Manish Pandey
Anil Kumar Gupta
Giuseppe Oliveto *Editors*

River, Sediment and Hydrological Extremes: Causes, Impacts and Management

Springer

Disaster Resilience and Green Growth

Series Editors

Anil Kumar Gupta, National Institute of Disaster Management, New Delhi, Delhi, India

SVRK Prabhakar, Climate Change Adaptation, Institute of Global Environment Strategies, Kanagawa, Japan

Akhilesh Surjan, College of Indigenous Futures, Arts and Society, Charles Darwin University, Darwin, Australia

Over the years, the relationship between environment and disasters has received significant attention. This is largely due to the emerging recognition that environmental changes-climate change, land-use and natural resource degradation make communities more vulnerable to disaster impacts. There is a need to break this nexus through environment based and sustainability inclusive interventions. Science – technology and economic measures for disaster risk management, hence, need to adapt more integrated approaches for infrastructure and social resilience. Environmental and anthropogenic factors are key contributors to hazard, risk, and vulnerability and, therefore, should be an important part of determining risk-management solutions.

Green growth approaches have been developed by emphasizing sustainability inclusion and utilizing the benefits of science-technology interventions along policy-practice linkages with circular economy and resource efficiency. Such approaches recognize the perils of traditional material-oriented economy growth models that tend to exploit natural resources, contribute to climate change, and exacerbate disaster vulnerabilities, Green growth integrated approaches are rapidly becoming as preferred investment avenue for mitigating climate change and disaster risks and for enhancing resilience. This includes ecosystem-based and nature-based solutions with potential to contribute to the resilience of infrastructure, urban, rural and peri-urban systems, livelihoods, water, and health. They can lead to food security and can further promote people-centric approaches.

Some of the synergistic outcomes of green growth approaches include disaster risk reduction, climate change mitigation and adaptation, resilient livelihoods, cities, businesses and industry. The disaster risk reduction and resilience outcome of green growth approaches deserve special attention, both for the academic and policy communities. Scholars and professionals across the domains of DRR, CCA, and green growth are in need of publications that fulfill their knowledge needs concerning the disaster resilience outcomes of green growth approaches. Keeping the above background in view, the book series offers comprehensive coverage combining the domains of environment, natural resources, engineering, management and policy studies for addressing disaster risk and resilience in the green growth context in an integrated and holistic manner. The book series covers a range of themes that highlight the synergistic outcomes of green growth approaches.

The book series aims to bring out the latest research, approaches, and perspectives for disaster risk reduction along with highlighting the outcomes of green growth approaches and including Science-technology-research-policy-practice interface, from both developed and developing parts of the world under one umbrella. The series aims to involve renowned experts and academicians as volume-editors and authors from all the regions of the world. It is curated and developed by authoritative institutions and experts to serve global readership on this theme.

Manish Pandey • Anil Kumar Gupta •
Giuseppe Oliveto
Editors

River, Sediment and Hydrological Extremes: Causes, Impacts and Management

Springer

Editors
Manish Pandey
Water Resources and Environmental
Division, Department of Civil Engineering
National Institute of Technology Warangal
Warangal, India

Anil Kumar Gupta
Centre for Excellence on Climate Resilience
Environment Climate and DRM Division
National Institute of Disaster Management
New Delhi, India

Giuseppe Oliveto
School of Engineering
University of Basilicata
Basilicata, Italy

Foreword

River, Sediment and Hydrological Extremes: Causes, Impacts and Management provides a comprehensive exploration of the intricate relationship between rivers, sediment dynamics, and hydrological extremes. This multidisciplinary work delves into the causes, impacts, and management strategies associated with these critical natural phenomena.

This book brings together leading experts from various disciplines to shed light on the complex interplay between rivers, sediment transport, and hydrological extremes. It covers a wide range of topics, including the role of climate change, land-use practices, and natural hazards in shaping hydrological patterns. The book also examines the impacts of hydrological extremes on ecosystems, infrastructure, and human communities, emphasizing the need for adaptive and resilient management approaches.

Moreover, *River, Sediment and Hydrological Extremes* delves into the intricate dynamics of sediment transport within river systems, exploring the linkages between sedimentation, erosion, and hydrological events. It highlights the significance of sediment as a valuable resource, while also addressing the challenges posed by excessive sedimentation, such as increased flood risk and reduced water quality.

One of the remarkable aspects of this work is its focus on management strategies. The authors present a range of approaches aimed at mitigating the impacts of hydrological extremes, managing sediment transport, and fostering sustainable river basin management. These strategies encompass both engineering solutions and ecosystem-based approaches, recognizing the need for integrated and adaptive management frameworks.

Overview of Book

The natural hazards posed by hydrologic events and river systems depend on the uncertainty of hydrological events. This ability is affected by change in climatic conditions. Climate change studies have revealed that the frequency of extreme weather phenomena with increasing damage to human assets has gradually grown worldwide. As a consequence, rainfall events concentrated in time and space are expected to lead to serious local flooding and sediment transport in many parts of the world. Floods are remarkable hydro-meteorological phenomena and forceful agents of geomorphic evolution in most physical geographical belts and, from the viewpoint of human society, among the most important environmental hazards. According to the Indian Environment Agency, floods rank as number one on the list of natural disasters in India over the past decade.

Floods and excess rainfall also change the patterns of erosion and deposition that are ultimately determined by base level, the lowest elevation to which the river can flow. Base level, in turn, is set by the interplay between tectonic deformation of the land surface and sediment supply—quantities that can vary in space and time. The above concept has serious implications for understanding the recent development of the major river systems. Large rivers with high sediment load flow south from the Himalayas into a series of narrow valleys that run parallel to the mountain front.

South Asia is one of the most risk-prone countries for river and sediment hazards. The geo-climatic variations of the region make the population vulnerable to flood and sediment and river-related disasters in varying degrees, intensities, and patterns. Sediment transport in rivers is one of the main causes of scouring and deposition and is always responsible for the failure of hydraulic structures and riverbank erosion. Therefore, precise estimation of erosion and scour is essential to reduce the hazards. Lack of preparedness and appropriate adaptation strategy makes people more risk-prone. The South Asia region needs to be concerned about the impacts of flood, sediments, and river hazards because a large portion of its population depends on sensitive sectors like agriculture and forestry for livelihoods and several other reasons. Because of this, the book *River, Sediment and Hydrological Extremes: Causes, Impacts and Management* will cover such aspects.

This book provides a platform for knowledge sharing in all areas related to rivers, sediment, and hydrological extremes. It will explain the hypothesis that river flow and sediment transport are intimately linked to erosion, scour, and sediment deposition. Sediment transport, erosion, and deposition are driven by local base-level changes and are highly variable in space and time.

This book is divided into three parts: (1) introduction and overview, (2) causes and impacts, and (3) river restoration, hydraulic structure stability, and flood risk management.

Under the Introduction and Overview part, Khundrakpam and Devi studied the Multi-Influencing Factor (MIF) (geospatial model), which is used for mapping and assessment of the flood-affected areas in the Iril River catchment of Manipur, India, for the period 2015–2021. The flood-affected area was observed to be highest in 2015, at 33.6 km^2 (1.13%), followed by 32.5 km^2 (1.09%) in 2017. Sudardeva and Pal studied the loss in Ecosystem Service Value (ESVs) under anthropogenic influences for Chennai and Hyderabad. They summarized the loss in ecosystem services that need urgent measures to enhance the sustainability of urban ecosystems through the restoration of waterbodies and effective land management practices. Bidyapati and Devi concluded that the vulnerability index of the Imphal East ranges from 130 to 173 (DRASTIC_AGRI) and 120 to 182 (DRASTIC_LU), indicating moderate to high vulnerability to groundwater contamination. Kiba et al. revealed that GIS can accurately predict the extent of flooding and produce flood maps, as well as flood damage estimation maps and flood hazard maps. Srikanth and Pal indicated that the spatiotemporal dynamics of meteorological variables could be used for long-term heatwave prediction, and both Support Vector Regression (SVR) and Random Forest (RF) models have the potential for reliable usage in this context. Kumari et al. suggested that Multi-Source Weather (MSWX) can be used in various climatic studies and hydrological modelling for areas or river basins where data are lacking or missing. Shukla focused on the behaviour of weakly nonlinear waves in mixed nonlinear fluids and further investigated the effect of van der Waals variables on wave evolution. Sharma and Swami presented a detailed study of the effects of measurement scale on temporal and spatial soil moisture analyses. The optimal measurement strategy for soil moisture measurement based on the optimal design for the study of spatiotemporal analysis will always be a trade-off between the accuracy and the cost of measurement. Patel and Sarkar concluded that the entropy-based approach could be utilized to determine the streamflow at any ungauged station on the Brahmani River, given the streamflow and stage at the upstream and downstream sites, respectively. Karna et al. observed that the deposition of fine sediments within the surface layer of bed material significantly impacts the aquatic life in the bed substrate. They utilized a numerical model to quantify the loss in the porosity of the surface layer bed material induced by this process.

In the second part, Goodarzi et al. studied river water flow prediction, which has been made by two GEP and Random Forest (RF) machine learning algorithms. The results of the two models were compared using five statistical indices. Hussain and Pal evaluated spatiotemporal variations in drought and assessed its risk over

Telangana using satellite data. The comparison of the Standardized Soil Moisture Index (SSMI) with SPI and SPEI shows that SSMI, when compared with the Standardized Precipitation Index (SPI) and Standardized Precipitation Evapotranspiration Index (SPEI), performs well in monitoring agricultural drought and can be used to develop effective drought warning and risk management. Okram and Devi studied drought-affected zones using satellite data and geographical information system (GIS) techniques in Thoubal district, Manipur (northeastern India), for the period 2013–2021. From the results, the study area was classified into five classes (severely dry, moderately dry, near normal, mildly wet, and moderately wet), and most of the study area experienced two drought conditions: moderate drought and near normal. Poonia et al. suggested that drought events across central and western parts of the country are severe and longer, whereas river basins in the southern part experience droughts more frequently but with low severity. The outcomes of this research offer crucial insights into drought hotspots with longer and more severe drought events across the study area and thus provide useful insights for policymakers to formulate comprehensive national drought mitigation and prevention strategies to safeguard a sustainable ecosystem. Barbhuiya et al. concluded that non-stationarity needs to be incorporated in the flood risk assessment framework for addressing the likely impacts of potential future climate change in water resources management. A comprehensive review of the different approaches for non-stationary flood frequency analysis is presented in this section. Gupta et al. quantified that the connection between extreme precipitation to moisture transport might help in the early prediction of extreme precipitation events over the Indian subcontinent. They evaluated the association between moisture transport and multi-day extreme precipitation events by quantifying moisture transport during the identified top-ranked multi-day extreme precipitation events. Deeksha et al. investigated that the emphasis of modern urban studies is changing from interpretation to information collection for effective decision-making, which will help readers grasp the issues associated with the existing system and the way forward to achieve sustainable development. This study will assist stakeholders and policymakers in taking necessary actions to preserve the present ecological equilibrium. Gajulapalli et al. studied sustainable land and water management in urban areas, along with emerging challenges. The active incorporation of new decentralized technologies, green infrastructure, and low-impact development to ensure the long-term reliability and resilience of our water resources must be prioritized. Ojha et al. investigated three-dimensional octant analysis used to clarify the function of bursting events in the particle entrainment process. The outcomes of this study provide an important and detailed view of turbulent flow structures in vegetation and non-vegetation zones in open channel flow. Barman et al. studied about recirculation region control behind a partially submerged cylinder due to wave against current. Moreover, the mean flow, fluctuating velocity, and velocity derivatives interact and exchange energy in a complex manner in the lock-on case.

Under river restoration, hydraulic structure stability, and flood risk management, Mishra and Tiwari obtained results that 4.106 mm^3 or 11.93% of storage volume had been lost from the usable storage volume of the Kaliasote reservoir. The rate of

sedimentation in the reservoir was also correlated with the empirical relationship of Varshney and Joglekar. Arjun et al. revealed better management of water resources in the Brahmaputra and Barak valleys in the Assam region needs detailed data and information about the river systems. However, the existing river database has a coarser resolution and lacks information, except for a few major rivers in Assam. Abhash et al. used Computational Fluid Dynamics (CFD) to simulate flow around a linear weir. The simulation results were compared with experimental results from the literature. The head-discharge relationship of the weir was also compared to the standard equations available in the literature. This study confirms the use of CFD as a tool for accurately predicting the flow patterns around hydraulic structures. Rathod et al. used an AI-based flood map generation tool for disseminating information and alerts to people in flood-prone areas. The system comprises several components, including hydrological and hydraulic models, AI-based flood map generation, and a mobile application for real-time alerts and geolocation-based messaging. This approach is scalable, cost-effective, and allows real-time monitoring for immediate responses to changing conditions, reducing the impact of floods and mitigating the risk of property damage and loss of life. Amin et al. studied extreme events that are part of the natural environment, creating diverse habitats through erosion and deposition processes. Human-induced climate change is predicted to increase average temperatures, leading to an increase in variables; therefore, a well-developed sustainable approach to managing risks is needed for the integrity of nature.

Contents

Part II   Causes and Impacts

**Part III   River Restoration, Hydraulic Structure Stability
             and Flood Risk Management**

Editors and Contributors

About the Editors

Manish Pandey graduated in Civil Engineering from Uttarakhand Technical University, India. He completed his master's and doctorate from Indian Institute of Technology Roorkee, India. Presently, Dr. Pandey is Assistant Professor at NIT Warangal since 2019. He has more than 5 years of teaching and research experience in experimental hydraulics and water resources engineering. He has authored more than 40 peer-reviewed journal papers and 20+ book chapters and conference proceeding papers. He has guided one PhD and five M.Tech students. Presently he is guiding four PhD and five M.Tech students. He was also awarded MOST postdoctoral research grant in 2018. He is an editorial board member of various national and international journals. Dr. Pandey is an active reviewer of several reputed peer-reviewed journals.

Anil Kumar Gupta is a sustainability risk management strategist working in the area of disaster management, environment, and climate resilience for more than 25 years with national, sub-national, and business administrations. He is currently a full Professor and Head of India's National Institute of Disaster Management (NIDM) Division of Environment and Disaster Risk Management. He is Programme Director of the Centre for Excellence on Climate Resilience and implementing projects, viz. CAP-RES (with DST, under National Knowledge Mission on Climate Change) and National Agriculture Disaster Management Plan (with Ministry of Agriculture & Farmer's Welfare). He was a recipient of Excellence Award by the Society of Environmental & Occupational Health, and bestowed with IDRC Canada's Think Tank Initiative Senior Fellowship 2011 for policy research.

Giuseppe Oliveto is Associate Professor of Hydraulic Engineering at the School of Engineering of University of Basilicata (Italy). Since 1992 he has been carrying out theoretical and experimental studies encompassing evolution and patterns of river networks, fluvial hydraulics, sediment transport, bridge hydraulics, and urban drainage hydraulics. He is the author of more than 100 papers in scientific journals and

conference proceedings. He is an editorial board member of various national and international journals. He was recognized as an outstanding reviewer by international journals. He has been awarded the Robert Alfred Carr Prize by the Council of the Institution of Civil Engineers (ICE), London (UK), for the paper "Temporal scour evolution at non-uniform bridge piers" published in the *Proceedings of the Institution of Civil Engineers - Water Management*, Volume 170, October 2017.

Contributors

Amiya Abhash Department of Civil Engineering, Indian Institute of Technology (BHU), Varanasi, Uttar Pradesh, India

Ankit Agarwal Department of Hydrology, Indian Institute of Technology Roorkee, Roorkee, Uttarakhand, India

S. P. Aggarwal North Eastern Space Applications Centre, Umiam, Meghalaya, India

Fatima Amin Environment, Climate and Disaster Risk Management (ECDRM) National Institute of Disaster Management, (NIDM) Ministry of Home Affairs, Govt. of India, New Delhi, India

Gokul Anand North Eastern Space Applications Centre, Umiam, Meghalaya, India

B. M. Arjun North Eastern Space Applications Centre, Umiam, Meghalaya, India

Biren Baishya Assam State Disaster Management Authority, Guwahati, Assam, India

Siddik Barbhuiya School of Infrastructure, Indian Institute of Technology, Bhubaneswar, Odisha, India

Diganta Barman North Eastern Space Applications Centre, Umiam, Meghalaya, India

Krishnendu Barman Department of Applied Mathematics with Oceanology and Computer Programming, Vidyasagar University, Midnapore, India

Anupal Baruah North Eastern Space Applications Centre, Umiam, Meghalaya, India

Ali Barzkar Department of Civil Engineering, Water Resources Management Engineering, Yazd University, Yazd, Iran

Haobam Bidyapati Department of Civil Engineering, National Institute of Technology, Imphal, Manipur, India

Shanti Swarup Biswal School of Infrastructure, Indian Institute of Technology, Bhubaneswar, Odisha, India

Ankit Chakravarti School of Civil and Environmental Engineering, Hachalu Hundessa Technology Campus, Ambo University, Ambo, Ethiopia

Susanta Chaudhuri Department of Geological Sciences, Jadavpur University, Kolkata, India

Sumanth Chinthala Department of Civil Engineering, NIT, Warangal, Telangana, India

Mushtaq Ahmad Dar Department of School Education J&K UT, Srinagar, Jammu and Kashmir, India

Koustuv Debnath Department of Aerospace Engineering and Applied Mechanics, Indian Institute of Engineering Science and Technology (IIEST), Shibpur, India

Deeksha Manipal School of Architecture and Planning, Manipal Academy of Higher Education, Manipal, Karnataka, India

Thiyam Tamphasana Devi Department of Civil Engineering, National Institute of Technology, Imphal, Manipur, India

Suryanarayana Gajulapalli Department of Civil Engineering, NIT, Warangal, Telangana, India

Mohammad Reza Goodarzi Department of Civil Engineering, Yazd University, Yazd, Iran

Manish Kumar Goyal Department of Civil Engineering, Indian Institute of Technology Indore, Indore, India

Sai Guguloth Department of Civil Engineering, National Institute of Technology Warangal, Warangal, India

Anil Kumar Gupta Centre for Excellence on Climate Resilience, Environment Climate and DRM Division, National Institute of Disaster Management, New Delhi, India

Hariom Gupta Department of Hydrology, Indian Institute of Technology Roorkee, Roorkee, Uttarakhand, India

Nitesh Gupta Department of Civil Engineering, Nirma University, Ahmedabad, India

P. Hussain Department of Civil Engineering, NIT, Warangal, Telangana, India

Nilav Karna AECOM, New Delhi, India

Sandhip Khundrakpam Department of Civil Engineering, National Institute of Technology, Manipur, India

Liza G. Kiba Department of Agricultural Engineering, SASRD, Nagaland University, Medziphema, India

Abhishek Kumar Department of Civil Engineering, National Institute of Technology, Rourkela, India

Pritam Kumar Department of Civil Engineering, National Institute of Technology, Rourkela, India

Alka Kumari Department of Hydrology, Indian Institute of Technology Roorkee, Roorkee, India

A. S. Lodhi Soil and Water Engineering Department, Jawaharlal Nehru Krishi Vishwa Vidhyalaya, Jabalpur, Madhya Pradesh, India

K. Mishra Department of Civil Engineering, Maulana Azad National Institute of Technology, Bhopal, India

Grace Nengzouzam Department of Agricultural Engineering, SET, Nagaland University, Dimapur, India

Amir Reza R. Niknam Department of Civil Engineering, Water Resources Management Engineering, Yazd University, Yazd, Iran

Nilay Nishant North Eastern Space Applications Centre, Umiam, Meghalaya, India

Aaditya Ojha Department of Civil Engineering, National Institute of Technology, Rourkela, India

Denish Okram Department of Civil Engineering, National Institute of Technology, Manipur, India

Padam Jee Omar FLoodkon Consultants LLP, Noida, India

Manali Pal Department of Civil Engineering, NIT, Warangal, Telangana, India

K. K. Pandey Department of Civil Engineering, Indian Institute of Technology (BHU), Varanasi, Uttar Pradesh, India

Manish Pandey NIT, Warangal, India

Pooja Patel School of Infrastructure, IIT Bhubaneswar, Argul, Khordha, Odisha, India

Sridhar Pilli Department of Civil Engineering, NIT, Warangal, Telangana, India

Vikas Poonia Department of Earth Sciences, Indiana University-Purdue University Indianapolis (IUPUI), Indianapolis, IN, USA

Akash Singh Raghuvanshi Department of Hydrology, Indian Institute of Technology Roorkee, Roorkee, Uttarakhand, India

Meenu Ramadas School of Infrastructure, Indian Institute of Technology, Bhubaneswar, Odisha, India

Nandineni Ramadevi Manipal School of Architecture and Planning, Manipal Academy of Higher Education, Manipal, Karnataka, India

Prem Ranjan Department of Agricultural Engineering, NERIST, Nirjuli, Arunachal Pradesh, India

Praveen Rathod Neram Civil Environmental Solution Pvt. Ltd., Mumbai, India

Sayahnya Roy Department of Aerospace Engineering and Applied Mechanics, Indian Institute of Engineering Science and Technology (IIEST), Shibpur, India

Arindam Sarkar School of Infrastructure, IIT Bhubaneswar, Argul, Khordha, Odisha, India

Anurag Sharma Department of Civil Engineering, National Institute of Technology, Rourkela, India

Sahil Sharma School of Engineering, Indian Institute of Technology, Mandi, India

Davood Shishebori Department of Industrial Engineering, Yazd University, Yazd, Iran

Anoop Kumar Shukla Manipal School of Architecture and Planning, Manipal Academy of Higher Education, Manipal, Karnataka, India

Satyavati Shukla Key Laboratory of Geospatial Informatics, Guilin University of Technology, Guilin, People's Republic of China

Triveni P. Shukla Department of Mathematics, National Institute of Technology, Warangal, Telangana, India

B. Srikanth Department of Civil Engineering, NIT, Warangal, Telangana, India

Sudardeva Department of Civil Engineering, NIT, Warangal, Telangana, India

Deepak Swami School of Engineering, Indian Institute of Technology, Mandi, India

H. L. Tiwari Department of Civil Engineering, Maulana Azad National Institute of Technology, Bhopal, India

Ravi Prakash Tripathi Department of Civil Engineering, Rajkiya Engineering College, Sonbhadra, Uttar Pradesh, India

Lixin Wang Department of Earth Sciences, Indiana University-Purdue University Indianapolis (IUPUI), Indianapolis, IN, USA

Part I
Introduction and Overview

Chapter 1
Flood Modeling Using MIF Method with GIS Techniques: A Case Study of Iril River Catchment, Manipur, India

Sandhip Khundrakpam and Thiyam Tamphasana Devi ⓘ

Abstract In the present study, a multi-influencing factor (MIF) (geospatial model) is used for mapping and assessment of the flood-affected areas in the Iril River catchment of Manipur, India, for the period of 2015–2021. The study region is in the plain valley part of the state, which is frequently prone to flooding due to its topographical landscape and rapid urbanization in recent years. In the MIF method, a major and minor influence is used to inter-relate the parameters and weight is calculated by using MIF score formula. Six parameters were used in MIF method, that is , slope, soil type, drainage density, rainfall, topographical wetness index (*TWI*), and *NDVI* (normalized vegetation index). Then each parameter is reclassified into five subclasses and ranking of 1–5 (low to high) is assigned to each subclass of the parameters. The predicted flood-affected areas were divided into four categories: very low, low, moderate, and high. The study region was found to be mostly affected by low to moderate flood (approximately 97%) in every year of the study period (2015–2021), which may not be a cause for concern. However, in terms of the magnitude of flood caused by the high category (as compared to the other flood classes), it was observed that the flood-affected area was highest in 2015, at 33.6 km^2 (1.13%), followed by 32.5 km^2 (1.09%) in 2017. And lower flood risk is thus observed in 2019 (0.74%) and 2021 (0.79%), respectively. Particularly, the predicted results for the year 2015 were compared and validated with literature and collected data, and a similar flood pattern was observed in this year.

Keywords GIS technique · MIF method · Weighted overlay · Iril catchment · GIS techniques

S. Khundrakpam · T. T. Devi (✉)
Department of Civil Engineering, National Institute of Technology, Manipur, India

1.1   Introduction

Rivers, sediment, and hydrological extremes are interlinked components of the Earth's natural systems that have significant impacts on the environment and human societies (Das and Umamahesh 2022). The causes of river sedimentation and hydrological extremes, such as floods (Saikumar et al. 2022) and droughts, are complex and can be influenced by various natural and human-induced factors, including climate change (Sinha et al. 2020; Das and Umamahesh 2018), land use changes, and water management practices. These processes can have significant impacts on river ecosystems, water quality, infrastructure, and human livelihoods. Understanding the drivers and impacts of river sedimentation and hydrological extremes is crucial for effective management strategies. Integrated approaches that consider the interactions between rivers, sediment, and hydrological extremes are essential for sustainable river basin management. This may involve measures such as river channel modifications, sediment trapping structures, floodplain zoning, and effective water resource management to mitigate the adverse impacts of these processes on the environment and society. Additionally, incorporating local knowledge, stakeholder engagement, and participatory approaches are critical for developing robust management plans that account for the diverse needs and perspectives of communities living in riverine areas.

Flooding is a primary natural disaster (Khan et al. 2011) and an event of hydrological extremes that has been occurring in all parts of the world. Excess water overflows the rivers and lakes to cause flooding, and several forms of sediment are transported along with the excess flow. Sediments deposited on the downstream side of the river is the major cause of disturbance in the ecosystem of water resource management (Jonkman and Dawson 2012; Kondolf et al. 2014). To solve most of the problems faced in management of hydrological extreme events such as flood or drought is the rightfully management of siltation and sediment deposition of river environment (Hauer et al. 2018). When a flood occurs, it not only takes the lives of humans and animals, but it also has long-term impacts on the ecosystem of living things. The infrastructure damage caused by the flood cannot be revived to its normal life expectancy, which again interrupts the various policies and programs planned by the government or other stakeholders and, therefore, significantly affects the overall economy of the region or state (Lechowska 2018).

Timely management and frequent monitoring with preventive measures for flooding are becoming crucial in areas where flood events are common (Behera and Devi 2022). With advanced technology, tools, and techniques along with the satellite imagery, flood events can be predicted or modeled (Munawar et al. 2022). And one of the techniques for flood modeling is using GIS tools with satellite data, and within this GIS platform (Sinha et al. 2008; Khan et al. 2011; Ajin et al. 2013; Ouma and Tateishi 2014; Hamdi et al. 2019; Hammami et al. 2019; Dash and Sar 2020), there are several multi-criteria decision-making methods (MCDM) such as AHP (analytic hierarchy process) (Danumah et al. 2016; Souissi et al. 2020; Senan et al. 2023) and MIF (multi-influencing factors) (Taheri et al. 2020; Singh et al.

2021; Singh and Devi 2022) which are commonly used for modeling of hydrological extreme events (flood and drought). The impacts of the multi-influencing factor (MIF) method on river, sediment, and hydrological extremes (Das and Umamahesh 2017; Bronstert et al. 2018; Jarajapu et al. 2022) are manifold. It helps in identifying the vulnerabilities of river and sediment systems to different factors and their interactions. It can also provide insights into the cascading effects of changes in one factor on other factors, allowing for more informed decision-making in river and sediment management. Additionally, the MIF method aids in identifying potential mitigation measures and interventions to reduce the negative impacts of human activities on rivers and sediment systems. MIF method enables a better understanding of the underlying causes of floods, such as changes in precipitation patterns due to climate change, alterations in land use and land cover, and modifications to river channels and floodplains. This understanding can help in identifying areas that are more vulnerable to floods and areas where flood risk may be increasing due to human activities. This information can inform flood mapping efforts (Mangukiya and Sharma 2022) and help in prioritizing resources for flood management.

Mitra et al. (2022) conducted an assessment on the performance of the GIS-based AHP method for flood modeling in the Dinajpur District of West Bengal. In their study, it was observed that 20% is categorized as high flood-risk and 27% as medium flood-risk zone in the district. They concluded that the limitations of MCDM can be improved using high-resolution satellite data, selecting suitable methods for a specific region, conducting sensitivity analysis, and applying machine learning techniques. Despite having such limitations, MCDM can be used successfully and reliably for flood modeling in any region. MIF method is mostly used for drought modeling (Pandey et al. 2021), groundwater modeling (Magesh et al. 2012; Anbarasu et al. 2020; Borah and Deka 2022), and very few in other areas such as suitability assessment for urban settlement (Singh et al. 2021). As the concept of MIF method is similar with other MCDM, there will be no exponential error in applying this method for flood modeling. Therefore, in the present study, an attempt is made to check the performance of MIF method in flood modeling. Thus, in this study, flood risk mapping and assessment (for the years 2015, 2017, 2019, and 2021) using the MIF method in a GIS environment is conducted in the Iril River catchment of Manipur (the north-eastern part of India).

1.2   Study Area

The study area (Iril catchment) is located in the districts of Senapati, Imphal east and west, and Ukhrul of Manipur state (northeastern part of India) shown in Fig. 1.1.

Geographical area lies between latitude 24°40′ N to 25°25′ N and longitude 93° 55′ E to 94°20′ E. The catchment area is estimated to be around 2985.5 km^2. The pour point to delineate the catchment area is taken at the Lamboikhul Tiger Camp (on the riverbed under the Eereima Suspension Bridge) having latitude 24°55′58.38″
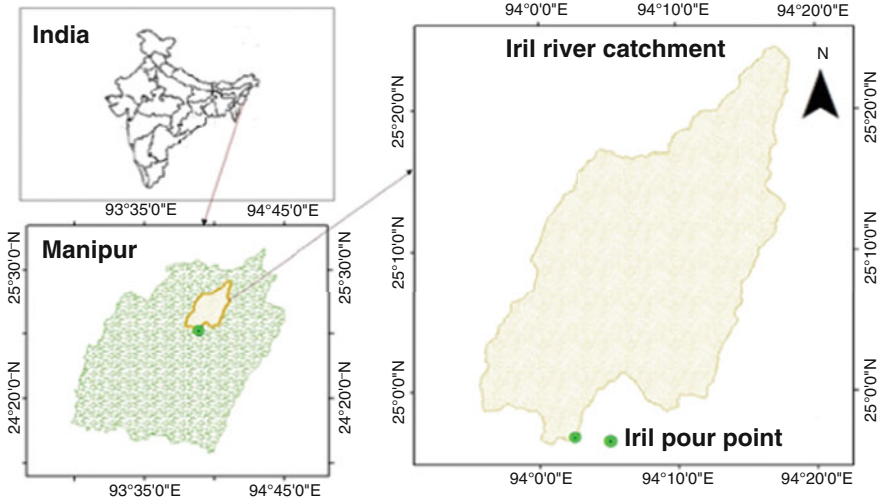
Fig. 1.1 Study area (Iril River catchment)

N and longitude 94°2′46.41″E which is marked in Fig. 1.1. As the study region is valley area of the state, the ecosystem of water resource management is affected by major rivers and its tributaries. In the state, there are 15 major rivers and streams (166.77 km^2 which is around 0.75% of the total geographical area).

The Barak river basin (Barak valley) to the west, the Manipur river basin in Central Manipur, the Yu river basin in the east, and a portion of the Liyai river basin in the north are the major river basins of the state, and urban drinking water supply is mostly (90%) from these rivers.

1.3   Data Used and Method

The collected data and its sources are provided in Table 1.1. The collected data are DEM (digital elevation model), Landsat 8/9 (2017, 2019, 2021) from USGS (US Geological Survey), Earth Explorer, rainfall (Directorate of Environment and Climate Change, Government of Manipur), and ESDAC (European Soil Data Centre). The Landsat 8/9 data were taken for the month of October of the studied period.

The data collected from different sources (Table 1.1) is utilized and processed through image processing for the required format using GIS tools (ArcGIS10.3®). In order to generate the secondary data from the primary data, IDW (inverse distance weighting) algorithm is used which is within the GIS platform. Then, the generated parameters, that is, rainfall, slope, soil type, drainage density, TWI (topographic wetness index), and NDVI (normalized difference vegetation index) are converted to

Table 1.1 Data used with its source

Sl. No.	Data	Source	Resolution	Extracted data
1.	DEM	USGS, Earth Explorer	Spatial (30 m)	Slope, drainage density
2.	NDVI	USGS, Earth Explorer Landsat 8/9	Temporal (2015, 2017, 2019, 2021)	NDVI
3.	Rainfall	Directorate of Environment and Climate Change	Temporal (2015, 2017, 2019, 2021)	Rainfall
4.	TWI	USGS, Earth Explorer	Spatial (30 m)	TWI
5	Soil type	ESDAC (European Soil Data Centre)	Spatial (30 m)	Soil type of study Iril catchment
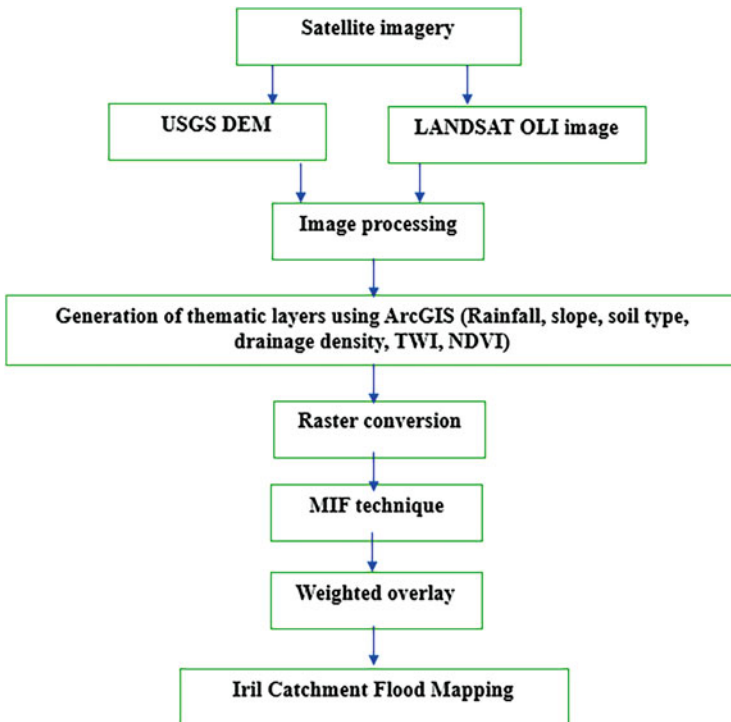
Fig. 1.2 Flowchart of methodology

raster format and the MIF score is calculated and overlaid by giving their respective weights to generate the flood risk map (for the years 2015, 2017, 2019, and 2021). The flowchart of methodology is provided in Fig. 1.2.

1.4 MIF Method

Prediction and mapping of flood-affected zones in the study region using MIF method includes collection of required data from different sources, generation of database (selection of input parameters), and finally developing flood risk map. MIF method is used by computing the interrelationship between the influencing factors which are categorized by two factors, that is, major (B) and minor (A) influence, and MIF score or weight is calculated by using Eq. 1.1. Influential factors are considered to assign the weight to each parameter. Figure 1.3 shows the interrelationship between these effects and their factor.

Major effect represents direct influence of one factor over another, and minor effect represents indirect influence. The major and minor effects are classified based on their holding capacity and the characteristics of the surface and subsurface features. The major factor is assigned a value of 1 and minor factor is assigned as 0.5. These values are combined to calculate the MIF score of each layer (parameters) using the following equation:

$$\text{MIF score} = \frac{(A+B)}{\sum(A+B)} \times 100 \tag{1.1}$$

1.5 MIF Weights

The major purpose of MIF method is to give the weightage to the given parameters which is affecting to cause flood. The effectiveness of the quality of prioritization has a direct impact on the available resources. In most situations, the decision-maker's primary judgment is used. In this study, experts' and decision-makers' "technical skills and know how" to solve the problems are considered. Several field surveys

Fig. 1.3 Interrelationship of parameters by MIF method
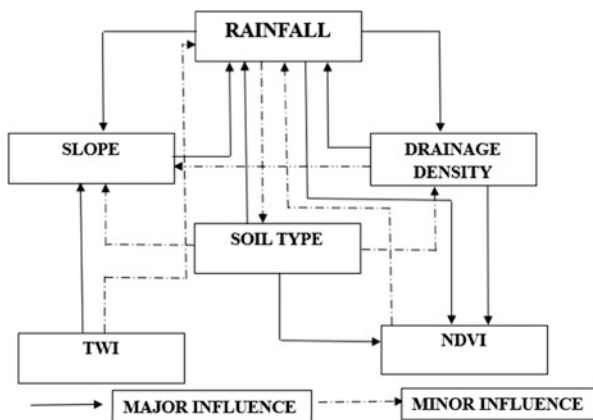
Table 1.2 Effect of different influencing factors and their corresponding scores

Factor	Minor effect (A)	Major effect (B)	(A + B)	Weight
NDVI	0.5	0	0.5	4
Slope	0	1	1	8
TWI	0.5	1	1.5	12
Drainage density	0.5	1 + 1	2.5	21
Soil type	0.5 + 0.5	1 + 1	3	25
Rainfall	0.5	1 + 1 + 1	3.5	30
			$\sum = 12$	$\sum = 100$

were conducted in and around the study area interacting with the people of local communities. With the understanding resulted from the community interaction and consultation with them, the weights are assigned to the selected input parameters on the scale of 1–5 (very low to very high class).

Table 1.2 shows the effect caused by different influencing factors (minor effect, A, and major effect, B), and the weight is calculated by using Eq. 1.1. The calculated weights are provided in Table 1.3 and each parameter is reclassified into five classes. Using the assigned ranks and weights, these thematic layers (input parameters) are overlaid by using weighted overlay method, and finally a flood risk map (flood-affected area) is generated for the years 2015, 2017, 2019, and 2021.

1.6 Input Parameters: Theoretical Background

Six input parameters are considered for the flood modeling in this study, and the theoretical concept of each parameter is provided in the following section.

1.6.1 Slope

The slope of a terrain is a critical aspect in determination of its dependability and is a measure of its steepness of any plane. The direction and quantity of surface runoff or subsurface drainage which reaches an area are determined by the slope. The contribution of rainfall to stream flow is dominated by slope. It regulates the length of overland flow, infiltration, and subterranean flows which are all examples of flow. Slope is presented in percentage and calculated as "rise" divided by "run" multiplied by 100. Slope is also generally expressed in degrees.

Table 1.3 Assigned MIF rankings and weights for flood mapping

Criteria	Units	Year 2015	2017	2019	2021	Ranges	Class rating	Weight (%)
NDVI	Level	−1–0	−1–0	−1–0	−1–0	Very high	5	4
Slope	%	0–6	0–6	0–6	0–6	Very high	5	8
		6–16	6–16	6–16	6–16	High	4	
		16.01–40	16.01–40	16.01–40	16.01–40	Moderate	3	
		40.01–60	40.01–60	40.01–60	40.01–60	Low	2	
		60.1–183.8	60.1–183.8	60.1–183.8	60.1–183.8	Very low	1	
TWI	Level	−0.58–5	−0.58–5	−0.58–5	−0.58–5	Very high	1	12
		5.1–9	5.1–9	5.1–9	5.1–9	High	2	
		9.1–11	9.1–11	9.1–11	9.1–11	Moderate	3	
		12–19	12–19	12–19	12–19	Low	4	
		20–21	20–21	20–21	20–21	Very low	5	
Drainage density	km/km^2	0–2	0–2	0–2	0–2	Very low	1	21
		2.1–4	2.1–4	2.1–4	2.1–4	Low	2	
		4.1–4.5	4.1–4.5	4.1–4.5	4.1–4.5	Moderate	3	
Soil type	Level	Clay Loam	Clay Loam	Clay Loam	Clay Loam	Moderate	3	25
Rainfall	mm	59.87–402.7	83.3–600	761–914	1040–1100	Very low	1	30
		402.8–642.7	601–1000	915–1010	1100–1140	Low	2	
		642.8–833.7	1000–1400	1020–1090	1150–1180	Moderate	3	
		833.8–1030	1410–1700	1100–1160	1190–1210	High	4	
		1031–1309	1710–2230	1170–1240	1220–1250	Very high	5	

1.6.2 Drainage Density

The physical characteristics of a catchment area are described through drainage density. Thus, the potential of water carried over by the landscape is related to drainage density and is an important parameter for understanding the ecosystem of water resource management in that region. If the density is high, the catchment region will be more prone to degradation, ending in deposition on the deeper grounds. It is calculated as stream length divided by basin area and its unit is km/km^2.

1.6.3 Soil Type

Soil texture is an essential component and property of soils. Based on soil texture, soil types are classified primarily as sand, silt, and clay. Clay soils are far less transparent and hold water for a greater amount of time than sandy soils. It demonstrates that the locations with clay soils are more prone to flood. When measurements are unavailable, the feel and appearance of the soil can be used to infer soil moisture. Soil moisture serves as the boundary between the land surface and atmosphere, and it is important in the division of rainfall into runoff and water storage in groundwater.

1.6.4 TWI

Topographic wetness index (*TWI*) is commonly used to quantify topographic control on hydrological processes. *TWI* (Nsangou et al. 2022) indicates the amount of water that is accumulated on a specific area and expressed as index. Its high value gives high potential and low value gives low potential of water accumulation. It ranges from −3 to 30 and it is calculated as

$$\text{TWI} = \ln \frac{U_{as}}{\tan \beta} \qquad (1.2)$$

where U_{as} is the area contributing to its upstream side and β is slope gradient.

1.6.5 Rainfall Distribution

Heavy rains, which prohibit natural watercourses from channeling surplus water, are the most prevalent primary cause of flood. The amount of runoff generated by a catchment is related to the amount of rain received in that catchment. Heavy rains

raise the level of water in rivers and lakes abruptly. When the water level exceeds the riverbanks or dams, the water begins to overflow, resulting in river-based flood. Volume of flood is contributed by the overflows from all the water bodies during heavy and continuous rainfall.

1.6.6 NDVI

The *NDVI* index analyzes and assesses the presence of live greenery using reflected light in the visible (*VIS*) and near-infrared wavelengths (*NIR*). Simply, *NDVI* is a gauge of the greenness of vegetation, as well as its richness and health. Thus, *NDVI* is calculated as

$$\text{NDVI} = \frac{(\text{NIR} - \text{VIS})}{(\text{NIR} + \text{VIS})} \tag{1.3}$$

1.7 Result and Discussion

In this section, the generated input parameters with the finally modeled flood risk map will be presented and accordingly will discuss the result.

1.7.1 Result

1.7.1.1 Generated Input Parameters

Generated slope (%, which is "rise" divided by "run" multiplied by 100) and drainage density (km/km^2) map is provided in Fig. 1.4.

Drainage density is high for the major streams (Iril river) and nearby to the river and its tributaries. Soil type (Fig.1.5a) was generated using ESDAC (European Soil Data Centre) data and classified as clay loamy soil, and *TWI* is shown in Fig.1.5b. It is observed that the entire study region is covered by clay loam soil, which has the combined properties of low drainage capacity, moderate fertility, and good water-holding potential.

By IDW method, the rainfall ranges of the given study area are derived and provided in Fig. 1.6 for the years 2015, 2017, 2019, and 2021, respectively. High rainfall is concentrated mostly in northern part of the study region in all the studied years. Highest rainfall goes up to around 2230 mm in a year which is observed in the year 2017 followed by 1309 mm in the year 2015. Medium rainfall is observed in 2019 and 2021; and lowest is observed in the year 2015 (60 mm per year) followed
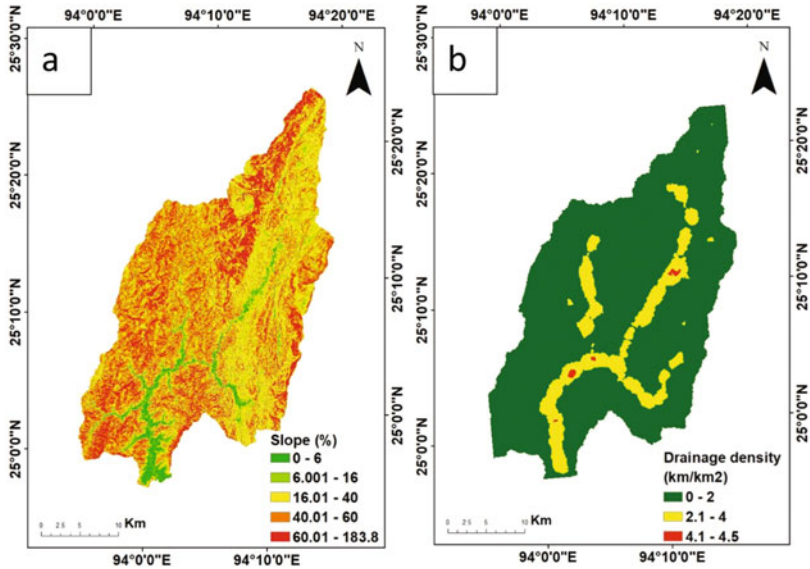
Fig. 1.4 (**a**) Slope and (**b**) drainage density
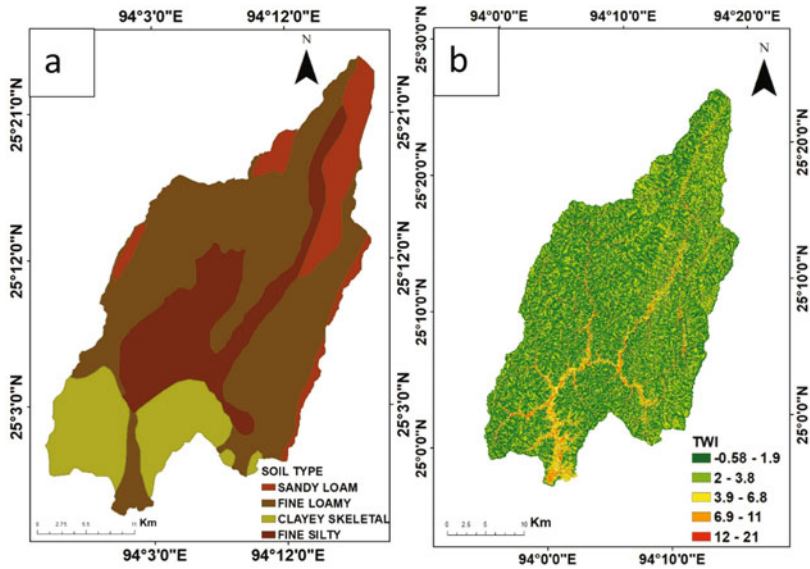
Fig. 1.5 (**a**) Soil type and (**b**) *TWI*

by in the year 2017 which is around 83 mm. So there is a large uneven distribution of rainfall in these years which suggest uncertain climatic conditions. However, in the years 2019 and 2021, the minimum rainfall observed is around 761 mm–1040 mm
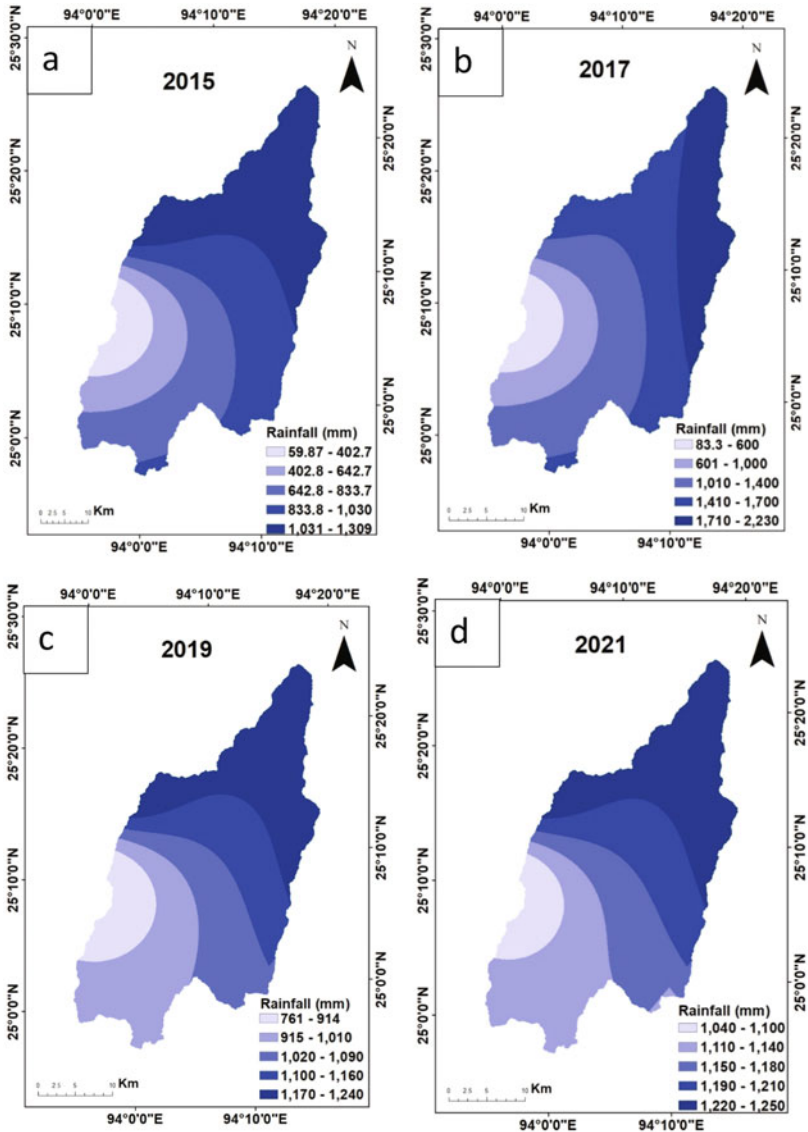
Fig. 1.6 Rainfall for the years (**a**) 2015, (**b**) 2017, (**c**) 2019, and (**d**) 2021

and maximum is 1240 mm–1250 mm, respectively, which indicates moderate climate conditions as per web report of the Indian Meteorological Department (IMD 2022).

Then, the *NDVI* (range of −1–0) of these years have been calculated and found that it has less vegetation at the month of October (Fig. 1.7) which is the month of every year taken (temporal scale) in this study.
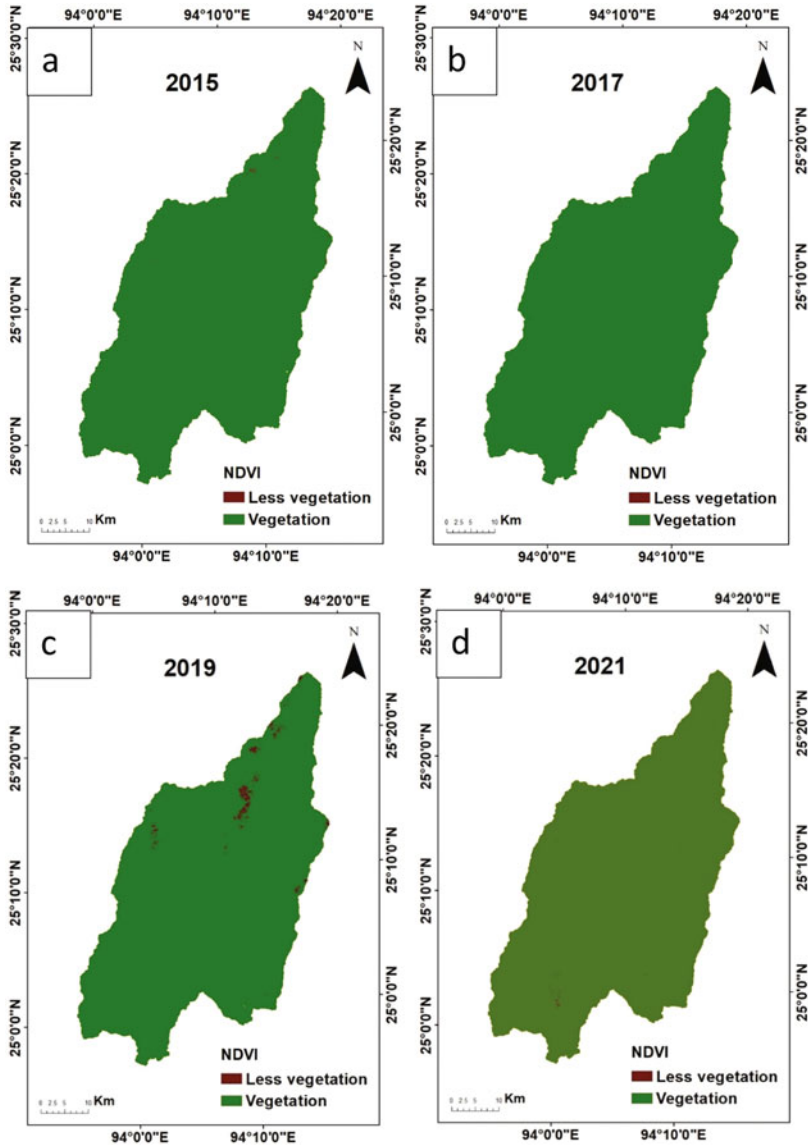
Fig. 1.7 NDVI for the years (**a**) 2015, (**b**) 2017, (**c**) 2019, and (**d**) 2021

1.7.1.2 Prediction of Flood

The predicted flood risk map for the years 2015, 2017, 2019, and 2021 is shown in Fig.1.8a–d. Flood-affected zone is classified as very low, low, moderate, and high.
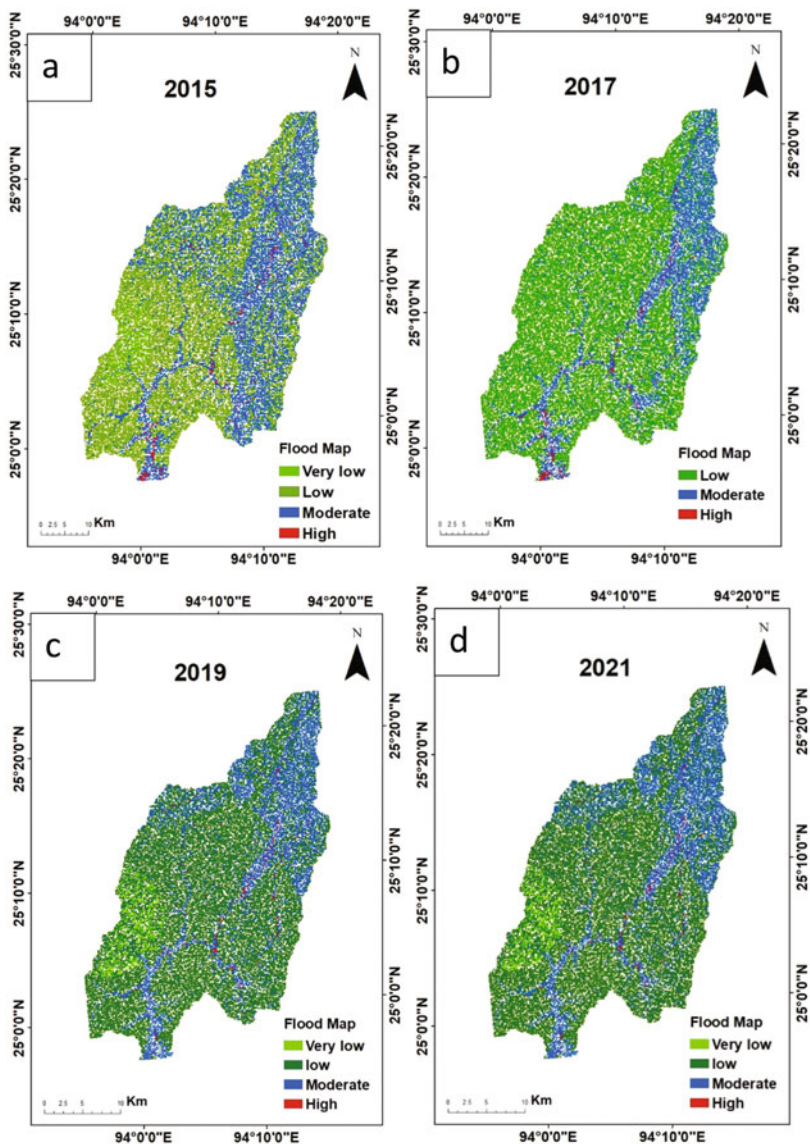
Fig. 1.8 Flood risk map for the years (**a**) 2015, (**b**) 2017, (**c**) 2019, and (**d**) 2021

Table 1.4 shows the predicted flood area in km^2 and percentage (%) for the years 2015, 2017, 2019, and 2021. Northwest side of the study region are more prone to flood as compared to southeast side.

From Fig.1.8, in all the years (2015, 2017, 2019, and 2021), it is affected by low to moderate flood and very small areas by high flood. Figure 1.9 shows the area of

Table 1.4 Predicted flood-affected area

| Flood class | Flood-affected area | | | | | | | |
| | (km^2) | | | | (%) | | | |
	2015	2017	2019	2021	2015	2017	2019	2021
Very low	39.2	49.00	72.00	58.30	1.32	1.64	2.41	1.95
Low	1941.9	1900.3	1973.2	1957.9	65.04	63.66	66.09	65.58
Moderate	970	1003.7	918.3	945.7	32.49	33.62	30.76	31.68
High	33.6	32.5	22	23.6	1.15	1.08	0.74	0.79
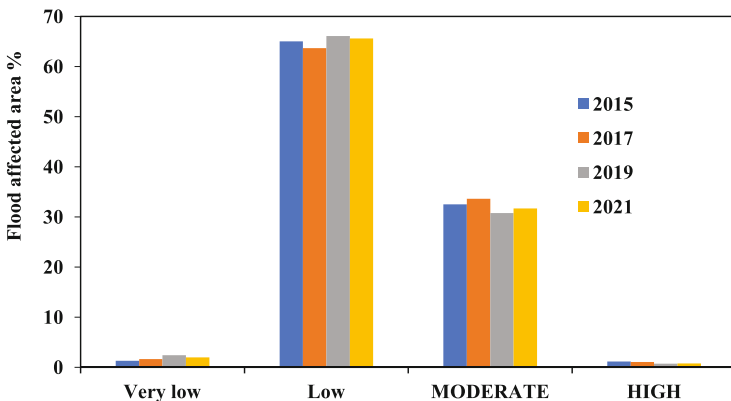
Fig. 1.9 Predicted flood affected area (%)

predicted flood in percentage (%). But the high category flood is the most significant to cause damage to agricultural activities as well as to properties. Thus, it is effective to study further, selecting only the flood-affected areas classified as high risk in the present study. Therefore, the flood-affected area in 2015 is observed to be the highest, at 33.6 km^2 (1.15%), followed by the year 2017 at 32.5 km^2 (1.28%) in the category of high flood as compared with other years, which is shown in Fig. 1.9.

1.8   Discussion

By considering multiple influencing factors such as *NDVI*, *TWI*, rainfall, slope, drainage density, and soil type, we can create a more comprehensive flood mapping model that takes into account various hydrological, topographic, and environmental factors that affect flood dynamics. Integrating these factors into a combined approach can provide a more accurate and holistic understanding of flood-prone areas, which can be valuable for flood risk assessment, preparedness, and management. It was found out that flood is affected mostly by rainfall with MIF score of 30 which gives more weightage to it and NDVI is less affected with a score of 4.

Moreover, the study region is in the valley plain part of the state where its terrain is 90% hilly. Soil erosion or soil loss from the sloppy hills is a frequent phenomenon during rainy seasons, and these sediment particles flow down to the plain valley through streams, rivers, and its tributaries as river discharge. High-intensity rainfall causes heavy landslide as most of the soil types in the state is alluvial soil (a type of loose soil) and can be easily disturbed by a slight continuous rainfall. Thus, sediments come along with the river discharge deposited in the low-lying areas, and therefore, the space occupied by the excess river water becomes smaller and then flood occurred. Such phenomenon create disturbance to the ecosystem of water resource management. There are several factors for soil erosion such as deforestation, human encroachment, climate change, and development activities. It is impossible to mitigate all these factors affecting to soil erosion, but it is always possible to minimize or slow down the process of soil erosion which includes monitoring the cutting down of trees and agricultural practices in hilly areas and application of strict laws for conservation of forest area while taking place of any developmental activities (road development, infrastructure planning, etc.). If these provisions are in place, flood occurrence can be minimized effectively.

1.9 Validation

The predicted (present study), simulated result (literature) and ground data (IFCD) were compared for the respected years (2015, 2017, 2019, and 2021). For the year 2015, the predicted area inundated by flood water is 39.4km^2 with the simulated discharge of 2452.87 m^3/s which is very high compared with the other years in both the cases (predicted and simulated). The collected ground data is also highest (2414.15 m^3/s) in the year 2015 as compared with other years. Thus, this very high flood classification for the year 2015 is compared with the simulated SWAT model (Behera and Devi 2022) result and ground data, and it has been found out that they match the same result (high flood class) (Table 1.5).

1.10 Conclusion

The predicted flood affected is highest in the year 2015 followed by 2017, 2021, and 2019. Thus, it is concluded that throughout the year, this study region is affected by low to high flood intensity. Indeed MIF method can be effectively used for flood modeling apart from the common application in drought modeling. Therefore, further wide application of MIF method in flood modeling is encouraged so that its effectiveness could be improved. As the study region is in the valley plain part of the state which is frequently subjected to flooding, and as evidenced in recent years of flood events in the region, it is suggested that the agricultural activities as well as other infrastructural services should be well planned and monitored.

Table 1.5 Flood class based on predicted, simulated, and observed data

Year	Present study (high flood, km^2)	Predicted discharge (SWAT model)[a] (m^3/s)	Observed discharge (IFCD)[b] (m^3/s)	Validation remarks		
				Present study (MIF model)	SWAT model[a]	Ground data[b]
2013	–	907.981	922.863	–	No flood	No flood
2014	–	929.45	914.9501	–	No flood	No flood
2015	33.6	2452.87	2414.15	**Very high flood**	**Very high flood**	**Very high flood**
2017	32.5	–	–	High flood	–	–
2019	22	–	–	High flood	–	–
2021	23.6	–	–	High flood	–	–

[a] Predicted discharge (swat model), result taken from Behera and Devi (2022)
[b] Observed discharge (IFCD) or ground data, result collected from Irrigation and Flood Control Department (IFCD), Government of Manipur

1.11 Future Scope

As GIS technology continues to advance and become more accessible, and with increasing concerns about climate change and flood hazards, the MIF method can provide valuable insights for flood mapping and mitigation efforts. The MIF method allows for the integration of multiple influencing factors, such as elevation, slope, land use, rainfall, and proximity to rivers or coastlines, which can result in more accurate flood mapping compared to single-factor methods. With the availability of high-resolution data and improved algorithms, the accuracy of flood mapping using the MIF method is expected to increase, aiding in better flood prediction and planning. As climate change continues to affect weather patterns and precipitation levels, flood risks are projected to increase in many regions. The MIF method can be used to assess the vulnerability of different areas to flooding under changing climate conditions. By incorporating climate change scenarios into the MIF method, it can help in identifying areas that may be more prone to flooding in the future, facilitating proactive measures for climate change adaptation and resilience planning. Therefore, the scope of the application of the MIF method can be achieved with one of the following objectives in future studies for flood modeling and assessment:

1. Integrated Decision Support System: The MIF method can be integrated into decision support systems that provide real-time flood monitoring and early warning systems. By combining MIF-based flood mapping with real-time data on precipitation, river levels, and weather forecasts, decision-makers can have access to up-to-date information for flood response and emergency management. This can enable more effective and timely decision-making in flood-prone areas.

2. Urban Planning and Infrastructure Development: Urban areas are often at higher risk of flooding due to impervious surfaces and inadequate drainage systems. The MIF method can be used in urban planning and infrastructure development to identify flood-prone areas and guide the location of critical infrastructure such as roads, buildings, and utilities. This can help reduce the exposure and vulnerability of urban areas to floods and support sustainable urban development.

3. Community Engagement: The MIF method can involve local communities in flood mapping efforts, allowing them to contribute their knowledge and experience of local flood hazards. Community engagement can enhance the accuracy and relevance of flood mapping results and also raise awareness and understanding of flood risks among local residents. This can promote community resilience and preparedness and facilitate participatory decision-making in flood risk management.

4. Insurance and Risk Assessment: Flood mapping using the MIF method can support insurance companies and risk assessment agencies in determining flood risk zones and calculating insurance premiums. Accurate flood mapping can help in estimating potential losses due to floods, assisting in risk management, and underwriting decisions. Insurance companies can also use flood mapping results to promote risk reduction measures among policyholders, leading to more resilient communities.

References

Ajin RS, Krishnamurthy RR, Jayaprakash M, Vinod PG (2013) Flood hazard assessment of Vamanapuram river basin, Kerala, India: An approach using remote sensing & GIS techniques. Adv Appl Sci Res 4(3):263–274

Anbarasu S, Brindha K, Elango L (2020) Multi-influencing factor method for delineation of groundwater potential zones using remote sensing and GIS techniques in the western part of Perambalur district, southern India. Earth Sci Inf 13:317–332. https://doi.org/10.1007/s12145-019-00426-8

Behera PK, Devi TT (2022) Study on Impact of Urbanization by SWAT Model in Iril River, Northeast India. In: Jha R, Singh VP, Singh V, Roy LB, Thendiyath R (eds) Hydrological modeling, Water science and technology library, vol 109. Springer, Cham. https://doi.org/10.1007/978-3-030-81358-1_29

Borah H, Deka S (2022) Exploration of potential zones of groundwater in Jamuna Watershed, Assam, by applying multi-influencing factor technique. J Indian Soc Remote Sens 51:75–91

Bronstert A, Agarwal A, Boessenkool B, Crisologo I, Fischer M, Heistermann M, Köhn-Reich L, López-Tarazón JA, Moran T, Ozturk U, Reinhardt-Imjela C (2018) Forensic hydro-meteorological analysis of an extreme flash flood: The 2016-05-29 event in Braunsbach, SW Germany. Sci Total Environ 630:977–991

Danumah JH, Odai SN, Saley BM, Szarzynski J, Thiel M, Kwaku A, Kouame FK, Akpa LY (2016) Flood risk assessment and mapping in Abidjan district using multi-criteria analysis (AHP) model and geoinformation techniques, (cote d'ivoire). Geoenvironmental Disasters 3(1) https://doi.org/10.1186/s40677-016-0044-y

Das J, Umamahesh NV (2017) Uncertainty and nonstationarity in streamflow extremes under climate change scenarios over a river basin. J Hydrol Eng 22(10):04017042

Das J, Umamahesh NV (2018) Assessment of uncertainty in estimating future flood return levels under climate change. Nat Hazards 93:109–124

Das J, Umamahesh NV (2022) Investigating risk, reliability and return period under the influence of large scale modes, and regional hydrological variability in hydrologic extremes. Hydrol Sci J 67(1):65–81

Dash P, Sar J (2020) Identification and validation of potential flood hazard areas using GIS-based multi-criteria analysis and satellite data-derived water index. J Flood Risk Manag 13(3):1–14

Hamdi SA, Ahmad SA, Saleh GJIA (2019). Analysis of basin geometry in Ataq Region, Part of Shabwah Yemen: using remote sensing and geographic information system techniques. Bull Pure and Appl Sci. 38 F (Geology), No.1, 2019: P.1–15, 2019

Hammami S, Dlala M, Zouhri L, Souissi D, Souei A, Zghibi A, Marzougui A (2019) Application of the GIS based multi-criteria decision analysis and analytical hierarchy process (AHP) in the flood susceptibility mapping (Tunisia). Arab J Geosci 12:1–16

Hauer C, Leitner P, Unfer G, Pulg U, Habersack H, Graf W (2018) The role of sediment and sediment dynamics in the aquatic environment. In: Riverine ecosystem management. Springer, Cham. https://doi.org/10.1007/978-3-319-73250-3_8

IMD (2022) Statewise rainfall information, a web report. Indian Meteorological Department

Jarajapu DC, Rathinasamy M, Agarwal A, Bronstert A (2022) Design flood estimation using extreme Gradient Boosting-based on Bayesian optimization. J Hydrol 613:128341

Jonkman SN, Dawson RJ (2012) Issues and challenges in flood risk management—editorial for the special issue on flood risk management. Water 2012(4):785–792

Khan SI, Hong Y, Wang J, Yilmaz KK, Gourley JJ, Adler RF, Brakenridge GR, Policelli F, Habib S, Irwin D (2011) Satellite remote sensing and hydrologic modeling for flood inundation mapping in lake Victoria basin: implications for hydrologic prediction in ungauged basins. IEEE Trans Geosci Remote Sens 49:85–95

Kondolf GM, Gao Y, Annandale GW, Morris GL, Jiang E, Zhang J, Cao Y, Carling P, Fu K, Guo Q, Hotchkiss R, Peteuil C, Sumi T, Wang HW, Wang Z, Wei Z, Wu B, Wu C, Yang CT (2014) Sustainable sediment management in reservoirs and regulated rivers: experiences from five continents. Erath's Future 2(5):256–280. https://doi.org/10.1002/2013EF000184

Lechowska E (2018) What determines flood risk perception? A review of factors of flood risk perception and relations between its basic elements. Nat Hazards 94:1341–1366. https://doi.org/10.1007/s11069-018-3480-z

Magesh NS, Chandrasekar N, Soundranagam JP (2012) Delineation of groundwater potential zones in Theni district, Tamil Nadu, using remote sensing, GIS and MIF techniques. Geosci Front 3(2):189–196

Mangukiya NK, Sharma A (2022) Flood risk mapping for the lower Narmada basin in India: a machine learning and IoT-based framework. Nat Hazards 113(2):1285–1304

Mitra R, Saha P, Das J (2022) Assessment of the performance of GIS-based analytical hierarchical process (AHP) approach for flood modelling in Uttar Dinajpur district of West Bengal, India. Geomat Nat Haz Risk 13(1):2183–2226. https://doi.org/10.1080/19475705.2022.2112094

Munawar HS, Hammad AWA, Waller ST (2022) Remote sensing methods for flood prediction: a review. Sensors (Basel) 22(3):960

Nsangou D, Amidou K, Zakari M, Ngoupayou JRN (2022) The Mfoundi watershed at yaoundé in the humid tropical zone of Cameroon: a case study of urban flood susceptibility mapping. Earth Systems and Environment 6(2):99–120. https://doi.org/10.1007/s41748-021-00276-9

Ouma OY, Tateishi R (2014) Urban flood vulnerability and risk mapping using integrated multi-parametric AHP and GIS: methodological overview and case study assessment. Water 6(6):1515–1545

Pandey P, Tiwari SK, Pandey HK, Chaurasia AK, Singh S (2021) Identification of potential recharge zones in drought prone area of bundelkhand region, India, Using SCS-CN and MIF technique under GIS-frame work. Water Conserv Sci Eng 6:105–125

Saikumar G, Pandey M, Dikshit PKS (2022) Natural river hazards: their impacts and mitigation techniques. In: River dynamics and flood hazards: studies on risk and mitigation. Springer, Singapore, pp 3–16

Senan CPC, Ajin RS, Danumah JH, Costache R, Arabameri A, Rajaneesh A, Sajinkumar KS, Kuriakose SL (2023) Flood vulnerability of a few areas in the foothills of the Western Ghats: a comparison of AHP and F-AHP models. Stoch Env Res Risk A 37(2):527–556. https://doi.org/10.1007/s00477-022-02267-2

Singh, NM, Devi TT (2022) Assessment and Identification of drought prone zone in a Low Laying Area by AHP and MIF method: A GIS based study, IOP Conference Series: Earth and Environmental Science, 1084 012047. https://doi.org/10.1088/1755-1315/1084/1/012047

Singh L, Saravanan S, Jennifer JJ, Abijith D (2021) Application of multi-influence factor (MIF) technique for the identification of suitable sites for urban settlement in Tiruchirappalli City, Tamil Nadu, India. Asia-Pac J Reg Sci 5(3):797–823. https://doi.org/10.1007/s41685-021-00194-8

Sinha R, Bapalu GVS, L.K. and Rath, B. (2008) Flood risk analysis in the Kosi River basin, north Bihar using the multi-parametric approach of analytical hierarchy process (AHP). J Indian Soc Remote Sens 36(4):335–349

Sinha J, Das J, Jha S, Goyal MK (2020) Analysing model disparity in diagnosing the climatic and human stresses on runoff variability over India. J Hydrol 581:124407

Souissi D, Zouhri L, Hammami S, Msaddek MH, Zghibi A, Dlala M (2020) GIS-based MCDM–AHP modeling for flood susceptibility mapping of arid areas, southeastern Tunisia. Geocarto Int 35(9):991–1017. https://doi.org/10.1080/10106049.2019.1566405

Taheri K, Missimer TM, Taheri M, Moayedi H, Mohseni PF (2020) Critical zone assessments of an alluvial aquifer system using the multi-influencing factor (MIF) and analytical hierarchy process (AHP) models in western Iran. Nat Resour Res 29(2):1163–1191. https://doi.org/10.1007/s11053-019-09516-2

Chapter 2
A Case Study on Estimating the Ecosystem Service Values (ESVs) Under Anthropogenic Influences for Chennai and Hyderabad

Sudardeva and Manali Pal

Abstract Ecosystem services are inevitable to all biota on the earth and possess a value of approximately 125 trillion USD. Although the complete valuation of ecosystem services in monetary terms is uncertain, they are sine qua non to frame policies regarding the utilization of resources in a sustainable way. Moreover, the continuous urban growth imparts variations to the urban ecological land use and land cover (LULC) and urban ecosystem functions that possess serious challenges. However, studies on quantifying ecosystem services and assessing them under anthropogenic influence are scarce, especially for the metropolitans in India. In this scenario, we selected Chennai metropolitan area (CMA) and the Greater Hyderabad Municipal Corporation (GHMC), two rapidly urbanizing metropolitan areas with increasing anthropogenic activities observed since last decade, for quantifying the ecosystem service value (ESV). The study applied the approach proposed by Costanza R et al. (Nature, 1997;387:253–260) that uses the spatiotemporal variations of LULC to compute the ESV. The LANDSAT data products are used to generate LULC for the CMA and GHMC for each decade since 1995–2022 (to mark the economic transition for the country), for example, for the years 1995, 2005, 2015 and 2022. The study reveals the drastic changes in the area of individual classes. Vegetation has shrunken noticeably between 1995 and 2022, followed by waterbodies for both the areas. Due to urbanization, the builtup is found to be increased in an unregulated way that reduces ESV. The substantial loss in ESV questions the resilience of the study areas, and this trend continues till the end of the observation period. The findings summarize the loss in ecosystem services that need urgent measures to be taken to enhance the urban ecosystem sustainability through the restoration of waterbodies and effective land management practices.

Keywords Ecosystem services · Ecosystem functions · Ecosystem service values · Anthropogenic activities · Urbanization

Sudardeva · M. Pal (✉)
Department of Civil Engineering, NIT, Warangal, Telangana, India

2.1   Introduction

The ecosystem is a biophysical system, defined by the complex interaction of biotic and abiotic components in a physical environment to form a new bubble in life form. The interdependency of biotic components among themselves and with the abiotic components defines the behaviour of a biological organism in the ecosystem. The behaviour of these components results in ecosystem functioning through which ecosystem services are derived in the form of goods and services. These ecosystem services (ES) are inevitable for the existence of life forms; they are direct and indirect benefits drawn from nature and enjoyed by humans for their livelihood. Even though all biotic components influence ecosystem functioning, human beings influence the system on a greater scale due to the large-scale utilization of services offered by the ecosystem. Hence, the quantification of the association between rapid urban growth and ecosystem services plays an essential role for the urban sustainability and development related to planning and policies. A study by Costanza et al. (1997) listed 17 ecosystem services that are derived from a single or a combination of two or more ecosystem functions. Another study by Rudolf S. de Groot categorized ecosystem functions into the regulation function (maintenance of essential ecological process and life support system), habitat functions (providing habitat for plants and animal species), production functions (provision of natural resources) and information functions (providing opportunities for evolution). The definitions of individual ecosystem services offered under each categorization are as follows:

1. **Regulation functions:** Those functions which regulate the essential ecosystem process through which basic life system is supported are termed as regulation functions. The services that are derived from bio-geochemical cycles and other bio-spheric processes to the ecosystem include gas regulation, climate regulation, disturbance prevention, water regulation, water supply, soil formation, soil retention, nutrient regulation, waste treatment, pollination and biological control.
2. **Habitat functions:** The ecosystem services that enable the life forms to get habituated with normal living in order to reproduce and proliferate among themselves such that there is a conservation in biodiversity and genetic diversity are known to as habitat functions.
3. **Production functions:** The livelihood of human is supported by intake of biomass which is a direct result of synthesis from primary producers and secondary producers. They include food, raw materials, genetic resources, medicinal resources and ornamental resources.
4. **Information functions:** These functions provide essential reference function that is transferred as information to humans in the process of evolution. The services generated provide values to life and help us in understanding the need for existence of ecosystem. They include recreation, aesthetic information, cultural and artistic information, spiritual and historic information, science and education.

The above listed services may not be able to catalogue all the ecosystem services, since there are a lot of unidentified benefits used by human in the ecosystem. The

dynamics of ecosystem along with the human influence urges us to look into the idea of ecosystem sustainability. To implement them in the society, the resources and services availed so far have to be utilized in a sustainable manner. There is a need for an account of the ecosystem services in terms of monetary value for prioritising human made decisions over development and conservation. The value of the world's ecosystem services and natural capital are estimated based on willingness to pay by the resource utilizers (Costanza et al. 1997, 2008, 2014). The study by De Groot et al. (2002, 2010, 2012) and by Kreuter et al. (2001), Liu et al. (2012) created ecosystem service valuation database by analysing the previous work on the valuation in monetary terms. The values of ecosystem services are updated from his earlier work by Costanza et al. (2011), considering consumer price index, and provided the factor of conversion as 1.38 from the year 1997 to 2011. A limited number of studies have been found on this problem statement, particularly for India, and the examples are as follows: Das and Das (2019) studied the impacts of urbanization and its dynamics on ecosystem services for Malda town in West Bengal, India. Sannigrahi et al. (2019) assessed the spatiotemporal variation in ESV for a natural reserve Sundarbans region, derived from spatiotemporal data of land use and land cover (LULC). Hence the valuation of ecosystem services depends on LULC Sannigrahi et al. (2020a, 2020b), and Sannigrahi et al. (2017, 2019) compared different supervised machine learning classification techniques to derive ecosystem service values (ESVs).

The study aims to present the trend in LULC of each category for a period of four decades (1995–2022) since the introduction of major economic reforms (1991) in India (Vikramani 2006). The change in the area occupied by each ecosystem class significantly impacts the functioning of the ecosystem, which further affects the extraction of ecosystem services. The more the natural element persists in the ecosystem, the least it is disturbed. But the needs of humans heavily influence LULC. It is essential to view and plan developmental initiatives in a sustainable way that alters the ecosystem of an urban area such that it should be a balance between resource utilization and extraction of ecosystem services. The study will state the current state of ecosystem functions and ESV derived from LULC. It will aid us to formulate indices that will help the local government to monitor and frame policies to achieve Sustainable Development Goal (SDG) concerning the urban area to make cities and human settlements inclusive, safe, resilient and sustainable. Furthermore, the change in LULC deteriorates the ecosystem and makes them prone to hazards. Since the increase in builtup area is associated with the increase in population, which in turn results in increase in demand of resources of water and energy, this additional demand in the existing system increases the stress on groundwater through extensive drafting, thus resulting in reduced baseflow component of the stream and may disturb the perennial nature of the stream. Additionally, the relationship between builtup and impervious surfaces is related to the increase in flood scenarios and land surface temperature (LST) that can affect the hydrological extremes. The valuation of ES would help in framing policy in an urban area for sustainable land use management practices. However, as mentioned earlier, the studies concerning the assessment of ES for urban region in India are limited.

Hence, this study has taken up to estimate the ESV for two metropolitans, namely, the Greater Hyderabad Municipal Corporation (GHMC) and Chennai Metropolitan Area (CMA) which has undergone rapid unregulated urbanization. The major objectives of the study are as follows:

1. To investigate the changes in LULC due to urbanization for the study area, that is, GHMC and CMA, over the last two decades, that is, 1995–2022
2. To estimate and detect the trends in ESVs offered by individual LULC classes and individual ecosystem functions

2.2 Rational of the Study

Industrialization and its associated urbanization have made lives of human being more comfortable than ever before, and they significantly impacted human way of consuming and utilizing resources. This anthropogenic utilization has brought severe degradation of the ecosystem and reduced the services offered by the ecosystem (Chopra et al. 2022). Since this is the age of sustainable development, a prior knowledge on services offered by the ecosystem is needed to draft policies for optimal and environment-friendly utilization of resources. This study attempts to estimate the ecosystem service values of two Indian metropolises and analyse the trend in the services between two decades, that is, 1995–2022. It also attempts to highlight the impacts of change in LULC triggered by economic opportunities on ecosystem service values.

2.3 Limitation of the Study

Valuation of ecosystem services involves the process of identifying the ecosystem services and assigning a monetary value to them. This study considers only a list of 17 ecosystem services based on a study performed by Costanza et al. (1997). The study excludes some of the services from the process limiting the idea of valuing the entire ecosystem. The values of ecosystem services are considered in terms of US Dollar (USD) and are not converted to Indian Rupee (INR) according to the present consumer price index.

2.4   Materials and Methods

2.4.1   Study Area

2.4.1.1   Greater Hyderabad Municipal Corporation

Hyderabad is the capital city and most populous city in the Indian state of Telangana. The Greater Hyderabad Municipal Corporation (GHMC) is an urban conglomeration comprising of two main cities, that is, Hyderabad and Secunderabad, along with its suburbs shown in Fig. 2.1. The study area is holding 9.7 million human habitants and spreads over an area of 550 km^2, which is further divided into 6 zones and 30 circles for administration convenience. It extends between 17°20′N to 17°60′N latitude and 78°23′E to 78°68′E longitude and receives an average precipitation of 840mm (Agilan et al. 2015). The river Musi which originates in Vikrabad flows in the city that acts as natural carrier to drain the water. The GHMC experiences an arid climate with mean monthly temperature varying 22.6°C in January and 32.3°C in May (Warrier et al. 2011). The average elevation is 580m above mean sea level and is located in Deccan plateau.

The study area serves as an industrial hub for pharma and life sciences, food processing and service sector, since it is stressed with 27% of state's population living in 0.8% of state's area. It shares almost half (43.5%) of total gross state domestic product (GSDP) of Telangana. The economic growth attracted population inside and outside the state of Telangana that resulted in unregulated land use practices.

2.4.1.2   Chennai Metropolitan Area

Chennai is one of the oldest municipal corporations in the world and serves as the capital of the Indian state of Tamil Nadu. The Chennai Metropolitan Area (CMA) comprises Greater Chennai Corporation, Avadi Corporation, Tambaram Corporation and its suburbs, which accounts for 12 million people spread over 1182 km^2 and
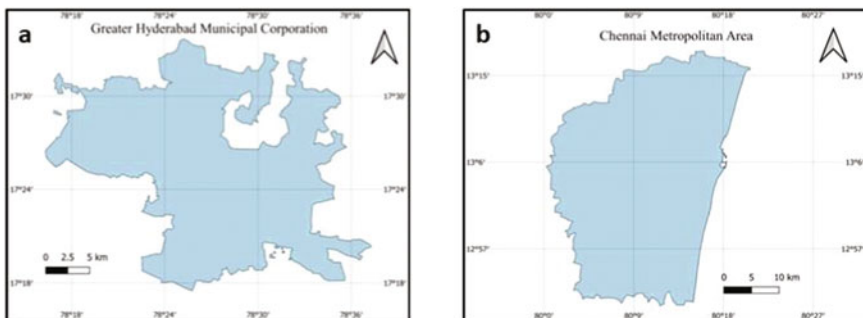
Fig. 2.1 Location of study area – (**a**) GHMC and (**b**) CMA
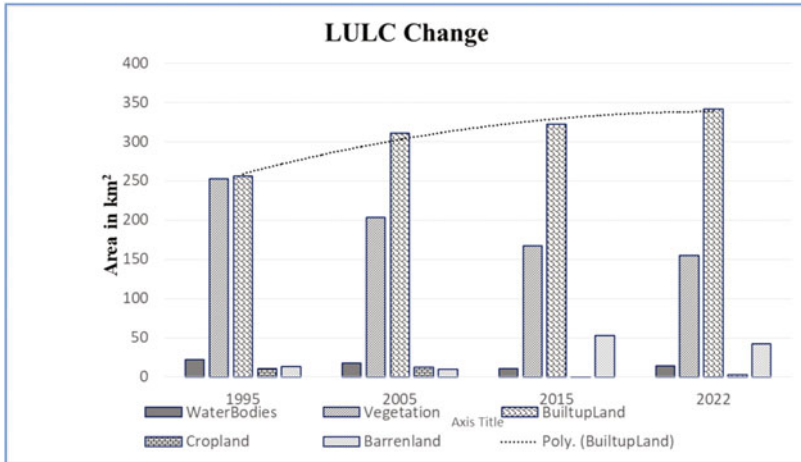
Fig. 2.2 Trend in LULC variation for GHMC from 1995 to 2022

shown in Fig. 2.2. The study area experiences a tropical wet and dry climate and is highly humid because of its location. It receives rainfall on an average of about 1400 mm where 60% of it occurs between October and December, that is, due to northeast monsoon (Devi et al. 2019). Three rivers Cooum, Adayar and Kosasthailayar flow in the study area and drains into the Bay of Bengal. Buckingham Canal once served as a navigational channel runs parallel to the coast. Heavy industrialization and urbanization in post-independence period sound the need for ecosystem valuation.

2.4.2 Data Source and LULC Classification

The estimation of ESVs depends on the accurate measurement of proportionate area that falls under each ecoregion, since an ecoregion offers unique ecosystem services. Remote sensing data products are reliable source for quantifying area under each ecoregion. For the study, geometrically and radiometrically calibrated Landsat data are obtained from the US Geological Survey (USGS) Earth Explorer that is for different time periods. The detail description of Landsat data used in the study is given in Table 2.1. The data for the month of January (with cloud cover less than 10%) are considered for the analysis for the years 1995, 2005, 2015 and 2022, in order to eliminate the seasonal variation and to maintain consistency in classification.

The data are classified into five LULC classes, that is, waterbodies, vegetation, builtup, cropland and barrenland, using a supervised machine learning algorithm, namely, support vector machine (SVM). The LULC classification using SVM has produced better accuracy (Sannigrahi et al. 2019) comparing with other techniques

Table 2.1 Description of the record of Landsat data for different years used in the study

Year	Data	Sensor	Month of image acquisition	Spatial resolution (m)
1995	Landsat 5	TM	January 1995	30
2005	Landsat 5	TM	January 2005	30
2015	Landsat 8	OLI	January 2015	30
2022	Landsat 9	OLI	January 2022	30

like Artificial Neural Network, Decision Tree and Maximum Likelihood Classification. Google Earth Engine is used to classify the images, since it reduces the tedious task of data handling. The cloud-based setup helps us to derive and store the output without need for handling many temporary data.

The platform's code editor is used to obtain the Landsat data and filtered for minimal cloud cover. An average of 200 training point is considered for individual class, that is, waterbodies, cropland, vegetation, builtup and barrenland, and Support Vector Machine (SVM) classifier (libsvm) is used for the supervised classification. The classified data for the years of 1995, 2005, 2015 and 2022 are used to obtain the proportionate area under each class and are analysed for spatiotemporal variations in an individual classed over the time period of study. The year 1995 was taken as reference period to define the variation in LULC classes and estimated as follows:

$$\triangle \text{LULC}_i = \frac{\text{LULC}_{\text{final}} - \text{LULC}_{\text{initial}}}{\text{LULC}_{\text{initial}}} \times 100$$

where $\triangle \text{LULC}_i$ is the change in an individual LULC observed during the time frame and $\text{LULC}_{\text{final}}$ and $\text{LULC}_{\text{initial}}$ is the particular LULC unit at the beginning and ending of the study. The average overall accuracy assessment of supervised classification for the study areas of CMA and GHMC is 73% and 55%, respectively. The accuracy can be enhanced by a more apparent distinction between cropland and barrenland, as non-cultivable areas are classified as barrenland. The flaws in the classification limit the study.

2.4.3   Estimation of Ecosystem Service Values

Ecosystem service value is estimated as the summation of product of the ecosystem coefficient (for LULC classes and ecosystem services) with proportionate area of LULC classes. We considered 17 ecosystem services offered by individual LULC classes and the value for ecosystem service coefficient obtained from Sannigrahi et al. (2019) are listed in Table 2.2. And the ESV can be mathematically computed with the following equation:

Table 2.2 Ecosystem service value for different LULC classes in US$/ha/year

Ecosystem services	Waterbodies	Vegetation	Cropland	Barrenland	Builtup
Gas regulation	0	0	0	10.06	0
Climate Regulation	13	6	215	0	26
Disturbance Regulation	81	0	0	0	0
Water regulation	166	0	0	15.1	1
Water supply	12	10	234	0	0
Erosion control	88	8	74	10.06	0
Soil formation	0	0	370	0	0
Nutrient cycling	51	0	0	0	0
Waste treatment	82	11	208	50.32	0
Pollination	0	5	12	0	0
Biological control	26	5	17	0	0
Habitat service	66	184	0	10.06	0
Food production	17	181	1269	0	0
Raw material	15	8	115	0	0
Genetic service	3	184	546	0	0
Recreation	60	4	43	0	161
Cultural service	54	25	0	5.03	0

$$\mathrm{ESV}_i = \sum_{j=1}^{17} aV_{ck} \times A_i$$

where ESV_i is the ecosystem service value offered by an individual class and V_{ck} is the ecosystem service coefficient for individual ecosystem service in US$/ ha/year:

$$\mathrm{ESV}_{total} = \sum_{i=1}^{5} a\mathrm{ESV}_i$$

ESV_{total} in a year is the total ecosystem service value offered by all individual LULC classes from their services. The change in ESV ($\triangle \mathrm{ESV}_i$) is calculated as follows:

$$\triangle \mathrm{ESV}_i = \frac{\mathrm{ESV}_{final} - \mathrm{ESV}_{initial}}{\mathrm{ESV}_{initial}} \times 100$$

2.5   Results and Discussion

2.5.1   Classification and Spatiotemporal Changes of LULC

2.5.1.1   GHMC

In the year 1995, the LULC class vegetation and builtup are found to be the predominant land cover category (46.5% and 46%) followed by waterbodies (4%), and then cropland and barrenland are the least ones. The dominance of builtup in LULC is found in 2005, and vegetation class is found to have considerable loss in proportion of area as shown in Fig. 2.2.

During the years 1995–2022, builtup area has increased 33% at the cost of vegetation and waterbodies changing the study area landscape with builtup as the dominant category.

The spatiotemporal changes in the study area are presented in Fig. 2.3. Even though the reduction in area of waterbody is observed, the rate of decrease in the area from 2015 to 2022 is very low compared to the rate of decrease from 2005 to 2015. The area under waterbodies, vegetation and cropland has shrunken to 36.05%, 38.69% and 75.13%, respectively, during the period of study between 1995 and 2022. Meanwhile the area under builtup and barrenland are found to increase 32.98% and 218.02% during the study. The decade of 2005–2015 has witnessed sharp transition in area under each LULC class, that is, the area under waterbodies, cropland and vegetation has been transformed into other LULC classes.

2.5.1.2   CMA

The Chennai Metropolitan Area had builtup as the dominant land category occupying 32.48% of total area followed by cropland, vegetation, barrenland and then waterbodies (29.62%, 14.91%, 13% and 10.14%), respectively, in 1995. The areas under builtup and barrenland are found to increase during the study period of 1995–2022 amounted to 36.46% and 42%, respectively, as seen in Fig. 2.4. Vegetation, cropland and waterbodies are found to follow decreasing trends throughout the study period, and estimated percentage losses in the area compared with the reference year are 24.8%, 30% and 45.96%, respectively. The increasing area under builtup and barrenland could be attributed with the decrease in the area associated with the LULC class of vegetation, cropland and waterbodies (Fig. 2.5).
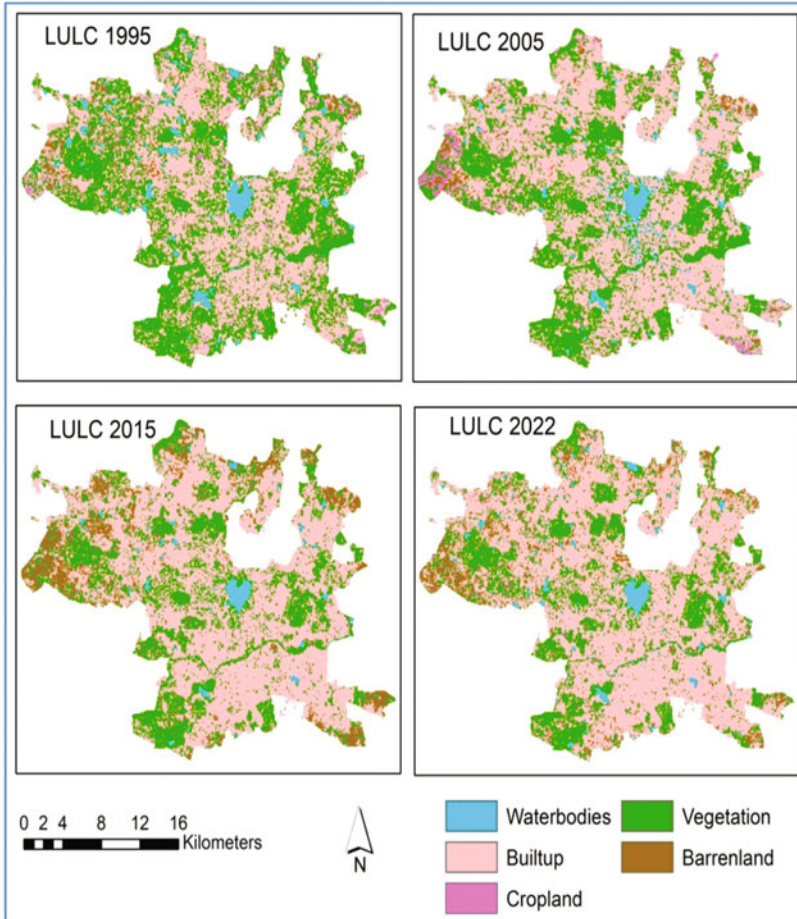
Fig. 2.3 Spatiotemporal variation of LULC observed in GHMC (1995–2022)

2.5.2 Ecosystem Service Values

2.5.2.1 GHMC

Figure 2.6 depicts the ESV derived from each LULC in GHMC. Waterbodies provide 14 ecosystem services out of 17 considered for this study, and it contributes to 1.8 million US Dollars (USD) in the year 1995 (Costanza et al. 1997) and gradually reduced to 1.7 million USD in 2005, 1.8 million USD in 2015 and 1.14 million USD in 2022. Vegetation provides 12 ecosystem services and contributed 18.16 million USD in the year 1995. It is the highest contributed LUCC class to ESV and then decreasing throughout the study period as 16.95 million USD in 2005,
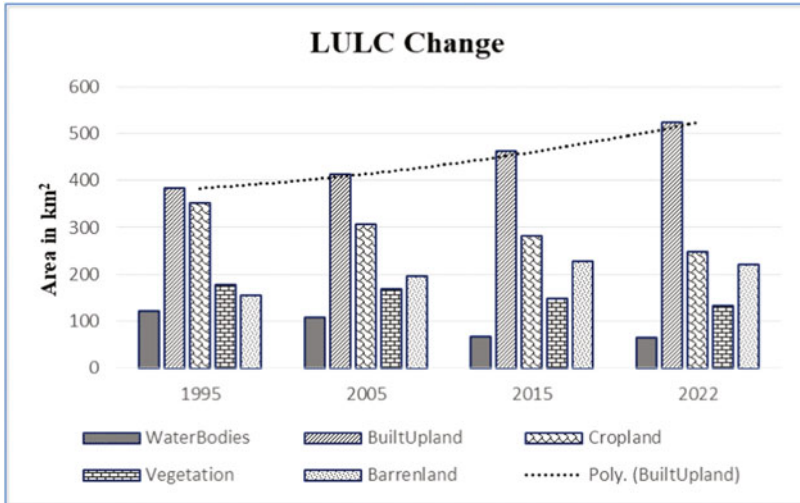
Fig. 2.4 Trend in LULC variation for CMA from 1995 to 2022

14.31 million USD in 2015 and 10.23 million USD in 2022 indicating the rate of decrease in ESV increasing as the time progressed.

Climate regulation, water regulation and recreation are the services provided by the builtup class. The valuation of these services is estimated around 4.5 million USD in 1995 and found to be a decreased till the end of the study period (4.9 million USD in 2005, 5.88 million USD in 2015 and 7.1 million USD in 2022). The rate of increase in ESV was found to be increased during later time period of study (2005–2015, 2015–2022). Though builtup is a dominant land use category, the net ecosystem services derived from it were less compared with another existing natural ecosystem. From this study, it is evident that there is a linkage between LULC and ecosystem service values. The reduction in the area of waterbodies (37.67%) has reflected in ESV, that is, the share in total ESV dropped from 6.45% in 1995 to 5.73% in 2022. Vegetation has drastically minimized in area by 43.6% where almost half of the area are converted into other eco-class. The contribution of vegetation to ESV dropped from 74% to 55% indicating the overall loss to the study area. The ecosystem services provided by vegetation have been following a decreasing trend throughout the period. The area under builtup found to be increased 33% during the period 1995–2022, the share to the total area calculated as 46.13% in 1995, 55.9% in 2005, 57.8% in 2015 and 61.8% in 2022.

The ESV_{total} is estimated 28.87 million USD in the year 1995 and 18.49 million USD in the year 2022 showing decreasing trend with an overall loss of 28.52% (10.38 million USD). The primary contribution of ESV is derived from vegetation followed by builtup, cropland and waterbodies, and this order continued even though there is net decrease in contribution from the individual classes except builtup. Production functions contribute higher share in ESV followed by information functions, habitat functions and regulation functions throughout the study as
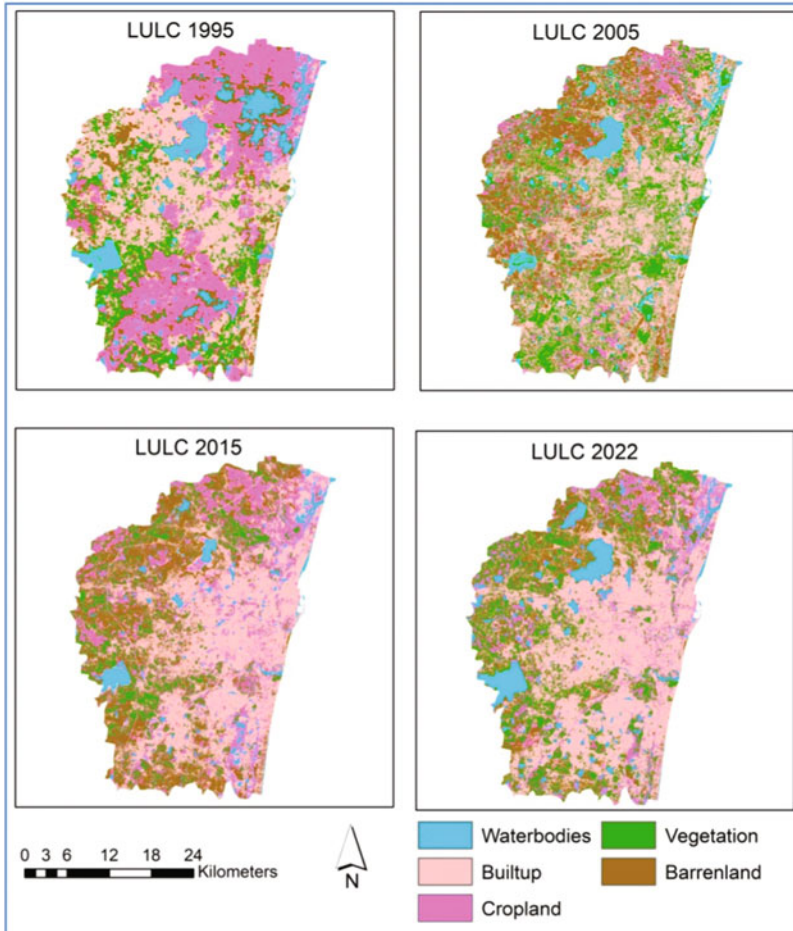
Fig. 2.5 Spatiotemporal variation of LULC observed in CMA (1995–2022)

shown in Fig. 2.7. The fivefold increase of area in barrenland observed between 2005 and 2015 has found to be decreased 20% during 2015–2022, along with the increase in builtup. This could be reasoned as the barrenland serves as an intermediate transition class towards the conversion of vegetation and cropland into builtup.

2.5.2.2 CMA

Cropland holds the highest share in contributing services to the ecosystem and is estimated to be 109 million USD in the year 1995, 94.9 million USD in 2005, 87.5 million USD in 2015 and 76.5 million USD in 2022 as shown in Fig. 2.8. Though cropland shares higher ESV among other eco-classes, there is constant decrease in
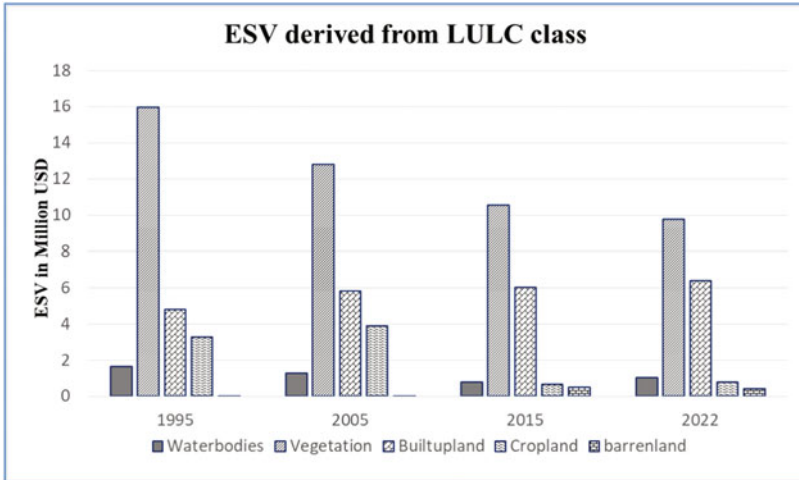
Fig. 2.6 The ESVs derived from LULC for GHMC
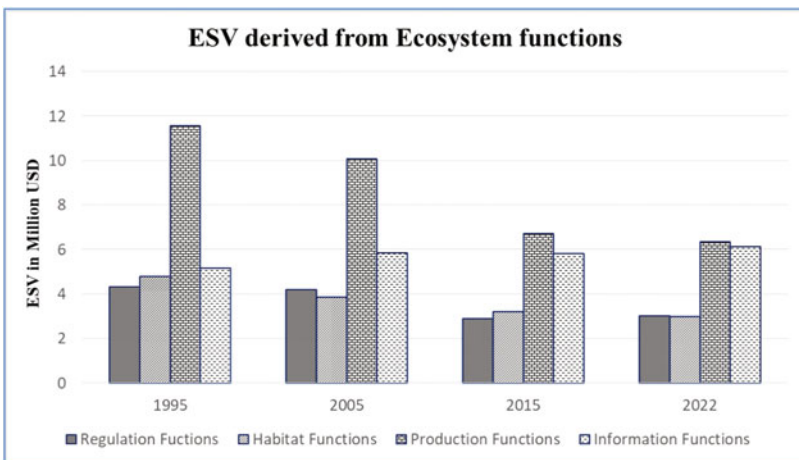
Fig. 2.7 The ESV derived from ecosystem functions for GHMC

ESV (30%) during the study period. The increase in ESV derived from the builtup does not significantly increase the total ESV as shown in Fig. 2.8.

This is a result of significant reduction in the area occupied by the cropland. Vegetation is the next highest contributor of ES in the CMA accounting 11.18 million USD, 10.56 million USD, 9.4 million USD and 8.4 million USD, and this eco-class too followed the decreasing trend in ESV as cropland during the study. Contradictorily, ESVs derived from builtup on the barrenland are found to be increasing throughout the study. This is reflected from decreasing trend in the area
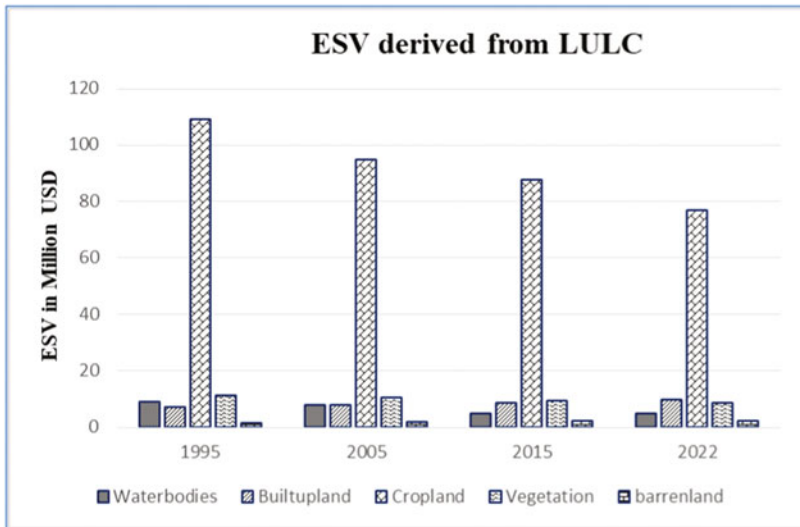
Fig. 2.8 The ESV derived from LULC class for CMA

occupied by the waterbodies and increasing trend in area occupied by the buildup and barrenland during the study.

The ESV for the CMA is estimated as 138.03 million USD in the year 1995 and found decreased as 123 million USD in 2005, 112.91 million USD in 2015 and then 101 million USD in 2022. The loss incurred in ESV amounts during the study of 36.24 million USD (26.25%) is attributed to the increase in the builtup and barrenland whose ecosystem services contribution is minimum. Figure 2.9 clearly shows that the production function dominates other ecosystem functions in generating ESV but follows decreasing trend throughout the study. This trend is followed by regulation functions and habitat functions except information function, where ESV contribution is found with increasing trend throughout the study. Regulation functions that regulate and maintain the ecosystem through its services (climate regulation, water regulation and supply, disturbance regulation and waste Treatment) are found to have subsequent decrease in generation of ESVs between 1995 and 2022. This fact questions the resilience of the study area in climate change-induced extremes. The decrease in regulation function indicates loss in basic life support services derived from the ecosystem.

2.6   Conclusion

In this study, we have calculated the spatiotemporal ESVs of Greater Hyderabad Municipal Corporation (GHMC) and Chennai Metropolitan Area (CMA) from the different LULC data for the period 1995–2022. The monetary values for
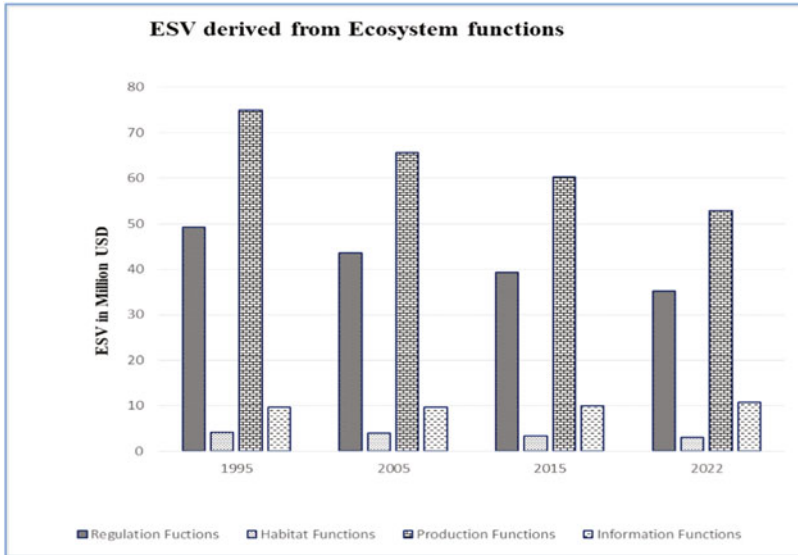
Fig. 2.9 The ESV derived from ecosystem functions for CMA

17 ecosystem services are calculated using ecosystem service coefficient values obtained from Sannigrahi et al. (2019). At instant builtup is the dominant land use category in the study, followed by vegetation and waterbodies, respectively. Due to the expansions in builtup, the ecosystem services such as climate regulation and recreation have increased during 1995–2022, whereas the decrease in ESV such as water regulation, water supply, erosion control, nutrient cycling, raw material and genetic services is observed due to shrinkage in the area under waterbodies and vegetation. It also describes the impact of human interference on ecosystem and natural capital. The study reveals that the area of our interest has undergone unregulated land use practices due to anthropogenic activities, since builtup is the only class found increased throughout the period of study. The study concludes that anthropogenic activities on LULC have severe impact on ecosystem functions and its derived ecosystem services. It is observed that years between 2005 and 2015 witnessed sharp transition in LULC and it could be reasoned with flowering economic activities. However, the reason has to be validated with further studies. The change detection analysis study on LULC would be able to quantify the transformation of one class into another and it limits the present study. Lastly, the study points that there is an overall loss in ESV derived from ecosystem services due to anthropogenic activities, 6 (clean water and sanitation, good health and well-being, sustainable cities and communities, climate action, life below water, life on land) out of 17 Sustainable Development Goals are more affected. The result of this study would be helpful in understanding the LULC dynamics and its associated changes in the ESV values to frame policies to attain ecosystem sustainability.

References

Agilan V, Umamahesh NV (2015). Detection and attribution of non-stationarity in intensity and frequency of daily and 4-h extreme rainfall of Hyderabad, India. J Hydrol, 530, 677–697. https://doi.org/10.1016/j.jhydrol.2015.10.028

Chopra B, Khuman YSC, Dhyani S (2022) Advances in ecosystem services valuation studies in India: learnings from a systematic review. Anthropocene Sci 1(3):342–357. https://doi.org/10.1007/s44177-022-00034-0

Costanza R, d'Arge R, De Groot R, Farber S, Grasso M, Hannon B, Limburg K, Naeem S, O'neill RV, Paruelo J, Raskin RG (1997) The value of the world's ecosystem services and natural capital. Nature 387(6630):253–260. https://doi.org/10.1038/387253a0

Costanza R, Pérez-Maqueo O, Martinez ML, Sutton P, Anderson SJ, Mulder K (2008) The value of coastal wetlands for hurricane protection. Ambio:241–248. https://doi.org/10.1016/j.gloenvcha.2021.102328

Costanza R, Kubiszewski I, Ervin D, Bluffstone R, Boyd J, Brown D et al (2011) Valuing ecological systems and services. F1000 biology reports 3. https://doi.org/10.3410/B3-14

Costanza R, De Groot R, Sutton P, Van der Ploeg S, Anderson SJ, Kubiszewski I, Farber S, Turner RK (2014) Changes in the global value of ecosystem services. Glob Environ Chang 26:152–158. https://doi.org/10.1016/j.gloenvcha.2014.04.002

Das M, Das A (2019) Dynamics of urbanization and its impact on urban ecosystem services (UESs): a study of a medium size town of West Bengal, Eastern India. J Urban Manag 8(3):420–434. https://doi.org/10.1016/j.jum.2019.03.002

De Groot RS, Wilson MA, Boumans RM (2002) A typology for the classification, description and valuation of ecosystem functions, goods and services. Ecol Econ 41(3):393–408. https://doi.org/10.1016/S0921-8009(02)00089-7

De Groot RS, Alkemade R, Braat L, Hein L, Willemen L (2010) Challenges in integrating the concept of ecosystem services and values in landscape planning, management and decision making. Ecol Complex 7(3):260–272. https://doi.org/10.1016/j.ecocom.2009.10.006

De Groot R, Brander L, Van Der Ploeg S, Costanza R, Bernard F, Braat L, Christie M, Crossman N, Ghermandi A, Hein L, Hussain S (2012) Global estimates of the value of ecosystems and their services in monetary units. Ecosyst Serv 1(1):50–61. https://doi.org/10.1016/j.ecoser.2012.07.005

Devi NN, Sridharan B, Kuiry SN (2019). Impact of urban sprawl on future flooding in Chennai city, India. J Hydrol, 574, 486–496. https://doi.org/10.1016/j.jhydrol.2019.04.041

Kreuter UP, Harris HG, Matlock MD, Lacey RE (2001) Change in ecosystem service values in the San Antonio area, Texas. Ecol Econ 39(3):333–346. https://doi.org/10.1016/S0921-8009(01)00250-6

Liu Y, Li J, Zhang H (2012) An ecosystem service valuation of land use change in Taiyuan City, China. Ecol Model 225:127–132. https://doi.org/10.1016/j.ecolmodel.2011.11.017

Sannigrahi S, Rahmat S, Chakraborti S, Bhatt S, Jha S (2017) Changing dynamics of urban biophysical composition and its impact on urban heat Island intensity and thermal characteristics: the case of Hyderabad City, India. Model Earth Syst Environ 3:647–667. https://doi.org/10.1016/j.jenvman.2019.04.095

Sannigrahi S, Chakraborti S, Joshi PK, Keesstra S, Sen S, Paul SK, Kreuter U, Sutton PC, Jha S, Dang KB (2019) Ecosystem service value assessment of a natural reserve region for strengthening protection and conservation. J Environ Manag 244:208–227. https://doi.org/10.1016/j.jenvman.2019.04.095

Sannigrahi S, Zhang Q, Joshi PK, Sutton PC, Keessstra S, Roy PS, Pilla F, Basu B, Wang Y, Jha S, Paul SK (2020a) Examining effects of climate change and land use dynamic on biophysical and economic values of ecosystem services of a natural reserve region. J Clean Prod 257:120424. https://doi.org/10.1016/j.jclepro.2020.120424

Sannigrahi S, Zhang Q, Pilla F, Joshi PK, Basu B, Keessstra S, Roy PS, Wang Y, Sutton PC, Chakraborti S, Paul SK (2020b) Responses of ecosystem services to natural and anthropogenic

forcings: a spatial regression based assessment in the world's largest mangrove ecosystem. Sci Total Environ 715:137004. https://doi.org/10.1016/j.scitotenv.2020.137004

Vikramani A (2006) India's economic growth history: fluctuations, trends, break points and phases. Indian Econ Rev 41:81–103. https://www.jstor.org/stable/29793855

Warrier CU, Babu MP (2011) A comparative study on isotopic composition of precipitation in wet tropic and semi-arid stations across southern India. J Earth Syst Sci 120, 1085–1094. https://doi.org/10.1007/s12040-011-0121-2

Chapter 3
Groundwater Vulnerability Mapping Using Modified DRASTIC Model: A GIS-Based Case Study of Imphal East District, Manipur, India

Haobam Bidyapati and Thiyam Tamphasana Devi ⬤

Abstract In this study, modified DRASTIC models (DRASTIC_AGRI and DRASTIC_LU models, AGRI stands for agriculture and LU stands for landuse) with GIS (Geographical Information System) tools were used to evaluate the vulnerability of groundwater (contamination and quality) in Imphal East District, Manipur, India, for the recent period (2021–2022). For the DRASTIC_AGRI model, seven input parameters (depth of water, net recharge, types of aquifer media, types of soil media, topographical slope, impact of the vadose zone and hydraulic conductivity) were used, and additionally, one more parameter (land use/land cover) is used in the DRASTIC_LU model. Out of these parameters (except hydraulic conductivity), data were collected from different government organisations, and for hydraulic conductivity, field measurements were performed using a field instrument (a Mini Disc Infiltrometer) at different locations within the study area. In order to construct the modified DRASTIC indexes, weights (1–5) and ratings (1–10) are assigned to these input parameters, and finally, using weighted overlay analysis, the indexes are derived. A Delphi method (Aller et al. 1985) is used to determine these ratings and weights. The results reveal that the vulnerability index of Imphal East ranges from 130 to 173 (DRASTIC_AGRI) and 120–182 (DRASTIC_LU), which indicates moderate to high vulnerability to groundwater contamination. The predicted index values are validated ($R^2 = 0.948$, $R^2 = 0.934$) using TDS (total dissolved solids), which is one of the major contributing parameters to groundwater pollution. It is concluded that even though the study region is not industrialised, urbanisation and human activities (including the use of pesticides in agricultural practises) may escalate the contamination of groundwater in this region, which needs to be checked regularly as well as widely to reduce the contamination further.

H. Bidyapati · T. T. Devi (✉)
Department of Civil Engineering, National Institute of Technology, Imphal, Manipur, India

Highlights
- First study on the application of DRASTIC_AGRI model and DRASTIC_LU model with GIS techniques for groundwater vulnerability mapping in the study region and very few in entire North East India

3.1   Introduction

The relationship between rivers, sediment, hydrological extremes and groundwater is complex and interconnected (Gupta et al. 2023). The ecosystem of water resources is disturbed by several factors, and its two major extreme events (floods and droughts) are significant. River plays a major role for source of water as well as sweeping away the overflow discharge of the catchment which controls and reduces the amount of flood in the region (Saikumar et al. 2022). Groundwater can play a critical role in maintaining river flow during periods of drought, as it can act as a natural storage reservoir and slowly release water into the river over time (Saikumar et al. 2022). However, excessive sediment accumulation in the riverbed can reduce the rate of groundwater recharge and lead to a decline in water table levels, which can in turn exacerbate drought conditions (Saikumar et al. 2022). Hydrological extremes, such as floods, can also impact groundwater quality by introducing contaminants into the subsurface, which can then migrate and impact nearby drinking water wells (Gupta et al. 2023). Effective management of river sediment and hydrological extremes can help to maintain healthy groundwater resources by reducing sedimentation and the risk of groundwater contamination (Saikumar et al. 2022). Additionally, groundwater management strategies, such as recharge wells and aquifer storage and recovery, can help to increase groundwater storage and recharge rates, providing a buffer against hydrological extremes and supporting healthy river ecosystems (Gupta et al. 2023). In case of drought (scarcity or non-availability of surface water), the main source of water is groundwater (Singh and Devi 2022). Due to natural (laterals seepage of polluted water, siltation and sedimentation, etc.) as well as anthropogenic activities, that is , the use of pesticides in agricultural practice (Farooqi et al. 2009; Urseler et al. 2022) and in animal farming, conversion of native land to agriculture (Novotny 1999) and dumping of sewage on the ground without treatment (Reynolds et al. 2007; Dregulo and Bobylev 2021), groundwater is polluted. Siltation and sedimentation of river caused by soil erosion and loss lead to contamination of groundwater (Pal et al. 2022; Raju 2022; Wang et al. 2022). Various chemicals (pharmaceuticals and personal care products) present and flows along with the sediment are potential risks to groundwater and eventually to human health and aquatic life (Xie et al. 2022). Thus, assessment on groundwater vulnerability to contamination and pollution becomes an essential part

for monitoring as well as for preventive measures to the groundwater pollution. The use of satellite data with GIS (Geospatial Information System) techniques is a well-known approach for modelling the groundwater vulnerability (Indulekha et al. 2019; Ahirwar et al. 2022). And one the commonly used GIS based model is DRASTIC (each letter represents the major factors affecting the transfer of contamination) for modelling of groundwater vulnerability (first time introduced by Aller et al. (1985), Ersoy and Gultekin (2013), Machdar et al. (2018), Malik and Shukla (2019) and Bera et al. (2021)). Then with the development of technology as well as the data source, DRASTIC model has been revised/modified (Wang et al. 2022; Khosravi et al. 2021; Pal et al. 2022) in many forms: (i) DRASTICA which includes the anthropogenic influence (Singh 2015) and gives the highest importance to that influencing factor (in the present study, agriculture is considered as anthropogenic influence, and soil type is the most affecting factor to agriculture and therefore highest weight is given to soil types and model is named as DRASTIC_AGRI); (ii) DRASTIC_LU in which an additional parameter, land use (LU), is used (present study; Saha and Alam 2014); (iii) pesticide_DRASTIC which is a pollutant's oriented model (Barbulescu 2020); (iv) DRASTICM which includes the lineament influence denoted by M (Mendoza and Barmen 2006); and (v) and in general CDRASTIC model where C denotes composite model (Malakootian and Nojari 2020), etc. to improve the accuracy of results.

Sarkar and Pal (2021) applied agricultural DRASTIC_AGRI and modified DRASTIC (which uses additional parameters such as LU and other composite parameters) to assess the groundwater vulnerability of the Malda area in West Bengal, India. Standard weights (1–5) are used to indicate the use of pesticides in agricultural activities (Aller et al. 1985). Pesticide applications were said to occur in agricultural DRASTIC_AGRI, and it is utilised in agricultural regions, while the original DRASTIC is employed in industrial and urban locations. They justified that DRASIC_AGRI was used because most of the study area is covered by agriculture land. In the result they observed that 43.16% of areas have low vulnerability (ranging from 95 to 143), and 20.51% of areas have high vulnerability (ranging from 170 to 197). Baghapour et al. (2016) applied DRASTIC_LU to assess the groundwater vulnerability (nitrate pollution) in the Shiraz aquifer located in Fars province, Iran. It was observed that the nitrate index ranged from 6.4 to 185 and was classified as very low (70), low (70–110) and medium (110–145). Further, it was interpreted that 6.45% of the total area is under moderate vulnerability, and the remaining 81.9% are under very low to low vulnerability. They concluded that nitrate concentration is high with a high volume of agricultural activities (use of pesticides) and shallow groundwater depth (rise of groundwater level), and to overcome the nitrate pollution of groundwater, they suggested some measures, which include an effective drainage system (improvement of the existing drainage system) in the region as well as improvements in fertiliser management (plantation of crops with high nitrate use efficiency).

In the present study region, where the major rivers are prone to siltation and sedimentation due to several factors (primarily soil erosion and loss due to urbanisation, landslides and pesticides from agricultural practises), it is very likely that the

groundwater is contaminated. Therefore, in this chapter, an assessment of the groundwater vulnerability (in terms of contamination) of Imphal East district, Manipur, is conducted using a modified DRASTIC model (DRASTIC_AGRI and DRASTIC_LU) with GIS techniques.

3.2 Study Area

Imphal East district (Fig. 3.1) is one of the districts of Manipur (northeastern state of India) that has a total population of 4,52,661 people (Census, 2011) and geographical area of around 709 km^2. It is located at an altitude of 790 m above sea level Imphal East, Manipur, India is located at latitude 24.780654 N and longitude 93.967437 E. A subtropical to temperate climate may be found there and the temperature is between 0 °C and 40 °C. The southwest tropical monsoon's effect is a phenomenon that the region encounters. The monsoon season's heaviest rain falls between May and August of every year. The region resembles a flat, long, narrow valley with solitary hills that rise up towards the south.
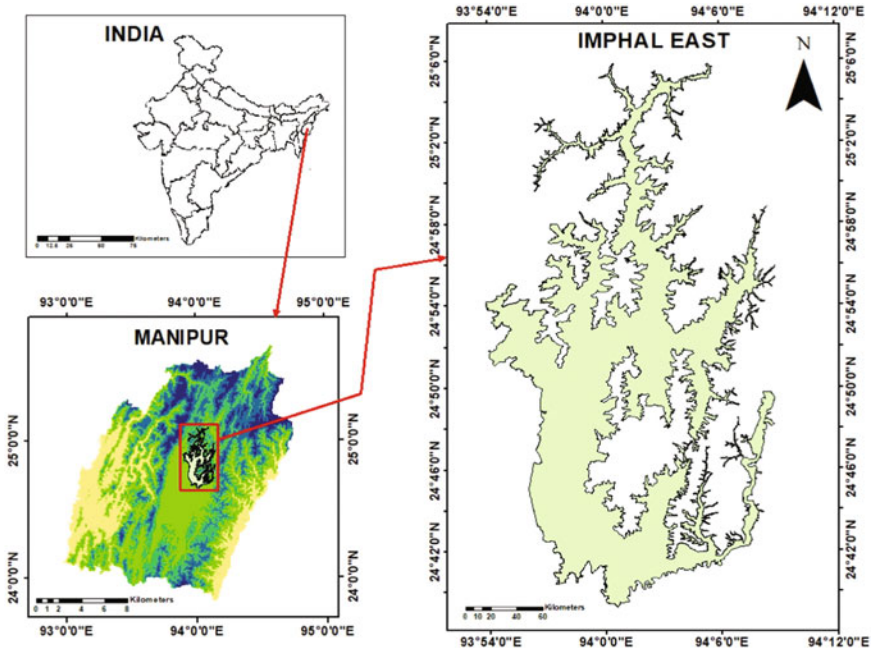
Fig. 3.1 Imphal East district map (MARSAC, Government of Manipur)

3.3 Methodology

DRASTIC model has different modified versions, and the models in this study are two of them IDRASTIC_AGRI and DRASTIC_LU. The data used and equations of DRASTIC_LU model and DRASTIC_AGRI model with theoretical background to assess the groundwater vulnerability in this study are presented in this section.

3.3.1 DRASTIC Model

DRASTIC model is used to evaluate vertical vulnerability mapping, and each letter in this model represents the required input parameters to get the final output. Therefore, D represents depth to water, R as net recharge, A as aquifer media, S as soil media, T as topography, I as impact of vadose zone and C as hydraulic conductivity. It is presumed that all these input parameters significantly affect the health of groundwater (pollution or contamination of groundwater) and play an important role in the overall results. In this model, each component (input parameters) is given a weighting multiplier to balance and enhance its importance. Thus, a scale of 1–5 as weight and a scale of 1–10 as ratings normally are assigned to each input parameter and are provided in Table 3.2 in the Result and Discussion section. After weights and rank are assigned to these input parameters, weighted overlay analysis is performed, and the weighted total of the seven elements results in the final vulnerability index as the DRASTIC index (D_i) is given as

$$D_i = D_r D_w + R_r R_w + A_r A_w + S_r S_w + T_r T_w + I_r I_w + C_r C_w \qquad (3.1)$$

where D_i is the DRASTIC index for a mapping unit w weighting factor for each parameter r rating for each parameter D, R, A, S, T, I and C, the seven parameters, that is, D is the depth of water, R is the net recharge, A is the aquifer media, S is the soil media, T is the topography, I is the vadose zone impact and C is the hydraulic conductivity, respectively.

3.3.2 DRASTIC_AGRI Model

In this modified model, vulnerability index is generated with different weights from the original DRASTIC model. Since weights are assigned according to the importance of the particular model, highest weight is assigned to the parameter that is important to the agriculture.
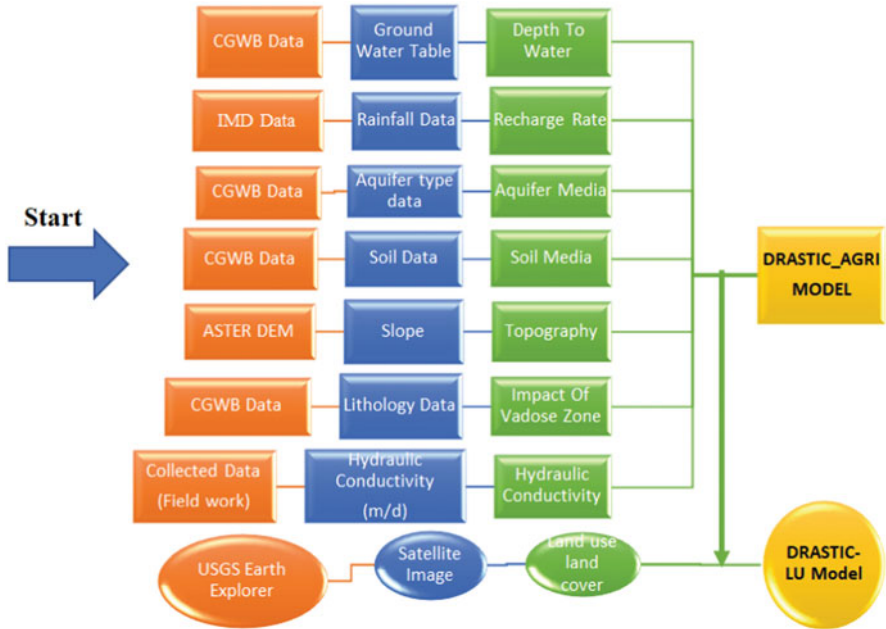
Fig. 3.2 Structure of data used in DRASTIC_AGRI and DRASTIC_LU models

3.3.3 DRASTIC_LU Model

In this modified model, vulnerability index is generated by adding land use/land cover (LULC) to the original DRASTIC model having assigned weights and rating for different parts of LULC. Then, weighted overlay analysis is performed with the eight parameters in GIS platform. DRASTIC_LU vulnerability index is given as

$$D_{LU} = D_r D_w + R_r R_w + A_r A_w + S_r S_w + T_r T_w + I_r I_w + C_r C_W + L_r L_w \qquad (3.2)$$

where L represents land use/land cover (Fig. 3.2).

3.3.4 Data Used

The data used (input parameters) with its sources and mode of derivation and extraction is provided in Table 3.1. The description of these input parameters provides the insight meaning of the characteristics possessed. The collected data retrieved from different sources were again processed through GIS tool (ArcGIS®).

Field work is conducted to calculate the hydraulic conductivity. Mini disk infiltrometer (MDI) is used for the measurement (Fig. 3.3). It has a suction tube on

Table 3.1 Sources of data used

Parameters (data)	Mode	Sources
Depth to water	Interpolation	Collected data (depth to water table) from the booklet issued by CGWB (Central Groundwater Board), Imphal East, 2018
Net recharge	Integration	Rainfall data collected from CGWB, 2018, as per IMD (Indian Meteorological Department) from 2013 to 2017
Aquifer media	Digitisation	Aquifer data From booklet – East District by CGWB, 2018
Soil	Digitisation	Soil data from *Groundwater Information Booklet* Imphal East District, Manipur, by the Ministry of Water Resource, 2013
Topography (slope)	Spatial analyst tool	Developed from SRTM data in ArcGIS using spatial analyst tool with resolution30
Impact of vadose zone	Digitisation	Collected the lithology data from booklet – Imphal East District by CGWB, 2018
Hydraulic conductivity	Digitisation	Collected the data by using the mini disk infiltrometer (MDI), performing the experiment in different locations of Imphal East and calculated the hydraulic conductivity value using graph in excel sheet
Land use/land cover (LULC)	Spatial analyst tool	Developed from ESRI data (Sentinel-2 10m,) in ArcGIS using spatial analyst tool for 2021

top (7 cm) of suction regulation tube (10.2 cm) followed by mariotte tube (28 cm) and stainless steel porous disk (4.5 cm diameter, 3 mm thick). Water should be poured in regulation tube up to 10 cm and suction tube is inserted according to soil porosity nature. Volume of the mariotte tube in initial time is noted and volume is noted every 30 s. It can be continued until the difference of the initial and final volume is less than 30 ml. Then the cumulative is calculated by difference of initial and final volume divided by area of the infiltration. Thereafter, hydraulic conductivity is calculated by cumulative infiltration divided by area (from the Van Genuchten parameters according to the suction type and soil type). Different locations were selected for the measurement of hydraulic conductivity in the study region, and Fig. 3.3 shows the MDI at measurement site, that is, Napet Pali (local name).

3.4 Result

In this section, the derived input parameters in the form of raster and vector from the collected ground data will be provided along with the final weighted overlay result of groundwater vulnerability map. All the input parameters were derived using IDW (inverse distance weighting) method in ArcGIS®. The assigned weights and ranks of the parameters are also provided in table.

Fig. 3.3 Measurement of hydraulic conductivity using MDI at site

3.4.1   Input Parameters

3.4.1.1   Depth of Water

For mapping of parameter, *D*, depths (m) of certain locations of the study area are collected from CGWB (2018). Depth ranges from 0 to 9 m. Then using the coordinates of the locations, interpolation is done by IDW shown in Fig. 3.4 and classified as per Table 3.2.

3.4.1.2   Net Recharge

Next parameter, *R*, is calculated by the summation of rainfall for the year 2021. After the summation, the data is added in the tool, and then net recharge mapping is done
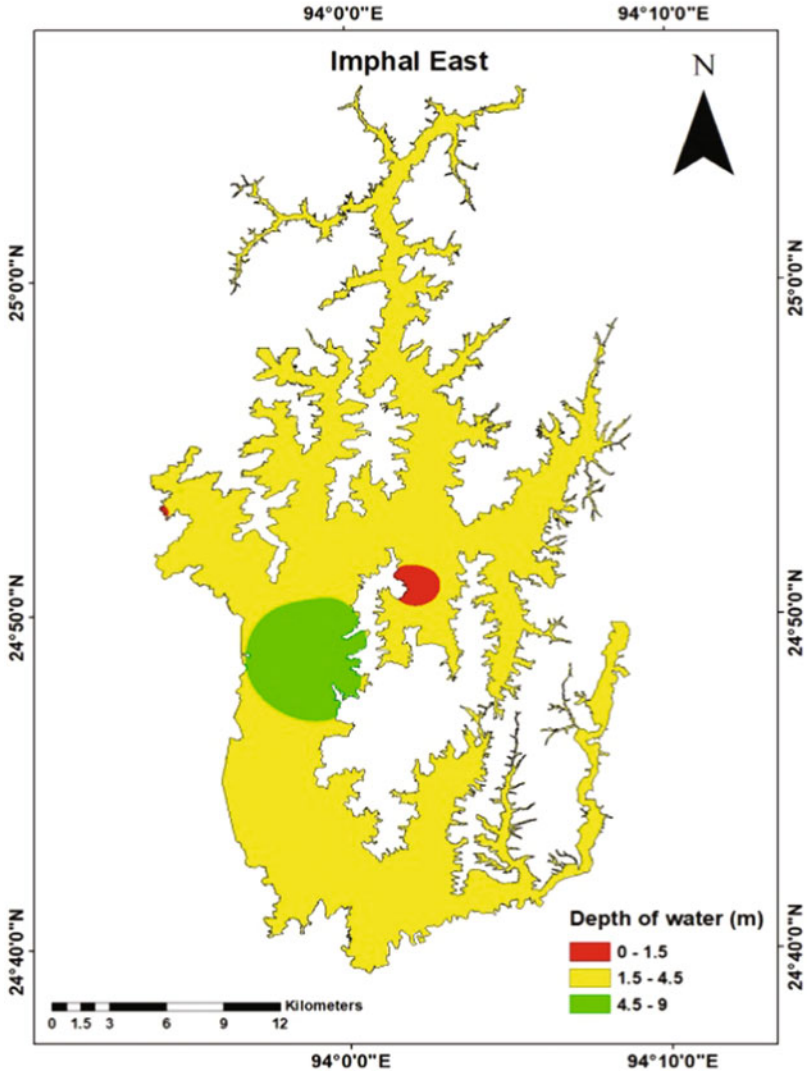
Fig. 3.4 Depth of water (m) map

through IDW using the coordinates of the study area, hence providing the map in Fig. 3.5. The sum of annual rainfall is about 1099 mm in the study area.

Table 3.2 Weight and rank assigned to the input parameters of DRASTIC-LU model and DRASTIC_AGRI models (Aller et al. 1985)

Parameters	Range	DRASTIC-LU		Agriculture DRASTIC	
		Weight	Rating	Weight	Rating
Depth of water (m)	0–1.5	5	10	5	10
	1.5–4.5		9		9
	4.5–9		7		7
Net recharge (mm)	10–99	4	9	4	9
Aquifer media	Sand, medium	3	10	3	10
	Sand, coarse		9		9
	Sand, gravel		8		8
	Gravel		7		7
Soil media	Loamy sand	2	6	5	6
Topography (% slope)	0–2	1	10	3	10
	2–6		9		9
	6–12		5		5
	12–18		3		3
	>18		1		1
Impact of vadose zone	Shale and siltstone	5	6	4	6
	Sand, silt and clay		3		3
Hydraulic conductivity (m/d)	0–4.1	3	1	2	1
Land use/land cover (LULC)	Water body	5	1	–	–
	Barren land		1		–
	Wet land		1		–
	Agriculture		8		–
	Built-up		7		–
	Crop land		7		–

3.4.1.3 Aquifer Media

Aquifer media is the medium that is beneath the water table of the ground, and Imphal East is mostly covered by sand and gravel (CGWB 2018). Like the other parameters, mapping is done through IDW shown in Fig. 3.6 for aquifer media.

3.4.1.4 Soil Media

Soil media data is collected from CGWB (2018) & Ground water Information (2013) and interpolated using IDW. Soil type of the study area is mostly covered by loamy sand. The map of the soil type is shown in Fig. 3.7.
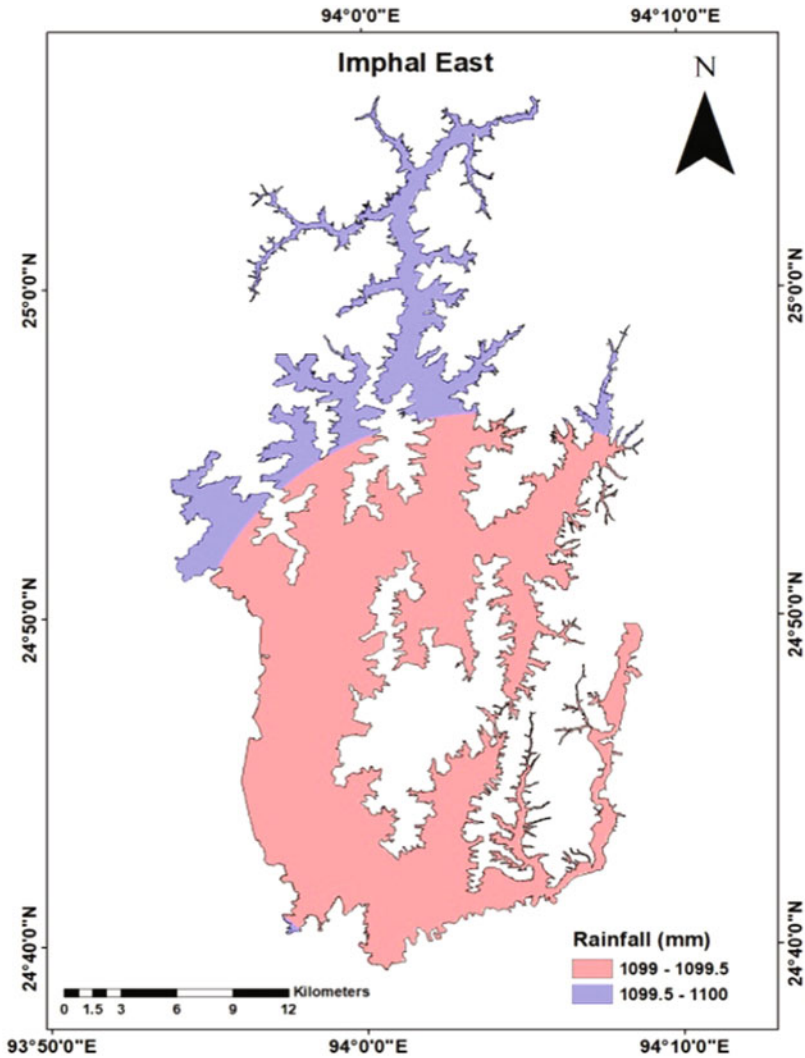
Fig. 3.5 Rainfall (mm) map

3.4.1.5 Topography

Topography is the percentage slope. The DEM (digital elevation model) is downloaded from earth explorer website.

Using the slope tool in ArcGIS, the percentage has been calculated and further classified as per Table 3.2. The map in Fig. 3.8 represents the slope in percentage of the area ranges from 0 to >18.
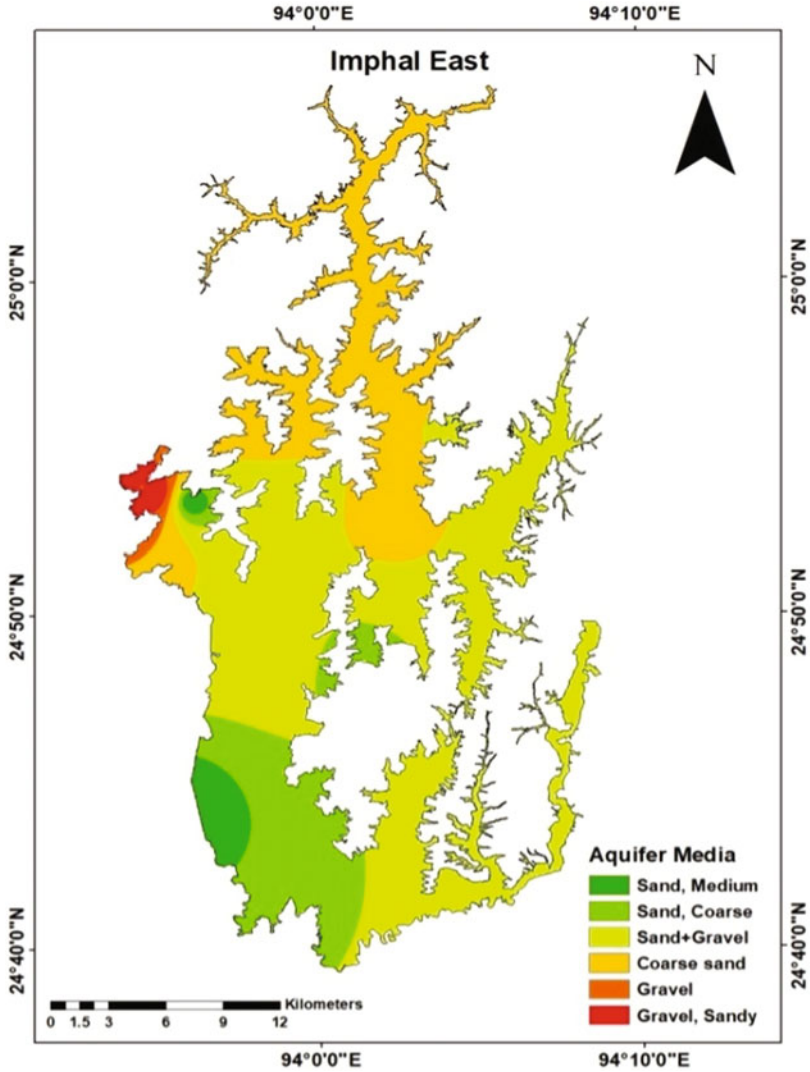
Fig. 3.6 Aquifer media map

3.4.1.6 Impact of Vadose Zone

Impact of vadose zone is the zone just beneath the soil surface which is followed by
the aquifer media. For Imphal East, sand silt and clay and shale and siltstone
constitute the vadose zone which are shown in Fig. 3.9.
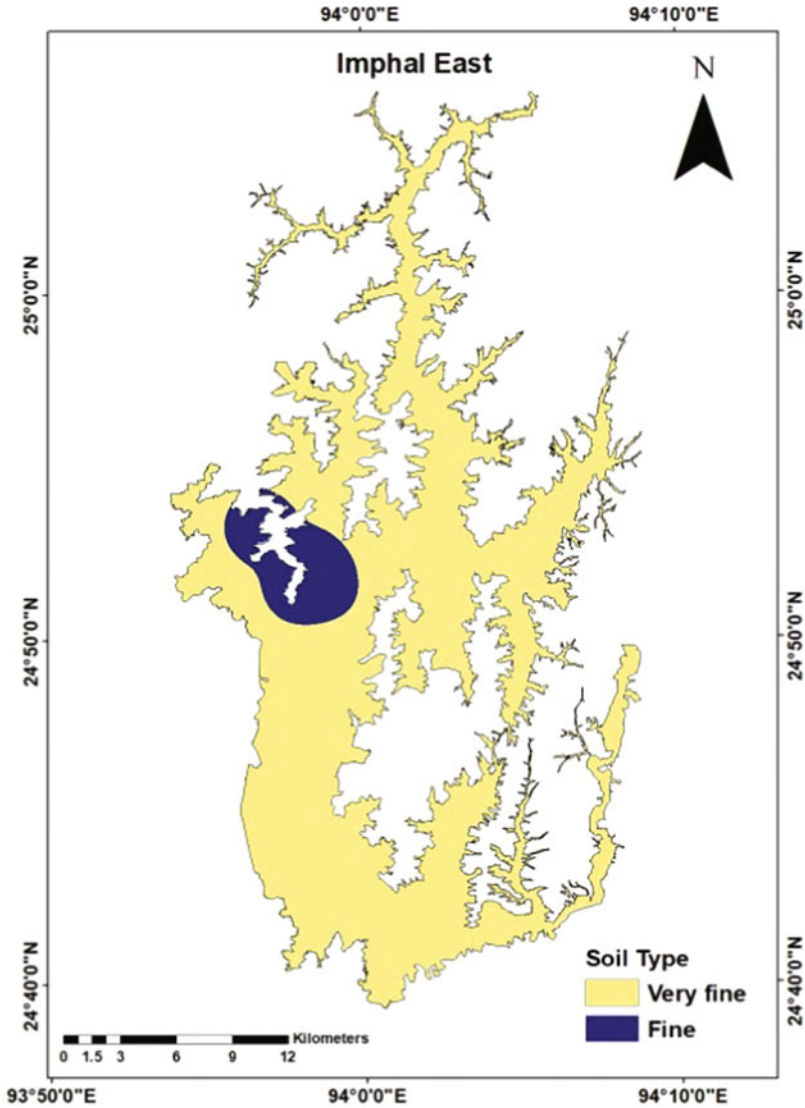
Fig. 3.7 Soil type map

3.4.1.7 Hydraulic Conductivity

Hydraulic conductivity is calculated using the mini MDI at different locations of the study area. In the field work, the volume change is the tube of the mini disk infiltrometer noted in the time interval of 30 s. Then, the collected data is analysed in excel sheet and value of hydraulic conductivity is provided in m/d. Interpolating the values of it, map is generated provided in Fig. 3.10.
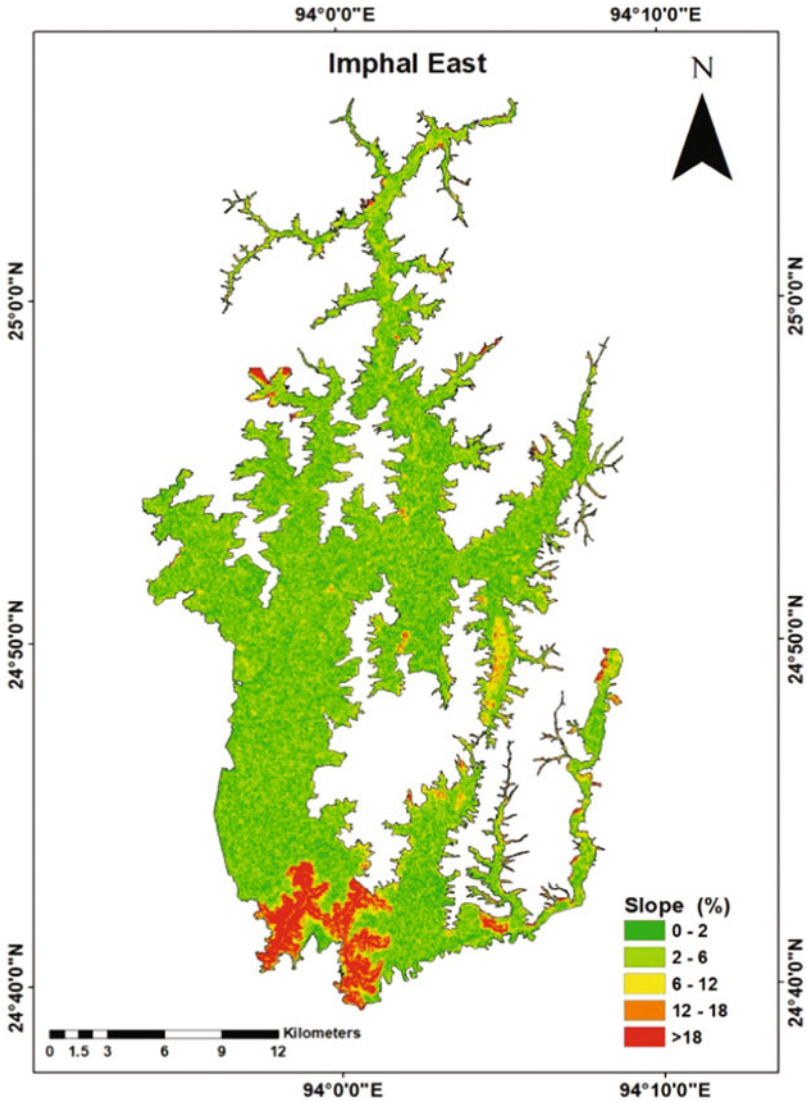
Fig. 3.8 Slope (%) map

3.4.1.8 Land Use/Land Cover

Another parameter for DRASTIC-LU model, LULC, is included with the seven parameters. And the weight assigned to this parameter is 5 which is the highest range of the assigned weight in DRASTIC model. Different parts of LULC include water body, barren land, wet land, agriculture, built-up and crop land as shown in Fig. 3.11. This parameter is prepared from ESRI data in spatial analyst tool for
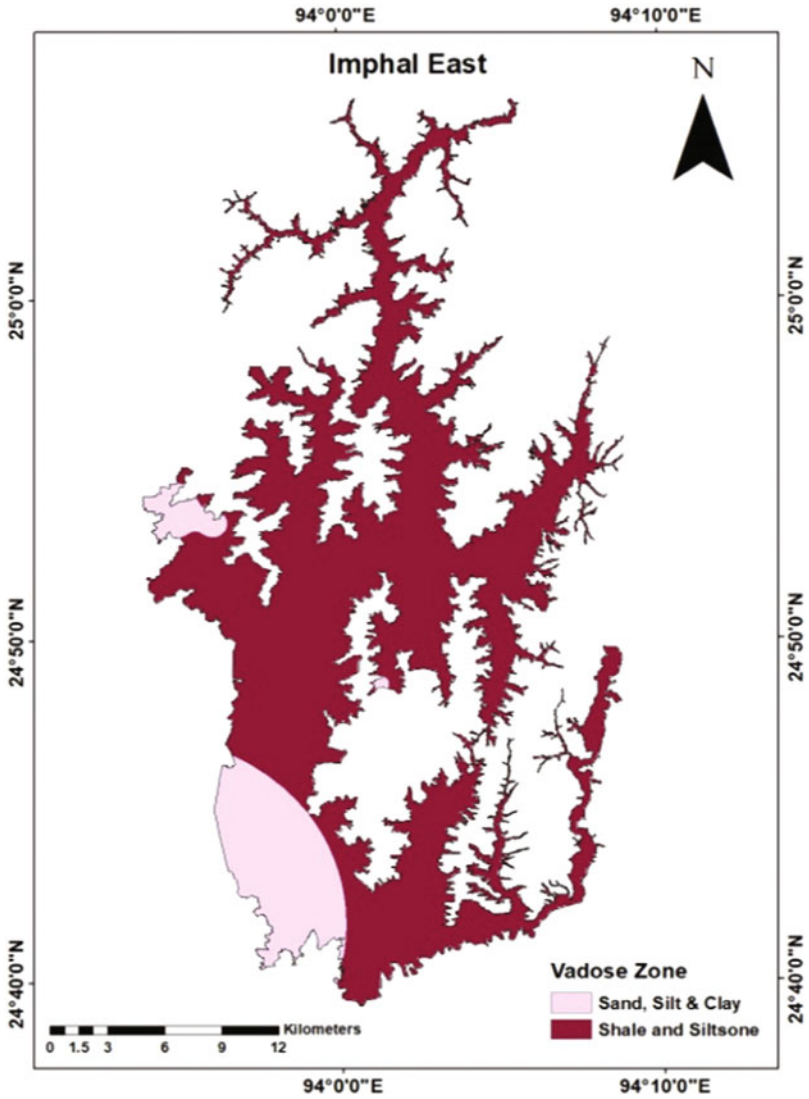
Fig. 3.9 Vadose zone map

2021. After generating all the required parameters, the respective weights and ranks are assigned which are shown in Table 3.2.
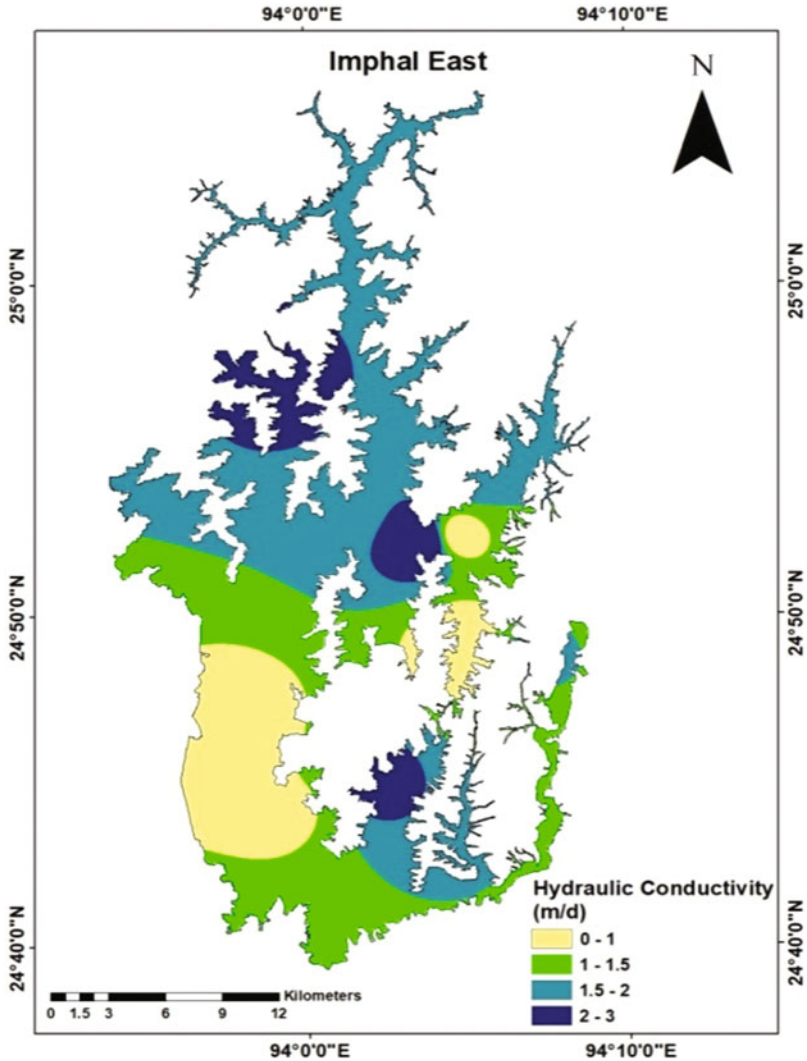
Fig. 3.10 Hydraulic conductivity (m/d) map

3.4.2 DRASTIC_AGRI Vulnerability Index

Using the above seven maps (Figs. 3.4, 3.5, 3.6, 3.7, 3.8, 3.9 and 3.10), a weighted overlay analysis is performed and generated a final map (Fig. 3.11). After reclassifying the seven maps according to their relative rates from 1 to 10 which was given in Table 3.2, the maps are layered over to the raster calculated in spatial analyst tool. As per the assigned weights in Table 3.2, the weights are multiplied with their rates, and then, the DRASTIC_AGRI vulnerability index is calculated and
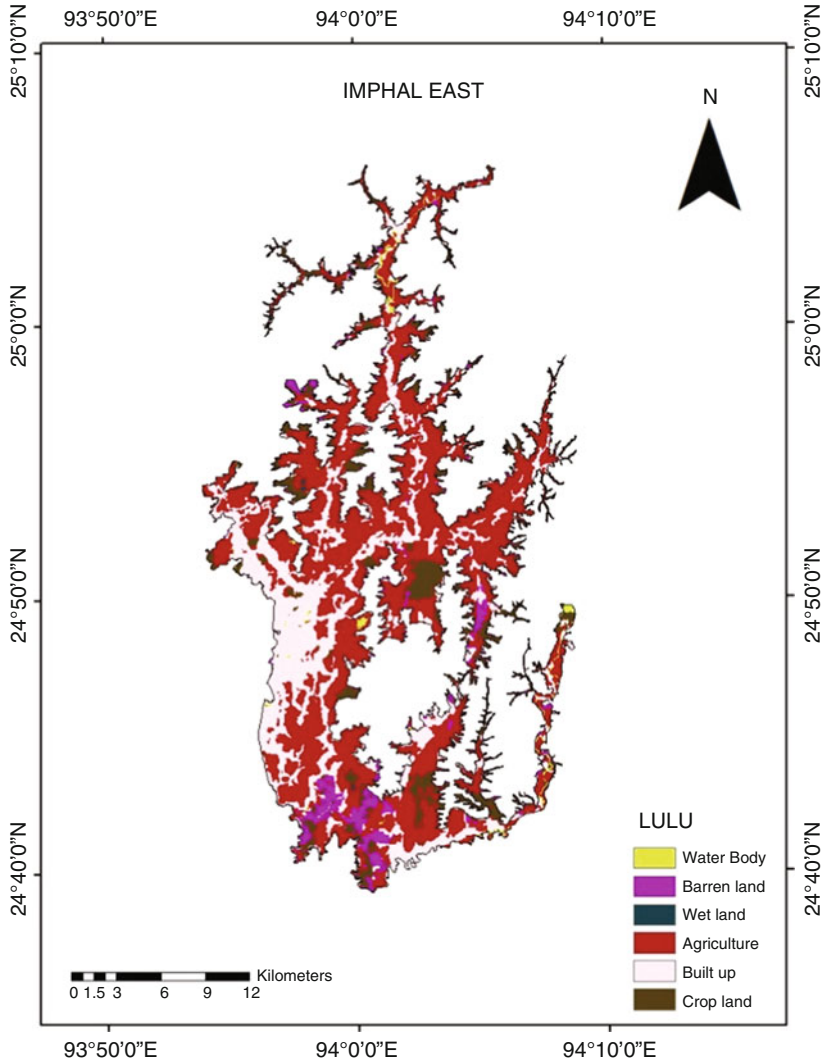
Fig. 3.11 LULC map

is given in Fig. 3.12. It shows different levels of vulnerable area in the study region and is classified into three levels as low vulnerability (8%), moderate vulnerability (12%) and high vulnerability (80%) presented in Fig. 3.11. It is observed that the index ranges from 130 to 173 and the northern part of the district is comparatively high from other parts of the district.
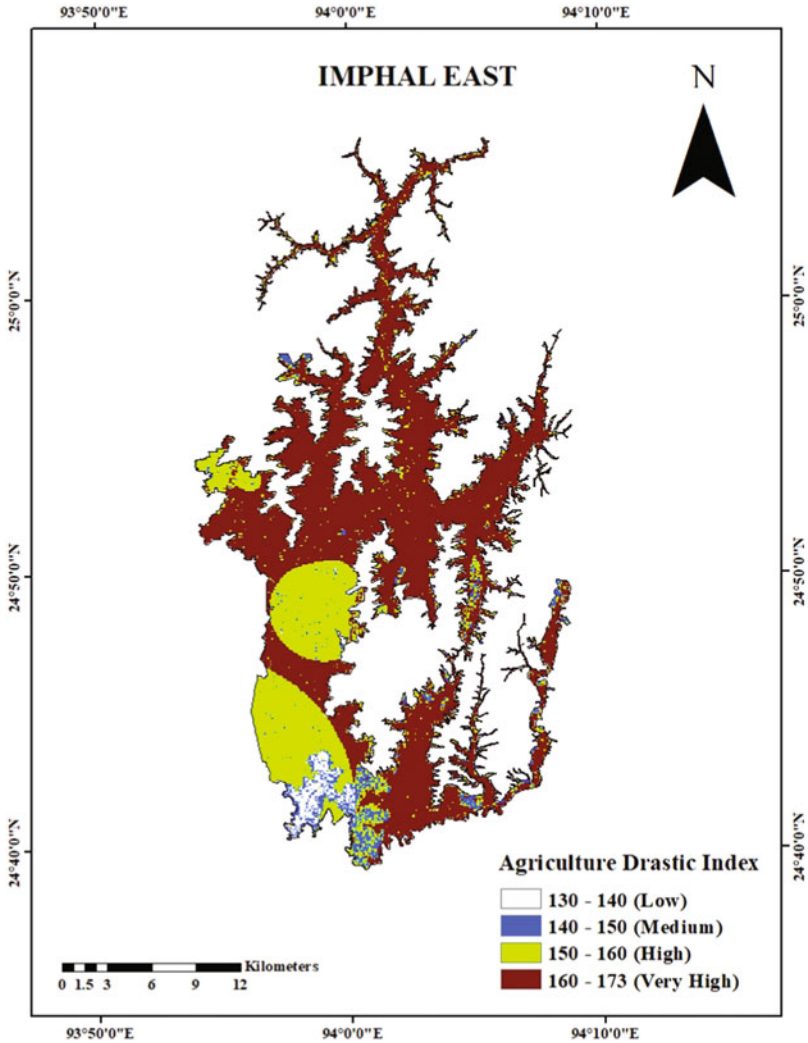
Fig. 3.12 DRASTIC_AGRI vulnerability index map

3.4.3 DRASTIC-LU Vulnerability Index

Using the eight parameters (Figs. 3.4, 3.5, 3.6, 3.7, 3.8, 3.9, 3.10 and 3.11) which are included in the LULC map, an overlay map is performed and a final map is generated (Fig. 3.12). And procedure is repeated as same as the above index, but in this index, LULC is included and the weights assigned to the eight parameters which are different from DRASTIC_AGRI model because the importance of the parameter to the corresponding index is different. But the rating is same as shown in Table 3.2 and DRASTIC-LU index ranges from 120 to 182 (Fig. 3.13).
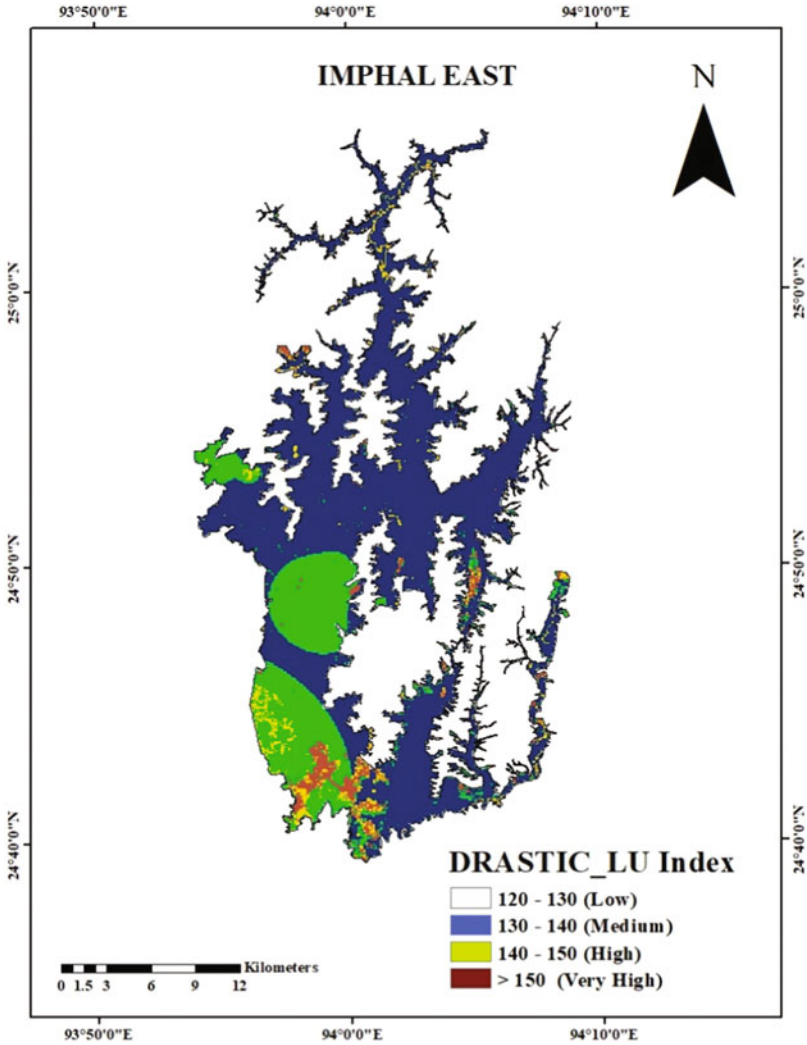
Fig. 3.13 DRASTIC_LU index map

3.4.4 Validation

Total dissolved solid (TDS) is the presence of different qualities which include salts, minerals, metals and other dissolved substances in a given volume of water. It is considered to be one of the parameters for health of water. To validate the vulnerability of the study area, the presence of chemical in groundwater like nitrate, ph, TDS, etc. can prove the pollution of groundwater if the index and chemical value is linearly correlated. In thus study, the predicted DRASTIC_AGRI and DRASTIC_LU indexes are plotted with TDS data collected from the Central Ground
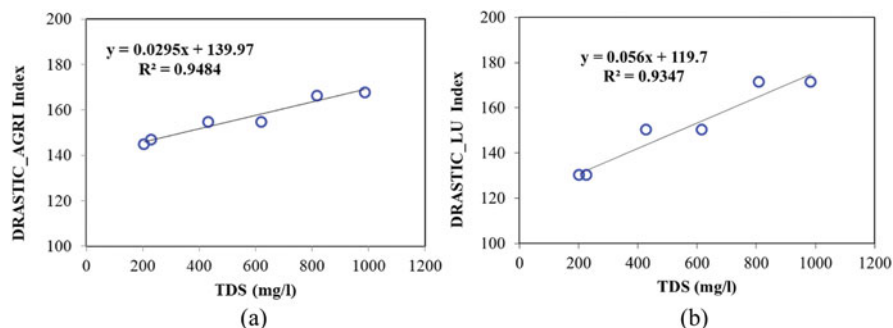
Fig. 3.14 Comparison of modelled DRASTIC indices and TDS value: (a) DRASTIC_AGRI and (b) DRASTIC_LU model

Table 3.3 Predicted groundwater vulnerability of DRASTIC_AGRI and DRASTIC_LU model

Vulnerability category	DRASTIC_AGRI		DRASTIC_LU	
	Area	%	Area	%
Low	7.236	1.895	12.351	3.240
Medium	18.278	4.787	19.201	5.038
High	100.491	26.320	83.949	22.026
Very high	255.794	66.997	265.638	69.696

Fig. 3.15 Comparison of groundwater vulnerability between DRASTIC_AGRI and DRASTIC_LU models
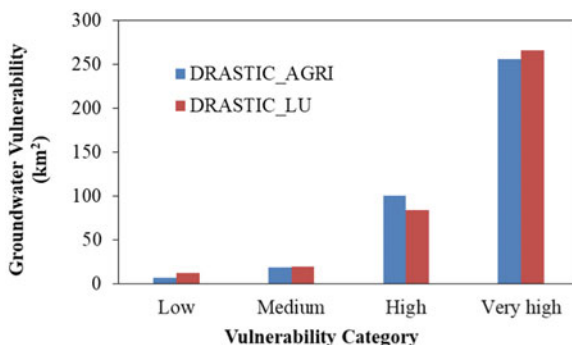
Water Board (CGWB), Government of India, for the year 2018 and are shown in Fig. 3.14a and b, respectively. Both the figures depicted that the predicted indexes (it directly indicates the quality of groundwater) are linearly correlated ($R^2 = 0.934$, $R^2 = 0.948$) with the collected ground data of TDS (mg/l) and are considered reasonable for modelling and simulation studies.

3.5 Discussion

The predicted groundwater vulnerabilities of DRASTIC_AGRI and DRASTIC_LU are compared and presented in Table 3.3. The area-wise predicted vulnerability is also plotted in Fig. 3.15. Out of the four classified categories (low, medium, high and

very high) of groundwater vulnerability, in both models, the very category is the highest in area (67%). This is a clear indication that the study region is significantly affected by groundwater contamination and is a warning sign to all concerned stakeholders. Even the high vulnerability category has reached up to 22% (DRASTIC_LU) or 26% (DRASTIC_AGRI). From Fig. 3.15, it depicts that the two methods predict equal amount of vulnerability.

As the purpose of the two models is different, they give different ranges of vulnerability. As the R^2 value is higher in the DRASTIC_AGRI model when compared with the TDS value than in the other model (DRASTIC_LU), it can be interpreted that DRASTIC_AGRI is slightly more efficient in predicting groundwater vulnerability in this study region. Therefore, DRASTIC_LU is over predicting, which can also be understood from the higher predicted index range by this model, that is, the index range predicted by DRASTIC_LU (index range is 120–182) is higher than that predicted by DRASTIC_AGRI (index range is 130–173), which means that the assumption of this model by giving more emphasis on LULC can be unsuitable. This also indicates that there is no significant effect of LULC in this study region. Farmers and local people can use this data to grow and select suitable crops in the region.

3.6 Future Scope

DRASTIC_LU and DRASTIC_AGRI are modified from the original DRASTIC model, which is a more accurate and better version. Likewise, different modified models are available in GIS technology, and these are the future scope of the model. For advanced technology, the AHP (analytic hierarchy process) method can also be used in this model with different weights and ranks for different parameters of the model. The AHP model considers the effect of each DRASTIC factor on the vulnerability cycle and provides a comparison of the values of the variables, the normalisation and the computing consistency ratio (CR). When applying the AHP method, the power of significance (as per Saaty's scale) between the two variables is filled in a matrix format using ground truth data, field characteristics and subject matter specialists' views, which may make the approach more efficient than the other models. Such values have been simplified to reflect the influence of the subjectivity involved in the weight assignment process. In any model, seven parameters will remain the same, which act as base parameters, and in a modified (new model) model, the required parameter, which is more weighted to the contamination of groundwater, is added. Similarly, different methods, that is, (i) overlay and index-based methods (applied in this present study), (ii) process-based simulation models, (iii) statistical methods and (iv) hybrid methods, can be applied and compared for an efficient result that can be completely relied upon for any management planning. Another future scope would be expanding the study area to other districts of the state so that a larger scenario of groundwater can be understood in the state, which will help in efficient planning of groundwater vulnerability monitoring strategies.

3.7 Conclusion

As the DRASTIC_AGRI index ranges from 130 to 173, it indicates high vulnerability to groundwater pollution and contamination in the region, which may affect agricultural practises and yield. Similarly, the calculated DRASTIC_LU index ranges from 120 to 182, which indicates that groundwater contamination is high and may affect the overall ecosystem of water resource management in the region. Therefore, agricultural practices should be monitored, especially in terms of crop and fertiliser management (reducing or avoiding pesticides), and proper zoning should be done for low vulnerability (pesticides allowed with conditions) and high vulnerability (pesticides free). Then, zone-wise and its agricultural practices may be adopted. It is also not recommended to use the groundwater directly before it is treated, and further to confirm its chemical presence, a laboratory test may be conducted.

References

Ahirwar R, Malik MS, Shukla JP (2022) Groundwater vulnerability assessment of Hoshangabad and Budni industrial area, Madhya Pradesh, India, using geospatial techniques. Applied Water Sci 12:250. https://doi.org/10.1007/s13201-022-01771-8

Aller L, Bennett T, Lehr JH, Petty RJ (1985) DRASTIC: A standardized system for evaluating groundwater pollution potential using hydrogeologic settings. US EPA, Environmental Research Laboratory, Ada, Oklahoma, EPA/600/2-85/0108

Baghapour MA, Nobandegani AF, Talebbeydokhti N, Bagherzadeh S, Nadiri AA, Gharekhani M, Chitsazan N (2016) Optimization of DRASTIC method by artificial neural network, nitrate vulnerability index, and composite DRASTIC models to assess groundwater vulnerability for unconfined aquifer of Shiraz Plain. Iran J Environ Health Sci Eng 14:13

Barbulescu A, Nazzal Y, Howari F (2020) Assessing the Groundwater Quality in the Liwa Area, the United Arab Emirates. MDPI 12:10

Bera A, Mukhopadhyay BP, Chowdhury P, Ghosh A, Biswas S (2021) Groundwater vulnerability assessment using GIS-based DRASTIC model in Nangasai River Basin, India with special emphasis on agricultural contamination. Ecotoxicol Environ Saf 214:1–11

Census (2011) District population report, Government of Manipur

Central Ground Water Board (CGWB) (2018) Ministry of Jal Shakti. Aquifer Mapping and Management Plan Imphal East District, Manipur

Dregulo AM, Bobylev NG (2021) Integrated Assessment of Groundwater Pollution from the Landfill of Sewage Sludge. J Ecol Eng 22:68–75. https://doi.org/10.12911/22998993/128872

Ersoy AF, Gültekin F (2013) DRASTIC-based methodology for assessing groundwater vulnerability in the Gümüşhacıköy and Merzifon basin (Amasya, Turkey). Earth Res J 17:33–40

Farooqi A, Masuda H, Siddiqui R, Naseem M (2009) Sources of arsenic and fluoride in highly contaminated soils causing groundwater contamination in Punjab, Pakistan. Arch Environ Contam Toxicol 56:693–706

Ground Water Information Booklet Imphal East District, Manipur by Ministry of Water Resources (2013)

Gupta LK, Pandey M, Raj PA, Shukla AK (2023) Fine sediment intrusion and its consequences for river ecosystems: a review. J Hazardous Toxic Radioactive Waste 27(1):04022036. https://doi.org/10.1061/(ASCE)HZ.2153-5515.0000729

Indulekha VP, Thomas CG, Anil KS (2019) Utilization of water hyacinth as livestock feed by ensiling with additives. Indian J Weed Sci 51:67–71

Khosravi K, Sartaj M, Karimi M, Levison J, Lofti A (2021) A GIS-based groundwater pollution potential using DRASTIC, modified DRASTIC, and bivariate statistical models. Environ Sci Pollut Res 28:50525–50541

Machdar I, Zulfikar T, Rinaldi W, Alfiansyah Y (2018) Assessment of groundwater vulnerability using DRASTIC Model and GIS : A case study of two sub-districts in Banda Aceh city. Indonesia; IOP Conf: Material Sci Eng 334:012032

Malakootian M, Nozari M (2020) GIS-based DRASTIC and composite DRASTIC indices for assessing groundwater vulnerability in the Baghin aquifer, Kerman. Iran J European Geosci Union 20:20–2351

Malik MS, Shukla JP (2019) GIS modeling approach for assessment of groundwater vulnerability in parts of Tawa river catchment area, Hoshangabad, Madhya Pradesh. India Groundw Sustai Dev 9:100249

Mendoza JA, Barmen G (2006) Assessment of groundwater vulnerability in the Rıo Artiguas basin, Nicaragua. Environ Geol 50:569–580. https://doi.org/10.1007/s00254-006-0233-1

Novotny V (1999) Diffuse pollution from agriculture - A worldwide outlook in USA. Water Sci Tech 39:1–3

Pal SC, Chakrabortty R, Arabameri A, Santosh M, Saha A, Chowdhuri I, Roy P, Shit M (2022) Chemical weathering and gully erosion causing land degradation in a complex river basin of Eastern India: an integrated field, analytical and artificial intelligence approach. Nat Hazards 110:847–879. https://doi.org/10.1007/s11069-021-04971-8

Raju NJ (2022) Arsenic in the geo-environment: A review of sources, geochemical processes, toxicity and removal technologies. Environ Res 203:111782. https://doi.org/10.1016/j.envres.2021.111782

Reynolds T, Barrett S, Dray L, Evans A, Kohler M, Morales MV (2007) Modelling Environmental and Economic Impacts of Aviation: Introducing the Aviation Integrated Modelling Project. 7th AIAA Aviation Tech, Integration and Operations Conf, Northern Ireland, 18–20 September 2007

Saha D, Alam F (2014) Groundwater vulnerability assessment using DRASTIC and Pesticide DRASTIC models in intense agriculture area of the Gangetic plains, India. Environ Monit Assess 186:8741–8763

Saikumar G, Pandey M, Dikshit PKS (2022) Natural river hazards: their impacts and mitigation techniques. In: River dynamics and flood hazards: studies on risk and mitigation. Springer, Singapore, pp 3–16

Sarkar M, Pal C (2021) Application of DRASTIC and Modified DRASTIC Models for Science Modeling Groundwater vulnerability of Malda District in West Bengal. J Indian Soc Remote Sens 49:1201–1219

Singh AK (2015) Advances in Indian Coldwater Fisheries and Aquaculture. J FisheriesSciencescom. 9(3):048–054

Singh NM, Devi TT (2022) Assessment and Identification of Drought Prone Zone in a Low Laying Area by AHP and MIF Method: A GIS Based Study. IOP Conf. Series: Earth and Environmental Science, p 1–12

Urseler N, Bachetti R, Morgante V, Agostini E, Morgante C (2022) Groundwater quality and vulnerability in farms from agricultural-dairy basin of the Argentine Pampas. Environ Sci Pollut Res 29:63655–63673

Wang N, Liu Q, Xie B, Huang X, Xiao D (2022) Tannin-coated PVA/PVP/PEI nanofibrous membrane as a highly effective adsorbent and detoxifier for Cr(VI) contamination in water. Sep Purif Technol 303:122164. https://doi.org/10.1016/j.seppur.2022.122164

Xie J, Liu Y, Wu Y, Li L, Fang J, Lu X (2022) Occurrence, distribution and risk of pharmaceutical and personal care products in the Haihe River sediments, China. Chemosphere 302: 134874. https://doi.org/10.1016/j.chemosphere.2022.134874

Chapter 4
Flood Hazard Mapping Using Hydraulic Models and GIS: A Review

Liza G. Kiba, Grace Nengzouzam, and Prem Ranjan

Abstract Floods are a natural event and are among the most frequent and destructive disasters, causing major infrastructure losses and disrupting livelihoods around the world. Floods are most often caused by extreme hydro-metrological and natural forces, but over the past decade, climate change and human response have added new dimensions. There is a wide array of flood risk management methods that can reduce this destruction, which requires estimating flood risks and their impacts. Preventive measures such as efficient land use planning, flood mapping, and implementation of other agronomical and engineering structures are essential in mitigating the hostile impacts of flood. Flood hazard estimation and mapping can be carried out using various methods depending on data, resources, and time availability. In contrast, flood assessment with the creation of the Geographic Information Systems (GIS) database for the flood zone and hydraulic modelling software such as HEC-RAS and HEC-HMS has proven to be useful for flood assessment. GIS can accurately predict the extent of flooding and produce flood maps, as well as flood damage estimation maps and flood hazard maps. Flood hazard maps can be analysed to provide advance warnings for general preparation and, if needed, evacuation. It is, therefore, one of the most significant tools for flood risk management.

Keywords Floods · GIS · HEC-RAS · HEC-HMS · Flood hazard maps

L. G. Kiba (✉)
Department of Agricultural Engineering, SAS, Nagaland University, Medziphema, India

G. Nengzouzam
Department of Agricultural Engineering, SET, Nagaland University, Dimapur, India

P. Ranjan
Department of Agricultural Engineering, NERIST, Nirjuli, Arunachal Pradesh, India

4.1 Introduction

Flood, a natural catastrophe, affects several regions of the globe, both developed and developing countries. Any natural phenomenon can be defined as a hazardous event if it occurs with the likelihood of causing loss or damage settlements. Flood hazards are among the most common and destructive disasters, causing extensive damage and disrupting livelihoods worldwide. The impact of floods can vary worldwide due to geographical, agricultural, and economic reasons. Although flood calamities are primarily caused by natural events, their repercussions have been increased as a result of human activities. Urbanisation in developing countries and the rapid growth of the associated population lead to the increase of uncontrolled and unplanned development activities (Shah et al. 2020). The development activities involve floods, and flood in plain areas in the cities can potentially increase loss of life and damaging properties. Thus, to minimise the risk of flooding and associated hazards and losses, it is essential to disseminate accurate and reliable information to the public in the form of flood inundation maps. The primary purpose of flood risk assessment is to gain a good understanding of the likelihood of floods of a given intensity occurring over a long period of time. Through this approach, individuals can implement precautionary measures and actions to minimise the impact of floods.

The mixture of human vulnerability and physical exposures results in flood hazards. It is difficult to control floods, but we can take measures to minimise their impact. Identifying the right measures to deal with floods is a difficult task. The stages involved in flood disaster management include prediction, preparedness, prevention, reduction, and damage assessment. The flood peril areas can be identified by flood hazard assessment and mapping. It also improves flood risk management and disaster preparedness. The anticipated degree and depth of flooding in a particular site under different scenarios can be assessed through flood hazard assessments and mapping.

Changing land use planning, creating emergency response plans, implementing specific flood protection measures, etc. are measures that can improve flood management preparedness. Flood risk assessments can be broadened to assess specific risks, taking into account the socio-economic characteristics of exposure areas.

The generation of flood inundation map is greatly promoted from the development of modelling and remote sensing (RS) and geographic information system (GIS) techniques (Bera et al. 2012). The flood risk areas can be identified by combining hydrologic models with RS and GIS by using hydrological models such as Hydrologic Engineering Centres-River Analysis System (HEC-RAS) and Hydrologic Engineering Centres-Hydrologic Modelling System (HEC-HMS). Apart from the identification of areas under flood hazard, floods can also be predicted.

For flood hazard assessment and mapping, the key components required are digital elevation models (DEMs) for generating the topographical features of the region and hydrological models for simulating several flood events and its effects. Generating flood inundation maps is greatly influenced by the resolution of the DEM, as higher-resolution DEMs tend to produce more reliable and precise maps

compared to lower-resolution DEMs (Ogania et al. 2019). Apart from DEM, various dataset such as land cover data, soil data, and meteorological data are also needed. GIS software such as ArcGIS, QGIS, and IGIS may be required for generation of maps. This software can also act as a visualisation tool.

Topographic data may be gathered (satellite data) or existing topographic datasets may be used. The use of GIS software enables the mapping of the depth and extent of flooding by measuring local land elevations in response to extreme water levels. Hydrological and historical data on floods, precipitation patterns, and climate data are required to simulate flood modelling, and these variables are used to estimate flooding depth and extent in various scenarios. This identification of high-risk flood zones allows planners to improve awareness and response. Integrated approaches that incorporate flood hazard assessments and associated maps can be implemented by land use and development planners to improve flood preparedness, enhance land developments, and increase community awareness.

This paper has presented the different case studies related to flood disaster management and successful implementation of GIS for mapping hazard maps. This work reflects the effectiveness and applicability of different flood hazard mapping methodologies. Successful implementation of flood hazard mapping will not only provide essential information on flood hazards but also enhance management and land use planning measures by limiting development in flood-prone areas.

4.2 Methodology

Flood hazard management is a critical task that involves identifying potential flood-prone areas and taking preventive measures to minimise flood risk. The following three phases can explain the methodology involved in developing a flood hazard map: (a) preparing/acquiring a DEM using ArcGIS, (b) simulating flood flows for various return periods using hydraulic models, and (c) producing flood risk maps by integrating the output from phase (a) and phase (b).

The initial phase is creating a flood hazard map (FHM) consisting of collecting and organising appropriate data. This involves acquiring data on the study region, topography, hydrology, land use, rainfall patterns, and climate data, from a range of sources, such as satellite imagery, ground surveys, and existing databases. The collected data is then processed and structured into an appropriate format for use in flood hazard modelling.

The second phase involves the utilising of the collected data to establish a flood hazard model. RS and GIS techniques are utilised to process the data and create a hydrological model that can forecast water behaviour in the area. The main objective of the model is to define and predict the higher-risk area of flooding.

The third phase incudes the generation of FHM based on the second phase which shows the areas at higher risk of flooding and the potential degree of the flood. The map can also be used to identify areas where flood mitigation measures are needed, such as constructing flood walls or implementing land use changes. The map can
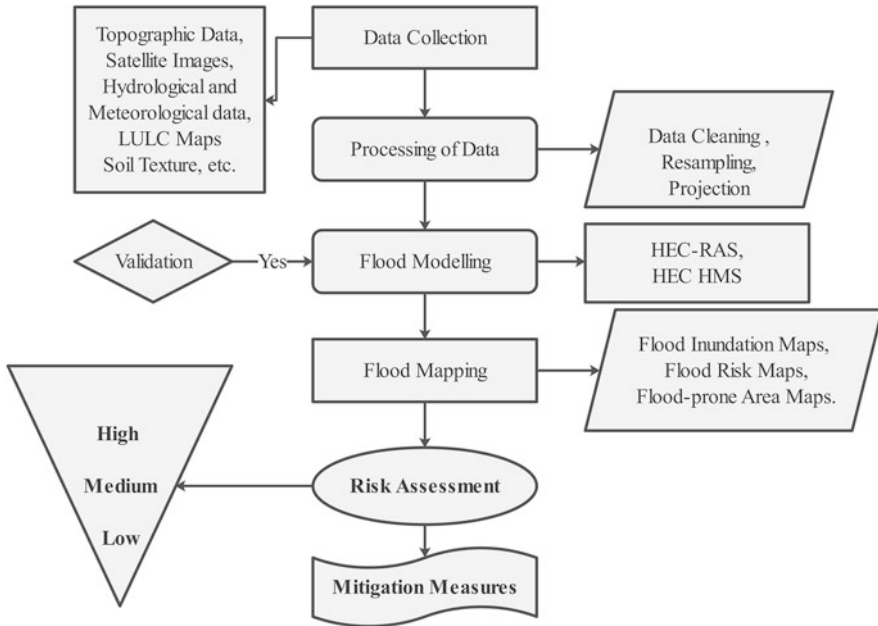
Fig. 4.1 Flowchart of flood hazard management

also be used for emergency planning and response, as it helps authorities to identify areas that are most at risk and to develop appropriate measures to mitigate the impact of flooding. The steps involved in flood hazard management using remote sensing (RS)-GIS and hydrological modelling are shown in Fig. 4.1.

4.3 HEC-RAS and HEC-HMS Model

The hydraulic model HEC-RAS, developed by the US Army Corps of Engineers (USACE), is commonly utilised to estimate the hydraulic characteristics of streams and rivers; this model allows the user to input data and obtain output on the screen and conduct further investigations. Besides the energy conservation equation, HEC-RAS needs data on river cross-sections and upstream flow rate to determine the depth and mean velocity of the river (Fan et al. 2009). By using GIS, the variation of water levels along the channel, which can be superimposed on a DEM of the region, can be computed by HEC-RAS to determine the extent and depth of flooding.

The hydraulic model of flood-prone areas using HEC-RAS in RS and GIS was created to generate the flood hazard maps for northern Thailand's Ping River Basin (Duan et al. 2012). The flood-inundated areas and flood depths of Chiang Mai province for the year 2005 were prepared by employing the HEC-RAS

one-dimensional flood model. The accuracy of model was validated by cross-checking the model outputs with the RS image.

In another study carried out for Greece, the flood-inundated area maps were generated for different areas, where both the similarities and differences were showed (Panagoulia et al. 2013). The hydrologic processes for the given return period were simulated by using HEC-HMS software, and hydrographs were prepared. Several simulations related to the hydraulics of open channel flow were conducted using ArcGIS-compatible HEC-RAS software. They concluded that prioritising and planning flood protection measures in the early phase are vital in generating flood inundation maps.

HEC-RAS model along with GIS was used for the Mert River Basin, Turkey, to prepare the flood hazard maps (Demir and Kisi 2015). They employed ArcGIS software to digitise the topographical data and finally generate DEM. Using HEC-RAS software, simulation of flood values was performed. Their output was integrated to prepare the flood risk maps.

HEC-RAS was integrated with GIS to delineate flood depths and degrees for Nam Phong River in northeast Thailand (Nut and Plermkamon 2015). The steady flow simulated flood along 148 km of the river and floodplain mappings for different return periods were derived. The researchers concluded that incorporating hydraulic simulation with GIS could improve the efficiency and accuracy of floodplain mapping and management. Moreover, ArcGIS and HEC-RAS provide powerful tools for planners and decision-makers.

Romali et al. (2018) evaluated the competence of the HEC-HMS model in flood risk assessment by comparing the observed historic data with the simulated result for certain flood events of Segamat Town, Malaysia. Using Nash-Sutcliffe model efficiency as a performance indicator, both model calibration and validation were carried out. The calibration and validation periods were evaluated using Nash-Sutcliffe efficiency values of 0.90 and 0.76, respectively.

The one-dimensional HEC-RAS model in combination with GIS was also used to create FHM of Ajay River basin, where parts of Jharkhand and West Bengal contribute to the drainage basin (Chakraborty and Biswas 2020). They classified FHM in five distinct categories based on various return periods, that is, very low, low, moderate, high, and very high. The damage to land use and population was quantified in detail with the aid of the map produced based on distinct classifications.

Multispectral data from Landsat-8 OLI and Sentinel-2, as well as DEM data from Aster (30 m) and Cartosat (10 m), were used in HEC-RAS and RAS mapper to make flood inundation maps of the sub-watershed Imphal River Basin in Manipur (Bipinchandra et al. 2019). The study's results gave a good look at how floods affect the area where the study was done.

A framework was made to use GIS, HEC-HMS, and HEC-RAS to model floods on a regional scale in the Indian city of Hyderabad (Rangari et al. 2019). Flood inundation maps were made based on three floods that happened in the city: one in July 1989, one in August 2000, and one in August 2008. Flood inundation maps were made that showed both the areas at risk and the places where flooding was likely to happen.

HEC-RAS 5.0.7 and Global Flood Monitoring System (GFMS) tools were employed to identify flood risk zones and delineate flood extent in Prayagraj, India, at the conjunction of River Gange and Yamuna (Sangam) (Kumar et al. 2020). When compared, the estimated data was found to be in close proximity to the observed data indicating the applicability of HEC-RAS and GFMS data/tools together.

4.4   Other Methods

Flood risk maps for the Guwahati Municipal Corporation (GMC) Area, Assam, were prepared by performing field surveys and contacting several governmental bodies to collect information and identify the major causes of the flood (Barman and Goswami 2009). Using Erdas and ArcGIS, they generated the FHM by integrating the collected information and presented the flood-vulnerable areas of the study area.

Another study was carried out for Dikrong River Basin in Arunachal Pradesh where flood-prone areas were mapped using GIS (Bhadra et al. 2011). A comparison was made between the generated inundation maps with already published maps under Brahmaputra Board Master Plan for the study area. They observed a very low differences (<5%) between modelled and reported map inundation areas, indicating successful application. They also determined that using GIS techniques is a cost-effective and dependable approach for producing flood inundation maps in areas with undulating topography such as Dikrong.

In order to create composite flood hazard index for Ghana, an additive model was proposed where topographical, land cover, and demographic data were used (Forkuo 2011). A district-level map of flood-prone areas and maximum flood hazard zones were generated using GIS. The study further reconfirms the conclusion made by other researchers (Barman and Goswami 2009; Bhadra et al. 2011) on the applicability of GIS in flood hazard mapping.

Flood inundation maps were developed for the Dep River Basin, Nigeria, where flood occurs at different severities every year (Daffi et al. 2014). Using GIS software, they generated flood-inundated area maps based on different return periods for the river basin. They found that area under agriculture sector was affected the maximum ($68.82–146.10 \text{ km}^2$ for return periods of 2–1000 years).

To create a high-resolution FHM, Giustarini et al. (2015) created a high-resolution hazard map by using a global inundation model from the European Centre for Medium-Range Weather Forecasts and a large collection of ENVISAT ASAR imagery. Their study showed that the combination of these methods was more beneficial than the conventional numerical modelling approach for producing high-resolution flood hazard maps.

As an advancement in the flood inundation mapping using Landsat-7 and Google Earth images along with extensive field survey, Ullah and Zhang (2020) delineated the inundated areas of the Panjkora River Basin, eastern Hindu Kush, Pakistan. The study involved locating 154 flood stations, where 70% of them were used for

constructing the model and the remaining 30% for validation purposes. Flood-prone areas were identified based on eight parameters, including elevation, slope, drainage density, rainfall, normalised difference vegetation index (NDVI), land use, and topographic wetness index (TWI). The correlation between flood occurrences and each parameter was analysed, resulting in a reliable model with a success and prediction rate of more than 82%.

4.5 Conclusion

In the present study, different kinds of literature have been reviewed where different hydrological models and software have been used to identify flood-inundated areas and flood hazard mapping. Usage of hydrological models can explicitly account for the role of hydraulic structures and provide additional information, such as flow depth, velocity, and volume of flow which can be useful for other applications.

The increase in flood frequency throughout the world is a major concern. Identifying the flood-vulnerable areas is the preliminary step for comprehensive flood risk management. A better understanding of the return period and flood extent and the adoption of mitigation policies are necessary to minimise the risk. Lack of use of flood modelling techniques and faulty land use has worsened the flood situation in most parts of the world. Further, rapid urbanisation and deforestation vastly contribute to the increased flood hazards. A clear understanding and awareness of current and potential flood risks result in society mobilising local energies in building resilience. Therefore, knowledge of flood hazards is vital for taking preventive measures.

A careful, sustainable urban planning, redirection measures on flood risk management, and monitoring programmes are essential to improve flood preparedness and thereby enhance land developments and promote community awareness. While flood hazard mapping does not reduce the risk of flooding, it will certainly increase awareness to the community. Flood hazard mapping complements and reinforces other adaptive strategies including emergency planning, flood protection, and evacuation planning. For any flood control and mitigation measures, there is a need to take human behaviour into consideration to better respond to flood risk. A lack of understanding of the benefits of flood hazard mapping may also be an impediment to implementation. In addition, flood mitigation strategies cannot be restricted to the construction of infrastructure or the development of plans using a top-down approach. Local governments and policymakers need to adopt integrated risk management strategies that can be much more effective when local communities are involved.

References

Barman P, Goswami DC (2009) Flood Zone Mapping of Guwahati Municipal Corporation Area using GIS technology. 10th ESRI India User Conference. Geography in Action

Bera K, Pal M, Bandyopadhyay J (2012) A case study of Mongalkote Blocks, Burdwan, West Bengal, India. Int J Sci Res Publ 2(11):1–9

Bhadra A, Choudhury S, Kar D (2011) GIS in flood hazard mapping—a case study. World Acad Sci Eng Technol, International Journal of Geological and Environmental Engineering 5:861–866

Bipinchandra M, Romeji N, Loukrakpam C (2019) Flood hazard risk assessment an mapping of a sub-watershed of Imphal River Basin, Manipur, India: A Multi-resolution Approach. Part of Lecture Notes in Civil Engineering book series (LNCE), Vol. 33

Chakraborty S, Biswas S (2020) Application of Geographic Information System and HEC-RAS in Flood Risk Mapping of a Catchment. Part of the Lecture Notes in Civil Engineering book series (LNCE), Vol. 33

Daffi R, Otun J, Ismail A (2014) Flood hazard assessment of River Dep floodplains in North-Central Nigeria. Int J Water Resour Environ Eng. 6(2):67–72

Demir V, Kisi O (2015) Flood hazard mapping by using geographic information. Adv Meteorol 2016:9. Article ID 4891015

Duan M, Zhang J, Liu Z, Aekakkararungroj A (2012) Use of remote sensing and GIS for flood hazard mapping in Chiang Mai Province, Northern Thailand. p 203–208

Fan C, Ko CH, Wang WS (2009) An innovative modeling approach using Qual2K and HEC-RAS integration to assess the impact of tidal effect on River Water quality simulation. J Environ Manag 90:1824–1832

Forkuo EK (2011) Flood hazard mapping using aster image data with GIS. Int J Geomatics Geosci 1 (4):932–950

Giustarini L, Chini M, Hostache R, Pappenberger F, Matgen P (2015) Flood hazard mapping combining hydrodynamic modeling and multi annual remote sensing data. Remote Sens 7: 14200–14226

Kumar N, Kumar M, Sherring A, Suryavanshi S, Ahmad A, Lal D (2020) Applicability of HEC RAS 2D and GFMS for flood extent mapping: a case study of Sangam area, Prayagraj, India. Model Earth Syst Environ 6:397–405

Nut N, Plermkamon V (2015) Floodplain mapping using HEC-RAS and GIS. Int J Environ Rural Dev 6(1):153–158

Ogania JL, Puno GR, Alivio MBT, Taylaran JMG (2019) Effect of digital elevation model's resolution in producing flood hazard maps. Global J Environ Sci Manag 5(1):95–106

Panagoulia D, Mamassis N, Gkiokas A (2013) Deciphering the Floodplain Inundation Maps in Greece. 8th International Conference Water Resources Management in an Interdisciplinary and Changing Context. European Water Resources Association

Rangari VA, Sridhar V, Umamahesh NV, Patel AK (2019) Floodplain Mapping and Management of Urban Catchment Using HEC-RAS: A case study of Hyderabad city. The Institution of Engineers (India), p 49–63

Romali NS, Yusop Z, Ismail AZ (2018) Hydrological Modelling using HEC-HMS for Flood Risk: Assessment of Segamat Town, Malaysia. IOP Conf. Series: Materials Science and Engineering, 318: 012029. https://doi.org/10.1088/1757-899X/318/1/012029

Shah SMH, Mustaffa Z, Teo FY, Imam MAH, Yusof KW, Al-Qadami EHH (2020) A review of the flood hazard and risk management in the South Asian Region, particularly Pakistan. Scientific African, p 2468–2276

Ullah K, Zhang J (2020) GIS-based flood hazard mapping using relative frequency ratio method: a case study of Panjkora River Basin, eastern Hindu Kush, Pakistan. PLoS One 15(3). https://doi.org/10.1371/journal.pone.0229153

Chapter 5
A Case Study on the Prediction of Heatwave Days Using Machine Learning Algorithms over Telangana

B. Srikanth and Manali Pal

Abstract This study aims to develop a heatwave prediction models for 7-, 15-, and 30-day lead times using machine learning algorithms, that is, support vector regression (SVR) and random forest (RF) for Telangana, a semiarid region vulnerable to heatwaves. The study uses five meteorological variables, namely, geopotential height, U-wind, V-wind, air temperature, and relative humidity for four atmospheric pressure levels (1000, 925, 850, and 700 hPa) from 1990 to 2019 as predictors. The input data is obtained from ECMWF Reanalysis Version 5 (ERA5), and the spatially averaged daily maximum temperatures of summer (i.e., for the months of April, May, and June) are obtained from the India Meteorological Department (IMD) as predictand. The Principal Component Analysis is used on spatially averaged meteorological variables to reduce the number of closely related variables for different pressure levels. The study shows significant accuracy in predicting the total number of annual heatwave days (HWDs) for Telangana for seven-day lead time, but model performances decrease with increasing lead time. Despite spatiotemporal variations in the connections between heatwaves and predictors, the models are satisfactory, and SVR outperforms RF in predicting HWDs. The study's findings indicate that the spatiotemporal dynamics of meteorological variables could be used for long-term heatwave prediction, and both SVR and RF models have the potential for reliable usage in this context.

Keywords Heatwave days · Machine learning algorithm · Random forest · Support vector regression

B. Srikanth · M. Pal (✉)
Department of Civil Engineering, NIT, Warangal, Telangana, India
e-mail: sb712007@student.nitw.ac.in

73

5.1 Introduction

Heatwaves (HWs) are days for a particular place experiencing abnormally high temperature that exceeds its long-term normal value that is calculated based on the maximum average temperature for a given base period of 30 years. These extreme heat events have serious and deadly consequences for various systems such as human health, agriculture, energy demand, and forest ecosystems and also significant impact on hydrological extremes, particularly in regions with already limited water resources. During a heatwave, high temperatures can increase evaporation rates, leading to decreased soil moisture and lower water levels in rivers, lakes, and reservoirs. This can exacerbate existing drought conditions, leading to a greater risk of water scarcity and water-related conflicts (Afroz et al. 2022). Additionally, high temperatures can increase the likelihood of intense rainfall events, leading to flash floods and landslides in areas with insufficient drainage capacity. These hydrological extremes can have significant economic, social, and environmental consequences, including damage to infrastructure and buildings, loss of crops, and increased risk of waterborne diseases. Therefore, it is essential to consider the potential impacts of heatwaves on hydrological extremes in planning for future water management and adaptation strategies. In recent years, heatwaves have become more common globally and have resulted in many fatalities. For instance, in 2003, a severe heatwave in Western Europe led to the death of over 70,000 people (Coumou and Rahmstorf 2012). Similarly, the 2010 heatwave in Russia, which lasted for a month (Dole et al. 2011; McMichael and Lindgren 2011) and the 2009 heatwave in Southeastern Australia caused the death of 54,000 and 374 people, respectively. In India, heatwave is a significant concern, particularly in the northern and central regions (Das and Umamahesh 2022; Das et al. 2022). The country experiences heatwaves every year, and they have become more frequent and severe in recent years, with temperatures regularly exceeding 45 °C in many regions. This extreme heat can cause heatstroke, dehydration, and other health problems, especially among vulnerable populations such as the elderly, children, and those with pre-existing medical conditions and who also experienced many fatalities due to various occurrences of these HWs. For example, the HW occurred in 1988 killed approximately 1300 people (De and Mukhopadhyay 1998) and in 1998 and 2003 killed approximately 2042 (Jenamani 2012) and 3054 people, respectively; and the toll was 2248 across different parts of the country, in the HWs that occurred in 2015 (Guha et al. 2016). Heatwaves in India also have a significant impact on the agricultural sector, as they can cause crop failures, loss of livestock, and damage to infrastructure. This, in turn, can lead to food shortages and price hikes, affecting the livelihoods of many farmers and their families. Thus, it can have a negative impact on the overall economy, as they can disrupt transportation and energy systems, and reduce productivity in various sectors. In addition, the increased demand for electricity during heatwaves can put a strain on the power grid, leading to power outages and blackouts.

Based on scenario-based projection studies, it is expected that global temperatures will increase by 1.4–5.8 °C (De Perez et al. 2018), which could result in a

significant rise in the number of heat-related deaths and illnesses (Meehl et al. 2009; Zhang et al. 2017). The Intergovernmental Panel on Climate Change (IPCC) assessment suggests that the frequency and length of warm days have been increasing since the 1950s and that most of Asia will experience more temperature extremes. Over recent decades, areas with high population density, particularly urban regions, have been more severely affected by these extreme temperatures (Christidis et al. 2015; Mishra et al. 2015). Heatwaves in India typically occur from March to May, which is the pre-monsoon season, and have varying levels of intensity, duration, and negative impacts on different parts of the country (Pai et al. 2013; Basha et al. 2017). A study by Rohini et al. (2016) and Das et al. (2020) used a gridded dataset to investigate the "excessive heat factor," which included both the "excess heat index" and "heat stress index" from 1961 to 2013. The research found that while the frequency and duration of heatwaves are increasing in some parts of central and northwestern India, there were no significant trends in the rest of the country. Khan et al. (2019) suggest that heatwaves could cause even more harm in the coming decades, not just in Asia but also in neighboring regions. To address the challenges posed by heatwaves in India, it is crucial to take steps to mitigate their effects. Therefore in implementing early warning systems, there is a need for the development of a robust model for forecasting heatwaves as a potential climate change mitigation measure.

In general, there are two main approaches commonly used for predicting heatwaves: (a) dynamic climate models and (b) statistical models. Dodla et al. (2017); Ahsan Khan et al. (2020); Naveena et al. (2021) employed the Weather Research and Forecasting (WRF) model, a type of dynamic climate model, to predict heatwaves up to 72 h in advance. Their study found that the root mean square error (RMSE) values ranged from 0.8 to 2.24 K. Similarly, Amna et al. (2013); Mandal et al. (2019) used a multi-model dynamical ensemble prediction system for heatwave prediction but found that the system's accuracy decreased for extreme forecast probabilities beyond a one-week lead time. Although dynamic climate models can capture complex interactions between the atmosphere, land, and ocean due to their physical basis, they are computationally demanding, requiring significant investment in data assimilation and a longer time for model building and parameterizations. Recently, a few studies have started to use machine learning (ML) algorithms for the same (Das and Nanduri 2018; Pandey et al. 2020, 2022). Khan et al. (2019) applied quantile regression forest (QRF) and random forest (RF) models in Pakistan, using synoptic climate variables to predict heatwaves at different time lags. The QRF model demonstrated accuracy in predicting heatwave triggering and departure dates for lead times of 1–10 days. Similarly, Khan et al. (2021) developed a climate change resilient heatwave prediction model using support vector regression (SVR), RF, and artificial neural network (ANN). The study found that SVR performed better than RF and ANN in predicting heatwave days and has the potential to provide accurate forecasting in the context of climate change (Sharma and Goyal 2017; Das and Nanduri 2018; Pandey and Md Azamathulla 2021; Singh et al. 2022). Further, in a study by Jacques-Dumas et al. (2022), a convolutional neural network was trained using 1000 years of climate

model outputs to forecast extreme heatwave occurrences. The model demonstrated the ability to predict heatwaves at three different levels of intensity as early as 15 days ahead of the event. Asadollah et al. (2021) utilized decision tree (DT), random forest (RF), and AdaBoost regression and decision tree (ABR-DT) to predict heatwaves and found that ABR-DT outperformed the other models even when one or multiple variables were removed. Imran Khan and Maity (2022) used a combination of one-dimensional neural network (Conv 1D) and long short-term memory (LSTM) neural network and found that the model's efficiency decreased to 50% when predicting more than five days ahead. These machine learning algorithms are efficient in recognizing highly nonlinear relationships between predictors and predictands and have been used extensively to predict various climate variables, such as wind, evapotranspiration, and extreme events. Therefore, considering the benefits of using these ML algorithms, along with the limited number of studies performed using them, the present study aims to predict heatwaves using support vector regression (SVR) and random forest (RF) for the state of Telangana and evaluate the models' performance for the same.

5.2   Materials and Methods

5.2.1   Methodology

Two ML algorithms, namely, SVR and RF, are used in this study to predict heatwave days (HWDs) for the study area. HWDs are defined as the daily maximum temperature exceeding the 95th percentile of the maximum temperature for at least five consecutive days, using the maximum temperature of the base year as a reference (Khan et al. 2019). The study focused on the months of April, May, and June (AMJ) and analyzed the HWDs for the period between 1990 and 2019 in the study area. In order to predict heatwaves, this study uses five climatic variables, namely, geopotential height, U-wind, V-wind, air temperature, and relative humidity, for four pressure levels, that is, 1000, 925, 850, and 700 hPa, for the time period of 1990–2019, thus concluding with 20 input variables as predictors. The redundancy due to these many numbers of predictors is avoided by the use of the principal component analysis (PCA) that helps to discard the effect of multidimensionality. Figure 5.1 depicts the steps of the overall methodology used in this study.

5.2.1.1   Support Vector Regression (SVR)

The nonlinearity is addressed by the SVR by mapping them into a higher-dimensional space using kernel functions such as polynomial, radial, sigmoid, and linear (Manali Pal et al. 2020). The polynomial and radial kernels are commonly used in SVR-based prediction models. The mathematical representation of SVR
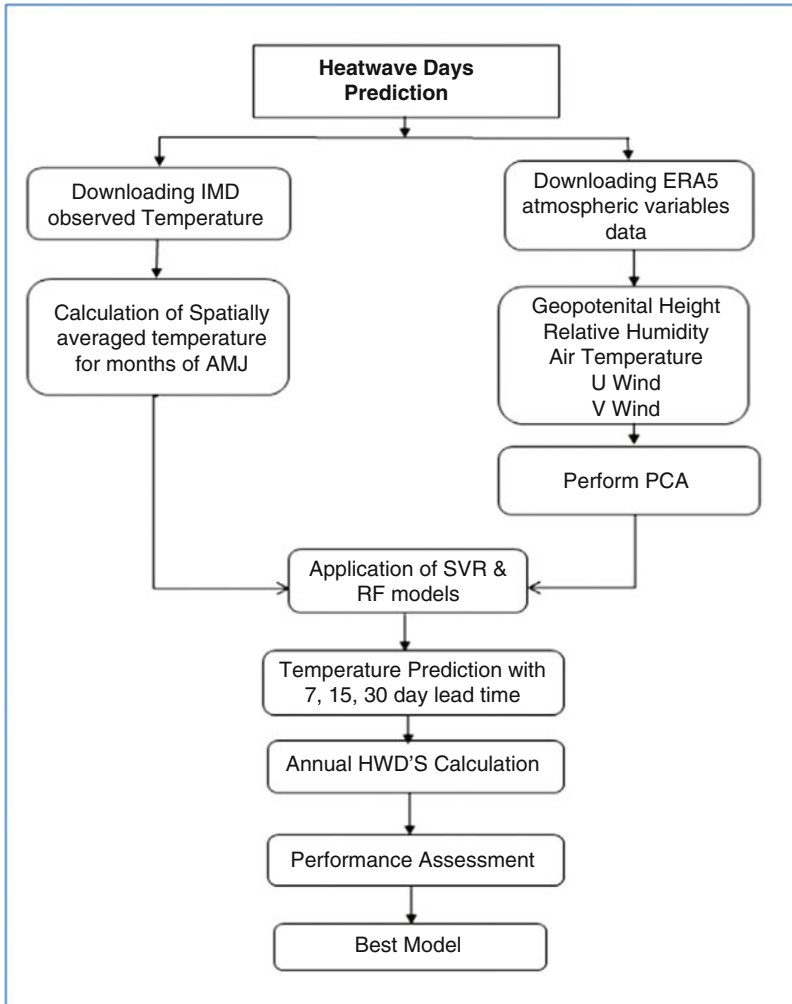
Fig. 5.1 The flowchart of overall methodology

involves finding a regression function, ($f(x) = (w, x) + b$), that describes the observed output y with an error tolerance of $\in$. Here, $[(x_1, y_1), (x_2, y_2). \ldots (x_i, y_i). \ldots (x_l, y_l)]$ represent a training dataset with x_i and y_i as input and output vectors, respectively, and l is the number of data pairs. To achieve this, the original input domain is mapped to a higher-dimensionality space where the function underlying the data is assumed to be linear. The transformed SVR problem in this space is solved by optimizing the following equation (Wang et al. 2007):

$$\text{Minimize } \frac{1}{2}\|w\|^2 + C\sum_{i=1}^{l}\left(\varepsilon_i + \varepsilon_i^*\right)$$

$$\text{Subject to}\begin{cases} Y_i - \sum_{j=1}^{K}\sum_{i=1}^{L}w_j x_{ji} - b \le \,\in + \varepsilon_i, \\ \sum_{j=1}^{K}\sum_{i=1}^{L}w_j x_{ji} - y_i \le \,\in + \varepsilon_i^*, \\ \varepsilon_i, \varepsilon_i^* \ge 0, \end{cases}$$

C is the capacity parameter cost, which is a positive constant that determines the degree of penalized loss when a training error occurs to tune the trade-off between model complexity and tolerance to empirical errors; ε_i, ε_i^* are the slack variables, which measure the distance (in the target space) of the training samples lying outside the insensitive tube from the tube. The equation below represents the functional dependency:

$$f(x) = \sum_{j-1}^{K} w_j x_j + b$$

where K is the number of support vectors. The optimization problem is solved using the dual formulation subject to constraints in the loss function and introducing the Lagrange multipliers, α_i and α_i^*. By solving the optimization problem, the final prediction function is

$$f'(x) = \sum_{i \in N}\left(\alpha_i - \alpha_i^*\right)k(x_i, x) + b$$

where $k(\ldots)$ is kernel function which computes nonlinear dependence between the two input variables x_i and x where x_i are the "support vectors" and b is the bias. In the present study, the radial basis function (RBF) kernel is used in the prediction of HWDs, and it can be mathematically represented with kernel width $-\gamma$, as,

$$k(x_i, x) = \exp\left(-\gamma\|x - x_i\|^2\right), \gamma > 0$$

5.2.1.2 Random Forest (RF)

RF is a collection of learning methods that generates several decision trees collectively used to execute a classification or regression. It is a decision tree-based ML algorithm that consists of many individual decision trees that operates as an ensemble. In RF, many uncorrelated trees will outperform any of the individual trees; the

low correlation being important as a better result can be achieved. There are two known ensemble methodologies, boosting and bagging (Asadollah et al. 2021). Bagging and boosting are two techniques that are often used in conjunction with RF to improve its performance.

Here is a summary of the steps taken in RF to construct a regression model: (1) bootstrapping samples from training data and random selection of m ($< p$) variables at each split, n number trees $T(\theta_t)$ are constructed, where θ_t denotes the parameter. It controls the growth of the tth tree (2). The prediction is produced from the nth single tree's average output as

$$f(x) = \widehat{E}(Y|X = x) = \sum_{i=1}^{n} \omega_i(x)Y_i \tag{5.1}$$

where

$$\omega_i(x) = \frac{\sum_{t=1}^{ntree} \omega_i(k, \theta_t)}{n_{\text{tree}}}, \omega_i(x, \theta) = \frac{1(x_i \in R_l(k, \theta))}{\left(j : x_{j \in R_1}(x, \theta)\right)} \tag{5.2}$$

The random selection of m ($<p$) predictors at each split is a key concept of RF, which provides an enhancement over bagging (Khan et al. 2019).

5.2.1.3   The Performance Metrics

The accuracies of the predictions of the models are assessed by the root mean square error (RMSE), mean square error (MSE), and Pearson's coefficient of correlation (R), between the observed and the predicted values. The mathematical expressions of the metrics are provided as follows.

The RMSE is computed by the following equation:

$$\text{RMSE} = \sqrt{\frac{1}{N} \sum_{i=1}^{N} (x_i - \widehat{x_i})^2}$$

where N is the number of observations, x_i is actual value, and $\widehat{x_i}$ is predicted value.

MSE is the average squared difference between the predicted values and the actual values in a dataset. MSE is calculated by taking the difference between the predicted value and the actual value for each data point, squaring the difference, and then taking the mean of these squared differences. A smaller MSE indicates a better fit of the model to the data, and it can be computed by the following equation:

$$\text{MSE} = \sum \frac{(y_i - \ldots y)^2}{n}$$

where y_i = predicted value and $\ldots y$ = actual value.

The Pearson's correlation coefficient (R) is a measure of the strength and direction of a linear relationship between two variables. It is commonly used to assess the degree to which one variable is related to another and can be used to identify trends or patterns in data. The values of coefficient of correlation vary between -1 and 1, where $-1/1$ indicates a perfect negative/positive correlation, and a value of 0 indicates no correlation. Coefficient of correlation (R) is given by below equation:

$$R = \frac{\sum\limits_{i=1}^{N} (y_i - \overline{y}) \left(\widehat{y}_i - \widehat{\overline{y})}\right)}{\sqrt{\frac{1}{N} \sum\limits_{i=1}^{N} (y_i - \overline{y})^2 \left(\widehat{y}_i - \overline{\widehat{y}}\right)^2}}$$

where y_i is the actual value, $\widehat{y}$ is the predicted value of y, and $\overline{y}$ and $\overline{\widehat{y}}$ are the mean values of the actual and predicted values, respectively.

5.2.2   Study Area and Data Source

5.2.2.1   Telangana

Telangana, a state located in the southern part of India, is known for its hot and dry climate and state stretches between 15°46′N to 19°47′N latitude and 77°16′E to 81° 43′E longitude. Telangana is one of the regions in India that is highly susceptible to heatwaves due to its geographical location, which makes it prone to the scorching heat of the sun. The state has been witnessing an increase in the frequency and intensity of heatwaves in recent years, which is a cause for concern. According to the India Meteorological Department (IMD), in 2019, the state witnessed over 200 heatwave days, which is significantly higher than the previous years (Fig. 5.2).

5.2.2.2   Data Collection

The study utilizes the Indian Meteorological Department's (IMD) data, that is, maximum daily temperature during summer (April, May, June) from 1990 to 2019. The data has a spatial resolution of $1° \times 1°$. To predict the temperature, the study employs a daily time series of five meteorological variables – geopotential height, U-wind, V-wind, air temperature, and relative humidity. These variables were extracted from the European Centre for Medium-Range Weather Forecasts Reanalysis Version 5 (ERA5) for four pressure levels – 1000, 925, 850, and
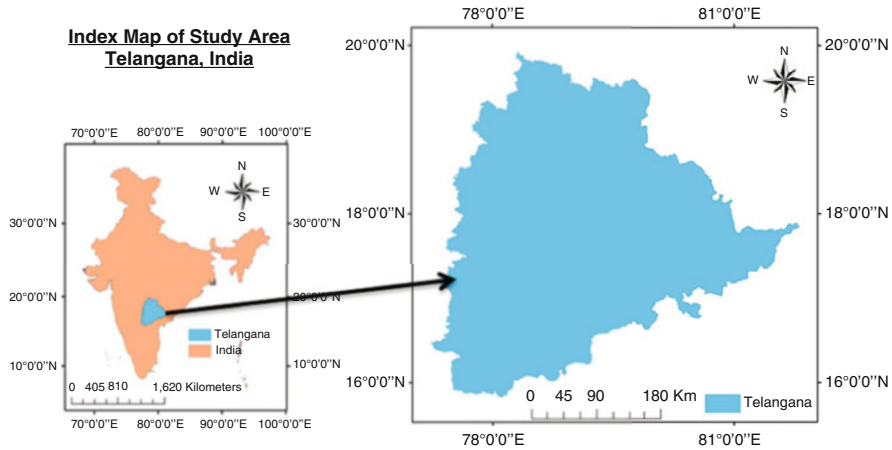
Fig. 5.2 The study area

Table 5.1 Atmospheric variables used for the selection of heatwave predictors

Atmospheric variables	Symbol	Pressure level (hPa)
Air temperature	Air	1000, 925, 850, and 700
Geopotential height	hgt	1000, 925, 850, and 700
Relative humidity	rhum	1000, 925, 850, and 700
U-wind	uwnd	1000, 925, 850, and 700
V-wind	vwnd	1000, 925, 850, and 700

700 hPa – for the same time period of 1990–2019. ERA5 provides a comprehensive record of the global atmosphere, land surface, and ocean waves since 1950 (Table 5.1).

5.3   Results

5.3.1   SVR Model Development

The SVR model developed by using the 21 years of data, that is, from a period of 1990 to 2010 (training period), and remaining 9 years of data, that is, from 2011 to 2019, is used for testing the models. The model is fitted without loss of the generality by selecting the optimal kernel function, that is, the Gaussian kernel with optimal parameter. It is tuned generally with three parameters, that is, box constraint, kernel scale, and epsilon. The epsilon values represent the error tolerance, and the box constraints are positive numeric values that aid to prevent overfitting. Kernel scale represents the width of kernel. Estimated box constraint, kernel scale, and epsilon values for the developed model are 9.81, 3.36, and 0.0043, respectively, for 30-day

lead time; 11.23, 1.71, and 0.21 for 15-day lead time; and 9.08, 3.43, and 0.93 for 7-day lead time.

5.3.2   RF Model Development

The RF model is constructed using 21 years of data spanning from 1990 to 2010 as the training period. The model was then tested using the remaining nine years of data, covering the period from 2011 to 2019. Random forest is generally defined by number of decision trees that model can generate, maximum number of splits that can be made in each decision tree, and number of variables that are randomly sampled for each split in the decision tree. To get the optimum combination of above three parameters, the RF has optimized hyperparameters which randomly selects all three parameters and establish an objective function. The parameters with minimum error in objective function are declared as optimum parameters, and model will be developed using those parameters. The parameters that are optimized in model are as follows: The number of variables to sample is the number of predictors to select at random for each split, which is taken as 2 for regression. Maximum number of splits is maximum number of decision splits (or branch nodes) per tree, and default value is considered as number of observations – 1. It is useful for controlling the complexity of the trees in the model. The number of learning cycles is the number of times that each tree in the model will be trained on the data which is taken as 100 for fitting the model.

5.3.3   Prediction of Maximum Temperature and Annual HWDs

This study aims to evaluate the predictive capabilities of SVR and RF models for predicting heatwaves in Telangana for the months of April, May, and June with different lead times of 7, 15, and 30 days. Spatially averaged temperature time series were generated using observed temperature data from the IMD, which are then predicted using SVR and RF models with the abovementioned lead times. Figures displaying time series plots of both observed (IMD) and predicted temperatures with SVR and RF during the training and testing periods are presented below (Figs. 5.3, 5.4, 5.5, 5.6, 5.7, and 5.8):

According to observed IMD data, HWDs were observed in the years of 1995, 1998, 2003, 2005, 2010, 2012, and 2015. The SVR and RF models, on the other hand, can only capture HWDs in the years 1995, 1998, 2003, and 2015. The year 2015 has the maximum numbers of HWDs (13 days) for the state calculated from IMD observed temperature, during the months of April, May, and June. A number of spatially averaged HWDs predicted by SVR and RF for the same year and time
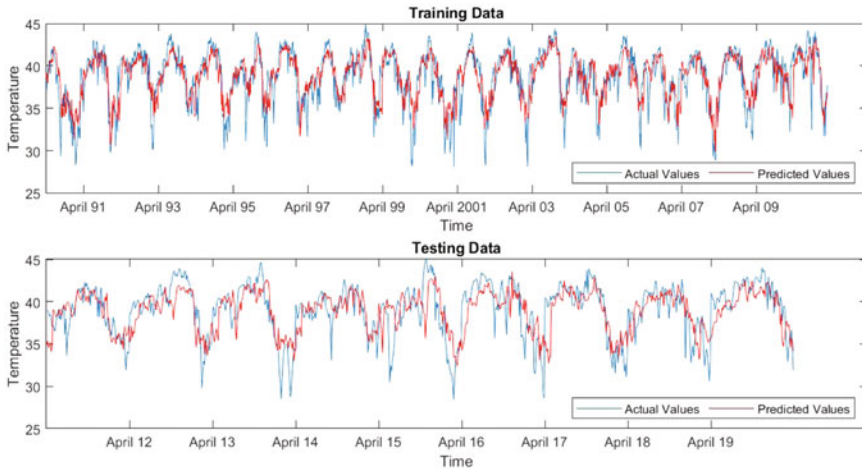
Fig. 5.3 Time series plot of observed and predicted temperature by SVR with seven-day lead time
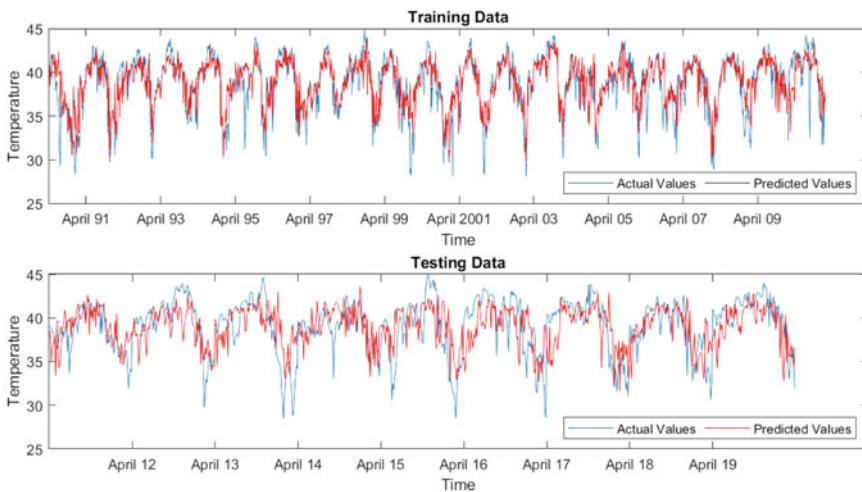
Fig. 5.4 Time series plot of observed and predicted temperature by SVR with 15-day lead time

period (AMJ) are 6 and 8 for seven-day lead time, respectively. The comparison between the numbers of observed and predicted HWDs from both the models has been presented in Fig. 5.9.

To evaluate the performance of SVR and RF models in predicting temperature, three performance metrics – correlation coefficient (R), root mean square error (RMSE), and mean square error (MSE) – are used. During the training periods, the ranges of R for all three lead times are found to be 0.64–0.78 and 0.88–0.89 for SVR and RF, respectively. During model testing periods, the same range is from 0.5–0.67 for SVR and 0.49–0.66 for RF. The ranges of RMSE for all three lead times
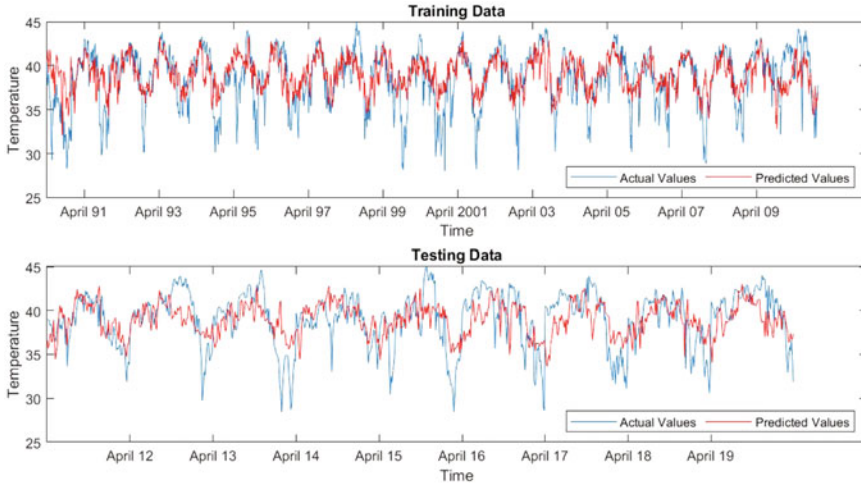
Fig. 5.5 Time series plot of observed and predicted temperature by SVR with 30-day lead time
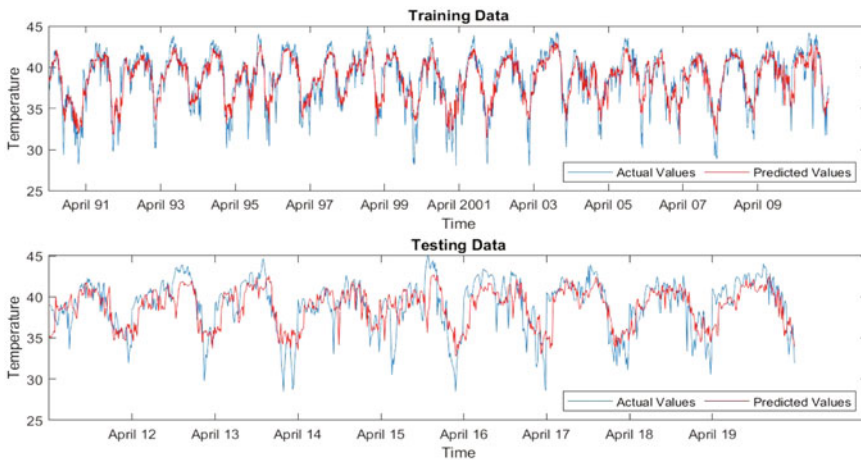
Fig. 5.6 Time series plot of observed and predicted temperature by RF with seven-day lead time

during training periods are 2.01–2.53 and 1.55–1.70 for SVR and RF, respectively. During model testing periods, the same are 2.35–2.70 for SVR and 2.37–2.78 for RF. It is observed that the RMSE values changed in the range of 2.7 °C and 2.78 °C for SVR and RF, respectively, for lead times 7–30 days. The average values of performance metrics for both models are presented in Tables 5.2 and 5.3. It is observed that the model performance decreases with the increase in lead time for both SVR and RF. While comparing between the two models, it is observed that the
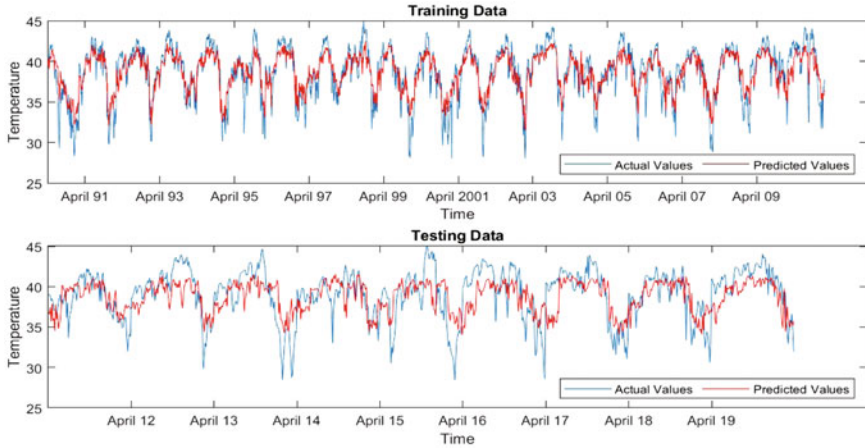
Fig. 5.7 Time series plot of observed and predicted temperature by RF with 15-day lead time
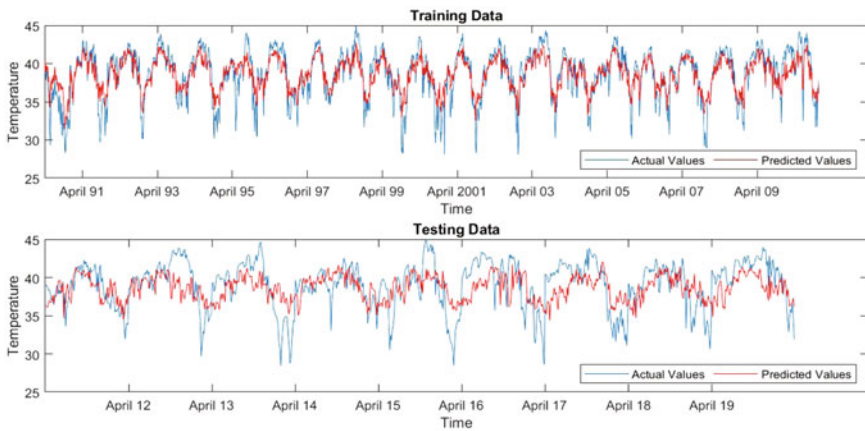
Fig. 5.8 Time series plot of observed and predicted temperature by RF with 30-day lead time

RF tends to overfit as the lead time increases whereas although the performance of SVR decreases, it does not show model overfitting.

Figure 5.10 shows the spatial distribution of observed and predicted temperature from SVR and RF, respectively, for seven-day lead times for the date June 4, 1995, that had experienced the heatwave (according to the definition mentioned above). It shows that both the models are not able to capture the highest observed temperature, that is, 41 °C.
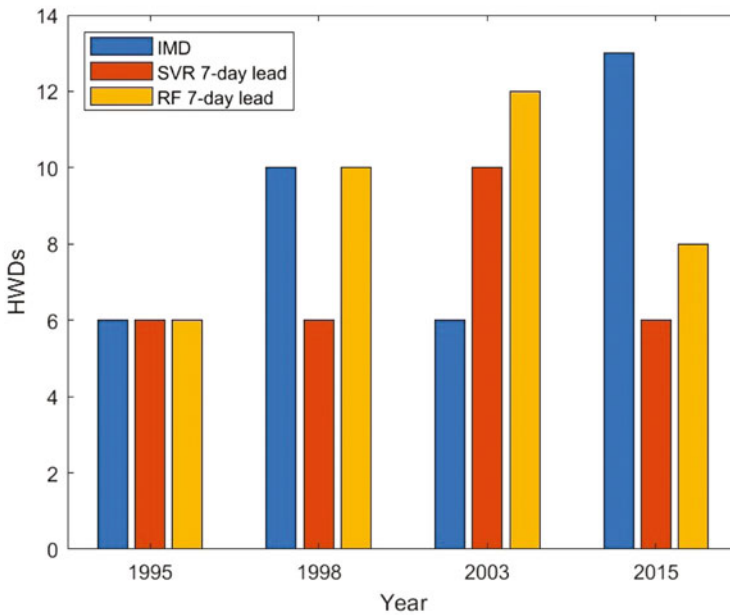
Fig. 5.9 The comparison between the numbers of observed and predicted HWDs from SVR and RF

Table 5.2 Performance metrics of SVR model for the lead times of 7, 15, and 30 days

	CC train	CC test	RMSE train	RMSE test	MSE train	MSE test
7	0.78	0.67	2.02	2.35	4.11	5.50
15	0.78	0.53	2.02	2.73	4.09	7.48
30	0.57	0.50	2.68	2.74	7.21	7.51

Table 5.3 Performance metrics of RF model for the lead times of 7, 15, and 30 days

Lead	CC train	CC test	RMSE train	RMSE test	MSE train	MSE test
7	0.88	0.66	1.55	2.37	2.43	5.62
15	0.89	0.58	1.59	2.58	2.54	6.69
30	0.89	0.49	1.71	2.78	2.91	7.76

5.4 Discussion

In this study, SVR and RF models are employed to predict the maximum temperature and forecast the number of HWDs in Telangana during summer (April to June). These two machine learning techniques have proven to be highly effective in solving a range of intricate problems. The outcomes have demonstrated the ML models'
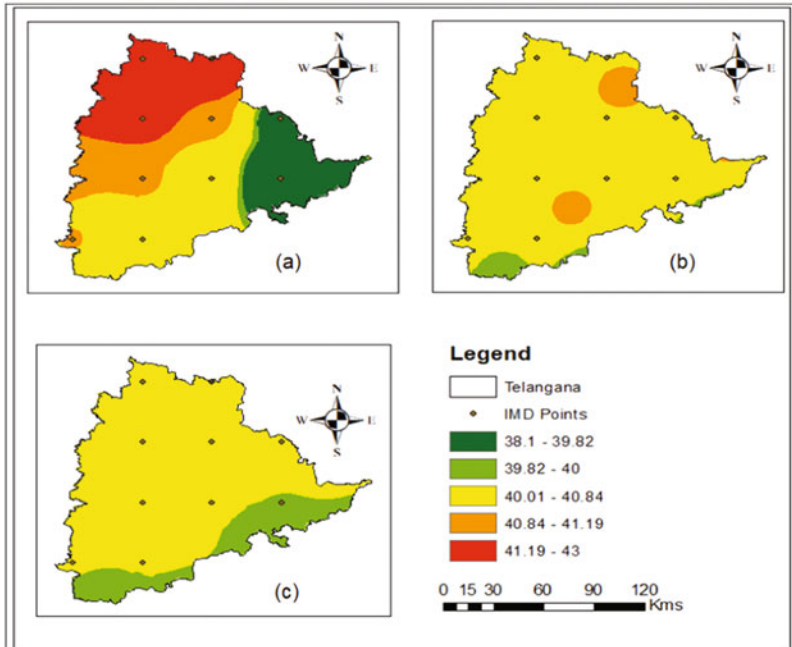
Fig. 5.10 The spatial distribution of (**a**) IMD observed, (**b**) SVR, and (**c**) RF predicted temperature for seven-day lead time on June 4, 1995

capability to predict the maximum temperature and fluctuation of HWDs from year to year. Both the models are able to predict maximum temperature and HWDs accurately up to a lead time of seven days. However, beyond that, the models' performance decreases, that is, it is not able to accurately predict the temperature or HWDs. The evaluation comparing both the models is done by using three performance metrics – correlation coefficient (R), root mean square error (RMSE), and mean square error (MSE) – and these performance metrics demonstrated that SVR possesses a high degree of accuracy in predicting temperature and HWDs compared to RF.

5.5 Conclusions

In this study, the heatwave prediction capabilities of SVR and RF are investigated for Telangana, spanning from 1990 to 2019. The study aims to assess the models' performances for lead times of 7, 15, and 30 days during April, May, and June. The observed temperature data from the IMD are utilized to calculate a time series of the average cumulative annual heatwave days. The same was predicted for SVR and RF models with lead times of 7, 15, and 30 days. The SVR model is able to capture the

five heatwave events out of seven whereas the RF model is able to capture four heatwave events. The results of the study suggest that SVR and RF machine learning algorithms can be used to predict heatwave days for Telangana by employing meteorological variables such as air temperature, relative humidity, geopotential height, u-wind, and v-wind as predictors. However, performance metrics indicate that the models' performance decreases with increasing lead times. The study found that both SVR and RF models demonstrated acceptable performances for up to seven days of lead time, with RMSE values of 2.36 °C and 2.37 °C for SVR and RF, respectively, during testing periods. In comparing the performance of the two models, SVR is found to be more efficient for this specific study.

5.6 Future Scope

The limitations of the current study can lead to future scope in terms of enhancing the model. For example, the model development has not considered the temporal variation of spatial correlation between the predictors and predictand along with the influences of teleconnections and that can be incorporated in future studies. These gaps in the study indicate potential areas for future research to address the abovementioned limitations. Additional research can be undertaken to compare the predictive capabilities of SVR and RF with other machine learning models when it comes to forecasting heatwaves. The efficacies of SVR, RF, and other statistical models can be contrasted with that of dynamical models to highlight their respective strengths and weaknesses.

References

Afroz M, Chen G, Anandhi A (2022) Drought- and heatwave associated compound extremes: A review of hotspots, variables, parameters, drivers, impacts, and analysis frameworks. Front Earth Sci 10:1–25. https://doi.org/10.3389/feart.2022.914437

Ahsan Khan N, Sajadul Alam Saimon M, Naqib Jimmy A, Fatema Lubna K, Abul Kalam Mallik M, Sajadul Alam M, Islam T, Ahmad I, Fatema K, Analyst G, Science E, Author A (2020) Study on heat wave and its thermodynamic features over bangladesh using numerical weather prediction model (NWPM). Int J Sci Bus. https://doi.org/10.5281/zenodo.3839997

Amna S, Samreen N, Khalid B, Shamim A (2013) Numerical climate modeling and verification of selected areas for heat waves of Pakistan using ensemble prediction system. J Phys Conf Ser 439(1). https://doi.org/10.1088/1742-6596/439/1/012041

Asadollah S, Khan N, Sharafati AS, Chung S, Wang ES, Xiao J (2021) Prediction of heat waves using meteorological variables in diverse regions of Iran with advanced machine learning models. Stoch Env Res Risk A 7(36):1959–1974

Basha G, Kishore P, Ratnam MV, Jayaraman A, Kouchak AA, Ouarda TBMJ, Velicogna I (2017) Historical and projected surface temperature over India during the 20th and 21st century. Sci Rep 7(1). https://doi.org/10.1038/s41598-017-02130-3. Nature Publishing Group

Christidis N, Jones GS, Stott PA (2015) Dramatically increasing chance of extremely hot summers since the 2003 European heatwave. Nat Clim Chang 5:46–50

Coumou D, Rahmstorf S (2012) A decade of weather extremes. Nat Clim Chang 2(7):491–496

Das J, Nanduri UV (2018) Assessment and evaluation of potential climate change impact on monsoon flows using machine learning technique over Wainganga River basin, India. Hydrol Sci J 63:1020–1046. https://doi.org/10.1080/02626667.2018.1469757

Das J, Umamahesh NV (2022) Heat wave magnitude over India under changing climate: Projections from CMIP5 and CMIP6 experiments. Int J Climatol 42:331–351. https://doi.org/10.1002/joc.7246

Das PK, Podder U, Das R, Kamalakannan C, Rao GS, Bandyopadhyay S, Raj U (2020) Quantification of heat wave occurrences over the Indian region using long-term (1979–2017) daily gridded (0.5° × 0.5°) temperature data—a combined heat wave index approach. Theor Appl Climatol 142(1–2):497–511. https://doi.org/10.1007/s00704-020-03329-7

Das J, Manikanta V, Umamahesh NV (2022) Population exposure to compound extreme events in India under different emission and population scenarios. Sci Total Environ 806. https://doi.org/10.1016/j.scitotenv.2021.150424

De US, Mukhopadhyay RK (1998) Severe heat wave over Indian subcontinent in 1998 in a perspective of global climate. Curr Sci 75:1308–1311

De Perez EC, Van Aalst M, Bischiniotis K, Mason S, Nissan H, Pappenberger F, Stephens E, Zsoter E, Van Den Hurk B (2018) Global predictability of temperature extremes. Environ Res Lett 13(5). https://doi.org/10.1088/1748-9326/aab94a

Dodla VB, Satyanarayana GC, Desamsetti S (2017) Analysis and prediction of a catastrophic Indian coastal heat wave of 2015. Nat Hazards 87(1):395–414. https://doi.org/10.1007/s11069-017-2769-7

Dole R, Hoerling M, Perlwitz J, Eischeid J, Pegion P, Zhang T, Quan XW, Xu T, Murray D (2011) Was there a basis for anticipating the 2010 Russian heat wave? Geophys Res Lett 38(6). https://doi.org/10.1029/2010GL046582

Guha-Sapir, D. & Below, R. Hoyois Ph. EM-DAT: The international Disaster database-www.emdat.be – Université Catholique de Louvain – Brussels – Belgium. (Accessed 17th February 2016)

Imran Khan M, Maity R (2022) Hyrbid deep learning approach for multi-step-ahead prediction for daily maximum temperature and heatwaves. Theor Appl Climatol 149:945–963. https://doi.org/10/1007/s00704-022-04103-7

Jacques-Dumas V, Ragone F, Borgnat P, Abry P, Bouchet F (2022) Deep learning-based extreme heatwave forecast. Front Climate 4:1–20. https://doi.org/10.3389/fclim.2022.789641

Jenamani RK (2012) Analysis of Ocean-Atmospheric features associated with extreme temperature variations over east coast of India- A special emphasis to Orissa heat waves of 1998 and 2005. Mausam 63:401–422

Khan N, Shahid S, Juneng L, Ahmed K, Ismail T, Nawaz N (2019) Prediction of heat waves in Pakistan using quantile regression forests. Atmos Res 221:1–11

Khan N, Shahid S, Ismail TB, Behlil F (2021) Prediction of heat waves over Pakistan using support vector machine algorithm in the context of climate change. Stoch Env Res Risk A 35(7): 1335–1353. https://doi.org/10.1007/s00477-020-01963-1

Mandal R, Joseph S, Sahai AK, Phani R, Dey A, Chattopadhyay R, Pattanaik DR (2019) Real time extended range prediction of heat waves over India. Sci Rep 9(1). https://doi.org/10.1038/s41598-019-45430-6

McMichael AJ, Lindgren E (2011) Climate change: present and future risks to health, and necessary responses. J Intern Med 270(5):401–413

Meehl GA, Tebaldi C, Walton G, Easterling D, McDaniel L (2009) Relative increase of record high maximum temperatures compared to record low minimum temperatures in the US. Geophys Res Lett. 36(23). https://doi.org/10.1029/2009GL040736

Mishra V, Ganguly AR, Nijssen B, Lettenmaier DP (2015) Changes in observed climate extremes in global urban areas. Environ Res Lett 10(2):024005. https://doi.org/10.1088/1748-9326/10/2/024005

Naveena N, Satyanarayana GC, Raju AD, Umakanth N, Srinivas D, Rao KS, Suman M (2021) Prediction of heatwave 2013 over Andhra Pradesh and Telangana, India using WRF model. Asian J Atmos Environ 15(3):1–12

Pai DS, Nair A, Ramanathan AN (2013) Long term climatology and trends of heat waves over India during the recent 50 years (1961-2010). MAUSAM. 64(4). https://doi.org/10.54302/mausam.v64i4.742

Manali Pal, Rajib Maity, Ratnam, J.V.,Masami Nonaka, & Swadin,K.B.(2020). Long-lead prediction of ENSO Modoki index using machine learning algorithms. Sci Rep, DOI: https://doi.org/10.1038/s41598-019-57183-3

Pandey M, Md Azamathulla H (2021) Discussion of "Gene-Expression Programming, Evolutionary Polynomial Regression, and Model Tree to Evaluate Local Scour Depth at Culvert Outlets" by Mohammad Najafzadeh and Ali Reza Kargar. J Pipeline Syst Eng Pract 12:07021001. https://doi.org/10.1061/(asce)ps.1949-1204.0000532

Pandey M, Zakwan M, Sharma PK, Ahmad Z (2020) Multiple linear regression and genetic algorithm approaches to predict temporal scour depth near circular pier in non-cohesive sediment. ISH J Hydraul Eng 26:96–103. https://doi.org/10.1080/09715010.2018.1457455

Pandey M, Jamei M, Ahmadianfar I et al (2022) Assessment of scouring around spur dike in cohesive sediment mixtures: A comparative study on three rigorous machine learning models. J Hydrol 606:127330. https://doi.org/10.1016/j.jhydrol.2021.127330

Rohini P, Rajeevan M, Srivastava AK (2016) On the variability and increasing trends of heat waves over India. Sci Rep 6:26153. https://doi.org/10.1038/srep26153

Sharma A, Goyal MK (2017) A comparison of three soft computing techniques, Bayesian regression, support vector regression, and wavelet regression, for monthly rainfall forecast. J Intell Syst 26:641–655. https://doi.org/10.1515/jisys-2016-0065

Singh UK, Jamei M, Karbasi M et al (2022) Application of a modern multi-level ensemble approach for the estimation of critical shear stress in cohesive sediment mixture. J Hydrol 607:127549. https://doi.org/10.1016/j.jhydrol.2022.127549

Wang W, Men C, Weizhen L (2007) Online prediction model based on support vector machine. Neurocomputing 71:550–558

Zhang Y, Yu C, Bao J, Li X (2017) Impact of temperature on mortality in Hubei, China: a multi-county time series analysis. Sci Rep 7:45093. https://doi.org/10.1038/srep4509

Chapter 6
Quantifying the Reliability of Reanalysis Precipitation Products Across India

Alka Kumari, Akash Singh Raghuvanshi, and Ankit Agarwal

Abstract For conducting hydroclimatological investigations, consistent time series of climate datasets are required. Precise measurement of precipitation is crucial for numerous purposes, including climate and land use change studies, environmental and agricultural research, the management of natural hazards, and the planning of water resources and hydrological systems. Reanalysis products have been released worldwide to investigate the validity of reanalysis on a global and regional basis. In this study, we investigated the ability of various reanalysis products to simulate spatiotemporal precipitation patterns over India from 1980 to 2021. We compared different precipitation reanalysis products, namely, the fifth generation of ECMWF global atmospheric reanalysis (ERA5), modern-era retrospective analysis for research and application, Land version 2 (MERRA-2-Land), climate forecast system reanalysis (CFSR), Japanese global atmospheric reanalysis project (JRA55), and Multi-Source Weather (MSWX) with gridded Indian Meteorological Department dataset using various descriptive indices and found that MSWX was a better representative of IMD data than other reanalysis products. ERA5 and MERRA2-Land showed satisfactory results for PBias, RMSE, and correlation coefficient. However, further studies are necessary to validate these findings on a basin scale. Overall, this research suggests that MSWX can be used in various climatic studies and hydrological modeling for areas or river basins where data is lacking or missing.

A. Kumari · A. S. Raghuvanshi · A. Agarwal (✉)
Department of Hydrology, Indian Institute of Technology Roorkee, Roorkee, India
e-mail: ankit.agarwal@hy.iitr.ac.in

6.1   Introduction

Precipitation data is a crucial input for hydrological models that simulate river discharge, sediment transport, and other hydrological extremes. Accurate precipitation data is necessary for managing water resources, mitigating floods and droughts, and assessing the impact of climate change on the water cycle. However, precipitation measurements are often limited by the number and location of rain gauges, leading to uncertainty in precipitation estimates, particularly in remote and poorly instrumented areas. This uncertainty can result in inaccurate estimates of river flow, sediment transport, and other hydrological processes, which can lead to inadequate water resource management and increased vulnerability to floods and droughts. To manage this problem, we have to first find most reliable alternate dataset for accuracy. The hydroclimatological investigation, including climatic trend analysis, agro-hydrological modeling, and atmospheric and climatic studies demand consistent time series of climate datasets across the globe/region (Hordofa et al. 2021; Saini et al. 2022). For many applications, such as climate and/or land use change studies, agricultural and environmental research, and natural hazard and hydrological and water resources planning, reliable precipitation measurements are essential (Saikumar et al. 2022). Precipitation measurements play a major role as important input data for hydrologic, climatological, and agricultural studies, particularly focusing on precipitation-induced natural disasters such as droughts, floods, and landslides (Aragão et al. 2007; Habib et al. 2012; Hong et al. 2006; Wu et al. 2012; Sharma and Goyal 2016). They provide important information to hydrologists, meteorologists, climatologists, and other decision-makers regarding magnitude, frequency, and impact (Wong et al. 2017). This data is also helpful in water resource planning and management, which is directly or indirectly related to agriculture, disaster mitigation, and preparedness. Despite having utmost importance in hydrological and climatological studies, the scientific community continues to have difficulties measuring rainfall at fine resolution scales due to its significant spatiotemporal variability (Guo et al. 2015).

Conventionally, precipitation data is measured through rain gauge networks. And these networks measure accurate precipitation amounts for specific locations, but their usage is restricted for regional and global applications due to their inhomogeneous distribution and small sampling areas (Anagnostou et al. 2010; Gupta et al. 2023). However, there is typically a shortage of temporally consistent ground-based observed precipitation data in mountainous and underdeveloped/developing nations (Viney and Bates 2004). Owing to high spatiotemporal variability in precipitation across India, it is quite challenging to have reliable homogeneous distributed precipitation data available for a long period (Zambrano et al. 2017). Climate datasets can be obtained from observations, satellite measurements, and reanalysis. In order to bridge the disadvantages of conventional and weather radar systems, numerous reanalysis and satellite-derived precipitation products have been developed. Satellite precipitation products have outstanding spatial coverage but also contain errors, mostly due to instrumental errors, temporal sampling errors, sensor calibration

errors, and algorithm errors (Gebremichael et al. 2005). In that case, reanalysis precipitation products can be used as an alternative to satellite precipitation products for studying the Earth's hydroclimatic system (Hodges et al. 2011). Reanalysis datasets are created by combining data from various sources, including satellites, radiosondes, and ground observations, and predictions made using climate and land surface models (Ghodichore et al. 2019). ERA5 (the fifth generation of ECMWF global atmospheric reanalysis), MERRA-2-Land (modern-era retrospective analysis for research and application, Land version 2), CFSR (climate forecast system reanalysis), JRA55 (Japanese global atmospheric reanalysis project), and MSWX (Multi-Source Weather) are some of the reanalysis datasets.

The reanalysis products use data assimilation techniques to blend past atmospheric and surface observations to create homogenous four-dimensional variables that are an integral part to numerical weather prediction systems. They provide improved understanding of weather patterns, aid in the identification of long-term trends, improve weather forecasting, enhance climate and hydrological modeling, and improve disaster preparedness. These reanalysis precipitation products are developed on global scale, and their applicability varies spatially as well as temporally. Therefore, numerous studies have been conducted evaluating the performance of the existing reanalysis products in India. Ghodichore et al. (2018) evaluated variability for the timescale of seasonal and annual to check the spatial and temporal patterns along with the temperature and precipitation trends using IMD gridded data of duration 34 years. This was done for six global reanalyses, best of all found was MERRA-land product for precipitation. On the other hand, for temperature datasets, JRA-55 and ERA-interim were found to be better performing. Ghodichore et al. (2019) evaluated six different reanalysis datasets to determine their ability to capture precipitation and moisture patterns over India. They used statistical metrics to analyze datasets from a 34-year period and found that all reanalyses captured the overall precipitation pattern over India but struggled with orographic rainfall over mountainous areas. MERRA-Land and ERA-Interim were identified as the two datasets that performed the best over India. Mahto and Mishra (2019) conducted an evaluation of reanalysis products for streamflow and annual water budget in two basins located in diverse climatic settings in India. They found that during the monsoon season, ERA-5 outperforms other reanalysis products for precipitation, maximum temperature, evapotranspiration, and soil moisture.

With the development of new data assimilation techniques and advancements in model parameterizations, numerical weather prediction systems continue to advance (Kalnay and Cai 2003). The recent addition of MSWX reanalysis data, which is believed to be the improved version of ERA5 (Beck et al. 2022), requires revaluation of the datasets for their performance in India. Therefore, it is crucial to investigate if the recent improvements and developments of reanalysis products are suitable for hydrological applications, as well as their accuracy and limitations, and thoroughly scrutinize their applicability to different world regions (Hodges et al. 2011).

In this study, we compare different reanalysis precipitation products with IMD dataset on a national scale by using various descriptive indices, including maximum precipitation, mean precipitation, skewness, standard deviation, PBias (percent bias),

RMSE (root mean square error), CDF (cumulative distribution function), and correlation coefficients. Our work of evaluating reanalysis data at a national scale can have important implications for better understanding of historical weather patterns in India, including the variability and trends of different weather variables such as temperature, precipitation, and wind. It can also be used as an input to climate models, improving the accuracy and reliability of climate projections that help policymakers and decision-makers plan for the potential impacts of climate change. So the aim of this study is to evaluate different reanalysis datasets with IMD dataset using descriptive indices.

6.2   Study Area and Data Used

The Indian subcontinent is the seventh largest country in the world with a total area of 3,287,590 km^2, spanning from 7°N to 38°N latitude and 64°E to 98°E longitude. The Arabian Sea borders India on the southwest and the Bay of Bengal on the southeast. The Himalayas are located in the northeast, northwest, and north. According to annual data from the Meteorological Department, India receives an average rainfall of 118 cm (Fig. 6.1). India's climate varies greatly across the country, with a predominantly tropical climate characterized by varying temperatures and rainfall. The northern region experiences a subtropical climate, with hot summers and cold winters, while the central and western parts are arid and receive minimal rainfall. On the other hand, Southern India has a tropical wet climate with substantial rainfall during the monsoon season from June to September. Coastal areas are susceptible to cyclones and storms during the monsoon season, and the northeast region, particularly the state of Meghalaya, receives the highest amount of precipitation.

We compared five reanalysis products: ERA5, MERRA-2-Land, CFSR, JRA55, and MSWX. These products cover the time period from 1980 to 2021 and are detailed in Table 6.1. To validate the accuracy of the datasets, we used the IMD gridded data with a spatial resolution of 0.25° × 0.25°, which has a daily temporal resolution. The IMD gridded data was generated using Shepard's interpolation technique to interpolate daily rainfall data collected from approximately 6955 hydrometeorological stations across India. The IMD gridded data is widely used as a reference dataset for comparison with other gridded rainfall datasets in India and is known for its ability to capture precipitation amounts in the Western Ghats and Himalayan orographic belts (Yumnam et al. 2021).

ERA-5 is the latest atmospheric reanalysis developed by the European Centre for Medium-Range Weather Forecasts and covers the period from 1979 onward. It has recently been utilized in hydroclimatic applications and assessments and includes improvements over ERA-Interim, such as enhancements in horizontal and vertical resolutions, an upgraded radiative transfer model, and analysis based on a ten-member ensemble 4D-Var. CFSR, developed by NCEP, is a third-generation product that utilizes a coupled climate atmosphere-ocean-land surface system
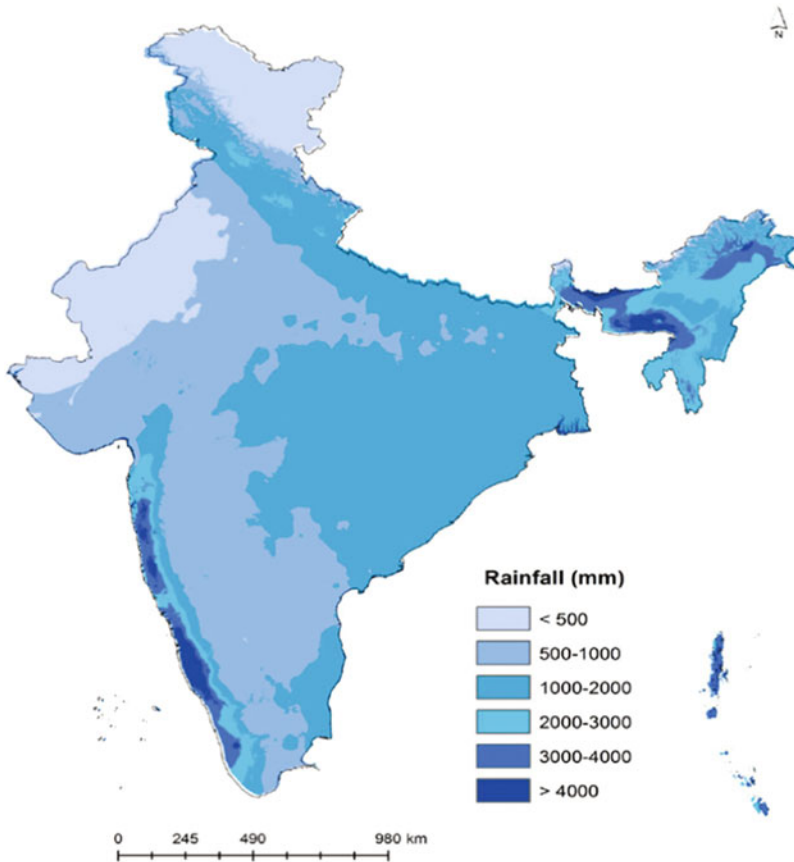
Fig. 6.1 A map illustrating the average annual rainfall across India (Reddy et al. 2015)

featuring interactive sea ice components. The data assimilation process of CFSR is executed through a three-dimensional VAR method and it assimilates satellite radiance data. MERRA-2 includes significant improvements compared to the original MERRA reanalysis, incorporating observation-based precipitation data products to rectify precipitation on the land surface. MERRA-2 has two distinct types of precipitation estimates: M2AGCM, produced by the atmospheric general circulation model, and M2CORR, corrected precipitation perceived by the MERRA-2 land surface. JRA-55, developed by the Japanese Meteorological Agency, is a global atmospheric reanalysis project that uses advanced four-dimensional VAR data assimilation and variance bias correction techniques for satellite data. It offers data from 1958 to the present and is an improvement over the previous Japanese 25-year reanalysis. Finally, MSWX is a comprehensive worldwide gridded meteorological dataset that provides highly detailed 0.1° resolution readings on near-surface weather conditions. It incorporates bias-correction techniques and offers medium-range and long-range forecast ensembles. The historical portion of the MSWX

Table 6.1 Detailed information about various datasets used. Here acronyms are defined as follows: ERA5 (the fifth generation of ECMWF global atmospheric reanalysis), MERRA-2 Land (modern-era retrospective analysis for research and application, Land version 2), CFSR (climate forecast system reanalysis), JRA55 (Japanese global atmospheric reanalysis project), and MSWX (Multi-Source Weather) are some of the reanalysis datasets

S. no.	Reanalysis products	Spatial resolution/ coverage	Variable	Organization
1.	MERRA-2 Land (period—1980–present)	$(0.5° \times 0.625°)$/ global	Total precipitation from atm model physics $(kg\ m^{-2}s^{-1})$	NASA
2.	CFSR (period—(CFSR: 1979–2010) and (CFSv2: 2011–present))	$(0.5° \times 0.5°)$/ global	Total precipitation $(kg\ m^{-2})$	NCEP
3.	JRA55 (period—1959–present)	$(0.563° \times 0.562°)$/ global	Total precipitation (mm/day)	JMA
4.	ERA5 (period—1979–present)	$(0.25° \times 0.25°)$/ global	Total precipitation (mm)	ECMWF
5.	MSWX (period—1979–present)	$(0.1° \times 0.1°)$/ global	Precipitation (mm/day)	–

record relies on ERA5 data that has been bias corrected and downscaled using high-resolution reference climatology.

6.3 Methods and Methodology

For the study period from 1980 to 2021, multiple datasets with varying spatial resolutions (IMD, ERA5, CFSR, MERRA-2, JRA5, and MSWX) were acquired from different sources. These datasets were preprocessed by clipping them to the study area and then resampling them to a standard spatial resolution of 0.25° using a first-order conservative remapping technique. The purpose of this was to facilitate comparison with the reference dataset (IMD).

To evaluate the accuracy of the reanalysis datasets, various descriptive indices such as Pbias, RMSE, correlation coefficient, and extreme precipitation (95th percentile) were used. Pbias measures the average deviation of the simulated datasets from the reference dataset, with an ideal value of 0. A positive value indicates underestimation, while a negative value indicates overestimation. RMSE indicates the concentration of data around the line of best fit, while the correlation coefficient represents the relationship between two variables. A value of 1 represents perfect correlation, 0 indicates no correlation, and − 1 indicates a negative correlation. The results of these indices are summarized in Table 6.2 (Prakash 2019; Prakash et al. 2012, 2015; Setti et al. 2020).

Table 6.2 Formulae used for various descriptive indices

Descriptive indices	Formulae
Skewness (C_s)	$\dfrac{n\sum_{i=1}^{n}\left(Y_i - \overline{Y}\right)^3}{(n-1)(n-2)S_Y^3}$
Percent bias (PBias)	$\dfrac{\sum_{i=1}^{n}\left(Y_i^{\text{ref}} - Y_i^{\text{sim}}\right)^2 \times 100}{\sum_{i=1}^{n}\left(Y_i^{\text{ref}}\right)}$
Root mean square error (RMSE)	$\sqrt{\dfrac{1}{n}\sum_{i=1}^{n}\left(Y^{\text{ref}} - Y^{\text{sim}}\right)^2}$
Correlation coefficient (R)	$\dfrac{\sum_{i=1}^{n}\left(Y_i^{\text{ref}} - \overline{Y}^{\text{ref}}\right)\left(Y_i^{\text{sim}} - \overline{Y}^{\text{sim}}\right)}{\sqrt{\sum_{i=1}^{n}\left(Y_i^{\text{ref}} - \overline{Y}^{\text{ref}}\right)^2} \times \sqrt{\sum_{i=1}^{n}\left(Y_i^{\text{sim}} - \overline{Y}^{\text{sim}}\right)^2}}$

where $Y_i, \overline{Y}$, Y^{ref}, $Y^{\text{sim}}, \overline{Y}^{\text{ref}}$ and $\overline{Y}^{\text{sim}}$ represents the precipitation, mean precipitation, reference precipitation (IMD), simulated precipitation (reanalysis), mean reference precipitation, and mean simulated precipitation.

Table 6.2 presents several descriptive indices used to evaluate the accuracy of the simulated datasets (reanalysis datasets) against the reference dataset (IMD dataset). These indices include mean precipitation, maximum precipitation, standard deviation, skewness, Pbias, RMSE, and correlation coefficient. Pbias measures the average capability of the simulated datasets to overestimate or underestimate the reference dataset, with an ideal value of 0. Values greater than 0 indicate underestimation, while values less than 0 indicate overestimation. RMSE represents the standard deviation of predicted errors and shows how well the data is concentrated around the line of best fit. The correlation coefficient indicates the degree of correlation between two variables and can range from -1 to 1, with 1 representing the best correlation, 0 indicating no correlation, and -1 representing a negative correlation. For the evaluation of extreme precipitation, we used 95th percentile criteria for comparing different reanalysis datasets with IMD dataset (Choi, 2004).

6.4 Results and Discussion

In this study, we first computed descriptive indices such as maximum precipitation, mean precipitation, standard deviation, percent bias (PBias), skewness, root mean square error (RMSE), and correlation. In the box-plot of maximum precipitation, Fig. 6.2a shows that CFSR tends to slightly overestimate the maximum precipitation, while ERA5 and MSWX slightly underestimate it. On the other hand, MERRA2-Land and JRA55 significantly underestimate the maximum precipitation. Moving on to mean precipitation in Fig. 6.2b, CFSR and JRA55 showed a slight overestimation, while ERA5, MERRA2-Land, and MSWX exhibited mean precipitation levels close to those of the IMD dataset. Figure 6.2c reveals that ERA5 and MERRA2-Land tend to underestimate the standard deviation, while CFSR overestimates it. On the other hand, MSWX and JRA55 provide standard deviations that are similar to those of the IMD dataset. In Fig. 6.2d, MERRA2-Land and JRA55 are found to underestimate
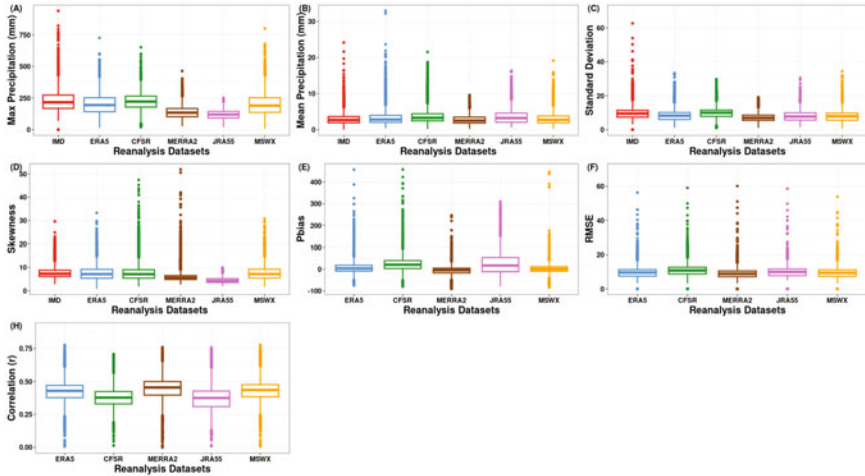
Fig. 6.2 Box-plot of various descriptive indices viz maximum precipitation (**a**), mean precipitation (**b**), standard deviation (**c**), and skewness (**d**), PBias (**e**) RMSE (**f**) and Correlation (**h**) of different reanalysis products of ERA5, CFSR, MERRA2, JRA55, and MSWX for Baitarani River Basin

skewness, while ERA5, CFSR, and MSWX exhibit skewness levels that are comparable to the IMD dataset. Moving on to the evaluation of Pbias, root mean square error, and correlation, as displayed in Fig. 6.2. E, F, and G, it is clear that MSWX performed the best compared to the other reanalysis products. However, MERRA2-Land and ERA5 also produced satisfactory results in these metrics.

Further, five datasets were used to calculate the daily precipitation distribution for the cumulative density function (CDF) from 1980 to 2021. The CDF plot of daily precipitation for MSWX closely resembles the IMD product, while MERRA2-Land overestimates and the other reanalysis precipitation products underestimate it. These results suggest that MSWX is a better representation of the IMD dataset, as depicted in Fig. 6.3. The daily precipitation distribution for percent bias (PBias) was plotted for the five datasets from 1980 to 2021. Based on Fig. 6.4, the PBias spatial map indicates that MERRA2-Land and MSWX outperform other reanalysis products, as they demonstrate consistently low values of PBias across the entire country. In contrast, the Pbias maps for CFSR, ERA5, and JRA55 exhibit high values of PBias for certain pixels. Specifically, ERA5 displays high PBias values in the northeast region, CFSR shows high values in certain parts of the northeast and south India due to high rainfall in those areas, and JRA55 displays high values in some portions of the north and northwest due to less rainfall in those areas. Thus, MERRA2-Land and MSWX are more preferable.

The daily precipitation distribution for root mean square error (RMSE) from 1980 to 2021 was plotted for the five datasets (as shown in Fig. 6.5). RMSE is the standard deviation of residuals (predicted errors), and it tells us how our data is concentrated around the line of best fit. All reanalysis precipitation products exhibited a high value
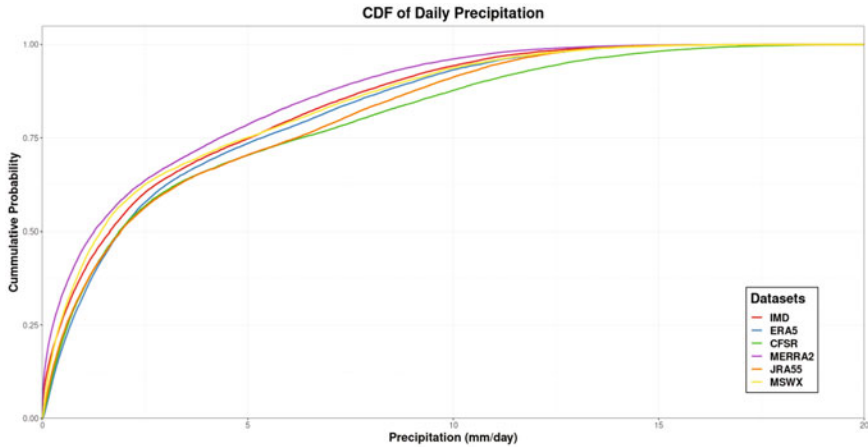
Fig. 6.3 Cumulative distribution function (CDF) curve for all reanalysis precipitation products, namely, the fifth generation of ECMWF global atmospheric reanalysis (ERA5), modern-era retrospective analysis for research and application, Land version 2 (MERRA-2 Land), climate forecast system reanalysis (CFSR), Japanese global atmospheric reanalysis project (JRA55), and Multi-Source Weather (MSWX) and IMD product for comparison

of root mean square error in the northeastern regions and Western Ghats due to higher rainfall in these areas. Among the five reanalysis products, MERRA2-Land gives better results (as shown in Fig. 6.5). In southern Peninsular India as well as in western regions, all the reanalysis products show low RMSE values, whereas in Meghalaya, RMSE values are very high.

The daily precipitation distribution for the correlation coefficient (R) was visualized for the five datasets from 1980 to 2021. The correlation coefficient describes how two variables are related to one another, whether they are increasing, decreasing, or increasing and decreasing. The correlation coefficient ranges from −1 to 1, where 1 represents the best correlation, 0 indicates no correlation, and − 1 signifies a negative correlation. The spatial map of correlation indicates that MERRA2-Land performed the best, showing good correlation across India. ERA5 and MSWX also demonstrated good correlation in many regions of India, such as Central India, the Western Ghats, and some parts of northeast India. On the other hand, CFSR and JRA55 exhibited good correlation in certain parts of the eastern region and Western Ghats but low correlation in some parts of the north and south. Notably, the Western Ghats demonstrated the highest correlation, while the northeast part of the country displayed the lowest correlation because northeast part of India, situated in Himalayan region, has higher elevation, complex terrain, with many mountains and valleys affecting the precipitation patterns. The Western Ghats is a mountainous region, having lower elevation than former that receives a lot of rainfall due to its location in the path of monsoon winds, while the northeast part of India is not located directly in the path of monsoon winds. The Western Ghats experiences monsoon seasons that are more predictable, whereas the northeast region of India
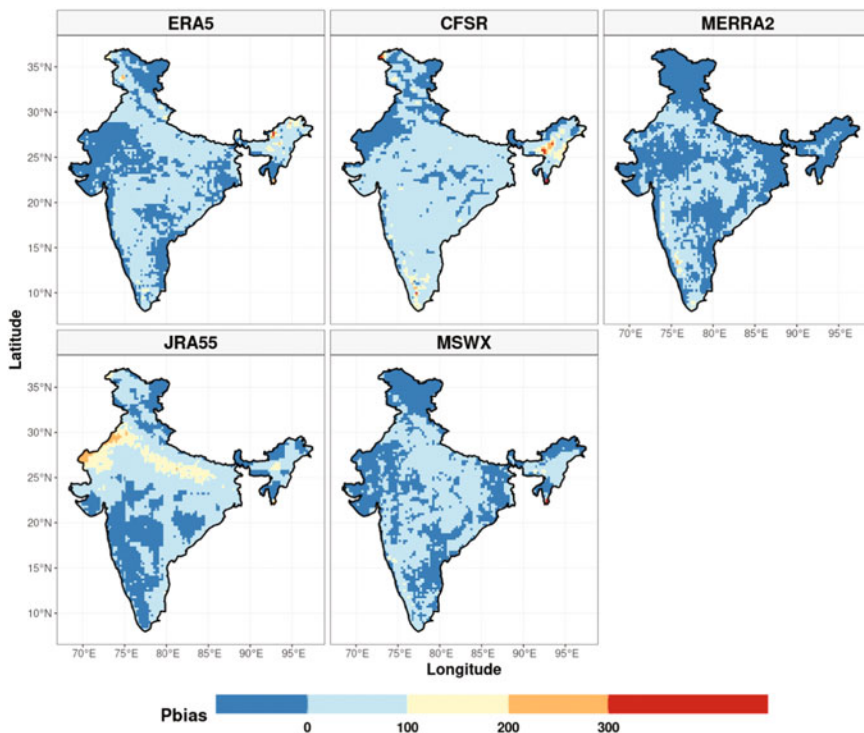
Fig. 6.4 Spatial map of Pbias for five reanalysis products, namely, the fifth generation of ECMWF global atmospheric reanalysis (ERA5), modern-era retrospective analysis for research and application, Land version 2 (MERRA-2 Land), climate forecast system reanalysis (CFSR), Japanese global atmospheric reanalysis project (JRA55), and Multi-Source Weather (MSWX)

may encounter more irregular and unpredictable precipitation patterns, possibly caused by regional climate variability. It may be difficult to capture these patterns accurately which could be a cause of reduced correlation between the observed and reanalysis data, as illustrated in Fig. 6.6.

Spatial distribution for extreme precipitation (95th percentile) was visualized for the five datasets from 1980 to 2021 in Fig. 6.7. For northeastern region and Western Ghats, we find that ERA5 and CFSR overestimate whereas MERRA2 land, JRA55, and MSWX underestimate the extreme precipitation. All the five reanalysis datasets are underestimating the extreme precipitation in Jammu and Kashmir regions. JRA55 overestimate the extreme precipitation over the western semiarid region, while remaining other reanalysis datasets are giving results close to IMD dataset. Moreover, MERRA2 land, ERA-5, and MSWX perform better for extreme precipitation in India than the other reanalysis products (Mahto and Mishra 2019).
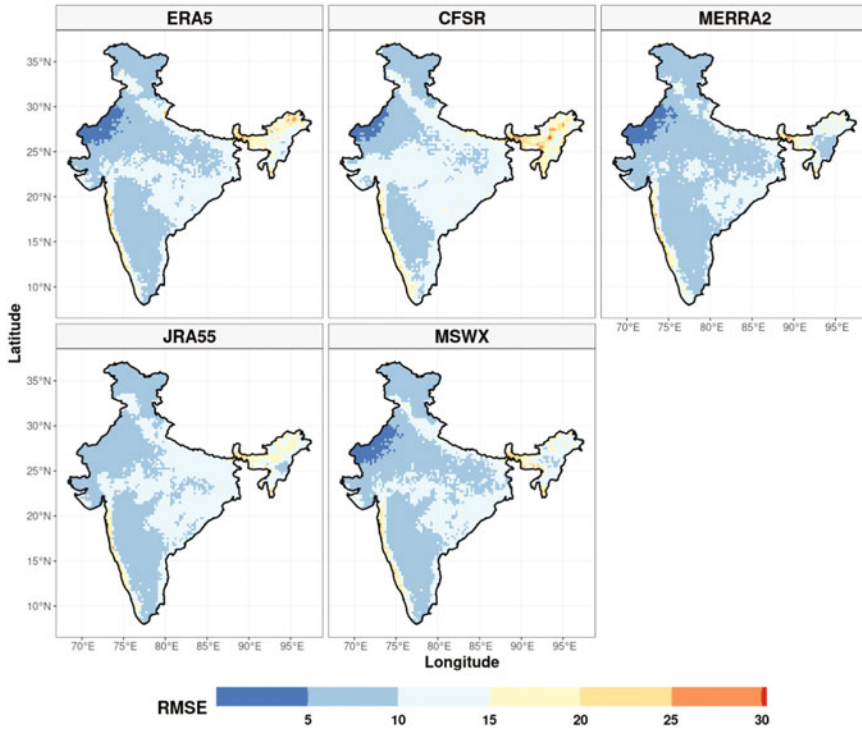
Fig. 6.5 Spatial map of RMSE for five reanalysis products, namely, the fifth generation of ECMWF global atmospheric reanalysis (ERA5), modern-era retrospective analysis for research and application, Land version 2 (MERRA-2 Land), climate forecast system reanalysis (CFSR), Japanese global atmospheric reanalysis project (JRA55), and Multi-Source Weather (MSWX)

6.5 Conclusion

The purpose of this study was to assess the reliability of five reanalysis precipitation products in comparison to the IMD dataset as the reference data, at a national scale in India. We examined various descriptive indices and CDF plots of the different datasets to evaluate their performance. Our results indicate that MSWX performed the best in terms of maximum precipitation, mean precipitation, standard deviation, and skewness. However, MERRA2-Land had slightly better results than MSWX in terms of PBias, RMSE, and correlation. Nevertheless, MSWX remained the best performing dataset overall. ERA5 performed satisfactorily but was slightly less accurate than MSWX, and CFSR and JRA55 performed poorly. Regarding the CDF plot, MSWX had the best results, followed by ERA5. In terms of the spatial maps of PBias, RMSE, and correlation, MERRA2-Land outperformed the other reanalysis precipitation products. In conclusion, our study found that MERRA2-Land, MSWX, and ERA5 were the most reliable reanalysis precipitation products for national scale analysis in India. However, more studies on smaller scales should
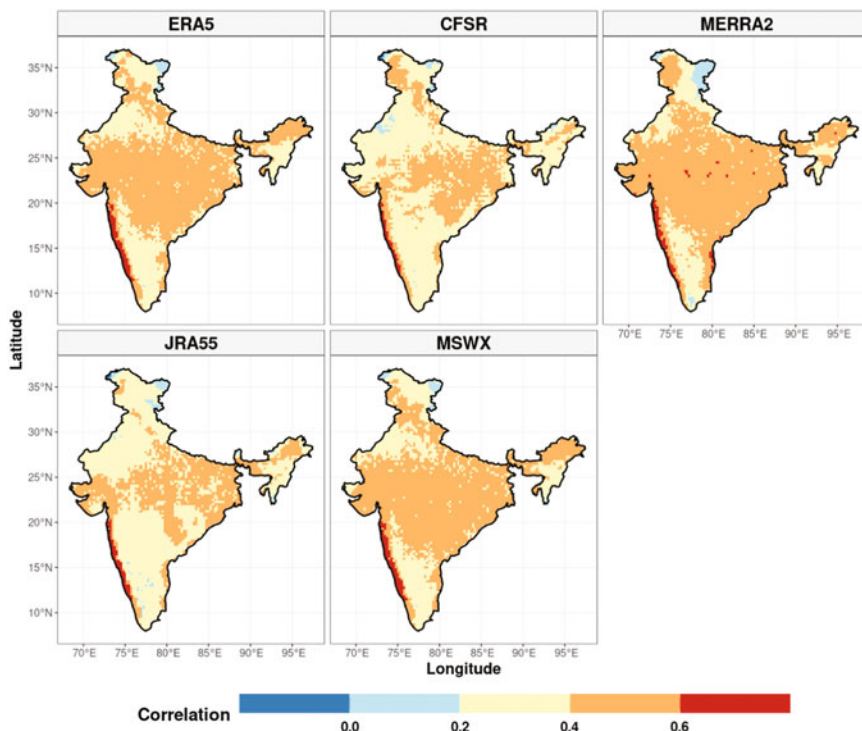
Fig. 6.6 Spatial map of correlation coefficients between IMD products and five reanalysis products, namely, the fifth generation of ECMWF global atmospheric reanalysis (ERA5), modern-era retrospective analysis for research and application, Land version 2 (MERRA-2 Land), climate forecast system reanalysis (CFSR), Japanese global atmospheric reanalysis project (JRA55), and Multi-Source Weather (MSWX)

be conducted to verify these findings, as evaluating reanalysis datasets at the basin scale is crucial for effective water resources management, agriculture, hydrological modeling, and climate change impact assessment. Precise precipitation datasets are required for accurate calculation of irrigation needs, crop yields, and drought management. Effective water resources management on a basin scale can help protect biodiversity and maintain ecosystem services. Further, these results are considered as an input to various climate and hydrological models as future study for improving the accuracy and reliability of projections that help policymakers and decision-makers plan for the potential impacts.
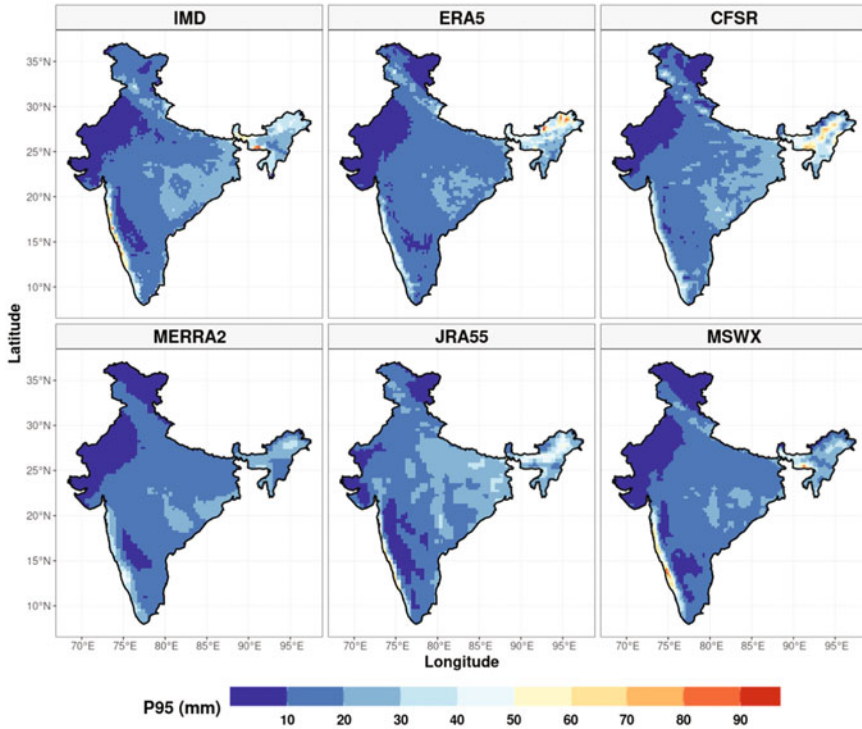
Fig. 6.7 Spatial map showing extreme precipitation (95th percentile) value of IMD products and five reanalysis products, namely, the fifth generation of ECMWF global atmospheric reanalysis (ERA5), modern-era retrospective analysis for research and application, Land version 2 (MERRA-2 Land), climate forecast system reanalysis (CFSR), Japanese global atmospheric reanalysis project (JRA55), and Multi-Source Weather (MSWX)

Data Availability Statement

The datasets used in this paper are freely available. The gridded rainfall datasets for Indian subcontinents are made available on https://imdpune.gov.in/cmpg/Griddata/Rainfall_25_Bin.html. **Declaration of Conflict of Interest** The authors declare no conflicts of interest relevant to this study.

Author Contributions All the authors contributed equally.

References

Anagnostou EN, Maggioni V, Nikolopoulos EI, Meskele T, Hossain F, Papadopoulos A (2010) Benchmarking high-resolution global satellite rainfall products to radar and rain-gauge rainfall estimates. IEEE Trans Geosci Remote Sens. 48(4 PART 1):1667–1683. https://doi.org/10.1109/TGRS.2009.2034736

Aragão LEOC, Malhi Y, Roman-Cuesta RM, Saatchi S, Anderson LO, Shimabukuro YE (2007) Spatial patterns and fire response of recent Amazonian droughts. Geophys Res Lett 34(7):1–5. https://doi.org/10.1029/2006GL028946

Beck HE, Van Dijk AIJM, Larraondo PR, McVicar TR, Pan M, Dutra E, Miralles DG (2022) Global 3-hourly 0.1 bias-corrected meteorological data including near-real-time updates and forecast ensembles. Bull Am Meteorol Soc 103(3):E710–E732. https://doi.org/10.1175/BAMS-D-21-0145.1

Choi Y (2004) Trends on temperature and precipitation extreme events in Korea. J Korean Geograph Soc 39(5):711–721

Gebremichael M, Krajewski WF, Morrissey ML, Huffman GJ, Adler RF (2005) A detailed evaluation of GPCP 1° daily rainfall estimates over the Mississippi River basin. J Appl Meteorol 44(5):665–681. https://doi.org/10.1175/JAM2233.1

Ghodichore N, Vinnarasi R, Dhanya CT, Roy SB (2018) Reliability of reanalyses products in simulating precipitation and temperature characteristics over India. J Earth Syst Sci 127(8): 1–21. https://doi.org/10.1007/s12040-018-1024-2

Ghodichore N, Dhanya CT, Vinnarasi R (2019) Examination of mean precipitation and moisture transport in reanalysis products over India. ISH J Hydraul Eng 25(1):51–61. https://doi.org/10.1080/09715010.2017.1364983

Guo H, Chen S, Bao A, Hu J, Gebregiorgis AS, Xue X, Zhang X (2015) Inter-comparison of high-resolution satellite precipitation products over Central Asia. Remote Sens 7(6):7181–7211. https://doi.org/10.3390/rs70607181

Gupta LK, Pandey M, Raj PA, Shukla AK (2023) Fine sediment intrusion and its consequences for river ecosystems: a review. J Hazard Toxic Radioact Waste. 27(1):04022036. https://doi.org/10.1061/(ASCE)HZ.2153-5515.0000729

Habib E, Haile AT, Tian Y, Joyce RJ (2012) Evaluation of the high-resolution CMORPH satellite rainfall product using dense rain gauge observations and radar-based estimates. J Hydrometeorol 13(6):1784–1798. https://doi.org/10.1175/JHM-D-12-017.1

Hodges KI, Lee RW, Bengtsson L (2011) A comparison of extratropical cyclones in recent reanalyses ERA-Interim, NASA MERRA, NCEP CFSR, and JRA-25. J Clim 24(18): 4888–4906. https://doi.org/10.1175/2011JCLI4097.1

Hong Y, Alder R, Huffman G (2006) Evaluation of the potential of NASA multi-satellite precipitation analysis in global landslide hazard assessment. Geophys Res Lett 33(22):1–5. https://doi.org/10.1029/2006GL028010

Hordofa AT, Leta OT, Alamirew T, Kawo NS, Chukalla AD (2021) Performance evaluation and comparison of satellite-derived rainfall datasets over the Ziway lake basin, Ethiopia. Climate 9(7). https://doi.org/10.3390/cli9070113

Kalnay E, Cai M (2003) Impact of urbanization and land-use. Nature 425(6939):528–531. https://doi.org/10.1038/nature01649.1

Mahto SS, Mishra V (2019) Does ERA-5 outperform other reanalysis products for hydrologic applications in India? J Geophys Res Atmos 124(16):9423–9441. https://doi.org/10.1029/2019JD031155

Prakash S (2019) Performance assessment of CHIRPS, MSWEP, SM2RAIN-CCI, and TMPA precipitation products across India. J Hydrol 571(January):50–59. https://doi.org/10.1016/j.jhydrol.2019.01.036

Prakash S, Mahesh C, Gairola RM, Pal PK (2012) Comparison of high-resolution TRMM-based precipitation products during tropical cyclones in the North Indian Ocean. Nat Hazards 61(2): 689–701. https://doi.org/10.1007/s11069-011-0055-7

Prakash S, Mitra AK, Momin IM, Pai DS, Rajagopal EN, Basu S (2015) Comparison of TMPA-3B42 versions 6 and 7 precipitation products with gauge-based data over India for the southwest monsoon period. J Hydrometeorol 16(1):346–362. https://doi.org/10.1175/JHM-D-14-0024.1

Reddy, C. S., Jha, C. S., Diwakar, P. G., & Dadhwal, V. K. (2015). Nationwide classification of forest types of India using remote sensing and GIS. Environ Monit Assess. 187(12). DOI: https://doi.org/10.1007/s10661-015-4990-8

Saikumar G, Pandey M, Dikshit PKS (2022) Natural river hazards: their impacts and mitigation techniques. In: River dynamics and flood hazards: studies on risk and mitigation. Springer, Singapore, pp 3–16

Saini G, Jagadeesh P, Saikumar G (2022) Trend assessment of rainfall over mumbai and pune cities. In: River dynamics and flood hazards: studies on risk and mitigation. Springer, Singapore, pp 587–606

Setti S, Maheswaran R, Sridhar V, Barik KK, Merz B, Agarwal A (2020) Inter-comparison of gauge-based gridded data, reanalysis and satellite precipitation product with an emphasis on hydrological modeling. Atmosphere 11(11):1–26. https://doi.org/10.3390/atmos11111252

Sharma A, Goyal MK (2016) A comparison of three soft computing techniques, Bayesian regression, support vector regression, and wavelet regression, for monthly rainfall forecast. J Intell Syst 26(4):641–655

Viney NR, Bates BC (2004) It never rains on Sunday: the prevalence and implications of untagged multi-day rainfall accumulations in the Australian high quality data set. Int J Climatol 24(9): 1171–1192. https://doi.org/10.1002/joc.1053

Wong JS, Razavi S, Bonsal BR, Wheater HS, Asong ZE (2017) Inter-comparison of daily precipitation products for large-scale hydro-climatic applications over Canada. Hydrol Earth Syst Sci 21(4):2163–2185. https://doi.org/10.5194/hess-21-2163-2017

Wu H, Adler RF, Hong Y, Tian Y, Policelli F (2012) Evaluation of global flood detection using satellite-based rainfall and a hydrologic model. J Hydrometeorol 13(4):1268–1284. https://doi.org/10.1175/JHM-D-11-087.1

Yumnam K, Guntu RK, Rathinasamy M, Agarwal A (2021) Quantile-based bayesian model averaging approach towards merging of precipitation products. J Hydrol 127206. https://doi.org/10.1016/j.jhydrol.2021.127206

Zambrano F, Wardlow B, Tadesse T, Lillo-Saavedra M, Lagos O (2017) Evaluating satellite-derived long-term historical precipitation datasets for drought monitoring in Chile. Atmos Res 186(November 2016):26–42. https://doi.org/10.1016/j.atmosres.2016.11.006

Chapter 7
Dynamics of Weakly Nonlinear Waves Propagating in the Region with Mixed Nonlinearity

Triveni P. Shukla

Abstract Our research focuses on the behavior of weakly nonlinear waves in mixed nonlinear fluids. We use a multiple-scale approach together with the equation of state for a van der Waals fluid to obtain a transport equation from the Navier-Stokes equations. Using the resulting transport equation, we further investigate the effect of van der Waals variables on wave evolution.

Keywords Asymptotic expansion · Evolution equation · Expansion shock · Double sonic shock · Non-ideal fluid

7.1 Introduction

The degree of natural hazards associated with hydrologic events and river systems is dependent on the uncertainty of hydrological events, which can be affected by changes in climatic conditions (Das et al. 2022; Gupta et al. 2022). According to climate change research, the frequency of extreme weather phenomena has been increasing worldwide, leading to more damage to human assets. Shock waves often play a significant role during water hazards (Saikumar et al. 2022). The study of waves and nonlinear dynamics is relevant to a wide range of physical systems, including rivers and other fluid flows. Understanding the dynamics of weakly nonlinear waves is crucial for analyzing sediment transport, or studying the interaction between different types of waves, such as surface waves and internal waves.

Perturbation expansions with multiple scales are often used to study nonlinear systems of partial differential equations (PDEs) for which a discussion of approximate solutions is of considerable interest. Nonlinear waves in real fluids have been the subject of many theoretical and experimental studies, starting from the work of Colonna et al. (2007), Thompson (1971), and Thompson and Lambrakis (1973) which have attracted the attention and their collaborators among several others

T. P. Shukla (✉)
Department of Mathematics, National Institute of Technology, Warangal, Telangana, India
e-mail: tpshukla@nitw.ac.in

(Colonna et al. 2007; Cramer 1989, 1991; Cramer et al. 1986; Kluwick 1991, 2001; Kluwick and Meyer 2010).

There has been widespread interest in the nonlinear wave phenomena mainly through the so-called evolution equations, derived from a large system of PDEs, representing an important aspect of the original system (Cramer and Sen 1992; Cramer and Webb 2007; Kluwick and Cox 1998). The pioneering work on the evolution equations in which both quadratic and cubic nonlinearities are present has been carried out by Cramer and Sen (1992) and Kluwick and Cox (1998); these works are mainly based on the fact that the fundamental derivative (Thompson 1971) is the following:

$$\tilde{\Xi}(\overline{\rho}, \overline{s}) \equiv 1 + \frac{\overline{\rho}}{\overline{c}} \left(\frac{\partial \overline{c}}{\partial \overline{\rho}} \right)_{\overline{s}}, \tag{7.1}$$

where $\overline{\rho}$ is the fluid density, $\overline{s}$ the entropy, and $\overline{c}$ the local speed of sound, which lies close to $\tilde{\Xi} = 0$ and may change sign in a single pulse for the fluids with high specific heat (Cramer et al. 1986; Cramer and Kluwick 1984; Kluwick 1991, 2001; Kluwick and Cox 1998).

In recent years, much attention has been paid toward the study of wave propagation in van der Waals fluids (Colonna and Guardone 2006; Taniguchi et al. 2010; Zhao et al. 2011). Shock formation and conditions under which such discontinuous solutions are admissible are of particular interest in nonideal fluids. This becomes more interesting because some discontinuous solutions which cannot be accounted for by the ideal fluids make their appearance in nonideal fluids (for instance, due to violation of second law of thermodynamics, expansion shocks are not admissible in ideal fluids but such shocks are allowed as admissible discontinuities in a non-ideal case provided that $\tilde{\Xi} < 0$ (Thompson and Lambrakis 1973)). It would be interesting to know how the quadratic and cubic nonlinearity parameters, and subsequently the evolutionary behavior of waves, are influenced by the real gas effects; this analysis, however, remains missing in the literature.

Here, using the related procedures, referred to as above, we study weakly nonlinear waves in a van der Waals fluid in which $\tilde{\Xi}$ changes sign in the transition region. The chapter is organized as follows: basic equations and formulation of the problem are given in Sect. 7.2; the unperturbed medium ahead of the wave is governed by the usual Navier-Stokes equations with viscosity and thermal conduction supplemented by the equation of state for a van der Waals fluid. In Sect. 7.3, the methodology presented in Cramer and Sen (1992) and Kluwick and Cox (1998) remains fundamental to all that follow, and it is desirable to discuss it anew at this time in the present setup, emphasizing the features we wish to use and develop. A nonlinear parabolic equation is derived that governs the evolution of small disturbances on unperturbed states; the evolution equation contains both quadratic and cubic nonlinearities inherent in the system. Using van der Waals equation of state, explicit expressions for these parameters are obtained. In Sect. 7.4, Riemann's solutions of the associated kinematic equation are presented with a rectangular

pulse initial distribution; the wave evolution exhibits different wave patterns involving sonic expansion and sonic compression shocks, in which an extreme edge of an expansion or compression fan is a shock wave, the precursor waves, and their interaction with wave-fans. It may be pointed out that the shock-related phenomena studied here cannot be accounted for by the ideal gas model. Indeed, in the present study, the expansion shocks, across which there is a decrease in pressure, sonic shocks which propagate with a speed identical to either the upstream or downstream convected sound speed, and precursor waves that leave the shock tangentially make their appearance unlike the ideal fluid formalism. The interaction times of shocks and wave-fans, strengths and speeds of shocks, widths of wave-fans, and the eventual decay rate of the amplitude of merged shocks are investigated under the influence of the van der Waals parameters. Finally, in Sect. 7.5, a numerical treatment of the parabolic equation is presented in the hyperbolic limit using a weighted essentially non-oscillatory (WENO) scheme (Jiang and Shu 1996). The viscous solution is compared with the solution of the associated inviscid equation; effects of the van der Waals parameters upon the evolution of signal profiles, their interaction, and decay behavior are presented.

7.2 Problem Formulation

The basic equations governing the unsteady, one-dimensional flow of a real fluid obeying the van der Waals equation of state are the Navier-Stokes equations:

$$\overline{\rho}_{\overline{t}} + \overline{u}\,\overline{\rho}_{\overline{x}} + \overline{\rho}\,\overline{u}_{\overline{x}} = 0,$$
$$\overline{u}_{\overline{t}} + \overline{u}\,\overline{u}_{\overline{x}} + \frac{\overline{p}_{\overline{\rho}}}{\overline{\rho}}\overline{\rho}_{\overline{x}} + \frac{\overline{p}_{\overline{s}}}{\overline{\rho}}\overline{s}_{\overline{x}} = \frac{4}{3}\frac{\mu}{\overline{\rho}}\overline{u}_{\overline{x}\overline{x}}, \qquad (7.2)$$
$$\overline{s}_{\overline{t}} + \overline{u}\,\overline{s}_{\overline{x}} = \frac{1}{\overline{\rho}\,\overline{T}}\left\{\frac{4}{3}\mu(\overline{u}_{\overline{x}})^2 + \left(k\overline{T}_{\overline{x}}\right)_{\overline{x}}\right\},$$

where $\overline{u}$ is the particle velocity, $\overline{p} = \overline{p}(\overline{\rho}, \overline{s})$ the pressure, $\overline{T} = \overline{T}(\overline{\rho}, \overline{s})$ the temperature, k the coefficient of heat conduction, and μ the coefficient of viscosity. The variables $\overline{x}$ and $\overline{t}$ denote, respectively, the space coordinate and time; the subscripts denote the partial derivatives.

For a van der Waals fluid, the pressure and the temperature are given by Quartapelle et al. (2003):

$$\overline{p} = K_0 \delta \frac{\overline{\rho}^{1+\delta} \exp(\delta \overline{s}/\mathrm{R})}{\left(1 - \overline{b}\overline{\rho}\right)^{1+\delta}} - \overline{a}\overline{\rho}^2, \qquad \overline{T} = K_0 \delta \frac{\overline{\rho}^{\delta} \exp(\delta \overline{s}/\mathrm{R})}{\left(1 - \overline{b}\overline{\rho}\right)^{\delta}}, \qquad (7.3)$$

where K_0 is a constant and $\delta = \mathrm{R}/c_v$ with R as the specific gas constant and c_v the specific heat at constant volume; the value of δ lies in the interval $0 < \delta \leq 2/3$ with

$\delta = 2/3$ for a mono-atomic fluid. The parameter $\overline{a}$ represents a measure of attraction between each particle that leads to added pressure due to intermolecular forces of attraction, and the parameter $\overline{b}$ denotes the effective volume of each particle.

Introducing the non-dimensional variables,

$$x = \frac{\overline{x}}{L}, p = \frac{\overline{p}}{\overline{p}_0}, \rho = \frac{\overline{\rho}}{\overline{\rho}_0}, t = \frac{\overline{t}\sqrt{\overline{p}_0/\overline{\rho}_0}}{L}, u = \frac{\overline{u}}{\sqrt{\overline{p}_0/\overline{\rho}_0}}, s = \frac{\overline{s}}{\overline{s}_0}, T = \frac{\overline{T}}{\overline{T}_0}, a$$

$$= \frac{\overline{a}\overline{\rho}_0^2}{\overline{p}_0}, b = \overline{b}\overline{\rho}_0, \tag{7.4}$$

system 7.2 can be written using vector matrix notation as

$$U_t + A(U)U_x = \frac{1}{Re}M(U)U_{xx} + \frac{1}{Re}N(U)[W(U)]_x U_x, \tag{7.5}$$

where $U = (\rho, u, s)^{tr}$ and **M, N,** and **W** are square matrices of order 3 with components denoted by $A_{ij}, M_{ij}, N_{ij},$ and W_{ij}, respectively, whose non-zero entries are given below:

$$A_{11} = A_{22} = A_{33} = u, \quad A_{12} = \rho, \quad A_{21} = \frac{p_\rho}{\rho}, \quad A_{23} = \frac{p_s}{\rho},$$

$$M_{22} = \frac{4}{3\rho}, \quad M_{31} = \frac{1}{Pr}\frac{RT_\rho}{T\rho\overline{s}_0}, \quad M_{33} = \frac{1}{Pr}\frac{RT_s}{T\rho\overline{s}_0},$$

$$N_{31} = \frac{1}{Pr}\frac{R}{T\rho\overline{s}_0}, \quad N_{32} = \frac{4}{3T\rho}\frac{\overline{p}_0}{\overline{T}_0\overline{\rho}_0\overline{s}_0}, \tag{7.6}$$

$$W_{11} = T_\rho, \quad W_{13} = T_s, \quad W_{22} = u,$$

with $Re := \frac{\overline{\rho}_0 L \sqrt{\overline{p}_0/\overline{\rho}_0}}{\mu}$ and $Pr := \frac{\mu R}{k}$ as the Reynolds number and Prandtl number, respectively.

7.3 Derivation of Evolution Equation

We look for asymptotic solutions of the system 7.5 of the form

$$U_i = U_i^{(0)} + \epsilon U_i^{(1)} + \epsilon^2 U_i^{(2)} + O(\epsilon^3), \tag{7.7}$$

where $U^{(0)} = (1, 0, 1)^{tr}$ refers to a constant background state and ϵ is a small parameter, $0 < \epsilon < < 1$, which may be regarded as the strength of the perturbed disturbance. The coefficient matrices $A, M, N,$ and W can be expanded about the constant state $U = U^{(0)}$ as

$$Y_{ij}(U) = Y_{ij}^{(0)} + Y'_{ijk}\left(\epsilon U_k^{(1)} + \epsilon^2 U_k^{(2)}\right) + Y''_{ijkl}\epsilon^2 U_k^{(1)} U_l^{(1)} + O\left(\epsilon^3\right), \qquad (7.8)$$

where i,j, and k vary from 1 to 3 and Y may denote any of the matrices A, M, N, and W. Further, we consider the following expansions:

$$\begin{aligned} Y'_{ijk} &= Y'_{ijk_0} + \epsilon Y'_{ijk_1} + O\left(\epsilon^2\right), \\ Y''_{ijkl} &= Y''_{ijkl_0} + \epsilon Y''_{ijkl_1} + O\left(\epsilon^2\right). \end{aligned} \qquad (7.9)$$

In the sequel, as pointed out in Cramer and Sen (1992) and Kluwick and Cox (1998), we refer to the critical points in the neighborhood where the quadratic steepening parameter $\tilde{\Gamma}$ is $O(\epsilon)$ that is,

$$\tilde{\Gamma} \equiv \frac{L_i A'_{ijk} R_j R_k}{L.R} = O(\epsilon), \qquad (7.10)$$

and consider the situation when the nonlinear distortions of disturbance, with perturbed strength $O(\epsilon)$, make their appearance noticeable over time scale of order $O(\epsilon^{-2})$; accordingly, we look for a far-field description near the wavefront and introduce the reference system $\xi = x - \lambda t$ and $\tau = \epsilon^2 t$ with λ as an eigenvalue of $A^{(0)}$. The new reference system achieves the purpose of shifting attention to the vicinity of the wavefront for large time. For small dissipative effect, we consider the Reynolds number $Re = O(\epsilon^{-2})$. In terms of the transformed variable ξ and τ, system Eq. 7.5 takes the form:

$$\epsilon^2 \frac{\partial U}{\partial \tau} + (A - \lambda I)\frac{\partial U}{\partial \xi} = \frac{1}{Re}M(U)U_{\xi\xi} + \frac{1}{Re}N(U)[W(U)]_\xi U_\xi. \qquad (7.11)$$

In view of the development, Eqs. 7.7 and 7.11 yield the following systems of PDEs at order $O(\epsilon^k)$, $k=1,2,3$:

$$\begin{aligned} O(\epsilon) &: G_{ij}U_{j\xi}^{(1)} = 0, \\ O\left(\epsilon^2\right) &: G_{ij}U_{j\xi}^{(2)} = -A'_{ijk_0}U_{j\xi}^{(1)}U_k^{(1)}, \\ O\left(\epsilon^3\right) &: G_{ij}U_{j\xi}^{(3)} = -U_{i\tau}^{(1)} - A'_{ijk_0}U_{j\xi}^{(1)}U_k^{(2)} - A'_{ijk_0}U_k^{(1)}U_{j\xi}^{(2)} - A'_{ijk_1}U_{j\xi}^{(1)}U_k^{(1)} \\ &\qquad - A''_{ijkl_0}U_{j\xi}^{(1)}U_k^{(1)}U_l^{(1)} + \frac{1}{\epsilon^2 Re}M_{ij}^{(0)}U_{j\xi\xi}^{(1)}, \end{aligned}$$

$$(7.12)$$

where $G_{ij} = A_{ij}^{(0)} - \lambda\delta_{ij}$.

The solvability condition for Eq. 7.12 requires that

$$det(G) = 0; \tag{7.13}$$

the eigenvalue λ takes the values, $-c_0$, 0, and $+c_0$, where $c_0 := \sqrt{\left(\frac{\partial p}{\partial \rho}\right)_0}$ is the speed of sound in the medium; hereafter, we will study the right moving wave which corresponds to the eigenvalue c_0. For c_0 to be real and nonzero, the term inside the square root must be positive, which in view of equation of state (Eq. 7.3) $_1$ requires that

$$\frac{(1 + \delta)(1 + a)}{1 - b} - 2a > 0; \tag{7.14}$$

it may be noticed that the inequality (Eq. 7.14) holds true in the domain $\{a, b, \delta : 0 < a \leq 1, 0 < b < 1, 0 < \delta \leq 2/3\}$. The left and the right eigenvectors of $A^{(0)}$ corresponding to the eigenvalue c_0 are

$$L = (c_0, 1, p_{s0}/c_0), R = (1/c_0, 1, 0)^{tr}. \tag{7.15}$$

Equation (7.12) implies that the solution vector $U^{(1)}$ is collinear to the right eigenvector R, that is,

$$U^{(1)} = V(\xi, \tau)R, \tag{7.16}$$

where $V(\xi, \tau)$ is the wave amplitude function, which is determined at the next order.

The solvability conditions for $U_i^{(2)}$ and $U_i^{(3)}$ require that the RHS of (12) $_2$ and (12) $_3$ be orthogonal to the left eigenvector L; this, indeed, imposes the conditions

$$\frac{L_i A'_{ijk_0} R_j R_k}{L.R} = 0, \tag{7.17}$$

and

$$(L \cdot R)V_\tau + L_i A'_{ijk_0} R_k U_{j,\xi}^{(2)} V + L_i A'_{ijk_0} R_j U_k^{(2)} V_\xi + L_i A'_{ijk_1} R_j R_k VV_\xi$$
$$+ L_i A''_{ijkl_0} R_j R_k R_l V^2 V_\xi - \frac{1}{\epsilon^2 Re} L_i M_{ij}^{(0)} R_j V_{\xi\xi} = 0, \tag{7.18}$$

where the terms containing $U_{j,\xi}^{(2)}$ and $U_k^{(2)}$ can be determined in terms of V^2 and V, respectively (see Cramer and Sen (1992) and Kluwick and Cox (1998)), and the resulting transport equation turns out to be of the following form:

Table 7.1 Behavior of Γ and Λ under the influence of van der Waals parameters a and b

	Increases with b	Decreases with a
Γ	$0 < a \leq 1, 0 < b < 1, 0 < \delta \leq 2/3$	$0 < a \leq 1, 0 < b < 1/9, 0 < \delta \leq 2/3$
Λ	$0 < a \leq 1, 0 < b < 1, 0 < \delta \leq 2/3$	$0 < a \leq 1, 0 < b < 1/12, 0 < \delta \leq 2/3$

$$V_\tau + (f(V))_\xi = \nu V_{\xi\xi}, \tag{7.19}$$

where $f(V) = \frac{\Gamma}{2}V^2 + \frac{\Lambda}{6}V^3$ with

$$\Gamma = \frac{\tilde{\Gamma}}{\epsilon} = \frac{\tilde{\Xi}_0}{\epsilon} = \frac{1}{2\epsilon}\frac{(1+\delta)(2+\delta)(1+a) - 6a(1-b)^2}{(1+\delta)(1+a)(1-b) - 2a(1-b)^2} = O(1), \tag{7.20}$$

$$\Lambda = \frac{(1+\delta)(2+\delta)(1+a)(6b+\delta-3) + 12a(1-b)^3}{2\left[(1+\delta)(1+a)(1-b) - 2a(1-b)^2\right]^{3/2}} = O(1), \tag{7.21}$$

being the quadratic and cubic nonlinearity parameters, and

$$\nu = \frac{1}{\epsilon^2 Re}\left[\frac{4}{3} + \frac{1}{Pr}\frac{\delta^2(1+a)}{(1+\delta)(1+a) - 2a(1-b)}\right] = O(1); \tag{7.22}$$

here $\tilde{\Xi}_0$ is the value of $\tilde{\Xi}$ evaluated at the unperturbed state. Using basic calculus tools, the behavior of Γ and Λ, influenced by the van der Waals parameters a and b, with the constraints given by Eq. 7.14, can be summarized in Table 7.1.

We restrict our discussion for the values of a, b, and δ lying in the intervals $0 < a \leq 1$, $0 < b < 1/12$, and $0 < \delta \leq 2/3$ for which Γ and Λ are monotonic.

It may be remarked that no analytical representation of the solution of Eq. 7.19 is feasible (Crighton 1986); however a few solutions of the associated kinematic equation, which appear to be novel, have been discussed in Cramer and Kluwick (1984) and Cramer et al. (1986). In the following section, using the related methodologies, we study the associated kinematic equation analytically to investigate the effects of the van der Waals parameters on the evolutionary behavior of waves that finally develop and obtain the numerical solutions, in Sect. 7.5, of parabolic Eq. 7.19, which is more amenable for numerical study.

7.4 Kinematic Shocks Associated with the Evolution Equation

In this section, we analyze the wave patterns evolving as solutions of the Cauchy problem for the kinematic equation associated with Eq. 7.19, by considering that there is no viscous term, and using the initial data

$$
V(\xi, 0) = \begin{cases} \Pi & \xi \in (-1, 1) \\ 0 & \text{otherwise,} \end{cases}
\tag{7.23}
$$

where $\Pi \in \mathrm{IR}$. Typically two Riemann problems are solved each at $\xi = -1$ and $\xi = 1$. Since the flux function is non-convex and contains an inflection point, solution is constructed by considering the effective flux function through a convex-hull (respectively, a concave-hull), which can be best described by the rest position of an elastic string stretched tightly below (respectively, above) the curve on the interval $[0, \Pi]$ (or $[\Pi, 0]$ if $\Pi < 0$), for instance, see Fig. 7.1 and Ref. (Zheng 2001). The portion of the hull that agrees with the flux function represents a centered wave-fan, whereas the straight line segment represents a shock satisfying the Oleinik's entropy condition (Oleinik 1959):
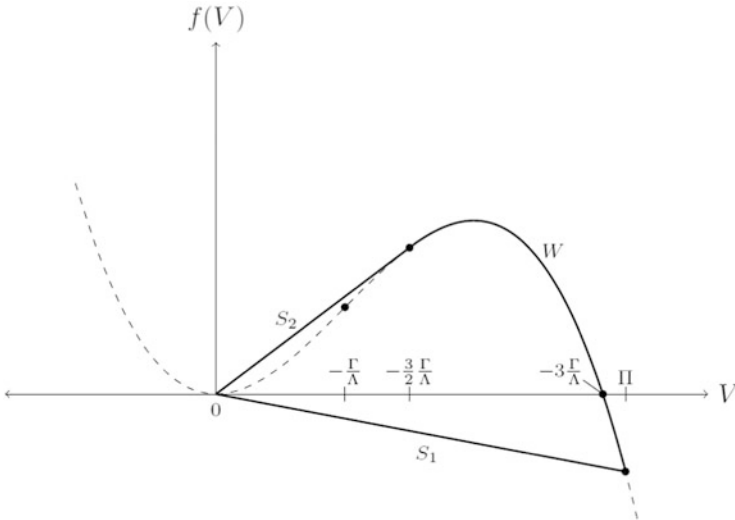
Fig. 7.1 Illustration for the flux function and construction of convex/conclave-hull (in Case 4); $-\frac{\Gamma}{\Lambda}$ is the inflexxion point, $-\frac{3}{2}\frac{\Gamma}{\Lambda}$ the point of tangency, S_1 the expansion shock, S_2 the expansion shock, S_2 the sonic compression shock, and W the compression fan

$$\frac{f(V)-f(V_l)}{V-V_l} \geq \frac{d\xi_s}{d\tau} \geq \frac{f(V)-f(V_r)}{V-V_r}, \tag{7.24}$$

where V_l and V_r are the left and the right states of the shock, respectively; here ξ_s denotes the position on the shock. The expression for the shock speed is then given by the Rankine-Hugoniot condition, and it turns out that

$$\frac{d\xi_s}{d\tau} = \frac{\Gamma}{2}(V_l + V_r) + \frac{\Lambda}{6}(V_l^2 + V_l V_r + V_r^2). \tag{7.25}$$

The strength σ of a shock can be defined as the magnitude of the jump:

$$\sigma := V_l - V_r. \tag{7.26}$$

Since the flux function is cubic in V, the graph of $f(V)$ possesses only one inflection point; so the equality in Eq. 7.24 holds only on one side depending upon the sign of Λ and the shock is reffered to as a sonic shock. For a given state V, the state V^t(say), which can be connected through a sonic shock at V^t, is uniquely determined as

$$V^t = -\frac{1}{2}\left(3\frac{\Gamma}{\Lambda} + V\right). \tag{7.27}$$

Equation 7.27, in view of Eq. 7.25, yields the sonic shock speed

$$\frac{d\xi_s}{d\tau} = \frac{\Lambda}{8}\left(V + 3\frac{\Gamma}{\Lambda}\right)\left(V - \frac{\Gamma}{\Lambda}\right). \tag{7.28}$$

Since Γ and Λ depend on the van der Waals parameters a and b (Table 7.1), the shock speed and consequently the interaction time of waves, width of wave-fan, and shock strength are also influenced.

Several cases can be discussed depending upon the initial condition and the signs of Γ and

Λ; in fact if one case is discussed, others can be explained in an analogous manner. Here we discuss the problem for which $\Gamma > 0$ and $\Lambda < 0$. As we increase Π from negative to a positive value, the solution can be classified into four cases depending upon some critical values of V (see Fig. 7.1); accordingly, we discuss the following cases:

(1) $\Pi \leq -\frac{\Gamma}{\Lambda}$, (2) $-\frac{\Gamma}{\Lambda} \leq \Pi \leq -\frac{3}{2}\frac{\Gamma}{\Lambda}$, (3) $-\frac{3}{2}\frac{\Gamma}{\Lambda} \leq \Pi \leq -3\frac{\Gamma}{\Lambda}$, (4) $\Pi \geq -3\frac{\Gamma}{\Lambda}$.

7.4.1   Case 1 ($\Pi \leq -\frac{\Gamma}{\Lambda}$)

Depending upon whether $\Pi < 0$ or $\Pi > 0$, two sub-cases may be considered. If $\Pi < 0$, a compression shock emanates from $\xi = -1$ connecting $V = 0$ to $V = \Pi$; at $\xi = 1$ a centered expansion fan connects $V = \Pi$ to $V = 0$ continuously. However, if $\Pi > 0$, the wave pattern is reversed; at $\xi = -1$ a centered expansion fan W, described by the characteristics

$$\xi = \left(\Gamma V + \Lambda \frac{V^2}{2} \right) \tau - 1, \qquad 0 \leq V \leq \Pi, \tag{7.29}$$

connects $V = 0$ to $V = \Pi$, while at $\xi = 1$ a compression shock S_1 emanates connecting $V = \Pi$ to $V = 0$ (see Fig. 7.2a). In each case, the shock and the wave-fan start interacting after some time, but their interactions are essentially the same for both the cases. Hereafter, we consider the situation when $\Pi > 0$; the compression shock S_1, which emanates from $\xi = 1$, propagates with speed

$$\frac{d\xi_s}{d\tau} = \Gamma \frac{\Pi}{2} + \Lambda \frac{\Pi^2}{6}. \tag{7.30}$$

The leading characteristic of the expansion fan W, carrying the value $V = \Pi$, hits the shock at
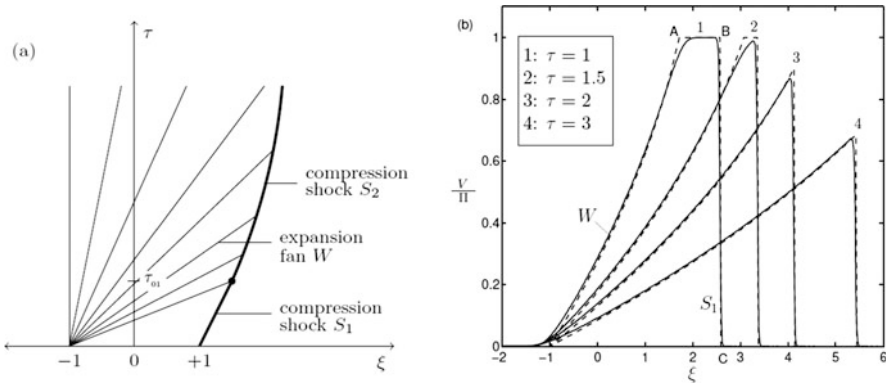
Fig. 7.2 Case 1; (**a**) illustration of analytical solution in $\xi - \tau$ plane; thick and thin lines represent shocks and characteristics of the wave-fan, respectively; (**b**) numerical comparison of viscous (solid line) and inviscid (dashed line) solutions with $a = 0.01$, $b = 0.01$, $\delta = 0.4$ and $\Pi = 1$, which yield $\tau_{01} = 1.7553$; the horizontal and vertical lines, for instance, AB and BC in Profile 1, correspond to the constant state and a shock, respectively, whereas W corresponds to the expansion fan

$$\tau_{01} = \frac{12}{\Pi(3\Gamma + 2\Pi\Lambda)}. \tag{7.31}$$

For $\tau > \tau_{01}$, the shape and speed of the shock S_1 get altered because of its interaction with the characteristics of the wave-fan W. Consequently, the staright shock S_1 assumes the form of a curved shock S_2, the speed of which can be determined with the help of Eq. 7.25 with $V_r = 0$ and V_l given by wave-fan Eq. 7.29. Since at the shock S_2, ξ is a function of τ, the left state V_l can be obtained as a function of τ

$$V_l = V(\xi_s(\tau), \tau) \equiv \phi(\tau). \tag{7.32}$$

Thus the speed of S_2, in terms of ϕ, is given by

$$\frac{d\xi_s}{d\tau} = \Gamma\frac{\phi}{2} + \Lambda\frac{\phi^2}{6}. \tag{7.33}$$

Equation 7.29 also yields an expression for the shock speed as

$$\frac{d\xi_s}{d\tau} = \left(\Gamma\phi + \Lambda\frac{\phi^2}{2}\right) + \tau(\Gamma + \Lambda\phi)\frac{d\phi}{d\tau}, \tag{7.34}$$

which, together with Eq. 7.33 and the condition $\phi(\tau_0) = \Pi$, yields the following expression for $\phi(\tau)$:

$$\tau\phi^2(3\Gamma + 2\Lambda\phi) = 12\Pi. \tag{7.35}$$

Equation 7.35 shows that the shock amplitude $\phi(\tau)$ decays to zero like

$$\phi \sim 2\left(\frac{\Pi}{\Gamma}\right)^{\frac{1}{2}}\tau^{-\frac{1}{2}} \quad as \ \tau \to \infty. \tag{7.36}$$

It may be noticed from Eq. 7.31 that an increase in b shortens the interaction time τ_{01}, whereas an increase in a delays the same. Indeed, an increase in b triggers the physical mechanism that causes the speed of the shock S_1 and width of the wave-fan W to increase; however, the strength of the shock S_2 decreases, rather than increases, with b. In contrast, an increase in a has exactly opposite effects. Since the curvature of the curved shock S_2 changes for different values of a and b, dependence of the speed of the shock S_2 upon these parameters is non-monotonic. The strength of shock S_1 is fixed (i. e. , Π) and does not depend upon a or b. Finally the influence of a and b upon the eventual decay of wave profile is examined; indeed, the expression (Eq. 7.36) shows that the wave decays at a faster rate with an increase in b, whereas an increase in a is capable of counteracting the decay rate. These observations show

that the effects of van der Waals parameters a and b, which are opposite in nature, can influence the wave pattern significantly.

7.4.2   Case 2 ($- \frac{\Gamma}{\Lambda} \leq \Pi \leq - \frac{3}{2} \frac{\Gamma}{\Lambda}$)

Since $- \frac{\Gamma}{\Lambda}$ is the inflection point, the state $\Pi > - \frac{\Gamma}{\Lambda}$ cannot be joined with the state $V = 0$ directly with a fan; indeed, the transition requires the introduction of an expansion shock S_1 followed by a centered expansion fan W (see Fig. 7.3a). Thus, a complete waveform that evolves at $\xi = -1$ consists of a centered expansion fan W connecting $V = 0$ to $V = V^t$ with a sonic expansion shock S_1 at its right edge joining $V = V^t$ to $V = \Pi$; here V^t is the value of V for which the chord joining (Π, $f(\Pi)$) and ($V^t, f(V^t)$) is tangent to the graph of $f(V)$ at $V = V^t$. A compression shock S_2 emanates from $\xi = 1$, connecting $V = \Pi$ to $V = 0$. The strength and speed of the shock S_1 are

$$\sigma = \frac{3}{2}\left(\Pi + \frac{\Gamma}{\Lambda}\right), \qquad \frac{d\xi_{S_1}}{d\tau} = \frac{\Lambda}{8}\left(\Pi + 3\frac{\Gamma}{\Lambda}\right)\left(\Pi - \frac{\Gamma}{\Lambda}\right). \qquad (7.37)$$

The expansion shock S_1 collides with the compression shock S_2 of strength Π at time

$$\tau_{02} = -\frac{48}{\Lambda}\left(\Pi + 3\frac{\Gamma}{\Lambda}\right)^{-2}. \qquad (7.38)$$
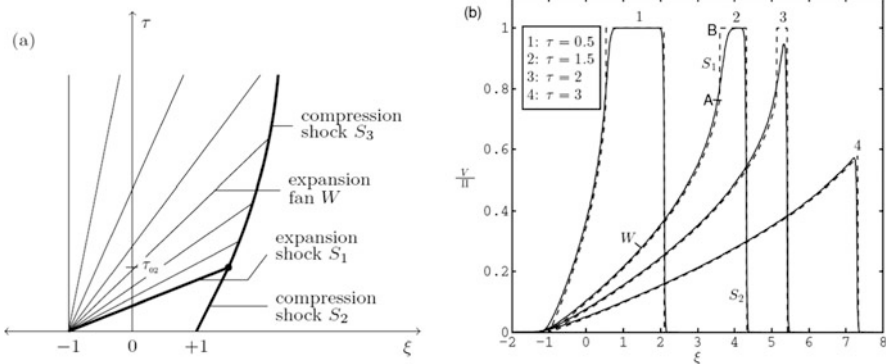
Fig. 7.3 Case 2; (**a**) illustration of analytical solution in $\xi - \tau$ plane, thick lines represent shocks and thin lines represent the characteristics of the wave-fan; (**b**) numerical comparison of viscous (solid line) and inviscid (dashed line) solutions with $a = 0.01$, $b = 0.01$, $\delta = 0.4$ and $\Pi = 1.8$, which yield $\tau_{02} = 2.3227$; the vertical line segment AB in Profile 2 corresponds to the sonic expansion shock S_1.

The collision gives rise to a merged shock S_3, beyond $\tau = \tau_{02}$, with a reduced speed and strength. Shock S_3 interacts with the expansion fan for $\tau > \tau_{02}$. On account of this interaction, the shape and the speed of the resulting shock get altered, which can be obtained by invoking the Rankine-Hugoniot condition (Eq. 7.25) and the characteristic family (29) with $0 \leq V \leq -\frac{1}{2}\left(\Pi + 3\frac{\Gamma}{\Lambda}\right)$; this leads to an evolutionary behavior for ϕ, namely:

$$\Lambda\phi^2\left(\phi + \frac{3}{2}\frac{\Gamma}{\Lambda}\right) = \frac{6\Pi}{\tau}, \tag{7.39}$$

with $\phi(\tau_{02}) = \Pi$. It can be seen that the speed of the resultant shock S_3 is less than that of the shock S_2; Eq. 7.39 shows that the shock amplitude ϕ decays to zero like $\tau^{-\frac{1}{2}}$ as $\tau \to \infty$; in fact

$$\phi \sim 2\left(\frac{\Pi}{\Gamma}\right)^{\frac{1}{2}}\tau^{-\frac{1}{2}} \quad as\ \tau \to \infty. \tag{7.40}$$

It is clearly seen from expression (Eq. 7.38) that the effects of a and b on the interaction time τ_{02} are qualitatively similar to the effects of a and b on τ_{01}. Also, it follows that the speeds of shocks S_1 and S_2 and the width of the wave-fan W increase, whereas the strengths of shocks S_1 and S_3 decrease with an increase in b; in contrast, the effect of the van der Waals parameter a is just opposite to that of b. It may be remarked that the strength of shock S_2 is not at all influenced by the van der Waals parameters. The final decay of the wave profile is exactly the same as in the previous case.

7.4.3   Case 3 ($-\frac{3}{2}\frac{\Gamma}{\Lambda} \leq \Pi \leq -3\frac{\Gamma}{\Lambda}$)

In this case, the initial discontinuity located at $\xi = -1$ splits into an expansion fan W_1 and a sonic expansion shock S_1, located on the extreme right edge of the fan W_1 (see Fig. 7.4a). Similarly at $\xi = 1$, because of the stability condition (Eq. 7.24), a single shock cannot connect $V = \Pi$ to $V = 0$, and thus a sonic compression shock S_2, followed by a centered compression fan W_2, described by

$$\xi = \left(\Gamma V + \Lambda\frac{V^2}{2}\right)\tau + 1, \qquad -\frac{3}{2}\frac{\Gamma}{\Lambda} \leq V \leq \Pi, \tag{7.41}$$

evolves at $\tau = 0$. The shock S_1, described by Eq. 7.37, first intersects the extreme left characteristic of the wave-fan W_2, carrying $V = \Pi$, at time
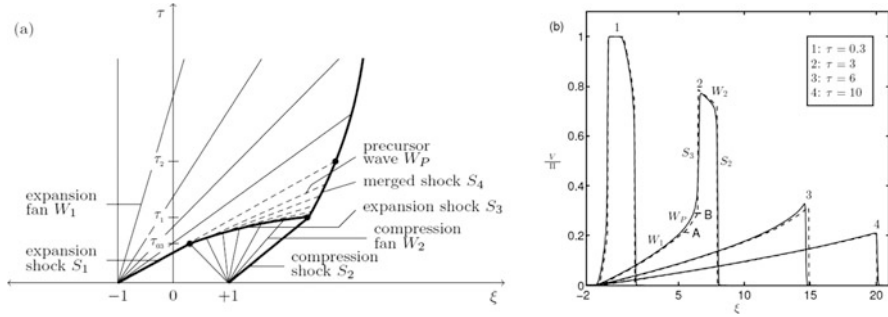
Fig. 7.4 Case 3; (**a**) illustration of analytical solution in $\xi - \tau$ plane, thick lines represent shocks and thin lines represent the characteristics of the wave-fan; (**b**) numerical comparison of viscous (solid line) and inviscid (dashed line) solutions with $a = 0.01$, $b = 0.01$, $\delta = 0.4$ and $\Pi = 3.2$, which yield $\tau_{03} = 0.7345$, $\tau_1 = 5.7768$, and $\tau_2 = 9.2417$; the curved portion AB in Profile 2 corresponds to the precursor wave W_P

$$\tau_{03} = -\frac{16}{3\Lambda}\left(\Pi + \frac{\Gamma}{\Lambda}\right)^{-2}. \tag{7.42}$$

For $\tau > \tau_{03}$, the speed of the resultant shock S_3 cannot be less than $f'(V^t)$ because of the limitations imposed by the Oleinik condition. Indeed, for $\tau > \tau_{03}$, the shock S_3 becomes curved on account of its interaction with the wave-fan W_2. The solution in the region between the characteristic on the right edge of W_1 and the curved shock S_3 is given by a non-centered expansion-fan, called the precursor wave W_P, whose characteristics are tangent to the shock S_3; a similar construction can be found in a work by Ballou (1970). So the shock S_3 is a sonic shock; its interaction with the wave-fan W_2 is described by (37) and (41) to yield

$$\left(\phi + \frac{\Gamma}{\Lambda}\right) = \left(\Pi + \frac{\Gamma}{\Lambda}\right)\left(\frac{\tau}{\tau_0}\right)^{-\frac{3}{8}}, \tag{7.43}$$

where ϕ satisfies $\phi(\tau_{03}) = \Pi$. The shock S_3 collides with shock S_2 that carries the value $\phi = -\frac{3}{2}\frac{\Gamma}{\Lambda}$; using this value of ϕ in (43), we get the time of collision as

$$\tau_1 = \tau_{03}\left(-\frac{2\Lambda}{\Gamma}\left(\Pi + \frac{\Gamma}{\Lambda}\right)\right)^{\frac{8}{3}}. \tag{7.44}$$

The equation of the curved shock S_3 can be obtained, by invoking Eqs. 7.41 and 7.43, as

$$\sigma = \frac{3}{2}\left(\Pi + \frac{\Gamma}{\Lambda}\right)\left(\frac{\tau}{\tau_{03}}\right)^{-\frac{3}{2}}, \qquad \xi_s = \frac{\Lambda}{2}\left[\left(\Pi + \frac{\Gamma}{\Lambda}\right)^2\left(\frac{\tau}{\tau_{03}}\right)^{-\frac{3}{4}} - \frac{\Gamma^2}{\Lambda^2}\right]\tau$$

$$+ 1, \qquad \tau_{03} \le \tau \le \tau_1. \tag{7.45}$$

The sonic compression shock S_2, which was of constant strength till $\tau = \tau_1$, also weakens on account of its interaction with S_3 for $\tau > \tau_1$; indeed for $\tau > \tau_1$, the merged shock S_4 interacts with the precursor wave W_P. The flow in the precursor wave region is governed by the following equation:

$$\xi(\tau) = \left(\Gamma V_l + \Lambda \frac{V_l^2}{2}\right)(\tau - \tilde{\tau}) + \xi_s(\tilde{\tau}), \tag{7.46}$$

where V_l is the value of V that precursor waves carry, $\xi_s(\tilde{\tau})$ is the shock location, and $\tilde{\tau}$ is the time when characteristics (precursor waves) leave the shock S_3; the expression for $\tilde{\tau}$ can be obtained from Eq. 7.43. Finally, the equation that describes the precursor wave region is given by the following expression:

$$\xi(\tau) = \left(\Gamma V_l + \Lambda \frac{V_l^2}{2}\right)\tau - 2^{\frac{1}{3}}\left(\frac{\Pi + \frac{\Gamma}{\Lambda}}{V_l + \frac{\Gamma}{\Lambda}}\right)^{\frac{2}{3}} + 1, \qquad -\frac{1}{2}\left(\Pi + 3\frac{\Gamma}{\Lambda}\right) \le V_l \le$$

$$-\frac{3}{4}\frac{\Gamma}{\Lambda}, \qquad \tau_{03} \le \tau \le \tau_2, \tag{7.47}$$

where τ_2 is the time that brings an end to the interaction process between W_P and S_4.

The speed of the merged shock S_4, which connects the precursor wave to the constant density region, is given by $d\xi_s/d\tau = \Gamma V_l/2 + \Lambda V_l^2/6$, $\tau_1 \le \tau \le \tau_2$; this, in view of Eq. 7.47, yields the following ODE for ϕ:

$$\frac{d\phi}{d\tau} = -\frac{\phi(2\Lambda\phi + 3\Gamma)}{6\left[\tau(\Gamma + \Lambda\phi) + \chi(\Gamma + \Lambda\phi)^{-\frac{5}{3}}\right]}, \qquad \chi$$

$$= \frac{2^{\frac{4}{3}}}{3}\Lambda(\Gamma + \Lambda\Pi)^{\frac{2}{3}}, \qquad \tau_1 \le \tau \le \tau_2. \tag{7.48}$$

Solution of Eq. 7.48, satisfying the condition, $\phi = -\frac{3}{2}\frac{\Gamma}{\Lambda}$ at $\tau = \tau_1$, can be written in the following implicit form, describing the merged shock wave S_4:

$$\tau\phi^2\left(\phi + \frac{\Gamma}{\Lambda}\right)^{\frac{2}{3}} = -\frac{9}{\Lambda^{8/3}}\chi, \qquad \tau_1 \le \tau \le \tau_2. \tag{7.49}$$

This interaction of precursor waves with the shock S_4 ends where the characteristic of the precursor wave, carrying the value $V = -(3\Gamma/\Lambda + \Pi)/2$, meets the merged shock S_4 at time τ_2 given by

$$\tau_2 = -48\Lambda^{-1}\left(\Pi + 3\frac{\Gamma}{\Lambda}\right)^{-2}. \tag{7.50}$$

The merged shock, after time τ_2, starts interacting with the wave-fan W_1; this interaction rule can be obtained as in Case 2, and the long time behavior is described by

$$\phi \sim 2\left(\frac{\Pi}{\Gamma}\right)^{\frac{1}{2}}\tau^{-\frac{1}{2}} \quad as\ \tau \to \infty. \tag{7.51}$$

An increase in the value of the parameter b causes the interaction time τ_{03}, speeds of shocks S_1 and S_2, strength of the shock S_2, and the width of the wave-fan W_1 to increase, whereas it induces a reduction in τ_1 and τ_2; strengths of the shocks S_1, S_3, and S_4; and width of the wave-fan W_2. However, an increase in the value of the parameter a shows effects opposite to that of b. Again, the effects of a and b upon the decay behavior are qualitatively similar to the previous cases.

7.4.4   Case 4 ($\Pi \geq -3\frac{\Gamma}{\Lambda}$)

Unlike the earlier cases, where an expansion fan at $\xi = -1$ was required, the present case requires no such fan. In fact, it requires only an expansion shock S_1, connecting $V_l = 0$ to $V_r = \Pi$; at $\xi = 1$, a compression-fan W is headed by a sonic compression shock S_2 (see Fig. 7.5a). Initially the shock S_1, emanating from $\xi = -1$, moves toward the left with a constant speed until it meets the characteristic located on the left edge of the wave-fan W_2 at time
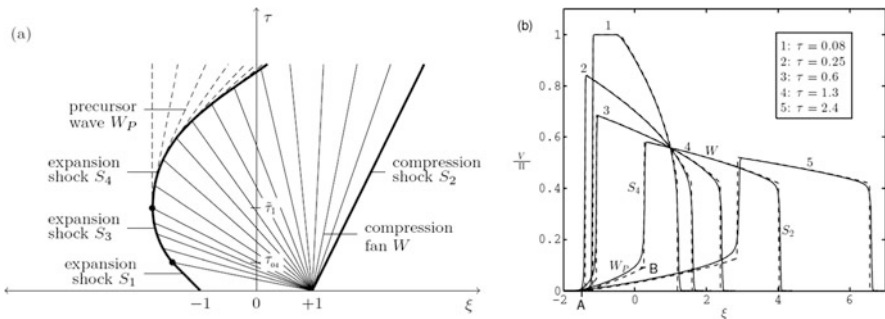
Fig. 7.5 Case 4; (**a**) illustration of analytical solution in $\xi - \tau$ plane, thick lines represent shocks and thin lines represent the characteristics of the wave-fan; (**b**) numerical comparison of viscous (solid line) and inviscid (dashed line) solutions with $a = 0.01$, $b = 0.01$, $\delta = 0.4$ and $\Pi = 5.5$, which yield $\tau_{04} = 0.1302$, $\tilde{\tau}_1 = 0.2574$, and $\tilde{\tau}_2 = 10.3761$; the curved portion AB in Profile 4 corresponds to the precursor wave W_P, whereas S_2, W, and S_4 correspond to their counterparts in (**a**)

$$\tau_{04} = -\frac{12}{\Pi(3\Gamma + 2\Pi\Lambda)}. \qquad (7.52)$$

The shock S_1, on account of its interaction with the compression wave-fan W, slows down and assumes a curved shape S_3; indeed, the shock S_3 becomes stationary when it meets the characteristic of W, carrying the value $V = -3\Gamma/\Lambda$, at time

$$\tilde{\tau}_1 = \frac{4}{9}\frac{\Lambda^2}{\Gamma^3}\Pi. \qquad (7.53)$$

For $\tau > \tilde{\tau}_1$, the shock S_3 moves to the right and assumes the form of a sonic shock S_4 with a reduced strength. As discussed in Case 3, a non-centered wave-fan W_P (precursor wave) needs to be introduced between the shock S_4 and the constant state on the left. The location ξ_s of the curved shock S_4 and its strength σ are given by

$$\xi_s = \frac{\Gamma^2}{2\Lambda}\left[4\left(\frac{\tilde{\tau}_1}{\tau}\right)^{\frac{3}{4}} - 1\right]\tau + 1, \qquad \sigma = -3\frac{\Gamma}{\Lambda}\left(\frac{\tilde{\tau}_1}{\tau}\right)^{\frac{3}{2}}, \qquad \tilde{\tau}_1 \leq \tau \leq \tilde{\tau}_2, \quad (7.54)$$

where $\tilde{\tau}_2$ is the time at which shocks S_2 and S_4 collide. Further interaction of the sonic shock S_4 with the wave-fan W can be obtained as in Case 3; the interaction ends when the shock meets the characteristic of wave-fan W, carrying the value $V = -3\Gamma/(2\Lambda)$, at time

$$\tilde{\tau}_2 = \frac{4^{\frac{11}{3}}}{9}\frac{\Lambda^2}{\Gamma^3}\Pi. \qquad (7.55)$$

For $\tau > \tilde{\tau}_2$, shocks S_2 and S_4 merge into a single shock, referred to as the merged shock, which has $V = 0$ on one side and precursor on the other side, merging from behind; indeed the merged shock for $\tau > \tilde{\tau}_2$ is described by the following implicit relation:

$$\tau\phi^2(\Gamma + \Lambda\phi)^{\frac{2}{3}} = \frac{4}{\Gamma^{1/3}}\Pi, \qquad \tau > \tilde{\tau}_2, \qquad (7.56)$$

showing thereby that the wave eventually decays like

$$\phi \sim 2\left(\frac{\Pi}{\Gamma}\right)^{\frac{1}{2}}\tau^{-\frac{1}{2}} \qquad as \ \tau \to \infty; \qquad (7.57)$$

indeed, the decay behavior, influenced by the van der Waals parameters a and b, remains similar to the earlier cases. The new feature in this case is this that in contrast to Case 3, the interaction of precursor wave W_P with the merged shock will never end in a finite time.

In this case, an increase in b leads to an increase in interaction time τ_{04}, speeds of both the shocks S_1 and S_2, and strengths of shocks S_2, S_3, and S_4, whereas the interaction times $\tilde{\tau}_1$ and $\tilde{\tau}_2$, the strength of the merged shock, and width of the wave-fan W decrease with an increase in b; as noted in Case 3, here also, the van der Waals parameter a has opposite effects on the wave evolution.

7.5   Numerical Solution

This section is devoted to the numerical solutions of parabolic Eq. 7.19, in the hyperbolic limit $\nu \to 0$, for all the four cases discussed in Sect. 7.4 using a weighted essentially non-oscillatory (WENO) scheme. Values of the van der Waals parameters a and b are carefully taken from the intervals presented in Sect. 7.3, so that by varying the values of these parameters, the value of Π does not fall out of the range under consideration. In each of these cases, three sets of computations are performed; in the first set, solution is given at various times (with fixed values of $a = 0.01$ and $b = 0.01$) in order to provide a complete picture of the evolutionary behavior of the signal profile. In the second (respectively, third) set, parameter a (respectively, b) is varied while keeping b (respectively, a) and τ fixed.

The numerical scheme is based on an essentially non-oscillatory (ENO) scheme. The key idea of ENO schemes is to use the "smoothest" stencil among several candidates to approximate the fluxes at cell boundaries to a higher-order accuracy and at the same time to avoid oscillations near shocks. The weighted essentially non-oscillatory (WENO) scheme uses a convex combination of all the candidate stencils instead of approximating the numerical flux using only one candidate stencil so that the order of accuracy is improved. Here we use a fifth-order WENO scheme (Jiang and Shu 1996) to solve parabolic Eq. 7.19 with the initial condition (Eq. 7.23) by treating the flux function, outlined as above, and approximating the second derivative by the central difference scheme. The scheme of Jiang and Shu is presented here for the sake of completeness. On discretizing the space into uniform meshes $\xi_{\frac{1}{2}} < \xi_{\frac{3}{2}} < \ldots < \xi_{N-\frac{1}{2}} < \xi_{N+\frac{1}{2}}$ with $\Delta\xi = \xi_{j+\frac{1}{2}} - \xi_{j-\frac{1}{2}} = \text{constant}$, the numerical scheme can be described as

$$V_\tau = -\frac{1}{\Delta\xi}\left(\widehat{f}_{j+\frac{1}{2}} - \widehat{f}_{j-\frac{1}{2}}\right) + \frac{V_{j-1} - 2V_j + V_{j+1}}{\Delta\xi^2}, \qquad (7.58)$$

where $\widehat{f}$ is monotonic numerical flux. Since the flux function $f(V)$ is non-monotonic (see Fig. 7.1), we split it into two monotonic parts using the global Lax-Friedrichs flux splitting as

Table 7.2 Values of $a_{k,l}^r$ and C_k^r with $r = 3$

k	$l = 0$	$l = 1$	$l = 2$	C_k^3
0	1/3	−7/6	11/6	1/10
1	−1/6	5/6	1/3	6/10
2	1/3	5/6	−1/6	3/10

$$f^{\pm}(V) = \frac{1}{2}(f(V) \pm \alpha V); \quad \alpha = \max |f'(V)|. \tag{7.59}$$

The numerical flux then takes the form $\widehat{f}_{j+\frac{1}{2}} = \widehat{f}_{j+\frac{1}{2}}^+ + \widehat{f}_{j+\frac{1}{2}}^-$, where $\widehat{f}^{\pm}$ are given by

$$\widehat{f}^{\pm} = \sum_{k=0}^{r-1} w_k q_k^r \left(f_{j+k-r+1}^{\pm}, \ldots, f_{j+k}^{\pm} \right), \tag{7.60}$$

with

$$q_k^r(g_0, \ldots, g_{r-1}) = \sum_{l=0}^{r-1} a_{k,l}^r g_l, \quad w_k = \frac{\alpha_k}{\alpha_0 + \ldots + \alpha_{r-1}}, \quad \alpha_k$$

$$= \frac{C_k^r}{(\epsilon' + IS_k)^2}, \quad 0 \le k, l \le r - 1. \tag{7.61}$$

The quantities w_k defined as above are the weights, ϵ' is a small positive real number introduced to maintain denominator nonzero, and IS_k is a smoothness measurement of the flux function on the kth stencil. Equation 7.60 gives the fifth-order WENO scheme, with $r=3$, for which $a_{k,l}^r$ and C_k^r are given in Table 7.2 and IS_k are given as follows:

$$IS_0 = \frac{13}{12}(f_{j-2} - 2f_{j-1} + f_j)^2 + \frac{1}{4}(f_{j-2} - 4f_{j-1} + 3f_j)^2,$$
$$IS_1 = \frac{13}{12}(f_{j-1} - 2f_j + f_{j+1})^2 + \frac{1}{4}(f_{j-1} - f_{j+1})^2, \tag{7.62}$$
$$IS_2 = \frac{13}{12}(f_j - 2f_{j+1} + f_{j+2})^2 + \frac{1}{4}(3f_j - 4f_{j+1} + f_{j+2})^2.$$

For the illustration of the solution in Case 1, we take $\Pi = 1$; both inviscid and viscous solutions at various times are depicted in Fig. 7.2b exhibiting that at $\tau = 1$, when the interaction of shock with the wave-fan has not yet started, the constant density region is still present and the viscous solution is in excellent agreement with the inviscid solution. At $\tau = 1.5$, Profile 2 in Fig. 7.2b shows that the interaction process has already started for the viscous solution, while it has yet to start for the inviscid solution. Once the interaction starts for the inviscid solution, both the solutions are in excellent agreement as is evident from Profiles 3 and 4 in Fig. 7.2b. The decay behavior of the wave is displayed in Fig. 7.6a, showing therein
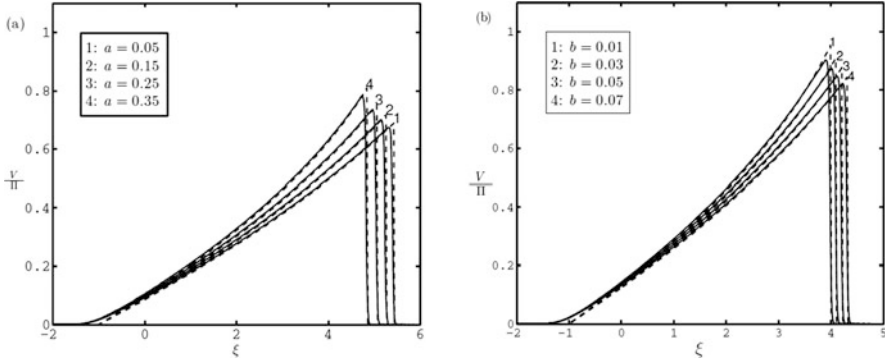
Fig. 7.6 (**a**) Case 1, signal profile for different values of a with $b = 0.02$, $\delta = 0.4$, $\Pi = 1$, and $\tau = 3$; (**b**) Case 1, signal profile for different values of b with $a = 0.1$, $\delta = 0.4$, $\Pi = 1$, and $\tau = 2$; dashed ($- - -$) and solid (——) lines represent inviscid and viscous solutions, respectively
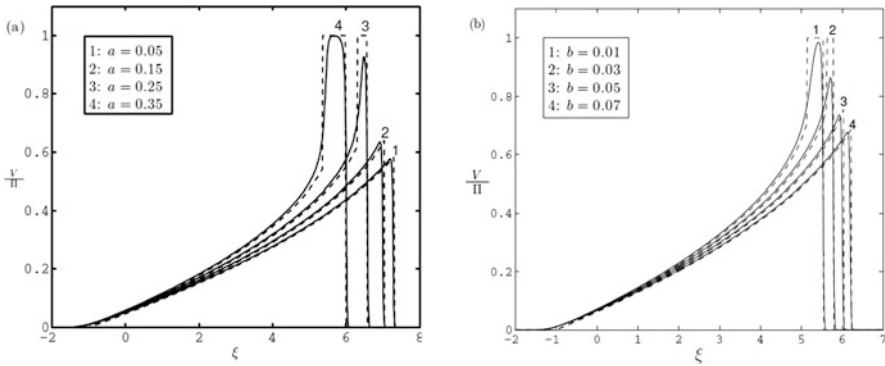
Fig. 7.7 (**a**) Case 2, signal profile for different values of a with $b = 0.02$, $\delta = 0.4$, $\Pi = 1.8$, and $\tau = 3$; (**b**) Case 2, signal profile for different values of b with $a = 0.1$, $\delta = 0.4$, $\Pi = 1.8$, and $\tau = 2.2$; dashed ($- - -$) and solid (——) lines represent inviscid and viscous solutions, respectively

that it slowed down under the influence of the van der Waals parameter a as predicted by the analytical results in Sect. 7.4.1. Similarly, Fig. 7.6b displays that the decay rate is enhanced by an increase in van der Waals parameter b, which is confirmed by analytical solution presented in Sect. 7.4.1.

Numerical solution of Eqs. 7.19 and 7.23, in the hyperbolic limit, for Case 2 with $\Pi = 1.8$ is depicted in Fig. 7.3b. Sonic shock is present till $\tau_{02} = 2.3227$ where it interacts with the wave-fan; indeed both viscous and inviscid solutions are seen to be in excellent agreement. Again a and b have the same effect on the decay of the wave amplitude as in the previous case (see Fig. 7.7a and b, which validate the conclusions drawn in Sect. 7.4.2).

Numerical solutions of viscous and inviscid equations, in Case 3 with $\Pi = 3.2$, are plotted in Fig. 7.4b; the variety of phenomena that can arise is seen through the signal profiles plotted therein. After the interaction time $\tau_{03} = 0.7345$, precursor
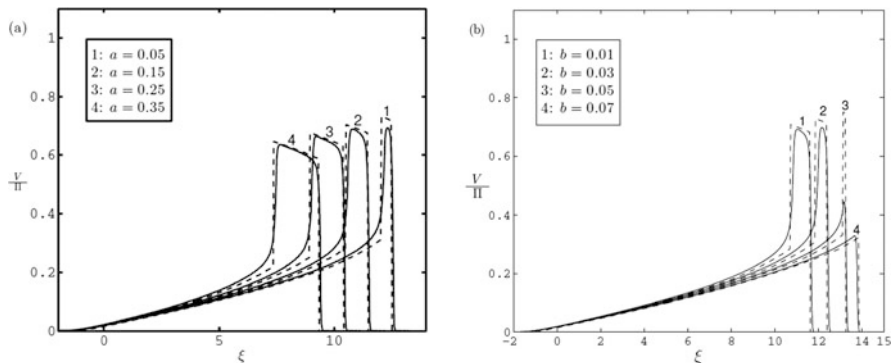
Fig. 7.8 (**a**) Case 3, signal profile for different values of a with b = 0.02, $\delta = 0.4$, $\Pi = 3.2$, and $\tau = 5$; (**b**) Case 3, signal profile for different values of b with a = 0.1, $\delta = 0.4$, $\Pi = 3.2$, and $\tau = 5$; dashed (− − −) and solid (——) lines represent inviscid and viscous solutions, respectively

waves evolve and persist in the system till time $\tau_2 = 9.2417$. At time $\tau_1 = 5.7768$, the interaction of wave-fan W_2 with the shock S_1 is over; for $\tau > 5.7768$, the precursor wave W_P interacts with the merged shock S_4 and causes it to slow down and decay in strength. Once again the inviscid and viscous solutions are seen to be in excellent agreement. Figure 7.8a and b validate the conclusions drawn in Sect. 7.4.3 relating to the dependence of shock speed/strength on the van der Waals parameters.

Finally for Case 4, the wave profiles of the numerical solution are depicted in Fig. 7.5b for $\Pi = 5.5$. The shock S_3 moves toward the left until it becomes stationary at time $\tilde{\tau}_1 = 0.2574$; the shock path then reverses and the shock propagates through the wavefront as a sonic shock S_4. For $\tau > 0.2574$, the precursor waves evolve in the system and remain there forever. Shock S_4 intersects the shock S_2 at time $\tilde{\tau}_2 = 10.3761$ and thereafter the precursor wave interacts with the merged shock. The point of intersection through which the Profiles 1–4 pass is the point where the characteristic of the wave-fan W is vertical carrying the value $V = -2\frac{\Gamma}{\Lambda}$ (see Fig. 7.5a and b). Numerical solutions, presented in Fig. 7.9a and b, confirm the analytical conclusions presented in Sect. 7.4.4.

7.6   Conclusion

In this work, we have used the method of multiple scales to derive the transport equation governing the amplitude of a weakly nonlinear wave in a dissipative medium; indeed the transport equation includes both quadratic and cubic nonlinearities which are responsible for a complex structure of evolving waves that are distinctly different from the ideal gas case where only quadratic nonlinearity is present. Exact analytic solutions of the kinematic equation associated with the parabolic transport equation are obtained, evolving from an initial condition representing a rectangular wave pulse; these are illustrated in Figs. 7.2a, 7.3a,
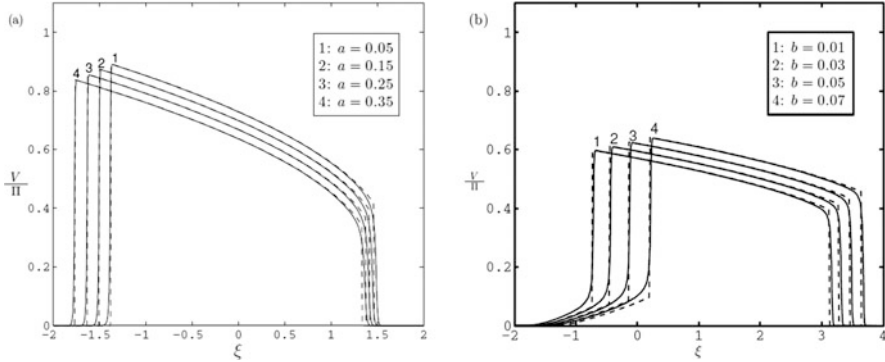
Fig. 7.9 (**a**) Case 4, signal profile for different values of *a* with b = 0.02, δ = 0.4, Π = 5.5, and τ = 0.2; (**b**) Case 4, signal profile for different values of *b* with a = 0.1, δ = 0.4, Π = 5.5, and τ = 1.0; dashed (– – –) and solid (———) lines represent inviscid and viscous solutions, respectively

7.4a, and 7.5a. The IVP of course differs from the classical Riemann problem, where a single discontinuity separates two different constant states; illustrative Cases 1–4 show that the initial discontinuity suffers a partial disintegration into a sonic shock (expansive or compressive) followed by a centered wave-fan, which is either an expansion or a compression fan. Interactions of shock waves with the wave-fans are of particular interest; precursor waves are present as a result of interaction of the waves emerging from the initial line carrying values of the density function corresponding to different convexities of the flux function. Wave evolution, in particular the width of the wave-fans, shock speeds/strengths, and the shock decay, influenced by the van der Waals parameters, have been depicted in Figs. 7.2, 7.3, 7.4, and 7.5. Indeed, Figs. 7.2b, 7.3b, 7.4b, and 7.5b depict the numerical results in the limit of vanishing viscosity for four typical cases leading to sonic shocks, precursor waves, and wave-fans.

The effects of van der Waals parameters are investigated on shock strengths, shock speeds, widths of wave-fans, interaction times, and the decay of the wave profiles. The interaction times, depending on the initial data, increase/decrease with an increase in van der Waals parameter *b*. Speeds of straight shocks and widths of expansion fans increase, whereas widths of compression fans decrease with an increase in *b*. Shocks get strengthened/weakened, with an increase in *b*, depending upon the initial data, whereas the eventual decay of wave becomes faster with an increase in *b* in all the cases. In contrast the effects of van der Waals parameter *a* on the wave evolution are just opposite to that of *b*.

The parabolic equation is solved numerically using the fifth-order WENO scheme; the numerical results are in excellent agreement with the analytical solutions. Indeed, the inviscid theory predicts the correct behavior of viscous solution when the dissipation coefficient is small; the numerical results confirm our conclusions relating to the crucial role played by the van der Waals parameters and the manner in which they influence the overall evolutionary and decay behavior of wave profiles.

References

Ballou DP (1970) Solutions to nonlinear hyperbolic Cauchy problems without convexity conditions. Trans Am Math Soc 152(2):441–460

Colonna P, Guardone A (2006) Molecular interpretation of nonclassical gas dynamics of dense vapors under the van der Waals model. Phys Fluids 18(5):56101

Colonna P, Guardone A, Nannan NR (2007) Siloxanes: a new class of candidate Bethe-Zel'dovich-Thompson fluids. Phys Fluids 19(8):86102

Cramer MS (1989) Negative nonlinearity in selected fluorocarbons. Physics of Fluids A Fluid Dyn 1(11):1894–1897

Cramer MS (1991) Nonclassical dynamics of classical gases. In: Nonlinear waves in real fluids. Springer, Cham, pp 91–145

Cramer MS, Kluwick A (1984) On the propagation of waves exhibiting both positive and negative nonlinearity. J Fluid Mech 142:9–37

Cramer MS, Sen R (1992) A general scheme for the derivation of evolution equations describing mixed nonlinearity. Wave Motion 15(4):333–355

Cramer MS, Webb C (2007) A modified Zabolotskaya–Khokhlov equation for systems having small quadratic nonlinearity. Wave Motion 44(5):323–339

Cramer MS, Kluwick A, Watson LT, Pelz W (1986) Dissipative waves in fluids having both positive and negative nonlinearity. J Fluid Mech 169:323–336

Crighton DG (1986) The Taylor internal structure of weak shock waves. J Fluid Mech 173:625–642

Das J, Manikanta V, Nikhil Teja K, Umamahesh NV (2022) Two decades of ensemble flood forecasting: a state-of-the-art on past developments, present applications and future opportunities. Hydrol Sci J 67(3):477–493

Gupta LK, Pandey M, Raj PA, Shukla AK (2022) Fine sediment intrusion and its consequences for river ecosystems: a review fine sediment intrusion and its consequences for river ecosystems: a review. October. https://doi.org/10.1061/(ASCE)HZ.2153-5515.0000729

Jiang G-S, Shu C-W (1996) Efficient implementation of weighted ENO schemes. J Comput Phys 126(1):202–228

Kluwick A (1991) Nonlinear waves in real fluids. Springer, Cham

Kluwick A (2001) Rarefaction shocks. In: Handbook of shock waves. Amsterdam, Elsevier, pp 339–411

Kluwick A, Cox EA (1998) Nonlinear waves in materials with mixed nonlinearity. Wave Motion 27(1):23–41

Kluwick A, Meyer G (2010) Shock regularization in dense gases by viscous–inviscid interactions. J Fluid Mech 644:473–507

Oleinik OA (1959) Uniqueness and stability of the generalized solution of the Cauchy problem for a quasi-linear equation. Uspekhi Matematicheskikh Nauk 14(2):165–170

Quartapelle L, Castelletti L, Guardone A, Quaranta G (2003) Solution of the Riemann problem of classical gas dynamics. J Comput Phys 190(1):118–140

Saikumar G, Pandey M, Dikshit PKS (2022) Natural river hazards: their impacts and mitigation techniques. In: River dynamics and flood hazards: studies on risk and mitigation. Cham, Springer, pp 3–16

Taniguchi S, Mentrelli A, Ruggeri T, Sugiyama M, Zhao N (2010) Prediction and simulation of compressive shocks with lower perturbed density for increasing shock strength in real gases. Phys Rev E 82(3):36324

Thompson PA (1971) A fundamental derivative in gas dynamics. Phys Fluids 14(9):1843–1849

Thompson PA, Lambrakis KC (1973) Negative shock waves. J Fluid Mech 60(1):187–208

Zhang X, Shu C-W (2010) On positivity-preserving high order discontinuous Galerkin schemes for compressible Euler equations on rectangular meshes. J Comput Phys 229(23):8918–8934

Zhao N, Mentrelli A, Ruggeri T, Sugiyama M (2011) Admissible shock waves and shock-induced phase transitions in a van der Waals fluid. Phys Fluids 23(8):86101

Zheng Y (2001) Systems of conservation laws: two-dimensional Riemannian problems. Springer, Cham

Chapter 8
Spatial and Temporal Variability of Soil Moisture, Its Measurement and Methods for Analysis: A Review

Sahil Sharma and Deepak Swami

Abstract The review article here presents a detailed study of the effects of the measurement scale on temporal and spatial soil moisture analysis. The dynamism of soil moisture remains critical in its application in agronomy, climate, environment and hydrology. The variations of soil moisture (spatially and temporally) are captured by various measurement techniques from the point scale to the continental scale. The robust sampling strategies are of great importance as it helps in the identification of the variability and study of the effects of heterogeneities. A comprehensive comparison of the methods for assessing variability in soil moisture for its spatial and temporal stability is carried out. The soil moisture variability methods' applicability and advantages and disadvantages are discussed. The scale of the study determines the statistical measurement methods to be applied. The factors affecting soil moisture variability are accurately determined using correlation analysis. Ultimately, the feel campaign strategy for soil moisture measurement based on optimal design for the study of spatiotemporal analysis will always be a trade-off between the accuracy and the cost of measurement, considering the scales of the study.

Keywords Watershed soil moisture · Field campaign strategy · Spatial and temporal stability · Scale of measurement · Correlation · ANOVA

8.1 Introduction

The dynamics of the near-surface soil moisture is an essential information to assess the soil moisture interaction with its surroundings. Though the soil moisture is minimal (Western et al. 2002), its contribution to the various natural phenomena is invaluable. The study of soil moisture is important to understand and maintain a balance between water energy interactions between the surface and atmosphere

S. Sharma (✉) · D. Swami
School of Engineering, Indian Institute of Technology, Mandi, India
e-mail: deepak@iitmandi.ac.in

(Vereecken et al. 2014). The understanding of soil moisture is fundamental for the study of the following fields:

1. Meteorology: soil moisture assists in maintaining the fluxes between the lithosphere and atmosphere (Famiglietti et al. 1998; Teuling et al. 2007; Hu and Si 2014a; b).
2. Hydrology: by quantifying the distribution of the precipitation into runoff, infiltration, groundwater recharge and pedogenesis in catchments (Aubert et al. 2003; Tyagi et al. 2013).
3. Agriculture: soil moisture variations determine the irrigation patterns, forecasting the yield, estimating evapotranspiration and forecasting flood and drought conditions (Brocca et al. 2010; Heathman et al. 2011).
4. Soil microbiology: the microbial cycles and their processes are controlled by the variations in soil moisture (Rodriguez-Iturbe et al. 1999; Schjønning et al. 2003; Lin et al. 2005). The consequent effect of these processes can further be associated with agronomy.

The dynamics of soil moisture have high importance; hence it is necessary to be understood. The dynamics can be defined as the capacity of the soil to regulate freshwater (precipitation) into surface and subsurface flow. Numerous studies identified behavioural characteristics of soil moisture. Spatiotemporal studies are conducted at various measurement scales to conceptualise soil moisture variability.

The scale of measurement of soil moisture is divided into the meteorological scale (which considers the larger areas) and small catchment scales (which considers the smaller field scales and small plots) (Brocca et al. 2007). Further, the scales of soil moisture studies have been divided into the field or local scale (Nielsen et al. 1973; Bell et al. 1980; Pandey and Pandey 2010; Heathman et al. 2011; Hu et al. 2010), catchment or the watershed scale (Western et al. 2002; Brocca et al. 2011; Rosenbaum et al. 2012; Hu and Si 2014a, b; Zucco et al. 2014), regional scale (Fernández-Martinez and Ceballos 2005; Brocca et al. 2007; Brocca et al. 2009) and continental scale (Reynolds 1974; Entin et al. 2000; Wagner et al. 2008; Li and Rodell 2013; Shouqin et al. 2014).

Based on the several field components and different study scales, most studies majorly concentrate on spatiotemporal behaviour of soil moisture and associated physical controls. The physical controls affecting soil moisture can be classified as physiographic factors (topography, climate), soil characteristics (texture, classification), cropping patterns and types, quality (method of measurement) and quantity (spatial and temporal extent) of measurement.

In estimating spatiotemporal characteristics of soil moisture, enormous measuring efforts are required. The techniques' applicability depends on the measurement scale and the required study accuracy. Gravimetric method, time domain reflectometers and sensor-based soil moisture measurements have applicability from field scale to lower catchment scales (Mohanty et al. 2000; Vereecken et al. 2014). For larger catchment areas and regional scales, geophysical methods like ground penetrating radars are best suited (Vereecken et al. 2014). The remote sensing technique has profound applicability for continental-scale studies (Wigneron et al. 2003; Loew

et al. 2006; Vereecken et al. 2014). The study's accuracy depends on the soil moisture measurement method and the study's scale. The increase in the study scale reduces the in-depth study of the area; as a result, the measurement accuracy decreases with the scale (Jonard et al. 2018). Methods like gravimetric and sensor-based methods are found to be the most accurate. The remote sensing-based technology requires field validation with the in situ soil moisture observations to arrive at conclusive results (Gasch et al. 2017). Based on the in situ results, modelling techniques are being developed to reduce the cost of obtaining soil moisture values (Woods et al. 1997; Lidard et al. 2001; Ursulino et al. 2019). Further, other methods based on land properties (terrain attributes) and pedological properties (texture) can be used to predict soil moisture variation (Zhu et al. 2012). Another new method developed to understand soil moisture dynamics is the wireless sensor network at various depths.

Weather extremes cause immense loss to flora and fauna, including human habitats. The weather extremes cause floods and droughts on a large scale, both locally and globally. Soil moisture is an important indicator of hydrologic extremes, as lower soil moisture values indicate drought conditions, while floods can be caused by saturation conditions in the field. The upper soil moisture layers show high variability, while the lower layers are better indicators of droughts and floods. Further, studies identified that the temperature extremes can be identified based on the antecedent soil moisture values. The soil moisture conditions of the spring season can influence the extreme temperatures of the summer season.

The spatial and temporal soil moisture values are analysed using various statistical measures. The statistical measures are subdivided into the following categories (Brocca et al. 2007):

1. Statistical analysis: to evaluate the probability density function and obtain the variability
2. Geostatistical analysis: to obtain the variation of soil moisture values based on the study distance (continuous or erratic)
3. Regression analysis: to determine the factors affecting the soil moisture variability

The numerous field campaigns comprehended that analytical analysis is essential for both spatial and temporal extents (Brocca et al. 2011). Studies have been conducted for longer temporal patterns and limited spatial extent (Teuling et al. 2006; De Lannoy et al. 2007; Hu et al. 2010; Brocca et al. 2011) and shorter temporal studies and larger spatial extents (Jacobs et al. 2004; Choi and Jacobs 2007; Jacobs et al. 2010; Famiglietti et al. 2008; Merlin et al. 2008; Panciera et al. 2008).

The specific objective of this study is to provide a comprehensive evaluation of the available literature on the techniques available for evaluating the spatiotemporal variability of soil moisture. This understanding is useful for increased crop growth, managing irrigation strategies and utilising the surface and subsurface flow. The review paper is divided into the following sections:

Section 8.2 presents an overview of the database.

Section 8.3 provides insight into various soil moisture measurement techniques.

Section 8.4 highlights the techniques for estimating the optimal sampling locations for computing spatial and temporal data.

Section 8.5 describes the methodology of spatiotemporal analysis used to evaluate the effect of the various factors on the soil moisture evaluations.

Section 8.6 outlines a detailed conclusion from the literature.

8.2   Overview of Reviewed Articles

Various peer-reviewed journals were considered for preparing a detailed review of soil moisture studies. The list of the articles is published in Table 8.1. The list of journals mentioned is recognised and cited by researchers worldwide. The following articles are selected to explain the methods involved in soil moisture measurement and the various statistical tools associated with computing soil moisture variability and stability studies. The articles further give an insight into the various physiographic factors affecting soil moisture stability. The articles thus effectively explain the statistical tools used in the spatiotemporal soil moisture analysis.

Figure 8.1 details the number of papers considered in the study yearly. The study increased in soil moisture since 2000, with the maximum number of publications on the spatiotemporal study of soil moisture in 2011 and 2014. Figure 8.2 plots a bar chart between the research article's study topic and the number of papers on the same topic. The graph depicts that the maximum weightage is given to spatiotemporal soil moisture studies, which consider the complete understanding of measurement techniques to factors affecting the stability and variability of soil moisture. At the same time, fewer research articles are considered case studies for the basic concepts of soil moisture and measurement techniques, factors affecting soil moisture variability and stability and study domains considering spatial and temporal patterns individually. This is because the complete spatiotemporal study comprehensively evaluates the other four cases of basic concepts, factors, spatial study and temporal study. Thus limited articles are selected for the basic concepts, factors affecting soil moisture and the studies of spatial and temporal distribution patterns of soil moisture.

8.3   Techniques for Measurement of Soil Moisture

During the previous 50 years, considerable progress has been made in soil moisture measurement techniques (Robinson et al. 2008; Vereecken et al. 2008). The soil moisture measurement techniques can be divided into two basic categories: direct and indirect measurements. The gravimetric method is the only direct and basic method for soil sampling wherein soils are weighed before and after oven drying. The temperature will be maintained at 105 °C for 24 h, and soil moisture is expressed in units of the ratio of m^3 of water to m^3 of soil. The calculations of the gravimetric

Table 8.1 List of journals selected for review

S. No.	Name of journal	19/20 impact factor	Number of papers
1	*Journal of Hydrology*	4.540	63
2	*Water Resources Research*	4.270	38
3	*Hydrological Processes*	3.160	16
4	*Geophysical Research*	3.360	12
5	*Remote Sensing and Environment*	8.430	12
6	*Geoderma*	4.848	9
7	*Hydrology and Earth System Sciences*	4.540	9
8	*Advances in Water Resources*	4.020	8
9	*Journal of American Society of Soil Sciences*	2.020	6
10	*Catena*	4.270	7
11	*Journal of Vadose Zone*	3.450	7
12	*Eco Hydrology*	2.767	3
13	*Environmental Earth Science*	2.000	3
14	*Soil and Tillage Research*	5.180	3
15	*Water Research*	9.130	3
16	*Agricultural Sciences*	0.290	2
17	*Agricultural Water Management*	3.990	2
18	*Journal of Agronomy*	3.050	2
19	*Canadian Journal of Soil Sciences*	1.171	2
20	*Environmental Geology*	0.110	2
21	*International Journal of Agriculture and Biological Engineering*	1.620	2
22	*Soil Science*	1.560	2
23	*Geosciences*	12.210	2
24	*Transaction of Geoscience and Remote Sensing*	6.120	2
25	*Sensors*	3.510	2
26	*American Society of Agricultural Engineers*	1.381	2
27	*Australian Journal of Soil Research*	1.690	1
28	*Earth Planet Science*	4.823	1
29	*Environmental Modeling and Software*	4.870	1
30	*European Journal of Soil Science*	2.800	1
31	*Forest Ecology and Management*	3.170	1
32	*Great Plains Research*	–	1
33	*Hilgardia*	–	1
34	*Hydrological Sciences*	2.186	1
35	*IEEE Journal on Geoscience and Remote Sensing*	2.48	1
36	*Irrigation Science*	3.04	1
37	*Journal of American Water Resources Association*	2.472	1
38	*Journal of Arid Environments*	1.830	1
39	*Journal of Arid Land*	1.444	1
40	*Journal of Climate*	5.707	1
41	*Journal of Earth System Sciences*	1.423	1

Table 8.1 (continued)

S. No.	Name of journal	19/20 impact factor	Number of papers
42	*Journal of Forestry Research*	1.689	1
43	*Journal of Hydrologic Engineering*	1.56	1
44	*Nonlinear Process in Geophysics*	1.650	1
45	*Observation and Measurement of Eco Hydrological Processes*	–	1
46	*Physics and Chemistry of Earth*	2.308	1
47	*Plos One*	2.740	1
48	*Procedia Engineering*	0.970	1
49	*Remote Sensing and Special Information Sciences*	0.930	1
50	*Reviews of Geophysics*	21.45	1
51	*Scientia Agricola*	1.680	1
52	*Soil Research*	1.670	1
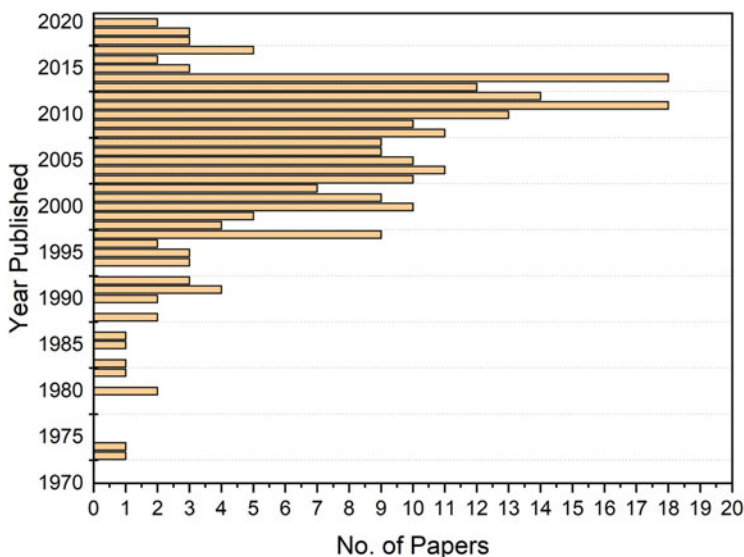
Fig. 8.1 Papers list year wise

method are easy to perform, but the method is time-consuming and destructive. The indirect methods are classified based on the measurement mechanism: contact (invasive) and contact-free (proximal). Where sensors are in direct contact with the soil are termed contact-based methods and in which no direct contact is made are categorised as contact-free methods. Further, gradually with time, the modelling and simulation techniques have been developed to obtain the values of soil moisture based on the other physical parameter involved. The methods involved in soil moisture measurements are as follows:

Fig. 8.2 Number of papers based on study area
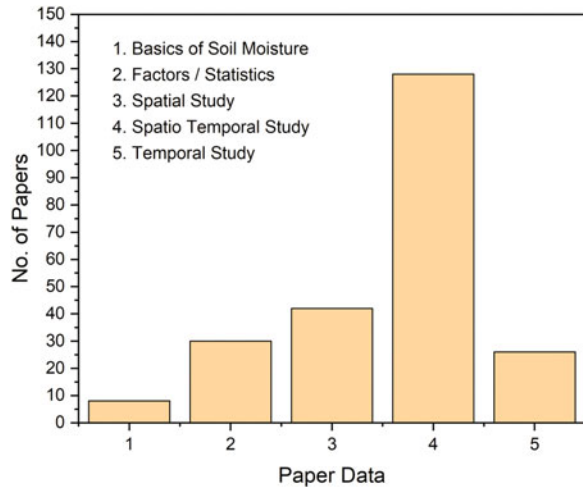
8.3.1   Point Scale Measurement Methods

The most common soil moisture measurement techniques apply the principle of electromagnetics. Soil moisture is the principal factor on which soil dielectric permittivity depends, which is fundamental to electromagnetic wave propagation in the field (Jonard et al. 2018). The field of influence of these methods is generally in the range of 1 cm. Following are the types of point scale measurement equipments:

8.3.1.1   Time Domain Reflectometer (TDR) or Frequency Domain Reflectometer

The TDR introduced by Topp et al. (1980) works on the principle of propagation of velocity of electromagnetic waves using the probe by inserting the probe inside the soil surface. The waves are emitted from a pulse generator, and the travel time is measured in the available length of the probe. The electromagnetic properties of the soil (Robinson et al. 2003) affect travel time. The applicability of TDR is large as much of the previous works of literature (Brocca et al. 2007, Brocca et al. 2009, 2011; Lawrence and Hornberger 2007; Hu and Si 2014a, b; Zucco et al. 2014) have made use of the field campaigns. The TDR probes are inserted directly into the soil for in situ measurements at the desired soil depth. The permittivity of soil is strongly related (Fig. 8.3) to the water content. The TDR measures the velocity of propagation of a high-frequency signal. The velocity is calculated using the following equation:
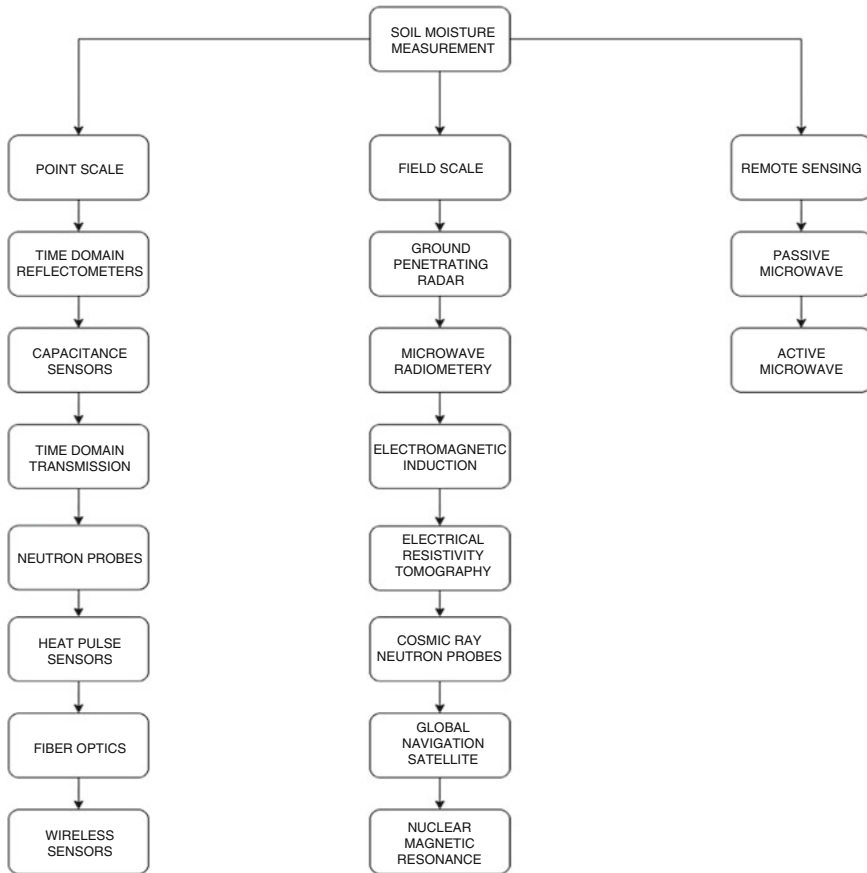
Fig. 8.3 Soil moisture measurement techniques

$$v = \frac{c}{\sqrt{k}} \tag{8.1}$$

where c is the velocity of light and k is the dielectric constant of soil.

The apparent dielectric constant gives the volumetric water content based on Topp et al.'s (1980) equation by determining the travel time in the available length wave guide.

The TDR is independent of soil texture, temperature and salt content. The TDR can further be used for long-term measurements. The biggest disadvantage of TDR is that the instrument is highly costly.

8.3.1.2 Capacitance Sensors

Capacitance-based sensors are a very common instrument to measure soil moisture based on the resistivity of the soil medium surrounding the sensor prong. Based on capacitance, these sensors capture the dielectric constant variation of dry soil and water. The charging time between the starting voltage and the applied capacitor is used to evaluate soil permittivity. The available frequency for the operating range is 50–150 MHz. The soil's dielectric permittivity and electrical conductivity govern the sensor output (Kelleners et al. 2005; Kizito et al. 2008).

The capacitance sensors are low in cost, sensitive to small changes, simple in construction and adjustable. Remote instruments can read the readings, and water content can be determined at any depth. The disadvantage is that they are sensitive to changes in environmental conditions such as temperature and humidity, that is, their long-term stability is inadequate.

8.3.1.3 Time Domain Transmission (TDT) or Frequency Domain Transmission

In the case of TDT sensors, the electromagnetic waves propagate in a loop or a closed transmission line. It measures the time from the start to the end of the loop. TDT is considered to be accurate as compared to TDR and capacitance sensors. The TDT work at higher frequencies resulting in better measurement quality (Blonquist Jr et al. 2005). The TDT sensors measure the transmission compared to TDR, which measures the reflections. The TDT sensors, compared to TDR, fare well, as existing multiple reflections do not influence them. Furthermore, the TDT sensors can measure delay time based on the TDR methodology.

8.3.1.4 Neutron Probes

It is based on estimating the number of hydrogen nuclei in the soil. It consists of a nuclear unit suspended from a cable with a neutron as the source and detector. Detecting the slow neutrons returning to the probe estimates the amount of hydrogen present (Kachanoski and de Jong 1988; Reichardt et al. 1997; Grant et al. 2004; Hu et al. 2010). The neutron comprises a nuclear unit, suspension cable, neutron source and detector, housing for receptors and shield for transportation of the radioactive device. The nuclear unit is lowered to known depth intervals. The source starts scattering and deflected, and this deflection is related to soil moisture. Measurements using the neutron probe are accurate for soil moisture determination, and it has a large sphere of influence; also, the measurements are not affected by temperature, soil type and pH. The disadvantages are that as it is a radioactive source, licenses are required, equipment is costly and the equipment is properly calibrated.

8.3.1.5   Heat Pulse Sensors

The heat pulse sensor method applies the principle of soil thermal properties. The heat pulse method can either be a single or dual probe. The dual probe method is most widely applicable, and it consists of two parallel probes made of a stainless tube, one of which consists of the heating element and the other thermocouple. As the source of heat and the travel distance are known, temperature fluctuations provide heat capacity (Heitman et al. 2003). The dual probe method is most widely applicable for obtaining thermal conductivity and diffusivity of soil, while the single probe only measures the conductivity.

8.3.1.6   Fibre Optic Sensors

It is based on the principle of reflection of light signal or attenuation. The instrument is based on a thermal hygrometer made of a polymeric membrane which assists in avoiding direct contact with the soil (Leone et al. 2007). The fibre optic sensors can detect soil moisture in various soil types and variable ground conditions. The advantages of fibre optics are that they are inexpensive and can measure the water over longer distances; further, the losses due to leakages are minimised.

8.3.1.7   Wireless Sensor Networks

In this case, an ensemble of soil moisture measuring sensors is used in the field; the wireless technology transmits signals to the main server. These sensors have applicability for studies in regions of high temporal resolution and large areas, particularly in monitoring eco-hydrological processes (Bogena et al. 2010; Jin et al. 2014). The wireless sensors have applicability in the field of agriculture, horticulture, etc. These sensors do not reveal the local information well because of the spacing requirements.

8.3.1.8   Tensiometer

A tensiometer is used to measure the soil water or soil suction. It consists of a water-filled tube and ceramic through which water movement occurs. The movement of water to and from the cup determines the suction pressure. A zero reading indicates fully saturated soil; the more the soil is drier, the higher the reading.

   The tensiometer is a low-cost instrument most applicable for continuous measurement at a particular location, assisting irrigation scheduling. Most of the tensiometers work from 0 to 100 kPa, which helps measure the saturated condition but not the drier conditions. Further, the instrument requires a regular check.

8.3.2 Field Scale Hydro-geophysical Methods

This methodology utilises the applicability of geophysics to determine the hydrological parameters. Further, to overcome the cost-intensive multiple-point measurements, geophysical methods have been employed. The hydro-geophysical methods are the following:

8.3.2.1 Ground Penetrating Radar (GPR)

The GPR is based on the principle of propagation of electromagnetic waves in the subsurface explained by Maxwell's equation. The GPR works using two antennas, a transmitter and a receptor antenna. The velocity obtained is based on the material property and is utilised to get dielectric permittivity. Various forms of GPR can be used, like surface GPR, cross hole GPR and off-ground GPR (Huisman et al. 2003). The advantages of using a GPR are that it enables a high recording speed, is easy to handle and can be operated at various frequencies. The disadvantage of using a GPR is that the higher frequencies have limited penetration compared to lower frequencies; further, the performance is not good in clay; the terrain should not be undulating while using the GPR.

8.3.2.2 Ground-Based Microwave (L Band) Radiometry

The principle associated with the method is the radiance emitted from a terrestrial body at the horizontal and vertical polarisations, which depend on the soil's temperature (Schmugge et al. 1986). The brightness temperature depends on the effective permittivity of the soil, which evaluates the soil moisture content.

8.3.2.3 Electromagnetic Induction

This method works on the principle of a transmitter and receiver induction coil placed at the opposite ends of the instrument. The transmitter coil generates a magnetic field on supplying current, and the receiver coil detects the currents generated within the soil. The apparent soil conductivity of soil depends on the various soil attributes (Kachanoski and de Jong 1988; Sheets and Hendrickx 1995; Reedy and Scanlon 2003; Sherlock and Mcdonnell 2003).

8.3.2.4 Electrical Resistivity Tomography

This method works on the principle of measuring electrical conductivity differences by using electrodes. In the initial stages, the method was used for large explorations

in geology and groundwater, but Samouëlian et al. (2005) started its applicability in vadose zone studies.

8.3.2.5 Cosmic Ray Neutron Probes

Appropriate spatiotemporal soil moisture monitoring per the scale differences is difficult (Bogena et al. 2015). Cosmic ray neutron probes have been used to fill this void (Desilets et al. 2010; Zreda et al. 2008). The principle of the technique is based on the relative changes of fast neutrons, which has a strong correlation to soil moisture, and soil moisture has associated hydrogen.

8.3.2.6 Global Navigation Satellite System Reflectometry (GNSS-R)

GNSS-R works on measuring the reflections received from the Earth's surface signals using global navigation satellite systems such as GPS. GNSS-R is an all-weather worldwide applicable technology. GNSS sensors are inexpensive and lightweight and have low power consumption (Jonard et al. 2018).

8.3.2.7 Nuclear Magnetic Resonance

The principle of NMR is based on the observance of nuclei in a magnetic field. The presence of H protons in the soil is related to soil water. Thus NMR is used to evaluate soil moisture, porosity and pore size distribution (Jonard et al. 2018).

8.3.3 Remote Sensing Technique

The remote sensing method includes satellites, microwaves and other non-contact techniques. Remote sensing techniques allow measurements to be taken from a remote location, and the overall coverage of the area can be vastly increased. The disadvantage of the remote sensing technique is that the system is complex and costly. Further, the application of remote sensing is generally applicable to the top surface soil moisture.

8.3.3.1 Passive Microwave Remote Sensing

In this method of remote sensing, thermal radiance emitted from the Earth's surface is captured by radiometers, particularly at the frequency of 1–12 GHz (Njoku and Entekhabi 1996). Since thermal emission is a direct function of the thermodynamic temperature of surface soil emissivity, it is later processed to estimate soil

reflectivity. The penetration depth in this method depends upon the availability of surface soil moisture and the frequency of radiation; for a higher frequency, the penetration depth is short.

8.3.3.2 Airborne and Space-Borne Active Microwave Remote Sensing

Active microwave methods are based on radar techniques, and the resolution depends on the antenna size, incidence angle and pulse length (Ulaby et al. 1996). Advanced Synthetic Aperture Radar (ASAR) TerraSAR-X, Radarsat-2 and European Remote Sensing (ERS 2) are a few of the satellites used extensively. Scattering matrix data is ensembled to calculate the backscattering coefficient and later expressed in decibels. The active remote sensing techniques' accuracy is based on measured surface roughness (Dobson and Ulaby 1985; Hallikainen and Ulaby 1985).

8.3.4 Modelling Approaches

Numerous modelling techniques have been developed over the years. To overcome the complex interactions, modelling approaches have found applications with reduced evaluation time and costs. As per the literature, various modelling approaches have been used to estimate soil moisture. The modelling approach is based on solving the Richards equation:

$$\frac{\partial \theta}{\partial t} = \frac{\partial}{\partial z}\left[K(h)\left(\frac{\partial h}{\partial z} + 1\right)\right] - S(h) \tag{8.2}$$

where h is the water pressure head, θ is the volumetric water content, t is the time, $K(h)$ is the hydraulic conductivity and $S(h)$ is the sink term, generally the root water uptake or evapotranspiration losses.

The first-generation method of soil moisture modelling was based on a simplified dynamic model for estimating spatial variability, where a wetting front model was used (Clapp et al. 1983). Later, Leonard et al. (1987) used groundwater loading effects of agricultural management systems on the movement of chemicals in the root zones (GLEAMS). Rodriguez-Iturbe et al. (1991) modelled soil moisture using nonlinear dynamics. Entekhabi and Rodriguez-Iturbe (1994) used an analytical framework to characterise soil moisture, and this model used noise represented by rainfall and losses represented by runoff, percolation and evapotranspiration. Barling et al. (1994) use a quasi-dynamic wetness approach for moisture content determination. Verburg et al. (1996) used a soil water infiltration and movement model for measuring water movement (SWIM). Vancloster et al. (1994) used water and agrochemicals in the soil, crop and vadose movement for soil water movement.

Woods et al. (1997) based the modelling approach based on the topographic index. Dam et al. (1997) used soil water atmosphere plants to simulate water, solute and heat transport in the soil-atmosphere-plant environment. Avissar (1998) used soil vegetation atmosphere transfer schemes for soil moisture predictions. Walker et al. (2001) used retrieval algorithms based on direct insertion and the Kalman filter that uses the profile updates that are abused on the covariance. Lidard et al. (2001) used TOPMODEL based on the energy-water balance to understand the structure and scaling properties. Ridolfi et al. (2003) used a stochastic soil moisture dynamic approach to consider soil moisture balance. Buttafuoco and Castrignano (2005) studied the spatial variation in soil moisture by multivariate geostatistics. Cai et al. (2017) used a hyper-resolution land surface model, Hydroblocks, for upscaling the in situ point measurement data to the remote sensing level. The most widely and commonly used method is the Hydrus one-dimensional model, which uses the inverse method to estimate the soil parameters and simulate the data set to obtain the soil moisture values (Ursulino et al. 2019).

8.4   Optimal Locations for Spatial and Temporal Study

To understand the spatial and temporal variation of the soil moisture in a watershed, the optimality of the sampling locations must be studied. The researchers have adopted the following two basic methods for obtaining optimal locations. For the study of spatial data, the optimal locations are found using the student's t-distribution test. In the temporal study, the most commonly applied method is random sampling.

8.4.1   NRL Estimate for Watershed Mean Soil Moisture

Statistical approaches capture the spatial variability of mean watershed soil moisture. Gilbert (1987) gave the estimation of the specific value of absolute error based on the following equation, which uses an iterative procedure:

$$\text{NRL} = \left(t_{1 - \propto/2, \text{NRL} - 1} \frac{\sigma_E}{\text{AE}} \right)^2 \tag{8.3}$$

where σ_E is the standard error, AE represents the absolute error in percentage, $t_{1 - \propto/2, \text{NRL} - 1}$ is the students t distribution and $\propto$ is the significance level. If the standard error value is not available, CV is used to estimate NRL; in that case, the relationship between CV_k is also investigated. The relationship is given for evaluations of soil moisture and employed for soil moisture campaigns (Brocca et al. 2007; Famiglietti et al. 2008):

$$CV_K = K_{1,}e^{-K_2\overline{\theta_k}} \tag{8.4}$$

where k_1 and k_2 are model fitting parameters and where $\overline{\theta_k}$ is the watershed mean soil moisture on any day k^{th} day.

8.4.2 NRL Estimate for Temporal Pattern

Temporal evaluation of watershed means soil moisture within defined accuracy levels uses a random combination method (Brocca et al. 2010). The steps involved in the random combination method are the following:

1. Randomly selected soil moisture measurements at n sampling locations ($n \leq N$) from the available N observations for N_r replicates.
2. The time series of watershed mean soil moisture is estimated and results in the N_r time series.
3. The coefficient of determination, R^2, and root mean square difference for the N_r time series against benchmark time series based on total N locations are computed for the entire watershed.
4. The mean and standard deviation of the performance statistics are estimated.
5. The above steps are repeated till $n = N$:

$$RMSD = \sqrt{\frac{\sum_{k=1}^{M}\left(\frac{1}{n}\sum_{i=1}^{n}\left(\theta_{ik} - \overline{\theta_K}\right)\right)^2}{M}} \tag{8.5}$$

where k represents days, n is the number of locations, M is the number of field campaign days, θ_{ik} is the mean moisture at i point and k^{th} day and $\overline{\theta_k}$ is the watershed mean moisture on a particular day k.

8.5 Methods of Spatiotemporal Analysis of Soil Moisture and Evaluating the Effects of Physiographic Factors

Various spatial and temporal analysis methods have been used to identify the effect of factors affecting soil moisture variations. The methods given below evaluate the soil moisture variation concerning the physiographic factors. The soil moisture variables, the relative difference and the comprehensive evaluation criteria method are used for temporal stability analysis. The semi-variograms, correlation coefficient methods, empirical orthogonal functions and ANOVA (analysis of variance) identify

the weightage of the various physiographic factors and how soil moisture varies with the variation in physiographic factors.

8.5.1 Descriptive Statistics

Descriptive statistic methods describe the basic features of the data obtained during the study. They give an idea of the simple measures and representation of the particular population sample and summarise the data set. The basic descriptive statistic measures used are maxima, minima, mean, standard deviation, coefficient of variation and skewness to represent the data set's variation and to identify probability distribution and random variables.

8.5.2 Soil Moisture Variables

Several component mechanisms are applied to observe the spatiotemporal characteristics of the observed soil moisture. Soil moisture measurements in the field are divided based on the spatial and temporal extent. Following are the common terms associated with spatial measurements; a point is defined as the location where the measurements are taken. The site represents the mean of the group of points under observation. A combination of sampling sites forms a sampling location, also called the study area. A combination of sampling locations collectively forms a watershed. The terms associated with the temporal measurements are sampling day, a particular day on which sampling is carried out for any sampling location. A campaign is defined as the complete set of observations for the complete duration of time.

The basic terminologies associated with soil moisture evaluation concerning depth and locations are the following:

8.5.2.1 Based on Depth

$$M_a = \frac{1}{N_l N_t} \sum_{b=1}^{N_t} \sum_{c=1}^{N_t} M_{abc} \tag{8.6}$$

$$M_b = \frac{1}{N_s N_t} \sum_{a=1}^{N_s} \sum_{t=1}^{N_t} M_{abc} \tag{8.7}$$

$$M_{ab} = \frac{1}{N_t} \sum_{k=1}^{N_t} M_{abc} \qquad (8.8)$$

$$VP_{ac} = \sqrt{\frac{N_1 \sum_{b=1}^{N_1} (M_{ab})^2 - \left(\sum_{b=1}^{N_1} M_{ab} \right)^2}{N_1(N_1 - 1)}} \qquad (8.9)$$

$$VT_a = \sqrt{\frac{N_t \sum_{c=1}^{N_t} M_{a\,c} - \left(\sum_{c=1}^{N_t} M_{a\,c} \right)}{N_t(N_t - 1)}} \qquad (8.10)$$

$$VS_b = \sqrt{\frac{N_s \sum_{a=1}^{N_s} (M_{ab})^2 - \left(\sum_{a=1}^{N_p} M_{ab} \right)^2}{N_s(N_s - 1)}} \qquad (8.11)$$

$$G_a = \frac{M_{a3} - M_{a1}}{1.5} \qquad (8.12)$$

where a is the moisture measurement site (point), b is the moisture measurement layers, c is the moisture sampling day, N_s is the number of observation sites, N_t is the number of sampling events, N_1 is the number of sampling layers, M is the soil moisture, VP is the profiling variability of time-averaged soil moisture content, VT is the temporal variability of layer averaged, VS is the spatial variability and G is the profile gradient (Venkatesh et al. 2011a, 2011b).

8.5.2.2   Based on Location

The notations used in the following equations are i, soil measurement at a point; j, soil measurement at a location; k, soil measurement sampling day; N_p, point measurements at the sampling location j; N, total number of sampling locations in the watershed; and M, total number of field campaign days (Singh et al. 2019).

1. Mean soil moisture of a particular location j on a particular day: k

$$\overline{\theta_{jk}} = \frac{1}{N_p} \sum_{i-1}^{N_s} \theta_{ijk} \tag{8.13}$$

2. Watershed mean soil moisture on any day k^{th} day:

$$\overline{\theta_k} = \frac{1}{N} \sum_{j=1}^{N} \overline{\theta_{jk}} \tag{8.14}$$

3. Temporal mean for each sampling location:

$$\overline{\theta_j} = \frac{1}{M} \sum_{k=1}^{M} \overline{\theta_{jk}} \tag{8.15}$$

4. Coefficient of variation of kth sampling day:

$$\text{CV}_k = \frac{\sigma_k}{\theta_k} = \frac{\sqrt{\frac{1}{N-1} \sum_{j-1}^{N} \left(\overline{\theta_{jk}} - \overline{\theta_k} \right)^2}}{\overline{\theta_k}} \tag{8.16}$$

8.5.3   SEMI: Variograms

Semi-variogram depicts the spatial autocorrelation of the measured values. Each pair of locations is plotted, and the model is fitted through them. The semi-variograms are of the following types: linear, spherical and exponential models. A particular model type is selected based on the goodness of fit. The semi-variance is given by $\Upsilon(h)$, where n(h) is the number of samples, and h represents the distance h and z represents the property of the crop (Bhatti et al. 1991; Charpentier and Groffman 1992; Cosh and Brutsaert 1999; Anctil et al. 2002; Huisman et al. 2003; Kaleita et al. 2005; Bosch et al. 2006; Hu et al. 2011):

$$\Upsilon(h) = \frac{1}{2n(h)} \sum\nolimits_{i=1}^{n(h)} [z(x_i) - z(x_{i+h})]^2 \tag{8.17}$$

$$\Upsilon(h) = C_0 + C_1 \left[1.5 \left(\frac{h}{a} \right) - 0.5 \left(\frac{h}{a} \right)^3 \right], 0 < \; h < a, \tag{8.18}$$

$$\Upsilon(h) = C_0 + C_1, h \geq a \tag{8.19}$$

where parameter 'a' is known as the range, C_1 parameter represents the difference value of sill and nugget and C_0 is known as the nugget and is a model parameter.

Nugget is an effect associated with measurement errors or spatial sources of variation. A nugget effect is observed as the lag increases to an infinitesimally small separation distance because a semi-variogram gives a value greater than zero.

The range is defined as the critical distance after which there would be no correlation between the sample pairs.

Sill: The increase in the distance beyond which the value of semi-variance will remain constant.

For a random distribution of samples in space, the separation distance between the samples does not play any role. For correlated samples, the semi-variance will be increased with the increasing distances. Further, it may be noted that samples separated at a distance greater than the range show a random variation (Bhatti et al. 1991).

8.5.4 Relative Difference

Introduced by Vachaud in 1985, the method compares one value with another and further helps determine the percentage increase or decrease.

$$\mathrm{RD}_{ij} = \frac{\theta_{ij} - \langle \theta_j \rangle}{\langle \theta_j \rangle} \tag{8.20}$$

where RD_{ij} is the relative difference, θ_{ij} is the soil moisture at i location and j time and $\langle \theta_j \rangle$ is the spatial average of θ_{ij} at time j.

1. Mean relative difference: the ratio of relative differences to the number of observation times:

$$\mathrm{MRD}_i = \frac{1}{N} \sum_1^{N_1} \mathrm{RD}_{ij} \tag{8.21}$$

2. Variance of relative difference is the average of the squared differences from the relative difference means:

$$\sigma\left(RD_{ij}\right)^2 = \frac{1}{N_t - 1} \sum_1^{N_t} \left(RD_{ij} - MRD_i\right)^2 \qquad (8.22)$$

where N_t are the number of relative differences.

3. Standard deviation of relative difference is the square root of the variance of relative differences:

$$SDRD_i = \sqrt{\frac{1}{N_t - 1} \sum_{j=1}^{j=N_t} \left(RD_{ij} - MRD_i\right)^2} \qquad (8.23)$$

4. Standard deviation of mean relative difference is defined as the square root of the variance of mean relative difference to mean of mean relative difference:

$$SDMRD = \sqrt{\frac{1}{N_s - 1} \sum_{i=1}^{N_s} \left(MRD_i - m_{MRD}\right)^2} \qquad (8.24)$$

where N_s is the number of locations and m_{MRD} is the mean of the mean relative differences.

8.5.5 Spearman Rank Correlation

The coefficient is used to assess the spatial stability of a soil moisture field. As the name suggests, it is a correlation coefficient used to evaluate the correlation of the ranking of sites of one day with the next day. Therefore, evaluating the soil moisture distribution of the entire area of study (Vachaud et al. 1985; Rolston et al. 1991; Cosh et al. 2004; Schneider et al. 2008; Hu and Si 2014a; b; das Neves et al. 2016) is obtained by

$$r_s = 1 - \frac{6 \times \sum_{i=1}^{n} \left(R_{i,j} - R_{i,j'}\right)^2}{n(n^2 - 1)} \qquad (8.25)$$

where $R_{i,\,j}$ is the rank of soil moisture and $S_{i,j}$ at location i and day j and n is the total number of days. The obtained coefficient value indicates 0 and 1, where 0 is for no stability and 1 is for a stable soil moisture area.

8.5.6   Correlation Coefficient

Another method for assessing spatial stability is obtaining the correlation coefficient value. The range is similar to Spearman's rank, whereby 1 represents closely correlated while 0 gives uncorrelated patterns (Cosh et al. 2004):

$$r_{j,j'} = \frac{\sum_{i}\left(S_{i,j} - \overline{S}_{.,j}\right)\sum_{i}\left(S_{i,j'} - \overline{S}_{.,j'}\right)}{\sqrt{\sum_{i}\left(S_{i,j} - \overline{S}_{.,j}\right)^{2}}\ \sqrt{\sum_{i}\left(S_{i,j'} - \overline{S}_{.,j'}\right)^{2}}} \tag{8.26}$$

where $S_{i,j}$ and $S_{i,j'}$ are the soil moistures at times j and j' and $\overline{S}_{.,j}$ represents the average soil moisture for that across all sampling locations.

8.5.7   Comprehensive Evaluation Criteria (CEC)

The CEC is evaluated to identify the locations which are most time stable and identify these locations. Jacobs et al. (2004) considered the combination of mean relative difference and variance of relative difference. Further, the temporally stable locations which are to be used for soil moisture content are identified on the following basis:

$$\mathrm{CEC} = \sqrt{\left(\mathrm{MRD}_i\right)^2 + \sigma\left(\mathrm{RD}_{ij}\right)^2} \tag{8.27}$$

where MRD_i is the mean relative difference and $\sigma(\mathrm{RD}_{ij})^2$ is the variance of relative difference:

1. Location with the value of mean relative difference closest to zero (Vachaud et al. 1985).
2. The lowest standard deviation of relative difference is the highest temporally stable location (Starks et al. 2006; Heathman et al. 2009; Pan 2012).
3. Hu et al. (2010) stated that the location to temporally stable is based on mean absolute error.
4. The idea of root means square error after offset application was given (Gao et al. 2013).

8.5.8   Empirical Orthogonal Functions (EOFs)/Principal Components

The method is applied to large multidimensional data sets. The method can reduce the observed variability by breaking it into empirical orthogonal functions, invariant in time and principal components invariant in space (Yoo and Kim 2004; Perry and Niemann 2007). The EOFs identify the variability sources in the data, and based on those variables affecting variability, the data set is compressed (Preisendorfer and Mobley 1988). The applicability of EOFs is to identify both spatial and temporal anomalies.

8.5.8.1   Spatial Anomalies

It is evaluated by subtracting average soil moisture for a given observation from all the observations collected at that time. The steps involved in utilising the EOF analysis are the following:

1. Calculating the covariance matrix. The covariance matrix for the spatial anomaly is spatial covariance:

$$Z_i(t) = S_i(t) - \frac{1}{m} \sum_{j-1}^{m} S_j(t), \qquad (8.28)$$

   where $S_i(t)$ is the soil moisture observation at any time t and location i, m denotes the number of observations and $Z_i(t)$ denotes the spatial anomaly:

$$V_{t\tau} = \frac{1}{m} \sum_{i=1}^{m} Z_j(t) Z_i(\tau). \qquad (8.29)$$

   where $V_{t\tau}$ represents the spatial covariance at times t and τ.

2. The second step is diagonalising the covariance matrix (at m sampling locations and n sampling times):

$$Z = - \begin{bmatrix} Z_{11} & Z_{12} & \cdots & Z_{1n} \\ Z_{21} & Z_{22} & & \vdots \\ \vdots & & \ddots & \vdots \\ Z_{m1} & \cdots & \cdots & Z_{mn} \end{bmatrix} \qquad (8.30)$$

$$V = \frac{1}{m} Z^{\mathrm{T}} Z \qquad (8.31)$$

where V represents the spatial covariance matrix.

3. The coordinates of the spatial anomalies can be found by projecting the anomalies onto the rotated axis.
4. The original data set of spatial anomalies can be obtained by solving the following equation:

$$P_{\mathrm{j}} = \frac{l_{\mathrm{jj}}}{\sum\limits_{k-1}^{n} l_{kk}}, \qquad (8.32)$$

where l denotes the eigen values, P_j gives a portion of the variance in the jth column and E is the Eigen vector.

$$F = ZE \qquad (8.33)$$

$$Z = FE^{\mathrm{T}} \qquad (8.34)$$

8.5.8.2   Temporal Anomalies

The long-term average soil moisture at every location is subtracted to obtain the temporal anomalies. Here the analysis is done to get the soil moisture variations in time rather than space. After this, the same steps are repeated for the spatial anomalies:

$$Z'_{i}(t) = S_{i}(t) - \frac{1}{n} \sum\limits_{\tau=1}^{n} S_{i}(\tau) \qquad (8.35)$$

where $Z'_{i}(t)$ *is* the temporal anomaly and τ is an index of sample dates.

8.5.9 Analysis of Variance

The ANOVA tests whether statistical differences exist between mean group values. Analysis of variance test is used to identify the statistically significant parameters among the various physical and meteorological factors (Jacobs et al. 2004). The ANOVA test is used to differentiate between two or more data sets. One-way ANOVA test identifies significant differences of temporally stable values among the groups like soil depths, growth ages, etc. These groups are divided based on the degree of successive data (precipitation, insolation, air temperature, ground temperature, wind speed and elevation) and category data (soil, texture, land use types). The standardisation method standardises the value of any raw variable x; μ is the mean, and σ is the standard deviation:

$$X_{\text{standardized}} = \frac{X - \mu}{\sigma} \qquad (8.36)$$

EOF identifies dominant physical controls of soil moisture, and ANOVA assists in determining the ranges of these physical control parameters, which leads to the optimal design of an area soil moisture campaign.

8.5.10 Wavelet Analysis

The concept of wavelet analysis is based on the hypothesis that time series is a combination of c small blocks like wavelets in frequency ranges. Wavelet analysis is comparable to Fourier transforms, only for wavelet analysis's error from high- and low-frequency components is minimal. This analysis has found its application in the field of hydrology: soil moisture variations (Redding et al. 2002; Lauzon et al. 2004; Tang and Piechota 2009; Biswas and Si 2011; Gaur and Mohanty 2016), runoff studies (Labat et al. 2000a; b; Anctil and Tape 2004), El Nino studies (Torrence and Webster 1999), etc.

Continuous wavelet transform of soil moisture spatial series with an equal increment can be given as

$$W_i^Y(s) = \sqrt{\frac{\delta X}{s}} \sum_{i-1}^{N} Y_j \psi \left[(j-i) \frac{\delta X}{s} \right] \qquad (8.37)$$

where ψ [ ] is the mother wavelet function, δX is the incremental distance and N is the spatial series length:

$$\psi(\eta) = \pi^{-1/4} e^{i\omega\eta - 0.5\eta^2} \qquad (8.38)$$

ω is the dimensionless frequency and represents dimensionless space. The cross wavelet between two soil moisture sample series Y and Z is given by

$$\left|W_i^{YZ}(s)\right| = \left|W_i^Y(s)\overline{W_i^Z(s)}\right|$$

(8.39)

W_i^Y and W_i^Z are wavelet coefficients

$$R_1^2(s) = \frac{\left|S\left(s^{-1}W_i^{YZ}(s)\right)\right|^2}{S\left(s^{-1}\left|W_i^Y(s)\right|^2\right)S\left(s^{-1}\left|W_i^Z(s)\right|^2\right)}$$

(8.40)

S is a smoothing operator

$$S(W) = S_{scale}\left(S_{space}\left(W(s,\tau)\right)\right)$$

(8.41)

where τ denotes the location and S_{scale} and S_{space} denote the smoothing.

8.6 Discussion

Soil moisture serves as an input to meteorological, hydrological, agricultural and soil microbiological processes. The soil moisture measurement studies are helpful in describing soil moisture variation patterns over variable study scales ranging from point to watershed and further to continental scale. The preceding sections identified dielectric techniques as the most reliable measurement methods. The most common method is the TDR-based measurement technique, which is based on Topp's equation. The equation is said to be insensitive to porosity, saturation and mineral percentage. The disadvantages associated with the dielectric techniques are related to the accuracy range, sensitivity and necessary validations. Modern techniques require cumbersome mechanisation, and the instruments should be in direct contact with the soil without leaving any air gaps. The study identified that neutron probes are the most accurate, sensitive and effective for soil moisture measurement compared to the other techniques. The modelling approach provides a less time-consuming measurement technique, though the accuracy associated with it is comparatively lower. Beyond the measurement of soil moisture, the various techniques involved in understanding the spatiotemporal variation of soil moisture are identified. The statistical method is best suited to identify spatial optimal sampling, while random combination and bootstrapping give better results for temporal optimal sampling. The correlation methods help in identifying the relationship of soil moisture on one day with another day of the next month or next based on the study requirement. Similarly, the comprehensive evaluation criteria method identifies the temporal stable locations that are required for future soil moisture monitoring.

8.7   Future Scope

The soil moisture measurement techniques used to obtain the soil moisture values require huge field effort. Further, the obtained values are needed to compute the spatiotemporal soil moisture variations. The study focused primarily on field-scale soil moisture measurements. Limited literature mentions soil moisture modelling approaches; different modelling approaches based on the pedotransfer functions provide an efficient method compared to field-based observations. The modelling approach requires one-time-filed data to validate the computed soil moisture values based on the modelling study. Further, the methods used for computing the spatio-temporal analysis are generic, and many more approaches can be used to compute the spatial and temporal stability and variability patterns.

8.8   Conclusions

This study conducted a comprehensive literature survey to define the sampling strategy while highlighting the methodologies and factors affecting the soil moisture analysis. The field campaign must be organised with a fixed gridded pattern in the entire area for robust analysis, and the left-over area should be less than the size of a unit grid. Post-field sampling and identifying stable temporal locations are prerequisites to mapping spatiotemporal variations in soil moisture. The random combination method requires fewer input variables than statistical and bootstrap methods to identify stable temporal locations for the same accuracy. Temporally stable locations prominently depend on the percentage of clay and sand, rather than silt or gravel or texture class, and locations at higher elevations were found to be temporally stable compared to the valley. For temporal stability, the standard deviation of relative difference is a more suitable measure for the field with a dryer of mean, whereas mean absolute bias error is useful for the wetter mean soil moisture value.

The governing factors for soil moisture variations are meteorological factors, topographic features, land use, land cover and soil texture class. The literature states no particular ranking mechanism of a factor as combined effects of the governing factors are of more importance. For example, soil moisture variability may decrease with a few passive factors, such as the age of forests and vegetation growing period. However, for land cover, the soil moisture variability ranking from literature can be agricultural land > forest > grassland > shrubs, and among the soil hydraulic factors, hydraulic conductivity is the most sensitive parameter to account for the soil moisture variability.

A semi-variogram better represents the spatial variation in the soil moisture at a scale larger than a field. While correlating soil's spatial and temporal variation, empirical orthogonal functions were more useful than the regression-based method. Principal component analysis and correlation results show that the soil moisture

variations are higher than the mean value for landforms with small leaf area index and crop height. This literature review concludes that topography and evapotranspiration are correlated for wetter and dryer periods, respectively. Further, the sampling density should be higher for wetter than dryer areas, and soil organic content better predicts soil moisture. There is no steady relationship between temperature and surface soil moisture; however, the literature review indicates that spatial variation is more sensitive to ground temperature than air temperatures. Spatial anomalies are extremely useful to capture the local to field scale variation of soil moisture, whereas temporal anomalies identify the wet and dry conditions relative to their long-term tendency.

Additionally, to the several factors discussed above, the soil moisture values can be affected by dew, grazing, depth to moisture sample, sunshine hours, radiations and precipitation. These factors are important and should be cautioned while starting the field campaign. For spatiotemporal variability analysis, at least one complete seasonal cycle data (one year) is required.

The most accurate measurement method would be a thorough investigation of the area, but the same is labour-intensive. Remote sensing provides the remedy for the discussed cumbersome process, but accuracy decreases. The modelling approach minimises the labour cost of soil moisture field investigation, but the accuracy of modelled values is comparatively less compared to field data. Thus, there should be a trade-off between cost-effectiveness and accuracy based on the importance of the work under consideration.

References

Anctil F, Tape DG (2004) An exploration of artificial neural network rainfall-runoff forecasting combined with wavelet decomposition. J Environ Eng Sci 3(S1):121–128. https://doi.org/10.1139/S03-071

Anctil F, Mathieu R, Parent LÉ, Viau AA, Sbih M, Hessami M (2002) Geostatistics of near-surface moisture in bare cultivated organic soils. J Hydrol 260(1–4):30–37. https://doi.org/10.1016/S0022-1694(01)00600-X

Aubert D, Loumagne C, Oudin L (2003) Sequential assimilation of soil moisture and streamflow data in a conceptual rainfall–runoff model. J Hydrol 280(1–4):145–161. https://doi.org/10.1016/S0022-1694(03)00229-4

Avissar R (1998) Which type of soil–vegetation–atmosphere transfer scheme is needed for general circulation models: a proposal for a higher–order scheme. J Hydrol 212:136–154. https://doi.org/10.1016/S0022-1694(98)00227-3

Barling RD, Corporation W, Moore ID, Grayson B (1994) Soil water content In – A quasi-dynamic wetness index for characterizing the spatial distribution of zones of surface saturation and soil water content. Water Resour Res 30:1029–1044. https://doi.org/10.1029/93WR03346

Bell KR, Blanchard BJ, Schmugge TJ, Witczak MW (1980) Analysis of surface moisture variations within large-field sites. Wat Resour Res 16(4):796–810. https://doi.org/10.1029/WR016i004p00796

Bhatti AU, Mulla DJ, Frazier BE (1991) Estimation of soil properties and wheat yields on complex eroded hills using geostatistics and thematic mapper images. Remote Sens Environ 37:181–191. https://doi.org/10.1016/0034-4257(91)90080-P

Biswas A, Si BC (2011) Identifying scale specific controls of soil water storage in a hummocky landscape using wavelet coherency. Geoderma 165:50–59. https://doi.org/10.1016/j.geoderma.2011.07.002

Blonquist JM Jr, Jones SB, Robinson DA (2005) Standardizing characterization of electromagnetic water content sensors: Part 2 Evaluation of seven sensing systems. Vadose Zone J 4(4):1059–1069. https://doi.org/10.2136/vzj2004.0141

Bogena HR, Herbst M, Huisman JA et al (2010) Potential of wireless sensor networks for measuring soil water content variability. Vadose Zo J 9:1002–1013. https://doi.org/10.2136/vzj2009.0173

Bogena HR, Huisman JA, Güntner A, Hübner C, Kusche J, Jonard F, Vey S, Vereecken H (2015) Emerging methods for noninvasive sensing of soil moisture dynamics from field to catchment scale; a review. Wiley Interdisc Rev Water 2(6):635–647. https://doi.org/10.1002/wat2.1097

Bosch DD, Lakshmi V, Jackson TJ, Choi M, Jacobs JM (2006) Large scale measurements of soil moisture for validation of remotely sensed data: Georgia soil moisture experiment of 2003. J Hydrol 323:120–137. https://doi.org/10.1016/j.jhydrol.2005.08.024

Brocca L, Morbidelli R, Melone F, Moramarco T (2007) Soil moisture spatial variability in experimental areas of central Italy. J Hydrol 333:356–373. https://doi.org/10.1016/j.jhydrol.2006.09.004

Brocca L, Melone F, Moramarco T, Morbidelli R (2009) Soil moisture temporal stability over experimental areas in Central Italy. Geoderma 148:364–374. https://doi.org/10.1016/j.geoderma.2008.11.004

Brocca L, Melone F, Moramarco T (2010) Remote Sensing of Environment ASCAT soil wetness index validation through in situ and modeled soil moisture data in central Italy. Remote Sens Environ 114:2745–2755. https://doi.org/10.1016/j.rse.2010.06.009

Brocca L, Hasenauer S, Lacava T, Melone F, Moramarco T, Wagner W, Bittelli M (2011) Soil moisture estimation through ASCAT and AMSR-E sensors: an intercomparison and validation study across Europe. Remote Sens Environ 115(12):3390–3408

Buttafuoco G, Castrignano A (2005) Study of the spatio-temporal variation of soil moisture under forest using intrinsic random functions of order k. Geoderma. 128:208–220. https://doi.org/10.1016/j.geoderma.2005.04.004

Cai X, Pan M, Chaney NW, Colliander A, Misra S, Cosh MH, Crow WT, Jackson TJ, Wood EF (2017) Validation of SMAP soil moisture for the SMAPVEX15 field campaign using a hyper-resolution model. Water Resour Res 53(4):3013–3028. https://doi.org/10.1002/2016WR019967

Charpentier MA, Groffman PM (1992) Soil moisture variability within remote sensing pixels. J Geophys Res 97:987–995. https://doi.org/10.1029/92jd00882

Choi M, Jacobs JM (2007) Soil moisture variability of root zone profiles within SMEX02 remote sensing footprints. Adv Water Resour 30:883–896. https://doi.org/10.1016/j.advwatres.2006.07.007

Clapp RB, Hornberger GM, Cosby BJ (1983) Estimating spatial variability in soil moisture with a simplified dynamic model. Water Resour Res 19:739–745. https://doi.org/10.1029/WR019i003p00739

Cosh MH, Brutsaert W (1999) Aspects of soil moisture variability in the Washita '92 study region. J Geophys Res 104:751–757. https://doi.org/10.1029/1999JD900110

Cosh MH, Jackson TJ, Bindlish R, Prueger JH (2004) Watershed scale temporal and spatial stability of soil moisture and its role in validating satellite estimates. Remote Sens Environ 92:427–435. https://doi.org/10.1016/j.rse.2004.02.016

Dam JC, Huygen J, Wesseling JG, Feddes RA, Kabat P, Van Walsum PEV, Groenendijk P, Van Diepen CA (1997) Theory of SWAP version 2.0; Simulation of water flow, solute transport and plant growth in the soil-water-atmosphere-plant environment (No. 71). DLO Winand Staring Centre

das Neves HH, da Mata MGF, Guerra JGM, de Carvalho DF, Wendroth OO, Ceddia MB (2016) Spatial and temporal patterns of soil water content in an agroecological production system. Sci Agric 74:383–392. https://doi.org/10.1590/1678-992x-2016-0213

De Lannoy GJM, Houser PR, Verhoest NEC, Pauwels VRN, Gish TJ (2007) Upscaling of point soil moisture measurements to field averages at the OPE3 test site. J Hydrol 343:1–11. https://doi.org/10.1016/j.jhydrol.2007.06.004

Desilets D, Zreda M, Ferré TPA (2010) Nature ' s neutron probe: Land surface hydrology at an elusive scale with cosmic rays. Water Resour Res 46:1–7. https://doi.org/10.1029/2009WR008726

Dobson MC, Ulaby FT (1985) Microwave dielectric behavior of wet soil-part dielectric mixing models. https://doi.org/10.1109/TGRS.1985.289498

Entekhabi D, Rodriguez-Iturbe I (1994) Analytical framework for the characterization of the space-time variability of soil moisture. Adv Water Resour 17:35–45. https://doi.org/10.1016/0309-1708(94)90022-1

Entin JK, Robock A, Vinnikov KY, Hollinger SE, Liu S, Namkhai A (2000) Meteorological land surface. J Geophys Res 105:11865–11877. https://doi.org/10.1029/2000JD900051

Famiglietti JS, Rudnicki JW, Rodell M (1998) Variability in surface moisture content along a hillslope transect: Rattlesnake Hill, Texas. J Hydrol 210:259–281. https://doi.org/10.1016/S0022-1694(98)00187-5

Famiglietti JS, Ryu D, Berg AA (2008) Field observations of soil moisture variability across scales. Water Resour Res 44:1–16. https://doi.org/10.1029/2006WR005804

Fernández-Martinez J, Ceballos A (2005) Mean soil moisture estimation using temporal stability analysis. J Hydrol 312(1-4):28–38

Gao Z, Xu X, Wang J et al (2013) A method of estimating soil moisture based on the linear decomposition of mixture pixels. Math Comput Model 58:606–613. https://doi.org/10.1016/j.mcm.2011.10.054

Gasch CK, Brown DJ, Campbell CS, Cobos DR, Brooks ES, Chahal M, Poggio M (2017) A field-scale sensor network data set for monitoring and modeling the spatial and temporal variation of soil water content in a dryland agricultural field. Water Resour Res 53(12):10878–10887

Gaur N, Mohanty BP (2016) Land-surface controls on near-surface soil moisture dynamics: traversing remote sensing footprints. Water Resour Res. https://doi.org/10.1002/2015WR018095

Gilbert RO (1987) Statistical methods for environmental pollution monitoring. John Wiley & Sons, Hoboken, NJ. https://doi.org/10.2307/2531935

Grant L, Seyfried M, McNamara J (2004) Spatial variation and temporal stability of soil water in a snow-dominated, mountain catchment. Hydrol Process 18:3493–3511. https://doi.org/10.1002/hyp.5798

Hallikainen MT, Ulaby FT (1985) Microwave dielectric behavior of wet soil-part 1 : empirical models and experimental observations. IEEE Trans Geosci Remote Sens 23:25–34. https://doi.org/10.1109/TGRS.1985.289497

Heathman GC, Larose M, Cosh MH, Bindlish R (2009) Surface and profile soil moisture spatio-temporal analysis during an excessive rainfall period in the Southern Great Plains, USA. Catena 78:159–169. https://doi.org/10.1016/j.catena.2009.04.002

Heathman GC, Cosh MH, Han E, Jackson TJ, McKee L, McAfee S (2011) Field scale spatiotemporal analysis of surface soil moisture for evaluating point-scale in situ networks. Geoderma 170:195–205. https://doi.org/10.1016/j.geoderma.2011.11.004

Heitman JL, Basinger JM, Kluitenberg GJ, Ham JM, Frank JM, Barnes PL (2003) Field evaluation of the dualprobe heat-pulse method for measuring soil water content. Vadose Zone J 2(4):552–560

Hu W, Si BC (2014a) Can soil water measurements at a certain depth be used to estimate mean soil water content of a soil profile at a point or at a hillslope scale. J Hydrol 516:67–75. https://doi.org/10.1016/j.jhydrol.2014.01.053

Hu W, Si BC (2014b) Revealing the relative influence of soil and topographic properties on soil water content distribution at the watershed scale in two sites. J Hydrol 516:107–118. https://doi.org/10.1016/j.jhydrol.2013.10.002

Hu W, Shao M, Han F et al (2010) Geoderma Watershed scale temporal stability of soil water content. Geoderma 158:181–198. https://doi.org/10.1016/j.geoderma.2010.04.030

Hu W, Shao M, Han F, Reichardt K (2011) Spatio-temporal variability behavior of land surface soil water content in shrub-and grass-land. Geoderma 162(3-4):260–272

Huisman JA, Snepvangers JJJC, Bouten W, Heuvelink GBM (2003) Monitoring temporal development of spatial soil water content variation: comparison of ground pene*tr*ating radar and time domain reflectometry. Vadose Zo J 2:519–529. https://doi.org/10.2136/vzj2003.5190

Jacobs JM, Mohanty BP, Hsu EC, Miller D (2004) SMEX02: field scale variability, time stability and similarity of soil moisture. Remote Sens Environ 92:436–446. https://doi.org/10.1016/j.rse.2004.02.017

Jacobs JM, Hsu EC, Choi M (2010) Time stability and variability of electronically scanned thinned array radiometer soil moisture during Southern Great Plains hydrology experiments. Hydrol Process 24(19):2807–2819

Jin R, Li X, Yan B, Li X, Luo W, Ma M, Guo J, Kang J, Zhu Z, Zhao S (2014) A nested ecohydrological wireless sensor network for capturing the surface heterogeneity in the midstream areas of the Heihe River Basin, China. IEEE Geosci Remote Sens Lett 11(11):2015–2019. https://ur.booksc.me/book/30943520/2f7cf4#:~:text=10.1109/lgrs.2014.2319085

Jonard F, Bogena H, Caterina D, Garré S, Klotzsche A, Monerris A, Schwank M, von Hebel C (2018) Ground-based soil moisture determination. Springer, Cham. https://doi.org/10.1007/978-3-662-48297-1_2

Kachanoski RG, de Jong E (1988) Scale dependence and the temporal persistence of spatial patterns of soil water storage. Water Resour Res 24:85–91. https://doi.org/10.1029/WR024i001p00085

Kaleita AL, Tian LF, Hirschi MC (2005) Relationship between soil moisture content and soil surface reflectance. Trans ASAE 48:1979–1986. https://dr.lib.iastate.edu/handle/20.500.12876/1037

Kelleners TJ, Robinson DA, Shouse PJ (2005) Frequency dependence of the complex permittivity and its impact on dielectric sensor calibration in soils. Soil Sci Soc Am J 69:67–76. https://doi.org/10.2136/sssaj2005.0067a

Kizito F, Campbell CS, Campbell GS, Cobos DR, Teare BL, Carter B, Hopmans JW (2008) Frequency, electrical conductivity and temperature analysis of a low-cost capacitance soil moisture sensor. J Hydrol 352(3–4):367–378. https://doi.org/10.1016/j.jhydrol.2008.01.021

Labat D, Ababou R, Mangin A (2000a) Rainfall – runoff relations for karstic springs. Part I : convolution and spectral analyses. J Hydrol 238:123–148. https://doi.org/10.1016/S0022-1694(00)00321-8

Labat D, Ababou R, Mangin A (2000b) Rainfall – runoff relations for karstic springs. Part II : continuous wavelet and discrete orthogonal multiresolution analyses. J Hydrol 238:149–178. https://doi.org/10.1016/S0022-1694(00)00322-X

Lauzon N, Anctil F, Petrinovic J (2004) Characterization of soil moisture conditions at temporal scales from a few days to annual. Hydrol Process 18:3235–3254. https://doi.org/10.1002/hyp.5656

Lawrence JE, Hornberger GM (2007) Soil moisture variability across climate zones. Geophys Res Lett 34:1–5. https://doi.org/10.1029/2007GL031382

Leonard RA, Knisel WG, Still DA (1987) GLEAMS: groundwater loading effects of agricultural management systems. Trans ASAE 30(5):1403–1418. https://elibrary.asabe.org/abstract.asp?

aid=30578#:~:text=1403%2D1418.%C2%A0(doi%3A-,10.13031/2013.30578,-)%20%401
987%0AAuthors%3A

Leone AP, Menenti M, Buondonno A, Letizia A, Maffei C, Sorrentino G (2007) A field experiment on spectrometry of crop response to soil salinity. Agric Water Manag 89(1-2):39–48

Li B, Rodell M (2013) Spatial variability and its scale dependency of observed and modeled soil moisture over different climate regions. Hydrol Earth Syst Sci 17(3):1177–1188

Lidard CD, Pan F, Wood EF (2001) A re-examination of modeled and measured soil moisture spatial variability and its implications for land surface modeling. Adv Water Resour 24(9-10):1069–1083

Lin HS, Kogelmann W, Walker C, Bruns MA (2005) Soil moisture patterns in a forested catchment: a hydropedological perspective. Geoderma 131:345–368. https://doi.org/10.1016/j.geoderma.2005.03.013

Loew A, Ludwig R, Mauser W (2006) Derivation of surface soil moisture from ENVISAT ASAR wide swath and image mode data in agricultural areas. IEEE Trans Geosci Remote Sens 44 (4):889–899

Merlin O, Walker JP, Chehbouni A, Kerr Y (2008) Remote sensing of environment towards deterministic downscaling of SMOS soil moisture using MODIS derived soil evaporative efficiency. Remote Sens Environ 112(10):3935–3946. https://doi.org/10.1016/j.rse.2008.06.012

Mohanty BP, Famiglietti JS, Skaggs TH (2000) Evolution of soil moisture spatial structure in a mixed vegetation pixel during the Southern Great Plains 1997 (SGP97) Hydrology Experiment. Water Resour Res 36(12):3675–3686

Nielsen DR, Bigga JW, Erh KT (1973) Spatial variability of field-measured soil-water properties. Hilgardia 42(7):215–259. https://hilgardia.ucanr.edu/Abstract/?a=hilg.v42n07p215#:~:text=10.3733/hilg.v42n07p215

Njoku EG, Entekhabi D (1996) Passive microwave remote sensing of soil moisture. J Hydrol 184(1–2):101–129. https://doi.org/10.1016/0022-1694(95)02970-2

Pan F (2012) Estimating daily surface soil moisture using a daily diagnostic soil moisture equation. J Irrig Drain Eng 138(7):625–631

Panciera R, Walker JP, Kalma JD, Kim EJ, Hacker JM, Merlin O et al (2008) The NAFE'05/CoSMOS data set: toward SMOS soil moisture retrieval, downscaling, and assimilation. IEEE Trans Geosci Remote Sens 46(3):736–745

Pandey V, Pandey PK (2010) Spatial and temporal variability of soil moisture. Int J Geosci 01:87–98. https://doi.org/10.4236/ijg.2010.12012

Perry MA, Niemann JD (2007) Analysis and estimation of soil moisture at the catchment scale using EOFs. J Hydrol 334:388–404. https://doi.org/10.1016/j.jhydrol.2006.10.014

Preisendorfer RW, Mobley CD (1988) Principal component analysis in meteorology and oceanography, Developments in atmospheric science, vol 17. Amsterdam, Elsevier

Redding TE, Hope GD, Fortin MJ, Schmidt MG, Bailey WG (2002) Spatial patterns of soil temperature and moisture across subalpine forest-clearcut edges in the southern interior of British Columbia. Can J Soil Sci 83(1):121–130

Reedy RC, Scanlon BR (2003) Soil water content monitoring using electromagnetic induction. J Geosci Geoenviron Eng. 129(11):1028–1039. https://doi.org/10.1061/(ASCE)1090-0241 (2003)129:11(1028)

Reichardt K, Portezan O, Bacchi OOS (1997) Neutron probe calibration correction by temporal stability parameters of soil water content probability distribution. Sci Agric 54:17–21. https://doi.org/10.1590/s0103-90161997000300003

Reynolds SG (1974) A note on the relationship between size of area and soil moisture variability. J Hydrol 22(1–2):71–76. https://doi.org/10.1016/0022-1694(74)90096-1

Ridolfi L, D'Odorico P, Porporato A, Rodriguez-Iturbe I (2003) Stochastic soil moisture dynamics along a hillslope. J Hydrol 272:264–275. https://doi.org/10.1016/S0022-1694(02)00270-6

Robinson DA, Jones SB, Wraith JM, Or D, Friedman SP (2003) A review of advances in dielectric and electrical conductivity measurement in soils using time domain reflectometry. Vadose Zone J 2(4):444–475. https://doi.org/10.2113/2.4.444

Robinson DA, Lebron I, Kocar B, Phan K, Sampson M, Crook N, Fendorf S (2008) Time-lapse geophysical imaging of soil moisture dynamics in tropical deltaic soils: An aid to interpreting hydrological and geochemical processes. Water Resour Res 46:1–12. https://doi.org/10.1029/2008WR006984

Rodriguez-Iturbe I, Entekhabi D, Bras RL (1991) Nonlinear dynamics of soil moisture at climate scales: 1. Stochastic analysis Water Resources Research 27(8):1899–1906

Rodriguez-Iturbe I, Porporato A, Ridolfi L, Isham V, Coxi DR (1999) Probabilistic modelling of water balance at a point: the role of climate, soil and vegetation. Proc R Soc London Ser A 455 (1990):3789–3805

Rolston DE, Biggar JW, Nightingale HI (1991) Temporal persistence of spatial soil-water patterns under trickle irrigation. Irrig Sci 12(4):181–186

Rosenbaum U, Bogena HR, Herbst M (2012) Seasonal and event dynamics of spatial soil moisture patterns at the small catchment scale. Water Resour Res 48:1–22. https://doi.org/10.1029/2011WR011518

Samouëlian A, Cousin I, Tabbagh A, Bruand A, Richard G (2005) Electrical resistivity survey in soil science: a review. Soil Tillage Res 83(2):173–193. https://doi.org/10.1016/j.still.2004.10.004

Schjønning P, Thomsen IK, Moldrup P, Christensen BT (2003) Linking soil microbial activity to water-and air-phase contents and diffusivities. Soil Sci Soc Am J 67(1):156–165. https://doi.org/10.2136/sssaj2003.1560

Schmugge T, O'Neill PE, Wang JR (1986) Passive microwave soil moisture research. IEEE Trans Geosci Remote Sens 1:12–22. https://doi.org/10.1109/TGRS.1986.289584

Schneider JA, Randolph MF, Mayne PW, Ramsey NR (2008) Analysis of factors influencing soil classification using normalized piezocone analysis of factors influencing soil classification using normalized piezocone tip resistance and pore pressure parameters. J Geosci Geoenviron Eng 134(11):1569–1586. https://doi.org/10.1061/(ASCE)1090-0241(2008)134

Sheets KR, Hendrickx JM (1995) Noninvasive soil water content measurement using electromagnetic induction. Water Resour Res 31(10):2401–2409. https://doi.org/10.1029/95WR01949

Sherlock MD, Mcdonnell JJ (2003) A new tool for hillslope hydrologists: spatially distributed groundwater level and soil water content measured using electromagnetic induction. Hydrol Process 17(10):1965–1977. https://doi.org/10.1002/hyp.1221

Shouqin Z, Weihua Z, Jiake L, Chaofu W (2014) Temporal variation of soil water and its influencing factors in hilly area of Chongqing, China. Int J Agric Biol Eng 7(4):47–60. https://doi.org/10.3965/j.ijabe.20140704.006

Singh G, Panda RK, Mohanty BP (2019) Spatiotemporal analysis of soil moisture and optimal sampling design for regional-scale soil moisture estimation in a tropical watershed of India. Water Resour Res 55(3):2057–2078

Starks PJ, Heathman GC, Jackson TJ, Cosh MH (2006) Temporal stability of soil moisture profile. J Hydrol 324(1–4):400–411. https://doi.org/10.1016/j.jhydrol.2005.09.024

Tang C, Piechota TC (2009) Spatial and temporal soil moisture and drought variability in the Upper Colorado River Basin. J Hydrol 379:122–135. https://doi.org/10.1016/j.jhydrol.2009.09.052

Teuling AJ, Seneviratne SI, Williams C, Troch PA (2006) Observed timescales of evapotranspiration response to soil moisture. Geosci Phys Res Lett 33(23):1–5. https://doi.org/10.1029/2006GL028178

Teuling AJ, Hupet F, Uijlenhoet R, Troch PA (2007) Climate variability effects on spatial soil moisture dynamics. Geophys Res Lett 34:2–5. https://doi.org/10.1029/2006GL029080

Topp GC, Davis JL, Annan AP (1980) Electromagnetic determination of soil water content: measurements in coaxial transmission lines. Water Resour Res 16(3):574–582. https://doi.org/10.1029/WR016I003P00574

Torrence C, Webster PJ (1999) Interdecadal changes in the ENSO–monsoon system. J Clim 12(8): 2679–2690. https://doi.org/10.1175/1520-0442(1999)012<2679:ICITEM>2.0.CO;2

Tyagi JV, Qazi N, Rai SP, Singh MP (2013) Analysis of soil moisture variation by forest cover structure in lower western Himalayas, India. J For Res 24:317–324. https://doi.org/10.1007/s11676-013-0355-8

Ulaby FT, Dubois PC, Van Zyl J (1996) Radar mapping of surface soil moisture. J Hydrol 184(1–2):57–84. https://doi.org/10.1016/0022-1694(95)02968-0

Ursulino B, Montenegro MGL, Paiva Coutinho A, Hugo Rabelo Coelho V, Cezar dos Santos Araújo D, Cláudia Villar Gusmão A et al (2019) Modelling soil water dynamics from soil hydraulic parameters estimated by an alternative method in a tropical experimental basin. WaterSA 11(5):1007

Vachaud G, Passerat De Silans A, Balabanis P, Vauclin M (1985) Temporal stability of spatially measured soil water probability density function. Soil Sci Soc Am J 49:822–828. https://doi.org/10.2136/sssaj1985.03615995004900040006x

Vancloster M, Viane P, Diels J, Christiens K (1994) WAVE model for simulating water and agrochemical in the soil and vadose environment

Venkatesh B, Lakshman N, Purandara BK, Reddy VB (2011a) Analysis of observed soil moisture patterns under different land covers in Western Ghats, India. J Hydrol 397:281–294. https://doi.org/10.1016/j.jhydrol.2010.12.006

Venkatesh B, Nandagiri L, Purandara BK, Reddy VB (2011b) Modelling soil moisture under different land covers in a sub-humid environment of Western Ghats, India. J Earth Syst Sci 120:387–398. https://doi.org/10.1007/s12040-011-0076-3

Verburg K, Keating BA, Bristow KL, Huth NI, Ross PJ (1996) Modelling nitrate leaching under sugarcane using APSIM-SWIM. In Proceedings*/Eighth Australian Agronomy Conference Toowoomba, p 724

Vereecken H, Huisman J. A, Bogena H, et al 2008 On the value of soil moisture measurements in vadose zone hydrology: a review; Water Resour Res 44(4):1–21. doi: https://doi.org/10.1029/2008WR006829

Vereecken H, Huisman JA, Pachepsky Y, Montzka C, Van Der Kruk J, Bogena H, Weihermüller L, Herbst M, Martinez G, Vanderborght J (2014) On the spatio-temporal dynamics of soil moisture at the field scale. J Hydrol 516:76–96. https://doi.org/10.1016/j.jhydrol.2013.11.061

Wagner W, Pathe C, Doubkova M, Säbel D, Bartsch A, Hasenauer S, Blöschl G, Scipal K, Martínez-Fernández J, Löw A (2008) Temporal stability of soil moisture and radar backscatter observed by the Advanced Synthetic Aperture Radar (ASAR). Sensors 8(2):1174–1197. https://doi.org/10.3390/s80201174

Walker JP, Willgoose GR, Kalma JD (2001) The Nerrigundah data set: soil moisture patterns, soil characteristics, and hydrological flux measurements. Water Resour Res 37:2653–2658. https://doi.org/10.1029/2001WR000545

Western AW, Grayson RB, Blöschl G (2002) Scaling of soil moisture: a hydrologic perspective. Annu Rev Earth Planet Sci 30:149–180. https://doi.org/10.1146/annurev.earth.30.091201.140434

Wigneron J, Calvet J, Pellarin T (2003) Retrieving near-surface soil moisture from microwave radiometric observations : current status and future plans. Remote Sens Environ 85(4):489–506. https://doi.org/10.1016/S0034-4257(03)00051-8

Woods K, Kegelmeyer WP, Bowyer K (1997) Combination of multiple classifiers using local accuracy estimates. IEEE Trans Pattern Anal Mach Intell 19(4):405–410

Yoo C, Kim S (2004) EOF analysis of surface soil moisture field variability. Adv Water Resour 27: 831–842. https://doi.org/10.1016/j.advwatres.2004.04.003

Zhu Q, Liao K, Xu Y, Yang G, Wu S, Zhou S (2012) Monitoring and prediction of soil moisture spatial-temporal variations from a hydropedological perspective: a review. Soil Res 50:625–637. https://doi.org/10.1071/SR12228

Zreda M, Desilets D, Ferre TPA, Scott RL (2008) Measuring soil moisture content non-invasively at intermediate spatial scale using cosmic-ray neutrons. Geophys Res Lett. 35:1–5. https://doi.org/10.1029/2008GL035655

Zucco G, Brocca L, Moramarco T, Morbidelli R (2014) Influence of land use on soil moisture spatial – temporal variability and monitoring. J Hydrol:1–7. https://doi.org/10.1016/j.jhydrol.2014.01.043

Part II
Causes and Impacts

Chapter 9
Streamflow Estimation Using Entropy-Based Flow Routing Technique in Brahmani River, Odisha

Pooja Patel and Arindam Sarkar

Abstract The accurate streamflow measurement is crucial for designing hydraulic structures, for sediment transport studies and for flood management. The direct in situ streamflow measurement using velocity measuring devices involves huge cost and affects the safety of workers. Thus, indirect flow measurement techniques are the need of the hour to avoid these limitations and to obtain an accurate estimation of streamflow. This study makes use of a flow routing technique to determine a streamflow hydrograph at a downstream station on a reach, where only the water elevations are monitored, and the streamflow is measured at a river section lying upstream of it. The model is capable to incorporate a significant lateral inflow from tributaries even in the absence of monitored discharge on the tributaries. The flow routing method makes use of the entropy theory – a probabilistic approach – and is only applicable under a condition of constant entropy parameter obtained at the two most extreme river sections on a river reach. The entropy parameter is a cross-sectional representative constant, the variation of which indicates the changes in cross-sectional hydraulic and geometrical characteristics. The method has proven to provide accurate discharge estimation on Indian rivers in past studies; thus, it is applied to route the flow from station Jaraikela to Panposh on the Brahmani River with significant inflow from tributaries. The predicted flow hydrograph at Panposh is compared with the observed monthly mean flow hydrograph and numerically simulated flow hydrograph using two-dimensional (2D) Hydrologic Engineering Centre's River Analysis System (HEC-RAS). The two-dimensional HEC-RAS solves the flow continuity and momentum equation using inputs such as upstream flow hydrograph, calibrated channel bed roughness, river bathymetry, and downstream stage hydrograph. The obtained results showed high prediction accuracy of the entropy-based approach with advantages over a numerical model in terms of eliminating the iterative calibration of bed roughness and requiring lesser input data.

P. Patel · A. Sarkar (✉)
School of Infrastructure, IIT Bhubaneswar, Argul, Khordha, Odisha, India
e-mail: a20ce09016@iitbbs.ac.in; asarkar@iitbbs.ac.in

The results inferred that the entropy-based approach can be utilized to determine streamflow at any ungauged station on the Brahmani River, given the streamflow and stage at upstream and downstream sites, respectively.

Keywords HEC-RAS · Flow routing · Streamflow · Entropy theory

9.1 Introduction

The greatest civilizations of the world have risen around the great rivers such as Indus and Nile; thus, rivers are regarded as the lifelines of the world. With time, the rapid growth in population and increased human intervention around the rivers has polluted the rivers, disturbed aquatic life, and increased the fluvial hazards. Flood is the most common fluvial hazard/disaster which has been observed frequently across the country (such as Uttarakhand flood in 2013, Chennai flood in 2015, and Kerala flood in 2018) causing huge loss of life, property, and environmental damages (Saikumar et al. 2022). The rapidly changing climate in conjunction with the human intervention led to increased frequency of extreme flood events in rivers. To enhance the flood preparedness, the non-structural measures involving flood forecasting and early warning system are being adopted in recent times. Flood forecasting implies the precise and reliable estimation of discharge at the river sites for flood warning, flood control planning, and evacuation of people from risk-prone areas. Moreover, the discharge estimation is required for other aspects of water resources and its management such as water allocation, design and operation of hydraulic structures and water quality and aquatic habitat assessment (Agarwal et al. 2016; Sharma et al. 2022). In India, discharge is still being measured using area velocity method employing the point velocity measured using current meter. The measurement of discharge in rivers using current meter involves a lot of difficulties, especially on inaccessible sites, which can lead to measurement uncertainties. During high flows, the discharge measurement using flow measuring devices is difficult and dangerous for the operators. Other than that, the traditional measurement techniques require a huge amount of effort, time, and cost, leading to reduced frequency of measurement at a number of gauging stations, which can have a negative impact on water resources management studies. Therefore, the new methods are required to reduce the cost and increase the frequency of measurements, offering a nearly accurate estimation of discharge.

One of the most commonly used indirect flow estimation techniques is hydrologic Muskingum flow routing method. It considers the linear relationship between storage and discharge, which is not true for natural channels. Additionally, the comparison of hydraulic and hydrologic flow routing showed the former predicts streamflow with higher accuracy (Roohi et al. 2020). The hydraulic routing solves full continuity and momentum equation (St. Venant equation) to route the flow considering the temporal and spatial variation of flow along the river. The St. Venant

equation is a partial differential equation; thus, the determination of its exact solution is quite difficult and requires high computation platforms. The numerical softwares such as HEC-RAS, MIKE 11HD, and LISSFLOD-FP give its approximate solution with some assumptions using finite difference method. Previous studies indicate a rapid use of these models to determine the streamflow and to study the flood inundation in rivers (Parhi et al. 2012; Kumar et al. 2017). The advancement in computational hydraulics shows the coupling of GIS with the hydraulic model like HEC-RAS, where a remotely sense data – digital elevation model (DEM) – is used to extract the river bathymetric information to define the geometry of the river. Despite these advantages, HEC-RAS cannot be applied on the river having ungauged tributaries due to the absence of input boundary condition. In addition to that, the HEC-RAS is very sensitive to bed roughness, which is determined iteratively by matching the predicted and observed water levels at the downstream station. Moramarco and Singh (2001) developed a flow routing technique where the downstream discharge was determined using recorded upstream discharge, downstream water levels, and area of the cross-section at both the stations. Unlike HEC-RAS, it eliminated the iterative calibration of the bed roughness coefficient for a channel. The flow routing technique was derived using the entropic velocity distribution by Chiu (1991), where the entropy signifies the uncertainty accompanied with a random variable (say, point velocity in river cross-section). The entropy theory was used in many previous studies, recently, to solve various problems in hydrology (Agarwal et al. 2016, Li and Zheng 2016) and hydraulics (Singh 2015). The proposed entropic flow routing offered a quick discharge estimate; however, its application was limited to the reaches without any tributaries and a constant entropy parameter (M) throughout the reach. The M parameter is a non-dimensional parameter which reflects the change in geometric and hydraulic characteristics (Moramarco and Singh 2001) at a river cross-section. Later, the entropy-based routing technique is modified to extend its application on a river network with tributaries (Moramarco et al. 2005) having no measured data on it. Thus, the inflow from tributaries was approximated as the function of the length of the reach, travel time, and difference in the cross-sectional area of the downstream and upstream sections. Despite unmeasured upstream flow at tributaries, the modified entropy-based routing provided reasonable flow simulation on the river reaches with tributaries having significant lateral contribution to the most downstream station. The method is tested on the Mahanadi and Godavari Rivers for the reaches with and without tributaries (Patel and Sarkar 2022). The obtained results excellently matched with the observed flow at the downstream stations on the three considered reaches. Consequently, this study presents a case study where the entropy-based technique is applied on a reach on the Brahmani River. The obtained discharge hydrograph at the downstream station is validated with the observed downstream discharge record. Moreover, the numerical model HEC-RAS is also adopted for the same reach to approximate the discharge at the downstream station. Further, the prediction accuracy of both techniques is compared using different goodness-of-fit indices.

9.2   Rationale of the Study

The rapidly changing climate and warming of planet have led to increased frequency of extreme precipitations and, thus, the increased intensity of flooding in rivers. This frequent flooding poses heavy impact on aquatic lives, human societies, and economy. The quantification of flood discharge is crucial for the safety of hydraulic structure and its design. However, the traditional measurement of discharge is complex and cumbersome task as it involves velocity measurement across the river cross-section. During high flows, the discharge estimation through velocity measurements puts operator's life at risk, whereas the stage can still be measured remotely with enough accuracy. Thus, there is a need for such techniques which can improve the river discharge estimation making use of the remotely measured stage data at the considered site. As a result, the goals of the paper are as follows:

1. Prediction of discharge at a downstream station using locally measured stage and available observed upstream discharge on a reach in Brahmani River, Odisha
2. Modeling the similar reach in two-dimensional HEC-RAS to simulate the downstream discharge using unsteady flow routing
3. Comparative analysis of the two flow routing techniques for discharge simulation on the Brahmani River

9.3   Limitations of the Study

The study presented has following limitations:

1. The entropy-based flow routing technique applies on river reach with constant entropy parameter (M) and on a reach having no distributaries.
2. The flow routing does not involve its application on a reach having any hydraulic structures or reservoirs present.

9.4   Study Area

The Brahmani River is the second largest river in the State of Odisha and is a non-perennial river, lying between latitude 20°28' to 23°35'N and longitude 83°52' to 87°30'E. The river flows through Jharkhand, Chhattisgarh, and Odisha and drains to the Bay of Bengal with a total drainage area of 39, 033 km^2. The river has three major tributaries, named Sankh, Tikra, and Karo. The basin has a tropical climate influenced by the southwest monsoon from June to October. The average rainfall received by the basin is 1460 mm approximately. The basin observes maximum temperature between 38 and 43 °C and minimum temperature ranges between 10 and 15 °C.
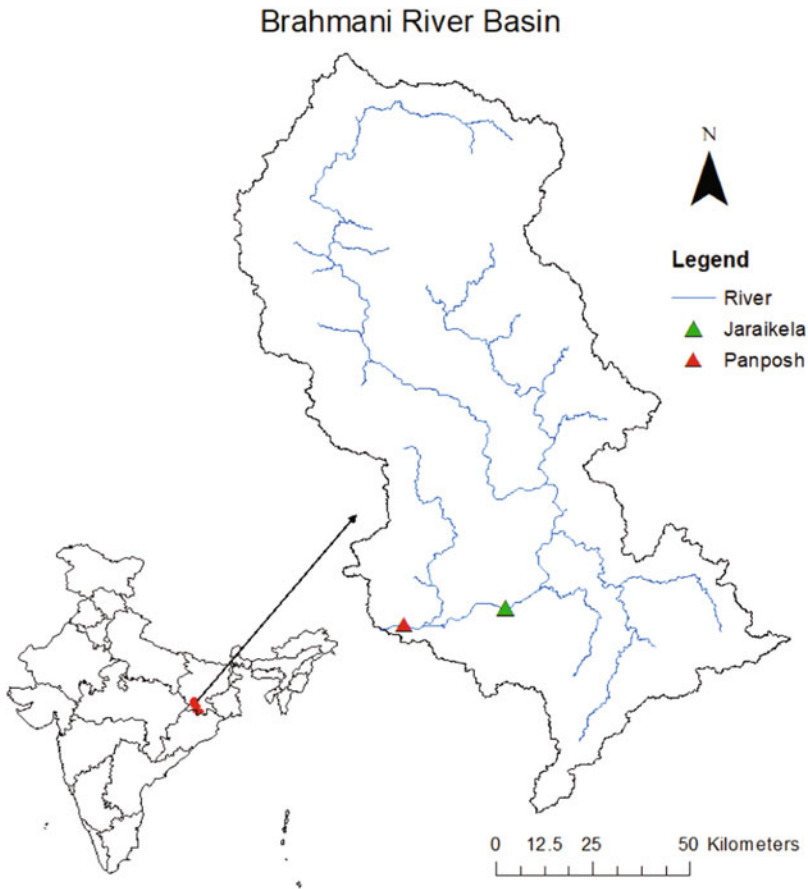
Fig. 9.1 Study area considered for flow routing

The hydrological data of the river is measured and maintained by the Central Water Commission (CWC), which is a central technical organization in the field of water resources. The basin has a total of eight stations, out of which, six are GDSQ (Gauge, Discharge, Sediment and Water Quality) measuring stations, one GQ, and one seasonal gauge measuring station. In this study, the flow routing is performed for the reach between Jaraikela and Panposh on the tributary of the Brahmani River (Koel River), as shown in Fig. 9.1.

9.5 Data Sources

The CWC measures discharge and stage at river sites on a daily basis. The measured discharge at the two stations on the Koel River, Jaraikela and Panposh, is obtained for the hydrological year of 2015–2016 from the Water Yearbook – Brahmani basin,

CWC. The discharge measurement is done by CWC utilizing the area velocity method, where the velocity measurements are made using the cup-type current meter. The depth of the flow is determined using the sounding rod for depths up to 3 m and by a log line beyond 3 m. The discharge is measured once a day for weekdays, whereas for the weekends, the discharge measurements are made using a discharge rating curve prepared from weekday measurements. For stage measurements, the datum of the site is fixed 1 or 2 m lower than the lowest bed level for the non-perennial streams. The river cross-section geometry by CWC is measured for the pre-monsoon (December–May) and post-monsoon (June–November) months. The available cross-sectional geometry is digitized to obtain the best-fit curve. Further, the cross-sectional area corresponding to the monthly average flow depth is calculated for each month utilizing the post- or pre-monsoon digitized curve at a considered site using integration on MATLAB. The riverbed slope at a river site is obtained from the digital elevation model (DEM) of year 2015 with a resolution of 30 m, procured from Bhuvan – Indian geo platform of ISRO. The river width and reach length are extracted from satellite imagery of the respective year using Google Earth Pro. The baseflow at each river site is obtained using the SWAT Baseflow filter, which uses the baseflow separation technique to segregate the baseflow from the input daily streamflow data. Moreover, the obtained daily baseflow is transformed to monthly mean baseflow for the discharge calculations using entropy-based routing technique.

9.6　Methodology

9.6.1　Entropy-Based Routing

The entropy derived flow estimation technique (Moramarco and Singh 2001) determines the downstream flow hydrograph employing upstream flow hydrograph and stage-area curve at both the extreme stations on a reach. The flow routing technique is derived from the entropic velocity distribution (Chiu 1991), which expresses the relation between average velocity (v_m) and maximum velocity (v_{max}) as follows:

$$v_m = \varnothing(M)v_{max} \quad \text{where,} \quad \varnothing(M) = \frac{e^M}{e^M - 1} - \frac{1}{M} \tag{9.1}$$

Xia (1997) calculated M using Eq. 9.1 on the upstream and downstream stations along an approximately straight river reach. Xia (1997) calculated the M parameter at two extreme sections on a reach and based on constant M concluded that the parameter remains constant throughout the straight reach. The constant M implies $\varnothing(M)$ to be constant; hence, the mean velocity at the downstream station is directly proportional to the mean upstream velocity. Thus, the discharge at the downstream sections (Q_d) can be written as

$$Q_d \propto \frac{A_u}{A_d} Q_u \qquad (9.2)$$

where Q_u is the upstream discharge, respectively, A_d is the cross-sectional area at downstream site, and A_u is the upstream cross-sectional area. Using Eq. 9.2, the flow routing model (Moramarco et al. 2005) is developed to calculate downstream flow at a time, t, given as follows:

$$Q_d(t) = \alpha \frac{A_u(t)}{A_d(t - T_L)} Q_u(t - T_L) + \beta \qquad (9.3)$$

where α and β are streamflow and baseflow parameters, respectively, and T_L is the time of travel by a flood wave from one end to another end of the reach. The parameters α and β are determined for the two boundary conditions as given below:

$$Q_d^b(t) = \alpha \frac{A_d^b}{A_u^b} Q_u^b + \beta \qquad (9.4)$$

$$Q_d^p(t) = \alpha \frac{A_d^p}{A_u^p} Q_u^p + \beta \qquad (9.5)$$

where Q^b and Q^P is peak baseflow and discharge, respectively, and A^b and A^P is area corresponding to Q^b and Q^P, respectively. Assuming $Q_d^b = Q_u^b$ in Eq. 9.4 for the nonuniform flow, the downstream peak flow (Q_d^p) can be expressed as the attenuated flow at upstream section in addition to the lateral inflow from tributaries (q_pL) during peak flow:

$$Q_d^p(t) = \left[Q_u^p(t) - Q^*\right] + q_pL \qquad (9.6)$$

The attenuation in upstream discharge (Q^*) is determined using Eq. 9.7 (Price 1973), where $K = L/2BS$ is the peak discharge attenuation parameter, Q_u^p is the upstream peak discharge, Δt_p is one-fifth of the time to peak t_p, and Q_1 and Q_{-1} are the discharge on either side of t_p at Δt_p:

$$Q^* = \frac{K}{(L/T)^3} Q_u^p \left| \frac{Q_1 + Q_{-1} - 2Q_u^p}{(t_p)^2} \right| \qquad (9.7)$$

The q_pL shows the lateral flow contribution from tributaries, which is calculated using Eq. 9.8–9.10 expressed by Moramarco et al. (2005) as follows:

$$q_p L = \frac{A_d(t_p) - A_u(t_p - T_L)}{T_L} \tag{9.8}$$

$$T_L = \frac{L}{c} \tag{9.9}$$

$$c = \frac{\partial Q_u}{\partial A_u} \tag{9.10}$$

The parameters are estimated by solving Eqs. 9.4–9.10, as mentioned above. Further, the discharge is estimated at any downstream station (using Eq. 9.3) on the same reach with calculated M approximately similar to that obtained at the upstream station. The only condition under which the entropic routing technique can be applied is that M, thus $\emptyset(M)$ at the two extreme sections of a river reach, should remain the same. Previous studies calculated the M parameter using measured velocity pairs (v_m and v_{max}); however, in absence of the available velocity data, Eq. 9.1 cannot be utilized. For such cases, the M parameter can be estimated utilizing measured discharge for previous years, assuming the statement regarding the M being constant at a gauging station and independent of flow dynamics (Xia 1997) to be true. Thus, the M is determined solving Eqs. 9.11–9.14 given below:

$$v_m e^{a_1} = \left(Me^M - e^M + 1\right)\left(e^M - 1\right)^{-2} \tag{9.11}$$

$$v_m = \frac{Q}{A} \tag{9.12}$$

$$a_1 = \ln\left(\frac{\mu}{v_*^2 D}\right) \tag{9.13}$$

$$v_* = \sqrt{gRS} \tag{9.14}$$

where v_* is the shear velocity, R is the hydraulic radius (assumed equal to the depth of water, D), S is the bed slope at the considered site, and μ is the kinematic viscosity of water. Thus, depending upon the constant M, a suitable reach is selected on the Brahmani basin to apply flow routing based on entropy theory.

9.6.2 Numerical Model: Two-Dimensional HEC-RAS

9.6.2.1 Overview of Model Setup Using HEC-RAS

The HEC-RAS is a two-dimensional (2D) model developed by the US Army Corps of Engineers (USACE) to demonstrate the hydrodynamics of flow in channels. It is one of the widely used softwares to simulate water depth (Sharma et al. 2022), discharge (Kumar et al. 2017), and sediment transport (Patel and Sarkar 2022) in river systems and is available freely in public domain. Two-dimensional HEC-RAS

solves diffusion or St. Venant equation to perform unsteady flow analysis for a river using finite difference method. The diffusion equation works fine for most flood applications; however, the St. Venant equation provides better results for shallow water flow problems. Thus, the St. Venant equation is solved to simulate the annual flow hydrograph at Panposh utilizing monitored flow at upstream station, Jaraikela, on the same reach. Equations 9.15 and 9.16 given below are the St. Venant equations, representing the law of conservation of mass and momentum, respectively:

$$\frac{\partial Q}{\partial X} + \frac{\partial A}{\partial t} = q \tag{9.15}$$

$$\frac{\partial Q}{\partial t} + \frac{\partial \left[\gamma \frac{Q^2}{A} \right]}{\partial X} + gA\frac{\partial H}{\partial X} + \frac{gQ|Q|}{c^2 AR} = 0 \tag{9.16}$$

where q is the lateral inflow, H is the stage, c is the Chezy coefficient, g is the acceleration due to gravity (9.81 m/s^2), γ is the momentum distribution coefficient, X is the longitudinal distance along the flow direction, and t is the elapsed time (s).

9.6.2.2   Geometric Data Input

The river modeling in HEC-RAS requires the river geometry and bathymetry information which is extracted from DEM given as input. The river geometry is drawn using satellite imagery as reference, representing flow line, bank line, and cross-sections demarcating the mainstream and floodplains. The modeling of river network requires the representation of tributary in the geometry from the point where measured data is available up to the point where it joins the main channel. In case of river networks with no observed discharge on the tributaries, the numerical model cannot be utilized to accurately estimate the downstream flow on a river reach.

9.6.2.3   Model Calibration

The riverbed roughness expressed as Manning's coefficient (n) is calibrated through an iterative process by running steady flow analysis multiple times for different n values. The n values for natural rivers vary within the range of 0.03–0.65 (Chow et al. 1988); thus, the n equivalent to 0.03, 0.04, and 0.05 are considered to calibrate the model. The n value for which the accurate stage at the downstream station is obtained is considered further for the unsteady discharge simulation at the downstream site. For the steady analysis, the boundary condition at downstream site is taken as normal depth, which can be assumed equal to river local bed slope (USACE 2016) of 0.003, whereas the upstream boundary condition is provided with a constant flow. The constant input flow equivalent to daily discharge at upstream site is randomly selected from the hydrological data of the years 2015–2016 for any

five days. The steady flow analysis is performed for the five different input flows at upstream to simulate the water level at downstream station. Thus, the water level obtained at the downstream station is matched with the observed water levels for each input discharge with different n. The n value accurately predicting water depth at the downstream station is considered for the unsteady flow analysis using two-dimensional HEC-RAS to simulate downstream discharge on a reach.

9.6.2.4 Unsteady Flow Analysis for Discharge Computation

The unsteady flow analysis requires detailed streamflow and stage time series at the upstream and downstream station, respectively. The computational period is provided from 01 June 2015 to 31 May 2016, with daily discharge as input at Jaraikela. The calibrated n value obtained from the steady flow analysis is used for discharge simulation. The uniform meshing of 50 m × 50 m is created throughout the river for the finite difference method to solve the St. Venant equation. The initial flow in the reach is provided equivalent to the lowest observed upstream discharge and corresponding elevation. It is done in order to avoid the instability in the model due to initial bad condition (dry channel). This implies that a discontinuity may occur while the channel adjusts the zero flow to the first input flow value at the upstream station during the start of the simulation. Thus, an initial ramp-up time period is provided for smooth transitioning of flow from zero to initial input discharge. The initial condition ramp-up hour of 10 h with a ramp-up fraction of 0.4 is provided to run the unsteady two-dimensional model. The computation time step (Δt) of the model is determined using the Courant condition for better accuracy of predictions. The Courant number (C_w) is defined as follows:

$$C_w = \frac{V_w \Delta t}{\Delta x} < 1 \tag{9.17}$$

where V_w is the velocity of flood wave and Δx is the distance between cross-sections. For this condition to satisfy, the time step should be

$$\Delta t = \frac{\Delta x}{V_w} \tag{9.18}$$

The V_w is calculated from average flow velocity by multiplying with a factor. The factor for natural channel equivalent to 1.5 is obtained from HEC-RAS user manual of version 5.0 (USACE 2016). The flood wave average velocity is calculated using the peak flow from the upstream input hydrograph and the corresponding cross-sectional area. Thus, the minimum time step of approximately 6.9 min is obtained, and the model is set to run with the computational time step of 6 min. Finally, using full continuity and momentum equations, the unsteady flow plan is created to route the flow from upstream to downstream station. The inflow from tributaries to downstream station is neglected due to the lack of measured flow on the tributaries.

Further, the discharge simulated after unsteady flow analysis is compared with the available measured discharge at Panposh.

9.6.3 Performance Evaluation Indices

The accuracy of the predictions by the model is determined using statistical metrics such as coefficient of determination (R^2) and Nash-Sutcliffe efficiency (NSE). These statistical metrics were also used in previous studies to check the goodness of fit of the predicted result (y^{pred}) with the observed datasets (y^{obs}). The value of NSE and R^2 being close to 1 indicates the accurate model prediction, whereas close to zero implies highly inaccurate model predictions. Tarpanelli et al. (2013), Singh and Cui (2015), and Vyas et al. (2020) utilized NSE, whereas Sharma et al. (2022) and Singh and Saravanan (2022) used R^2 to assess the predicted streamflow. The NSE and R^2 for the datasets are calculated using following equations:

$$\text{NSE} = 1 - \frac{\sum_{i=1}^{n} \left(y_i^{obs} - y_i^{pred}\right)^2}{\sum_{i=1}^{n} \left(y_i^{obs} - y_{mean}^{obs}\right)^2} \tag{9.19}$$

$$R^2 = \left[\frac{\sum_{i=1}^{n} \left(y_i^{obs} - y_{mean}^{obs}\right)\left(y_i^{pred} - y_{mean}^{pred}\right)}{\sqrt{\sum_{i=1}^{n} \left(y_i^{pred} - y_{mean}^{pred}\right)^2} \sqrt{\sum_{i=1}^{n} \left(y_i^{obs} - y_{mean}^{obs}\right)^2}}\right]^2 \tag{9.20}$$

where y_{mean}^{obs} is the mean observed flow.

9.7 Results

9.7.1 Entropy-Derived Flow Estimation

The flow routing technique derived from entropic velocity distribution presents a quick discharge estimation at an ungauged site using locally measured stage data. However, its application follows a necessary condition that parameter M should remain approximately constant at the extreme stations on a river reach. The calculated parameter M for the two considered stations Jaraikela and Panposh on the tributary of the Brahmani River is obtained as 14.4 and 13.8, respectively. The estimated value at the two considered stations is approximately constant; thus, the entropy-based flow routing is utilized for the reach between these two stations on Brahmani River basin, as shown in Fig. 9.1. The M parameter signifies the

Table 9.1 Geomorphological characteristics of considered reach (Jaraikela–Panposh) in Brahmani River basin

Characteristics	Magnitude
Reach length (L)	30.8 km
Average bed slope (S)	0.003 m/m
Average width (B)	550 m
Monthly mean peak flow	
Jaraikela Panposh	187.2 m^3/s 236.8 m^3/s

geometrical, morphological, and hydraulic characteristics of the river section (Farina et al. 2014; Greco and Moramarco 2016). The constant $\Phi(M)$ shows a certain state of equilibrium at a river site, achieved through the interaction and balance between the hydraulic and geometrical characteristics such as bed slope, width, flow depth, sediment concentration, and bed roughness (Choo et al. 2015). The constant M at upstream and downstream stations on a reach is just a criterion which should be checked before implementing the entropic flow routing on any reach (Moramarco et al. 2005). Once the criterion is met, the magnitude of the M parameter does not influence the output downstream discharge. This was found true for previous studies (Tarpanelli et al. 2013; Barbetta et al. 2012), which used a similar flow routing method without even calculating the M parameter for the sections on a river reach yet obtained downstream discharge with good accuracy.

The considered reach between Jaraikela and Panposh does not have any existing hydraulic structure; however, it receives a significant inflow from tributaries mainly during monsoon season. Hence, the lateral inflow (qL) is considered and calculated using Eq. 9.8, as stated in previous section. The required river characteristics for entropy-based routing are given in Table 9.1. The parameters α and β in Eq. 9.3 are calculated solving Eqs. 9.4 and 9.5 and thus obtained equal to 2.58 and -22.69 m^3/s, respectively. The calculated monthly mean flow at Panposh for the hydrological year of 2015–2016 is given in Fig. 9.3. The calculated statistical indices for Panposh are given in Table 9.2, which shows that the flow is simulated with higher accuracy having NSE and R^2 greater than 0.8.

9.7.2 HEC-RAS Flow Routing

The steady flow analysis is performed to determine the calibrated n for the reach. As mentioned previously, the reach has tributaries, but the inflow from it is not considered in modeling due to unavailable measured discharge. As a result, the simulated water depth at the downstream station using steady flow analysis with varying n may not be showing results with expected high accuracy. However, the results are still significantly accurate with NSE and R^2 being greater than 0.5 for all three values of n (Table 9.2). The obtained water depth at the downstream station, Panposh, is compared with the measured water depth in Fig. 9.2. The results showed

Table 9.2 Statistical indices showing the efficacy of models in streamflow predictions

	Flow routing technique		NSE	R^2
Calibration	HEC-RAS	$n = 0.03$	0.55	0.90
		$n = 0.04$	0.66	0.83
		$n = 0.05$	**0.76**	**0.91**
Validation	**Entropy-based routing**		**0.87**	**0.89**
	Two-dimensional HEC-RAS		0.78	0.77

Fig. 9.2 Comparison of predicted and observed water depth at Panposh
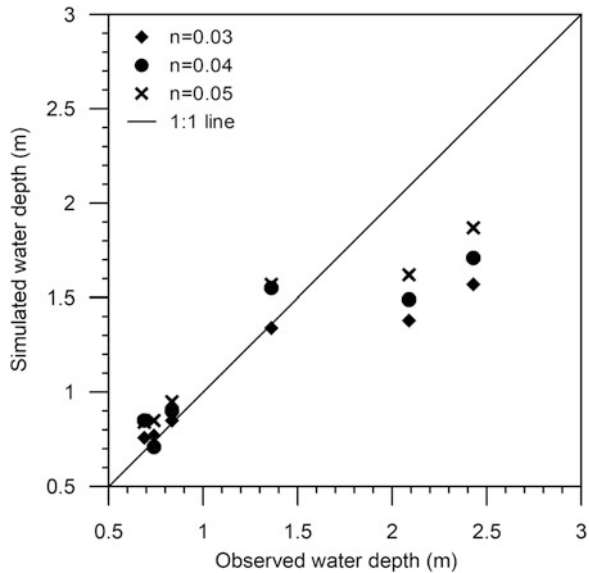
that the predicted water depth at Panposh is closely scattered around the 1:1 line for $n = 0.05$ (Table 9.2), thus offering the best predictions.

The unsteady flow analysis is performed in HEC-RAS for the selected river reach to simulate the monthly mean flow at Panposh taking $n = 0.05$ for the main channel. It is observed that the reach has tributaries but no measured flow; thus, the lateral flow contribution is neglected in unsteady flow simulation. The simulated flow at Panposh for the year of 2015–2016 is shown in Fig. 9.3, indicating that the flow is obtained with significant accuracy having R^2 and NSE >0.7 (Table 9.2).

9.8 Discussion

The two routing techniques employed in this study use a different representation of river reach, with HEC-RAS offering an accurate representation of river geometry extracted from DEM. The entropy-derived routing assumes a river with an average width, neglecting the river meandering and changes in cross-section. The distinct

Fig. 9.3 Predicted and
observed streamflow at the
downstream station Panposh
using two different routing
techniques
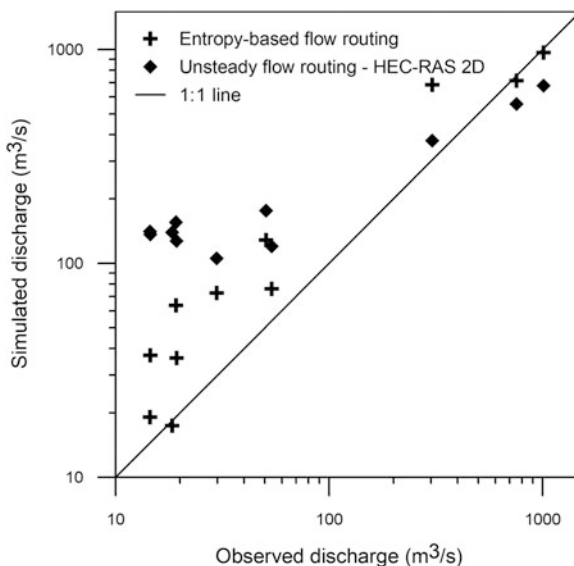
river representation by both models causes a difference in channel storage, which
affects the simulated flow. Despite HEC-RAS being superior to entropy-based
routing regarding channel representation, the latter performed comparatively better
than the former at Panposh (Fig. 9.3). It is because of the consideration of lateral flow
contribution from tributaries in a river network by the entropic routing. However, the
simulated flow by both the techniques agreed well with the observed discharge with
a negligible difference in calculated statistical metrics (Table 9.2) for the selected
reach.

The inherent assumption behind the constant M parameter is that the average
flow velocity at the upstream station is linearly associated with the downstream mean
flow velocity for a given time. The linear relationship is hampered in presence of a
flow controlling structure; thus, the entropic discharge estimation technique cannot
be implemented. However, the HEC-RAS is better for such complex engineered
reaches as it is compatible to define large storage or hydraulic structures. For natural
un-engineered channels, the entropic technique is assumed better than HEC-RAS
because of its simpler structure and disregarding the iterative calibration process to
determine n.

9.9 Recommendations

The results presented in this study and previous studies in literature are limited to
flow simulation at the downstream site on the reach. However, the linear relation
between the discharges at extreme stations on a reach indicates that the entropic

routing can be used to determine the discharge record at the ungauged station upstream of the gauged downstream station having recorded local stage series. Thus, it is recommended to examine the entropy-based method for inverse flow routing on river reaches as a future scope of the study.

9.10 Conclusions

The river restoration, water management, and fluvial hazard studies require the reliable and frequent estimate of the discharge at multiple river sites, which is difficult and cumbersome to measure using traditional techniques. Thus, the entropic discharge estimation technique can be employed at the river sites, which offers a noncontact discharge measurement. Moreover, this method can be utilized for such river networks whose modeling in numerical software is difficult due to unknown measured discharge at tributaries. The utilized new method gives discharge hydrograph at downstream station without the need of local rating curve and discharge contribution by tributaries, yet accounting for the lateral inflow to the downstream station. The method shows that the existence of linear relationship between the discharge at the stations on the extreme ends of a reach is an important characteristic for flood wave propagation. In case of a hydraulic structure, this relation may disrupt, leading to inapplicability of entropic flow routing on such reaches. The entropic flow estimation technique is compared with the numerical model HEC-RAS as well to underline the advantages and disadvantages of both the methods. The entropy-based routing technique has an advantage over numerical model when the ungauged tributaries are present; however, the numerical model may perform better for the engineered reaches having hydraulic structures present.

References

Agarwal A, Maheswaran R, Sehgal V et al (2016) Hydrologic regionalization using wavelet-based multiscale entropy method. J Hydrol 538:22–32. https://doi.org/10.1016/j.jhydrol.2016.03.023

Barbetta S, Franchini M, Melone F, Moramarco T (2012) Enhancement and comprehensive evaluation of the Rating Curve Model for different river sites. J Hydrol 464–465:376–387. https://doi.org/10.1016/j.jhydrol.2012.07.027

Chiu C (1991) Application of entropy concept in open-channel flow study. J Hydraul Eng 117:615–628. https://doi.org/10.1061/(asce)0733-9429(1991)117:5(615)

Choo TH, Hong SH, Yoon HC et al (2015) The estimation of discharge in unsteady flow conditions, showing a characteristic loop form. Environ Earth Sci 73:4451–4460. https://doi.org/10.1007/s12665-014-3731-6

Chow VT, Maidment DR, Mays LW (1988) Applied hydrology. McGraw-Hill, New York

Farina G, Alvisi S, Franchini M, Moramarco T (2014) Three methods for estimating the entropy parameter M based on a decreasing number of velocity measurements in a river cross-section. Entropy 16:2512–2529. https://doi.org/10.3390/e16052512

Greco M, Moramarco T (2016) Influence of bed roughness and cross section geometry on medium and maximum velocity ratio in open-channel flow. J Hydraul Eng:142. https://doi.org/10.1061/(asce)hy.1943-7900.0001064

Kumar N, Lal D, Sherring A, Issac RK (2017) Applicability of HEC-RAS & GFMS tool for 1D water surface elevation/flood modeling of the river: a Case Study of River Yamuna at Allahabad (Sangam), India. Model Earth Syst Environ 3:1463–1475. https://doi.org/10.1007/s40808-017-0390-0

Li F, Zheng Q (2016) Probabilistic modelling of flood events using the entropy copula. Adv Water Resour 97:233–240. https://doi.org/10.1016/j.advwatres.2016.09.016

Moramarco T, Singh VP (2001) Simple method for relating local stage and remote discharge. J Hydrol Eng 6:78–81. https://doi.org/10.1061/(asce)1084-0699(2001)6:1(78)

Moramarco T, Barbetta S, Melone F, Singh VP (2005) Relating local stage and remote discharge with significant lateral inflow. J Hydrol Eng. https://doi.org/10.1061/(asce)1084-0699(2005)10:1(58

Parhi PK, Sankhua RN, Roy GP (2012) Calibration of channel roughness for Mahanadi River, (India) using HEC-RAS Model. J Water Resour Protect 04:847–850. https://doi.org/10.4236/jwarp.2012.410098

Patel P, Sarkar A (2022) Entropy-based flow and sediment routing in data deficit river networks. Water Resour Manag 36:2757–2777. https://doi.org/10.1007/s11269-022-03174-5

Price RK (1973) Flood routing methods for British Rivers. Proc Inst Civ Eng 55:913–930. https://doi.org/10.1680/iicep.1973.4147

Roohi M, Soleymani K, Salimi M, Heidari M (2020) Numerical evaluation of the general flow hydraulics and estimation of the river plain by solving the Saint–Venant equation. Model Earth Syst Environ 6:645–658. https://doi.org/10.1007/s40808-020-00718-9

Saikumar G, Pandey M, Dikshit PKS (2022) Natural river hazards: their impacts and mitigation techniques. In: River dynamics and flood hazards: studies on risk and mitigation. Springer, Singapore, pp 3–16

Sharma A, Baruah A, Mangukiya N et al (2022) Evaluation of Gangetic dolphin habitat suitability under hydroclimatic changes using a coupled hydrological-hydrodynamic approach. Ecol Inform:69. https://doi.org/10.1016/j.ecoinf.2022.101639

Singh VP (2015) Entropy theory in hydraulic engineering: an introduction. In: Entropy theory in hydraulic engineering: an introduction. ASCE Virginia. https://doi.org/10.1061/9780784412725

Singh VP, Cui H (2015) Entropy theory for streamflow forecasting. Environ Process 2:449–460. https://doi.org/10.1007/s40710-015-0080-8

Singh L, Saravanan S (2022) Adaptation of satellite-based precipitation product to study runoff and sediment of Indian River watersheds. Arab J Geosci 15:1–21. https://doi.org/10.1007/s12517-022-09610-5

Tarpanelli A, Barbetta S, Brocca L, Moramarco T (2013) River discharge estimation by using altimetry data and simplified flood routing modeling. Remote Sens. https://doi.org/10.3390/rs5094145

USACE (2016) HEC-RAS river analysis system, Hydraulic reference manual, Version 5.0. US Army Corps of Engineers Hydrologic Engineering Centre, Davis CA

Vyas JK, Perumal M, Moramarco T (2020) Discharge estimation using tsallis and shannon entropy theory in natural channels. Water (Switzerland) 12. https://doi.org/10.3390/w12061786

Xia R (1997) Relation between mean and maximum velocities in a natural river. J Hydraul Eng 123:720–723. https://doi.org/10.1061/(asce)0733-9429(1997)123:8(720)

Chapter 10
Infiltration of Suspended Fine Sediments into Surface Layer of Coarse Sediment-Bedded Channel

Nilav Karna, A. S. Lodhi, Sai Guguloth, and Ankit Chakravarti

Abstract The deposition of fine sediments within the surface layer of bed material has a significant impact on the aquatic life that exists in the bed substrate. The current study conducted laboratory experiments to measure the sediment deposition process using a tilting flume. For the experiments, three different uniformly sized gravels were used. The accumulation of fine sediment particles within the pores of the coarse sediment bed surface moving as bed load was investigated at various equilibrium quantities of suspended load in the flow. The present study utilizes a numerical model to quantify the loss in porosity of surface layer bed material induced by this process. The entrainment of deposited particles by clear water inflow to the channel is also investigated. The findings of this study will be useful in future research on the ecological and environmental consequences of riverine systems.

Keywords Active bed layer · Coarse sediment bed · Suspended load · Porosity

---

N. Karna
AECOM, New Delhi, India

A. S. Lodhi (✉)
Soil and Water Engineering Department, Jawaharlal Nehru Krishi Vishwa Vidhyalaya, Jabalpur, Madhya Pradesh, India

S. Guguloth
Department of Civil Engineering, National Institute of Technology Warangal, Warangal, India
e-mail: gs712006@student.nitw.ac.in

A. Chakravarti
School of Civil and Environmental Engineering, Hachalu Hundessa Technology Campus, Ambo University, Ambo, Ethiopia
e-mail: ankit.chakravarti@ambou.edu.et

10.1 Introduction

Fine sediments such as silt and clay are mostly transported as suspended load by channel flows. Previous studies have strongly suggested the possibility of the exchange of fine sediment particles suspended in the flow and the sediments in the streambed (Gibson et al. 2009; Gupta et al. 2023). This exchange induces fine sediment in suspension to infiltrate into the pores of riverbed material, resulting in the deposition of fine particles inside the pores of the channel bed surface and its substrate (Einstein 1968; Diplas and Parker 1992; Gibson et al. 2007). Entrainment of the embedded fine particles occurs both during their deposition and consequent flow conditions (Cuthbertson and Ervine 2007; Pandey et al. 2018, 2019).

The aforementioned process is harmful to benthic fish, invertebrates, and other aquatic biotas that rely on these habitats as part of their life cycles (Chaudhuri et al. 2022; Lodhi et al. 2021a, b; Pourshahbaz et al. 2022; Rathburn and Wohl 2003). This process is also significant because of its effects on channel stability and downstream sediment deposition (Chapman 1988; Correia et al. 1992; Gibson et al. 2007; Pandey et al. 2022). Several field investigations have been conducted over the last three decades to investigate the mechanism of fine sediment penetration into river channel beds (Beschta and Jackson 1979; Frostick et al. 1984; Lisle 1989; Lodhi et al. 2021a; b). Garcia and Parker (1991) gave a thorough overview of previous research on this issue. Diplas and Parker (1992) studied the fine particle deposition on the surface layer and the release of fines from streambed material using a poorly sorted mixture with a median size (d_{50}) of 2.44 mm and a standard deviation of 2.75, and silica flour as fine sediment with d_{50} values of 0.08 mm and 0.11 mm was utilized. Diplas and Parker (1992) employed two kinds of fines to establish a seal inside the substrate, which was deeper for fines of 0.08 mm and shallower for fines of 0.11 mm. The highest depth measured for the seal was 5* d_{90}. In this case, d_{90} is the size of the sediment so that 90% of the particles are finer than this by weight.

Gibson et al. (2007) reported that the clogging occurred only in the thin upper layer of bed, which was not quantified. Dimensionless shear stress due to flow was observed by Gibson et al. (2007) to control the process and depth of clogging. Diplas (1994) discovered the highest fine deposition in the channel bed's pool and bar tail. Nevertheless, the entrainment of sediment was first noticed at the bar head and then at the pool and at the bar tail. The amount of fines collected was proportionate to the severity of the discharge. According to Diplas (1994), during flood-simulating events, fine particles are deposited within the channel bed and are entrained from a depth of 4*d_{90}. The exchange of stream water with the water in the pores of a subsurface channel bed is also called a hyporheic exchange. Gibson et al. (2007) observed changes in bed material composition caused by the collection of fine sediment particles that were previously circulating as suspended loads in the flow. Huang and García (2000) established an analytical model to investigate the contamination of gravel spawning grounds caused by fine deposition in the flow as suspended load. However, due to the assumptions used, the model does not have a

broad application. Packman and MacKay (2003) experimentally observed the kaolinite clay particle deposition in a coarse sediment bed. They looked into the correlation between stream-subsurface exchange flows, deposition of fines to the hyporheic zone, fine accumulation in the streambed, and bed structure alteration. There was a large deposit of clay inside the bed that was observed. However, blockage of bed material pores was observed to occur by bridging rather than bottom upward. It implies that even small volumes of suspended particles may significantly alter streambed habitat owing to fine sediment deposition in the bed surface layer.

Gibson et al. (2009)investigated the variance in vertical gradient of fine sediment accumulated in a 100-mm-thick gravel bed. The vertical trends of fine deposition inside gravel bed pores were shown to be significantly dependent on the nature of the suspended particles and active bed layer. Following that, Gibson et al. (2007) calculated the sand bridging threshold (described below) in a channel flow delivering fine particles in suspension with gravel as bed material. Cui et al. (2008) developed a statistical model to describe the fine sediment particle's entry into the fixed streambed. The results indicate that contact between the fine and coarse sediment is restricted to the near-bed surface area. The current work quantifies this relationship in the instance of a moveable bed situation. Through flume studies, Cui et al. (2008) found that fine penetration into the substrate of static bed material was independent on fine concentration in the flow. However, the current research analyzes these impacts using movable bed experiments. Furthermore, fine sediments migrated as bed load in Cui et al.'s (2008) trials but as suspended load in the current investigation. Detert and Parker (2010) calculated the amount of fine particles entrained by the flow from pores in a coarse material stratum. They indicated that testing data would be required to completely verify the sediment-cleaner mixture.

The nature of the bed material also has a significant impact on the process of fine sediment penetration from flow into the streambed. However, the effect of heterogeneous bed composition on fine material deposition has not been well addressed (Rathbun and Wohl 2003). The current study was done to solve these information gaps, and the development of a mathematical model would be valuable in estimating how often a coarse sediment bed of a particular thickness must be washed out for fine sediment particle removal and is useful for fish spawning.

Various initiatives are also planned to develop strategies for flushing sediments accumulated in existing storage reservoirs across the globe. The sediments accumulated in streams right beneath the dam are primarily clay, fine silt, and sand particles (Bechteler and Nujic 1998). These sediments must be managed in order to extend the life of the reservoirs. Reservoir flushing is a probable current activity, and it contributes a significant amount of fine suspended silt to river reaches downstream of the dam (Rathbun and Wohl 2003; Saikumar et al. 2022). When fine particles are discharged into the stream downstream of the dam, their contact with the streambed material reduces the porosity of the sediment bed, hampered aquatic life, and has influenced the dynamics of the sediment particles in the bed. Riverbed debris in downstream sections of the dam would be primarily mobile owing to high-intensity flows caused by reservoir flushing. Stream stability, biological, and environmental factors must be addressed before the operation plan for dam removal is determined.

10.2 Experimental Setup

An extensive set of experiments were conducted in the Hydraulics laboratory of the Indian Institute of Technology Roorkee, India, for the study of various processes of the flow of fines and suspended sediment through the coarse gravel bed of a channel. A recirculating (also has the facility of one way flow) tilting flume of 13.0 m length, 0.40 m width, and 0.60 m depth was selected for all experiment purposes.

Naturally available gravel and sand each with a specific gravity of 2.65 were used for the experiments. Three different but uniform size gravels each of median size (d_{50}) 5.2 mm, 2.7 mm, and 1.9 mm were used in individual experiments to form the coarse bed of the channel. The fine sediment used as suspended load was also uniform in size with a median diameter of 0.062 mm. The largest gravel was designated as L, the middle size gravel as M, the smallest gravel as S, and the suspended material as W for the recording purpose. Fine sediment was obtained by passing the raw sediment through a 0.09 mm sieve and retaining it on a 0.045 mm sieve. Curves of the particle size distribution for the sediment used in the experiments are given in Fig. 10.1. Gibson et al. (2009) specified a channel bed thickness of 10 cm. In the current study, a 15-cm-thick sediment bed was placed; this refers to a thickness that is considerably higher than the value of 5*d_{90} of various sediment conditions. A pre-calibrated orifice meter was installed in the return pipe to measure the channel discharge. A pointer gauge was used to measure the flow depths.
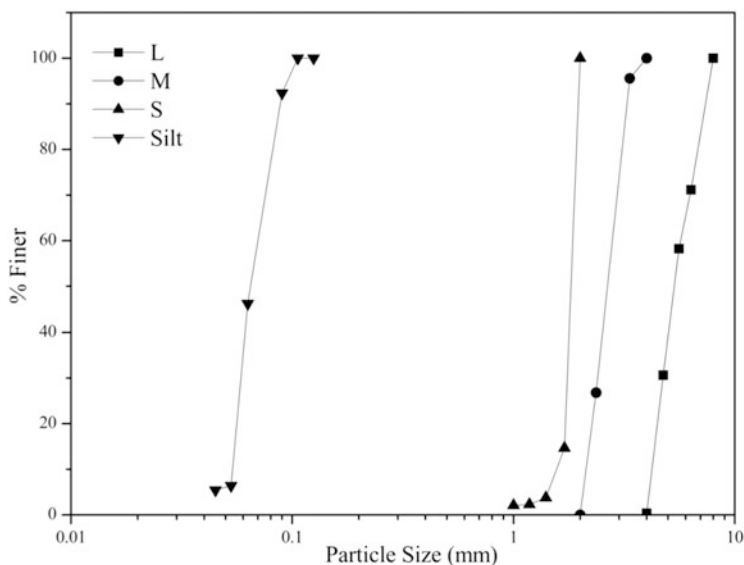
Fig. 10.1 Distribution of channel bed material's grains in size

10.2.1 Procedure

10.2.1.1 Suspended Sediment-Laden Runs

The desired coarse sediment, neatly washed with clear water and free from dust or any other unwanted particles, was placed throughout the channel bed to the height of 150 mm and leveled with the help of a wooden template starting from upstream to downstream. A predefined quantity of fine material was meticulously combined with water in the hopper tank situated at downstream of the canal for a predetermined amount of duration. Sediment was mixed in the downstream tank so that proper mixing of sediment and water could be ensured before the mixture entered the channel entrance through the return pipe. The water mixed with fine sediment was pumped from the collection tank to flume entrance through a return pipe. The desired discharge in the flow was controlled using the discharge valve in the return pipe and orifice meter. The depth of flow in the flume was controlled by operating the pre-calibrated tailgate.

The cross-sectional mean dispersed silt content in the flow was measured using a breadth integrating sampling positioned at the downstream end of the flume (Kothyari and Jain 2010). The experimental runs were conducted continuously for 6–8 h period. During each run, at regular interval, 5–7 samples of water flowing in the channel were collected in a 10 L capacity bucket through the width-integrating sampler. The fine sediment in the collected water was given sufficient time to settle down. The settled fine sediment was carefully removed from this mixture by filtering and oven-drying. The gravel, if any present in the collected sample, was separated from the fine sediment by sieving. The fine sediment thus collected was weighed on an electronic balance having 0.01 g least count, and the average proportion of the fine sediment in the water flow was estimated. An experimental run was supposed to reach equilibrium when the average concentration of suspended fines in the last three consecutive samples did not vary by more than $\pm 5\%$. The average of those last three concentration values was considered as equilibrium average concentration (C). Only experimental runs which attained equilibrium (deciphered after completion of the experiments of a series) were selected for further analysis.

Throughout the experimental run, the gravel bed material moved as bed load and was collected in the trap at the downstream end of the flume. Right from the start of the experiment, the bed load was collected every half an hour interval. The bed load collected was weighed and then fed upstream of the working section of the channel for the next half an hour to maintain the bed load continuity. This process was done for the full duration of the experiment.

The vertical variation of suspended sediment concentration was also measured in a few runs at two sections of the channel; the first section was located 2.5 m downstream of the entrance and the second was10 m downstream of the channel entrance (i.e., end of the flume). The value of suspended sediment concentration at a given point in the flow was measured by pumping the suspended sediment sample at that point using a Tullu pump. By pre-calibrating the pump, it was ensured that the

velocity of a sample of the suspended load at its entrance into the sampling tube was equal to the flow velocity at the point being sampled. The flow depth was traversed for measurement of suspended sediment concentration distribution by withdrawing the samples from different points (levels) in the flow at vertical spacing of 10 mm. The suspended sediment concentration distribution was, however, observed to be in equilibrium at both of these sections. For a specific hydraulic condition (discharge and slope), the successive experimental runs were carried out by increasing the suspended load concentration in the inflow till the surface layer pores got completely filled with fines.

The channel tailgate was completely lifted at the end of the experiment, and input to the flume was halted simultaneously by turning off the re-circulating pump. Because of the depletion scenario that occurred inside the flume, storage of the flume was emptied out easily with a high velocity. As a result, the potential of suspended fine deposition on the channel bed during flow draining was reduced. Volumetric samples of the gravel materials in the bed were taken in order to quantify the deposition of fine sediment within the pores of bed material. Due to their uniform surface, flume walls had little impact on the particles' settling process. A mixture of gravel and fines were picked up from three locations along the bed (3 m, 6 m, and 9 m) for the full depth of bed. The mixture contained within the surface area of 0.2 m × 0.4 m × 0.02 m was sampled. In order to facilitate the sampling process, two thin but hard aluminum sheets with 2 cm marking on the inner sides were fully inserted into the bed 20 cm apart. Proper care was taken to avoid disturbance in the structure within the bed layers. The channel bed was relaid by using parent bed material in its original position in the channel bed after quantifying the fine sediment in the sample. The outflow ($\approx$0.2 l/s) was again allowed to flow through the streambed to saturate the entire bed before the start of the next experimental run. In the subsequent runs of the series, bed samples for determining its composition were taken from the same locations. Though bed forms have an influence on the fine particle vertical fluxes infiltrating into pores of bed material, no significant bed forms were observed in any of the experimental runs of any series.

Following the completion of any particular series on suspended sediment-laden flow, tests for fine particle entrainment within the pores of the active bed layer were carried out. The outflow utilized for this purpose was not the same as the discharge used for the comparable set of sediment-laden runs. For each series, four entrainment runs were performed, each at successively increasing discharge. During these runs, the one-way flow system of the flume was brought into operation using a large overhead tank. At the end of each run, bed material samples were taken for analysis of residual particles deposited in the various levels of the bed. The composition of bed material was used in determining the channel bed porosity.

Once the specific set of tests has been completed, the gravel on the channel bed was completely taken out of the flume. The flume bed and gravel in the channel were washed with clear water to remove the fine particles that are existing in the bed layer. The channel bed was again prepared using the same or other gravels and made ready for the next set of experiments. Seven separate series of tests were carried out, with each series consisting of 10–12 experimental runs. The laboratory experiments done

in the absence of fine silt were denoted as 2LC1, 1MC1, and so on, whereas those in the presence of suspended fines were marked as 1SW4, 2MW7, and so on. Here first numeric stands for a series number; first alphabet is the type of gravel used; C is the clear water, W is for a sediment-laden run, and the last numeric is the run number. 2LC1 represents the first clear water experimental run of the second series on a bed composed of 5.2 mm gravel. Similarly, an experimental run with the name 1SW4 represents fourth sediment-laden run of the first series on a bed composed of 1.9 mm gravel. Whereas to denote entrainment runs, E is used. For example, 2ME2 designates the second entrainment run of second series of runs on a bed composed of 2.7 mm gravel.

10.2.2 Observations on the Infiltration Process of Suspended Sediment into the Pores of the Gravel Bed

10.2.2.1 Visual Analysis

Depending on the regularity and size of the sediment particles, the tiny suspended particles were demonstrated to penetrate into the openings of the gravel bed of the channel in two distinct ways. Channel bed consisting of homogeneous sediment of series $L\left(\frac{d_{15} \text{ of sediment}}{d_{85} \text{ bed material}} = 46\right)$, $M\left(\frac{d_{15} \text{ of sediment}}{d_{85} \text{ bed material}} = 24\right)$, and $S\left(\frac{d_{15} \text{ of sediment}}{d_{85} \text{ bed material}} = 20\right)$, fine sediment infiltrated unrestrained into the pores of the sediment bed, where d_{85} and d_{15} denote 85% and 15% of the sediment material finer the that diameter. As a result, d_{15}/d_{85} ranges from 12 to 14 met the condition specified by Gibson et al. (2009) for the occurrence of unhindered infiltration. A completely unobstructed mode of fine sediment infiltration was observed in all experimental runs with L and M size gravels on the channel bed; however, fine penetration into gravel S beds proceeded until the deposited fines "bridged" the spaces between the sediment particles of the bed, forming a "seal" that limited further fine infiltration to a larger depth. Our findings almost satisfied Gibson et al.'s (2009) requirements, which say that the bridging threshold is determined by the constriction ratio of $\frac{D_{c*}}{D_{85}} = 3$, where D_{c*} was determined by Kenney et al.'s (1985) expression, as the regulating constriction size. Both accumulation (intrusion) and infiltration of accumulated particulate silt take place at the same time during the latter phases of fine sediment ingress, and the asymptotic state is attained in which the quantity of fine sediment contained within the bed material does not fluctuate. In the context of the channel inflow, variations in the concentration of fine silt can lead to disturbances in the equilibrium. This process continues until the pores of the top layer of the active bed layer, which is 20 mm thick, are completely sealed with fines; this process is known as fine sediment limit deposition. If the suspended sediment content in the flow to the channel increases beyond this stage, fine sediment ripples form on the bed surface.

In a natural environment, the gaps between the coarse sediment particles would be partially filled with finer sediments (i.e., silt or sand) before the start of a fine

suspended sediment-laden inflow, thus restricting the entrance of suspended fines into pore spaces of the bed material.

10.2.2.2   Spatial Disparity of Quantity of Fine Sediment in the Active Bed Layer

The amount of fine particles infiltrated into gravel bed was reported as a percentage of the bed material. Figure 10.2 depicts the fluctuation of the quantity of fines infiltrated into the upper strata of the active bed layer with distance along the flow direction for the data series 2MW (see Eq. 10.1 presented below). As previously stated, nomenclatures such as 2MW designate the second series of experimental runs with fine sediment in suspension, while the channel bed was composed of sediment type M. According to Fig. 10.2, the fraction of fine silt inside the upper layers of the active bed layer was slightly more than 25%. However, greater quantities of fines (24%) were found in the top layers of the substrate (active layer) during the 1LW series experimental runs. The trend lines for the fraction of fines in the active bed layer are virtually horizontal, showing no major fluctuation along the flow direction, as shown in Fig. 10.2 and other figures for data from the 2MW and 1LW series (Karna et al. 2015b). It should be noted that the regional change in the composition of the bed layer during fine particle infiltration, as represented in Fig. 10.2, has not previously been examined by many researchers.

The arithmetic average (AEV) of the fine particle proportions in the top layers along the flow direction was calculated. Figure 10.3 depicts the fluctuation of AEV
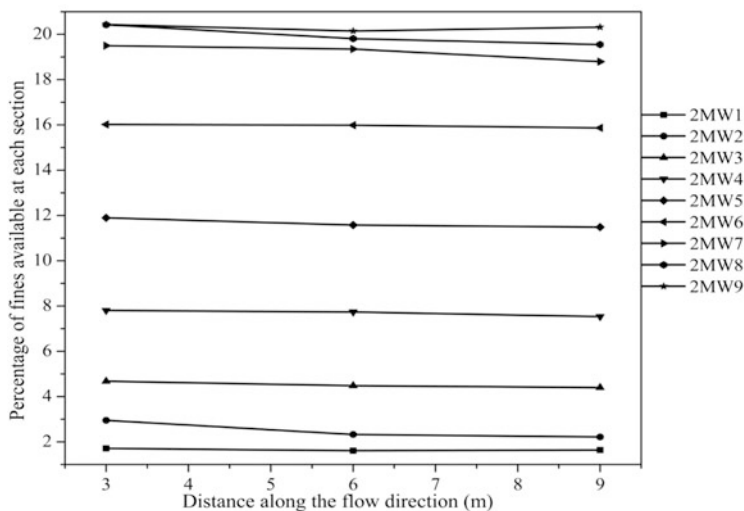
Fig. 10.2 Variation of the proportion of fine particles along the flow direction in active bed layer (series 2MW)
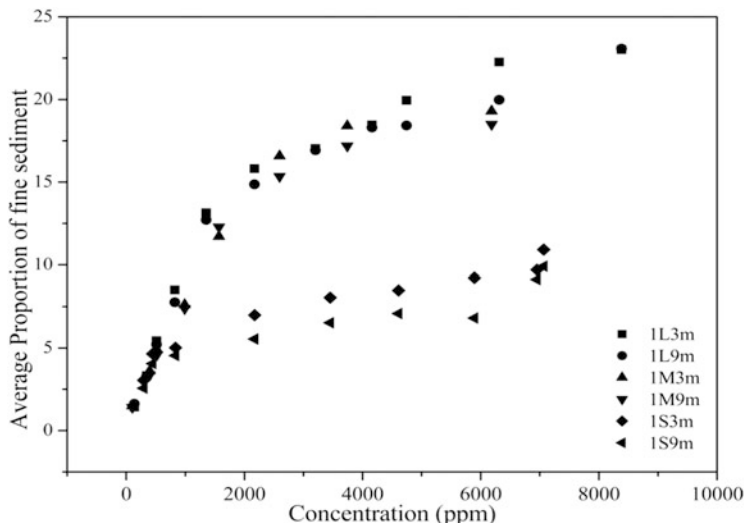
Fig. 10.3 Variation of the proportion of fines in active bed layer with its concentration in flow (series 1LW)

values at 3 m and 9 m with equilibrium concentrations of suspended fine particles for the series 1LW, 1MW, and 1SW data. The statistics from different series showed that the AEV values rise as the concentration of suspended silt in the flow increased. This implies that the suspended load transport rate in the flow controls the fraction of fines in the pores of granular material on the channel bed. Earlier, Diplas (1994) and Einstein and Chien (1953) found similar findings. It is also worth noting that the fraction of particles intruded into the active bed layer is less than the porosity of the bed material, which is 27% (for L series).

10.2.2.3   Entrainment of Suspended Particles from Coarse Sediment Pores in Bed Material

Figure 10.4 illustrates the temporal variation of the average fine particle content in the channel flow collected at the channel outflow during various entrainment runs. The findings of the experiments indicate that the typical concentration of fine sediment in suspension at the canal discharge dropped quickly; it indicates a rapid increasing entrainment rate. The bed looked to be fine-free at the conclusion of the sessions, which could be ascribed to the reduced value of C for the data from run 1SE1.

Despite the fact that the fine particles of sediment content in the flow had become almost insignificant by the end of the entrainment process, assessment of the bed
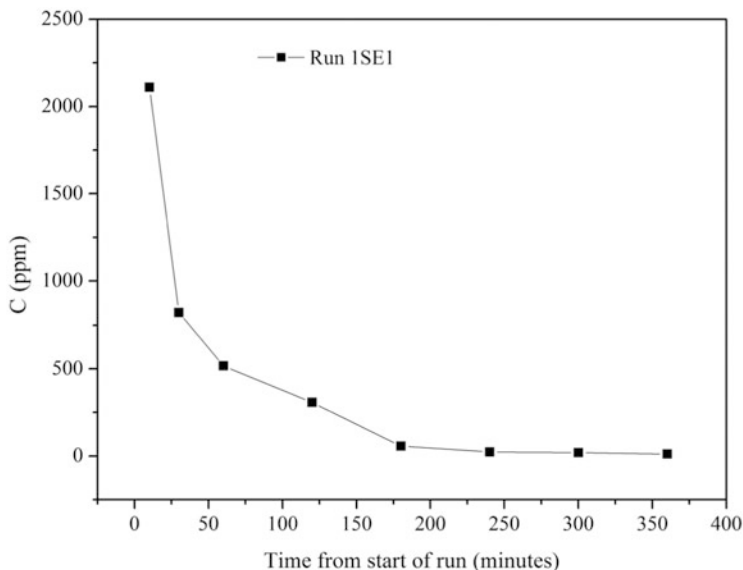
Fig. 10.4 Temporal variations of concentration of fines during sediment entrainment run (1SE1)

samples gathered at the last stage of the entrainment cycle showed that a few of the fine particles retained within the bed material fissures. According to Diplas and Parker's (1992)study, they discovered that fine sediments infiltrated into the pavement layer were only partially cleansed during the stage of the entrainment, whereas fine sediments penetrated into the sub-pavement layer stayed undisturbed (Diplas 1994; Karna et al. 2015a). This is due to the protection provided by small grit particles in the soil layer. Although fine sediment was much smaller than the parent bed material, larger sediment in bed material effectively disguised those silt particles. Greater flow shear force is necessary to clear these tiny particulates from the deeper strata of the bed surface (Einstein and Chien 1953). To increase shear stress on the bed, consecutive entrainment runs at rising high flow at larger velocities were performed. The depth of silt entrainment rises as the flow through the channel increased. However, subsequent increases in flow could not entice the deeper bed layer.

As previously stated, the samples of the bed material encompassing the complete thickness of the bed material were obtained to properly quantify the depth of fine sediment penetration into the substrate. Figure 10.5 depicts the change in fine sediment fractions in various strata of the bed layer for the 1SE1 run. It is obvious from these and figures for data from other similar experimental runs that the flow could not entirely entice the fine silt previously deposited in the channel bed material.
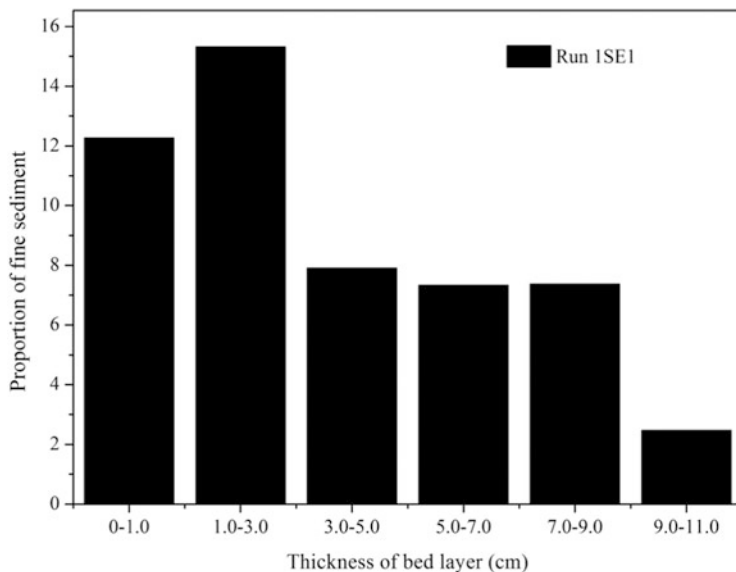
Fig. 10.5   Variation of proportion of fines in different layers after sediment entrainment run (*1SE1*)

10.3   Mathematical Simulation of Entrainment of Fine Particles and Their Deposition from Pores of the Coarse Sediment Bed

The change that occurs in the relative porosity of the active bed layer owing to routing of suspended fine sediment through the bed channel constituted of coarse particles has been analyzed. As a result, the difference in porosity throughout the depth of the bed and its substrate is not replicated. The development of a fine sediment barrier or shield within the sediment bed is also not depicted.

10.3.1   Active Bed Layer

The interchange of fine particles is primarily restricted to the thin top surface of the streambed. The thickness of the particle exchanging layer is determined by the sediment size, bed feature parameters, and flow characteristics. The active bed layer (substrate) or the mixing layer is the thin layer of bed material that actively participates in the exchange of sediment particles. The active layer thickness was assumed to be a function of flow depth developed by Rahuel et al. (1989) and Karim and Holly Jr (1986); however Diplas and Parker (1992) and Correia et al. (1992) connected it to particle size. The first factor seems to be true for a dune bed since dune height is proportional to flow depth, while the later appears to be valid for a

flatbed (Garde and Raju 2000). van Niekerk et al. (1992) investigated the relationship between sediment size and shear stress. Singh et al. (2004) developed a strategy that incorporates the methodologies above as follows:

$$\Delta z = 0.3\, h \left(1 - \frac{\tau_{oc}}{\tau_o} \right) + 2d_{50}$$ (10.1)

where τ_0 denotes the average shear stress caused by the flow, h represents the depth of the flow, and τ_c is the critical shear stress for the commencement of sediment particle motion. When d_{50} equals 1, the equation primarily relies on it, especially in flatbed scenarios like a static gravel bed. Additionally, when there's bed load transport, the equation always gives a value lower than one. This suggests that Eq. 10.1 effectively accounts for the influence of bed load transport on infiltration and the entrainment of fine sediment.

10.3.2 Governing Equations

Khullar (2002) developed the sediment continuity equation, which governs the process of variation in the average porosity caused by the routing of suspended particles through a nonuniform sediment bed. In developing the governing equations, the subsequent assumptions were made: the channel's active bed layer is predominantly involved in the process of fine particles entrainment and deposition, the flow is longitudinal, and simultaneous transport of bed material has no effect on the process of fine sediment infiltration into the pores of the bed material. The governing equation is as follows:

$$\frac{\partial p_g}{\partial t} + a_1 \frac{\partial Q_s}{\partial t} + a_2 \frac{\partial Q_s}{\partial x} = 0$$ (10.2)

where $a_1 = -\,1/(Ub\Delta z)$ and $a_2 = -1/(b\Delta z)$ where p_g denotes the porosity of the sediment bed, b the stream breadth, and Qs the suspended load transport rate consisting mainly of fine silt, U represents mean flow velocity and x the distance, and t denotes the duration of the flow. According to Khullar et al. (2013), Qs is a function of p_g as well as flow and sediment characteristics. The process of fine particle infiltration and intrusion into pores of the sediment bed and the substrate is therefore reproduced by varying Qs with x and t.

In conjunction with the dynamic equation of flow and the continuity equation, it would provide a series of nonlinear hyperbolic formulas that may be used to examine the routing of fine sediments in suspension under uniform/nonuniform flow and steady/unsteady flow circumstances. However, in the current analysis, only stable uniform flows are studied, and the values of flow parameters are therefore known a priori. As a result, just Eq. 10.2 must be solved here. Because an analytical solution

to Eq. 10.2 is not attainable, a numerical solution is developed with the goal of assessing the change in average porosity caused by fine sediment deposition (intrusion) inside the pores of bed material. As a result, porosity is regarded as the unknown variable in Eq. 10.2 and, on the other hand, pertains to the process of routing fine suspended sediments through coarse bed material under both equilibrium and nonequilibrium suspended load transport situations. The fine sediment is expected not to permeate below the active bed layer thickness indicated by Eq. 10.1.

A nondimensional suspended load transport law was developed by Khullar et al. (2013) who used to implement a correction factor for the interference of the mean size of the bed sediment mixture and the effects of sheltering exposure. The approach given by Khullar et al. (2013) is employed herein to determine and is so briefly detailed below for the sake of completeness:

$$\varphi_s = \frac{Q_s}{\gamma_s} \sqrt{\frac{\gamma_f}{\Delta\gamma_s g d^3}} \text{ and } \varphi_{s,i} = \frac{i_s Q_{s,i}}{i_b \gamma_s} \sqrt{\frac{\gamma_f}{\Delta\gamma_s g d_i^3}} \qquad (10.3)$$

where d represents mean size of the sediment particle, $\Delta\gamma_s = \gamma_s - \gamma_w$, with γ_s and γ_w are specific weights of sediment and water, $Q_{s,\ i}$ denotes the fraction wise suspended load transport rate (by weight) per unit width of the channel, and i_b and i_s are the proportions of d_i in bed material and suspended load respectively.

The suspended load transport rate for uniform non-cohesive sediment material is determined using the equation (Eq. 4) proposed by Samaga et al. (1986) and for nonuniform sediment bed conditions (Eq. 10.5) using Khullar (2002):

$$\varphi_s = f\left(\frac{\tau_o}{\Delta\gamma_s d}\right) \qquad (10.4)$$

$$\varphi_{s,i} = f\left(\frac{\tau_o}{\Delta\gamma_s d_i}, \xi_{s,i}\right) \qquad (10.5)$$

In the aforementioned expression, $\xi_{s,\ i}$ denotes the interference factor for sediment mixtures. The nondimensional bed shear stress (τ_{*i}) for the non-cohesive sediment materials is computed by using $\tau_{*i} = (\tau_o/\Delta\gamma_s d_i)$, where d_i represents the size of the non-cohesive sediment.

The steps listed below should be used to compute $Q_{s,\ i}$:

1. Calculate the mean size of the sediment particles d_a on the bed layer.
2. Calculate the critical shear stress (τ_c) using shield criteria for the incipient motion of the sediment particles.
3. Determine the shear stress ($\tau_0 = \gamma_e R_e S_f$) formed due to flow, where R_e denotes mean hydraulic radius and S_f represents friction slope.
4. Determine the τ_0/τ_c and d_i/d_0 values.

5. Calculate the $\xi_{s,i}(\tau_o/\tau_{oc})^{0.62}$ using below mentioned equation:

$$\log\left(\xi_{s,i}[\tau_o/\tau_{oc}]^{0.62}\right) = 0.703 + 0.54\log(d_i/d_a) + 0.03(\log[d_i/d_a])^2$$
$$+ 0.0308(\log[d_i/d_a])^3 \tag{10.6}$$

6. Calculate the value of $\xi_{s,i}(\tau_o/\Delta\gamma_s d_i)$ and also compute $\varphi_{s,\ i}$ using the equation proposed by Khullar et al. (2013):

$$\varphi_{s,i} = 28\left(\xi_{s,i}(\tau_o/\Delta\gamma_s d_i)\right)^6 \tag{10.7}$$

7. Compute the suspended load transport Q_s from the below expression:

$$Q_s = \sum i_s \, Q_{s,i} = \varphi_{s,i} \, i_b \, \gamma_s \, \sqrt{(\Delta\gamma_s/\gamma_f)gd_i^3} \tag{10.8}$$

10.3.3   Numerical Scheme

The MacCormack's (1969) finite difference numerical approach with two layers of predictor corrector steps is used to solve Eq. 10.2 using proper boundary and beginning conditions. The MacCormack's (1969) approach is straightforward and easy to apply. This system can readily accommodate general roughness and sediment discharge equations. Bhallamudi and Chaudhry (1991) present a full overview of the scheme.

10.3.3.1   Stability of Numerical Model

The current numerical strategy must meet the stability criterion defined as

$$S \leq \left(\frac{q}{h} + \sqrt{g\,h}\right)\frac{\Delta t}{\Delta x} \tag{10.9}$$

where S represents the bed evolution disruption propagation speed, g is gravity acceleration, q is discharge intensity, x is the computational spatial step size, and h is flow depth. The value of S is determined by Eq. 10.2 and is as follows: $S = \frac{U}{1 - \frac{Ub\Delta z}{\partial Q_s/\partial p_p}}$.

10.3.4   Model Application

The suggested numerical model is utilized to compute the change in average porosity of the bed layer, hence replicating the process of fine deposition and infiltration within coarse material gaps. The model findings are validated using the current study's experimental data.

10.3.4.1   Accumulation of Fine Particles Inside the Pores of the Sediment Bed

The model was originally used to assess changes in the active bed layer's average porosity. The following beginning and boundary conditions are utilized for this purpose:

Initial Conditions

In this instance, the original state was $p_a(m, 1) = 0.383)$ with $m = 1, \ldots, n$, where n is the entire amount of geographic grid processing units and

$$Q_s(l, 1) = 0.0 \tag{10.10}$$

Boundary Conditions

In order to create the temporary situation, fine sediment particles were eventually added to the flow at the upstream side of the flume for model implementation. The scenario is as follows $Q_{s1}^{k+1} = Q_{sN}^k + \Delta Q_s$, where ΔQ_s is the rate of increase of the inbound suspended load of a fine particle at the most upstream computational node, N is the downstream boundary computational node, 1 is the upstream boundary computational node, and k is the computational time level. This model application was difficult to apply on this criterion. It needed to be transformed into an equation so that the value could be found at the first processing point. By applying the backward difference to the geographic elements of the sediment continuity equation, Eq. 10.11 is produced for node 1:

$$p_{g1}^{k+1} = p_{g1}^k + a_2 \frac{\Delta t}{\Delta x} \left[(Q_{sN}^k + \Delta Q_s) - Q_{s1}^k \right] \tag{10.11}$$

because the components on the right-hand side of the preceding expression are known for time level k.

Following the procedures outlined above, a FORTRAN computer program was created. This software was originally evaluated for correctness using a small amount of sample data. The computational grid length that was employed was 1.0 m. The computing time step was chosen based on the Courant condition of stability, which is given by Eq. 10.9. It should be noted that using an S value equal to or less than unity produced no different results. The model might be used to calculate the average porosity of the sediment bed during transient phases and under equilibrium conditions of suspended load transit.

10.3.5 Contrast of Predicted and Measured Estimates of Equilibrium Porosity

In Fig. 10.6, the proposed numerical model is accurately replicating the actual values of asymptotic porosity, with the calculated values having a maximum deviation of 10% from the observed values. This suggests that the model is able to effectively quantify fluctuations in porosity values averaged throughout the active bed layer thickness. It is noteworthy that no model calibration was performed in order to produce the results shown in Fig. 10.6. The porosity of the bed material may vary throughout the depth below the streambed due to the variable rate of fine intrusion into them and "sealing" or "bridging" created during the fine deposition process in the pores. However, such differences are difficult to represent using the one-dimensional numerical model described here. The suggested numerical model
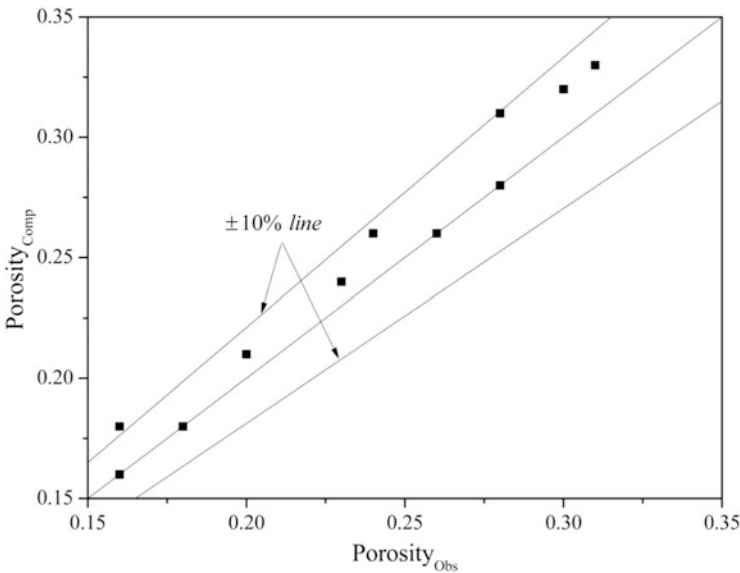
Fig. 10.6 Contrast of measured and calculated coarse soil porosity values

is used to estimate the average porosity values for the lengths of the experimental runs. The measured (residual) equilibrium porosity value is defined as the initial porosity of bed material minus the observed percent of fine silt inside the active bed layer at the conclusion of the respective experimental run. The results of the model are seen in Fig. 10.6, where it is demonstrated that the model is able to accurately capture the observed values of equilibrium porosity, with the calculated values.

10.3.6   Calculating Porosity of the Bed Layer for Transient Stage

Figure 10.7 depicts the time-dependent variation in estimated porosity at two distinct locations along the streambed during the 2MW5 trial session. The gap between the sections chosen for study is relatively short; the approximated values of equilibrium porosity at these sections do not differ considerably. During the transitory stage, only a slight variation is observed in the estimated values of porosity at the specified site, with porosity at the upstream portion being lower than that at the downstream section. This suggests that the rate of fine particles entry into the gaps of coarse particle is greater at upstream than downstream. Fine sediment rate in the flow would decline along the flow path due to particles penetrating the crevices of coarse sediment material. The sedimentation rate is delayed, and the excess porosity is higher when the lowest proportion of particulate material is suspended in the channel influx. Figure 10.7 demonstrates that with constant dispersed sediment quantities in
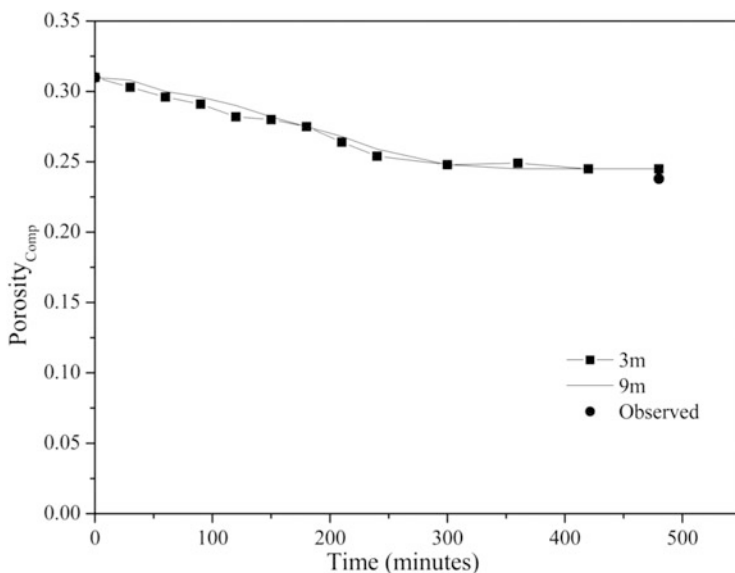
Fig. 10.7   Variation of porosity during transient stage (Run 2MW5)

approach flow, the state of equilibrium deposition proceeds along the flow path and is thus reached first at upstream sites. However, as shown by the testing findings in Fig. 10.2, the typical permeability of the substrate material should be nearly constant over the stream length during the balance period. Figure 10.7 also depicts the observed equilibrium porosity at the ninth section of the cycle. This shows that the model projected a reasonably accurate result, albeit one that was marginally greater than what was witnessed, as shown in Fig. 10.6.

10.4   Conclusions

Experiments have been conducted to investigate the changes in the composition of bed material caused by fine infiltration. It was discovered that the proportion of fines in the top layer of the active bed layer expands as the optimal content of embedded fines in the flow gets higher. Additionally, stratification in bed material is caused by fine particle infiltration into the gaps between the coarse sediment particles. However, these results are confined to studies on fine sediment with a consistent dimension of 0.062 mm. To further explore this process, a one-dimensional numerical model has been developed. This model uses a finite difference numerical approach proposed by MacCormack (1969) to solve the sediment continuity equation, with proper initial and boundary conditions. The model calculates the variation in the mean porosity of the active bed layer as a function of distance and time. Despite its potential, the model does have some limitations which should be taken into consideration.

References

Bechteler W, Nujic M (1998) Predicting reservoir sedimentation with 2D model Floodsim 国际泥沙研究: 英文版 1: 72–80
Beschta RL, Jackson WL (1979) The intrusion of fine sediments into a stable gravel bed. J Fish Board Can 36(2):204–210
Bhallamudi SM, Chaudhry MH (1991) Numerical modeling of aggradation and degradation in alluvial channels. J Hydraul Eng 117(9):1145–1164
Chapman DW (1988) Critical review of variables used to define effects of fines in redds of large salmonids. Trans Am Fish Soc 117(1):1–21
Chaudhuri S, Pandey M, Debnath K, Oliveto G (2022) A comparative study on equilibrium scour volume around circular cylinders in clay–sand mixed cohesive beds, at near-threshold velocity of sand–an experimental approach. Water Supply 22(8):6777–6791
Correia LP, Krishnappan BG, Graf WH (1992) Fully coupled unsteady mobile boundary flow model. J Hydraul Eng 118(3):476–494
Cui Y, Wooster JK, Baker PF, Dusterhoff SR, Sklar LS, Dietrich WE (2008) Theory of fine sediment infiltration into immobile gravel bed. J Hydraul Eng 134(10):1421–1429
Cuthbertson AJ, Ervine DA (2007) Experimental study of fine sand particle settling in turbulent open channel flows over rough porous beds. J Hydraul Eng 133(8):905–916

Detert M, Parker G (2010) Estimation of the washout depth of fine sediments from a granular bed. J Hydraul Eng 136(10):790–793

Diplas P (1994) Modelling of fine and coarse sediment interaction over alternate bars. J Hydrol 159(1–4):335–351

Diplas P, Parker G (1992) Deposition and removal of fines in gravel-bed streams. Dynamics of gravel-bed rivers. p 313–329

Einstein HA (1968) Deposition of suspended particles in a gravel bed. J Hydraul Div 94(5): 1197–1206

Einstein HA, Chien N (1953) Can the rate of wash load be predicted from the bed-load function? *Eos*. Trans Am Geophys Union 34(6):876–882

Frostick LE, Lucas PM, Reid I (1984) The infiltration of fine matrices into coarse-grained alluvial sediments and its implications for stratigraphical interpretation. J Geol Soc 141(6):955–965

Garcia M, Parker G (1991) Entrainment of bed sediment into suspension. J Hydraul Eng 117(4): 414–435

Garde RJ, Raju KGR (2000) Mechanics of sediment transportation and alluvial stream problems. Taylor & Francis, Milton Park

Gibson S, Abraham D, Heath R, Schoellhamer D, Petticrew EL, Krein A, Walling DE, Wörman A, Packman AI, Marklund L, Harvey JW, Stone SH, Wooster JK, Dusterhoff SR, Cui Y, Sklar LS, Dietrich WE, Malko M, Singh AK, Garde RJ (2007) Bed load transport of sediment mixtures. J Hydraul Eng 235(2):1003–1017

Gibson S, Abraham D, Heath R, Schoellhamer D (2009) Vertical gradational variability of fines deposited in a gravel framework. Sedimentology 56(3):661–676

Gupta LK, Pandey M, Raj PA, Shukla AK (2023) Fine sediment intrusion and its consequences for river ecosystems: a review. J Hazard Toxic Radioact Waste. 27(1):4022036

Huang X, García MH (2000) Pollution of gravel spawning grounds by deposition of suspended sediment. J Environ Eng 126(10):963–967

Karim MF, Holly FM Jr (1986) Armoring and sorting simulation in alluvial rivers. J Hydraul Eng 112(8):705–715

Karna N, Hari Prasad KS, Giri S, Lodhi AS (2015a) Effect of fine sediments on river hydraulics–a research review. ISH J Hydraul Eng 21(2):142–150

Karna N, Hari Prasad KS, Giri S, Lodhi AS (2015b) Intrusion of fine sediments into river bed and its effect on river environment–a research review. ISH J Hydraul Eng 21(2):142–150

Kenney TC, Chahal R, Chiu E, Ofoegbu GI, Omange GN, Ume CA (1985) Controlling constriction sizes of granular filters. Can Geotech J 22(1):32–43

Khullar NK (2002) Effect of wash load on transport of uniform and nonuniform sediments. Ph. D. Thesis, Indian Institute of Technology Roorkee. 33(2): 341–347

Khullar NK, Kothyari UC, Raju KGR (2013) Study of deposition of fine sediment within the pores of a coarse sediment bed stream. Int J Sediment Res 28(2):210–219

Kothyari UC, Jain RK (2010) Experimental and numerical investigations on degradation of channel bed of cohesive sediment mixtures. Water Resour Res 46(12)

Lisle TE (1989) Sediment transport and resulting deposition in spawning gravels, north coastal California. Water Resour Res 25(6):1303–1319

Lodhi AS, Jain RK, Sharma PK (2021a) Flow behavior around spur dyke founded in cohesive sediment mixtures. Proc Inst Civil Eng-Water Manag 174(1):1–14. https://doi.org/10.1063/1. 4964659

Lodhi AS, Jain RK, Sharma PK, Karna N (2021b) Influence of cohesion on scour at wake of partially submerged spur dikes in cohesive sediment mixtures. ISH J Hydraul Eng 27(2): 123–134

MacCormack RW (1969) The effect of viscosity in hypervelocity impact cratering, Paper 69–354. Am Inst. Aeronaut. and Astronaut., Cincinnati, Ohio

Packman AI, MacKay JS (2003) Interplay of stream-subsurface exchange, clay particle deposition, and streambed evolution. Water Resour Res 39(4)

Pandey M, Ahmad Z, Sharma PK (2018) Scour around impermeable spur dikes: a review. ISH J Hydraul Eng. 24(1):25–44. https://doi.org/10.1080/09715010.2017.1342571. Taylor and Francis Ltd.

Pandey M, Lam WH, Cui Y, Khan MA, Singh UK, Ahmad Z (2019) Scour around spur dike in sand–gravel mixture bed. Water 11(7):1417

Pandey M, Jamei M, Ahmadianfar I, Karbasi M, Lodhi AS, Chu X (2022) Assessment of scouring around spur dike in cohesive sediment mixtures: a comparative study on three rigorous machine learning models. J Hydrol 606:127330

Pourshahbaz H, Abbasi S, Pandey M, Pu JH, Taghvaei P, Tofangdar N (2022) Morphology and hydrodynamics numerical simulation around groynes. ISH J Hydraul Eng 28(1):53–61. https://doi.org/10.1080/09715010.2020.1830000

Rahuel JL, Holly FM, Chollet JP, Belleudy PJ, Yang G (1989) Modeling of riverbed evolution for bedload sediment mixtures. J Hydraul Eng 115(11):1521–1542

Rathburn S, Wohl E (2003) Predicting fine sediment dynamics along a pool-riffle mountain channel. Geomorphology 55(1–4):111–124

Saikumar G, Pandey M, Dikshit PKS (2022) Natural river hazards: their impacts and mitigation techniques. In: River dynamics and flood hazards: studies on risk and mitigation. Springer, Cham, pp 3–16

Samaga BR, Raju KGR, Garde RJ (1986) Bed load transport of sediment mixtures. J Hydraul Eng 112(11):1003–1017

Singh AK, Kothyari UC, Ranga Raju KG (2004) Rapidly varying transient flows in alluvial rivers. J Hydraul Res 42(5):473–486

van Niekerk A, Vogel KR, Slingerland RL, Bridge JS (1992) Routing of heterogeneous sediments over movable bed: model development. J Hydraul Eng 118(2):246–262

Chapter 11
River Water Flow Prediction Rate Based on Machine Learning Algorithms: A Case Study of Dez River, Iran

Mohammad Reza Goodarzi, Amir Reza R. Niknam, Ali Barzkar, and Davood Shishebori

Abstract Forecasting the river flow, especially during floods, will allow the officials to minimize the damages caused. Various methods have been used to predict the flow of river water. Many studies have been conducted in this field using artificial intelligence and machine learning methods, which show that these methods can also be very effective. In this study, river water flow prediction has been made by two GEP (gene expression programming) and random forest (RF) machine learning algorithms. The daily data of the last ten years of Dez River discharge in Iran were used, 75% of which were considered for training and 25% for testing. Finally, the predictability of each of the mentioned models has been investigated to select the best model. The results of the two models were compared using five statistical indices R, MAE, RMSE, Nash-Sutcliffe (NSE), and the agreement index (Ia). The accuracy values of R, MAE, RMSE, NSE, and Ia were 0.995, 17.337, 60.635, 0.954, and 0.986 for the GEP model and 0.926, 26.483, 26.483, 301.3, 26.483, 26.483, 17.337, and 0.986 for the random forest model. In some of the statistical indicators, a decrease in the values in the testing stage compared to the training stage can be observed. This may be due to significant fluctuations on some days of the year, such as a sharp increase in rainfall causing a substantial increase in the river flow rate. However, the GEP model has demonstrated good results in both the training and testing stages, indicating that it can effectively estimate flow rate values. Also, in addition to reasonable accuracy, this model has a higher speed than the random forest model for river flow estimation.

M. R. Goodarzi (✉)
Department of Civil Engineering, Yazd University, Yazd, Iran
e-mail: Goodarzimr@yazd.ac.ir

A. R. R. Niknam · A. Barzkar
Department of Civil Engineering, Water Resources Management Engineering, Yazd University, Yazd, Iran

D. Shishebori
Department of Industrial Engineering, Yazd University, Yazd, Iran
e-mail: Shishebori@yazd.ac.ir

Keywords Streamflow · Machine learning · GEP · Random Forest · Dez River

11.1 Introduction

River flow prediction is a crucial issue in hydrology, which is essential in managing, operating, and planning water resources. Due to Iran's climatic changes and weather conditions, rains occur every year, which have caused large floods and subsequent losses. Also, since flood control is based on predicting the incoming flow when a flood occurs, there is very little time to implement crisis management methods and reduce the damages caused by the flood. Therefore, runoff and subsequent floods are expected in the last few years by using the predicted data of atmospheric models. In this way, one of the strategies for managing the crises caused by floods is the quick and accurate prediction of runoff to reduce risk. Over the years, various statistical, hydraulic, and hydrological models have been developed, each with strengths and weaknesses (Chen et al. 2019; Desta et al. 2019; Gupta et al. 2020). The diverse factors affecting hydrological processes make applying all of them in the designed models challenging. Moreover, the presence of uncertainties and nonlinear relationships between variables has complicated the problem. Physical and conceptual hydrological models have been less emphasized due to the need for abundant information about various parameters and time-consuming calibration (Kong et al. 2019; Mohammady et al. 2018; Ravindranath et al. 2019). The importance of using new modeling methods in engineering is so much that it has been able to show its footprint in various fields of this field in recent years. These methods are common to the majority of engineering sciences. In water science and engineering, artificial intelligence models for modeling and predicting various hydrological parameters have attracted the attention of experts and researchers in this field. Among these, the flow rate can be mentioned as one of the most sensitive parameters. The importance of planning and managing water resources and the ever-increasing population growth and limited surface water resources in some countries have made a more accurate prediction of river flow using new modeling tools and methods an unavoidable necessity (Seyedian et al. 2014). Recently, machine learning algorithms have found many applications in various fields, including environmental and water resource management (Barzkar et al. 2021). Therefore, machine learning-based approaches such as artificial neural networks (ANNs), support vector machines (SVMs), and Bayesian networks (BNs) have been used as powerful tools to predict hydrological parameters (Pitta et al. 2016; Salas 1993; Wagena et al. 2020). With the advancement in machine learning algorithms in recent decades, numerous studies have investigated their potential in predicting hydrological parameters (Yaseen et al. 2015).

Several studies have reported that artificial neural networks and the M5 algorithm have been used to model the relationship between water level and flow rate. Bhattacharya and Solomatine (2005) reported higher accuracy in predicting hydrological parameters using these methods than conventional approaches. In a study by

Lin et al. (2006) on China's Lancang River, support vector machines, artificial neural networks, and ARMA modeling were used to predict long-term river flow. The results indicated that the support vector machine method outperformed other models in terms of accuracy. To predict river flow, Noori et al. (2011) utilized the support vector machine model and three input variable extraction methods, including forward selection, gamma test, and principal component analysis. The results suggested that the support vector machine model's accuracy improved with these preprocessing models. Kisi et al. (2013) conducted a study in Turkey to predict the daily flow of the Krokavak basin using gene expression programming (GEP), artificial neural network (ANN), and adaptive neuro-fuzzy inference system (ANFIS) models. The GEP model demonstrated superior performance compared to the other two methods. Chu et al. (2016) used support vector machine, autoregressive integrated moving average (ARIMA), and radial basis function neural network (RBFNN) models to predict the monthly and long-term flow of the upper Yellow River basin. A comparison of the results revealed that the support vector machine model had the best performance and the lowest simulation error for long-term and medium-term streamflows compared to the other two models. Atieh et al. (2017) conducted a study to predict the duration curves of ungauged basins using artificial neural network (ANN) and GEP models. The results indicated that GEP and ANN models were more sensitive to the drainage area, followed by the mean annual precipitation, the entropy disturbance index, and the shape. Goyal et al. (2017) investigated four models based on support vector regression to predict flow rates from two nearby karst springs in Greece. The model's performance was evaluated using the root mean square error and correlation coefficient. Finally, they concluded that the models used in their study performed better than the generalized regression neural network, radial basis function neural network, and ARIMA models. Das and Nanduri (2018) investigated statistical downscaling based on classification and regression to forecast monthly monsoon flow over a basin in India. The output of GCM models and the representative concentration path (RCP) scenario was used. Support vector machine (SVM) and relation vector machine (RVM) models were also used for downscaling. The results showed that with the increase in temperature, the sensitivity of the upper areas of the monsoon currents increased and showed a decreasing trend and medium and low flow in all scenarios showed an increase in the future period.

Adnan et al. (2021) conducted a study to estimate the monthly flow of KALAN and CHAKDARA stations located in the SWAT river basin, utilizing the Group Method of Data Handling-Neural Network (GMDH-NN), Dynamic Evolving Neural-Fuzzy Inference System (DENFIS), and Multi-Adaptive Regression Splines (MARS) models. The results indicated that DENFIS and MARS models had the best performances for the two mentioned stations, respectively. Yeditha et al. (2022) evaluated the development of rainfall-runoff models and one-day-ahead streamflow forecasting using two satellite precipitation datasets, GPM-IMERG and CHIRPS. Using daily rainfall data from 2000 to 2018, artificial neural networks, extreme learning machines (ELM), and long short-term memory (LSTM) models were developed for rainfall-runoff. Nash-Sutcliffe efficiency coefficient, correlation coefficient, and root mean square error were used to evaluate accuracy. The results showed that both satellite precipitation products could be used well with LSTM

and ELM models for rainfall-runoff modeling and streamflow forecasting. In another study, Barzkar et al. (2022) investigated drought events in different climatic conditions and formulated the standard precipitation-evapotranspiration index (SPEI) values for various climates using GEP, model tree (MT), and multiple adaptive regression spline (MARS) algorithms. Among these models, the M5MT algorithm provided the most accurate prediction of SPEI in all climates. Wei et al. (2022) employed the random forest algorithm to predict extreme seasonal rainfall during summer on the Yangtze River. The prediction models based on 14 atmospheric and oceanic indices were trained and tested using samples from 1951 to 2019. The results showed that the RF3 model, based on three indices, performed optimally in distinguishing between severe and non-extreme events. The decision trees in the RF3 model revealed the primary decision path leading to a severe rainfall event in the area.

This study aims to assess the daily flow of the Dez River, a significant tributary of the Karun River that has substantial agricultural land. Two robust machine learning algorithms, gene expression programming (GEP) and random forest (RF), were utilized to achieve this. The modeling was based on daily flow data obtained from the Tel Zang station. Eventually, the findings of the two models were compared using statistical indices to determine the superior model for predicting river flow.

11.2 Materials and Methodology

The Dez watershed stretches between 48°10′ to 50°21′ east longitude and 31°34′ to 34°07′ north latitude, covering an area of approximately 21,720 km². The elevation of the watershed ranges from 190 m to 4124 m, with an average elevation of 1676 m. This research focuses on a portion of the Dez watershed situated in Khuzestan province. The Telezang hydrometric station is positioned approximately 20 km upstream of the Dez dam and has been monitoring river flow since 1955. The Khuzestan Water and Power Organization provided the data and information necessary to construct and validate the models used in this study. The flow rates from various points along the river were collected in the field. This research utilizes the river's flow rate data recorded at the Telezang station from 2011 to 2022. The station's geographic coordinates are 48°46′48″ east longitude and 49°32′ north latitude. Additionally, Fig. 11.1 displays the study area's location. Also, the flowchart of the steps of this study can be seen in Fig. 11.2.

11.3 Gene Expression Programming

Ferreira introduced the gene expression programming (GEP) algorithm, based on the theory of Darwin, and evolved genetic programming, for the first time (Ferreira 2001). GEP is a type of data mining network that presents the relationship between
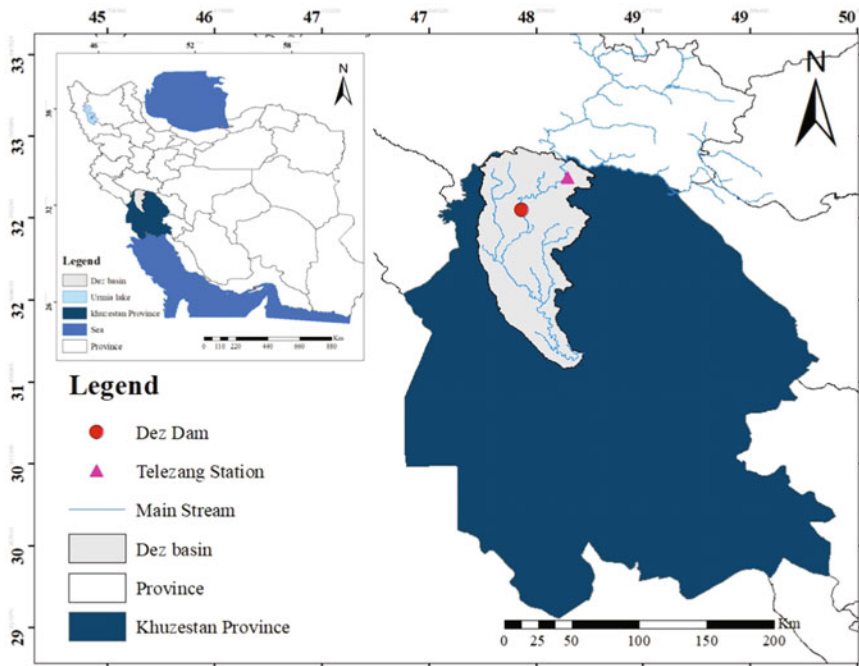
Fig. 11.1 Study area

parameters as a mathematical equation and does not have a black box structure. Moreover, this model is adaptable to different conditions, making it advantageous over neural networks (Danandeh Mehr et al. 2018). The algorithm provides an automatic programming technique for solving problems as a computer program and can optimize the structure of the model and its components. GEP uses a tree structure, whereas the genetic algorithm is based on the binary system, which is the fundamental structural difference between these two models (De Castro et al. 2005). The step-by-step execution process of GEP is as follows:

1. Generating an initial population of formulas by combining functions (mathematical operators used in the formulas) and terminals (problem variables and constant numbers)
2. Evaluating each individual in the population using fitness functions
3. Generating a new population using the equations

Figure 11.3 illustrates the GEP model calculation process. The process commences by selecting control parameters, including the function set, terminal set, fitness function, control parameters, and termination criteria. Before executing the evolutionary algorithm, the fitness function is determined, which leads to the creation of an initial population's random string, commonly referred to as a chromosome in genetic programming terminology. These strings are translated into a tree, and the results are compared to the fitness score of each chromosome. If the

Fig. 11.2 Flowchart of study steps
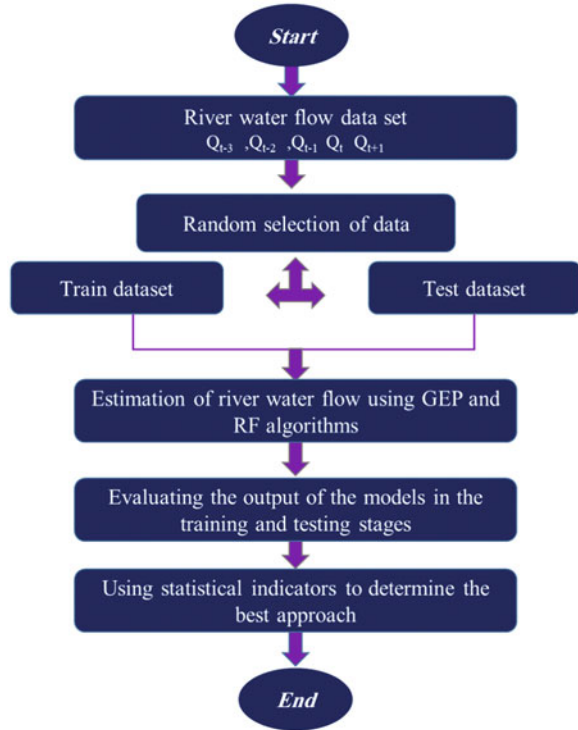
Fig. 11.3 Schematic diagram of the GEP algorithm (Iqbal et al. 2020)
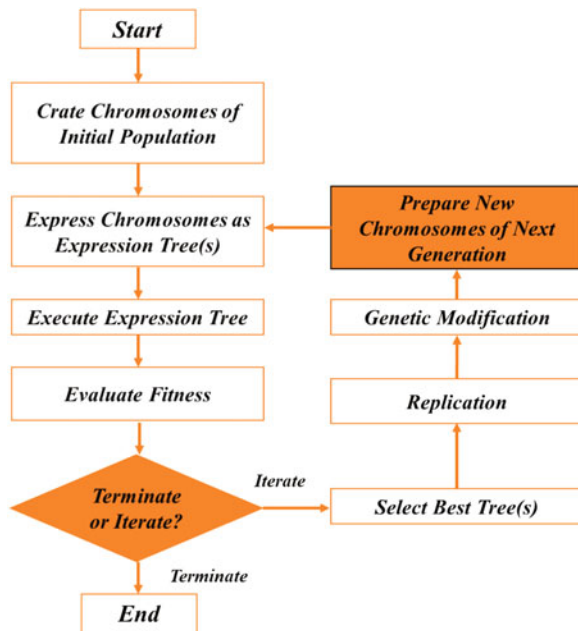
Table 11.1 Table of GEP model settings

Description of parameters	Setting of parameters
Function set	+ ▢ − ▢ × ▢ ÷
Linking function	Addition
Mutation rate	0.00138
Inversion rate	0.00546
One-point and two-point recombination rates	0.00277
Gene recombination	0.00277
Fitness function	RMSE
Head size	8
Number of gene	3
Number of chromosomes	30

fitness criterion is not met, the roulette wheel selection method is used to select a few chromosomes, which then undergo mutation to generate new generations. Alternatively, the chromosomes also become optimized if the variables are optimized with the fitness function (Iqbal et al. 2020).

In this particular study, the GEP model was employed to determine river flow by utilizing the GenXproTools5 software. Typically, the data was segregated such that 75% of it was reserved for the training phase while the remaining 25% was allotted for the testing phase. The model's implementation began by defining a set of initial parameters as per the user's requirements and ended based on the user-defined stop criteria. Thus, the selection of accurate and appropriate input parameters plays a crucial role in the precision and efficacy of the proposed model for river flow estimation. Consequently, the optimal combination of input parameters was obtained through trial and error. Table 11.1 illustrates the recommended settings for GEP modeling that are utilized for predicting river flow.

11.4 Random Forest (RF)

Tree-based methods are nonparametric statistical methods for classification and regression analysis using recurrent algorithms (Breiman 1984). Random forest (RF) is a tree-based method introduced by Breiman (2001) for addressing classification and regression issues. Some advantages of this model include estimating missing data, classifying significant variables, handling thousands of variables without eliminating them, running on large datasets, and being one of the most precise algorithms. The model's key feature is its superior performance in measuring variable importance for determining its role in predicting the response. This model creates a forest that contains multiple decision trees, which split the dataset into different parts. A decision tree is created for each segment, and the majority voting prediction of these trees is used for overall prediction, culminating in the final prediction (Cutler et al. 2007) (Fig. 11.4).
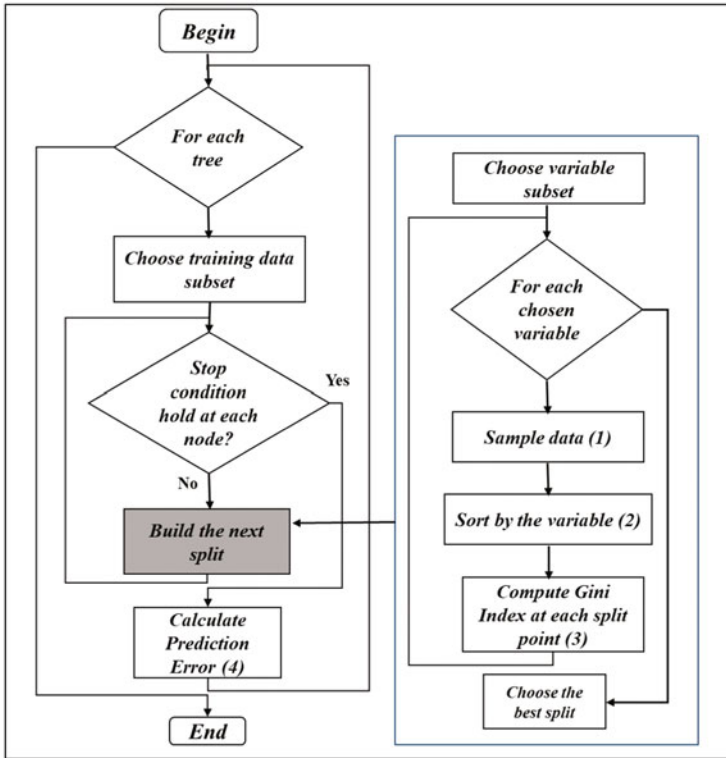
Fig. 11.4 Schematic steps of the RF model (Kunhare et al. 2020)

11.4.1 Performance Evaluation of Models Using Statistical Indicators

A wide range of indicators is available to assess the efficacy of machine learning models. In this study, several indicators, such as the coefficient of correlation (R), mean absolute error (MAE), root mean square error (RMSE), Nash-Sutcliffe coefficient (NSE), and agreement index (I_a), were employed to evaluate various approaches and ascertain the optimal approach for estimating river flow rate. The calculation method for each of these indicators is as follows:

$$R = \frac{\sum\limits_{1}^{n} \left(Q_O - \overline{Q}_O\right)\left(Q_F - \overline{Q}_F\right)}{\sqrt{\sum\limits_{1}^{n} \left(Q_O - \overline{Q}_O\right)^2 \cdot \sum\limits_{1}^{n} \left(Q_F - \overline{Q}_F\right)^2}} \tag{11.1}$$

$$\text{MAE} = \frac{\sum_{1}^{n} |Q_F - Q_O|}{N} \tag{11.2}$$

$$\text{RMSE} = \sqrt{\frac{\sum_{1}^{n} (Q_F - Q_O)^2}{N}} \tag{11.3}$$

$$\text{NSE} = 1 - \frac{\sum_{1}^{n} (Q_F - Q_O)^2}{\sum_{1}^{n} (Q_O - \overline{Q}_O)^2} \tag{11.4}$$

$$I_a = 1 - \frac{\sum_{1}^{n} (Q_F - Q_O)^2}{\sum_{1}^{n} \left(|Q_F - \overline{Q}_O| + |Q_O - \overline{Q}_O| \right)^2} \tag{11.5}$$

N represents the number of samples, Q_O is the observed actual values, Q_F is the calculated values, $\overline{Q}_O$ is the mean of observed actual values, and $\overline{Q}_F$ is the mean of calculated values. R is a dimensionless measure that ranges from -1 to 1 and is used to determine the strength and type of the relationship between quantitative variables. MAE is expressed in cubic meters per second and indicates the difference between two values. It has a value between $(+\infty, 0)$. RMSE, on the other hand, also has a value between $(+\infty, 0)$ and measures the difference between the predicted value and the recorded values. The closer the values are to zero, the higher the model's accuracy. NSE is a dimensionless and normalized parameter that assigns values between $(1, -\infty)$ and is sensitive to limit values. Lastly, I_a is a dimensionless parameter that has values between $(1, 0)$ and indicates the degree of freedom of the error, similar to NSE.

11.5 Results and Discussion

11.5.1 The Performance of the GEP

The GEP machine learning model has successfully demonstrated its performance in estimating hydrological parameters in recent years. The training and testing dataset was randomly selected from the initial river flow rate dataset, and since there was no missing or missing data, no preprocessing was needed. The dataset was relatively small and was based on the time series of the river flow rate for five consecutive days. Therefore, one day was considered the basic day (QT). According to this, three days ago (QT-3), two days ago (QT-2), one day before (QT-1), and the base day (Q_t) are selected as input variables, and one day after base day (QT +1) is selected as the output variable. Based on statistical indicators, the results of the GEP model in the

Table 11.2 Statistical indicators of the GEP model

Approach			Indices				
			R	MAE (m³/s)	RMSE(m³/s)	NSE	I_a
GEP	Q	Train	0.987	12.190	25.800	0.971	0.993
		Test	0.995	17.337	60.635	0.954	0.986
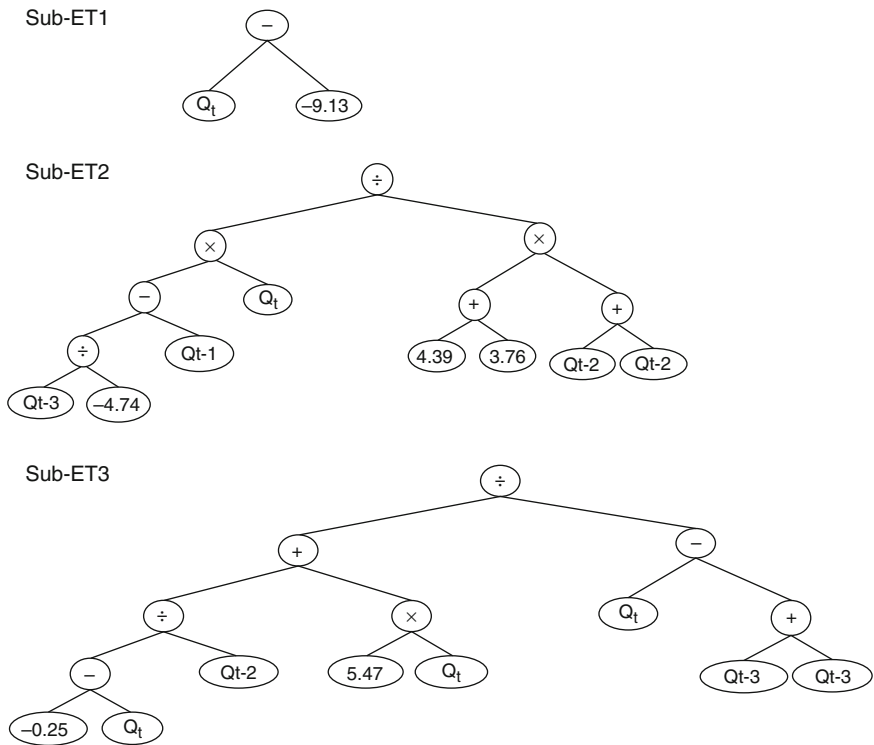
Fig. 11.5 The GEP model presents the tree structure for estimating the flow of the Dez River

training and testing stages are shown in Table 11.2. In some of the statistical indicators, a decrease in the values in the testing stage compared to the training stage can be observed. This may be due to significant fluctuations on some days of the year, such as a sharp increase in rainfall causing a substantial increase in the river flow rate. However, the GEP model has demonstrated good results in both the training and testing stages, indicating that it can effectively estimate flow rate values.

The GEP model's desired patterns are presented in a tree structure for the best model in Fig. 11.5, and the best-extracted equation for the amount of river flow from 5000 generations and three genes is presented in Eq. 11.6. Since GEP uses mathematical functions and operators, the empirical relations of this algorithm also include linear and nonlinear combinations of mathematical functions and operators. For example, empirical GEP relationships may involve linear combinations of
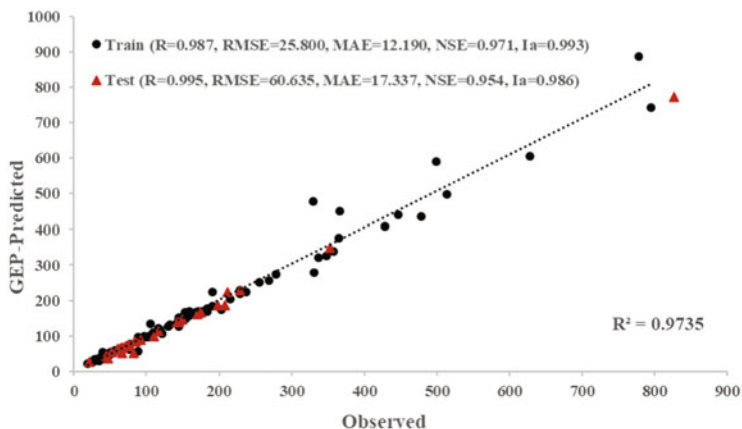
Fig. 11.6 Comparison of predicted values of the GEP model with observed values

mathematical functions such as addition, multiplication, and subtraction. Also, these relations may include nonlinear combinations of mathematical functions such as logarithmic and power functions (Ferreira 2006).

The evaluation of the model and its display between the observed and anticipated values are shown in Fig. 11.6. The GEP-based machine learning algorithm is a practical approach to evaluating the river flow. Model evaluation in machine learning is usually performed by regression analysis. Regression analysis indicates that the accuracy of each model is higher when it is closer to one (Farooq et al. 2020). Figure 11.6 shows that the regression line is about 1, and the model's accuracy for this set is 0.97. Based on this, it is evident that the estimated values align with the observed values in most cases, indicating the acceptable accuracy of this model in estimating daily values of the Dez River flow:

$$
\text{GEP} - Q = (Q_t - (-9 \cdot 13)) + \left(\frac{\left(\left(\left(\frac{Q_{t-3}}{-4 \cdot 74} \right) - Q_{t-1} \right) \times Q_t \right)}{((4 \cdot 39 + 3 \cdot 76) \times (Q_{t-2} + Q_{t-2}))} \right)
$$

$$
+ \left(\frac{\left(\frac{-0 \cdot 25 - Q_t}{Q_{t-2}} \right) + (5 \cdot 47 \times Q_t)}{Q_t - (Q_{t-3} + Q_{t-3})} \right) \tag{11.6}
$$

11.5.2 The Performance of the Random Forest (RF) Machine Learning Model

This study collected daily streamflow data from the Dez Basin Telezang station for 11 years (2011–2022). As mentioned, a random forest (RF) machine learning model
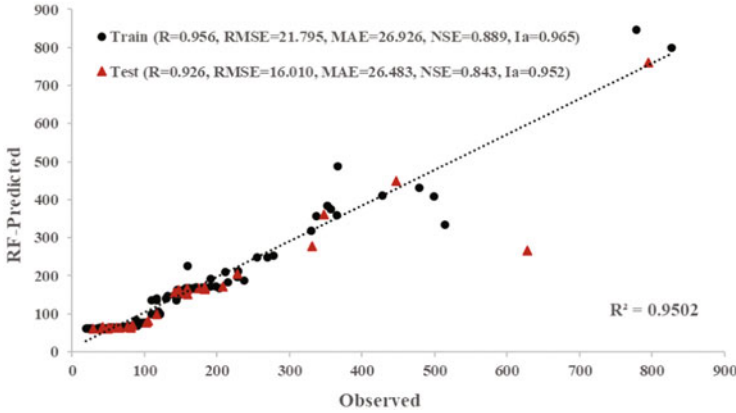
Fig. 11.7 Scatter plot of observed and simulated daily discharge values at the Telezang station using the random forest model

Table 11.3 Performance of random forest model on training and testing data

Approach			Indices				
			R	MAE (m^3/s)	RMSE (m^3/s)	NSE	I_a
RF	Q	Train	0.956	26.926	21.795	0.889	0.965
		Test	0.926	26.483	16.010	0.843	0.952

based on data mining methods was employed to estimate daily streamflow. For this purpose, 75% of the data was allocated for the training phase, and the remaining 25% was for the validation phase. The streamflow training set from three days before the baseline to the baseline day was selected as the predictor variable, and the streamflow training set from the day after the baseline was used as the target variable. Furthermore, Fig. 11.7 shows the scatter plot of observed values against simulated daily streamflow values by the random forest model for the validation data. The plot indicates that the majority of the simulated and observed values, except for a few points on the diagonal, are close to each other, demonstrating a good agreement between the observed and simulated values.

Additionally, Table 11.3 presents the values of five evaluation criteria used to quantify the performance of the RF model. The results in this table suggest that the model can estimate daily streamflow accurately at the Dez Telezang station, and the RF model performed well in streamflow estimation. This section discusses the validation process of the RF model to demonstrate its ability to estimate river flow.

Table 11.3 presents the correlation (R) for the training and test data, which are 0.956 and 0.926, respectively. The coefficient of determination (I_a) for the training and test data is determined to be 0.965 and 0.952, respectively, in this model. The Nash-Sutcliffe efficiency index is also obtained for the training and test data as 0.889 and 0.843, respectively. Furthermore, the RMSE and MAE indices are 21.795 and 26.926 for the training phase and 16.010 and 26.483 for the testing phase. Therefore,

since the test data is employed to evaluate model performance in research analysis, it can be concluded that the statistical indices, including I_a, R, NSE, RMSE, and MAE, obtained for precipitation and runoff in the test data are acceptable, and the performance of the random forest model at this station is appropriate.

11.5.3 Comparison of Prediction Performance Between GEP and RF

In order to ensure a suitable comparison of the two models' performance, a quantitative analysis was conducted in this section. Five evaluation metrics were used to compare them; the results are presented in Tables 11.2 and 11.3. The coefficient of determination for both models was almost the same during the testing phase, with a slight relative superiority of the GEP model. On the other hand, the GEP model's relative superiority was observed based on the I_a index despite a small difference in its value. The lower the value of the root mean square error (RMSE) metric, the better the model's performance. The RF model produced slightly better results in the testing phase, but in the validation phase, the RF model was considered the superior model due to its significant difference. This was possible because the random forest model was created from data subsets, and the final output is based on ranking or majority average, which mitigates the problem of overfitting. The model's performance is considered better when the Nash-Sutcliffe efficiency (NSE) metric values are closer to one. Therefore, it was observed that the GEP model performed better than the RF model.

Finally, based on the obtained results, it was determined that the GEP model performed better in most statistical indicators and was chosen as the superior model for river flow estimation. Moreover, Fig. 11.8 illustrates the observed and predicted daily river flow values. As depicted in the Fig. 11.8, there is no clear trend in the flow during the study period. In some years, the flow trend is increasing, while in some years, it is decreasing, and the river flow time series is fluctuating.

Hydrological modeling is one of the most important processes in water resource applications (Goodarzi et al. 2022). Policy-makers and decision-makers of each region can use the prediction of hydrological processes, such as river flow intensity that can lead to floods, as a possible measure to reduce flood damage. By being aware of the possible occurrence of floods, policy-makers and managers can make informed decisions, such as designing an off-stream reservoir to store excess water during high flows and help protect the area more against floods (Chebii et al. 2022).

One of the significant limitations of random forest is that too many trees can make the algorithm too slow for real-time predictions. These algorithms are fast to train, but predictions are slow after training. A more accurate forecast requires more trees, which results in a slower model. The speed of the random forest algorithm is fast enough in many real-world projects, but of course, there may be situations where project execution time is more critical and other methods are preferred.
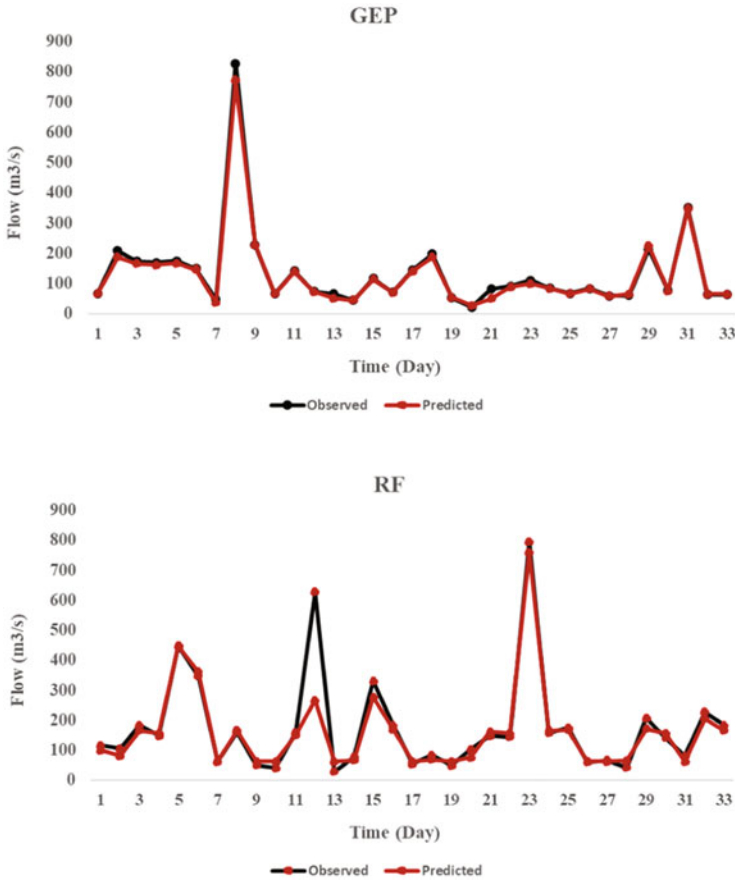
Fig. 11.8 Observed and computed daily river flow values

Also, in this study, due to the lack of sufficient data for the years before 2011, it was not possible to examine and predict changes with more data. It is suggested that in future studies, in addition to using data with a longer time frame, the performance of different machine learning techniques such as artificial neural network (ANN), support vector machine learning (SVM), adaptive neuro-fuzzy interface (ANFIS) and multivariate adaptive regression spline, and (MARS) should be investigated.

11.6 Conclusion

Accurately estimating river flow is crucial for hydrological cycle studies, water resource management, and allocation. In this study, GEP and RF modeling approaches were utilized to estimate the daily flow of the Dez River. The objective

was to demonstrate the differences between the two models and evaluate their ability to model daily river flow. The river streamflow daily data was collected from the Dez Basin Telezang station for 11 years (2011–2022). The data from five consecutive days were also used for the data used in the models. According to this, three days ago (QT-3), two days ago (QT-2), one day before (QT-1), and the base day (Q_t) are selected as input variables, and one day after base day (QT +1) is selected as the output variable. The findings indicated that the GEP model performed better than the RF model. The predicted value chart shows that the model accurately estimated the periodicity and cycles in the prediction data, demonstrating its excellent flow estimation capabilities. Also, several indices such as correlation coefficient (*R*), mean absolute error (MAE), root mean square error (RMSE), Nash-Sutcliffe coefficient (NSE), and agreement index (I_a) were used to check the accuracy of the models. The accuracy values of R, MAE, RMSE, NSE, and I_a were 0.995, 17.337, 60.635, 0.954, and 0.986 for the GEP model and 0.926, 26.483, 26.483, 301.3, 26.483, 26.483, 17.337, and 0.986 for the Random forest model. According to the results during training and testing, the GEP model showed more precision and can be a suitable alternative to conceptual models in situations with limited data and information. Furthermore, the GEP modeling approach was faster than the RF model and delivered results in less time.

Refrences

Adnan RM, Liang Z, Parmar KS, Soni K, Kisi O (2021) Modeling monthly streamflow in mountainous basin by MARS, GMDH-NN and DENFIS using hydroclimatic data. Neural Comput & Applic 33(7):2853–2871. https://doi.org/10.1007/s00521-020-05164-3

Atieh M, Taylor G, Sattar MAA, Gharabaghi B (2017) Prediction of flow duration curves for ungauged basins. J Hydrol 545:383–394. https://doi.org/10.1016/j.jhydrol.2016.12.048

Barzkar A, Shahabi S, Niazmradi S, Madadi MR (2021) A comparative study of remote sensing and gene expression programming for estimation of evapotranspiration in four distinctive climates. Stoch Env Res Risk A 35(7):1437–1452. https://doi.org/10.1007/s00477-020-01956-0

Barzkar A, Najafzadeh M, Homaei F (2022) Evaluation of drought events in various climatic conditions using data-driven models and a reliability-based probabilistic model. Nat Hazards 110(3):1931–1952. https://doi.org/10.1007/s11069-021-05019-7

Bhattacharya B, Solomatine DP (2005) Neural networks and M5 model trees in modelling water level–discharge relationship. Neurocomputing 63:381–396. https://doi.org/10.1016/j.neucom. 2004.04.016

Breiman L (1984) Classification and regression trees CA, Wadsworth International Groups

Breiman L (2001) Random forests. Mach Learn 45(1):5–32. https://doi.org/10.1023/ A:1010933404324

Chebii SJ, Mukolwe MM, Ong'or BI (2022) River flow modelling for flood prediction using artificial neural network in ungauged Perkerra catchment, Baringo County, Kenya. Water Pract Technol 17(4):914–929. https://doi.org/10.2166/wpt.2022.034

Chen Y, Marek GW, Marek TH, Moorhead JE, Heflin KR, Brauer DK, Gowda PH, Srinivasan R (2019) Simulating the impacts of climate change on hydrology and crop production in the Northern High Plains of Texas using an improved SWAT model. Agric Water Manag 221:13–24. https://doi.org/10.1016/j.agwat.2019.04.021

Chu, H., Wei, J., Li, T., & Jia, K. (2016). Application of support vector regression for mid- and long-term runoff forecasting in "Yellow River Headwater" Region. Procedia Eng, 154, 1251–-–1257. doi: doi: https://doi.org/10.1016/j.proeng.2016.07.452

Cutler DR, Edwards TC Jr, Beard KH, Cutler A, Hess KT, Gibson J, Lawler JJ (2007) Random forests for classification in ecology. Ecology 88(11):2783–2792. https://doi.org/10.1890/07-0539.1

Danandeh Mehr A, Nourani V, Kahya E, Hrnjica B, Sattar AMA, Yaseen ZM (2018) Genetic programming in water resources engineering: a state-of-the-art review. J Hydrol 566:643–667. https://doi.org/10.1016/j.jhydrol.2018.09.043

Das J, Nanduri UV (2018) Assessment and evaluation of potential climate change impact on monsoon flows using machine learning technique over Wainganga River basin, India. Hydrol Sci J 63(7):1020–1046. https://doi.org/10.1080/02626667.2018.1469757

De Castro L, Von Zuben F, Ferreira C (2005) Gene Expression Programming and the Evolution of Computer Programs. In (p 82–103). https://doi.org/10.4018/978-1-59140-312-8.ch005

Desta Y, Goitom H, Aregay G (2019) Investigation of runoff response to land use/land cover change on the case of Aynalem catchment, North of Ethiopia. J Afr Earth Sci 153:130–143. https://doi.org/10.1016/j.jafrearsci.2019.02.025

Farooq F, Nasir Amin M, Khan K, Rehan Sadiq M, Faisal Javed M, Aslam F, Alyousef R (2020) A comparative study of random forest and genetic engineering programming for the prediction of compressive strength of high strength concrete (HSC). Appl Sci 10(20):7330. https://www.mdpi.com/2076-3417/10/20/7330

Ferreira C (2001) "Gene expression programming: a new adaptive algorithm for solving problems". arXiv preprint cs/0102027

Ferreira C (2006) Gene Expression Programming: Mathematical Modeling by an Artificial Intelligence

Goodarzi MR, Niknam ARR, Sabaghzadeh M (2022) Chapter 11 - Rainfall-runoff modeling using GIS: a case study of Gorganrood Watershed, Iran. In: Zakwan M, Wahid A, Niazkar M, Chatterjee U (eds) Current directions in water scarcity research, vol 7. Elsevier, Amsterdam, pp 165–181

Goyal MK, Sharma A, Katsifarakis KL (2017) Prediction of flow rate of karstic springs using support vector machines. Hydrol Sci J 62(13):2175–2186. https://doi.org/10.1080/02626667.2017.1371847

Gupta A, Himanshu S, Gupta S, Singh R (2020) Evaluation of the SWAT Model for Analysing the Water Balance Components for the Upper Sabarmati Basin. In (p 141–151). https://doi.org/10.1007/978-981-13-8181-2_11

Iqbal MF, Liu Q-F, Azim I, Zhu X, Yang J, Javed MF, Rauf M (2020) Prediction of mechanical properties of green concrete incorporating waste foundry sand based on gene expression programming. J Hazard Mater 384:121322. https://doi.org/10.1016/j.jhazmat.2019.121322

Kisi O, Shiri J, Tombul M (2013) Modeling rainfall-runoff process using soft computing techniques. Comput Geosci 51:108–117. https://doi.org/10.1016/j.cageo.2012.07.001

Kong X, Zeng X, Chen C, Fan Y, Huang G, Li Y, Wang C (2019) Development of a maximum entropy-archimedean copula-based Bayesian network method for streamflow frequency analysis—a case study of the Kaidu River Basin, China. Water 11(1):42. https://www.mdpi.com/2073-4441/11/1/42

Kunhare N, Tiwari R, Dhar J (2020) Particle swarm optimization and feature selection for intrusion detection system. Sādhanā 45(1):109. https://doi.org/10.1007/s12046-020-1308-5

Lin J-Y, Cheng C-T, Chau K-W (2006) Using support vector machines for long-term discharge prediction. Hydrol Sci J 51(4):599–612. https://doi.org/10.1623/hysj.51.4.599

Mohammady M, Moradi HR, Zeinivand H, Temme AJAM, Yazdani MR, Pourghasemi HR (2018) Modeling and assessing the effects of land use changes on runoff generation with the CLUE-s and WetSpa models. Theor Appl Climatol 133(1):459–471. https://doi.org/10.1007/s00704-017-2190-x

Noori R, Karbassi AR, Moghaddamnia A, Han D, Zokaei-Ashtiani MH, Farokhnia A, Gousheh MG (2011) Assessment of input variables determination on the SVM model performance using PCA, Gamma test, and forward selection techniques for monthly stream flow prediction. J Hydrol 401(3):177–189. https://doi.org/10.1016/j.jhydrol.2011.02.021

Pitta S, Venkata Praveen T, Prasad M (2016) Artificial neural network model for rainfall-runoff - a case study. Int J Hybrid Inform Technol. 9:263–272. https://doi.org/10.14257/ijhit.2016.9.3.24

Ravindranath A, Devineni N, Lall U, Cook ER, Pederson G, Martin J, Woodhouse C (2019) Streamflow reconstruction in the upper Missouri River Basin using a Novel Bayesian Network Model. Water Resour Res 55(9):7694–7716. https://doi.org/10.1029/2019WR024901

Salas JD (1993) Analysis and modeling of hydrological time series. In: Maidment DR (ed) Handbook of hydrology. McGraw-Hill, New York, pp 19.1–19.72

Seyedian SM, Soleimani M, Kashani M (2014) Predicting streamflow using data-driven model and time series. Iran J Ecohydrol. 1(3):167–179. https://doi.org/10.22059/ije.2014.54219

Wagena MB, Goering D, Collick AS, Bock E, Fuka DR, Buda A, Easton ZM (2020) Comparison of short-term streamflow forecasting using stochastic time series, neural networks, process-based, and Bayesian models. Environ Model Softw 126:104669. https://doi.org/10.1016/j.envsoft.2020.104669

Wei W, Yan Z, Tong X, Han Z, Ma M, Yu S, Xia J (2022) Seasonal prediction of summer extreme precipitation over the Yangtze River based on random forest. Weather Clim Extrem 37:100477. https://doi.org/10.1016/j.wace.2022.100477

Yaseen ZM, El-shafie A, Jaafar O, Afan HA, Sayl KN (2015) Artificial intelligence based models for stream-flow forecasting: 2000–2015. J Hydrol. 530:829–844. https://doi.org/10.1016/j.jhydrol.2015.10.038

Yeditha PK, Rathinasamy M, Neelamsetty SS, Bhattacharya B, Agarwal A (2022) Investigation of satellite precipitation product driven rainfall-runoff model using deep learning approaches in two different catchments of India. J Hydroinf 24(1):16–37. https://doi.org/10.2166/hydro.2021.067

Chapter 12
A Case Study in Evaluating Spatiotemporal Variations in Drought and Its Risk Assessment over Telangana Using Satellite Data

Palagiri Hussain and Manali Pal

Abstract As the critical parameter of the agricultural drought process, soil moisture (SM) has the potential to monitor agricultural drought, which can provide practical support for water management. Microwave remote sensing showed capability in estimating geophysical properties like SM and paved the way for a continuous agricultural drought monitoring. ECMWF's (European Centre for Medium-Range Weather Forecasts) fifth-generation reanalysis data, ERA 5 Land data, provides monthly averaged global SM at 9 km resolution. Telangana state in India is a severely drought-prone state heavily impacted by significant water stress and water shortages due to frequent droughts. This increases the need for accurate agricultural drought characterisation in the state. Keeping in mind the necessity of drought monitoring system for Telangana and availability of large-scale ERA 5 SM data in this study, an agricultural drought index, namely, Standardised Soil Moisture Index (SSMI), is derived, to characterise agricultural drought in Telangana, India. SSMI's performance is then evaluated by comparing it with meteorological-based indices Standardised Precipitation Index (SPI) and Standardised Precipitation Evapotranspiration Index (SPEI). The comparison of SSMI with SPI and SPEI shows that SSMI when compared with SPI and SPEI performs well in monitoring agricultural drought and can be used to develop effective drought warning and risk management. Furthermore, to study the drought characteristics, run theory is applied for SSMI, SPI and SPEI to identify grid-wise drought events and characterise them in terms of duration (D_d), frequency (D_f), intensity (D_i) and peak (D_p). The results show that SPEI characterises an overall increase in D_d, D_f, D_s and D_p during 2003–2022 compared with SSMI and SPI, mainly due to the increasing potential evapotranspiration. In contrast, SSMI and SPI do not reveal this phenomenon since SM and rainfall alone does not exhibit a significant change overall. For all the four drought characteristics, D_d, D_f, D_s and D_p, SPEI showed greater drought risk whereas SPI/SSMI indicated lower drought risk in terms of D_d and D_s. This also

P. Hussain · M. Pal (✉)
Department of Civil Engineering, NIT, Warangal, Telangana, India

suggests that drought occurred more frequently but with shorter duration and more severity in Telangana from 2003 to 2022. All indices can roughly capture the major drought events, but SPEI-detected drought events are overall more severe than SSMI. There is strong heterogeneity in the spatial distribution of drought events as identified by all the indices. These findings could contribute to a better understanding of spatiotemporal patterns of agricultural droughts and provide a reference for future drought for the study area.

12.1   Introduction

Hydrologic hazards refer to extreme occurrences involving water distribution, movement and occurrences, resulting in adverse economic, social and environmental impacts, as well as loss of life (Wilhite 2000). Floods, droughts, landslides and river scour and deposition are examples of hydrologic hazards. Unlike other hazards, drought is the most intricate yet least comprehended, and it affects a vast geographical region, causing harm to more people than any other hazard (Hagman et al. 1984). The onset and end of a drought event are hard to determine, as the effects develop slowly over an extended period, lasting years even after the event's conclusion. A drought can last for a short or long time, ranging from a few weeks to several years, and it can have catastrophic consequences for water supplies and the agriculture sector. Drought is a naturally occurring event where there is a lack of water during the process of water distribution. The occurrence of drought is a multifaceted and gradual process that can have far-reaching consequences. It can result in devastating impacts on agriculture with decreased crop yields, food scarcity and environmental degradation, ultimately causing significant economic and societal harm (Mishra and Singh 2010; Kim et al. 2015; Park et al. 2016; Das et al. 2022a, 2022b; Kumari and Shukla 2023; Saikumar et al. 2023). It is crucial to analyse the characteristics of drought events to enable governments to implement preventive measures against such events. Drought frequency analysis can aid in the selection of appropriate measures for providing relief during droughts and managing drought risks. Drought event identification and characterisation are necessary to perform such drought frequency analysis.

Drought event identification and characterisation rely on the use of appropriate drought indices to analyse and understand the occurrence and impact of drought events. In general, droughts are typically classified based on different water factor deficits (Wu et al. 2020; Das et al. 2021). Meteorological drought occurs when there is a prolonged lack of precipitation. On the other hand, agricultural drought refers to a situation where crops are unable to receive sufficient water during a crucial growth phase, leading to stunted growth, crop yield reduction or even crop failure due to

declining soil moisture (SM) (Ding et al. 2021). The steps in drought event identification and characterisation include the selection of suitable drought indices and extraction of relevant characteristics (duration, frequency, intensity and peak) associated with drought events.

At present, various studies on drought event identification and characterisation have utilised only Standardized Precipitation Evapotranspiration Index (SPEI) and Standardized Precipitation Index (SPI) (Zhang et al. 2020; Jamro et al. 2019; Ma et al. 2023; Bisht et al. 2019; Wang et al. 2017; Xu et al. 2015; Zhou et al. 2014; Sharma and Goyal 2020; Hinge et al. 2022), which may not provide an accurate depiction of the spatiotemporal patterns of different drought events. Therefore, it is crucial to choose drought indices that are effective in characterising both meteorological droughts and agricultural droughts. In this study along with the two meteorological drought indices SPEI and SPI, one agricultural drought index Standardised Soil Moisture Index (SSMI) is used for drought event identification. Both the SPI and SPEI are both capable of analysing drought over multiple timescales. However, the SPI only takes into account precipitation, and thus, it cannot fully capture drought conditions caused by rising temperatures. On the other hand, the SPEI is more appropriate for assessing the impact of global warming on the severity of meteorological drought because it considers both precipitation and evapotranspiration (Yao et al. 2018). SSMI is used as agricultural drought index as it can have multiple timescales and can show more comprehensive agricultural drought state (Tao and Zhang 2020). The SPI and SPEI are used in this study because agricultural drought links various characteristics of meteorological drought to agricultural impacts directly, focusing on rainfall shortages (SPI), differences between actual and potential evapotranspiration (SPEI), soil water deficits (SSMI), etc. (Łabędzki and Bąk 2014).

The run theory is used in this study for drought identification and characterisation. Run theory is a time series analysis method, which has been widely used in the drought identification process (Zhang et al. 2020; Jamro et al. 2019; Ma et al. 2023; Bisht et al. 2019; Wang et al. 2017; Xu et al. 2015; Zhou et al. 2014). Its basic problem is determining the threshold level. In previous studies, only a single threshold level is set in the run theory (Zhang et al. 2020; Jamro et al. 2019; Ma et al. 2023). This single threshold procedure is simple, but it is tending to over-/incomplete identifying the drought events, affecting the accuracy of the results. Therefore, it is necessary to further optimise and test the more thresholds for drought identification. This would ensure greater consistency between the identified drought events and those that have occurred in reality.

12.2   Rational of the Study

Prior studies have primarily focused on individual drought events, with limited attention given to exploring the connections among various types of drought. Nevertheless, given the impact of climate change and human activities, the

associations between different types of droughts are likely to be affected, yet research on the response relationships and underlying mechanisms is inadequate. This study aims to identify and characterise both meteorological and agricultural drought events using ERA 5 Land data. Various studies on droughts have primarily relied on data collected from observation stations. Although this information is considered dependable, the number of meteorological stations within these networks is often insufficient to provide a comprehensive representation of the spatial distribution of meteorological parameters (Shi et al. 2020). With respect to spatial coverage, grid-based datasets can serve as an alternative to station observations for drought event identification (Shi et al. 2020). So, in this study, ERA 5 Land gridded rainfall, temperature and SM data is used to derive SPI, SPEI and SSMI to identify and characterise meteorological and agricultural drought events.

The state of Telangana in India is highly vulnerable to drought and relies primarily on rainfall as a water source. In 2015, the Telangana government declared seven out of its ten districts to be experiencing drought conditions (Anuradha 2016). In recent years, nearly half of the mandals in Telangana have reported inadequate rainfall, with two-thirds of the population engaged in agriculture, which is particularly susceptible to the impacts of droughts. This increases the need for accurate drought event identification and characterisation in the state. Given the importance of identifying and characterising drought in Telangana, and the availability of extensive ERA 5 reanalysis data, this study aims to apply the run theory in conjunction with the SPI, SPEI and SSMI to characterise and identify drought events in this drought-prone state.

12.3   Limitations of the Study

This study employs a multi-threshold run theory approach based on the SPI, SPEI and SSMI which is used to identify drought events. Typically, run theory uses a single threshold; however, our study utilises multiple thresholds. As SPI, SPEI and SSMI have same classification levels in terms of mild, moderate, severe and extreme wet/drought conditions, using multiple threshold run theory does not pose any issues. Nonetheless, implementing multi-threshold run theory with other drought indices that have different classification levels can be challenging. Although some other drought indices offer more detailed insights by taking into account more climatic variables, we could not utilise them due to this limitation.

12.4   Study Area

The state of Telangana (Fig. 12.1) is a semi-arid Indian state that experiences severe droughts frequently. Its primary source of water is rainfall, and it is situated between 15.83°N to 19.91°N and 77.24°E to 81.79°E. Most of the state's land is semi-arid
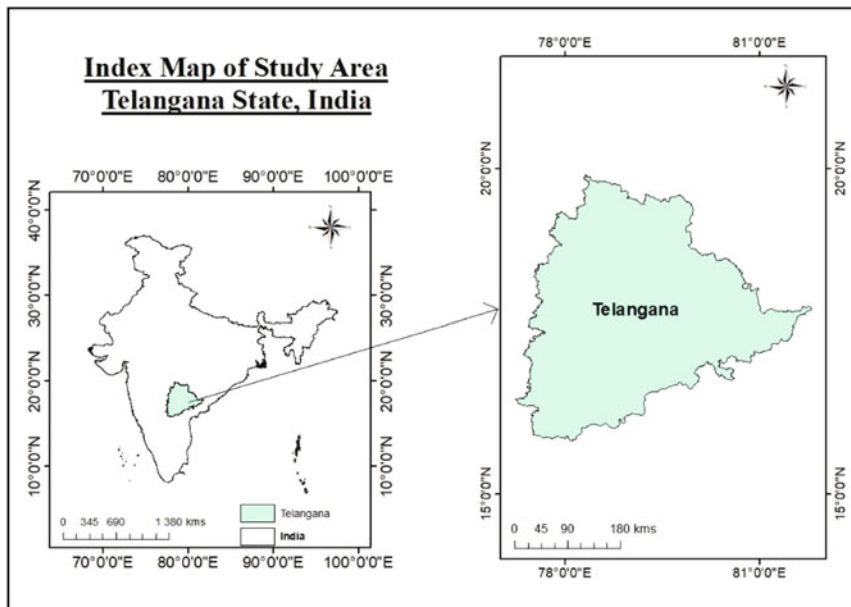
Fig. 12.1 Study area map

due to low ground water levels and little rainfall, and it is drained by the two major rivers Godavari and Krishna as well as numerous smaller rivers. With an average annual rainfall of 905.4 mm, the monsoon season in the state lasts from June through September. The State's total geographic area is 276.95 lakh acres, of which 49.07% is under cultivation and 24.07% is covered by forest, and 9.02%, 7.46% and 5.42% of all land is either fallow, used for non-agricultural purposes and land unusable for cultivation, respectively (Telangana State at a Glance 2021, Telangana government). The remaining 4.96% is made up of cultivable waste, permanent pastures and other grazing lands. In Telangana, red soils predominate making up for 48% of the total land area. Black cotton soils (25%), alluvium (20%) and rocks and boulders (7%) are the other soil types found in the state. Major monsoon crops grown in Telangana include cotton, paddy, maize, soybeans and pulses. Major rabi crops in the state include paddy, groundnuts and Bengal gram (Agriculture Action Plan 2021–2022 (2022), Telangana Government). The state's crop production is primarily composed of food crops. The agricultural crisis in Telangana is made worse by the state's 8–9 months of dry weather each year.

12.5 Materials and Methods

12.5.1 Datasets

Monthly gridded rainfall, temperature and SM datasets are used in this study to derive SPI, SPEI and SSMI. Monthly gridded rainfall in m, 2 m air temperature in K and volumetric soil in m^3/m^3 for Telangana from 1991 to 2022 is extracted from ERA5 Land monthly data. The ERA5 is a reanalysis data and stands for the fifth generation of the European Reanalysis (ERA) dataset. It is produced by the European Centre for Medium-Range Weather Forecasts (ECMWF) and is based on a combination of satellite and ground-based observations, as well as numerical weather prediction models. The dataset is available at a spatial resolution of $0.1°$ (approximately 10 km) and covers the period from 1950 to the present day (Table 12.1).

12.5.2 Drought Indices

The Standardised Soil Moisture Index (SSMI), Standardised Precipitation Index (SPI) and Standardised Precipitation Evapotranspiration Index (SPEI) are used to determine drought characteristics (duration, frequency, intensity and peak) for Telangana. Both the SPI (McKee et al. 1993; McKee 1995) and SPEI (Vicente-Serrano et al. 2010) are used in this study to quantify the meteorological drought and SSMI for agricultural drought identification. The SPI and SSMI uses the two-parameter Gamma distribution to fit the cumulative monthly rainfall and SM time series. Once the gamma probability density function is fitted to monthly rainfall and SM time series, SPI and SSMI are computed mathematically as following equation:

$$SPI = \frac{RF_{mn} - \overline{RF_m}}{\sigma_m}$$

Table 12.1 Datasets used in the study

Datasets used	Data product	Spatial/temporal coverage	Source
ERA5 Land	Rainfall (m) Temperature (K, 2 m air) Soil moisture (m^3/m^3, 0–7 cm)	0.1°/monthly	https://cds.climate.copernicus.eu/ (Muñoz-Sabater et al. 2021)

Table 12.2 Classification of SPI and SPEI for different drought levels (McKee et al. 1993; McKee 1995; Vicente-Serrano et al. 2010)

Level of drought	SPI, SPEI
Extreme wet	≥ 2.0
Severe wet	1.5–2
Moderate wet	1–1.5
Mild wet	0.5–1
Near normal	−0.5–0.5
Mild dry	−1––0.5
Moderate dry	−1.5– −1
Severe dry	−2––1.5
Extreme dry	≤ -2.0

$$\text{SSMI} = \frac{\text{SM}_{mn} - \overline{\text{SM}_m}}{\sigma_m}$$

where RF_{ij} and SM_{ij} are the rainfall and SM for the mth grid and n^{th} time period. $\overline{\text{RF}_m}$ and $\overline{\text{SM}_m}$ are the mean rainfall and SM for the mth grid and σ_m is the standard deviation of rainfall and SM for the mth grid for SPI and SSMI, respectively. The ERA5 Land monthly gridded rainfall and monthly gridded SM from 1991 to 2022 are used in this study to derive SPI and SSMI from 2001 to 2022.

The calculation of the SPEI is analogous to that of the SPI. However, in place of rainfall data, the monthly difference between the amount of precipitation and potential evapotranspiration (PET) is used, resulting in the climatic water surplus/deficit (wb = RF_m − PET_m). This data is then fitted using a three-parameter log-logistic distribution. Once the *wb* series is fitted using log-logistic distribution, SPEI is calculated as

$$\text{SPEI} = V - \frac{C_0 + C_1 V + C_2 V^2}{1 + d_1 V + d_2 V^2 + d_3 V^3}$$

In the above equation, $V = \sqrt{-2\ln(P)}$ for $P \leq 0.5$ and C_0, C_1, C_2, d_1, d_2 and d_3 are constants. *P* here is the probability of exceeding a determined *wb* value. If $P > 0.5$, then *P* is replaced by $1 - P$.

ERA5 Land monthly gridded rainfall and temperature from 1991 to 2022 is used in this study to derive SPEI. Both indices use the probability density functions to fit the time series (*RF* for SPI and RF − PET for SPEI) and then use the inverse standard normal distribution to transfer the cumulative probability density functions to the drought index value. Positive/negative values of the SPI and SPEI indicate wet/dry conditions. Different levels of drought based on SPI and SPEI are shown in Table 12.2. R Studio is used to calculate SPI, PET and SPEI provided the inputs ERA 5 rainfall and ERA 5 temperature.

12.5.3 Run Theory

Drought events and their characteristics, including annual drought frequency (D_f), annual drought duration (D_d), drought intensity (D_s) and drought peak (D_p) at each grid, are determined by run theory (Guerrero-Salazar and Yevjevich 1975). The schematic diagram of the determination of drought events and their characteristics based on the SPI, SPEI and SSMI time series is shown in Fig. 12.2. Run theory is applied using multiple thresholds at $x_0 = -0.5$, $x_1 = -1$, $x_2 = 0.5$ using three indices where x_0, x_1 and x_2 are indices' values (Ma et al. 2023). Using these three thresholds at x_0, x_1, x_2, drought events are identified as follows using run theory:

Step 1: Check if the monthly SPI/SPEI/SSMI value is below x_0. If yes, it indicates occurrence of drought and mark it as a potential drought event. Based on this, drought events E1, E2, E3, E4, E5 and E6 are selected as shown in Fig. 12.2.

Step 2: Remove any minor drought event from above selected events in step 1, which only lasts for one month and does not reach the threshold x_1. Accordingly E1 is considered as minor drought event and E2, E3, E4, E5 and E6 are screened for next step.

Step 3: Combine any adjacent drought events which have an interval of one month and do not reach the threshold x_2, into one drought event. Accordingly, E2 and E3 are combined into one event.

So, finally from Fig. 12.2, E2–E3, E4, E5 and E6 are the four drought events identified based on run theory with multiple thresholds.
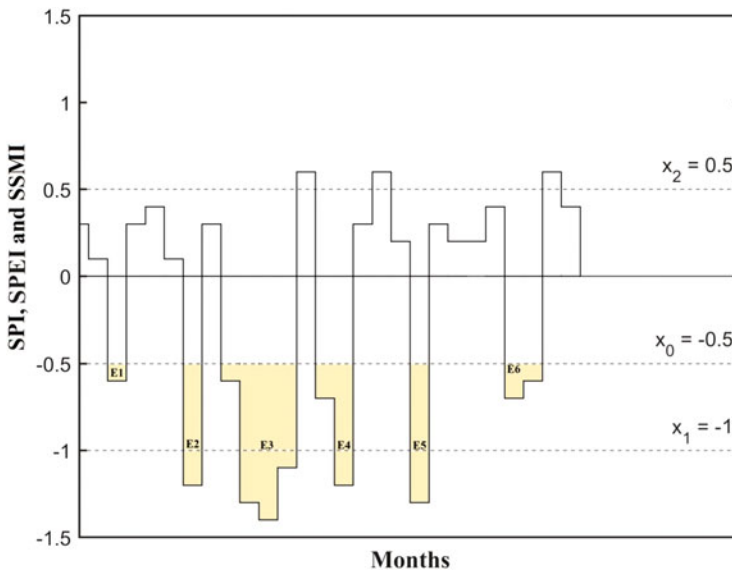
Fig. 12.2 The schematic diagram showing the identification of drought events

Fig. 12.3 Overall
methodology workflow
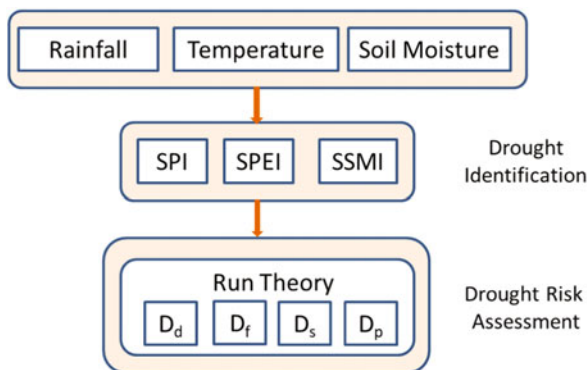
Once the drought events are identified, drought parameters D_f, D_d, D_s and D_p are determined. Annual drought frequency (D_f) is the number of drought events in the study period divided by the number of years. Drought duration for a single drought event is the difference between the start time (t_s) and the end time (t_e) of drought event. Annual drought duration (D_d) is the total duration of drought events in months divided by the total number of years. Drought intensity (D_s) for each drought event is determined as sum of SPEI values divided by drought duration for that particular drought event. Drought peak (D_p) at each grid is the smallest SPEI value for the entire time period.

The overall methodology of the study is shown in Fig. 12.3 where SPI, SPEI and SSMI are derived using rainfall, temperature and SM data. Run theory is then applied to these three indices and the drought characteristics, D_f, D_d, D_s and D_p, are determined.

12.6 Results

In this study, the monthly state averaged SPI, SPEI and SSMI for Telangana state from 2003 to 2022 is calculated and presented in Fig. 12.4. All the three indices have same classification of different classes of drought from mild drought ($-1 \leq$ SPI/SPEI/SSMI ≤ -0.5), to moderate drought ($-1.5 \leq$ SPI/SPEI/SSMI ≤ -1), to severe drought ($-2 \leq$ SPI/SPEI/SSMI ≤ -1.5) and to extreme drought (SPI/SPEI/SSMI ≤ -2). Irrespective of classes of drought (near normal, mild, moderate, severe and extreme), all the indices are able to show a synchronous pattern in representing drought (negative SPI/SPEI/SSMI) or wet conditions (positive SPI/SPEI/SSMI) with a monthly delay of one or two months by SSMI. This time delay by SSMI shows the translation of meteorological drought represented by SPI/SPEI to agricultural drought represented by SSMI. However, many severe meteorological drought events did not lead to agricultural drought. This may be due to water storage or
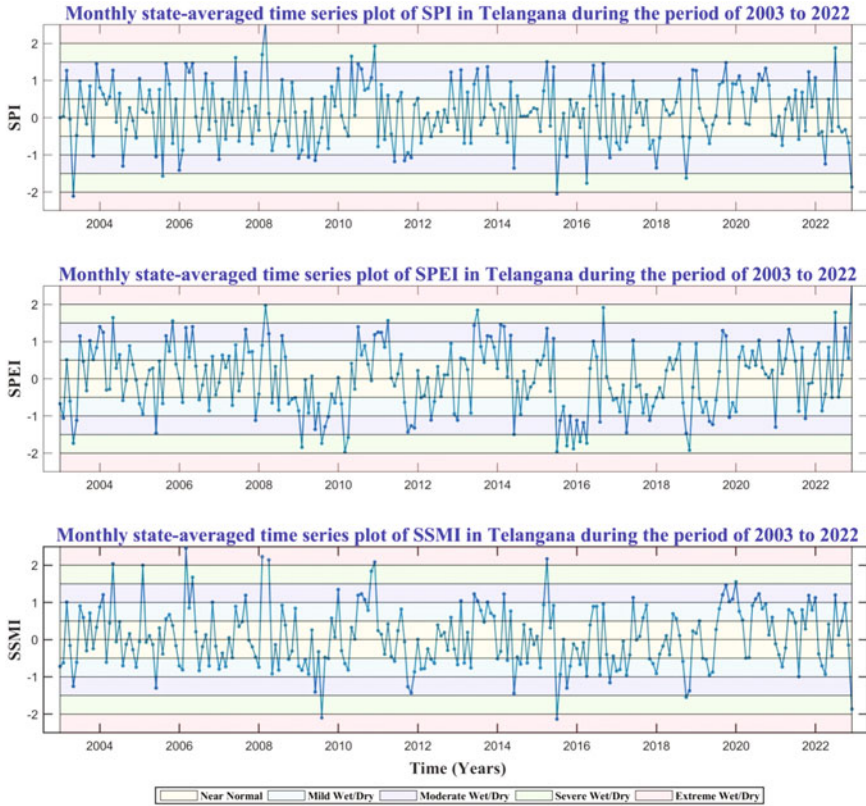
Fig. 12.4 Monthly state-averaged time series plot of SPI, SPEI and SSMI in Telangana during the period of 2003–2022

groundwater recharge, and the propagation time of meteorological drought to agricultural drought is different under different land-use types (Zhou et al., 2021).

Drought event identification and characterisation are a prerequisite to drought frequency analysis and are related to drought risk often characterised by its duration, frequency, intensity and spatial extent (Xu et al. 2015). In this study, using run theory drought events are identified for Telangana, and annual drought duration (D_d), annual drought frequency (D_f), drought intensity (D_s) and drought peak (D_p) are calculated. Figure 12.5 displays the spatial patterns of drought characteristics D_d, D_f, D_s and D_p determined from drought events identified by one-month SPI, SPEI and SSMI over Telangana from 2003 to 2022. In Fig.12.5, high meteorological/agricultural drought risk is represented by blue colour and low meteorological/agricultural drought risk by yellow colour for all the four drought characteristics. In terms of drought peak (D_p), all the three indices show very low values (blue
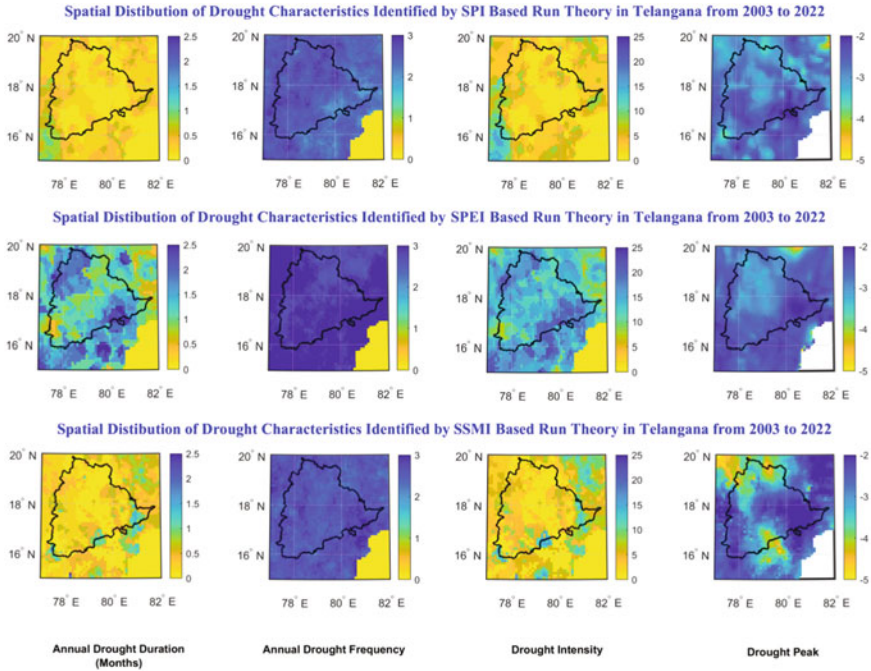
Fig. 12.5 Annual drought duration (D_d), annual drought frequency (D_f), drought intensity (D_s) and drought peak (D_p) as determined by multi-threshold run theory

colour). It means in terms of dry only conditions, that is, if there is a drought, there is higher risk of extreme droughts for the entire Telangana represented by SPI/SPEI with SSMI indicating even more intense drought risk at very few regions indicated by yellow colour. In terms of drought frequency (D_f) too, all the three indices indicated higher meteorological/agricultural drought risk (blue colour). The spatial distribution of D_s is consistent with that of D_d for all the three indices. For all the four drought characteristics, D_d, D_f, D_s and D_p, SPEI showed greater drought risk whereas SPI/SSMI indicated lower drought risk in terms of D_d and D_s. This also suggests that drought occurred more frequently (higher D_f) but with shorter duration (lesser D_d by SPI, SSMI) and more severity (higher D_p) in Telangana from 2003 to 2022. For meteorological drought risk analyses, SPEI and SPI showed different spatial pattern. This is due to input parameters provided to calculated SPI and SPEI. SPEI considers both rainfall and precipitation; SPI considers only rainfall. Because of this meteorological drought risk assessed by SPEI based run theory, it should be considered more accurate than that of SPI-based run theory.

12.7 Conclusions

The drought indices, that is, SPI, SPEI and SSMI, are analysed for the relation between meteorological drought and agricultural drought. The translation of meteorological drought to agricultural drought is represented by a time delay of a month or two by SSMI compared to SPI and SPEI. The investigation into the relation between meteorological drought and agricultural drought provides better understanding of the process of drought propagation and could aid in enhancing drought preparedness and alleviation measures.

The SPI, SPEI and SSMI are also analysed to identify drought event characterisation over Telangana to assess drought risk in terms of D_d, D_f, D_s and D_p. The SPI and SSMI displayed a similar pattern in all the four drought characteristics. All the three indices displayed similar spatial distribution of D_s and D_d. The SPEI characterises higher values in D_d, D_f, D_s and D_p which can be largely attributed to increasing PET. In contrast, the SPI did not demonstrate these higher patterns, as it solely considers rainfall and does not show a higher D_d and D_s. This emphasises the significance of PET in explaining the spatial aspects of drought dynamics. These findings indicate that the escalating PET has the potential to intensify drought conditions, indicating a worrisome future considering the projected increase in PET due to a warming climate (Li et al. 2020). Thus, it is plausible that the SPEI may be more appropriate than the SPI index to assess drought risk related to climate change.

12.8 Future Scope and Recommendations

In this study, the time delay between meteorological drought and agricultural drought was seen only by a time series analysis, and any linear or nonlinear relationship between them was not performed. A correlation analysis between both the droughts would have given more in-depth results of how drought is translated from meteorological drought to agricultural drought. Given the influence of climate change and human interventions, the relationship between these two types of droughts and their propagation is complex and is not limited to linear correlation but may also involve nonlinear connections (Leng et al., 2015). Zhou et al. (2021) revealed that the translation time from meteorological to agricultural drought varied across different land-use categories. Thus, it is crucial to account for both linear and nonlinear relationships between different droughts. Drought risk in this study is assessed individually in terms of D_d, D_f, D_s and D_p. But the better risk assessment will be calculated by a joint probability distribution between any of these two characteristics ($D_d\_D_f$, $D_d\_D_s$, $D_d\_D_p$, $D_s\_D_f$, $D_f\_D_p$, $D_d\_D_p$) or three characteristics ($D_d\_D_f\_D_s$, $D_d\_D_f\_D_p$, $D_d\_D_s\_D_p$) from the four drought characteristics.

Long-term plans are necessary for reducing the risk of drought, and early warning should be viewed as a means of effectively reducing the increasing susceptibility of

communities and assets. Regarding early warning systems for drought, it is widely acknowledged that establishing an efficient system is crucial for identifying risks and closely monitoring farmers' vulnerability levels. A dependable and lasting drought early warning system relies on multi-level governance, institutional setups and frameworks that utilise risk assessment characteristics like D_d, D_f, Ds and D_p for gradual hazards like drought.

References

Agriculture Action Plan 2021–2022 (2022) Department of Agriculture, Government of Telangana. https://agri.telangana.gov.in/open_record_view.php?ID=959

Anuradha UV (2016) Telangana Drought 2016. South Asia Network on Dams, Rivers and People

Bisht DS, Sridhar V, Mishra A, Chatterjee C, Raghuwanshi NS (2019) Drought characterization over India under projected climate scenario. Int J Climatol 39(4):1889–1911

Das S, Das J, Umamahesh NV (2021) Nonstationary modeling of meteorological droughts: application to a region in India. J Hydrol Eng 26. https://doi.org/10.1061/(asce)he.1943-5584.0002039

Das S, Das J, Umamahesh NV (2022a) Copula-based drought risk analysis on rainfed agriculture under stationary and non-stationary settings. Hydrol Sci J 67:1683–1701. https://doi.org/10.1080/02626667.2022.2079416

Das S, Das J, Umamahesh NV (2022b) Investigating the propagation of droughts under the influence of large-scale climate indices in India. J Hydrol 610. https://doi.org/10.1016/j.jhydrol.2022.127900

Ding Y, Gong X, Xing Z, Cai H, Zhou Z, Zhang D, Sun P, Shi H (2021) Attribution of meteorological, hydrological and agricultural drought propagation in different climatic regions of China. Agric Water Manag 255:106996

Guerrero-Salazar PLA, Yevjevich VM (1975) Analysis of drought characteristics by the theory of runs (Doctoral dissertation, Colorado State University. Libraries)

Hagman G, Beer H, Bendz M, Wijkman A (1984) Prevention better than cure. Report on human and environmental disasters in the Third World. 2

Hinge G, Piplodiya J, Sharma A et al (2022) Evaluation of hybrid wavelet models for regional drought forecasting. Remote Sens 14. https://doi.org/10.3390/rs14246381

Jamro S, Dars GH, Ansari K, Krakauer NY (2019) Spatio-temporal variability of drought in Pakistan using standardized precipitation evapotranspiration index. Appl Sci 9(21):4588

Kim H, Park J, Yoo J, Kim TW (2015) Assessment of drought hazard, vulnerability, and risk: a case study for administrative districts in South Korea. J Hydro Environ Res 9(1):28–35

Kumari C, Shukla R (2023) Nature Based Solutions (NBS) to achieve food security and SDGs in drought prone subtropical area

Łabędzki L, Bąk B (2014) Meteorological and agricultural drought indices used in drought monitoring in Poland: a review. Meteorology Hydrology and Water Management. Res Oper Appl 2(2):3–13

Leng G, Tang Q, Rayburg S (2015) Climate change impacts on meteorological, agricultural and hydrological droughts in China. Glob Planet Chang 126:23–34

Li L, She D, Zheng H, Lin P, Yang ZL (2020) Elucidating diverse drought characteristics from two meteorological drought indices (SPI and SPEI) in China. J Hydrometeorol 21(7):1513–1530

Ma Q, Li Y, Liu F, Feng H, Biswas A, Zhang Q (2023) SPEI and multi-threshold run theory based drought analysis using multi-source products in China. J Hydrol 616:128737

McKee TB (1995) Drought monitoring with multiple time scales. In Proceedings of 9th Conference on Applied Climatology, Boston, 1995

McKee TB, Doesken NJ, Kleist J (1993, January) The relationship of drought frequency and duration to time scales. In Proceedings of the 8th Conference on Applied Climatology 17(22): 179–183

Mishra AK, Singh VP (2010) A review of drought concepts. J Hydrol 391(1–2):202–216

Muñoz-Sabater J, Dutra E, Agustí-Panareda A, Albergel C, Arduini G, Balsamo G, Boussetta S, Choulga M, Harrigan S, Hersbach H, Martens B, Miralles DG, Piles M, Rodríguez-Fernández NJ, Zsoter E, Buontempo C, Thépaut JN (2021) ERA5-Land: a state-of-the-art global reanalysis dataset for land applications. Earth Syst Sci Data 13(9):4349–4383

Park S, Im J, Jang E, Rhee J (2016) Drought assessment and monitoring through blending of multi-sensor indices using machine learning approaches for different climate regions. Agric For Meteorol 216:157–169

Saikumar G, Pandey M, Dikshit PKS (2023) Natural river hazards: their impacts and mitigation techniques. p 3–16. https://doi.org/10.1007/978-981-19-7100-6_1

Sharma A, Goyal MK (2020) Assessment of drought trend and variability in India using wavelet transform. Hydrol Sci J 65:1539–1554. https://doi.org/10.1080/02626667.2020.1754422

Shi H, Chen J, Li T, Wang G (2020) A new method for estimation of spatially distributed rainfall through merging satellite observations, raingauge records, and terrain digital elevation model data. J Hydro Environ Res 28:1–14

Tao R, Zhang K (2020) PDSI-based analysis of characteristics and spatiotemporal changes of meteorological drought in China from 1982 to 2015. Water Resour Protect 36(5):50–56

Telangana State at a Glance 2021 by Directorate of Economics and Statistics, Government of Telangana, https://www.telangana.gov.in/PDFDocuments/Telangana-State-at-a-Glance-2021.pdf

Vicente-Serrano SM, Beguería S, López-Moreno JI (2010) A multiscalar drought index sensitive to global warming: the standardized precipitation evapotranspiration index. J Clim 23(7): 1696–1718

Wang X, Zhang Y, Feng X, Feng Y, Xue Y, Pan N (2017) Analysis and application of drought characteristics based on run theory and Copula function. Trans Chin Soc Agric Eng 33(10): 206–214

Wilhite DA (2000) Chapter 1 drought as a natural hazard: concepts and definitions. Drought Mitigation Center Faculty Publications, p 69

Wu M, Li Y, Hu W, Yao N, Li L, Liu DL (2020) Spatiotemporal variability of standardized precipitation evapotranspiration index in mainland China over 1961–2016. Int J Climatol 40(11):4781–4799

Xu K, Yang D, Xu X, Lei H (2015) Copula based drought frequency analysis considering the spatio-temporal variability in Southwest China. J Hydrol 527:630–640

Yao N, Li Y, Lei T, Peng L (2018) Drought evolution, severity and trends in mainland China over 1961–2013. Sci Total Environ 616:73–89

Zhang L, Wang Y, Chen Y, Bai Y, Zhang Q (2020) Drought risk assessment in Central Asia using a probabilistic copula function approach. Water 12(2):421

Zhou Y, Liu L, Zhou P, Jin J, Li J, Wu C (2014) Identification of drought and frequency analysis of drought characteristics based on palmer drought severity index model. Trans Chin Soc Agric Eng 30(23):174–184

Zhou K, Li J, Zhang T, Kang A (2021) The use of combined soil moisture data to characterize agricultural drought conditions and the relationship among different drought types in China. Agric Water Manag 243:106479

Chapter 13
Drought Modeling Through Drought Indices in GIS Environment: A Case Study of Thoubal District, Manipur, India

Denish Okram and Thiyam Tamphasana Devi

Abstract In this study, drought-affected zones were modeled using satellite data and geographical information system (GIS) techniques in Thoubal district, Manipur (north eastern part of India), from 2013 to 2021. Different drought indices, that is, standard precipitation index (*SPI*), temperature condition index (*TCI*), normalized difference vegetation index (*NDVI*), vegetation condition index (*VCI*), NDVI deviation (Dev_{NDVI}), and vegetation health index (*VHI*), were used in the modeling. From the results, the study area has been classified into five classes (severely dry, moderately dry, near normal, mildly wet, and moderately wet), and mostly the study area witnesses two drought conditions, that is, moderate drought and near normal. Thus, drought-like conditions occurred in the years 2015, 2016, 2018, 2019, 2020, and 2021 while in the years 2013 and 2014, the study area experienced both moderate drought and near normal condition in different parts of the district, and in 2017, the whole district received a sufficient amount of precipitation and experienced a near normal condition. A comparison of the predicted results with the collected data was done, and it was observed that the crop yield is high when the near normal condition is predicted for the year 2017. In support of the validation of predicted results, a community opinion-based survey was also conducted by interacting with the local people at various parts of the study area. Their opinions of crop production affected either by drought or flood are found to be relevant with the predicted results of the present study.

Keywords Drought modeling · Drought indices GIS techniques · Thoubal district · Satellite data

D. Okram · T. T. Devi (✉)
Department of civil Engineering, National Institute of Technology, Manipur, India

13.1 Introduction

River, sediment, and hydrological extremes are closely linked, as these strong interrelationships can lead to a range of natural hazards (Das et al. 2022a, b, c) such as reduced water availability, impacts on agricultural productivity, damage to infrastructure, loss of life, and injury. The impacts of these hazards can be significant and long-lasting and can have far-reaching economic, social, and environmental consequences. Rivers and its tributaries are similar with the veins of human and carry everything along with the flow including sediments, which is one of the most problems creating discharges. Sediment discharge in rivers is due to soil erosion in upstream side of the river, which is caused by the escalating anthropogenic influence (Saikumar et al. 2022). Long-term continuous deposition of sediments decreases water depth and becomes a caused for hydrological extreme events such as drought. Drought is one of the hydrological extreme events that impact the ecosystem of water resources management and living things on earth in the short term as well as in the long term (Saikumar et al. 2022). It is defined as prolonged shortages of water supply due to the lack of significant precipitation, over utilization of water, siltation, and sedimentation of rivers and lakes and interrupted weather patterns that disturb the water cycle. It is also a slow recurring and unpredictable disaster that leads to serious impacts on livestocks, humans, and the environment throughout the world and is more powerful than other natural disasters (Temesgen et al. 2001). Meteorological (Das et al. 2021a) and agricultural drought (Goyal and Sharma 2016; Sharma and Goyal 2020; Das and Umamahesh 2022) causes change in climate patterns, precipitation deficits, and increased evapotranspiration. Managing these hazards requires a comprehensive approach that considers the underlying causes of hydrological extremes (Das et al. 2022a, b; c). This includes implementing measures such as water conservation practices, sediment management strategies, and drought control structures to mitigate the impacts of these phenomena. It also involves improved communication and collaboration between stakeholders, including governments, water resource managers, and communities. Some of the most challenging problems that human societies currently encounter are rising food demand due to increase in population (Das et al. 2022a, b, c) and environmental stressors, which have prompted new studies to look at how droughts affect food production (Orimoloye 2022). Another major problem faced all over the world is the drying up of rivers and lakes (Bond et al. 2008; Wu et al. 2021; Gupta et al. 2023), which are the main source of water supply to all the living lives. India is also a country that depends on agriculture, and India's agriculture is solely dependent on fresh water resources, which is likely a result of irregular rainfall patterns and extended droughts (Purohit et al. 2021; Das et al. 2022a, b, c; Rawat et al. 2022).

Today, several technologies are developed to predict and model the drought pattern, and one of the most reliable and effective is integrated approach of satellite data with geographical information system (GIS) techniques (Yin et al. 2014; Singh and Devi 2022; Zhao et al. 2022) through drought indices (Ihinegbu and Ogunwumi 2022; Zhang et al. 2023) such as standard precipitation index (SPI), normalized

difference vegetation index (*NDVI*), temperature condition index (*TCI*), vegetation condition index (*VCI*), vegetation health index (*VHI*), etc. or through multi criteria decision-making methods such as analytic hierarchy process (AHP) and multi-influencing factors (MIF). Drought modeling can help inform the development of effective management strategies by providing information on the onset, duration, and severity of drought conditions (Das et al. 2022a, b, c; Sharma and Goyal 2020). This information can be used to inform decision-makers about water allocation, drought preparedness measures, and the implementation of drought response plans. Unlike many natural disasters, drought is barely noticeable and is difficult to recognize when the drought will start, and the end of a drought can take around days, months, or even more as the onset of the drought is gradual (Mosley 2015; Das et al. 2021a; b). Most of the droughts occur when usual weather patterns are disturbed, which leads to a drastic change in the water cycle. Therefore, nowadays, satellite-based remote sensing techniques are used to assess high spatial resolution and high temporal resolution for observing the Earth (Gao et al. 2021). The surface characteristics of land and atmosphere can be derived from remotely sensed images. Currently, researchers are demanding for an increasing development of remote sensing data (high-resolution images) for effective drought monitoring.

Hammouri and El-Naqa (2007) conducted a study on the assessment of drought conditions prevailing in Amman-Zarqa basin, northern Jordan, using different drought indices using GIS and remote sensing techniques. In this study, the drought was assessed using two different indices (*SPI* and *NDVI*). Using *SPI,* drought severity has been analyzed, and for selected rainfall stations, the annual *SPI* values for 6 and 12 months from 1975 to 2000 have been analyzed and found an important phenomenon that the dry seasons return in a similar way year after year. The months of October, November, December, January, and February were used in an investigation of *NDVI* drought severity for the years 1981–2003. According to the study's findings, the Amman-Zarqa basin is now experiencing drought conditions. Kloos et al. (2021) in the south east region of Germany, Central Europe, conducted research on agricultural drought detection using moderate-resolution imaging spectro-radiometer (MODIS)-based vegetation health indices. The main goal of this project is to monitor agricultural drought utilizing (MODIS) *NDVI,* land surface temperature (*LST*), *TCI, VCI*, and *VHI*on water scarce regions and the scope where these drought indices can be used to identify drought conditions. In order to assess the derived drought indices *VCI, TCI*, and *VHI,* soil moisture index data from 2001 to 2020, combined with yield data for agricultural crops and land use data, were employed, and it is observed that in the years 2003, 2015, and 2018, the study area was unusually hot or dry, enduring severe drought conditions, which lead to a great loss in agriculture. Abuzar et al. (2017) conducted a study on Drought Risk Assessment Using Remote Sensing and GIS: A Case Study of District Khushab, Pakistan. By the use of temporal images from *NDVI* (2003, 2009, and 2015) based on Landsat enhanced thematic mapper (ETM) and meteorological based *SPI*, this work makes an effort to identify areas that are geographically and temporally at risk for drought in agriculture, in addition to drought due to weather. The study area was separated into three zones: no drought, slight drought, and moderate drought. Between the

NDVI, SPI, and rainfall anomaly, a correlation analysis was conducted. A spatial temporal drought risk map was created after correlating rainfall and NDVI. The vegetation cover classes were calculated using this NDVI, and a trend in their shift was also discovered. Using SPI values over a 15-year period, drought risk was detected. NDVI and SPI readings were used in a linear combination weighted approach to evaluate the impact of the drought. The results showed that 41% of the district has no drought, 28% has a slight drought, and 30% has a moderate drought. According to the study, the southern portion of District Khushab had a deficit in rainfall and little vegetation, making it the region with the highest prevalence of drought. Patil et al. (2021) conducted a study on the analysis of agricultural drought intensity and geographic extent in Manganga watershed of Maharashtra, India. The major goal of the study is to use VHI, which incorporates NDVI, VCI, LST, and TCI, to examine the severity of the agricultural drought. Clear Landsat satellite data availability for the research area is taken into account for the temporal analysis of drought. In this work, Landsat data are used to examine the Vegetation Health Index during the dry seasons of 2001, 2010, 2015, 2017, and 2019. The analysis makes precise measurements of how changes in the drought analysis affect the NDVI, LST, and VHI using satellite data, and it is found that mild and moderate drought conditions are predominant across the entire study area in exception of the nearby areas along the river. Singh and Devi (2022) conducted a study on estimating drought-prone areas in low-lying topography of India's north-eastern region (Imphal west district in Manipur state). In their study, it was observed in the year 2019 that a condition similar to drought with a terrible amount of available surface water arises, which seriously affects the agriculture and to the livelihood of the region. To forecast drought-prone areas, two methods were used, that is, AHP and MIF. The drought zone region was summarized considering several parameters (like rainfall, temperature, slope, infiltration, vegetation cover, density, soil) as acute (22.8% by AHP and 39.4% by MIF), moderate (60.1% and 54.7%), critical (16.1% and 5.5%), and extreme (0.9% and 0.3%). After analyzing all the data, it is recommended that MIF approach is more precise displaying 43.7% of drought zones are acute and 51.32% are moderate drought-prone areas.

The aim of this study is to evaluate drought using satellite data and GIS techniques in Thoubal district, Manipur, and the main objective of this study is to identify and map drought-prone area using drought indices, that is, SPI, TCI, NDVI, VCI, VHI, and Dev_{NDVI}(NDVI deviation) for the nine conjugative years, that is, from 2013 to 2021.

13.2 Study Area

Thoubal district (Fig. 13.1) is one of Manipur's districts in northeastern India. The district is located in eastern Manipur Valley, where it makes up a bigger portion of the state. The district covers an area of 324 km^2. It is located between 23°45′–24°45' N latitudes and 93°45′–94°15′ E longitudes. The district is generally located at an
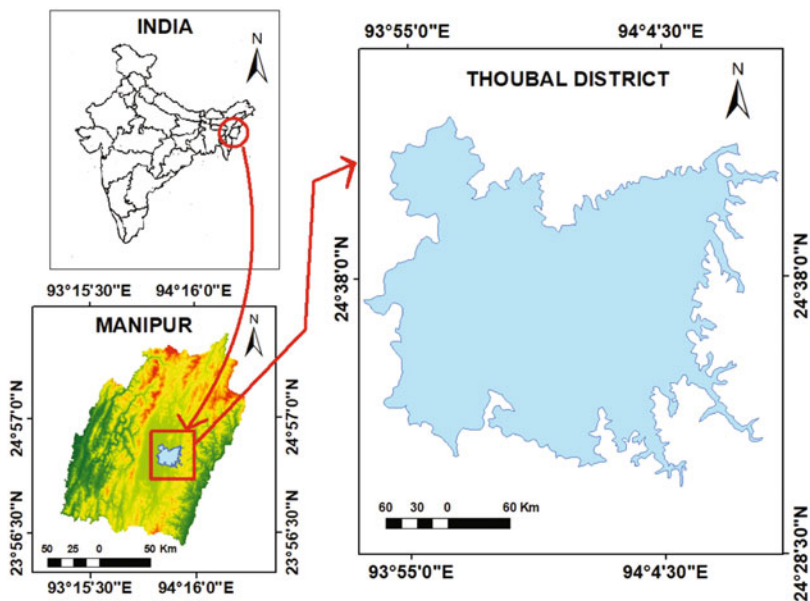
Fig. 13.1 Location of study area (Thoubal District)
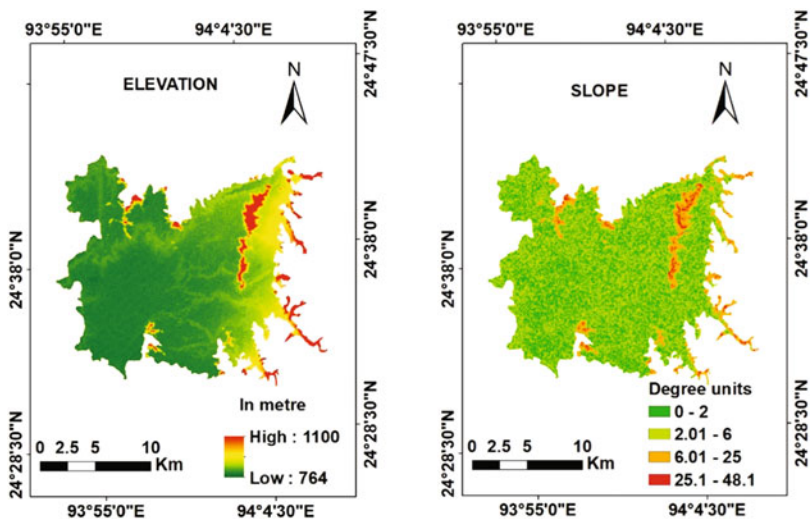
Fig. 13.2 DEM (left) and slope map (right)

altitude of 790 meters above mean sea level. The district hardly has some hillocks and hills with allow height. Of these, Punam Hill is located at a height of 1009 m above sea level. Fig. 13.2 shows the digital elevation model (DEM) and slope of the study area.

The major rivers in the study area are the Imphal river originating from Senapati district and the Thoubal river emerging from the hill ranges of Ukhrul district flows through Thoubal district. It has a moderate climate varying seasonally. The major source of income for the population of Manipur depends on agriculture and the activities concerning to it. Seventy percent of the population in the district is associated with farming since the topography of Thoubal district facilitates irrigation significantly. Sugarcane, pineapple, and rice are the most cultivated crops. Animal husbandry and fishing also support to the economy of the district.

13.3 Methodology

The study is conducted using two different sources, that is, metrological data and satellite data, and Fig. 13.3 displays a conceptual breakdown of the methodology that was used. Metrological data has been collected for nine conjugative years from 2013 to 2021. Annual rainfall for nine rain stations has been used to derive *SPI*. In our study area, there is only one rainfall station, so we have collected other eight rainfall stations from another district as well. For every station, *SPI* has been
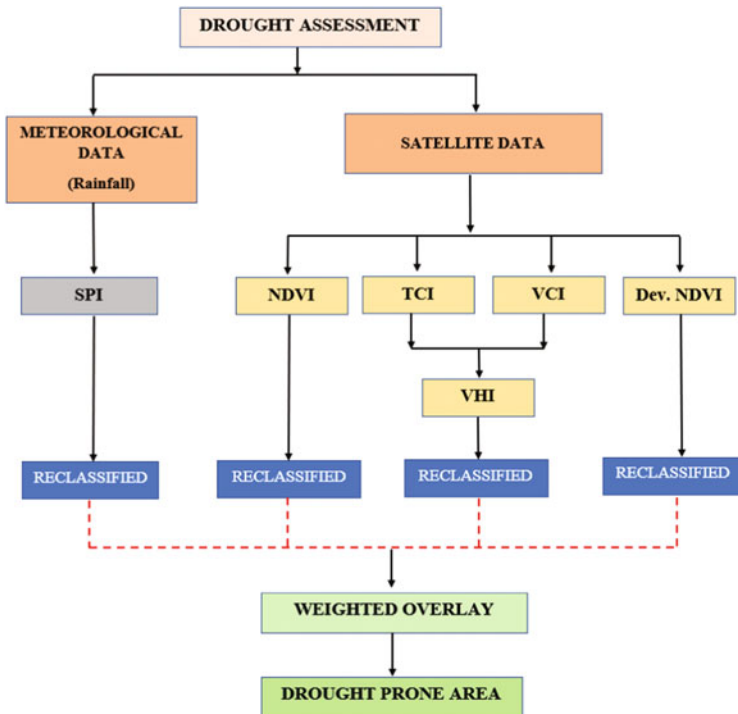
Fig. 13.3 Flowchart of methodology

calculated, and those calculated *SPI* are being interpolated with the help of inverse distance weighting (IDW) through GIS tool (ArcGIS®). From the interpolated *SPI* map, our study area is been extracted. From the satellite data again, two sources have been used: (i) MODIS data and (ii) Landsat-8 data. MODIS data has been collected for 9 years (2013–2021), and from those data, *LST* (maximum and minimum) has been derived, and using a formula given in Eq. 13.3, *TCI* from 2013 to 2021 has been calculated. From the Landsat-8 data, *NDVI* has been derived using GIS tool for nine conjugative years, that is, 2013–2021. From *NDVI, VCI* and *Dev*$_{NDVI}$ have been calculated for the same 9 years, and from *TCI* and *VCI, VHI* is again calculated. All the indices have been reclassified, and using weighted overlay tool, drought-prone zone is predicted.

13.3.1 Drought Indices

13.3.1.1 SPI

The *SPI* is a drought monitoring precipitation data over a period of time. It has an intensity scale where the *SPI* positive values denote wet conditions and the *SPI* negative values show drought conditions. Its purpose is to standardize the rarity of current drought. The formula of *SPI* is given in Eq. 13.1 as:

$$SPI = \frac{(X_i - X_{i\ mean})}{\sigma} \tag{13.1}$$

where X_i = significant precipitation, X_{imean} = average precipitation, σ = standard deviation of the selected time. The range of *SPI* value is given in Table 13.1.

13.3.1.2 NDVI

The *NDVI* is a commonly used vegetation index to understand vegetation health. It computes the difference between visible and near-infrared to determine the density of green vegetation. High *NDVI* values show dense green vegetation, while the lesser values denote sparse vegetation like barren areas, snow, or sand. The formula used to compute *NDVI* is as shown in Eq. 13.2:

$$NDVI = \frac{(NIR - Red)}{(NIR + Red)} \tag{13.2}$$

where *NIR* = near-infrared light and *Red* = visible red light. The range of *NDVI* value is given in Table 13.1.

Table 13.1 Meteorological drought classification using *SPI* values (McKee et al. 1993), *NDVI* (Aziz et al. 2018) and *TCI, VCI, VHI* (Bhuiyan et al. 2008), *Dev*$_{NDVI}$ (Berhan et al. et al. 2011)

SPI	Drought category	NDVI	Drought category	TCI, VCI, VHI.	Drought category	Dev$_{NDVI}$	Drought category
>2	Extremely wet	≥0.6	Extremely wet	≥40	No drought	>0.1	Extremely wet
1.50–1.99	Very wet	0.4–0.6	Wet	<40	Mild drought	>−0.05 to ≤0.1	Near normal
1.00–1.49	Moderately wet	0.2–0.4	Moderate	<30	Moderate drought	>−0.2 to ≤0.05	Moderate dry
0.99–0	Mild wet	0–0.2	Dry	<20	Severely drought	≤−0.2	Extreme dry
0–0.99	Mild dry	<0	Extremely dry	<10	Extremely drought		
−1.00––1.49	Moderate dry	–	–	–	–		
−1.5––1.99	Severe dry	–	–	–	–		
−2 and less	Extreme dry	–	–	–	–		

13.3.1.3 TCI

TCI is an index used to estimate vegetation stress affected by temperature and stress caused by extreme amount of wetness. They are determined relating to maximum value and minimum value of temperature. The unfavorable conditions are denoted by high temperature, while the favorable situation is shown by low temperature. The expression of *TCI* is given in Eq. 13.3:

$$TCI_j = \frac{(LST_{max} - LST_j)}{(LST_{max} - LST_{min})} * 100 \qquad (13.3)$$

where *LST* is land surface temperature. LST_{max} and LST_{min} values are based on the long-term record of remote sensing images during a specific time period *j*. The range of *TCI* value is given in Table 13.1.

13.3.1.4 VCI

VCI is used to identify drought conditions and to assess the outbreak of drought particularly in regions where drought events are confined and imprecise. It provides details on the beginning, extent, and the intensity of drought based on the vegetation alterations and compared them to historical values. The formula used to compute *VCI* is shown in Eq. 13.4:

$$VCI = \frac{NDVI_j - NDVI_{min}}{NDVI_{max} - NDVI_{min}} \qquad (13.4)$$

where $NDVI_j$ is the image of $NDVI$ value for a particular month/year. $NDVI_{max}$ and $NDVI_{min}$ are the maximum and minimum value of $NDVI$ from all the image within the data set. The range of VCI value is given in Table 13.1.

13.3.1.5 VHI

VHI shows the extent of the drought based on the condition of the vegetation health and the impact of temperature on plant condition. A decline in VHI signifies poor vegetation condition and rising temperature, which implies stressed vegetation health, and an extended length of time would be a sign of drought. VHI is given in Eq. 13.5

$$VHI = a * VCI + (1 - a) * TCI \qquad (13.5)$$

where $a = 0.5$. The range of VHI value is given in Table 13.1.

13.3.1.6 Deviation NDVI

On the other end of the spectrum, wetness intensity can be described as the $NDVI$ deviation (Dev_{NDVI}) from its long-term mean. The difference between the long-term $NDVI$ for that particular month and the current time's $NDVI$ is used to calculate this deviation. It is expressed in Eq. 13.6.

$$Dev_{NDVI} = NDVI_j - NDVI_{mean} \qquad (13.6)$$

where $NDVI_j$ is the image of $NDVI$ value for a particular month/year and $NDVI_{mean}$ is the mean value of $NDVI$ from the entire image within the data set. The range of Dev_{NDVI} value is given in Table 13.1.

13.3.2 Materials Required

The data required with spatial and temporal resolution for this study and their sources are given in Table 13.2.

Table 13.2 Data source used in the study

Sl. No.	Data	Source	Resolution (spatial/temporal)	Extracted data type
1.	STRM DEM	USGS, Earth Explorer	Spatial (30 m resolution)	Slope
3.	Landsat 7/8	USGS, Earth Explorer	Temporal (2013–2021)	NDVI
4	LST	MODIS	Temporal (2013–2021)	TCI
4.	Meteorology	DoECC, Manipur	Temporal (2013–2021)	Rainfall and Temperature
5.	District Map of Manipur	MARSAC, Manipur	Spatial (30 m resolution)	District Map of Thoubal
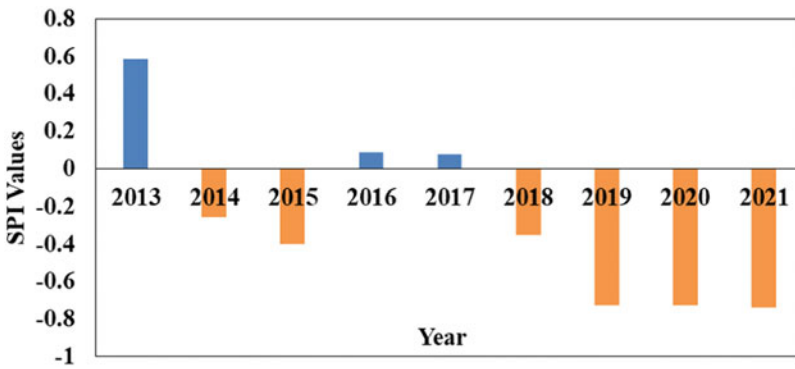
Fig. 13.4 *SPI* values (2013–2021)

13.4 Results

In this section, understanding how rainfall deviations, vegetation density, and temperature are determined and how drought indices like *SPI*, *NDVI*, and *TCI* behave during the study period were analyzed.

13.4.1 Drought Assessment

13.4.1.1 SPI Map

The annual *SPI* value (2013–2021) was examined to demonstrate the spatial pattern during these years. Fig. 13.4 illustrated *SPI* for Thoubal district. IDW approach was used to interpolate the obtained *SPI* value in order to determine the drought zone (Fig. 13.5a–i). There is no sign of drought in 2013 and 2017 as the *SPI* value of 2013 and 2017 lies between the range of 0–0.99, which is a sign of mild wet as shown in
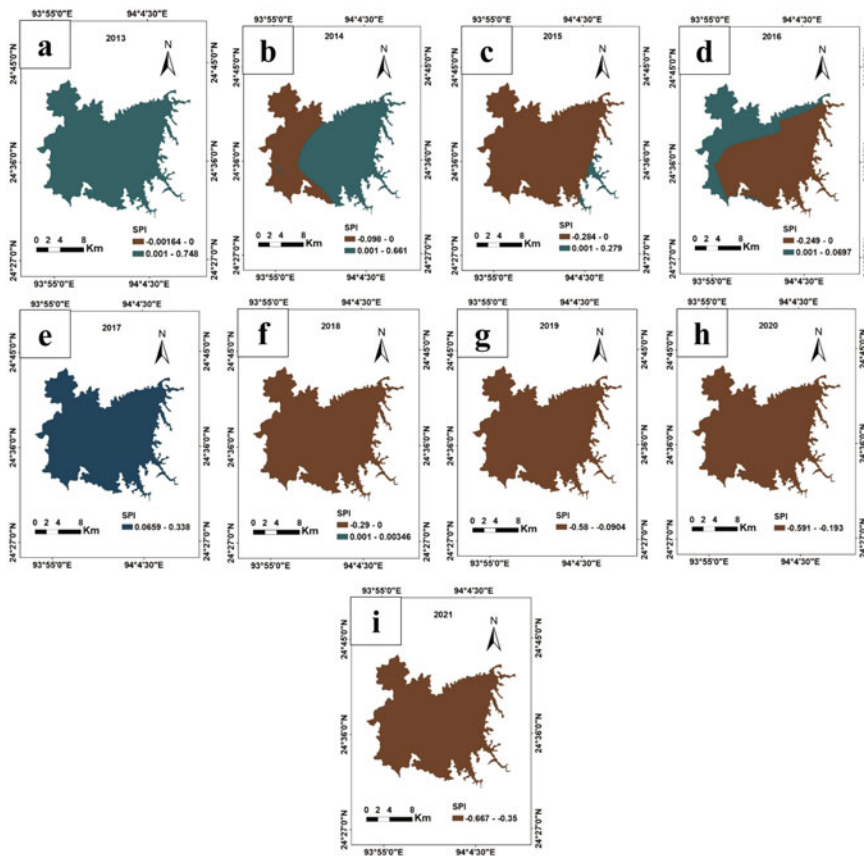
Fig. 13.5 (**a–i**) *SPI* map (2013–2021)

Fig. 13.5a and e. While in 2014 and 2016, some region of Thoubal district face mild wet, and some region face mild drought as shown in Fig. 13.5b and d. In the past 4 years, that is, 2018, 2019, 2020, and 2021, Thoubal district faced mild drought as shown in Fig. 13.5f–i.

13.4.1.2   NDVI

After analyzing the result of *NDVI* (Fig. 13.6) from Landsat-8 image for the month of November (2013–2021), it was found out that in the year 2013, 2019, 2020, and 2021, the *NDVI* value is mostly in the range of 0–0.2, which indicates moderate condition as per the drought indices value provided in Table 13.1. The years 2014, 2015, 2016, and 2018 exhibited mixed conditions with only 2017 showing a noticeable difference, ranging from 0.2 to 0.4 and a greater than 0. It indicates that some parts are extremely dry, and some areas are in moderate condition.
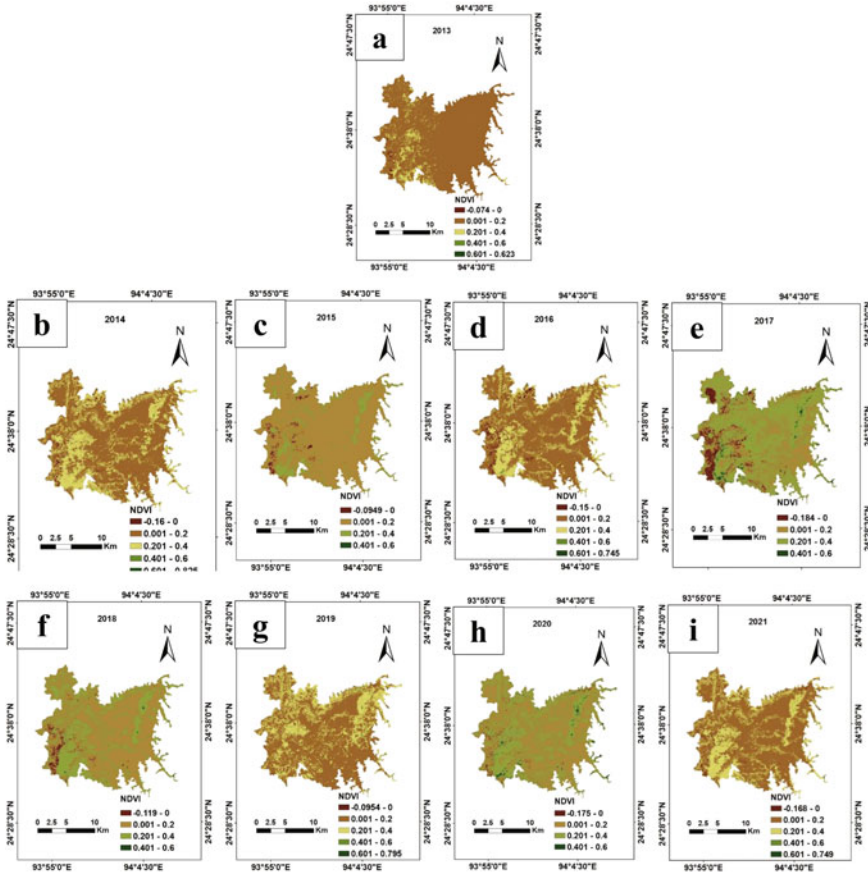
Fig. 13.6 (**a–i**) *NDVI* map (2013–2021)

13.4.1.3   TCI

After analyzing the results of *TCI* derived from MODIS data, as shown in Fig. 13.7, it was found that in the years 2013, 2014, 2015, 2017, 2018, and 2021, the values mostly fell within the range of no drought as indicated in Table 13.1. In 2019, some parts of the study area do not have a data, and in 2018 and 2020, it was found out that there is a mix situation among no drought, mild drought, moderate drought, severely drought, and extreme drought.

13.4.1.4   VCI

The occurrence of drought was examined from 2013 to 2021 using *VCI*, which indicates vegetation condition at a specific period comparing to its best and the worst
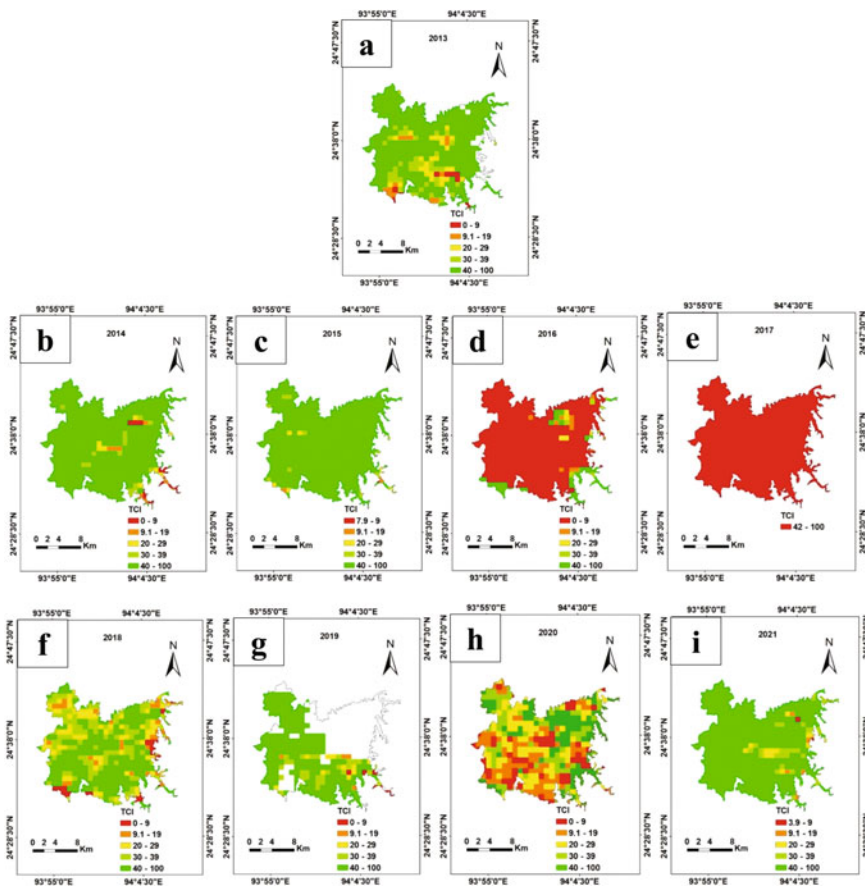
Fig. 13.7 (**a–i**) *TCI* map (2013–2021)

condition. The result of this study shows that in the years 2014, 2018, 2020, and 2021, there were no drought cases as the majority of the *VCI* values of the district lies between 41 and 100, and in 2015, 2016, and 2019, there is a mixed condition. In 2017, some small regions in western part of the district are under extreme drought, while the remaining parts of the district are in no drought condition. In the year 2013, majority of the area faces extreme drought cases where the *VCI* value is between 0 and 10 (Fig. 13.8).

13.4.1.5 *Dev*$_{NDVI}$

The results of drought risk assessment using deviation *NDVI* (*Dev*$_{NDVI}$) from 2013 to 2021 have found that in the years 2014, 2015, 2016, 2018, 2020, and 2021, there was near normal condition of drought (−0.049 to 0.1), and in 2017 and 2019, there is
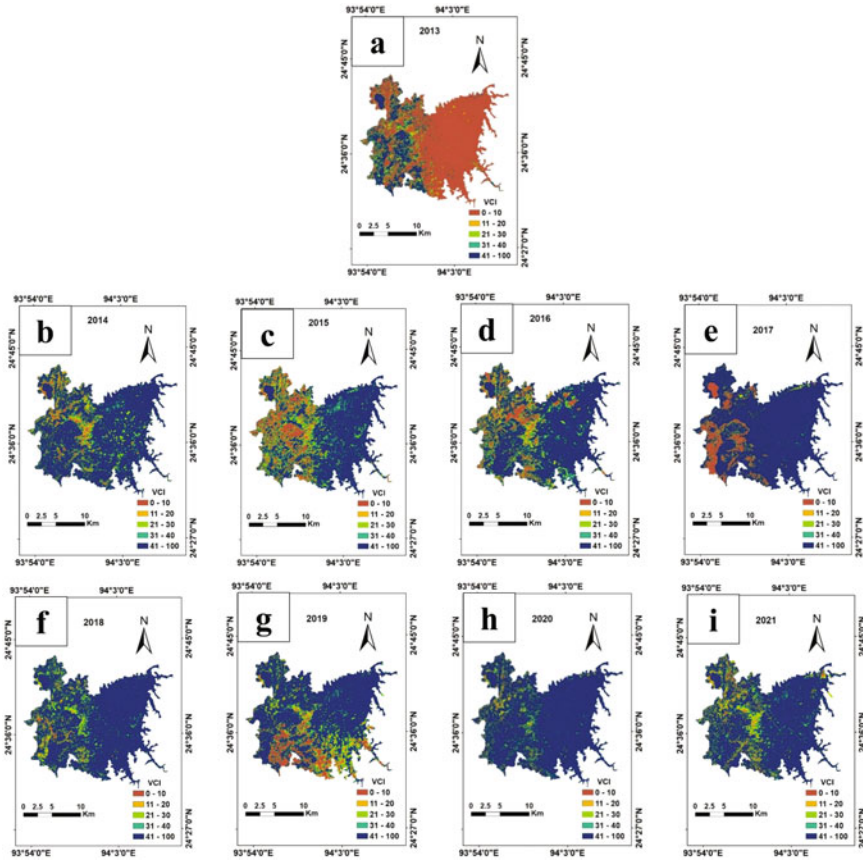
Fig. 13.8 (**a–i**) *VCI* map (2013–2021)

a kind of a mix situation having moderate drought to extreme wet condition. While in the year 2013, majority of the study area experiences moderate drought where the value lies between −0.19 and −0.05, and some regions in western side have near normal condition (Fig. 13.9).

13.4.1.6 VHI

After analyzing the *VHI* data from 2013 to 2021, the results indicate that the no drought conditions dominate over other drought conditions in the years 2014, 2015, 2017, 2018, 2019, 2020, and 2021 where the *VHI* values range between 41 and 100. In 2013, there is a mix situation between moderate to no drought conditions, while in 2016, the western region of the study area experienced extreme drought, and majority of the eastern region faces moderate to extreme drought conditions where the value lies between 0 and 30 (Fig. 13.10).
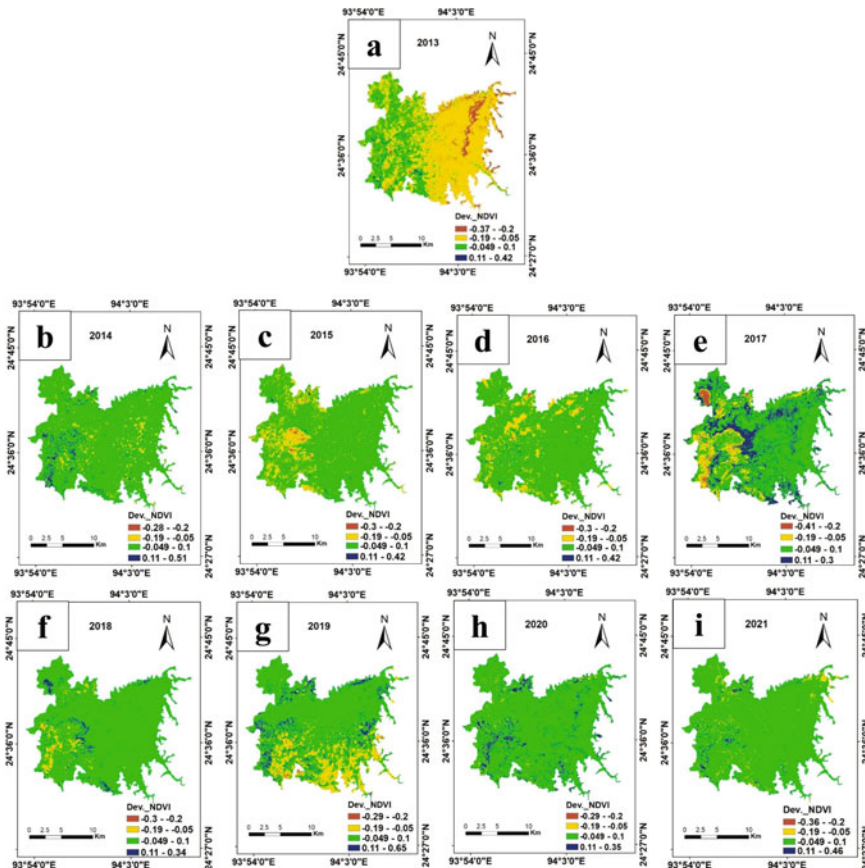
Fig. 13.9 (**a–i**) Dev_{NDVI} map (2013–2021)

13.4.2 Overlay Analysis

For a period of 9 years (2013 to 2021) and through weighted overlay analysis combining *SPI*, *NDVI*, *VHI*, and Dev_{NDVI} thematic layers, the final map for each year (Fig. 13.8) is calculated. In the overlay analysis, *SPI* is given as 40% weight, *NDVI* as 30%, *VHI* as 20%, and Dev_{NDVI} as 10% (Aziz et al. 2018). It is observed that from 2013 to 2014, the district can be divided into two categories, namely, near normal condition and moderate dry condition. In 2013, the western part of the district is in near normal, and majority of the eastern region is in moderate dry condition, while in 2014, the western part is moderate dry, and the eastern region is in near normal condition. In 2017, the whole district receives sufficient rainfall and is in near normal condition. For the years 2015, 2016, 2018, 2019, 2020, and 2021, the district is in moderate dry arising a drought-like condition (Fig. 13.11).
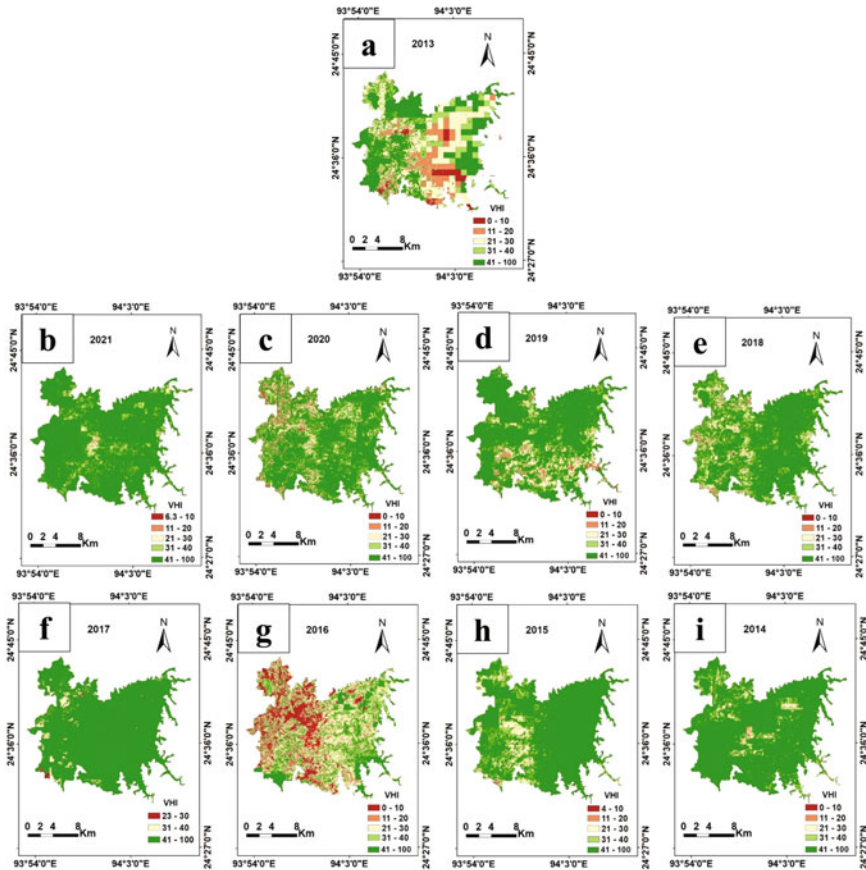
Fig. 13.10 (**a**–**i**) *VHI* map (2013–2021)

13.5 Validation

The predicted drought has been compared with the ground data values, which have been taken from the Department of Agriculture, Government of Manipur, as shown in Fig. 13.12. A survey has also been done in various parts of the study area within the local community including locations such as Heirok Part-3 Ngarouthen, Heirok Part-2 Khunou, Langmeithet Mamang Leikai, Langmeithet Maning Leikai, and Ukhongshang Laikol leirak (local manes). In the survey, the first author interacted with several people whose profession is agriculture and who are also familiar with agricultural practices from several years. They have been asked about the difficulties faced during the farming season, which may be due to flood or drough-like situation, that is, scarcity available surface water (in the study region, main source of water for agriculture is only surface water) or excess water during growing season. After the survey has been conducted, it was found out that in the years 2015, 2016, 2018,
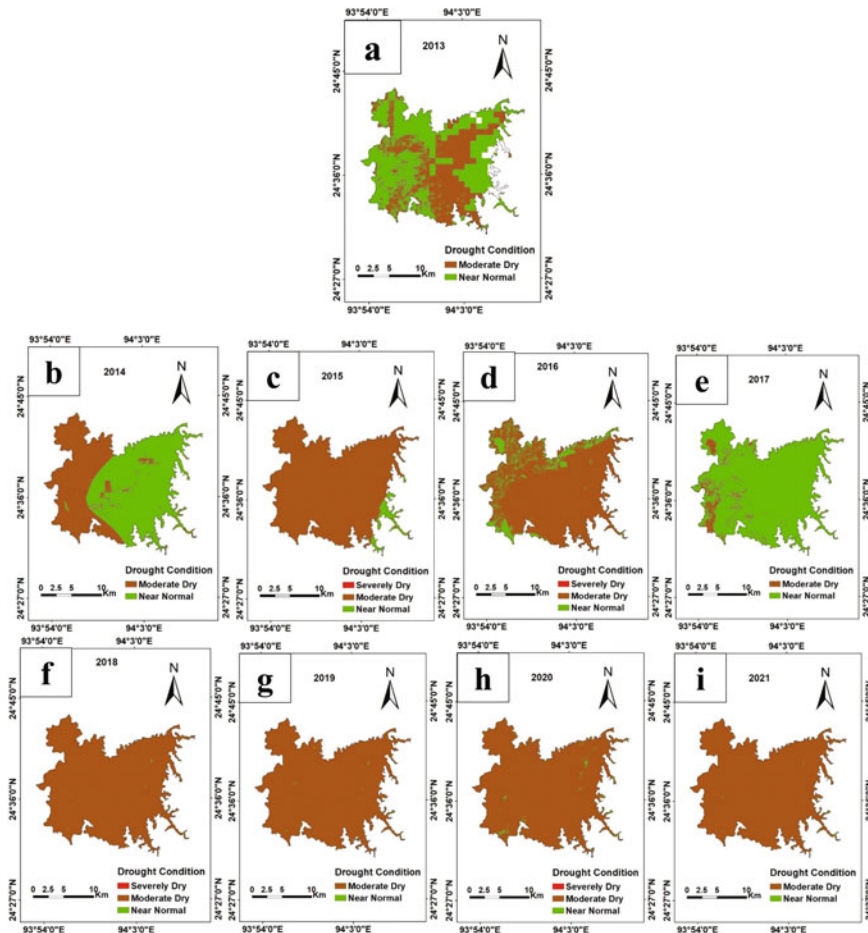
Fig. 13.11 (**a–i**) Drought analysis map (2013–2021)

2019, 2020, and 2021, a drought-like situation was witnessed in the study region, while in the year 2017, the whole district receives sufficient amount of rainfall and is in near normal condition. Such findings are also matched with present study of predicted drought-affected zone in a particular year, which is evident in Fig. 13.12. In the year 2017, crop production is high as per collected ground data, and there is highest area of near normal as per prediction; thus, this graph follows the pattern of high crop production in low drought prediction in the years 2013, 2015, and in 2017. But in the year 2019, crop production is low, and there is also low drought prediction. So, it may be due to other factors that the crop production is low and is not necessarily due to drought. And in the year 2020, drought prediction is comparatively high, but crop production is also high, and this is the exception in the results of this drought prediction study.
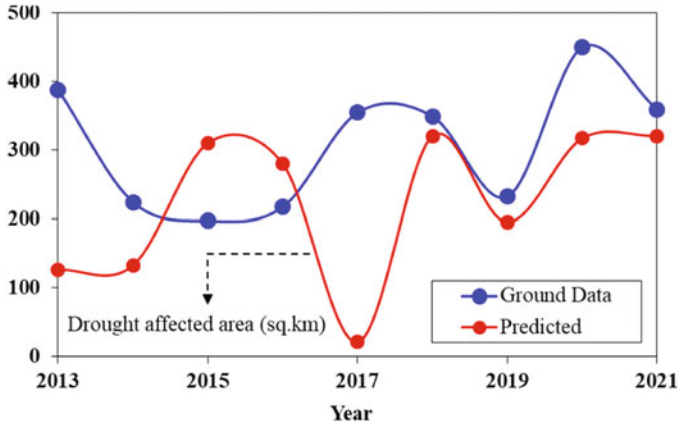
Fig. 13.12 Crop production (ground data) in drought-affected areas (predicted result)

13.6 Discussion

The drought monitoring tools and indices play an important role in executing drought conditions, and the use of GIS and remote sensing is recommended as they make it accessible to examine the data for reachable and inaccessible regions. The study shows that remote sensing and meteorological drought indices were able to indicate drought events. The drought events were determined by considering various drought indicators like *SPI*, *NDVI*, *TCI*, *VCI*, *VHI,* and *Dev*$_{NDVI}$. According to *SPI*, the rainfall of the district varies spatially and temporarily, and the highest rainfall was recorded in 2017, while the least was in 2016. In addition to this, *TCI* derived from MODIS was examined, and it was found that there is a mix of situations among no drought, mild drought, severe drought, and extreme drought. Furthermore, several studies of *NDVI* were conducted to detect and assess agricultural drought. *NDVI* is one of the most commonly used remote sensing indices to detect and quantify the presence of greenness and vegetation density. It is derived from satellite images and based on the intensities of light reflected in the near-infrared (NIR) and red (RED) ranges. In the year 2013, the district had the minimum density of vegetation coverage, or sparse vegetation, while in the year 2017, the district indicated the densest vegetation coverage, signifying sufficient precipitation occurred. Lastly, *NDVI* is recommended for global agricultural drought monitoring as it helps monitor changes in lighting conditions, surface slopes, and many other factors. The *NDVI* is used in the calculation of *VCI*, which contrasts the *NDVI* with the range of values seen during the same time period in previous years. It is applicable for the evaluation of vegetation stress and the study of vegetation reactions. From the *VCI* results, it was found out that in 2013, the majority of the area faced extreme drought cases where the *VCI* values were between 0 and 10. The *VHI* displays the amount of moisture and the temperature or thermal condition of vegetation as calculated using *VCI* and *TCI*.

From the results of *VHI,* it was found that there were no other drought conditions in the years 2014, 2015, 2017, 2018, 2019, 2020, and 2021, while in 2016, the western part of the study area experienced extreme drought, and the majority of the eastern region faced moderate to extreme drought conditions. From the results of $Dev_{\text{NDVI in 2013,}}$ the majority of the study area experienced moderate drought. The output from the above study displays that the Thoubal district faced drought-like conditions in the years 2018, 2019, 2020, and 2021, while in the year 2017, the district received sufficient amounts of precipitation with a maximum density of vegetation. More than 70% of the population is directly or indirectly engaged in agricultural activities. Therefore, analyzing and studying the changes in hydrological extremities is very important. After analyzing the study area using drought indices for the past 9 years, it was found out that Thoubal District is a prevailing area of drought, so proper planning of water resource management is needed. The irrigation system needs to be well planned, and regular maintenance is needed for those areas in which irrigation systems are already provided. Farmers can adopt sustainable practices such as using drought-resistant crops, implementing efficient irrigation techniques, and practicing soil conservation. Raise awareness through programs with the help of local clubs and governments.

13.7   Future Scope

Drought is a natural disaster that affects many parts of the world, and its impact is expected to increase due to climate change. Drought indices are used to quantify drought severity and assess its impacts on water resources, agriculture, and other sectors. With the availability of satellite data and advances in remote sensing technology, there are many opportunities to improve drought modeling using drought indices such as the following:

1. By developing new and improved drought indices that can capture the complexity of drought processes. For example, current drought indices mainly rely on precipitation and temperature data, but there are other factors such as soil moisture, vegetation cover, and evapotranspiration that can affect drought severity. Developing new indices that incorporate these factors could improve the accuracy of drought modeling.
2. By improving the spatial resolution of drought modeling using drought indices. Most current drought indices are based on large-scale data, such as weather station observations or satellite data with coarse spatial resolution. However, with the availability of high-resolution satellite data, it is possible to develop drought indices at a finer spatial scale, which can be useful for local decision-making.
3. Finally, future research could focus on integrating drought modeling with decision support systems. Drought is a complex phenomenon that affects multiple sectors, and decision-making requires the integration of different sources of

information. By integrating drought modeling with decision support systems, stakeholders can make informed decisions on water allocation, crop management, and other aspects of drought management.

13.8   Conclusion

Thoubal district faced drought like conditions in the years 2018, 2019, 2020, and 2021, while in 2017, the district receives sufficient amount of precipitation with maximum density of vegetation. Among the studied indices, *NDVI* is recommended for global agricultural drought monitoring as it helps to change in lighting conditions, surface slopes, and many other factors. More than 70% of the population is directly or indirectly engaged in agricultural activities and therefore more focused, and studies on agricultural drought in this region are needed. Specifically for the study region, it is suggested to construct bore-wells, which can be effectively used as an alternate source of water for various purposes, including small-area farming of crops. It is also important to note that surface water is the only and widely used source of water in this region, which indicates the high potential of using groundwater as another source, especially during drought-like situations.

References

Abuzar MK, Mahmood AS, Sarwar F, Saleem AR, Khubaib N, Malik AH, Khalil T, Shaista S (2017) Drought risk assessment using GIS and remote sensing: a case study of District Khushab, Pakistan. In proceedings: 15th International Conference on Environmental Science and Technology, Rhodes, Greece, 31 August - 2 September 2017

Aziz A, Umar M, Khan MS, Javed MN, Gao H, Mansha M, Farhan SB, Iqbal I, Abdullah S (2018) Assessment of drought conditions using HJ-1A/1B data: a case study of Potohar region, Pakistan. Geomatics Nat Hazards Risk 9(1):1019–1036

Berhan G et al (2011) Using satellite images for drought monitoring: a knowledge discovery approach. J Strateg Innov Sustain 7:135–153

Bhuiyan C, Singh RP, Kogan FN (2006) Monitoring drought dynamics in the Aravalli Region (India) using different indices based on ground and remote sensing data. Int J Appl Earth Obs Geoinf 8(2):289–302

Bond NR, Lake PS, Arthington AH (2008) The impacts of drought on freshwater ecosystems: an Australian perspective. Hydrobiologia 600:3–16. https://doi.org/10.1007/s10750-008-9326-z

Das J, Umamahesh NV (2022) A non-stationary based approach to understand the propagation of meteorological to agricultural droughts. Water Resou Manag. https://doi.org/10.1007/s11269-022-03297-9

Das S, Das J, Umamahesh NV (2021a) Nonstationary modeling of meteorological droughts: application to a region in India. J Hydrol Eng 26(2):05020048

Das S, Das J, Umamahesh NV, N.V. (2021b) Identification of future meteorological drought hotspots over Indian region: a study based on NEX-GDDP data. Int J Climatol 41(12): 5644–5662

Das J, Manikanta V, Umamahesh NV (2022a) Population exposure to compound extreme events in India under different emission and population scenarios. Sci Total Environ 806:150424

Das S, Das J, Umamahesh NV (2022b) Investigating seasonal drought severity-area-frequency (SAF) curve over Indian region: incorporating GCM and scenario uncertainties. Stoch Env Res Risk A 36(6):1597–1614

Das S, Das J, Umamahesh NV (2022c) Investigating the propagation of droughts under the influence of large-scale climate indices in India. J Hydrol 610:127900

Gao M, Knobelspiesse K, Franz BA, Zhai P-W, Martins V, Burton SP, Cairns B, Ferrare R, Fenn MA, Hasekamp O, Hu Y, Ibrahim A, Sayer AM, Werdell PJ, Xu X (2021) Adaptive data screening for multi-angle polarimetric aerosol and ocean color remote sensing accelerated by deep learning. Front Remote Sens 2:757832. https://doi.org/10.3389/frsen.2021.757832

Goyal MK, Sharma A (2016) A fuzzy c-means approach regionalization for analysis of meteorological drought homogeneous regions in western India. Nat Hazards 84:1831–1847

Gupta LK, Pandey M, Raj PA, Shukla AK (2023) Fine sediment intrusion and its consequences for river ecosystems: a review. J Hazard Toxic Radioact Waste. 27(1):04022036. https://doi.org/10.1061/(ASCE)HZ.2153-5515.0000729

Hammouri N, El-Naqa A (2007) Drought assessment using GIS and remote sensing in Amman-Zarqa basin, Jordan. Jordan J Civil Eng 1(2):142–152

Ihinegbu C, Ogunwumi T (2022) Multi-criteria modelling of drought: a study of Brandenburg Federal State, Germany. Model Earth Syst Environ 8:2035–2049. https://doi.org/10.1007/s40808-021-01197-2

Kloos S, Yuan Y, Castelli M, Menzel A (2021) Agricultural drought detection with MODIS based vegetation health Indices in Southeast Germany. Remote Sens 13:3907. https://doi.org/10.3390/rs13193907

McKee TB, Doesken NJ, Kleist J (1993) The relationship of drought frequency and duration to time scales. In the proceedings of the Eighth Conference on Applied Climatology, pp 179–184, California. American Meteorological Society, Boston, MA. 17–22 January 1993

Mosley LM (2015) Drought impacts on the water quality of freshwater systems; review and integration. Earth Sci Rev 140:203–214. https://doi.org/10.1016/j.earscirev.2014.11.010

Orimoloye IR (2022) Agricultural drought and its potential impacts: enabling decision-support for food security in vulnerable regions. Front Sustain Food Syst 6:838824. https://doi.org/10.3389/fsufs.2022.838824

Patil AS, Patil AA, Patil SP, Saundade SD, Chugule KA, Katavare SB, Panhalkar SS (2021) Analysis of the agriculture drought severity and spatial extent using Vegetation Health Index (VHI) in Manganga watershed of Maharashtra. India Disaster Adv 14(2):36–47

Purohit SK, Panigrahi S, Sethy PK, Behera SK (2021) Time series forecasting of price of agricultural products using hybrid methods. Appl Artif Intell 35(15):1388–1406. https://doi.org/10.1080/08839514.2021.1981659

Rawat S, Ganapathy A, Agarwal A (2022) Drought characterization over Indian sub-continent using GRACE-based indices. Sci Rep. 12(1):15432

Saikumar G, Pandey M, Dikshit PKS (2022) Natural river hazards: their impacts and mitigation techniques. In: River dynamics and flood hazards: studies on risk and mitigation. Springer, Singapore, pp 3–16

Sharma A, Goyal MK (2020) Assessment of drought trend and variability in India using wavelet transform. Hydrol Sci J 65(9):1539–1554

Singh NM, Devi TT (2022) Assessment and Identification of Drought Prone Zone in a Low Laying Area by AHP And MIF Method: A GIS Based Study. IOP Conf. Series: Earth and Environmental Science; pp 1–12

Temesgen B, Mohammed M, Korme T (2001) Natural hazard assessment using GIS and remote sensing methods, with particular reference to the landslides in the Wondogenet Area, Ethiopia. Phys Chem Earth Part C Sol Terr Planetary Sci 26(9):665–675

Wu D, Li Y, Kong H, Meng T, Sun Z (2021) Scientometric analysis-based review for drought modeling, indices, types, and forecasting especially in Asia. Water 13(18):2593. https://doi.org/10.3390/w13182593

Yin Y, Zhang X, Lin D, Yu H, Wang J, Shi P (2014) GEPIC-VR model: a GIS-based tool for regional crop drought risk assessment. Agric Water Manag 144:107–119. https://doi.org/10.1016/j.agwat.2014.05.017

Zhang Y, Xie D, Zhao WH, Geng S, Lu H, Ma G, Huang J, Sian KTCLK (2023) Construction of an integrated drought monitoring model based on deep learning algorithms. Remote Sens 15(3): 667. https://doi.org/10.3390/rs15030667

Zhao Y, Zhang J, Bai Y, Zhang S, Yang S, Henchiri M, Seka AM, Nanzad L (2022) Drought monitoring and performance evaluation based on machine learning fusion of multi-source remote sensing drought factors. Remote Sens 14:6398. https://doi.org/10.3390/rs14246398

Chapter 14
Copula-Based Probabilistic Evaluation of Meteorological Drought Characteristics over India

Vikas Poonia, Lixin Wang, and Manish Kumar Goyal

Abstract This chapter describes the applicability of copula-based probabilistic methodology to model the dependence structure among drought characteristics for meteorological drought in India. The Plackett, Frank, and Gumbel copulas were used across 1162 pixels across 24 Indian river basins. We then analyzed the joint dependence of drought characteristics to extract significant features such as return periods and exceedance probability, which could be beneficial for the effective management and planning of water resource systems. Our findings suggest that drought events across Central and Western part of the country are severe and longer, whereas river basins in Southern part experience droughts more frequently but with low severity. The outcomes of this research offer crucial insights into the drought hotspots with longer and severe drought events across the study area and thus provides useful insights for policymakers to formulate comprehensive national-level drought mitigation and prevention strategies to safeguard the sustainable ecosystem.

Keywords Drought · Duration · Probabilistic approach · Severity · SPI

14.1 Introduction

Drought is an extreme and recurrent climate disaster that happens due to abnormal deficiency in precipitation (Das et al. 2022a; Huang et al. 2014; Wilhite 2000a, 2000b; Zhang and Zhang 2016) leading to significant losses in terms of economy, ecology, environment, and people, for example, forest fires, crop losses, desertification, and ecological degradation (Poonia et al. 2022; Yuan et al. 2017). Droughts are

V. Poonia (✉) · L. Wang
Department of Earth Sciences, Indiana University-Purdue University Indianapolis (IUPUI), Indianapolis, IN, USA

M. K. Goyal
Department of Civil Engineering, Indian Institute of Technology Indore, Indore, India

a prevalent occurrence, affecting over 50% of the Earth's surface (Kogan 1997). It is considered one of the most expensive natural disasters globally, causing an average of 6–8 billion USD in damages (Keyantash and Dracup 2002; Saikumar et al. 2022; Soľáková et al. 2014; Wilhite 2005). Compared to other natural disasters, drought has a much larger spatial extent, leading to significantly higher damages (Das et al. 2022b; Xu et al. 2015b). Drought is described as the most unpredictable and least understood natural disaster (Hagman 1984). There is no universal definition for drought (Wilhite 2000a, 2000b), and its definition varies regionally, exhibiting variations in climatic characteristics and integrating various socioeconomic, physical, and biological variables (Zeleke 2017). Due to its complex nature, drought is typically classified into three main categories: meteorological, agricultural, and hydrological droughts (Mishra and Singh 2010). However, in drought monitoring, the most emphasis is placed on meteorological drought, which refers to the absence or insufficiency of rainfall compared to long-term averages. Meteorological drought is the first to occur, and other two droughts are consequent to it. If the precipitation scarcity persists for an extended period, other forms of drought can occur subsequently, as noted by (Guo et al. 2017; Gupta et al. 2023; Purkayastha and Afzal 2022). Thus, this study is specifically focused on monitoring meteorological drought. The standardized precipitation index (SPI) is the most commonly used index among several meteorological drought indices due to its simplicity and flexibility, and it requires only precipitation as an input parameter (Mckee et al. 1993). In this study, the most widely used standardized precipitation index (SPI) is selected for drought characterization.

According to Mishra and Singh (2010), drought has a significant impact on various aspects over Asia, particularly in India, including the country's GDP, water availability, and food production. Thus, it is crucial to determine the frequency and severity of drought events that occur in India. Thus, it is crucial to determine the frequency and severity of drought events that occur in India. However, quantifying drought is challenging due to its elusive and complex behavior. Nonetheless, Dracup et al. (1980) have recognized two crucial characteristics of a drought event, namely, drought duration and drought severity. Since drought is a phenomenon that involves multiple variables; therefore, it is more appropriate to use multivariate techniques to model drought properties such as severity and duration. In the past, number of probabilistic techniques were used to analyze drought characteristics, but univariate analysis fails to reveal significant correlations. Therefore, a multivariate approach is recommended to develop a joint dependence that can describe the interconnections between different drought characteristics. However, most multivariate distributions are based on univariate approaches and have some drawbacks, such as the requirement for the marginal distributions to be identical (Salvadori and De Michele 2004). To address these drawbacks, the copula is appropriate approach for the multivariate analysis. Copula is a powerful tool that can combine multiple drought characteristics and has been found to be better to conventional multivariate approaches and become widely used in the field of hydrometeorology (Das and Das 2021; Guo et al. 2019; Hao and AghaKouchak 2013; Maeng et al. 2017; Sklar 1959a; b; Van de Vyver and Van den Bergh 2018). This allows for a more accurate representation of the

multivariate relationships between different variables. Many studies have demonstrated the effectiveness of copulas in studying hydro-climatic events, and detailed information can be found in these studies (Bisht et al. 2019; Goswami et al. 2018b; Jha et al. 2019). In this present study, we have chosen to use the copula-based approach instead of univariate analysis, and further details can be found in methodology section.

Both globally and in India, there has been an observed rise in drought events, with over one million square kilometers of India experiencing varying degrees of water stress and drought conditions (Mishra and Cherkauer 2010). To address this issue, several studies have utilized bivariate copulas to analyze drought frequency in some regions of India. Other studies, such as Xu et al., in 2015a,b, have focused on the variability of drought events in terms of their spatial and temporal aspects, with a focus on copula theory. In 2018, Goswami et al. conducted a drought characterization using copula approach for the Sikkim region of the Himalayas. Their findings indicated that extreme events are more likely to occur together in the future under different climatic scenarios. The impact of climate change on drought parameters, including severity and duration, can lead to non-stationarity, which may affect both drought vulnerability and resilience. In 2018, Sharma and Goyal investigated the impact of drought on ecosystem resilience over India. More recently, in 2019, Jha et al. employed a probabilistic approach based on copulas to forecast vegetation drought in India and evaluate vegetation resilience to disturbances. Das et al. (2020a; b) carried out a multivariate characterization of drought using copulas in the Himalayan states, allowing for a quantitative assessment of drought resilience. Bisht et al. (2019) showed that drought severity and duration in India would increase under changing climate scenarios. Therefore, there is an urgent need for an India-level multivariate drought characterization.

Numerous investigations using copulas have been conducted on the occurrence of drought in various areas of central and western India. However, since rainfall patterns are diverse across various regions of India, a thorough assessment of drought using copulas would require various marginal distributions. Consequently, the dependence structure between drought characteristics such as duration and severity would vary across different regions of the country. To facilitate effective drought mitigation strategies and risk management, a comprehensive nationwide drought investigation is required, including the computation of return periods. Thus, this study aims to investigate the dependence among meteorological drought characteristics in various regions of India using a multivariate approach. The study also conducts a comprehensive evaluation of drought risk on a national scale to calculate the return period and exceedance probability of meteorological droughts.

14.2   Study Area and Data Used

Climate change has a significant impact on river basins around the world, leading to changes in their ecosystems and water balance. The hydrological characteristics of a region play a critical role in how vegetation responds to climate instability, making it useful to assess river basins based on their vulnerability. Thus, for this study, the 24 major river basins in India were chosen as study area (Fig. 14.1). The Indian Meteorological Department (IMD4) provided monthly gridded precipitation data with a resolution of $0.5° \times 0.5°$ covering the period from 1982 to 2013. The IMD data was derived from daily precipitation data collected and has been used in several recent studies (Kumar et al. 2021; Poonia et al. 2021a, b; Das et al. 2020c; Shivam et al. 2019). IMD data is commonly used for drought analysis due to its ability to effectively capture the rainfall variability across the country, which makes it a more accurate dataset (Mishra and Liu 2014).

14.3   Methodology

The SPI is widely used as a meteorological drought index, and for this study, a 12-month time scale drought index based on SPI is utilized. The SPI-12 is preferred as it reflects long-term precipitation patterns and is commonly associated with reservoir, groundwater, and streamflow levels. As climatological and hydrological characteristics are mutually dependent, multivariate assessment is necessary to understand their dependence. Drought being a complex and multivariate extreme event, effective tools such as copulas are required to model its dependence characteristics. Therefore, a copula tool is employed in this analysis. Primarily, a trend analysis was conducted on drought severity and duration through MK Test using the
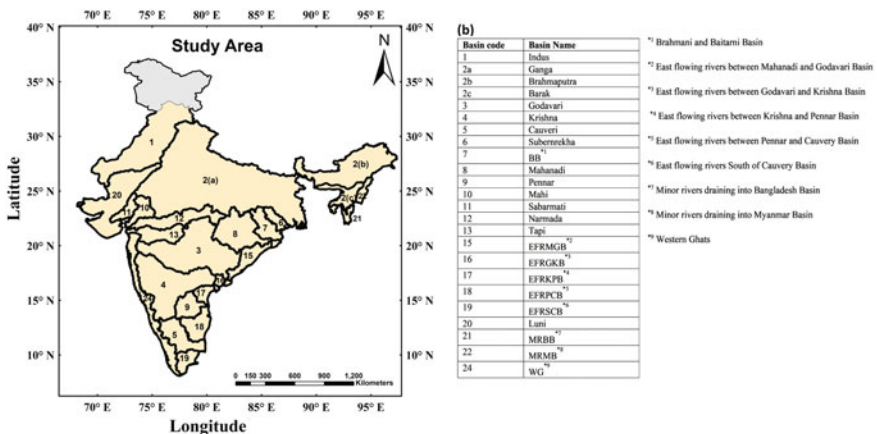
Fig. 14.1   River basins of India

MK test from 1982 to 2013. However, this trend analysis suggested that an additional efficient methodology is needed to fully understand the drought condition over India. Further, various copulas are employed and selected the best copula for each pixel across India (Goswami et al. 2018a). Finally, using different copulas, several bivariate probabilistic computations, such as joint return periods and exceedance probabilities, were examined.

14.3.1 Computation of Drought Properties and Trend Assessment

According to Shiau (2006), drought duration (d) is defined when the SPI consistently less than the specific threshold, that is, SPI equals to zero for a particular length of time, whereas severity (s) can be computed calculated by adding up the negative SPI values, that is, $s_n = \sum_{n=1}^{d} SPI_n$. The severity and duration of a drought event are determined by the same criteria as defined by Shiau (2006). For this study, the trend analysis was conducted to examine whether there is any monotonic trend in drought severity and duration utilizing MK trend analysis test.

14.3.2 Copula Modeling

It is crucial to recognize that the drought variables are interrelated, so relying merely on univariate analysis is insufficient to fully investigate drought. Therefore, this study incorporates bivariate analysis to assess the joint dependence among drought characteristics. The copula tool was utilized in this study, which offers a robust approach to construct a bivariate distribution. A theorem, proposed by Sklar in 1959a,b, states that a d-dimensional CDF can be computed as:

$$F(x_1, x_2 \ldots \ldots x_n) = C\big(F_1(x_1), F_2(x_2), F_3(x_3) \ldots . F_n(x_p)\big) \tag{14.1}$$

Three copulas named as Plackett, Frank, and Gumbel were selected for this analysis. These copulas offer numerous advantages, like model negatively and positively correlated variables and offer greater flexibility (Zhang and Singh 2007). Before modeling the joint distributions, it is crucial to determine the suitable marginal distribution of the data. For the present study, five marginals (lognormal, gamma, Weibull, exponential, and normal distributions) were fitted to the drought characteristics, and the best one was determined through KS test. Further, parameters for all three copulas were determined. The performance of each copula was evaluated using two indices, that is, AIC and BIC. These indices are commonly used to compare the model performance (Poonia et al. 2021c; Das et al. 2020b; Goswami

et al. 2018b). The joint dependence of different drought variables was assessed to determine useful properties such as return period and exceedance probability.

14.3.3 Probabilistic (Exceedance Probability) Assessment

The copula-based analysis of drought properties provides crucial information for drought management, such as the probability of both duration and severity of a drought simultaneously surpassing certain limits. In present study, exceedance probability (Eq. 14.2) was computed, which refers to the likelihood that both drought duration and severity surpass a specific threshold. Specifically, the exceedance probability was calculated at the 25th, 50th, 75th, and 95th percentile values of drought duration and severity for all basins.

$$F(D \geq d, S \geq s) = 1 - F_D(d) - F_S(s) + C(F_D(d), F_S(s)) \qquad (14.2)$$

14.3.4 Return Period Analysis

The return period is the average time between two successive drought events. In the univariate case, the return period of drought severity and drought duration can be computed using Eqs. 14.3 and 14.4, respectively, proposed by Shiau and Shen (2001):

$$T_S = \frac{E(L)}{1 - F_s(S)} \qquad (14.3)$$

$$T_D = \frac{E(L)}{1 - F_d(D)} \qquad (14.4)$$

where T_S and T_D are the expected return period of drought severity and duration, respectively. Also, E(L) is the anticipated drought interarrival time.

In this study, we have also computed the bivariate return period T_{DS} (duration and severity surpassing a certain threshold) as given by Shiau (2006) (Eq. 14.5):

$$T_{DS} = \frac{E(L)}{P(D \geq d, \quad S \geq s)} = \frac{E(L)}{1 - F_D(d) - F_S(s) + C(F_D(d), F_S(s))} \qquad (14.5)$$

14.4 Results and Discussion

14.4.1 Drought Properties and Trend Assessment

Prior to undertaking probabilistic computation, we first calculated the average drought variables, namely, severity and duration, obtained from observed meteorological droughts (Fig. 14.2).

Our investigation revealed that the average drought duration and severity are more prominent over Eastern India. Our preliminary examination indicates that assessing drought characteristics based solely on drought duration and severity may provide only limited information; thus, it would be more effective to employ multivariate technique. The lack of a significant trend in drought severity and duration (Fig. 14.3) suggests that the random fluctuations in drought characteristics make it challenging to explain their joint dependence structure. This further emphasizes the need for a more advanced methodology, such as copula analysis, to understand and manage drought across Indian river basins.

14.4.2 Bivariate Analysis of Probability

After obtaining the joint probabilities, the next step is to calculate exceedance probabilities by Eq. 14.5 for distinct severity and duration thresholds at each grid location across India. Fig. 14.4 demonstrates the exceedance probability for different drought properties where they simultaneously exceed different thresholds (25th,
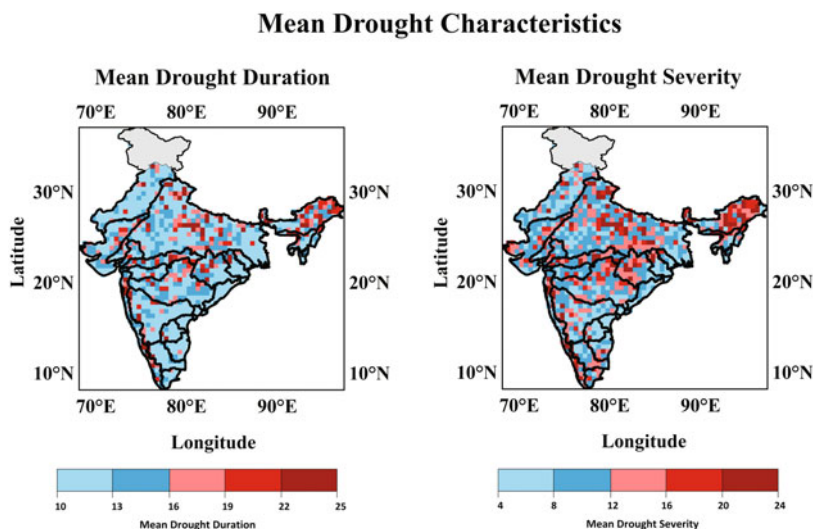
Fig. 14.2 Mean drought characteristics across Indian river basins from 1982 to 2013
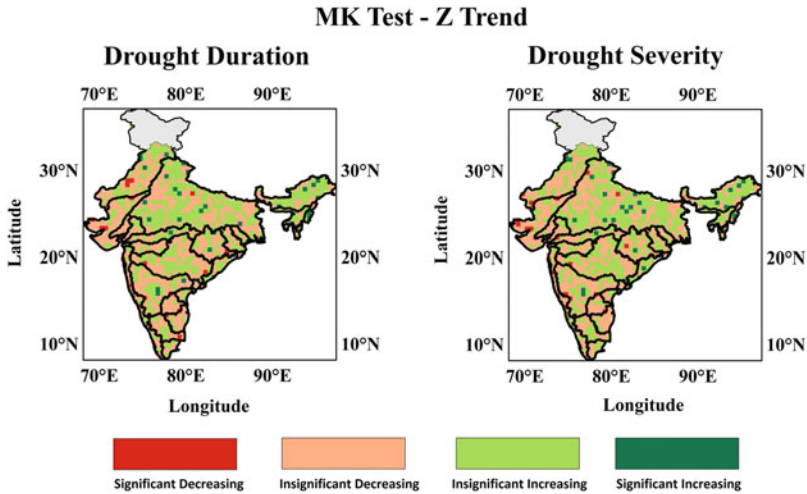
Fig. 14.3 Basin-wise trend assessment of drought characteristics from 1982 to 2013

50th, 75th, and 95th percentile). Here, we focus on the 50th percentile outcomes because it delivers more accurate finding. The findings indicate that the majority of the study area are prone to meteorological drought conditions. Thus, it implies that a shortage of precipitation poses a significant risk to these regions. In the lower exceedance probability scenario (25th percentile), almost the entire study area shows a high probability of meteorological drought. This could be attributed to the increase in average temperature and the decrease in seasonal and annual rainfall in recent years (Mallya et al. 2015). According to Niranjan Kumar et al. (2013), there has been a usual rise in the occurrence of meteorological droughts in modern time. Results suggest that simultaneous exceedance of drought characteristics is more useful than analyzing them separately. This is because the joint analysis provides a better understanding of the combined impact of duration and severity on drought occurrence, which can help in developing more effective drought management strategies. Therefore, it is important to consider both variables together when assessing the severity and duration of drought events.

14.4.3   Bivariate Analysis of Return Period

This part focuses on the calculation of the joint return period. Fig. 14.5 illustrates the joint return period for severity and duration at different percentile thresholds. The findings suggest that the regions of Eastern India (MRBB, Barak, and Brahmaputra) and Western India (Luni, Sabarmati, Mahi, and Tapi) have the longest return period for all thresholds. Longer drought inter-arrival times are related to extreme events with greater drought severity and duration. Additionally, Western Ghats, Narmada,

Exceedance Probability
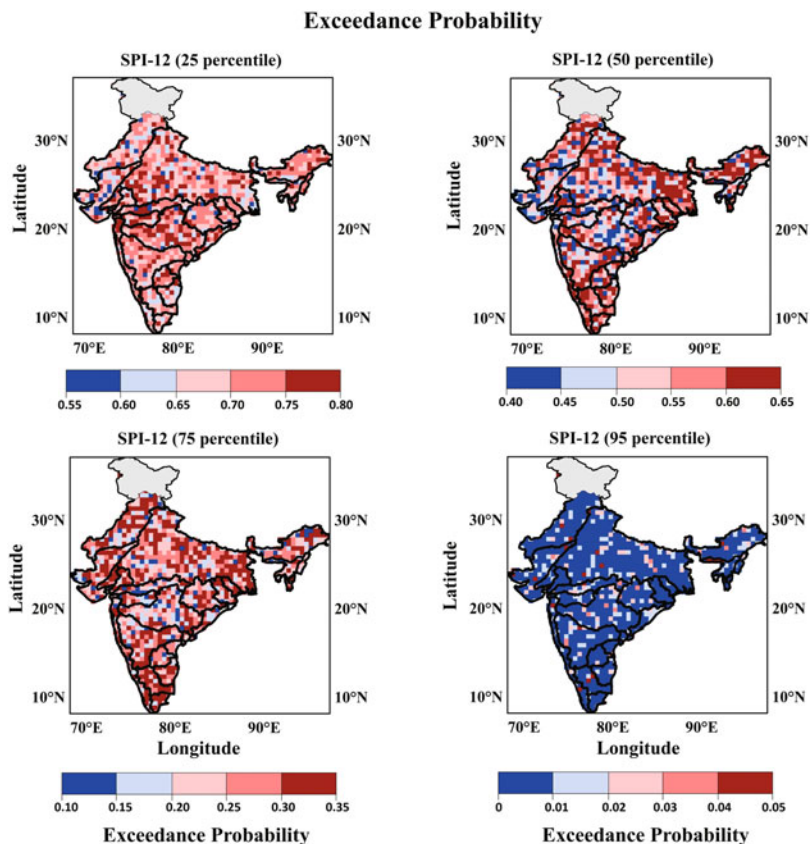
Fig. 14.4 Exceedance probabilities for drought characteristics (severity and duration) surpassing their different threshold values

and Indus also demonstrate the longest return period. The Western Ghats, in particular, has a longer return period due to its high rainfall, ecological diversity, and evergreen forests. Additionally, this part of the country is well recognized for its resilience to hydroclimatic disturbances, as noted in studies by Jha et al. (2019) and Sharma and Goyal 2018a, b. On the other hand, South Indian basins, such as Krishna, EFRPCB, and Cauveri, as well as BB and Sabarmati basins also demonstrate a lesser return period. The findings from Amrit et al. (2018) also support the shorter return period in Southern India, where frequent droughts occur every 5–6 years in a significant part of the region. The joint return period results can aid policymakers and stakeholders in formulating better drought management guidelines and designing water resource systems in drought-prone areas.

Joint Return Period
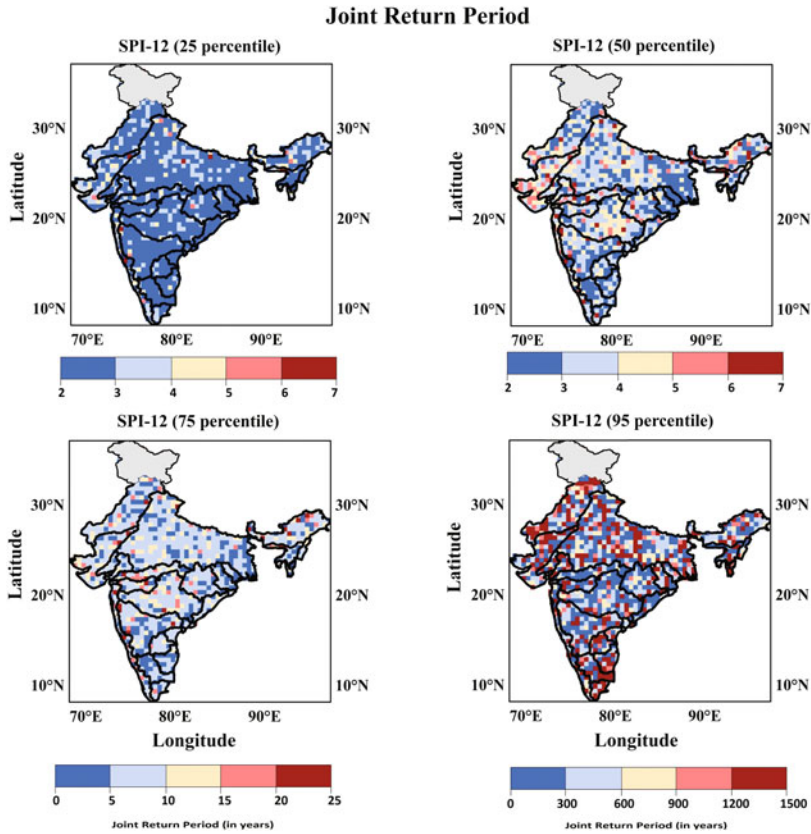
Fig. 14.5 Joint return period for drought characteristics (severity and duration) surpassing their different threshold values

14.5 Conclusion

The current research focuses on conducting a nationwide drought assessment of India during the period 1982–2013 by employing copula-based probabilistic model. We employ various copulas to determine the joint dependence among drought properties. From this, a joint PDF is constructed, which is further used to calculate exceedance probability as well as recurrence interval at different thresholds of drought properties. The research revealed that it is necessary to use different marginal distributions to model the drought characteristics for all 1162 grid points across India. It was also determined that only one copula model is inadequate to capture the joint dependence at higher levels; therefore, three copulas were employed in this analysis. To better understand the likelihood of drought occurrence, return period and exceedance probability analysis was carried out.

Our findings conclude that southern river basins are highly susceptible to drought. This is consistent with the results of Mallya et al. (2015), where they found a rise in drought occurrence in different regions across the country. Our analysis revealed that Southern River basins exhibit larger exceedance probability but lesser recurrence interval when compared to Western India. It implies that droughts are longer and severe in Central and Western River basins of India, while less severe and more frequent over Southern River basins of the country. The western India is more prone to drought due to scarce vegetation and are highly vulnerable to agricultural droughts, and this is consistent with the findings of Jha et al. (2019). Additionally, the river basins in Southern India situated over arid regions frequently experience droughts. Thus, our analysis suggests that droughts have a significant impact on India, particularly in the Western and Southern parts of the country. In this analysis, we have used bivariate copula, which was effective in exploring the interaction between drought duration and severity; however, it may be ineffective to capture the interactions between other properties. Hence, it is recommended to use trivariate copula in future drought research (Xu et al. 2015a). Overall, this analysis offers important information for policymakers and stakeholders in developing drought mitigation strategies at the national level, particularly in managing severe and longer drought events.

References

Amrit K, Pandey RP, Mishra SK, Kumre SK (2018) Long-term meteorological drought characteristics in Southern India. In: World Environmental and Water Resources Congress 2018. American Society of Civil Engineers, Reston, VA, pp 207–215. https://doi.org/10.1061/9780784481417.019

Bisht DS, Sridhar V, Mishra A, Chatterjee C, Raghuwanshi NS (2019) Drought characterization over India under projected climate scenario. Int J Climatol 39:1889–1911. https://doi.org/10.1002/joc.5922

Das S, Das J, Umamahesh NV (2021) Nonstationary modeling of meteorological droughts: application to a region in India. J Hydrol Eng 26:5020048

Das J, Jha S, Goyal MK (2020a) Non-stationary and copula-based approach to assess the drought characteristics encompassing climate indices over the Himalayan states in India. J Hydrol 580: 124356

Das J, Jha S, Goyal MK (2020b) On the relationship of climatic and monsoon teleconnections with monthly precipitation over meteorologically homogenous regions in India: Wavelet & global coherence approaches. Atmos Res 238:104889. https://doi.org/10.1016/j.atmosres.2020.104889

Das J, Poonia V, Jha S, Goyal MK (2020c) Understanding the climate change impact on crop yield over Eastern Himalayan Region: ascertaining GCM and scenario uncertainty. Theor Appl Climatol 142(1–2):467–482. https://doi.org/10.1007/s00704-020-03332-y

Das S, Das J, Umamahesh NV (2022a) Copula-based drought risk analysis on rainfed agriculture under stationary and non-stationary settings. Hydrol Sci J 67:1683–1701

Das S, Das J, Umamahesh NV (2022b) Investigating seasonal drought severity-area-frequency (SAF) curve over Indian region: incorporating GCM and scenario uncertainties. Stoch Environ Res Risk Assess. 36:1597–1614

Dracup JA, Lee KILE, Paulson EG (1980) On the Statistical Characteristics of Drought Events F ' kl 16: 289–296

Goswami UP, Bhargav K, Hazra B, Goyal MK (2018a) Spatiotemporal and joint probability behavior of temperature extremes over the Himalayan region under changing climate. Theor Appl Climatol 134:477–498. https://doi.org/10.1007/s00704-017-2288-1

Goswami UP, Hazra B, Goyal MK (2018b) Copula-based probabilistic characterization of precipitation extremes over North Sikkim Himalaya. Atmos Res 212:273–284. https://doi.org/10.1016/j.atmosres.2018.05.019

Guo H, Bao A, Liu T, Ndayisaba F, He D, Kurban A, De Maeyer P (2017) Meteorological drought analysis in the Lower Mekong Basin using satellite-based long-term CHIRPS product. Sustainability 9. https://doi.org/10.3390/su9060901

Guo Y, Huang S, Huang Q, Wang H, Wang L, Fang W (2019) Copulas-based bivariate socioeconomic drought dynamic risk assessment in a changing environment. J Hydrol 575:1052–1064. https://doi.org/10.1016/j.jhydrol.2019.06.010

Gupta LK, Pandey M, Raj PA, Shukla AK (2023) Fine sediment intrusion and its consequences for river ecosystems: a review. J Hazard Toxic Radioact Waste 27:4022036

Hagman G (1984) Prevention better than cure: report on human and natural disasters in the third world. Swedish Red Cross, Stockholm

Hao Z, AghaKouchak A (2013) Multivariate Standardized Drought Index: a parametric multi-index model. Adv Water Resour 57:12–18. https://doi.org/10.1016/j.advwatres.2013.03.009

Huang S, Hou B, Chang J, Huang Q, Chen Y (2014) Copulas-based probabilistic characterization of the combination of dry and wet conditions in the Guanzhong Plain. China J Hydrol 519:3204–3213. https://doi.org/10.1016/j.jhydrol.2014.10.039

Jha S, Das J, Sharma A, Hazra B, Goyal MK (2019) Probabilistic evaluation of vegetation drought likelihood and its implications to resilience across India. Glob Planet Change 176:23–35. https://doi.org/10.1016/j.gloplacha.2019.01.014

Keyantash J, Dracup JA (2002) The quantification of drought: an evaluation of drought indices. Bull Am Meteorol Soc 83:1167–1180. https://doi.org/10.1175/1520-0477(2002)083<1191:TQODAE>2.3.CO;2

Kogan FN (1997) Global Drought Watch from Space. Bull Am Meteorol Soc 78:621–636. https://doi.org/10.1175/1520-0477(1997)078<0621:GDWFS>2.0.CO;2

Kumar N, Poonia V, Gupta BB, Goyal MK (2021) A novel framework for risk assessment and resilience of critical infrastructure towards climate change. Technol Forecast Soc Change 165:120532. https://doi.org/10.1016/j.techfore.2020.120532

Maeng S, Azam M, Kim H, Hwang J (2017) Analysis of changes in spatio-temporal patterns of drought across South Korea. Water 9:679. https://doi.org/10.3390/w9090679

Mallya G, Mishra V, Niyogi D, Tripathi S, Govindaraju RS (2015) Trends and variability of droughts over the Indian monsoon region. Weather Clim Extrem 12:43–68. https://doi.org/10.1016/j.wace.2016.01.002

Mckee TB, Doesken NJ, Kleist J (1993) The relationship of drought frequency and duration to time scales. In AMS 8th Conference on Applied Climatology. American Metrological Society, Boston MA, pp 179–184. doi: citeulike-article-id:10490403

Mishra V, Cherkauer KA (2010) Retrospective droughts in the crop growing season: Implications to corn and soybean yield in the Midwestern United States. Agric For Meteorol 150:1030–1045. https://doi.org/10.1016/j.agrformet.2010.04.002

Mishra A, Liu SC (2014) Changes in precipitation pattern and risk of drought over India in the context of global warming. J Geophys Res-Atmos. https://doi.org/10.1002/2014JD021471

Mishra A, Singh V (2010) A review of drought concepts. J Hydrol 391:202–216. https://doi.org/10.1016/j.jhydrol.2010.07.012

Niranjan Kumar K, Rajeevan M, Pai DS, Srivastava AK, Preethi B (2013) On the observed variability of monsoon droughts over India. Weather Clim Extrem 1:42–50. https://doi.org/10.1016/j.wace.2013.07.006

Poonia V, Das J, Goyal MK (2021a) Impact of climate change on crop water and irrigation requirements over eastern Himalayan region. Stoch Environ Res Risk Assess 6. https://doi.org/10.1007/s00477-020-01942-6

Poonia V, Goyal MK, Gupta BB, Gupta AK, Jha S, Das J (2021b) Drought occurrence in Different River Basins of India and blockchain technology based framework for disaster management. J Clean Prod 312:127737. https://doi.org/10.1016/j.jclepro.2021.127737

Poonia V, Jha S, Goyal MK (2021c) Copula based analysis of meteorological hydrological and agricultural drought characteristics across Indian river basins. Int J Climatol 41(9):4637–4652. https://doi.org/10.1002/joc.v41.9 10.1002/joc.7091

Poonia V, Goyal MK, Jha S, Dubey S (2022) Terrestrial ecosystem response to flash droughts over India. J Hydrol 605:127402. https://doi.org/10.1016/j.jhydrol.2021.127402

Purkayastha S, Afzal MS (2022) Review of smooth particle hydrodynamics and its applications for environmental flows. J Inst Eng Ser A 103:921–941

Saikumar G, Pandey M, Dikshit PKS (2022) Natural river hazards: their impacts and mitigation techniques. In: River dynamics and flood hazards: studies on risk and mitigation. Springer, Cham, pp 3–16

Salvadori G, De Michele C (2004) Frequency analysis via copulas: theoretical aspects and applications to hydrological events. Water Resour Res 40:1–17. https://doi.org/10.1029/2004WR003133

Sharma A, Goyal MK (2018a) Assessment of ecosystem resilience to hydroclimatic disturbances in India. Glob Chang Biol 24:e432–e441. https://doi.org/10.1111/gcb.13874

Sharma A, Goyal MK (2018b) District-level assessment of the ecohydrological resilience to hydroclimatic disturbances and its controlling factors in India. J Hydrol 564:1048–1057. https://doi.org/10.1016/j.jhydrol.2018.07.079

Shiau JT (2006) Fitting drought duration and severity with two-dimensional copulas. Water Resour Manag 20:795–815. https://doi.org/10.1007/s11269-005-9008-9

Shiau JT, Shen HW (2001) Recurrence analysis of hydrologic droughts of differing severity. J Water Resour Plan Manag ASCE 127(1):30–40

Shivam G, Goyal MK, Sarma AK (2019) Index-based study of future precipitation changes over subansiri river catchment under changing climate. J Environ Informatics 34:1–14. https://doi.org/10.3808/jei.201700376

Sklar A (1959a) Fonctions de reprtition a n dimensions et leursmarges. Publ Inst Stat Univ Paris 8: 229–231

Sklar M (1959b) Fonctions de Répartition à n Dimensions et Leurs Marges. Publications de l'Institut Statistique de l'Université de Paris, pp 229–231

Soľáková T, De Michele C, Vezzoli R (2014) Comparison between parametric and nonparametric approaches for the calculation of two drought indices: SPI and SSI. J Hydrol Eng 19:04014010. https://doi.org/10.1061/(asce)he.1943-5584.0000942

Van de Vyver H, Van den Bergh J (2018) The Gaussian copula model for the joint deficit index for droughts. J Hydrol 561:987–999. https://doi.org/10.1016/j.jhydrol.2018.03.064

Wilhite DA (2000a) Chapter 1 drought as a natural hazard. Drought A Glob Assess, pp 147–162

Wilhite DA (2000b) Drought as a natural hazard: Concepts and definitions. In Drought: a global assessment, pp 3–18

Wilhite DA (2005) The role of disaster preparedness in national planning with specific reference to droughts. Springer, Cham

Xu K, Yang D, Xu X, Lei H (2015a) Copula based drought frequency analysis considering the spatio-temporal variability in Southwest China. J Hydrol 527:630–640. https://doi.org/10.1016/j.jhydrol.2015.05.030

Xu K, Yang D, Yang H, Li Z, Qin Y, Shen Y (2015b) Spatio-temporal variation of drought in China during 1961-2012: a climatic perspective. J Hydrol 526:253–264. https://doi.org/10.1016/j.jhydrol.2014.09.047

Yuan X, Zhang M, Wang L, Zhou T (2017) Understanding and seasonal forecasting of hydrological drought in the Anthropocene. Hydrol Earth Syst Sci 21:5477–5492. https://doi.org/10.5194/hess-21-5477-2017

Zeleke TT (2017) Trend and periodicity of drought over Ethiopia. Int J Climatol. https://doi.org/10.1002/joc.5122

Zhang L, Singh VP (2007) Bivariate rainfall frequency distributions using Archimedean copulas. J Hydrol 332:93–109. https://doi.org/10.1016/j.jhydrol.2006.06.033

Zhang Q, Zhang J (2016) Drought hazard assessment in typical corn cultivated areas of China at present and potential climate change. Nat Hazards 81:1323–1331. https://doi.org/10.1007/s11069-015-2137-4

Chapter 15
Nonstationary Flood Frequency Analysis: Review of Methods and Models

Siddik Barbhuiya, Meenu Ramadas, and Shanti Swarup Biswal

Abstract Recent changes in the climate, land use/land cover, and field-scale water resources allocation at the catchment scale have rendered the conventional hypothesis of the stationarity of hydrologic extremes unreliable. The current understanding of evolving patterns of hydrological variables has led to the development of nonstationary approaches, particularly in extreme event frequency analysis. A comprehensive review of the different approaches for nonstationary flood frequency analysis is presented in this chapter. The popular methods including generalized additive models for location, scale, and shape (GAMLSS) framework; probability-based approaches using Gumbel distribution and Log Pearson distribution III (LP 3), Bayesian approaches, r-largest, peaks-over-threshold, time-varying moments; among others are discussed. Additionally, the challenges associated with nonstationary hydrological frequency analysis and future research directions in the analysis of flood extremes are briefly addressed. It is evident that nonstationarity needs to be incorporated in flood risk assessment framework for addressing the likely impacts of potential future climate change in water resources management.

Keywords Flood frequency analysis · Climate change · Extreme events · Nonstationarity · Bayesian approach

15.1 Introduction

Among the fatal natural hazards, water resource-related extreme events such as floods, cyclones, and droughts have been known to be the costliest and most disastrous, across different parts of the world. Naturally occurring riverine flood and flash flood events are characterized by overflowing of rivers into the riverbanks as a result of heavy precipitation, inundating large areal extent comprising human settlements and natural ecosystems (Merz et al. 2021; Das et al. 2022). In fact, the

S. Barbhuiya · M. Ramadas (✉) · S. S. Biswal
School of Infrastructure, Indian Institute of Technology, Bhubaneswar, Odisha, India
e-mail: sab12@iitbbs.ac.in; meenu@iitbbs.ac.in; ssb14@iitbbs.ac.in

extreme events are also caused by anthropogenic influences such as urban floods, dam break, and coastal floods. Disastrous floods can leave unprecedented impacts on society and destruction of lives and also cause disruption to economic activities in the region (Mudelsee et al. 2003; Ray et al. 2019; Kuang and Liao 2020; Mangukiya and Sharma 2022; and Das et al. 2022 among others). In India, a significant portion of land, encompassing over 40 million hectares or 12% of the geographical area, is observed to be susceptible to flood events. Each year, floods claim the lives of more than 1600 people and inflict damages exceeding Rs. 5600 crores (73 million USD) (Central Water Commission 2018). Flood frequency analysis (FFA) has become an indispensable tool in assessing the potential impacts of these flood hazards and designing effective mitigation measures. In this regard, the term frequency or return period that expresses the exceedance probability of the flood event is used. Through FFA, the relationship among flood peaks, volumes, duration, and the associated return periods can be assessed, utilizing continuous long-term data of observed flow discharge or water levels in the river. In recent years, the phenomena of climate change, land use/land cover change, and water resource reallocation and different watershed-scale interventions have challenged the notion of stationarity of hydrological variables that is adopted in frequency analysis and extreme event modeling (Berghuijs et al. 2019; Milly et al. 2008; Villarini et al. 2009; Debele et al. 2017a). Significant rise in riverine flood hazard is projected for parts of sub-Saharan Africa, Asia, Europe, northern Russia, and specific regions in South and North America in future periods (Merz et al. 2021). Incidentally, the trends and change patterns of hydrological variables have been studied by numerous researchers in the form of detection and attribution studies and encouraged the choice of nonstationary approaches for modeling the changing risk of hydrological extremes such as floods and droughts (Mondal and Mujumdar 2012; Serinaldi and Kilsby 2015; Singh and Chinnasamy 2021). Therefore, these methods are increasingly being adopted for estimation of return period and risk associated with riverine flood hazards at local-to-regional scales (Lima et al. 2015; Mondal and Daniel 2019).

FFA methods accounting for nonstationarity have been applied to various case studies worldwide, demonstrating their usefulness in understanding and predicting the behavior of hydrological extremes in changing environments. The analysis includes finding the best estimates of the time-varying parameters of probability distributions that fit the flood variables (peak, volume, duration), using covariates such as time, temperature, or any suitable hydroclimatic variable. The popular methods and models adopted in nonstationary hydrologic frequency analysis include generalized additive models for location, scale, and shape (GAMLSS) framework, probability distribution-based models (Gumbel distribution, Log Pearson distribution III), Bayesian approaches, r-largest, peaks-over-threshold, time-varying moments, pooled FFA, local likelihood, and quantile regression. In one of the earlier studies by Strupczewski et al. (2001), the need to incorporate trend for accurate analysis of flood frequency is established, wherein the temporal trends in hydrological variables implying nonstationarity were investigated for FFA. They used annual peak discharge series, applying both the annual maximum series and partial duration series-based approaches for at-site frequency modeling. They had relied on the

Akaike information criterion (AIC) to identify the best nonstationary model among different models, while the maximum likelihood method was used for model parameter determination. The advancements in hydrological modeling over the last few decades include use of Bayesian approaches (Cheng et al. 2014; Sharma and Goyal 2017), as well as applications for regional flood frequency analysis, in the context of nonstationary analysis. The application of nonstationary analysis of extreme precipitation events in Mediterranean region is found in Tramblay et al. (2013), where a nonstationary peaks-over-threshold model was utilized with climatic variables as covariates. The authors used Poisson distribution and generalized Pareto distribution for modeling the occurrence and magnitude of heavy rainfall events, respectively, while the southern circulation patterns and monthly air temperature were adopted as covariates. They found that the nonstationary model with climatic covariates performed better than the classical stationary model and could simulate future climate scenarios for understanding impacts of such changes in future. The potential future changes in the covariates included in the model were also used to evaluate the possible future changes in extreme precipitation events in the study area. Das and Umamahesh (2017) had analyzed uncertainties and nonstationarity in future streamflow projections at river basin scale under climate change scenarios: representative concentration pathways (RCPs) 4.5 and 8.5 using the VIC-3 L model, they and found that while stationary models were suitable for RCP4.5, nonstationary approach was more appropriate for RCP8.5. Further, their study suggested that nonstationary return levels were reliable for designing low-capacity hydraulic structures and highlights the role of nonstationarity in improved hydrologic modeling and design. Similarly, a review of various return level-based metrics for hydrologic design under nonstationary conditions can be found in Mondal and Daniel (2019). Das and Umamahesh (2022) also studied the hydrological extremes in the Godavari River basin, India, incorporating physically based covariates such as the Indian Summer Monsoon Index and precipitation into the Generalized Extreme Value distribution to incorporate nonstationarity.

Comparison of stationary and nonstationary flood frequency approaches can provide useful insights on the drawbacks of stationary models that do not address climatic change. Currently, we can find numerous studies that use external covariates besides time, to improve results of FFA. In their study, Machado et al. (2015) analyzed historical flood records of the Tagus River in Spain and found that the estimates of extreme event magnitudes and frequencies are better modeled by including covariates of various climate and environmental drivers. They compared both stationary and nonstationary models including a GAMLSS model that incorporated both climate and catchment factors. The norming constants method (NCM) was adopted for nonstationary FFA of flow in the Wei River in China, by Xiong et al. (2015). In their study, the nonstationarity present in annual daily flow series and their effect on the annual maximum flood series were modeled. The authors had considered nonstationarity using additional explanatory climatic variables, tested the NCM on the flow data, and found that it outperformed the traditional stationary FFA models. Šraj et al. (2016) also compared among four different models for estimating flood quantiles at gauging sites in Slovenia. With significantly increasing trend in

annual maximum discharge series at these sites, nonstationarity-based analysis of extremes was imperative. In their study, Šraj et al. (2016) used the GEV distribution, with parameters dependent on time and annual precipitation as covariates. The maximum likelihood and Bayesian Monte Carlo Markov chain methods were used for parameter estimation. Comparison of results of FFA using GAMLSS method with different types of covariates is performed by Dègan et al. (2017), creating nonstationary models with time and principal components obtained from empirical orthogonal factor (EOF) analysis on climate variables (climate indices and temperature). Their study found the nonstationary model using principal components as covariates to be better at modeling change. These studies overall suggest that nonstationarity is important in the context of FFA, and significant difference exists between nonstationary and stationary estimates, with likely underestimation in case of the latter approach.

There are numerous instances when nonstationary approach has reduced the uncertainty involved in hydrologic design, specifically with advancements in Bayesian model-based analysis. It is possible that stationarity assumption could lead to unsafe designs for structures when trends are present in hydrologic variables, and potential variations in these trends also need attention of hydrologists. Singh and Chinnasamy (2021) performed nonstationary FFA of discharge of Periyar River in India using generalized extreme value distribution and covariates of annual precipitation, urban extent, and time. When compared with stationary analysis results, they observed that the trends in flows are present, and it is advantageous to adopt nonstationary FFA. A study by Guo et al. (2023) has compared the performance of nonstationary Bayesian regional flood frequency analysis (RFFA) coupled with the linear mixed effect (LME) model with the stationary generalized least squares (GLS) model. Indeed, the nonstationary LME-based Bayesian RFFA method performed better than the stationary GLS-based method with respect to the deviance information criterion (DIC). The nonstationary approach reduced uncertainty in design flood estimation and has been recommended for nonstationary FFA of ungauged sites.

The presented review of applications of nonstationary hydrologic frequency analysis suggests that incorporating nonstationarity in FFA is particularly relevant in the current scenario with possible future alterations in climatic variables and hydrologic processes. The studies also emphasize the choice of relevant covariate that drives the changes in these variables. There are several challenges associated with nonstationary FFA that are evident from the review of literature. Discerning among the natural, anthropogenic, and mixed drivers of nonstationarity is problematic, as these factors may be interlinked in complex ways, and requires substantial efforts for detecting trends and change points with limited data records. In fact, short-term trends and multi-decadal shifts in hydrological variables may complicate nonstationary analysis (Koutsoyiannis and Montanari 2015). Besides, the inadvertent use of nonstationary approach to shorter-term time series can lead to increased uncertainty (Serinaldi and Kilsby 2015).

This chapter aims at a comprehensive review of important nonstationary FFA approaches and their applications, challenges, and future research direction. The

popular GAMLSS framework, probability distribution-based models (Gumbel distribution, Log Pearson distribution III), Bayesian approaches, r-largest, peaks-over-threshold, and other methods: time-varying moments, pooled FFA, local likelihood, and quantile regression are included in the review. The objective of the review is to provide direction to hydrologists regarding the emerging methods in nonstationary hydrologic frequency analysis and their relative merits and demerits. With increasing focus on nonstationarity approaches in the face of changing climate, land use, and anthropogenic interventions, there is perennial need for developing more robust and flexible approaches that can be adapted across spatial scales too. It is also important to devise strategies for integrating the findings of nonstationary analysis into risk assessment and adaptation, so that the benefits of planning and management of water resources can be maximized, ensuring that communities are better prepared and more resilient to future hydrologic extreme events (Chen et al. 2021; Zhou et al. 2022).

15.2 Nonstationary Frequency Analysis Approaches

15.2.1 Generalized Additive Models for Location, Scale, and Shape (GAMLSS) Framework

15.2.1.1 Theory

The GAMLSS framework (Rigby et al. 2005) offers a flexible statistical framework for the estimation of distribution parameters of flood variables as functions of covariates, under assumptions of nonstationarity. The GAMLSS framework has been widely used to model different hydrological variables, such as precipitation, temperature, and streamflow (Archfield et al. 2016; Westra et al. 2014). In the GAMLSS framework, the response variable y is assumed to follow a specific distribution with parameters μ, σ, ν, τ (for location, scale, shape, and additional shape, respectively). Each parameter is modeled as a function of covariates (Rigby et al. 2005). The general GAMLSS model can be written as:

$$g_k(\theta_k) = X_k\beta_k + \sum_{i=1}^{p_k} s_{ik}(x_{ik}), \text{for } k = 1, 2, \ldots, K \qquad (15.1)$$

where y follows a specific distribution with parameter vector $\theta = (\mu, \sigma, \nu, \tau)$, g_k is a link function for the k-th ($k = 1, 2, \ldots, K$) parameter, θ_k is the k-th parameter of the distribution (location, shape, or additional shape), X_k is known model matrix for the k-th parameter, β_k is the parameter vector for the k-th parameter, $s_{ik}(x_{ik})$ is the smooth function of the covariance x_{ik} for the k-th parameter, and p_k is the number of covariates for the k-th parameter.

The GAMLSS model can accommodate different choices of probability distribution and link functions. The link functions g_k transform the distribution parameters to a scale on which the linear predictors can be modeled. The choice of link function depends on the range and interpretation of the distribution parameters. The smooth $s_{ik}(x_{ik})$ functions capture nonlinear relationships between the covariates and the distribution parameters (Wood 2006). These functions can be spline function or local regression function. Generally, in GAMLSS framework, the distribution parameters and smooth functions are estimated by maximizing a penalized likelihood function. This maximization process ensures the goodness of fit of the model (Rigby et al. 2005).

15.2.1.2   Scope

Debele et al. (2017a, 2017b) provide a detailed process of use of GAMLSS in flood frequency studies. The challenges of nonstationarity-based approach are discussed in Debele et al. (2017a), and they also suggest the GAMLSS framework as the most popular for nonstationary statistical analysis. The relative advantages and weaknesses are also presented in their work. A comparison of three methods—maximum likelihood, weighted least squares-two stage (WLS/TS), and GAMLSS for computation of design flood quantiles under nonstationarity was performed for Polish and Norwegian catchments by Debele et al. (2017b). Their study recommended using a multi-model approach to minimize errors associated with model formulation across different length datasets. While GAMLSS performed best in overall estimation of design flood quantiles with longer datasets, the WLS/TS provides better accuracy for shorter time series analysis. In another study, Chen et al. (2021) did flood frequency analysis for several gauging stations in the United Kingdom and examined the choice of covariates. The nine covariates chosen included rainfall variability-related and atmospheric circulation pattern-based variables, to model the inherent nonstationarity in flood records. Their study found that the simplest choice—a time-varying nonstationary flood model may not always be the most appropriate, and physically based covariates can offer better nonstationary models. Even the use of multiple covariates is recommended to improve the analysis, to simulate the effects of climate change. A framework for assessing the uncertainty of nonstationary FFA with possible application in hydrologic design, water supply, and reservoir regulation was proposed by Zhou et al. (2022), for the Hanjiang River of China. They combined GAMLSS, copula model, and Bayesian uncertainty processor (BUP) techniques for design flood estimation with information on uncertainty of the estimates. In this study, precipitation and reservoir index were covariates. Their framework addresses the modeling of uncertainty in nonstationary FFA.

15.2.2 FFA Using Probability Distributions

GEV distribution is widely used for modeling extreme events such as floods, droughts, and other hydroclimatic extremes. The GEV family includes three types of extreme value distributions, namely, the Gumbel, Frechet, and Weibull distributions. The Gumbel distribution has been widely used to model extreme event characteristics in a nonstationary context. Log Pearson distribution III (LP 3) is another popular choice of distribution for flood frequency analysis, which considers the skewness, kurtosis, and other moments of the variable data (Stedinger et al. 1993).

15.2.2.1 Generalized Extreme Value (GEV) Distribution

The cumulative distribution function (CDF) of the GEV distribution is given by Coles (2001):

$$F(x) = \exp\left\{ - \left(1 + \xi \cdot \left(\frac{x - \mu}{\sigma}\right) \right)^{-\frac{1}{\xi}} \right\} \tag{15.2}$$

where x is the random variable of interest, μ is the location parameter, σ is the scale parameter, and ξ is the shape parameter. In a nonstationary context, any of the parameters can be modeled as functions of time or other covariates. For example, suppose we have a covariate, t, representing time. We can model the location and scale parameters as functions of time in a linear fashion:

$$\begin{aligned} \mu(t) &= \mu_0 + \mu_1 t \\ \sigma(t) &= \sigma_0 + \sigma_1 t \\ \xi(t) &= \xi_0 + \xi_1 t \end{aligned} \tag{15.3}$$

where μ_0, μ_1, σ_0, σ_1, ξ_0, and ξ_1 are the regression coefficients to be estimated.

15.2.2.2 Gumbel Distribution

The Gumbel distribution probability density function (PDF) $f(x)$ and cumulative distribution function (CDF) $F(x)$ are as follows:

$$\begin{aligned} f(x) &= \frac{1}{\sigma} \, \exp[- (\frac{x - \mu}{\sigma}) - \exp(- \frac{x - \mu}{\sigma})]; F(x) \\ &= \exp[- \exp(- \frac{x - \mu}{\sigma})] \end{aligned} \tag{15.4}$$

where x is the random variable, μ is the location parameter, and σ is the scale parameter. Incorporating the time-varying parameters μ_t, σ_t previously discussed into these PDF and CDF expressions results in:

$$f(x, t) = \frac{1}{\sigma(t)} \left[\exp\left(-\frac{x - \mu(t)}{\sigma(t)} \right) - \exp\left(-\frac{x - \mu(t)}{\sigma(t)} \right) \right]; F(x, t)$$
$$= \exp\left[-\exp\left(-\frac{x - \mu(t)}{\sigma(t)} \right) \right] \tag{15.5}$$

This approach allows to account for nonstationarity in the data, provided the correct estimates of the parameters are obtained through the analysis.

15.2.2.3 Log Pearson Distribution III (LP 3)

The LP 3 distribution is specified by its parameters: location (μ), scale (σ), and shape (ξ). In this approach, the goal is to fit a Pearson type III distribution to the base-10 logarithms of the annual flood maxima. The parameters estimated are mean μ, standard deviation σ, and skew coefficient ξ of the log-transformed data (Griffis and Stedinger 2007). By setting parameters μ, σ, and ξ as functions of time or other covariates as previously discussed, it is possible to capture the changes in flood magnitudes and frequencies over time (Vogel and Wilson 1996). By incorporating time-varying parameters, the LP 3 distribution can better represent the nonstationary behavior of hydrological variables, providing more accurate flood frequency estimates in the context of changing conditions.

15.2.2.4 Scope

An important step of FFA is the choice of best distribution to represent the characteristics of the extreme events. There are numerous probability distributions that can be adopted and depend on the data and results of goodness of fit tests. In the study by Gruss et al. (2022) that performed annual maxima FFA for ten rivers in the Czech Republic and Poland, they compared three-parameter distributions including the log-normal, Weibull, generalized extreme value (GEV), and Pearson type III distributions. Their methodology was flexible as it allowed for the choice of best fit distribution for FFA. Nonstationary FFA models were found to be superior over stationary models for flood estimation, and among the distributions, Weibull and log-Normal distributions were found to be the most suitable for lower and upper quantiles, respectively.

15.2.3   Bayesian Models

15.2.3.1   Theory

Bayesian model framework has been employed to perform robust nonstationary FFA by integrating prior knowledge, uncertainty, and model updating based on new data (Khaliq et al. 2006; Salas et al. 2018). The analysis is used to estimate the posterior distribution of the parameters of the probability distributions and the time-varying functions. The framework is best suitable to model uncertainties related to hydrological FFA.

The posterior distribution of the parameters can be expressed as (Salas et al. 2018):

$$p(\theta|y) \propto p(y|\theta) * p(\theta) \tag{15.6}$$

where $p(\theta|y)$ is the posterior distribution, $p(y|\theta)$ is the likelihood function that represents the probability of observing the data y given the parameters θ, $p(\theta)$ is the prior distribution that encodes our knowledge about the parameters before observing the data, and y denotes the observed data.

15.2.3.2   Scope

Bayesian approaches have been successfully utilized to model distributions in flood frequency models involving GAMLSS, Gumbel, and LP 3 distributions (Khaliq et al. 2006). This allows for the incorporation of expert knowledge and historical information into the modeling process, which can lead to more accurate and reliable predictions of extreme events. In their FFA study, Lima and Lall (2010) demonstrated that the Hierarchical Bayesian models can provide accurate estimates of monthly/annual flood discharge probability distribution parameters for ungauged sites in Brazil. They performed nonstationary model development using reconstructed natural inflow series from over 40 gauging points representing a wider range of catchment areas. In fact, the developed regional-scale approach was used for augmenting records of flow at sites with missing data as well as to estimate flow at ungauged sites. Similarly, studies by Ouarda and El (2011) detail the scope of nonstationary frequency analysis models in hydrology, with a specific focus on the Bayesian approaches. They had used the nonstationary generalized maximum likelihood estimation method and the reversible jump Monte Carlo Markov Chain (MCMC) model for hydrologic frequency analysis.

15.2.4   Other Methods

Few other popular models used in nonstationary FFA are discussed in this section. The r-largest and peaks-over-threshold (POT) approaches have been useful for modeling nonstationary extreme events, using annual maxima as well as POT data (Douglas et al. 2000; Mudelsee et al. 2003).

The r-largest approach is a method for modeling extreme events by fitting a distribution to the r largest order statistics within a specified period (Douglas et al. 2000). This technique focuses on modeling the most extreme floods and provides a means of estimating the return levels associated with rare discharge levels. The peaks-over-threshold approach, on the other hand, models exceedances over a predefined threshold u using the generalized Pareto distribution (GPD) (Mudelsee et al. 2003). The GPD is described by its $f(x)$ and $F(x)$ as follows:

$$f(x) = \frac{1}{\sigma} \cdot \left(1 + \xi\left(\frac{x-u}{\sigma}\right)\right)^{-(1+\xi)^{-1}}; F(x) = 1 - \left(1 + \xi\left(\frac{x-u}{\sigma}\right)\right)^{-(1+\xi)^{-1}} \quad (15.7)$$

where the symbols as defined previously. Both the r-largest and POT approaches can be used in conjunction with Bayesian approach for analysis of floods with due consideration for uncertainty assessment.

Time-varying moments, pooled flood frequency analysis, local likelihood, and quantile regression also offer flexibility in modeling extreme events, under climate change, land use change, and human interventions, but are less popular methods for nonstationary flood frequency analysis (Hejazi and Markus 2009; Villarini et al. 2009; Vogel et al. 2011; Wilson et al. 2010).

Time-varying moments provide a method for estimating the moments of the underlying distribution as functions of time. Strupczewski et al. (2001) used the nonstationary approach by incorporating temporal trend in the first two moments of the distributions: mean and variance. The time-varying mean μ_t and variance σ_t^2 were modeled using smooth functions such as splines or linear regression.

Pooled flood frequency analysis is a method that combines data from multiple sites to improve the estimation of flood quantiles (Vogel et al. 2011). The pooling group is determined by a similarity criterion, such as geographical proximity or hydrological similarity. Flood quantiles are then estimated using a weighted average of the site-specific quantiles.

Local likelihood is a nonparametric approach that estimates the distribution parameters using a weighted likelihood function (Khaliq et al. 2006).

$$L(\theta) = \prod_i [f(y_i \mid \theta(x_i))]^{w(x_i,x)} \quad (15.8)$$

where $L(\theta)$ is the likelihood function, $f(y_i | \theta(x_i))$ is the probability density function, and $w(x_i, x)$ are the weights. The weights depend on the distance between the x_i observation and the point of interest x, typically following a kernel function.

Quantile regression models the quantiles of the response variable as a function of covariates, allowing for the estimation of flood quantiles under nonstationary conditions (Khaliq et al. 2006). The quantile regression model is specified as follows:

$$Q_y(\tau|X) = X\,\beta(\tau) \tag{15.9}$$

where $Q_y(\tau|X)$ is the conditional quantile function, τ is the quantile level, X is the matrix of covariates, and $\beta(\tau)$ are the quantile-specific coefficients.

15.3 Case Studies

15.3.1 Review of Literature

An exhaustive list of case studies that have contributed to the understanding and development of nonstationary flood frequency analysis is presented in Table 15.1. The compiled information showcases the evolution of the modeling approaches and the relative popularity of models and highlights the growing importance of nonstationary approaches in flood frequency analysis.

15.3.2 Application: Case Study of Barmanghat Subbasin, India

We present findings of case study of nonstationary and stationary FFA of discharge data of Barmanghat subbasin of the Narmada River Basin in this section. The basin area is predominantly agricultural land. In this case, we performed FFA on the annual maximum streamflow data using a temporal nonstationary GEV model. The location and scale parameters of the GEV distributions are modeled as linear functions of the time covariate, while the shape parameter remains constant. Normal priors are utilized for parameter estimation in this case study. This analysis is implemented using the nonstationary extreme value analysis (NEVA) software package developed by Cheng et al. (2014). This analysis provides posterior probabilities with uncertainty interval during estimation of return levels and utilizes Bayesian approach for parameter estimation of models.

Results presented in Fig. 15.1a show the flood discharge versus return level curves obtained from the FFA for time covariate value of 45 years from the initial observation (as an example). The Akaike Information Criterion (AIC) and Bayesian Information Criterion (BIC) performance metrics used to evaluate model efficiency both suggest that nonstationarity approach is best for streamflow analysis of Barmanghat. With an AIC value of 499.43, the nonstationary model is significantly better than the stationary model with AIC of 505.76. Similarly, the BIC value for the

Table 15.1 Overview of popular nonstationary flood frequency analysis studies

Author(s)	Objective	Methodology	Findings
Strupczewski et al. (2001)	Investigated time trends in hydrological nonstationarity	Maximum likelihood method	Trend incorporation necessary for accurate modeling
Lima and Lall (2010)	Developed hierarchical Bayesian models for regional and at-site trends	Hierarchical Bayesian models	Accurate estimation of parameters; useful for record augmentation
Ouarda and El (2011)	Discussed nonstationary frequency analysis models	Nonstationary GMLE method and reversible jump MCMC	Bayesian model efficient for hydrological quantiles
Tramblay et al. (2013)	Analyzed nonstationary model for heavy rainfall events	Poisson and generalized Pareto distribution	Nonstationary model with climatic covariates superior to stationary model
Xiong et al. (2015)	Developed NCM for nonstationary FFA	NCM	NCM outperformed traditional FFA models
Machado et al. (2015)	Evaluated stationary and nonstationary flood frequency approaches	Stationary and nonstationary models	Nonstationary modeling improved rare flood probability estimates
Šraj et al. (2016)	Compared models for flood quantile estimation	Stationary and nonstationary GEV models	Nonstationary model with annual precipitation had best performance
Debele et al. (2017b)	Analyzed seasonal flow maxima	Maximum likelihood, two-stage, and GAMLSS methods	GAMLSS exhibited better performance
Das and Umamahesh (2017)	Analyzed uncertainties in streamflow projections	VIC-3L model projections under RCPs 4.5 and 8.5	Stationary for RCP4.5; nonstationary for RCP8.5
Debele et al. (2017a)	Discussed challenges in nonstationarity models and practical requirements	GAMLSS package	GAMLSS useful, but issues remain in applicability
Dègan et al. (2017)	Analyzed nonstationary flood frequency	Stationary and nonstationary models	Nonstationary models crucial for long periods
Singh and Chinnasamy (2021)	Investigated nonstationarity of Periyar River	Stationary and nonstationary models	Nonstationary FFA methods recommended
Chen et al. (2021)	Revisited the stationary assumption in FFA	Nine candidate covariates in nonstationary models	Rainfall variability dominant driver for flooding
Gruss et al. (2022)	Compared distributions for stationary and non stationary data	Weibull, Log-Normal, GEV, and Pearson Type III-based models	Nonstationary models superior; Weibull and Log-Normal most suitable
Zhou et al. (2022)	Developed approach for nonstationary FFA uncertainty	GAMLSS, Copula, and BUP techniques	Reliable probabilistic interval estimations for design floods

Table 15.1 (continued)

Author(s)	Objective	Methodology	Findings
Das and Umamahesh (2022)	Examined hydrological extremes under nonstationary conditions	GEV distribution with physically based covariates	Nonstationary approach provided valuable insights
Guo et al. (2023)	Investigated performance of nonstationary Bayesian RFFA	LME and GLS models	Nonstationary LME-based Bayesian RFFA method performed better
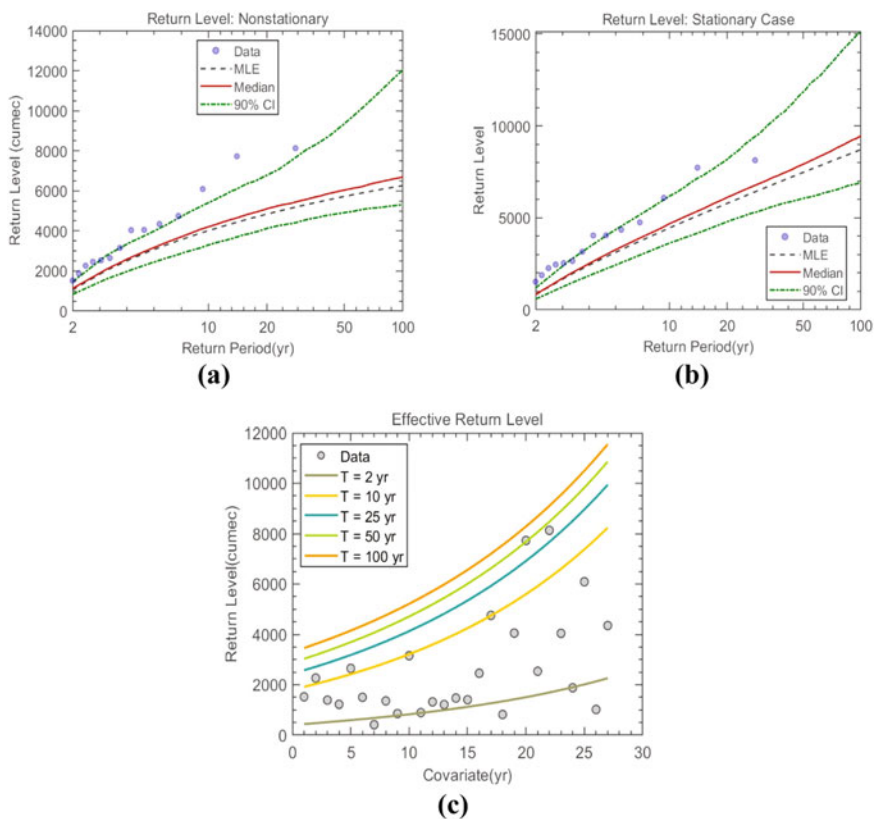
Fig. 15.1 Results of nonstationary and stationary FFA performed for Barmanghat Subbasin: (**a**) return level curves constructed based on a nonstationary model, (**b**) return level curves based on a stationary model, and (**c**) varying effective return levels as a function of time

nonstationary model (507.2) is also better than the stationary model with BIC of 509.64. The comparison of return levels between the presented nonstationary analysis (in Fig. 15.1a) and the stationary model (Fig. 15.1b) demonstrates the differences between results of both approaches. Fig. 15.1c further shows the changes in

effective return level as a function of time chosen as the covariate in the present case study.

15.4   Concluding Remarks

Nonstationary flood frequency analysis methods have become increasingly important in understanding and predicting hydrological extremes in changing environments. Various studies have been conducted worldwide, employing different approaches and techniques to address nonstationarity in flood frequency modeling. In summary, nonstationary flood frequency analysis methods have demonstrated their usefulness in various case studies, offering improved modeling accuracy and reducing uncertainty in the face of changing environmental conditions. These methods provide valuable insights for flood management, infrastructure design, and flood mitigation projects.

The vast amount of literature reviewed in this domain emphasizes that nonstationary flood frequency analysis is important for addressing the impacts of climate change, land use changes, and human activities in water resources management and has capability to provide reliable estimates of flood risk probabilities, design flood levels, and convey the associated uncertainties to users, compared to stationary approaches. Additionally, for integrating nonstationary flood frequency analysis into policy making, following parameters are required to be met: (i) understanding of local hydrological regimes and nonstationary factors; (ii) creation of public awareness on the importance of nonstationary flood frequency analysis; (iii) identification of appropriate nonstationary methods tailored to the study area; (iv) conversations with stakeholders, such as policymakers, engineers, and researchers for participatory resilience development; and (v) regular update and review of flood adaptation and mitigation policies and strategies to ensure their effectiveness and relevance.

15.4.1   Challenges

The comprehensive review of flood studies and existing approaches in nonstationary FFA has helped us to summarize the different challenges that are faced by hydrologists (Das et al. 2022). The major challenges are as follows:

- Data availability and quality: Nonstationary flood frequency analysis often requires long-term and high-quality data to capture the underlying trends and changes in hydrological extremes. However, acquiring such data is often challenging due to data gaps, inconsistencies, and limited spatial coverage.
- Selection of appropriate covariates: Identifying relevant and significant covariates that can explain the nonstationarity in flood frequency is a difficult task.

Researchers must carefully select the covariates based on their physical relevance and statistical significance in relation to the regional flood data.

- Model selection and validation: Numerous nonstationary models have been proposed in the literature, each with their own advantages and limitations. Choosing the appropriate model for a specific case and validating its performance are essential steps in nonstationary flood frequency analysis.
- Uncertainty quantification: Nonstationary flood frequency analysis has numerous sources of uncertainty, including those due to parameter estimation, model structure, and input data. Quantifying and accounting for these uncertainties is crucial for providing reliable and robust estimates of design floods.
- Computational complexity: Nonstationary flood frequency analysis often involves complex mathematical models and advanced statistical techniques that can be computationally demanding. Development of efficient algorithms and software packages is necessary for practical applications.

15.4.2 Future Direction

With the exhaustive review of applications and scope of nonstationary FFA carried out in this chapter, we have been able to assess the future scope of the research in this domain. Notably, the following important thrust areas are to be addressed in the analysis to utilize the maximum benefits of this exercise in hydrologic design and risk adaptation:

- Integration of climate change projections: Incorporating climate change projections into nonstationary flood frequency analysis can help assess the potential impacts of climate change on future flood risk and inform adaptation strategies.
- Development of regional nonstationary models: Developing regional nonstationary flood frequency models can help overcome data limitations and improve the estimation of flood quantiles for ungauged sites, which is particularly relevant for regions with limited data availability.
- Improvement of model performance and uncertainty quantification: Further research is needed to develop and evaluate new nonstationary models, as well as to refine existing ones and to improve their performance and uncertainty quantification in flood frequency analysis.
- Cross-disciplinary collaboration: Collaboration between hydrologists, meteorologists, and climate scientists can help better understand the drivers of nonstationarity in flood frequency and develop more accurate and robust models.
- Application of machine learning and artificial intelligence: The use of machine learning and artificial intelligence techniques can help identify patterns and relationships in large, complex datasets and may provide novel insights into nonstationary flood frequency analysis.

Ultimately, advancing the science of nonstationary FFA is essential for improving the design and management of water resources infrastructure and better adapting

to the impacts of natural and anthropogenic climate change on hydrological systems. By addressing the aforementioned challenges and research gaps and addressing the future scope for research in this domain, nonstationary FFA can be improved, standardized, and merged with flood risk management protocols to provide timely, accurate, and reliable estimates of flood risk and build the resilience of flood mitigation infrastructure.

References

Archfield SA, Hirsch RM, Viglione A, Blöschl G (2016) Fragmented patterns of flood change across the United States. Geophys Res Lett. https://doi.org/10.1002/2016GL070590

Berghuijs WR, Harrigan S, Molnar P, Slater LJ, Kirchner JW (2019) The relative importance of different flood-generating mechanisms across Europe. Water Resour Res. 55(6):4582–4593. https://doi.org/10.1029/2019WR024841

Central Water Commission (2018) Annual report 2018–19. Central Water Commission, Ministry of Water Resources, Government of India, New Delhi

Chen M, Papadikis K, Jun C (2021) An investigation on the non-stationarity of flood frequency across the UK. J Hydrol 597. https://doi.org/10.1016/j.jhydrol.2021.126309

Cheng L, AghaKouchak A, Gilleland E, Katz RW (2014) Non-stationary extreme value analysis in a changing climate. Clim Chang. https://doi.org/10.1007/s10584-014-1254-5

Coles S (2001) An introduction to statistical modeling of extreme values. Springer, London. https://doi.org/10.1007/978-1-4471-3675-0

Das J, Umamahesh NV (2017) Uncertainty and nonstationarity in streamflow extremes under climate change scenarios over a River Basin. J Hydrol Eng 22(10):1–13. https://doi.org/10.1061/(asce)he.1943-5584.0001571

Das J, Umamahesh NV (2022) Investigating risk, reliability and return period under the influence of large scale modes, and regional hydrological variability in hydrologic extremes. Hydrol Sci J 67(1):65–81. https://doi.org/10.1080/02626667.2021.1998512

Das J, Manikanta V, Nikhil Teja K, Umamahesh NV (2022) Two decades of ensemble flood forecasting: a state-of-the-art on past developments, present applications and future opportunities. Hydrol Sci J 67(3):477–493. https://doi.org/10.1080/02626667.2021.2023157

Debele SE, Bogdanowicz E, Strupczewski WG (2017a) Around and about an application of the GAMLSS package to non-stationary flood frequency analysis. Acta Geophys 65(4):885–892. https://doi.org/10.1007/s11600-017-0072-3

Debele SE, Multimodel GÁ, Monte Á (2017b) A comparison of three approaches to non-stationary flood frequency analysis. Acta Geophys 65(4):863–883. https://doi.org/10.1007/s11600-017-0071-4

Dègan A, Adéchinaalamou E, N'Tcha M'Po Y, Afouda A (2017) Non-stationary flood frequency analysis using additive terms for location, scale and shape parameters in the Ouémé River basin (Benin, West Africa). Int J Curr Eng Technol 7(2):556–570

Douglas EM, Vogel RM, Kroll CN (2000) Trends in floods and low flows in the United States: Impact of spatial correlation. J Hydrol 240(1–2):90–105. https://doi.org/10.1016/S0022-1694(00)00336-X

Griffis VW, Stedinger JR (2007) Log-Pearson type 3 distribution and its application in flood frequency analysis. II: Parameter estimation methods. J Hydrol Eng 12(5):492–500. https://doi.org/10.1061/(ASCE)1084-0699(2007)12:5(492)

Gruss Ł, Wiatkowski M, Tomczyk P, Pollert J, Pollert J (2022) Comparison of three-parameter distributions in controlled catchments for a stationary and non-stationary data series. Water (Switzerland) 14(3). https://doi.org/10.3390/w14030293

Guo S, Xiong L, Chen J, Guo S, Xia J, Zeng L, Xu CY (2023) Nonstationary regional flood frequency analysis based on the Bayesian Method. Water Resour Manag 37(2):659–681. https://doi.org/10.1007/s11269-022-03394-9

Hejazi MI, Markus M (2009) Impacts of urbanization and climate variability on floods in Northeastern Illinois. J Hydrol Eng 14(6):606–616. https://doi.org/10.1061/(asce)he.1943-5584.0000020

Khaliq MN, Ouarda TBMJ, Ondo J-C, Gachon P, Bobée B (2006) Frequency analysis of a sequence of dependent and/or non-stationary hydro-meteorological observations: a review. J Hydrol 329(3–4):534–552. https://doi.org/10.1016/j.jhydrol.2006.03.004

Koutsoyiannis D, Montanari A (2015) Meurtre par imprudence de concepts scientifiques: le cas de la stationnarité. Hydrol Sci J 60(7–8):1174–1183. https://doi.org/10.1080/02626667.2014.959959

Kuang D, Liao KH (2020) Learning from floods: linking flood experience and flood resilience. J Environ Manag 271:111025. https://doi.org/10.1016/j.jenvman.2020.111025

Lima CHR, Lall U (2010) Spatial scaling in a changing climate: a hierarchical Bayesian model for non-stationary multi-site annual maximum and monthly streamflow. J Hydrol 383(3–4):307–318. https://doi.org/10.1016/j.jhydrol.2009.12.045

Lima CHR, Lall U, Troy TJ, Devineni N (2015) A climate informed model for nonstationary flood risk prediction: application to Negro River at Manaus, Amazonia. J Hydrol 522:594–602. https://doi.org/10.1016/j.jhydrol.2015.01.009

Machado MJ, Botero BA, Benito G (2015) Flood frequency analysis of historical flood data under stationary and non-stationary modelling. Hydrol Earth Syst Sci. 2561–2576. https://doi.org/10.5194/hess-19-2561-2015

Mangukiya NK, Sharma A (2022) Flood risk mapping for the lower Narmada basin in India: a machine learning and IoT-based framework. Nat Hazards 113(2):1285–1304. https://doi.org/10.1007/s11069-022-05347-2

Merz B, Blöschl G, Vorogushyn S, Dottori F, Aerts JC, Bates P et al (2021) Causes, impacts and patterns of disastrous river floods. Nature Reviews Earth & Environment 2(9):592–609. https://doi.org/10.1038/s43017-021-00195-3

Milly PCD, Betancourt J, Falkenmark M, Hirsch RM, Kundzewicz ZW, Lettenmaier DP, Stouffer RJ (2008) Climate change: stationarity is dead: whither water management? Science 319(5863):573–574. https://doi.org/10.1126/science.1151915

Mondal A, Daniel D (2019) Return levels under nonstationarity: the need to update infrastructure design strategies. J Hydrol Eng 24(1):1–11. https://doi.org/10.1061/(asce)he.1943-5584.0001738

Mondal A, Mujumdar PP (2012) On the basin-scale detection and attribution of human-induced climate change in monsoon precipitation and streamflow. Water Resour Res. 48(10):2011WR011468. https://doi.org/10.1029/2011WR011468

Mudelsee M, Börngen M, Tetzlaff G, Grünewald U (2003) No upward trends in the occurrence of extreme floods in central Europe. Nature 425(6954):166–169. https://doi.org/10.1038/nature01928

Ouarda J, El S (2011) Bayesian nonstationary frequency analysis of hydrological variables 1. JAWRA. 47(3). https://doi.org/10.1111/j.1752-1688.2011.00544.x

Ray K, Pandey P, Pandey C, Dimri AP, Kishore K (2019) On the recent floods in India. Curr Sci 117(2):204–218. https://www.jstor.org/stable/27138236

Rigby RA, Stasinopoulos DM, Lane PW (2005) Generalized additive models for location, scale and shape. J R Stat Soc Ser C Appl Stat 54(3):507–554. https://doi.org/10.1111/j.1467-9876.2005.00510.x

Salas JD, Obeysekera J, Vogel RM (2018) Techniques for assessing water infrastructure for nonstationary extreme events: a review. Hydrol Sci J 63(3):325–352. https://doi.org/10.1080/02626667.2018.1426858

Serinaldi F, Kilsby CG (2015) Stationarity is undead: uncertainty dominates the distribution of extremes. Adv Water Resour 77:17–36. https://doi.org/10.1016/j.advwatres.2014.12.013

Sharma A, Goyal MK (2017) A comparison of three soft computing techniques, Bayesian regression, support vector regression, and wavelet regression, for monthly rainfall forecast. Int J Intell Syst 26(4):641–655. https://doi.org/10.1515/jisys-2016-0065

Singh N, Chinnasamy P (2021) Non-stationary flood frequency analysis and attribution of streamflow series: a case study of Periyar River, India. Hydrol Sci J 66(13):1866–1881. https://doi.org/10.1080/02626667.2021.1968406

Šraj M, Viglione A, Parajka J, Blöschl G (2016) The influence of non-stationarity in extreme hydrological events on flood frequency estimation. J Hydrol Hydromech. 426–437. https://doi.org/10.1515/johh-2016-0032

Stedinger JR, Vogel RM, Foufoula-Georgiou E (1993) Frequency Analysis of Extreme Events. In: Maidment DR (ed) Handbook of Hydrology. McGraw-Hill, New York, NY, USA, pp 18.1–18.66

Strupczewski WG, Singh VP, Feluch W (2001) Non-stationary approach to at-site flood frequency modelling I. Maximum likelihood estimation. J Hydrol 248(1–4):123–142. https://doi.org/10.1016/S0022-1694(01)00397-3

Tramblay Y, Neppel L, Carreau J, Najib K (2013) Non-stationary frequency analysis of heavy rainfall events in southern France. Hydrol Sci J 58(2):280–294. https://doi.org/10.1080/02626667.2012.754988

Villarini G, Serinaldi F, Smith JA, Krajewski WF (2009) On the stationarity of annual flood peaks in the continental United States during the 20th century. Water Resour Res 45(8):1–17. https://doi.org/10.1029/2008WR007645

Vogel RM, Wilson I (1996) Probability distribution of annual maximum, mean, and minimum streamflows in the United States. J Hydrol Eng 1(April):69–76

Vogel RM, Yaindl C, Walter M (2011) Nonstationarity: flood magnification and recurrence reduction factors in the United States. JAWRA J Am Water Resour Assoc 47(3):464–474. https://doi.org/10.1111/j.1752-1688.2011.00541.x

Westra S, Thyer M, Leonard M, Kavetski D, Lambert M (2014) A strategy for diagnosing and interpreting hydrological model nonstationarity. Water Resour Res 50(6):5090–5113. https://doi.org/10.1002/2013WR014719

Wilson D, Hisdal H, Lawrence D (2010) Has streamflow changed in the Nordic countries? - Recent trends and comparisons to hydrological projections. J Hydrol 394(3–4, 334):–346. https://doi.org/10.1016/j.jhydrol.2010.09.010

Wood SN (2006) On confidence intervals for generalized additive models based on penalized regression splines. Aust N Z J Stat 48(4):445–464. https://doi.org/10.1111/j.1467-842x.2006.00450.x

Xiong L, Du T, Xu C, Guo S (2015) Non-stationary annual maximum flood frequency analysis using the norming constants method to consider non-stationarity in the annual daily flow series. Springer, Cham. https://doi.org/10.1007/s11269-015-1019-6

Zhou Y, Guo S, Xu CY, Xiong L, Chen H, Ngongondo C, Li L (2022) Probabilistic interval estimation of design floods under non-stationary conditions by an integrated approach. Hydrol Res 53(2):259–278. https://doi.org/10.2166/nh.2021.007

Chapter 16
Multiday Extreme Precipitation Ranking and Association with Atmospheric Moisture Transport During Indian Summer Monsoon

Hariom Gupta, Akash Singh Raghuvanshi, and Ankit Agarwal

Abstract In recent years, the frequency of multiday extreme precipitation events has intensified over the Indian subcontinent. Variability in frequency, intensity, and duration of extreme precipitation events have an adverse impact on human society and the natural ecosystem. Therefore, it becomes essential to rank such extreme events based on their characteristics and understand the underlying atmospheric dynamics driving them. In this study, we ranked multiday extreme precipitation events during the Indian summer monsoon (ISM) season over the Indian subcontinent using a high-resolution daily precipitation dataset for 71 years period (1951–2021). Further, we attempt to evaluate the association between moisture transport and multiday extreme precipitation events by quantifying moisture transport during identified top-ranked multiday extreme precipitation events. Our analysis indicates strong moisture transport persisting over the extreme precipitation occurrence regions prior to and during the multiday extreme precipitation events. Quantifying the connection between extreme precipitation to moisture transport might help in the early prediction of extreme precipitation events and lower the associated risks.

Keywords Multiday extremes · Ranking · Moisture transport · Integrated vapor transport (IVT) · Indian summer monsoon

16.1 Introduction

Due to climate change, warmer temperatures lead to increased evaporation and atmospheric moisture, which can then lead to more intense rainfall, which is contributing to more frequent and intense extreme precipitation events. These events can lead to flooding, landslides, and other hazards and also have significant human

H. Gupta · A. S. Raghuvanshi · A. Agarwal (✉)
Department of Hydrology, Indian Institute of Technology Roorkee, Roorkee, Uttarakhand, India
e-mail: ankit.agarwal@hy.iitr.ac.in

impacts that can cause significant damage to infrastructure, homes, and other property. Managing extreme precipitation events requires a multifaceted approach that involves several strategies, and infrastructure improvements such as building levees, improving drainage systems, and reinforcing buildings can help to minimize the impact of extreme precipitation. Early warning systems can help to alert communities to the potential for extreme precipitation, allowing for evacuation or other preparedness measures. Land-use planning and zoning can help to minimize the impact of extreme precipitation by avoiding development in flood-prone areas or requiring new construction to be built to higher standards to withstand flooding.

Most extreme rainfall indices across the west coast stations and north-western regions of the Indian Peninsula have exhibited notable positive trends. Over India, in the last 50 years, precipitation extremes have varied in heterogeneous ways (Joshi and Rajeevan 2006), thus becoming a major concern. Understanding the characteristics of precipitation extremes allows us to identify the impact causing extreme events, which requires attention and resources for mitigation and adaptation. Therefore, it is crucial to characterize and rank precipitation extremes to comprehend the risk and impact and examine the underlying drivers that contribute to their occurrence and intensification. In recent years, several techniques have been adopted to evaluate and rank precipitation extremes in various parts of the world. Beguería et al. (2009) adopted extreme value theory to evaluate the characteristics of extreme precipitation occurrences over north-eastern Iberian Peninsula. An equivalent threshold-based objective method was adopted for identifying regional extreme events (REE) while considering their impact area and duration (Ren et al. 2012). An index system was also established specifically for REE in this method. This index system was comprised of five indices, that is, extreme magnitude, maximum impacted area, cumulative intensity, accumulated area, and duration, as well as an integrated index and spatial location. An "event-adjusted" method based on the optimization of the time duration and the event area was developed by Müller and Kaspar (2014) in which the radius of a circle with the same diameter as the one over which the geometric mean is taken is multiplied by the common logarithm of the spatial geometric mean of the return periods, to measure the extremeness. Ramos et al. (2014) introduced a novel approach for ranking daily extreme precipitation on the basis of the affected area and the intensity at each grid point. This approach was further modified for multiday extreme events using accumulated normalized departure from climatology at shorter time scales (e.g., 3 days) and longer time scale (e.g. 5, 7, and 10 days) (Ramos et al. 2017). Similar approach was adopted to rank multiday precipitation extreme events in the Indian western Himalayas (IWH) (Raj et al. 2021) and for the identification and selection of wet spell events across Danube river basin (Ciric et al. 2017). In the above ranking methods, a typical Gaussian distribution was not achieved by normalized precipitation anomalies. Therefore, a new ranking method, based on the severity of the extreme precipitation days considering the magnitude of the precipitation above the 95th climatological percentile and the area affected by the same magnitude, was suggested (Ramos et al. 2018).

Atmospheric moisture transport plays a crucial role in the occurrence of extreme precipitation events. Being the primary component of the atmospheric branch of the water cycle, atmospheric moisture transport anomalies have a considerable impact on precipitation extremes. The Indian summer monsoon (ISM) is closely related to atmospheric moisture transport, as it involves the transport of moisture from the surrounding oceans to the Indian subcontinent. The Indian summer monsoon accounts for the majority of the annual rainfall (Turner and Annamalai 2012) over India (~ 80% of the annual rainfall) and contributes as the critical source of water for agriculture in the region (Hrudya et al. 2021). However, in recent years, India has experienced rise in frequency of extreme precipitation events during the Indian summer monsoon causing significant damage to infrastructure and loss of life. The importance of atmospheric moisture transport to extreme precipitation has become even more pronounced in recent years as a result of climate change. As global temperatures rise, the atmosphere is able to hold more moisture, which means that there is more moisture availability for transport and precipitation (Tabari 2020). This has led to an increase in the frequency and severity of extreme precipitation events in many parts of the world. Thus, understanding the linkages between extreme precipitation events and atmospheric moisture transport is essential. Recent study attempted to establish the link between precipitation over the continents and evaporation from the ocean using various major atmospheric moisture transport mechanisms, namely, atmospheric rivers (ARs) and low-level jets (LLJs) (Gimeno et al. 2016). With these references, the present study focuses on evaluating the rank of multiday extreme precipitation events over Indian subcontinent region during India summer monsoon (ISM). Further, the association between moisture transport and extreme precipitation is evaluated by assessing the spatiotemporal variability of atmospheric moisture during top ranked multiday events.

16.2   Study Area

India has a diverse physiography, with varied landforms, ranging from high mountain ranges, plateaus, plains, and coastal regions (as shown in Fig. 16.1). The country has a coastline of about 7500 km, which is home to several major ports. The West coast (WC) of India is bordered by the Arabian Sea, while the East coast (EC) is bordered by the Bay of Bengal. During the ISM, the Indian WC region, which makes up the windward side of the Western Ghats mountains, experiences extremely heavy rainfall, whereas the Southeast Indian region experiences rain-shadowing (Francis and Gadgil 2006). During ISM season, the country receives 75–80% of its total annual rainfall. Despite significant year-to-year variability, the intensity and frequency of extreme rainfall events during ISM have increased significantly over the past 50 years (Goswami et al. 2006). In addition, there is an increase in the rise of location-specific and widespread extreme precipitation due to large variability of the monsoon low-level westerlies over the Arabian Sea (AS), which provides the intense streams of moisture supply causing extreme rainfall events across the country (Roxy
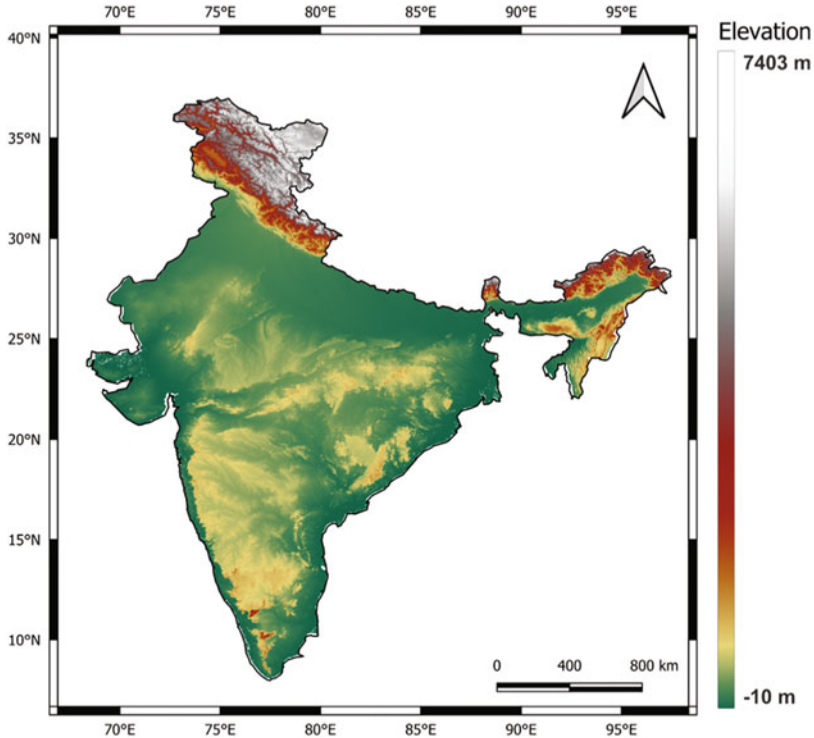
Fig. 16.1 Geographic map of Indian subcontinent depicting its elevation over different regions

et al. 2017; Sagar et al. 2017). Despite the importance of moisture supply from the AS (during ISM season) in triggering multiday extreme precipitation events over the Indian region, no research has thoroughly examined the relationship between multiday extreme precipitation events and atmospheric moisture transport over the Indian subcontinent.

16.3   Datasets and Methods

16.3.1   Precipitation Data

For the computation of multiday ranking events, daily gridded rainfall data developed by India Meteorological Department (IMD) at a spatial resolution of $0.25° \times 0.25°$ is used for ISM months, that is, from June to September (JJAS) for 1951–2021 period (Pai et al. 2014). These datasets were prepared with the use of daily rainfall records obtained from 6955 rain gauge stations over India (Pai et al. 2014). IMD data is considered as the more accurate dataset as it efficiently captures the temporal and spatial variability of precipitation in India (Pai et al. 2014).

16.3.2   Reanalysis Data

We used data from the most recent ERA-5 reanalysis (Hersbach et al. 2020) from the European Centre for Medium-Range Weather Forecasts (ECMFW) at 6-hourly temporal resolution (0 UTC, 6 UTC, 12 UTC, and 18 UTC) to obtain the values of zonal wind speed (u), meridional wind speed (v), and specific humidity (q) at multiple vertical levels of the troposphere (1000–300 hPa; 20 pressure levels) in order to quantify atmospheric moisture transport at 0.25° × 0.25° resolution. Compared to other reanalysis products, ERA-5 captures precipitation reasonably well during Indian summer monsoon (Mahto and Mishra 2019).

16.3.3   Ranking Multiday Extreme Precipitation

For the ranking of extreme precipitation events, we adopted the methodology developed by Ramos et al. (2018). This ranking method considered magnitude, spatial extent, and duration of the extreme precipitation events. For the estimation of ranking, only wet days (days with precipitation greater than 2.5 mm as per IMD) are considered. In this method, we calculate 95th percentile threshold from daily precipitation data for 1951–2021 period at each grid point and for each day of year during ISM to ensure a fair comparison among all grid point while evaluating precipitation anomaly. A three-step procedure is used to determine the ranks of extreme precipitation events across multiday accumulation periods.

Step 1: The extreme precipitation anomaly is computed for each day and each grid point as follow:

$$N95_{d,i,j} = P_{d,i,j} - P95_{t,i,j} \tag{16.1}$$

where $N95_{d,\,i,\,j}$ is the extreme precipitation anomaly on day d, at the grid point (i,j). $P_{d,\,i,\,j}$ is the daily accumulated precipitation of day d at grid point (i,j). $P95_{t,\,i,\,j}$ is the Julian daily 95th percentile of the precipitation for that grid point (i,j). A seven-day running mean of $P95_{t,\,i,\,j}$ is calculated before computing the anomalies in order to smoothen the highly variable $P95_{t,\,i,\,j}$ time series. Finally, for each day and for each grid point (i,j), an anomaly departure from 95th percentile threshold is obtained.

Step 2: The second step involves calculating the accumulated extreme precipitation anomalies (NCC) for a certain period p by calculating the sum of the anomalies (Eq. 16.1 – N95) over multiday periods (n) as follows:

$$NCC_{p,i,j} = \sum_{d=1}^{n} N95_{d,i,j} \tag{16.2}$$

We computed the accumulated extreme precipitation anomalies for 1-, 3-, 5-, and 7-day period. For example, the accumulated precipitation anomalies for 3 days on

August 5, 2006, corresponds to the sum of the extreme precipitation anomaly relative to August 3–5, 2006.

Step 3: Finally, the multiday extreme precipitation events are ranked based on a ranking index (R), which is defined as follows:

$$R = A \times M \tag{16.3}$$

where A is the area (in percentage) with accumulated extreme precipitation anomalies (*NCC*) greater than zero and M is the mean value of the extreme precipitation anomalies (*N*95) for all the grid points.

16.3.4 Atmospheric Moisture Transport

Atmospheric moisture transport is characterized by significant water vapor anomalies in the atmosphere. In the past, many studies have used water vapor imagery and column-integrated water vapor (IWV) observations to quantify atmospheric moisture transport and its mechanisms (Neiman et al. 2008, 2013; Ralph et al. 2004; Zhu and Newell 1998). Later, it was realized that IWV does not account the flux component, and the column-integrated water vapor transport (IVT), which includes horizontal winds in its computation, is used as the preferable measure in most contemporary research because it includes horizontal winds in its computation. IVT has certain benefits over IWV, including better relationships with precipitation and more accurate forecasts from numerical weather prediction models (Dettinger et al. 2011). IVT magnitude on a grid cell is computed as the magnitude of column-integrated zonal and meridional moisture fluxes, as given in Eq. 16.4:

$$\text{IVT} = \frac{1}{g}\sqrt{\left(\int_{1000hpa}^{300hpa} qu\, dp\right)^2 + \left(\int_{1000hpa}^{300hpa} qv\, dp\right)^2} \tag{16.4}$$

where IVT is magnitude of water vapor transport in $kg.\, m^{-1}s^{-1}$; q is specific humidity in $kg.\, kg^{-1}$; u and v are, respectively, zonal and meridional wind velocities in $m.\, s^{-1}$; dp is the pressure difference between two adjacent pressure levels in Pa; and g is the acceleration due to gravity (9.81 ms^{-2}).

16.4 Results and Discussions

In this section, multiday extreme precipitation events ranking over Indian subcontinent is presented in tabular format. The spatiotemporal patterns of top ranked multiday extreme precipitation events and corresponding multiday moisture transport is presented and discussed.

16.4.1   Ranking Multiday Extreme Precipitation Events

In Tables 16.1, 16.2, 16.3, and 16.4, the top ten cases of the rankings of precipitation extremes for different accumulated periods (1, 3, 5, and 7 days) are shown. Interestingly, many events are not independent, and they overlap at different durations. In addition, it is clear from Tables 16.1, 16.2, 16.3, and 16.4 that the different top ten ranks are dominated by four events that occurred, respectively, in July 1989, September 1995, July 2006, and August 2019. This dominance exerted by just a few extreme precipitation episodes is expected to occur at longer durations, since we analyze successive accumulated precipitation days over relatively long periods.

Table 16.1 The top ten events ranking of one-day accumulated extreme precipitation events

Date	% Area (*A*)	Mean (*M*)	*R* = *A**M	Rank
24-07-1989	12.08	46.89	566.39	1
05-09-1995	13.20	40.05	528.70	2
16-08-2011	9.35	56.24	525.55	3
23-07-1989	9.24	54.86	507.03	4
23-06-2007	9.28	53.44	496.11	5
09-08-2019	12.45	39.78	495.35	6
07-08-2007	7.81	60.30	471.06	7
04-09-1995	11.71	39.88	466.94	8
04-07-2006	6.96	63.93	445.11	9

The first column corresponds to the date of the event. Column *A* corresponds to the area (in %) of the domain that has extreme precipitation anomalies above N95. Column *M* corresponds to mean value of these extreme precipitation anomalies over area *A*. Column *R* corresponds to the final rank index used for ranking the days. The final column corresponds to the ranking of the event.

Table 16.2 The top ten events ranking of three-day accumulated extreme precipitation events

Date	% Area (*A*)	Mean (*M*)	*R* = *A**M	Rank
05-09-1995	9.24	94.86	876.64	1
05-08-2006	5.93	135.29	801.77	2
06-08-2006	7.21	105.03	757.35	3
24-07-1989	8.56	81.98	701.56	4
03-08-1997	5.41	118.76	642.27	5
06-09-1995	7.81	81.89	639.74	6
25-07-1989	8.50	75.20	638.91	7
04-08-2006	3.81	161.62	616.21	8
09-08-2019	8.60	69.99	601.82	9

The first column corresponds to the date of the event. Column *A* corresponds to the area (in %) of the domain that has extreme precipitation anomalies above N95. Column *M* corresponds to mean value of these extreme precipitation anomalies over area *A*. Column *R* corresponds to the final rank index used for ranking the days. The final column corresponds to the ranking of the event.

Table 16.3 The top ten events ranking of five-day accumulated extreme precipitation events

Date	%Area (A)	Mean (M)	R = A*M	Rank
07-08-2006	6.78	113.46	768.78	1
10-08-2019	4.43	141.11	625.73	2
06-09-1995	5.53	111.50	616.89	3
11–08-2019	4.06	133.63	542.71	4
13-08-2017	3.42	158.05	540.36	5
08-08-2006	6.01	89.79	539.57	6
09-08-2019	5.26	99.06	521.38	7
07-09-1995	5.14	97.73	502.24	8
27-09-1988	6.42	77.32	496.64	9

The first column corresponds to the date of the event. Column A corresponds to the area (in %) of the domain that has extreme precipitation anomalies above N95. Column M corresponds to mean value of these extreme precipitation anomalies over area A. Column R corresponds to the final rank index used for ranking the days. The final column corresponds to the ranking of the event.

Table 16.4 The top ten events ranking of seven-day accumulated extreme precipitation events

Date	Area	Mean	Rm	Rank
11–08-2019	3.61	154.67	557.67	1
10-08-2019	4.00	137.59	550.23	2
06-09-1995	4.21	115.23	484.72	3
05-09-1995	4.93	97.79	482.26	4
13-07-1962	3.13	146.02	456.87	5
12-08-2019	3.07	147.62	452.69	6
24-06-1974	1.28	325.87	418.65	7
07-09-1995	3.94	105.98	417.25	8
14-07-1962	2.74	145.50	397.97	9

The first column corresponds to the date of the event. Column A corresponds to the area (in %) of the domain that has extreme precipitation anomalies above N95. Column M corresponds to mean value of these extreme precipitation anomalies over area A. Column R corresponds to the final rank index used for ranking the days. The final column corresponds to the ranking of the event.

Therefore, two or three intense precipitation anomalous days will be sufficient to influence successive periods.

The one-day first rank event on July 24, 1989 (Fig. 16.2), was widespread, with 12.08% of Indian subcontinent showing extreme precipitation anomalies larger than $P95$. It reached an average extreme precipitation anomaly of 46.89 mm (Fig. 16.2). The event hit the central peninsula and west-coast section of India, with maximum precipitation more than 250 mm and with precipitation above 150 mm observed at several grid points. The same event is also present in the three-day ranking (rank 4 and 7) underlining that it was dominant at the daily scale, but precipitation on the day before and the day after was also relevant (Fig. 16.2). In this regard, any ranking methodology focusing on single-day duration would be limited in capturing its evolution. The absence of this event from further multiday ranking (five- and
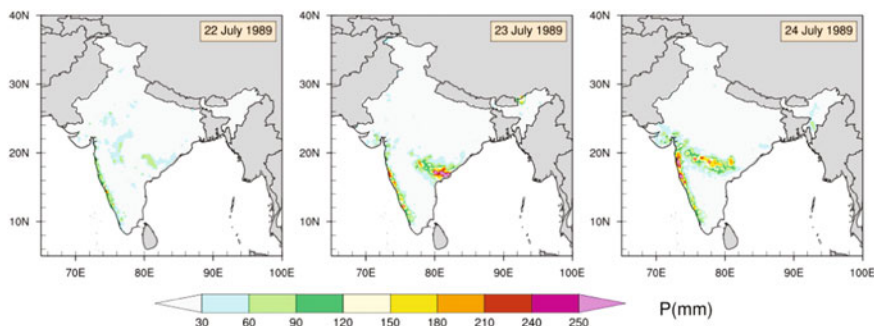
Fig. 16.2 Spatiotemporal variation of precipitation events 2 days prior to the top-ranked one-day accumulated extreme precipitation event. The magnitude of precipitation (mm) is shaded in different colors

seven-day ranking) shows that the extreme event occurred only for three to four continuous days (i.e., July 22–25).

Several events, which are not significant on a daily ranking, become significant, based on intensity and spatial extension at longer time durations (as shown in Tables 16.1, 16.2, 16.3, and 16.4). For instance, the total of five different events appeared in the three-, five-, and seven-day ranking categories that are absent in one-day ranking. The changes in the ranking of different duration highlight the importance of multiday ranking of extremes, as it is crucial to capture events of varying spatiotemporal characteristics. The extreme event of August 11, 2019, accounts for eight occurrences. The event was not a short-lived one and lasted for a considerably longer duration of 7 days from August 2 to August 11, 2019 (Fig. 16.8). Daily average extreme precipitation anomalies higher than 154.67 mm are present on all the days. Precipitation was localized and intense (Fig. 16.9) along west coast throughout 7 days. This prolonged event was related to the disastrous floods that took place in Odisha and Kerala between August 1 and 20 causing the death of 135 people and affecting 89.76 lakh people in total (https://weather.com/en-IN/india/news/news/2020-01-08-top-5-biggest-floods-affect-india-2019).

16.4.2 Moisture Transport During Extreme Precipitation Events

Top-ranked multiday extreme precipitation events identified as per the above criteria are shown in Figs. 16.2, 16.4, 16.6, and 16.8. Figs. 16.3, 16.5, and 16.7 and 9 show vertically integrated water vapor associated with this multiday extreme precipitation events. For the present analysis, the hilly regions of north-eastern parts of India and the Western Ghats were not considered for this analysis. It is interesting to see the asymmetry in the moisture convergence and associated rainfall, which is a characteristic of the monsoon low-pressure systems (Sagar et al. 2017).

Fig. 16.3 Atmospheric moisture transport 2 days prior to the top-ranked one-day accumulated extreme precipitation event. The magnitude of atmospheric moisture transport quantified by IVT (kg/m/s) is shaded in different colors, while the direction of atmospheric moisture transport is also shown with black color vector arrows
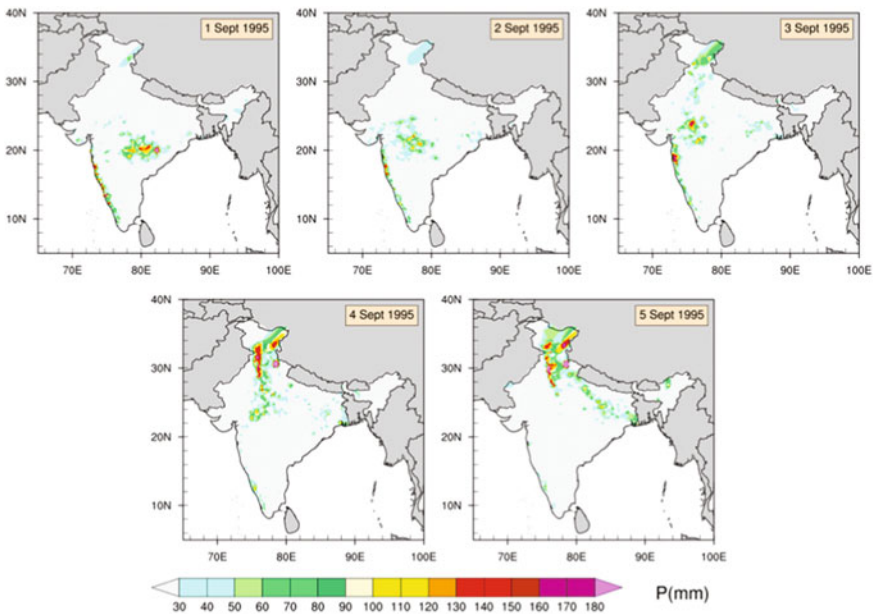
Fig. 16.4 Spatiotemporal variation of precipitation events 2 days prior to the top ranked three-day accumulated extreme precipitation event. The magnitude of precipitation (mm) is shaded in different colors

In addition, results show atmospheric moisture transport persisting for 2 days or more prior to the occurrence of multiday extreme precipitation events with peak IVT intensity ranging between 900 and 1000 kg/m/s (as shown in Figs. 16.3, 16.5, 16.7, and 16.9). The existence of consistent IVT values above 1000 kg/m/s during heavy precipitation events emphasizes that persistent nature of IVT will be an indication of the extent of extreme rainfall over a region. It is proved from the analysis that the existence of intense moisture transport, which is at least persisting for 24 h, may be the major reason for the occurrence of heavy precipitation. Our findings are in

Fig. 16.5 Atmospheric moisture transport 2 days prior to the top ranked three-day accumulated extreme precipitation event. The magnitude of atmospheric moisture transport quantified by IVT (kg/m/s) is shaded in different colors, while the direction of atmospheric moisture transport is also shown with black color vector arrows
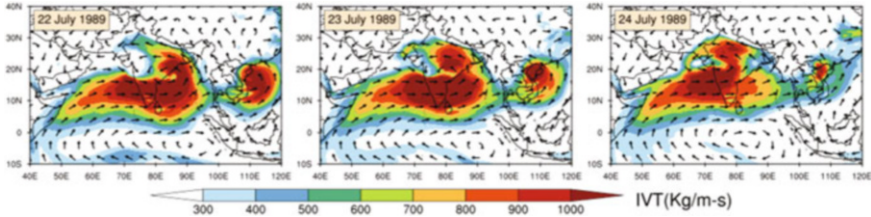

Fig. 16.6 Spatiotemporal variation of precipitation events 2 days prior to the top ranked 5-day accumulated extreme precipitation event. The magnitude of precipitation (mm) is shaded in different colors

coherence with recent studies (Sagar et al. 2017; Hazra et al. 2017) regarding extreme precipitation caused by low-level convergence and abundance of moisture in the atmosphere.
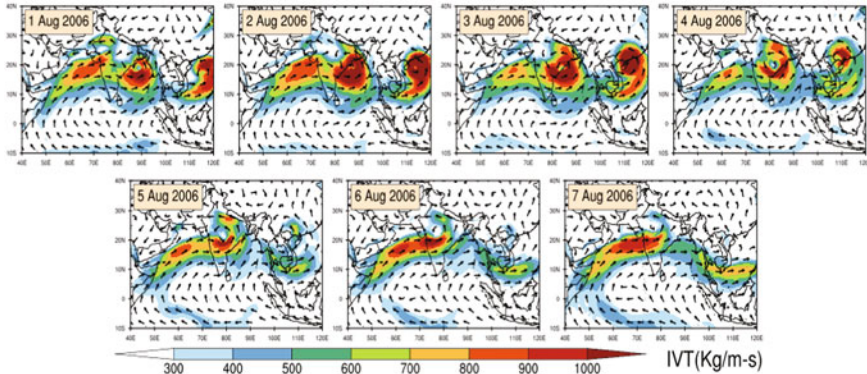
Fig. 16.7 Atmospheric moisture transport 2 days prior to the top-ranked five-day accumulated extreme precipitation event. The magnitude of atmospheric moisture transport quantified by IVT (kg/m-s) is shaded in different colors, while the direction of atmospheric moisture transport is also shown with black color vector arrows

16.5   Conclusions

We ranked multiday extreme precipitation events over India using a methodology similar to that used by Ramos et al. (2018). We considered both magnitude and spatial extent to rank events of different durations. We found that a few events received higher rankings due to their more significant precipitation amounts and impacts. Our ranking technique can help identify the timing of maximum impact and long-duration extremes. We also examined the association between atmospheric moisture transport and extreme precipitation events. Our results suggest that high moisture incursion over regions near cyclonic circulations increases specific humidity and contributes to the development of thunderstorms leading to multiday extreme precipitation. Our findings emphasize the importance of utilizing a multiday ranking scheme to accurately measure and monitor the spatial and temporal propagation of extreme precipitation events. The ranking database we created can also be useful for studying the impacts of extreme precipitation periods on wide areas and analyzing changes in atmospheric circulation throughout those days. Future studies will focus on looking into different synoptic scale meteorological patterns during multiday extreme precipitation events.
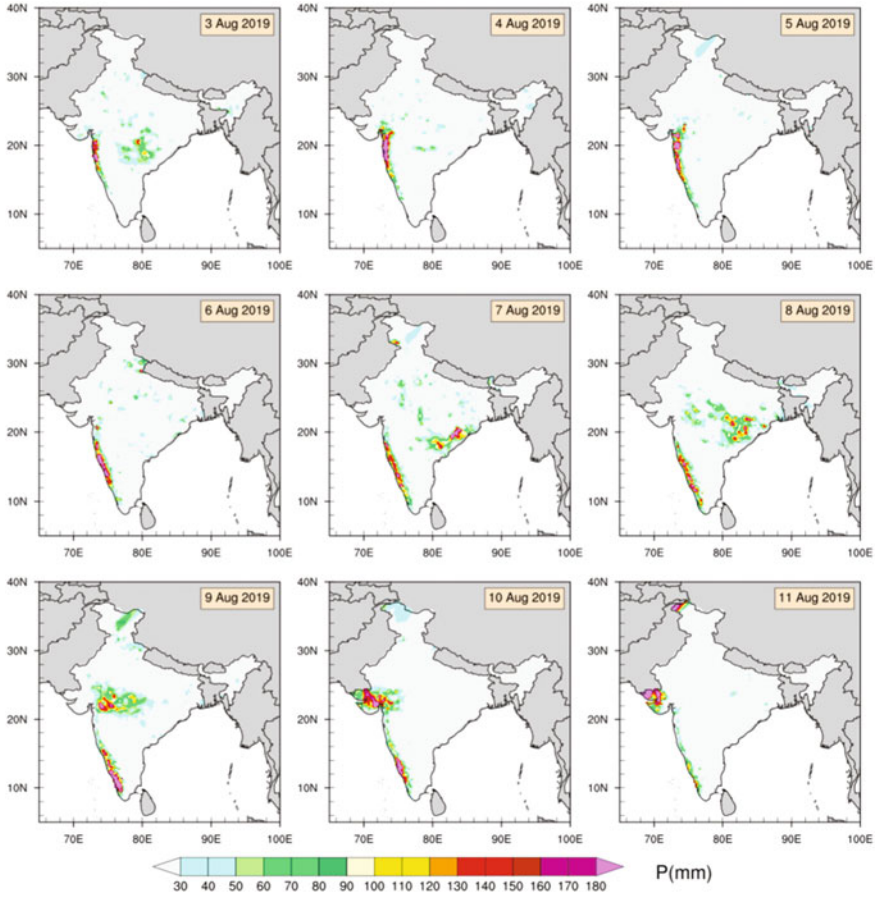
Fig. 16.8 Spatiotemporal variation of precipitation events 2 days prior to the top ranked seven-day accumulated extreme precipitation event. The magnitude of precipitation (mm) is shaded in different colors
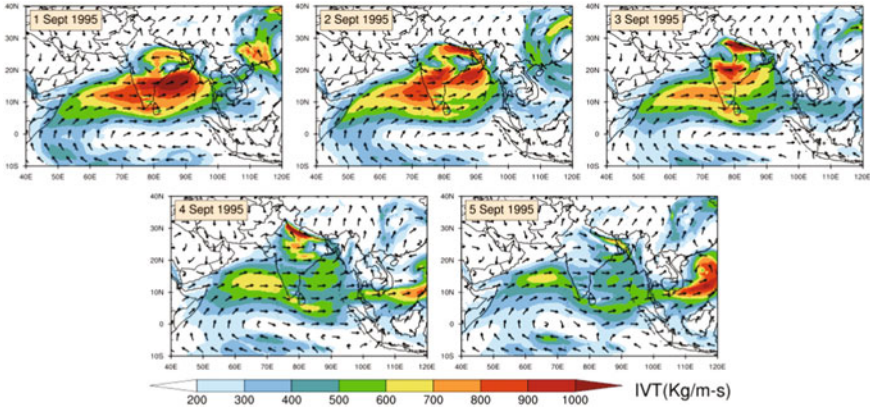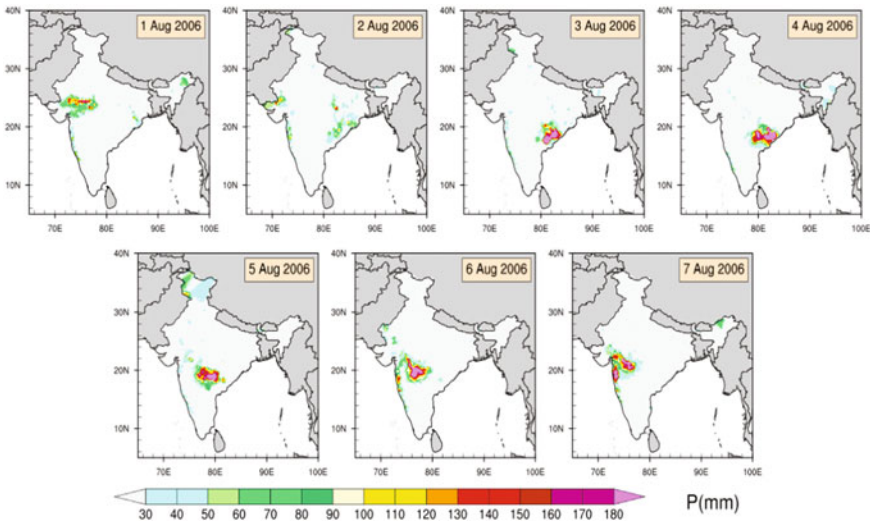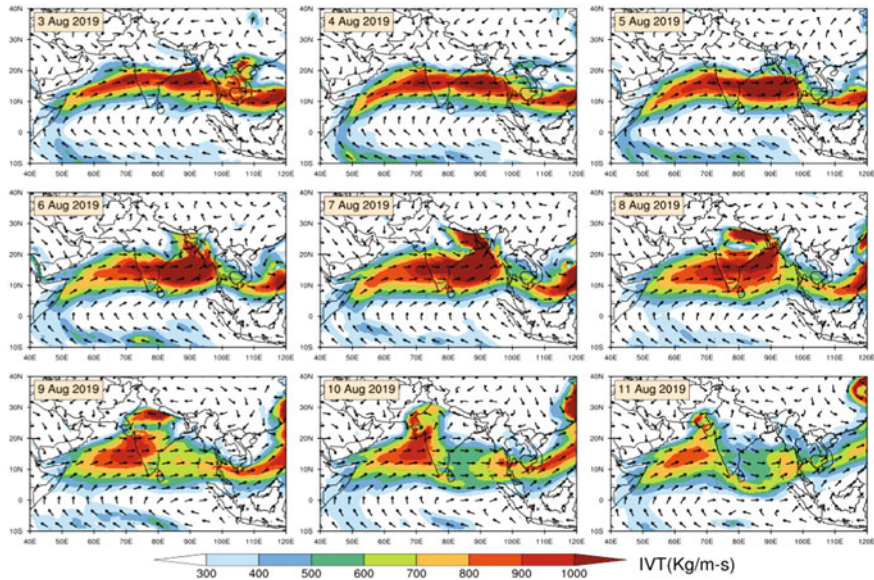
Fig. 16.9 Atmospheric moisture transport 2 days prior to the top ranked seven-day accumulated extreme precipitation event. The magnitude of atmospheric moisture transport quantified by IVT (kg/m/s) is shaded in different colors, while the direction of atmospheric moisture transport is also shown with black color vector arrows

Data Availability Statement

The datasets used in this paper are freely available. The gridded rainfall datasets for Indian subcontinents are made available on https://imdpune.gov.in/cmpg/Griddata/Rainfall_25_Bin.html. ERA5 reanalysis datasets are for Indian subcontinents are available on https://cds.climate.copernicus.eu/#!/search?text=ERA5&type=dataset

Declaration of Conflict of Interest The authors declare no conflicts of interest relevant to this study.

Author Contributions All the authors contributed equally.

References

Beguería S, Vicente-Serrano SM, López-Moreno JI, García-Ruiz JM (2009) Annual and seasonal mapping of peak intensity, magnitude and duration of extreme precipitation events across a

climatic gradient, northeast Spain. Int J Climatol 29(12):1759–1779. https://doi.org/10.1002/joc.1808

Ciric D, Nieto R, Ramos A, Drumond A, Gimeno L (2017) Wet spells and associated moisture sources anomalies across Danube River Basin. Water 9(8):615. https://doi.org/10.3390/w9080615

Dettinger MD, Ralph FM, Das T, Neiman PJ, Cayan DR (2011) Atmospheric rivers, floods and the water resources of California. Water 3(2):445–478. https://doi.org/10.3390/w3020445

Francis PA, Gadgil S (2006) Intense rainfall events over the west coast of India. Meteorog Atmos Phys 94:27–42. https://doi.org/10.1007/s00703-005-0167-2

Gimeno L, Dominguez F, Nieto R, Trigo R, Drumond A, Reason CJC, Taschetto AS, Ramos AM, Kumar R, Marengo J (2016) Major mechanisms of atmospheric moisture transport and their role in extreme precipitation events. Annu Rev Environ Resour 41(1):117–141. https://doi.org/10.1146/annurev-environ-110615-085558

Goswami BN, Venugopal V, Sengupta D, Madhusoodanan MS, Xavier PK (2006) Increasing trend of extreme rain events over India in a warming environment. Science 314(5804):1442–1445. https://doi.org/10.1126/science.1132027

Hazra A, Chaudhari HS, Ranalkar M, Chen J-P (2017) Role of interactions between cloud microphysics, dynamics and aerosol in the heavy rainfall event of June 2013 over Uttarakhand, India. Q.J.R. Meteorol. Soc 143:986–998. https://doi.org/10.1002/qj.2983

Hersbach H et al (2020) The ERA5 global reanalysis. Q J R Meteorol Soc 146(730):1999–2049. https://doi.org/10.1002/qj.3803

Hrudya PH, Varikoden H, Vishnu R (2021) A review on the Indian summer monsoon rainfall, variability and its association with ENSO and IOD. Meteorog Atmos Phys 133(1):1–14. https://doi.org/10.1007/s00703-020-00734-5

Joshi UR, Rajeevan M (2006) Trends in Precipitation Extremes over India, p 28

Mahto SS, Mishra V (2019) Does ERA-5 outperform other reanalysis products for hydrologic applications in India? J Geophys Res Atmos 124(16):9423–9441. https://doi.org/10.1029/2019JD031155

Müller M, Kaspar M (2014) Event-adjusted evaluation of weather and climate extremes. Nat Hazards Earth Syst Sci 14(2):473–483. https://doi.org/10.5194/nhess-14-473-2014

Neiman PJ, Ralph FM, Wick GA, Kuo Y, Wee T, Ma Z, Taylor GH, Dettinger MD (2008) Diagnosis of an intense atmospheric river impacting the Pacific northwest: storm summary and offshore vertical structure observed with COSMIC satellite retrievals. Mon Weather Rev 136(11):4398–4420. https://doi.org/10.1175/2008MWR2550.1

Neiman PJ, Ralph FM, Moore BJ, Hughes M, Mahoney KM, Cordeira JM, Dettinger MD (2013) The landfall and inland penetration of a flood-producing atmospheric river in Arizona. part i: observed synoptic-scale, orographic, and hydrometeorological characteristics. J Hydrometeorol 14:460–484. https://doi.org/10.1175/JHM-D-12-0101.1

Pai DS, Rajeevan M, Sreejith OP, Mukhopadhyay B, Satbha NS (2014) Development of a new high spatial resolution (0.25° × 0.25°) long period (1901-2010) daily gridded rainfall data set over India and its comparison with existing data sets over the region. MAUSAM. 65(1):1–18. https://doi.org/10.54302/mausam.v65i1.851

Raj S, Shukla R, Trigo RM, Merz B, Rathinasamy M, Ramos AM, Agarwal A (2021) Ranking and characterization of precipitation extremes for the past 113 years for Indian western Himalayas. Int J Climatol 41(15):6602–6615. https://doi.org/10.1002/joc.7215

Ralph FM, Neiman PJ, Wick GA (2004) Satellite and CALJET aircraft observations of atmospheric rivers over the eastern North Pacific Ocean during the winter of 1997/98. Mon Weather Rev. 132(7):1721–1745. https://doi.org/10.1175/1520-0493(2004)1322.0.CO;2

Ramos AM, Trigo RM, Liberato MLR (2014) A ranking of high-resolution daily precipitation extreme events for the Iberian Peninsula: ranking of the Iberian Peninsula daily precipitation. Atmos Sci Lett. https://doi.org/10.1002/asl2.507

Ramos AM, Trigo RM, Liberato MLR (2017) Ranking of multi-day extreme precipitation events over the Iberian Peninsula: multi-day extreme precipitation events Iberian Peninsula. Int J Climatol 37(2):607–620. https://doi.org/10.1002/joc.4726

Ramos AM, Martins MJ, Tomé R, Trigo RM (2018) Extreme precipitation events in summer in the Iberian Peninsula and its relationship with atmospheric rivers. Front Earth Sci 6:110. https://doi.org/10.3389/feart.2018.00110

Ren F, Cui D, Gong Z, Wang Y, Zou X, Li Y, Wang S, Wang X (2012) An objective identification technique for regional extreme events. J Clim 25(20):7015–7027. https://doi.org/10.1175/JCLI-D-11-00489.1

Roxy MK, Ghosh S, Pathak A, Athulya R, Mujumdar M, Murtugudde R, Terray P, Krishnan R, Rajeevan M (2017) A threefold rise in widespread extreme rain events over Central India. Nat Commun 8:708. https://doi.org/10.1038/s41467-017-00744-9

Sagar SK, Rajeevan M, Rao SVB (2017) On increasing monsoon rainstorms over India. Nat Hazards 85:1743–1757. https://doi.org/10.1007/s11069-016-2662-9

Tabari H (2020) Climate change impact on flood and extreme precipitation increases with water availability. Sci Rep 10:13768. https://doi.org/10.1038/s41598-020-70816-2

Turner A, Annamalai H (2012) Climate change and the South Asian summer monsoon. Nat Clim Change 2:587–595. https://doi.org/10.1038/nclimate1495

Zhu Y, Newell RE (1998) A proposed algorithm for moisture fluxes from atmospheric rivers. Mon Weather Rev. 126(3):725–735. https://doi.org/10.1175/1520-0493(1998)1262.0.CO;2

Part III
River Restoration, Hydraulic Structure Stability and Flood Risk Management

Chapter 17
Remote Sensing and Its Application on Soil: An Ecosystem Services

Deeksha, Anoop Kumar Shukla, Nandineni Rama Devi, and Satyavati Shukla

Abstract Ecosystem services are a necessary part of human life. Because these ecological services linked directly to human survival, we must understand the significance of their interaction, even though there is a large amount of literature on the subject, establishing a suitable knowledge foundation, which is vital. In this book chapter, we discussed importance of ecosystem services (ES) and its various forms and explored various remote sensing techniques and the models used to assess soil ES. As a result, we discover that the emphasis of modern urban studies is changing from interpretation to information collection for effective decision-making, which will help readers grasp the issues associated with the existing system and the way forward to achieve sustainable development.. This work will assist stakeholders and policymakers in taking necessary actions to preserve the present ecological equilibrium.

Keywords Ecosystem services · Remote sensing · GIS · Soil · River

17.1 Introduction

Soils are the Earth's greatest carbon reservoir, storing approximately 3.3 times more carbon than the atmosphere and 4.5 times more than total biomass. Wetlands play an important role in carbon sequestration, an ecological function that is seen as a critical environmental benefit in the context of global warming. Based on the land usage practise, temperature, structure, and terrain, the reservoir of soil organic carbon can operate as a source (through oxidation of carbon into CO^2 owing to soil exposure to

Deeksha · A. K. Shukla (✉) · N. Rama Devi
Manipal School of Architecture and Planning, Manipal Academy of Higher Education, Manipal, Karnataka, India
e-mail: deeksha.msapma2@learner.manipal.edu; anoop.shukla@manipal.edu; nandineni.rd@manipal.edu

S. Shukla
Key Laboratory of Geospatial Informatics, Guilin University of Technology, Guilin, PR, China

atmosphere) or a sink (by long-term retention of carbon as organic matter in soil) of atmospheric carbon dioxide.

Soil properties are one of the most critical environmental elements that have a significant influence on the structure and productivity of coastal wetlands. Topography, tidal or riverine sedimentation patterns, temperature, tidal regime, and long-term sea level fluctuations, as well as soil type and its physical, chemical, and biological qualities, may all contribute to aquatic vegetation ability to capture atmospheric carbon through photosynthesis.

The value of biodiversity is intrinsically connected to ecosystem services and individual well-being. Apart from incursion, additional risks to biodiversity include soil degradation, air degradation, and climatic changes. Ecosystem services (ES) are the advantages people receive from nature (Costanza et al. 1997; Daily 1997. To build a bridge between nature and society, ES combines human well-being and natural systems for ecological and economic growth. Changes in land use and land cover significantly influence ecosystem services, leading to deterioration (Deeksha and Shukla 2022; Gupta et al. 2023; Saikumar et al. 2022; Sharma and Goyal 2018; Shukla et al. 2018; Shukla et al. 2020). As a result, evaluating ecosystem services has been a focus of academic research for many years. Recent interventions also demonstrate the study's preparedness to advise policymakers in making critical decisions in the policymaking process, as well as the integration of ecology, geography, and economy.

ES is essential in ensuring an individual's well-being by providing security, satisfying fundamental necessities for day-to-day living, and maintaining strong social relationships. As half of the world's population lives in cities, urban ecosystems remain a significant topic of ecosystem service study. According to MEA (2005), over 60% of worldwide ES has been threatened or inappropriately exploited, and a similar trend is projected to continue for the foreseeable future. As a result, ES is now widely regarded as a critical component of land-use planning, ecological, environmental planning, and management.

The interaction between the ESs might be of two forms. The first is tradeoffs, in which an increase in one ES's influence leads to a decrease in another ES's effect. Second, there are synergies, which occur when the action of one ES increases the impact of another ES (Han et al. 2020). Understanding this link is crucial because it focuses on the interaction between ES by focusing on intrinsic bundles (Cord et al. 2017) rather than separate ES when similar relationships arise again throughout place and time. According to studies, tradeoffs and synergies are created by interactions between multiple ecosystems. Hence, ecosystem services cannot be regarded as autonomous. Researchers conclude that studying numerous ecosystem services is difficult (Braat and de Groot 2012; Bejagam et al. 2023; Das et al. 2023).

Several more paradigms for ES investigations have recently developed (Li et al. 2021). The Common International Classification of Ecosystem Services (CICES) includes multiple ES criteria to account for natural capital. The framework designed by the Intergovernmental Science-Policy Platform on Biodiversity and Ecosystem Services (IPBES) closely captures themes that link nature's contribution to humanity. To better comprehend ES, researchers developed a foundation framework for

worldwide ES research; hence, ES is divided into four categories: (i) provisioning ecosystem services, (ii) regulating ecosystem services, (iii) supporting ecosystem services, (iv) cultural ecosystem services.

Ecosystem services described as commodities that may be directly derived from nature, consumed, and have a commercial value. Water, food, timber, and biofuels are all examples of provisioning ecosystem services. Similarly, for the freshwater supply, ecosystem service provided an environment that works well (Abera et al. 2021). Precipitation, evaporation, and climatic fluctuation significantly influence the region's water output (Zhang et al. 2018). Water yield has a favorable relationship with evapotranspiration and soil conservation, as well as other components such as food production and wood.

Regulating ecosystem services may be described as the advantages derived from the ecosystem's process current affairs. Climate change, carbon storage, soil fertility, floods, and other examples will be given. The study's researcher (Bennett et al. 2009) stresses the interaction between regulating ecosystems and other ESs in terms of tradeoffs and synergies, as a result of which regulating ESs regarded as one of the essential metrics for assessing ecological resilience. Managing one ES component improves synergies with other ES parameters, particularly carbon storage, low flow, biodiversity, and so forth (Carter Berry et al. 2020). Carbon storage is a critical component in the worldwide service of climate management (Gómez-Baggethun and Barton 2013). Because of the ineffectiveness non-interpreting-scientific criteria, the practical application of carbon sequestration knowledge will take a step back in public governance. Carbon sequestration is a critical factor in global climate management. Because carbon is held in the terrestrial environment, researchers (Delibas et al. 2021) investigated the significance of soil in avoiding climate change by sequestering carbon. As a result, the carbon in the ground significantly influences geographical and nonspatial data. As a result, modeling and comparing various LULC scenarios can provide crucial information to policymakers in decision-making. This process may be re-scaled globally, regionally, and locally by linking various rationales to economic possibilities and regulatory legislation.

Researchers introduced cultural ecosystem services and examined and characterized it as "the non-material or intangible advantages humans gain from the ecosystem either spiritually, via cognitive growth, recreation, self-reflection or by enjoying aesthetically" (Gómez-Baggethun and Barton 2013; MEA 2005). Some of the services in this ES, such as recreation, have monetary value, while others do not. Many methods in which cultural ecosystems are incorporated in the research are functions that fulfil life information functioning (de Groot et al. 2012; Das et al. 2020). Furthermore, simplify the term by linking human sociocultural behaviors to psychological growth (Sen and Guchhait 2021). CES is also related to the intangible advantages individuals gain from nature as a result of engagement. Several researches on cultural ecosystem services focus on nature-based and aesthetic recreation services (TEEB 2010), with little attention paid to the spiritual value of landscape due to modeling limitations (Nelson et al. 2013).

Supporting ecosystem services are the underlying processes of the ecosystem that sustain life, such as photosynthesis, the nutrient cycle, and evolution; this is a critical

service that the ecosystem offers, allowing the rest of the ecosystem services to be delivered.

17.2   Soil Ecosystem Service

Soils are a crucial element of environments; therefore, understanding their processes requires multidisciplinary and transdisciplinary methods. Soil is generated when the lithosphere, biosphere, atmosphere, and hydrosphere collide. It manages the bulk of ecological processes in environments. It is host to a considerable part of the world's biodiversity, supplying the physical underpinning for many anthropogenic activities. Anthropogenic influences on soil have been worse since the dawn of agriculture (Brevik et al. 2015; Beyene et al. 2021). Man has used soil for centuries, and this legacy is widely recorded. Yet, despite such extensive use, a complete perspective on the subject has just lately evolved. Undoubtedly, all of various applications of soils have received considerable attention over the past, yet there is hardly any overlap from one research field toward another. Someone might propose that the absence of a holistic viewpoint is related to the reality that soil resources were not limited till the beginning of the twentieth decade, and thus, individuals did not automatically conceive of diverse soil usages as competing, including one another. Along with air and water health, soil conditions constitute one of the three factors of ecosystems. Water and air quality are primarily influenced by the amount of contamination they contain, which significantly affects the benefit of humans and animals, health, and ecological systems. Soil quality, on the other hand, is described rather more generally as "the ability of a soil to operate within ecological and territory constraints to sustain biological production, preserve ecological integrity, and encourage flora and fauna health."

Soil ES has been significantly damaged due to global warming and anthropogenic activity, threatening food safety in the future. Climate change will likely reduce soil quality by altering the soil-water-gas balance and lowering soil organic carbon. Nevertheless, the soil is indeed most excellent terrestrial carbon store and, if not maintained properly, may contribute significantly to greenhouse gas emissions. Agricultural development, unsustainable practices, alteration of natural environments in rural regions, and urban sprawl are all hastening soil deterioration, with negative consequences for soil value (Pereira et al. 2016).

Soils are an essential natural resource since they influence a country's financial position (Dominati et al. 2010). Soil natural capital is characterized as the soil's ability to deliver the ES necessary for specific land use, providing that sustainable practices are adopted (Hewitt et al. 2015).

Urban soils are impermeable, heavily contaminated, poisonous to plants and microorganisms, and threaten people's well-being (De Vries et al. 2013). Likewise, in mining-affected regions, soils may be incapable of supporting productive and functioning ecosystems. Soil ES of provision, regulation, and cultural relevance are particularly endangered in intensive agricultural areas, and more efficient techniques

that reduced soil ES deterioration are required. It is critical to restoring a few of these deteriorated regions prone to significant disruptions to reintroduce ES. This paper aims to examine the significance of soil ES and RS GIS application on the same.

17.3   Importance of Soil Ecosystem Service

Soils face intense stresses in metropolitan settings, reducing the quantity and quality of the ES they offer. Notwithstanding these challenges, these grounds significantly contribute to food grown in urban gardens, leading to long-term food security, urban resilience, and urban environment development. Management of soil functions is critical for agricultural output. Soil productivity and sensitivity to deterioration will be determined by their ability to preserve carbon, water, and nutrients. Healthy soils have more significant potential to absorb carbon, water, and nutrients; reduce greenhouse gas emissions; and fight pests and diseases. The ability of farming soils to control ES is declining as the region is surrounded by intensive crop production practices to raise animals and people expands. This excessive usage affects soils' long-term capability to manage functions critical to the sustainability of ecosystems and societies.

The ES value of soil is determined by its potential supply and how we handle it (Fig. 17.1). Grounds can bring just brief advantages that are not unsustainable or advantages that only become visible over time, depending on how we handle our property. Nonsustainable administration may devalue and deteriorate ecosystem soil services, whereas sustainable management can preserve or increase such facilities. Many methods for assessing soil ES have been developed for general soil services, although most of the assessments have been centered on agricultural landscapes. Those concepts are utilized to increase our understanding of agriculture practices' ability to transform agroecosystems and vice versa.

The value, devaluation, deterioration, preservation, or enhancement of soil ES is inextricably tied to land use planning. The primary reason for soil deterioration in urban and peri-urban settings are urban sprawl, which results in a variety of soil disservices, including sealing, contamination, ecosystem and habitat loss, and water and nutrient losses. Innovative types of urban design that utilize organic alternatives are required to limit the effects caused by humans and towns on soil functions, hence lowering land usage, the likelihood of medical conditions, and the expenses connected with them.

17.4   RS and GIS Implemented in Soil ES Studies

Remote sensing (RS) is a basic form of science that helps us acquire and analyze information about any object or phenomenon from a certain distance through the help of satellites. Today, we find various applications of remote sensing in
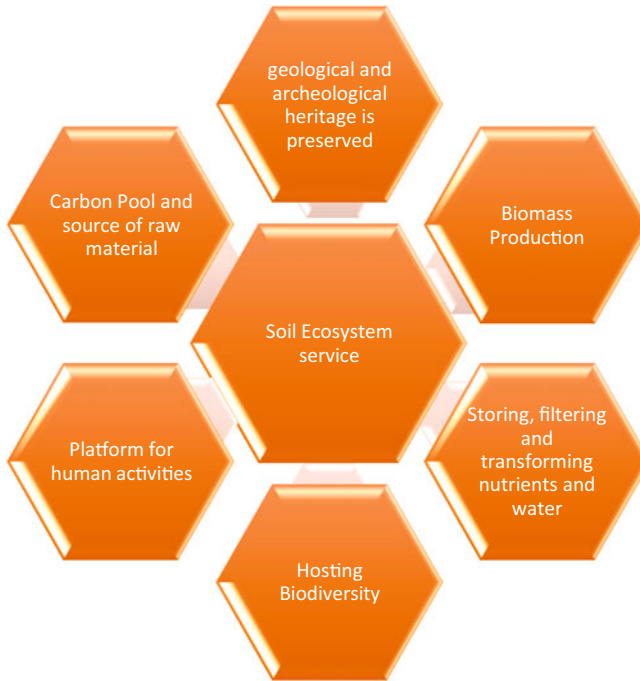
Fig. 17.1 Characteristics of soil ecosystem services

groundwater analysis, mining and mineral exploration, biophysical mapping, geo-logical planning and mapping, landslide hazard analysis, earthquake analysis, geo-morphology studies, etc. And the Geographic Information System (GIS) data model represents how we intend to look at the world and gives an understanding of how the world works. GIS data provides new representation for one or more aspects of the real world. The models created may be of the static type, where the input to the model and the processed output from the model pertains to a specific study area for the same period. These studies provide general indicators, impact factors, and weak points toward the current scenario study area like soil exploration, water contami-nation estimates, land use land cover (LULC) change studies, ecosystem service studies, etc. In this section, we shall understand the application of RS and GIS in studying ecosystem services.

Ecosystems may be investigated at several scales, including global, regional, and local. Global-level studies are conducted globally, but researchers recommend examining the services at the local level, which provides us with a better knowledge of the issue and aids in the implementation of suitable mitigation methods at the regional level. This contributes to achieving global sustainable goals (Jia et al. 2014). Although several research investigations have shed light on the interdependence of various ecosystem services in recent years, the merger of our existing knowledge reservoir and gaps remains insufficient (Lee and Lautenbach 2016).

Remote sensing and GIS implementations in ecosystem surveillance are increasingly widespread, overcoming the limits of old approaches and allowing observation of multiple spatiotemporal scales in a repeated and unbiased way (Lausch et al. 2016; Soubry et al. 2021). The inherent properties of GIS and RS allow for the synchronization of synoptic, geographically linked, and periodic observations. The data is used to understand man-environment interactions in a specific metropolitan area (Luederitz et al. 2015). RS-based evaluations are gaining popularity as a valid method for modeling, mapping, and evaluating ecosystems and their products (Pettorelli et al. 2014). The scenario includes assessing the potential of RS for protecting urban ecological integrity. As a result, the current study is meant to highlight the relevance and potential of remote sensing in measuring ES. It examines attitudes regarding RS in recent research on ecosystem services.

The ES model assists the researcher in quantifying, physically locating, and perhaps evaluating economic patterns. According to Daily, this knowledge is critical in helping urban planners, designers, and legislators understand the impact of urban growth on ES. There is a profusion of models and technologies available now that assist us in mapping and accessing ES and likewise (Signorello et al. 2020).

A growing body of research has tried to comprehend land-use developments and their influence on ES at the same time, which has assisted designers and policymakers in taking proper actions to address the issue. Satellite photos have been widely utilized as the most accurate technique for monitoring LULC and ES changes (Shukla et al. 2020; Verma and Raghubanshi 2019). Models are used to examine the interactions of ES (such as a tradeoff, synergies, bundles/clusters, and flows) and to bring forth advantages that humans experience for their well-being consciously (Dang et al. 2021). Enhancing ecosystem service management by objectively assessing interactions among multiple ES is highly valued.

The Integrated Valuation of Environmental Services and Tradeoffs (InVEST) tool was created inside the Natural Capital Project (Signorello et al. 2020). The InVEST model can display a spatially displayed map of the ESs. When compared to other models, the In-VEST model requires little experience; it provides a virtually exact evaluation with a minimum number of data input criteria and is useful in comprehending areas dealing with ecological processes. The In-VEST model is a helpful tool for evaluating small-scale and local research that produces meaningful and trustworthy results for LULC and ES. Using user-defined base settings like land usage, land cover, and climate variations, the InVEST toolbox is used to calculate roughly 14 ES for supply changes.

Soil and Water Assessment Tool (SWAT) is widely used to simulate hydrological processes (Notter et al. 2012). Furthermore, the model offers spatial discretization flexibility, allowing it to assess space locally, regionally, and globally. To measure ES changes, various models are utilized, including ARIES, LUCI, CA-Markov, SLEUTH, CLUES, and others.

Ecosystem services are studied quantitatively using mapping and modeling tools. Researchers also employed a mix of models to analyze ES, such as a combination of model mapping ES (such as InVEST, SWAT, and ARIES), model mapping urban expansion, and statistical modeling. LUSD-urban (Land Use Scenario

Dynamics-urban) is an urban expansion model that helps in a multi-scale simulation of urban development. LUSD-urban, together with Cellular Automata (CA) and system dynamics models, represents micro-scale evolutionary factors and macro-scale resource restrictions. This model has gone through several versions in recent years, with improved accuracy and a kappa index on average (Xie et al. 2018). SLEUTH (Slope, Land use, Exclusion, Urban extent, Transportation, and Hill shade) and CLUE-S are the other models (the Conversion of Land Use and its Effects at a Small regional area). Correlation analysis, regression analysis, and root mean square deviation are examples of statistical models. This model combination is effective for creating correlations among a few variables, but it is not regarded as practically feasible. InVEST, ARIES, and SWAT are the most well-known models.

LULC, soil data, topographical data, and hydrological data are the most widely utilized base data. This provides a comprehensive picture of several criteria, such as habitats, soil types, vegetation classes, and biomes. Additional types of data required for ES evaluation include census data, meteorological data such as precipitation data, which is used for water yield assessment, and digital elevation model (DEM), which is employed for Hydrology evaluation.

InVEST, SWATARIES (Artificial Intelligence for Ecosystem Services (ARIES), LUCI, and other models are utilized to obtain spatiotemporal ESs. According to the publishing trend, the InVEST model is widely utilized due to its input data criterion; it uses publicly available open-source data and has a mapping/modeling scale of 30 x 30 m. This strategy enables us access to various ecological services (water quality, soil erosion, carbon sequestration, biodiversity conservation, nutrients, agricultural produce, etc.).

17.5 The Methodological Framework Used to Study (Soil) ES

The methodological framework (Fig. 17.2) used to assess ecosystem services starts with the image acquisitions from earth observation satellite. Followed by spatial map preparation, LULC maps are created using satellite images and ERDAS Imagine image processing software. The map can be prepared using pixel-based image analysis (PBIA) or object-based image analysis (OBIA) method (Shukla et al. 2018). In PIBA framework, we have two types of map classification, that is, supervised classification and unsupervised classification.

Object-based image analysis (OBIA) and nearest neighbor (NN) classification are used to create land use land cover (LULC) maps. The categorization indices for OBIA are as follows: (1) the Normalized Difference Vegetation Index (NDVI), which estimates the density of green cover on a specific land parcel; (2) the Soil Adjustment Vegetation Index (SAVI), which corrects NDVI for the impact of soil brightness on the given land parcel and is employed where vegetation cover is poor; (3) Normalized Difference Water Index (MNDWI) modification, which aids in
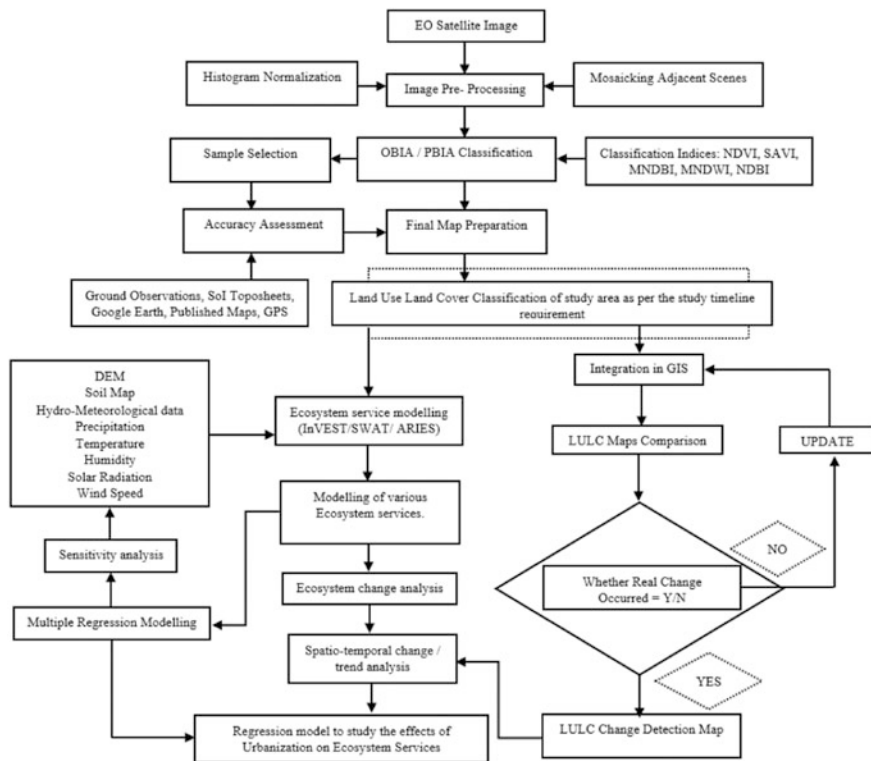
Fig. 17.2 Methodological framework used to study ES using RS and GIS

developing open water features by reducing built-up, vegetation, and soil land sounds; and (4) the Normalized Difference Built-Up Index (NDBI), which is a tool for mapping the urban built-up area.

The majority of studies relied on accessible "open data sources," according to key findings. The Landsat, MODIS, and Sentinel series were the most widely used for data collecting. Most research relied on open and accessible data repositories for this purpose, such as aerial photos and Google Earth imagery. The data is then processed, analyzed, and visualized using a GIS environment.

17.6   Discussion

From the study, we discovered that not only has the quantity of studies risen, but also the notion of ecosystem services has attracted an increasing range of study viewpoints. The concept of ecosystem services was originally meant to tie ecology and economics together by using economic terminology and a utilitarian rationale for conservation objectives. Considering these roots, it is not unexpected to observe the

dataset's persistent high representation of the ecological perspective; however, we did not witness the "domination by ecology and economy" as is commonly stated. Numerous academics have advocated for ecosystem services research to incorporate social sciences, citing the fundamentally social character of governance and the necessity to "work our way backwards from society and its unique requirements to environmental processes, rather than vice versa."

17.7   Conclusion

This chapter attempted to summarise the present state of soil ES research. It indicated potential areas for further soil ES study. The following can be inferred from this study: Plenty of research on soil and ecosystem services are found, though not all of them have investigated the direct relationship with soil qualities. Most investigations focused on provisioning and regulating ES, and most of the study was undertaken within Europe. Visualization of ecosystem services must begin at the lowest levels of education, when the influence of soil characteristics may be immediately integrated. The need to use soil data in all ES modeling investigations must be stressed. Upcoming soil and ecosystem service studies must concentrate on soil functioning in light of the United Nations' Sustainable Development Goals. This highlights the multifaceted importance of soil security in long-term environmental governance and decision-making. Soils are a complicated structure inextricably linked to biogeochemical cycles that isolating out the soil part in ES research may be insufficient. Understanding the ecological process and its benefits to civilization requires a comprehensive perspective.

The methods chosen to treat our fields may have a significant influence on soil ES. Non-sustainable usage can result in a substantial amount of disservices, an adverse effect on the ecological features of the land, soil qualities, functionalities, and services. On the opposite side, sustainable alternatives can potentially preserve or enhance such functions. Nonsustainable activities hasten the consequences of global warming on soil ES, whereas sustainable practises assist in ameliorating them. Soil ES is inextricably tied to sustainability, and the harm or benefit caused by our actions will be mirrored in our economic and social systems.

Notwithstanding this awareness, the soil ecosystem must be prioritized in the environment of sustainable growth. Similarly, additional attempts should be made to develop methods that can analyze soil functions in nonagricultural settings. Finally, the preservation and enhancement of soil ES depends on how sustainable our activities are, making it a long-term imperative to strike an equilibrium between food security and sustainability.

According to the findings, the emphasis of current urban studies is changing away from interpretation and toward information gathering for effective decision-making. The usage of RS and GIS for this purpose is growing in popularity. The LULC-based evaluation technique is frequently used to assess soil ES. The findings show that rich nations fund a disproportionately large amount of ES research. Researchers from

developed and developing countries choose free or open data sources for studying soil ES.

Nevertheless, information obstacles, a lack of RS- and GIS-based software, and a lack of capacity-building programs in developing countries obstruct any research attempts. It advocates for extraordinary solutions to encourage RS-based ES research in poor economies. The availability of open-source technology, such as Google Earth Engine, free database access, and other capacity-building initiatives, is crucial. As a way forward, work related to carbon sequestration in the wetland areas of Indian context can be undertaken to understand the use of RS and GIS tools in the wetland areas and to address present trends in this line of work.

References

Abera W, Tamene L, Kassawmar T, Mulatu K, Kassa H, Verchot L, Quintero M (2021) Impacts of land use and land cover dynamics on ecosystem services in the Yayo coffee forest biosphere reserve, southwestern Ethiopia. Ecosyst Serv 50:101338

Bejagam V, Singh A, Sharma A (2023) Spatiotemporal variability and controlling factors of ecosystem water use efficiency in India. Theor Appl Climatol.:1–15. https://doi.org/10.1016/j.ecoser.2021.101338

Bennett EM, Peterson GD, Gordon LJ (2009) Understanding relationships among multiple ecosystem services. Ecol Lett 12(12):1394–1404. https://doi.org/10.1111/j.1461-0248.2009.01387.x

Beyene TK, Jain MK, Yadav BK, Agarwal A (2021) Multiscale investigation of precipitation extremes over Ethiopia and teleconnections to large-scale climate anomalies. Stoch Env Res Risk A:1–17. https://doi.org/10.1007/s00477-021-02120-y

Braat LC, de Groot R (2012) The ecosystem services agenda:bridging the worlds of natural science and economics, conservation and development, and public and private policy. Ecosyst Serv 1(1):4–15. https://doi.org/10.1016/j.ecoser.2012.07.011

Brevik EC, Cerdà A, Mataix-Solera J, Pereg L, Quinton JN, Six J, Van Oost K (2015) The interdisciplinary nature of SOIL. SOIL 1(1):117–129. https://doi.org/10.5194/soil-1-117-2015

Carter Berry Z, Jones KW, Gomez Aguilar LR, Congalton RG, Holwerda F, Kolka R, Looker N, Lopez Ramirez SM, Manson R, Mayer A, Muñoz-Villers L, Ortiz Colin P, Romero-Uribe H, Saenz L, von Thaden JJ, Vizcaíno Bravo MQ, Williams-Linera G, Asbjornsen H (2020) Evaluating ecosystem service tradeoffs along a land-use intensification gradient in central Veracruz, Mexico. Ecosyst Serv 45. https://doi.org/10.1016/j.ecoser.2020.101181

Cord AF, Bartkowski B, Beckmann M, Dittrich A, Hermans-Neumann K, Kaim A, Lienhoop N, Locher-Krause K, Priess J, Schröter-Schlaack C, Schwarz N, Seppelt R, Strauch M, Václavík T, Volk M (2017) Towards systematic analyses of ecosystem service tradeoffs and synergies: main concepts, methods and the road ahead. Ecosyst Serv. 28:264–272. https://doi.org/10.1016/j.ecoser.2017.07.012. Elsevier B.V

Costanza R, d'Arge R, de Groot R, Farber S, Grasso M, Hannon B, Limburg K, Naeem S, O'Neill R v, Paruelo J, Raskin RG, Sutton P, van den Belt M (1997) The value of the 'world's ecosystem services and natural capital. Nature 387:253–260

Daily GC (1997) Daily_1997_Natures-services-chapter-1. In: Daily GC (ed) Societal dependence on natural ecosystems ('nature's services.). Island Press, Washington, DC

Dang AN, Jackson BM, Benavidez R, Tomscha SA (2021) Review of ecosystem service assessments: pathways for policy integration in Southeast Asia. Ecosyst Serv. 49. https://doi.org/10.1016/j.ecoser.2021.101266. Elsevier BV

Das J, Poonia V, Jha S, Goyal MK (2020) Understanding the climate change impact on crop yield over Eastern Himalayan Region: ascertaining GCM and scenario uncertainty. Theor Appl Climatol 142:467–482

Das J, Das S, Umamahesh NV (2023) Population exposure to drought severities under shared socioeconomic pathways scenarios in India. Sci Total Environ. 161566. https://doi.org/10.1016/j.scitotenv.2023.161566

de Groot R, Brander L, van der Ploeg S, Costanza R, Bernard F, Braat L, Christie M, Crossman N, Ghermandi A, Hein L, Hussain S, Kumar P, McVittie A, Portela R, Rodriguez LC, ten Brink P, van Beukering P (2012) Global estimates of the value of ecosystems and their services in monetary units. Ecosyst Serv 1(1):50–61. https://doi.org/10.1016/j.ecoser.2012.07.005

De Vries FT, Thébault E, Liiri M, Birkhofer K, Tsiafouli MA, Bjørnlund L, Jørgensen HB, Brady MV, Christensen S, De Ruiter PC, D'Hertefeldt T, Frouz J, Hedlund K, Hemerik L, Gera Hol WH, Hotes S, Mortimer SR, Setälä H, Sgardelis SP, Uteseny K, van der Putten WH, Bardgett RD (2013) Soil food web properties explain ecosystem services across European land use systems. Proc Natl Acad Sci U S A 110(35):14296–14301. https://doi.org/10.1073/pnas.1305198110

Deeksha, Shukla AK (2022) Ecosystem services: a systematic literature review and future dimension in freshwater ecosystems. Appl Sci (Switzerland) 12(17). https://doi.org/10.3390/app12178518

Delibas M, Tezer A, Kuzniecow Bacchin T (2021) Towards embedding soil ecosystem services in spatial planning. Cities 113. https://doi.org/10.1016/j.cities.2021.103150

Dominati E, Patterson M, Mackay A (2010) A framework for classifying and quantifying the natural capital and ecosystem services of soils. Ecol Econ 69(9):1858–1868. https://doi.org/10.1016/j.ecolecon.2010.05.002

Gómez-Baggethun E, Barton DN (2013) Classifying and valuing ecosystem services for urban planning. Ecol Econ 86:235–245. https://doi.org/10.1016/j.ecolecon.2012.08.019

Gupta LK, Pandey M, Raj PA, Shukla AK (2023) Fine Sediment intrusion and its consequences for river ecosystems: a review. J Hazard Toxic Radioact Waste. 27(1):04022036. https://doi.org/10.1061/(ASCE)HZ.2153-5515.0000729

Han H-Q, Liu Y, Gao H-J, Zhang Y-J, Wang Z, Chen X-Q (2020) Tradeoffs and synergies between ecosystem services: A comparison of the karst and non-karst area. J Mt Sci 17(5):1221–1234. https://doi.org/10.1007/s11629-019-5667-5

Hewitt A, Dominati E, Webb T, Cuthill T (2015) Soil natural capital quantification by the stock adequacy method. Geoderma 241–242:107–114. https://doi.org/10.1016/j.geoderma.2014.11.014

Jia X, Fu B, Feng X, Hou G, Liu Y, Wang X (2014) The tradeoff and synergy between ecosystem services in the Grain-for-Green areas in Northern Shaanxi, China. Ecol Indic 43:103–113. https://doi.org/10.1016/j.ecolind.2014.02.028

Shukla AK, Shekhar Prasad Ojha C, Mijic A, Buytaert W, Pathak S, Dev Garg R, Shukla S (2018) Population growth, land use and land cover transformations, and water quality nexus in the Upper Ganga River basin. Hydrol Earth Syst Sci 22(9):4745–4770. https://doi.org/10.5194/hess-22-4745-2018

Lausch A, Erasmi S, King DJ, Magdon P, Heurich M (2016) Understanding forest health with remote sensing-Part I-A review of spectral traits, processes and remote-sensing characteristics. Remote Sens. 8(12). https://doi.org/10.3390/rs8121029. MDPI AG

Lee H, Lautenbach S (2016) A quantitative review of relationships between ecosystem services. Ecol Indic. 66:340–351. https://doi.org/10.1016/j.ecolind.2016.02.004. Elsevier B.V

Li J, Zhang C, Zhu S (2021) Relative contributions of climate and land-use change to ecosystem services in arid inland basins. J Clean Prod 298. https://doi.org/10.1016/j.jclepro.2021.126844

Luederitz C, Brink E, Gralla F, Hermelingmeier V, Meyer M, Niven L, Panzer L, Partelow S, Rau AL, Sasaki R, Abson DJ, Lang DJ, Wamsler C, von Wehrden H (2015) A review of urban ecosystem services: Six key challenges for future research. Ecosyst Serv. 14:98–112. https://doi.org/10.1016/j.ecoser.2015.05.001. Elsevier

MEA (2005) Ecosystems and human well-being: synthesis. Island Press, Washington, DC

Nelson E, Bhagabati N, Ennaanay D, Lonsdorf E, Pennington D, Sharma M (2013) Modeling terrestrial ecosystem services. In: Encyclopedia of biodiversity, 2nd edn. Elsevier, Amsterdam., pp 347–361. https://doi.org/10.1016/B978-0-12-384719-5.00427-5

Notter B, Hurni H, Wiesmann U, Abbaspour KC (2012) Modelling water provision as an ecosystem service in a large East African river basin. Hydrol Earth Syst Sci 16(1):69–86. https://doi.org/10.5194/hess-16-69-2012

Pereira P, Ferreira AJD, Sarah P, Cerdà A, Walsh R, Keesstra S (2016) Preface: urban soils and sediments. J Soils Sediments. 16(11):2493–2499. https://doi.org/10.1007/s11368-016-1566-3. Springer Verlag

Pettorelli N, Laurance WF, O'Brien TG, Wegmann M, Nagendra H, Turner W (2014) Satellite remote sensing for applied ecologists: Opportunities and challenges. J Appl Ecol. 51(4): 839–848. https://doi.org/10.1111/1365-2664.12261. Blackwell Publishing Ltd.

Saikumar G, Pandey M, Dikshit PKS (2022) Natural river hazards: their impacts and mitigation techniques. In: River dynamics and flood hazards: studies on risk and mitigation. Springer, Singapore, pp 3–16

Sen S, Guchhait SK (2021) Urban green space in India: Perception of cultural ecosystem services and psychology of situatedness and connectedness. Ecol Indic 123. https://doi.org/10.1016/j.ecolind.2021.107338

Sharma A, Goyal MK (2018) Assessment of ecosystem resilience to hydroclimatic disturbances in India. Glob Chang Biol 24(2):e432–e441

Shukla AK, Ojha CSP, Garg RD, Shukla S, Pal L (2020) Influence of spatial urbanization on hydrological components of the upper Ganga River Basin, India. J Hazard Toxic Radioact Waste 24(4). https://doi.org/10.1061/(asce)hz.2153-5515.0000508

Signorello G, Marzo A, Prato C, Sturiale G, de Salvo M (2020) Assessing the hidden impacts of hypothetical eruption events at Mount Etna. Environ Sustain Indic 8. https://doi.org/10.1016/j.indic.2020.100056

Soubry I, Doan T, Chu T, Guo X (2021) A systematic review on the integration of remote sensing and gis to forest and grassland ecosystem health attributes, indicators, and measures. Remote Sens 13(16). https://doi.org/10.3390/rs13163262. MDPI AG

TEEB (2010) The economics of ecosystems and biodiversity

Verma P, Raghubanshi AS (2019) Rural development and land use land cover change in a rapidly developing agrarian South Asian landscape. Remote Sens Appl Soc Environ 14:138–147. https://doi.org/10.1016/j.rsase.2019.03.002

Xie W, Huang Q, He C, Zhao X (2018) Projecting the impacts of urban expansion on simultaneous losses of ecosystem services: a case study in Beijing, China. Ecol Indic 84:183–193. https://doi.org/10.1016/j.ecolind.2017.08.055

Zhang L, Cheng L, Chiew F, Fu B (2018) Understanding the impacts of climate and landuse change on water yield. Curr Opin Environ Sustain. 33:167–174. https://doi.org/10.1016/j.cosust.2018.04.017. Elsevier B.V

Chapter 18
Sustainable Land and Water Management in Urban Areas: Emerging Challenges

Suryanarayana Gajulapalli, Sumanth Chinthala, and Sridhar Pilli

Abstract In Indian urban areas, the water and land use are critical, finite, and entwined resources. Expeditious increasing urbanization propelled by globalization and the booming population has brought global problems such as climate change, a shortage of natural resources, deteriorated public health, and so forth. Among these overwhelming challenges, a major obstacle is meeting the basic needs of increasing urban populations while ensuring the integrity of ecosystems including land and water. Urban water management and land resource management play a pivotal role for a sustainable future. The traditional water infrastructure focused mainly on physical structures associated with drinking water supply and distribution and collection and disposal of wastewater and storm water. However, integration of the traditional components with the protection and restoration of natural systems, conservation, reuse, and reclamation is the need of the hour. Moreover, the active incorporation of new decentralized technologies, green infrastructure, and low impact development to ensure the long-term reliability and resilience of our water resources has to be prioritized. Since the urban areas are rapidly developing, we need to understand the emerging challenges and develop strategies to mitigate the ill effects at a faster pace. This chapter discusses various emerging challenges that may arise from the water and land use perspective.

Keywords Urban · Management · Water · Land use

18.1 Introduction

Rivers were considered as the lifelines in many countries. Ancient civilizations and empires were established on the banks of rivers and for many centuries, and those civilizations and empires have faced a lot of challenges due to the hydrological extremes and other issues(Saikumar et al. 2022). Even in the modern era, many cities

S. Gajulapalli · S. Chinthala (✉) · S. Pilli
Department of Civil Engineering, NIT, Warangal, Telangana, India
e-mail: sumanthchinthala@nitw.ac.in

are either directly or indirectly built depending on a major river. As the demand for resources increased, management of water, sediments, and hydrological extremes became more and more challenging, and as a result, the hazards that were resulted due to the natural and anthropogenic factors have affected many cities directly and indirectly.

Since the impacts of climate change are visible in various aspects, it is necessary for us to think about the sustainable practices, which can reduce the hydrological risks. Since rivers cannot be exclusively engineered without the management of land and water, there is an immediate necessity to integrate the land and water management in urban areas to ensure that the hydrological risks are minimized.

Generally, people migrate from villages to the cities for various work opportunities; as a result, urban population has rapidly increased, and it has had a negative impact on the urban people and environment. Presently, almost >50% of the global population lives in the cities (Falah et al. 2020). Globally, by 2030, around 60% of the population is accounting for the urban population (Seto et al. 2012). According to the United Nations, by the year 2050, urban growth will increase from 3.9 to 6.4 billion (Narimani et al. 2022), whereas the growth rates of urban lands will be twice as fast as those of urban populations.

It is estimated that between 2018 and 2050, more than 35% of India, China, and Nigeria people will settle in cities (Mohammad and Goswami 2021). Over the decades due to financial progress and the technology development, persistent growth of the urban cities in the regional and the city level has undergone many changes and raises the major challenge on to the structure and functional systems and subsystems (Chu and Tang 2005; Chen 2016). As a result, increase in the population density and land use patterns are contributing to urban climate changes and affect the meteorological factors (Kim and Brown 2021; Saikumar et al. 2022). On the other hand, countries like India are purely dependent on agriculture, and it requires a tremendous amount of water and land (Seto et al. 2012). Due to the increase of global population and a subsequent increase in anthropogenic activities and other factors, availability of fresh water has been significantly affected (John et al. 2021a; b). Moreover, for many medium- and low-income group countries, water shortage has emerged as a significant problem at the national level (John et al. 2021a; b). Additionally, the rampant increase of growing challenges in the form of urbanization, economic growth, population, and climate changes, etc. are disturbing the water flow cycle and land maintenance by exerting pressure on water resource management and land use patterns and biodiversity hotspots with built-up area (Fidani and Pancovska 2020; Gupta et al. 2023).

During the past decades, vast acceleration of urbanization and the increasing demand for built-up areas have led to increasingly serious conflicts between various types of land use (Seto et al. 2012). Moreover, high density of population, various types of land use patterns, and expansion of transport system and industrialization ushered in an unprecedented process of urbanization. As the result, the huge quantity of heat is stored in the city. It has been observed to reduce the large amount of heat and energy required. For instance, Urban dwellers consume more than 75% of total energy resources because of their activities in urban environments (Madlener and

Sunak 2011). One of these factors is the increase in energy demand in urban centers, which not only wastes millions of dollars in energy but also damages the health of the urban people (Ouda and Cekirge 2014). Some of the cities are now starting working toward sustainable paths, and in some of the cities, still it is a big challenge. Nevertheless, in the narrow range, some negative effects from the blue and green infrastructure are dominated by their positive impacts (de Souza and Torres 2021).

Green infrastructure (GI) is a comprehensive planning approach discussing the blue and green infrastructure including the greenspace and the water space. Strategically, the disparate types of natural elements are interconnected networks and provide multiple environmental and ecological and economic and social benefits to the people and wildlife (Walmsley 2006). Existing urban water systems in Sweden fulfill these fundamental requirements to a high degree. Over the last decade, the existing systems have been increasingly criticized from the viewpoint of sustainability. However, similar discussions have also arisen in the power and transportation sectors. A number of supplementary requirements for a sustainable urban water system have also been identified in various programs. They state that the system should (1) have a high degree of functional robustness and flexibility (2) to be adapted to local conditions and (3) be easy to understand and thus encourage responsible behavior by the users. This systems analysis project within the program is carried out by a group of framework for systems analysis of sustainable urban water management (Hellström et al. 2000).

18.2   Sustainable Development Goals

To address the present global challenges around the world, agenda for the 2030 sustainable development in 2015 United Nations has adopted the sustainable development goals (UN Sustainable Goals 2015). The urgent call for action for all developed and developing countries in a global partnership to achieve the 17 sustainable goals. However, on paper, Stockholm resilience center elucidates the interrelationships between various SDGs. The SDGs are grouped into three domains: economic, environmental, and social domains, and these three are interrelated with each other. However, sustainable progress in the economic layer can be achieved by the good progress in the other two layers vice versa. On several interrelated scales, to create the balance between economic, social, and environmental concern is essential to achieving the SDGs by 2030. Progress on many global concerns, such as climate change, food security, water resources, and sustainable energy, is hampered by poor economic or social conditions.

The SDGs have emphasized on land degradation, which is the one of the major problem in the local and regional level. It reflects the human resources, and also it has negative effects on the ecosystem and soil functionality. Land degradation is inherently related to the carrying capacity of ecosystem and sensitivity resilience and to the vulnerability of local communities, increasing the soil depletion other hand same rate the built up areas are increasing (Smrekar et al. 2016). This indicates that to
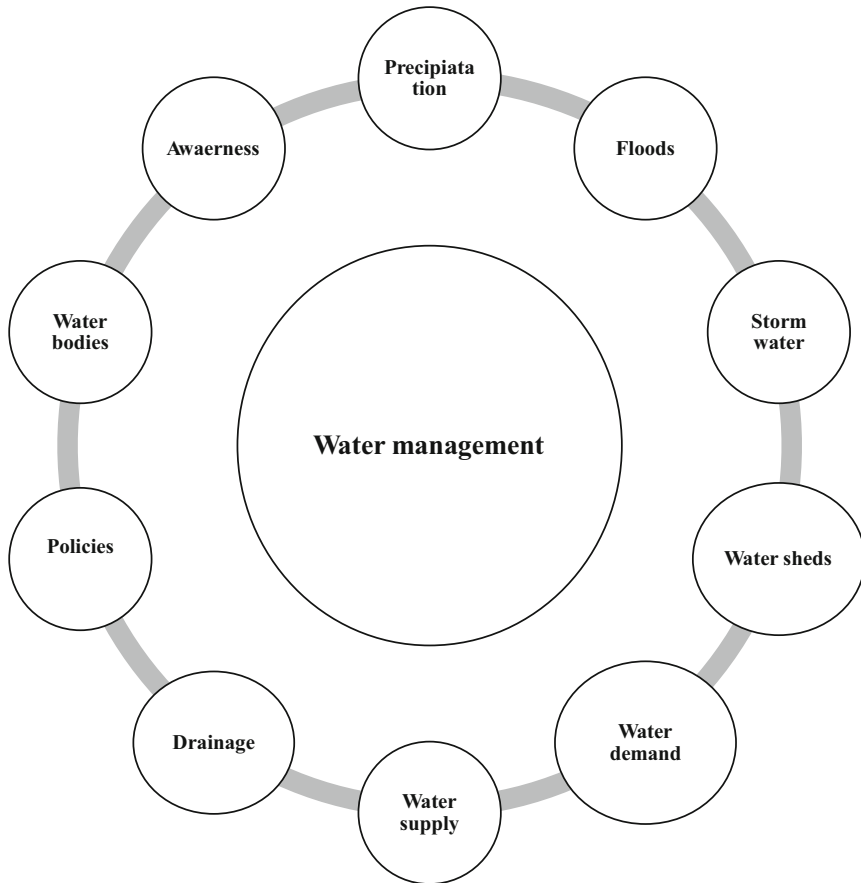
Fig. 18.1 Factors affecting water management

handle land degradation and other problems, factors affecting water and land management are to be identified. Figs. 18.1 and 18.2 show various factors affecting water and land management, respectively.

18.3 Rational of the Study

Every government has to provide clean water to the urban communities. Urban water management is to be water, and its constituents can be carefully used, reused, and returned to nature by different forms. The main aim of the sustainable urban water and wastewater system is necessary focusing the different aspects like (1) moving toward a nontoxic environment; (2) improve the drinking water—treatment and distribution; (3) conserving natural resources; (4) saving human resources; (5) saving
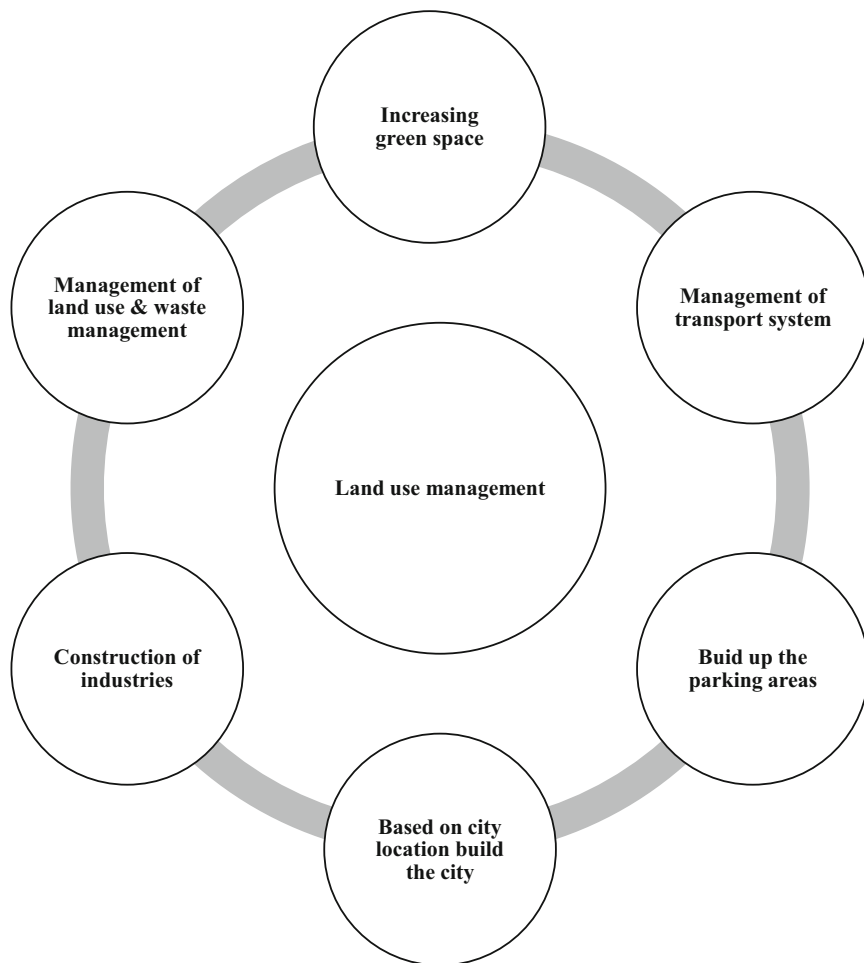
Fig. 18.2 Factors affecting the land use management

financial resources; (6) maximizing the biodegradable products; (7) improving health and hygiene; (8) improving wastewater and sludge—recovery of products; (9) build-up the planned infrastructure; (10) integrated waste management; (11) storm water management; (12) improve the land use patterns; (13) improve the air quality; (14) built the green infrastructure; (15) built the integrated transport system; and (16) awareness among the people. On the other hand, to build the economic infrastructure, the researchers and scientists are focusing on the integrated projects on the (1) use of products and by-products from the urban water treatment system (2) social-economical aspects, (3) risk assessment, and (4) communication technologies. A framework for system analysis of sustainable urban water management has been described by (Simpson et al. 2021).

In addition to that, developing the urban green and blue infrastructure is also responsible for the water quality and control of waterborne diseases. Urban green and blue infrastructure is responsible for the ecosystem service but not limited to the water retention and regulation, amelioration of biodiversity, carbon sequestration, and the thermal comfort in and around the build-up area (Li et al. 2017). In addition to that, restoration of the stream and river ecosystem services in the urban areas enhances the biodiversity and water quality and controls the waterborne disease (Haase 2015). Even though it is implemented in the small areas, it has improved the availability and quality of recreational space in and around areas. In cities, the main components of GBI land plots consist of the natural surfaces, permeable and unsealed blue water surfaces, and the green vegetation grounds (Puppim de Oliveira et al. 2022). While gray infrastructure can be easily replaced with GBI to give small-scale, cost-effective treatments, local governments and cities must learn to create their own, site-specific innovations. Therefore, it is necessary to comprehend the relationship between GBI, and especially in urban areas, naturally available green surfaces like trees and grasses are replaced by the artificial surfaces.

Overall, sustainable management of water and land in urban areas is essential for creating more livable, resilient, and environmentally sustainable cities. By adopting a range of strategies and engaging with communities, urban areas can work toward a more sustainable future for all. To remove wastewater from user's location to prevent unhygienic conditions and remove storm water to avoid damage from flooding, it is necessary to address the following.

Sustainable Urban Design: Sustainable urban design can help to maximize the use of land and water resources in cities. This may include designing buildings and public spaces to be more energy-efficient, integrating green spaces and public transportation systems, and utilizing low-impact development techniques to manage storm water runoff.

Efficient Water Use: Urban areas should aim to use water resources efficiently by adopting practices such as rain water harvesting, graywater reuse, and water-efficient landscaping. This can help to reduce demand on freshwater resources and minimize the need for energy-intensive water treatment and distribution systems.

Integrated Water Management: Integrated water management involves coordinating the management of different water sources, such as groundwater, surface water, and storm water. This can help to improve water quality, reduce flooding and erosion, and provide multiple benefits for the environment and communities.

Sustainable Land Use Planning: Sustainable land use planning involves developing land use policies that promote compact, walkable urban centers that are more efficient in their use of resources. This may involve implementing policies to encourage denser development, mixed-use zoning, and more efficient transportation systems, which can help to reduce the need for car travel and promote active transportation.

Community Engagement: Community engagement is critical for achieving sustainable water and land management in urban areas. Engaging with residents and stakeholders can help to identify their priorities and concerns, promote public

awareness of sustainability issues, and build support for sustainable practices and policies.

Sustainable water, storm water, energy, and infrastructure management in Indian communities is an important issue that has both present and future challenges. Some of the challenges that Indian communities face include the following:

Water Scarcity: India is one of the most water-stressed countries in the world, with many communities facing acute water shortages. As the population grows and climate change impacts become more severe, the challenge of managing water sustainably will only become more difficult.

Flooding: Many Indian communities are also at risk of flooding, particularly during the monsoon season. This can cause damage to infrastructure and homes and can also lead to health issues like waterborne diseases.

Energy Poverty: A large proportion of the Indian population still lacks access to reliable and affordable energy. This can make it difficult to meet basic needs like cooking and lighting and can also hinder economic development.

Poor Infrastructure: Many Indian communities lack basic infrastructure like roads, sanitation, and waste management systems. This can make it difficult to implement sustainable water and energy management strategies, as well as contribute to other social and economic issues. The information on technical innovations, policy proposals, strategies, and actions related to rainwater management was documented in Kazak et al. (2022).

18.4 Limitations

1. Dynamically changing land use and water use patterns will not allow the recovery of the water bodies.
2. Unauthorized usage/contamination of groundwater and surface water may lead to many hydrological issues resulting in the destruction of the water body.
3. Nonuniform cropping pattern creates an unpredictable demand for water and may create water shortage issues.
4. Water requirement for maintaining the green infrastructure and recently developed forest areas is often overlooked resulting in the damage to the recently developed green ecosystems.
5. Water requirements for large infrastructure projects and recreational purposes are not estimated resulting in sudden rise in demand for water resources.

18.5 Materials and Methods

Table 18.1 shows that the different types of methods are adopted to solve the water-related issues in various countries. These methods are discussed in detail in the subsequent sections.

Table 18.1 Various types of methodologies adopted worldwide to solve water-related issues

Sl no	Country	Methodology	Purpose	References
1	Latin America and Caribbean (LAC)	Managed Aquifer Recharge (MAR)	To maximize the natural storage	Valverde et al. (2018)
2	Implemented in many cities	Constructed wetlands	Strom water management and water treatment	Stefanakis (2019)
3	Guangdong, China	Water Resource-Withdrawal-GDP-Footprint (WRWGF)3	Mitigation of water shortage and pollution	Xian et al. (2022)
4	**Applicable to cities**	**City Water Resilience Framework (CWRF)**	Plan for strengthening urban water resilience	Saikia et al. (2022)
5	Implemented to excessive rain and flood cities	Urban storm water drainage systems	Protecting cities from excessive rainfalls and urban floods	Azari and Tabesh (2022)
6	Australia	Water-sensitive urban design (WSUD)	Local storm water management	Roy et al. (2008), Barton and Argue (2007)
7	Urban environment	Sustainable Drainage Systems (SuDS)	Designed to transport surface water, slow runoff down before it enters watercourses, they provide areas to store water in natural contours	usdrain.org/delivering suds/using suds/background/ sustainable drainage
8	South-eastern United States	Best management practice (bmp)	Reduce sediment and pollutant loading into streams	Anderson and Lockaby (2011)
9	Hydrology of urban catchments closer to predevelopment conditions	Low impact development (LID)	Utilizes distributed storm water controls	Performance and implementation of low impact development: A review
10	Australia	Integrated Urban Water Management (IUWM)	All parts of the water cycle, natural and constructed, surface and subsurface, recognizing them as an integrated system	Mitchell (2006)

18.6   Managed Aquifer Recharge (MAR)

MAR is adapted from the International Groundwater Resource Assessment Centre. It has to be willful recharged of aquifer for future recover or environmental benefits, and the main purpose of the MAR is to overcome the environmental imbalance of local groundwater demand of and availability withal securing drinking and irrigation

Table 18.2 Different types of main and specific MAR classification systems

	Main MAR methods	Specific MAR methods
Water infiltration	Well, shaft, and borehole recharge	Aquifer storage and recovery (ASR)/aquifer storage, transfer, and recovery (ASTR) shallow well/shaft/pit infiltration
	Spreading	Drains Irrigation, infiltration ponds, furrow and basins, flooding ditch
	Infiltration due to induced bank	Lake/river bank filtration, dune filtration
Water interception	In-channel modifications	Channel spreading, subsurface dams, recharge dams, sand dams
	Runoff harvesting	bunds, trenches, and rooftop rainwater harvesting barriers

water supply at any time by increasing the groundwater storage. Other hand, it includes the prevention of land subsidence, salt water intrusion, improvement of source water quality, and avoidance of direct potable reuse of treated wastewater by underground passage. This water source includes surface water from reclaimed water, rivers, lakes, and storm runoff. Water sources include surface water from rivers or lakes, storm water runoff, and reclaimed water. Thus, based on the water quality, pre-treatment might be necessary to recharging to an aquifer. This MAR classification system starting five main methods and associated specific MAR methods. The methods are discussed in detail in Table 18.2.

In the MAR, most modeling studies were carried out on the shaft, well, and borehole recharge and spreading methods, and these methods are frequently used to recharge the aquifers globally. This method is planning and establishing in different location in order to reduce the hazard risk such as low recovery efficiencies and clogging that lead to failure of facility.

18.6.1 Role of Constructed Wetland as Green Infrastructure in Urban Water Management

The basic concept of constructed wetland is able to remove various forms of pollutants like organic, trace elements, and nutrients through the series of physical, chemical, and biological process and enhance the water quality under controlled conditions. Nowadays, in some of the areas, the natural wetlands are seldom utilized for the treatment of light-contaminated wetlands. On a global basis, these are commonly avoided for the treatment of wastewater; these could affect irreversible damage to ecosystems. In general, the CWs are constructed in such a way as to simulate and increase the functions of natural wetlands. Urban designers, researchers, scientists, and architects designed their characteristics in such a way that they are more easily understood and implemented in the built-up environment. CWs represent a very interesting and effective development in the field of ecological

engineering. Based on the utility and function, CWs are divided in the three main areas.

Constructed Wetlands for Flood Control: Due to high rainfall, the system has reached the high runoff, and it will create the flood and damage the system. To avoid these issues, implement strategies to increase the infiltration volume and the capacity for storing storm water, while controlling the volume water reaching the sewers system and eventually treatment plants. It is found in many countries that the CWs significantly contribute to the IUWM and also have the ability to recycle the stored water volume. Constructed wetlands for wastewater treatment: CWs are the engineered developed systems designed to receive and purify wastewater from various sources exploiting the naturally occurring treatment processes. Internationally, many countries used the applications of CWs.

Constructed Wetlands for Habitat Creation: These programs are meant to create new habitat for wildlife. The major objective is to utilize CWs' ecological advantages rather than just their role as a therapeutic center. By luring in wildlife species, particularly birds, and establishing a green area, CWs' primary characteristics—the presence of water and vegetation—make them excellent for the establishment of a new ecological habitat or for the restoration of a degraded ecosystem. These systems can be used as public recreation and educational facilities, as well as a source of food and fiber. Many comparable facilities, like the CWs in the Greater Vancouver area, have been built in North America.

18.7 Water Resource-Withdrawal-GDP-Footprint

To fulfil the UN sustainable development goal by utilization, sustainable water practices are the basis of sustainable development. Using a thorough framework that considers both water quantity and quality, it is vital to evaluate the development of sustainable water consumption. Based on the graywater footprint to enunciate the water quality and quantity, the Water Resource-Withdrawal-GDP-Footprint (WRWGF) work is constructed, and China's largest economic province city Guangdong, which suffers from severe water pollution, investigated the sustainable water utilization.

18.7.1 City Water Resilience Framework (CWRF)

Due to the emerging challenges like rapid urban growth, degrading ecosystems and global health crisis like the recent pandemic, providing water services, and managing resources need much more than risk reduction and management (OECD 2014; UN 2018). CWRF is conceptualized within a five-step approach called the City Water Resilience Approach (CWRA) (ARUP 2019). These five steps include

understanding the system, assessing urban water resilience, development of action plan, and implementation of action plan and evaluate, learn, and adapt.

18.7.2 Urban Storm Water Drainage Systems

Urban floods are a natural disaster that cannot be prevented, but the damages can be minimized by implementing the right policies and actions. Hence, in order to reduce the danger of system failure and urban flooding, it is necessary to establish a better framework to assist decision-makers in evaluating and rehabilitating the USDS.

18.7.3 Water-Sensitive Urban Design

As there are many uses of the WSUD architecture, practitioners' definitions of WSUD frequently reflect this confusion. WSUD is described as "the integration of urban planning with the management, preservation and conservation of the urban water cycle, that guarantees that urban water management is attentive to natural hydrological and ecological processes" in the inter-government agreement on a National Water Initiative. The terms "water sensitive" and "urban design" are included in the term "water-sensitive urban drainage," according to (Wong 2006) in their proposal to the IWA/IAHR Joint Committee on Urban Drainage (Barton and Argue 2007).

Urban design is a well-known discipline that deals with the planning and architectural design of urban environments, addressing problems that have traditionally been dealt with in areas unrelated to water but that nevertheless interact with or have an impact on environmental effects on both land and water. In order to guarantee that water is given the proper importance during the urban design processes, WSUD introduces "sensitivity to water" into urban design. The words "water sensitive" define a new paradigm in integrated urban water cycle management that integrates various disciplines of engineering and environmental sciences associated with the provision of water services including the protection of aquatic environments in urban areas. Urban design choices and, by extension, water management techniques are governed by community values and goals. Collectively, WSUD integrates the social and physical sciences.

18.7.4 Sustainable Drainage Systems (SuDS)

SuDS can balance various opportunities and challenges in urban design and community development, improving different places and spaces by implementing sustainable development practices. Although it has been manage surface water that

account for the pollution, flood, wildlife and plants combined known as Sustainable Drainage Systems (SuDS). SuDS mimic nature and typically manage rainfall close to where it falls. Basically, these are designed for the slow runoff and conveyance of water. On the other hand, these provide the space to where the water soaks in the soil and undergoes evaporation and transpiration. Drainage systems known as SuDS are thought to be environmentally friendly because they harm the environment only temporarily or not at all. They are frequently seen as a series of management techniques, command systems, and strategies created to drain surface water effectively and sustainably, while reducing pollution and controlling the effect on the water quality of nearby bodies of water.

SuDS are more sustainable than traditional drainage methods because of the following reasons. Firstly, they manage runoff volumes and flow rates from hard surfaces so that flooding does not affect urbanization. They also provide natural flow regime to water courses, habitat for wildlife, opportunities for evapotranspiration from surface cover, and vegetation.

18.7.5   Best Management Practice (BMP)

It has been demonstrated that applying best management practices (BMP) significantly lowers the risk. The management of forests in the Southeast varies widely depending on the physiographic region, soil erosion, climate, and site wetness. And it is obvious that BMP reduce the amount of pollutants and sediment that enter streams.

According to scientific research, using forestry BMPs has lessened the influence on water quality. Managers are increasingly being expected to quantify the amount of sediment being retained by recommended BMPs, even though numerous studies have shown the qualitative value of BMPs. There are few studies that have specifically quantified BMP efficacy for use in models or estimates. We looked through the scientific literature for studies in the Southeast where the improvement in water quality was measured or where specific pathways for improvement were discovered in order to better understand the impact of BMPs. Although we acknowledge that it may also be determined by examining physical (temperature) and biotic responses, our review concentrated on BMP effectiveness to minimize sediment delivery. Although BMP may include a variety of procedural or policy approaches, our focus was on field-based solutions to isolate silviculture operations from streams (Anderson and Lockaby 2011).

18.8   Low Impact Development (LID)

Climate change exacerbates the effects of urbanization; hence, new storm water management strategies must be developed in order to lessen these effects. Low impact development is a new storm water management paradigm (LID). To bring the hydrology of urban catchments closer to pre-development conditions, LID makes use of dispersed storm water controls (typically green infrastructure), green areas, and natural hydrologic features. The review gives an overview of what is known about LID as a method for managing storm water and a way to combat climate change, as well as the state of research and application of this subject. Methods of optimization, modeling, monitoring, and the performance of LID alternatives are presented in order to provide readers a better knowledge of the wide range of factors that should be taken into account when designing low impact developments. Although LID has been widely used and has been successful in many instances, its advantages are still debatable. In order to provide an overview of LID and analyze its performance and application, this review synthesizes knowledge from a variety of sources.

18.8.1   Integrated Urban Water Management (IUWM)

In Indian cities, after the water contamination incidents like Bholakpur in Hyderabad, the centralized urban water supply in Indian cities has to focus on many interrelated issues and local factors to manage urban waters so that the hygiene of urban areas may be improved on similar lines with western countries (Mitchell 2006). Indian cities should consider all parts of water cycle including the natural, constructed, surface, and subsurface components in the integrated system. In case if any component is not included in the integrated system due to any reason, the long-term strategies may be formulated for their inclusion in the long run.

Secondly, the water requirements for both anthropogenic and ecological requirements have to be identified. In many Indian cities, the estimation for demand of water for ecological purposes is not carried out. As a result, during peak summer seasons, the water scarcity has affected a lot of wildlife.

In many instances, the local, cultural, and economic perspectives are often ignored by the policy makers. Additionally, the involvement of all stakeholders in planning and decision-making process is missing.

Examples are as follows:

1. Involving sport authority experts while conducting major sports events in the city and estimating the water consumption.
2. Involving authorities who organize religious/social/cultural/technical/business events in the city and taking their consent in estimating the water consumption.
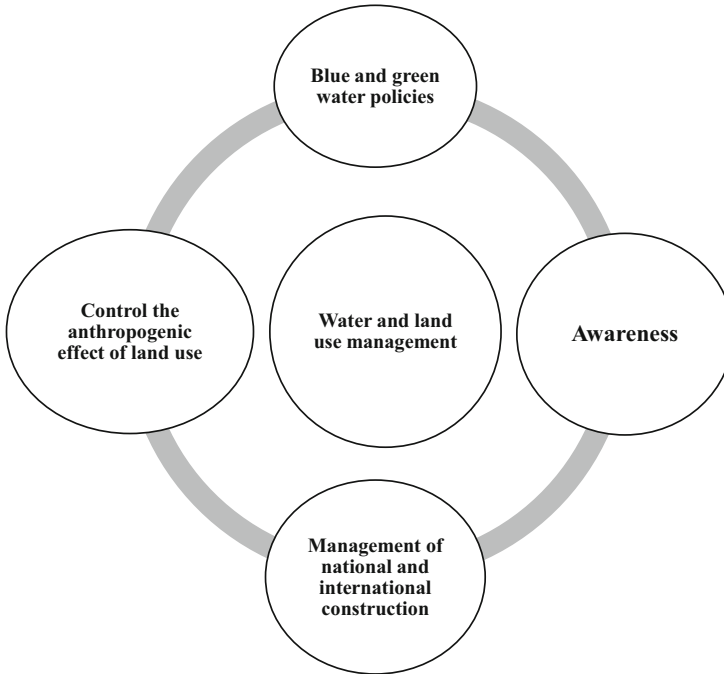
Fig. 18.3 Strategies to manage land and water

Creating awareness on sustainability to balance the environmental, social, and economic needs for short, medium, and long term.

The multifunctional elements of IUWM include groundwater management, maintenance of biodiversity, recreation, affordableness, greenhouse gas emissions, amenity, community satisfaction, ecosystem protection, energy usage, equity, pollution prevention and control, public health protection and sanitation, and water sharing (Mitchell 2006). However, for Indian context, more dimensions including nutrient/pollutant recovery from groundwater may be added to ensure that the groundwater sources are restored for future purposes. Fig. 18.3 summarizes various aspects of managing water and land management policies simultaneously.

18.9 Discussions and Recommendations

The water systems and usage of land near to the water bodies must be looked at as a single unit rather than considering them as independent units before carrying out any anthropogenic activity. While using the land, efforts must be made in such a way that the natural flow is not disturbed. Even if such disturbance is inevitable, the demarcation of the water body and land must be made. Further, in random sampling of

water bodies and monitoring of the recharge capacity, flow reduction has to be carried out on time to restore any damage that happens to the water network.

18.10   Conclusions

From the studies conducted, it is evident that management of water resources is going to become tougher in the coming years due to various reasons. To address the same, the following conclusions can be made:

1. *Think tanks*: International bodies generally talk about various short-term and long-term strategies to manage water resources. However, the decisions taken at international level take a lot of time to reach the local level due to various factors. To reduce the delays, think tanks are to be developed where the experts should converge on taking decisions based on the international scenario, national economy, local factors, administrative difficulties, and public acceptance. Social scientists and other relevant experts are to be involved at state and central level in the country to accelerate the strategies, which can address the issues of water management.
2. *Decentralized reusing/water reducing strategies:* They have to be encouraged at community level to keep a check on the rising water demand. For instance, the reusable cup project, which was initiated across many educational institutions across the world, has significantly reduced millions of gallons of water by reducing the need for a disposable container, which can be used only once. The entire water footprint of the disposable cup industry was significantly reduced. Similarly, there are many local solutions that reduce the water footprint significantly. However, it needs a lot of planning, implementation, and dedication by the local communities to show a significant impact.
3. *Mass restoration of water sources:* Mass restoration of water sources using conventional techniques is needed to check on depleting groundwater levels and many other hydrological parameters.
4. *Losses:* Losses at various levels can be addressed by working on efficient technologies, which can be retrofitted at various components in the water supply. The cost benefits of reducing the losses must be transferred to the public by providing some incentives.
5. *Safe water reuse strategies*: Research has to be carried out to investigate the strategies needed to reuse domestic water safely.

References

Anderson CJ, Lockaby BG (2011) The effectiveness of forestry best management. 35(cm)
ARUP (2019) Methodology City Water Resilience Assessment Acknowledgements

Azari B, Tabesh M (2022) Urban storm water drainage system optimization using a sustainability index and LID/BMPs. Sustain Cities Soc 76(June 2021):103500. https://doi.org/10.1016/j.scs.2021.103500

Barton AB, Argue JR (2007) A review of the application of water sensitive urban design (WSUD) to residential development in Australia. Aust J Water Resour 11(1):31–40. https://doi.org/10.1080/13241583.2007.11465309

Chen X (2016) An analysis of climate impact on landscape design. Atmos Clim Sci 06(03):475–481. https://doi.org/10.4236/acs.2016.63037

Chu YW, Tang JTH (2005) The internet and civil society: environmental and labour organizations in Hong Kong. Int J Urban Reg Res 29(4):849–866. https://doi.org/10.1111/j.1468-2427.2005.00625.x

de Souza DT, Torres PHC (2021) Greening and just cities: elements for fostering a south–north dialogue based on a systematic literature review. Front Sustain Cities 3(May). https://doi.org/10.3389/frsc.2021.669944

Falah N, Karimi A, Harandi AT (2020) Urban growth modeling using cellular automata model and AHP (case study: Qazvin city). Model Earth Syst Environ 6(1):235–248. https://doi.org/10.1007/s40808-019-00674-z

Fidani D, Pancovska VZ (2020) 2020 UBT International Conference Sustainable Management of Water Resources in Urban Areas as an Integrated Part of Urban Planning Sustainable Management of Water Resources in Urban Areas as an Integrated Part of Urban Planning: the Case

Gupta LK, Pandey M, Raj PA, Shukla AK (2023) Fine sediment intrusion and its consequences for river ecosystems: a review. J Hazard Toxic Radioact Waste. 27(1):4022036

Haase D (2015) Sustainability of water quality and ecology reflections about blue ecosystem services in cities. Sustain Water Q Ecol 5:77–83. https://doi.org/10.1016/j.swaqe.2015.02.003

Hellström D, Jeppsson U, Kärrman E (2000) A framework for systems analysis of sustainable urban water management. Environ Impact Assess Rev 20(3):311–321. https://doi.org/10.1016/S0195-9255(00)00043-3

John CK, Pu JH, Moruzzi R, Pandey M, Azamathulla HM (2021a) Reusable rainwater quality at the ikorodu area of lagos, Nigeria: Impact of first-flush and household treatment techniques. J Water Sanit Hyg Dev 11(5):732–745. https://doi.org/10.2166/washdev.2021.062

John CK, Pu JH, Pandey M, Moruzzi R (2021b) Impacts of sedimentation on rainwater quality: case study at Ikorodu of Lagos, Nigeria. Water Supply 21(7):3356–3369. https://doi.org/10.2166/ws.2021.093

Kazak JK, Dąbrowska J, Bednarek A (2022) Stormwater management in urban and rural areas. Water 14(21):3488. https://doi.org/10.3390/w14213488

Kim SW, Brown RD (2021) Urban heat Island (UHI) variations within a city boundary: a systematic literature review. Renew Sust Energ Rev 148(August 2020):111256. https://doi.org/10.1016/j.rser.2021.111256

Li F, Liu X, Zhang X, Zhao D, Liu H, Zhou C, Wang R (2017) Urban ecological infrastructure: an integrated network for ecosystem services and sustainable urban systems. J Clean Prod 163:S12–S18. https://doi.org/10.1016/j.jclepro.2016.02.079

Madlener R, Sunak Y (2011) Impacts of urbanization on urban structures and energy demand: What can we learn for urban energy planning and urbanization management? Sustain Cities Soc 1(1):45–53. https://doi.org/10.1016/j.scs.2010.08.006

Mitchell VG (2006) Applying integrated urban water management concepts: a review of Australian experience. Environ Manag 37(5):589–605. https://doi.org/10.1007/s00267-004-0252-1

Mohammad P, Goswami A (2021) Quantifying diurnal and seasonal variation of surface urban heat Island intensity and its associated determinants across different climatic zones over Indian cities. GISci Remote Sens 58(7):955–981. https://doi.org/10.1080/15481603.2021.1940739

Narimani N, Karimi A, Brown RD (2022) Effects of street orientation and tree species thermal comfort within urban canyons in a hot, dry climate. Eco Inform 69(March):101671. https://doi.org/10.1016/j.ecoinf.2022.101671

OECD (2014) Managing water for future cities: Policy Perspectives. https://www.oecd.org/environment/resources/Policy-Perspectives-Managing-Water-For-Future-Cities.pdf.

Ouda OKM, Cekirge HM (2014) Potential environmental values of waste-to-energy facilities in Saudi Arabia. Arab J Sci Eng 39(11):7525–7533. https://doi.org/10.1007/s13369-014-1311-4

Puppim de Oliveira JA, Bellezoni RA, Wan-Yu S, Bayulken B (2022) Innovations in urban green and blue infrastructure: tackling local and global challenges in cities. J Clean Prod 362 (March):132355. https://doi.org/10.1016/j.jclepro.2022.132355

Roy AH, Wenger SJ, Fletcher TD, Walsh CJ, Ladson AR, Shuster WD, Thurston HW, Brown RR (2008) Impediments and solutions to sustainable, watershed-scale urban stormwater management: lessons from Australia and the United States. Environ Manag 42(2):344–359. https://doi.org/10.1007/s00267-008-9119-1

Saikia P, Beane G, Gin R, Avello P, Ellis L, Shouler M, Ward R, Fisher S, Leten J, Jim A, Town C (2022) City water resilience framework: a governance based planning tool to enhance urban water resilience. Sustain Cities Soc:77. https://doi.org/10.1016/j.scs.2021.103497

Saikumar G, Pandey M, Dikshit PKS (2022) Natural river hazards: their impacts and mitigation techniques. In: River dynamics and flood hazards: studies on risk and mitigation. Springer, Cham, pp 3–16

Seto KC, Güneralp B, Hutyra LR (2012) Global forecasts of urban expansion to 2030 and direct impacts on biodiversity and carbon pools. Proc Natl Acad Sci U S A 109(40):16083–16088. https://doi.org/10.1073/pnas.1211658109

Simpson NP, Mach KJ, Constable A, Hess J, Hogarth R, Howden M, Lawrence J, Lempert RJ, Muccione V, Mackey B, New MG, O'Neill B, Otto F, Pörtner HO, Reisinger A, Roberts D, Schmidt DN, Seneviratne S, Strongin S, van Aalst M, Trisos CH (2021) A framework for complex climate change risk assessment. One Earth 4(4):489–501. https://doi.org/10.1016/j.oneear.2021.03.005

Smrekar A, Zorn M, Komac B (2016) Heritage protection through a geomorphologist's eyes: From recording to awareness raising. Acta Geogr Slov 56(1):123–127. https://doi.org/10.3986/AGS.3348

Stefanakis AI (2019) The role of constructed wetlands as green infrastructure for sustainable urban water management

UN (2018) The World's Cities in 2018. https://www.un.org/en/events/citiesday/assets/pdf/the_worlds_cities_in_2018_data_booklet.pdf.

Valverde JPB, Stefan C, Palma A, Eduardo N, Vivar HLP, M, C. R. (2018) Inventory of managed aquifer recharge schemes in Latin America and the Caribbean. Sustain Water Resour Manag 4(2):163–178. https://doi.org/10.1007/s40899-018-0231-y

Walmsley A (2006) Greenways: multiplying and diversifying in the 21st century. Landsc Urban Plan 76(1–4):252–290. https://doi.org/10.1016/j.landurbplan.2004.09.036

Wong THF (2006) Water sensitive urban design - the journey thus far. Austr J Water Resour 10(3):213–222. https://doi.org/10.1080/13241583.2006.11465296

Xian C, Fan Y, Zhang J, Zhang L (2022) Assessing sustainable water utilization from a holistic view : A case study of. Sustain Cities Soc 76(June 2021):103428. https://doi.org/10.1016/j.scs.2021.10342

Chapter 19
Nature of Bursting Events over a Rigid Bed with Emergent Vegetation

Aaditya Ojha, Abhishek Kumar, Pritam Kumar, and Anurag Sharma

Abstract The turbulent flow parameters and Reynolds stress analysis in flow over the smooth rigid bed with the emergent rigid vegetation in a straight channel have been investigated in this study. Higher-order turbulence parameters such as quadrant and octant analysis have been performed in the present study. Quadrant analysis shows that in the non-vegetation zone, sweep and ejection events have more dominant. In the vegetation zone, sweep and ejection have significant contributions as well as inward interaction event. Probability distribution shows that in the vegetation zone $P_{(3,0)}$ and $P_{(2,0)}$ have the least value, and in the vegetation zone, $P_{(1,0)}$ has the maximum value. Occurrence of probability analysis will show the contribution of the different classes of events in the three-dimensional bursting phenomena. This paper investigated three-dimensional octant analysis used to clarify the function of bursting events in the particle entrainment process. The outcomes of this study provide an important and detailed view of turbulent flow structures in vegetation and non-vegetation zone in an open channel flow.

Keywords Rigid vegetation · Bursting event · Octant analysis · Probability distribution · Quadrant analysis

19.1 Introduction

Aquatic plants have a significant impact on nutrient transport, flow patterns, and turbulence in rivers and canals, as well as on aesthetics, ecological restoration, and flood management (Tsujimoto 1999; Wang et al. 2021). In addition to create a habitat for aquatic life, vegetation also strengthens banks; reduces bank erosion, turbidity, and floods; and penetrates pollutants (Bennett et al. 2002; Gupta et al. 2023). One factor that alters the average and turbulent flow behavior of a channel is the presence of vegetation (Nepf 2012). The effect of vegetation on flow is

A. Ojha · A. Kumar · P. Kumar · A. Sharma (✉)
Department of Civil Engineering, National Institute of Technology, Rourkela, India
e-mail: sharmaan@nitrkl.ac.in

influenced by both the characteristics of the channel and the vegetation. Many studies have been conducted in the past on numerical methods for experiments utilizing real or artificial vegetation in flumes (Järvelä 2002; Meijer and Van Velzen 1999; Righetti and Armanini 2002; Khan et al. 2022). In main channels, floodplains, and wetland water basins, vegetation like grasses, bushes, and mangroves often grows. They enhance shear stress at the channel bed and raise hydraulic resistance to water flow. As a result, the open channel's conveyance capacity of the channel will be reduced. Additionally, the potential for sediment containment and deposition will be enhanced. Vegetation in coastal and riverine areas is crucial for sediment movement as well as ecosystem regulation. Vegetation in rivers is crucial to the ecosystem's restoration. Whether they are ecological, morphological, hydrological, or water quality factors, restoration must take into account several functions (Brookes et al. 1996; Aamir et al. 2022).

In rivers and open channels, vegetation increases the hydraulic resistance to the flow, causing an increase in flow depth and a decrease in flow velocity. As a result, vegetation is crucial for riverbank stability and energy loss during feeding occasions. The features of turbulence and vegetation cover affect sediment transport. In some areas along the river, there is frequent vegetation at various heights. Depending on the flow conditions, some vegetation may be emergent or submerged. As a result of momentum transfer between various vegetation layers, this results in complex flow dynamics (Luhar et al. 2008; Pasha and Tanaka 2016; Pasha et al. 2018; Chembolu et al. 2019; Chatelain and Proust 2021; Sohrabi et al. 2022).

River flood risk and environmental management presently focus on how riparian vegetation affects biological and flow processes in channels. Prior research mainly examined and simulated vegetation that was uniform in height while submerged or emerging, which is contrary to the behavior of real river and floodplain systems. Conversely, there are several plant heights that simultaneously experience emergent and submerged environments. Consequently, an important scientific method for assessing the impact of vegetation in open channel flows would be properly studied on the hydrodynamics of vegetated flow in open channels under more realistic circumstances (Tsujimoto and Kitamura 1990; Nepf 1999; Carollo et al. 2002; Nezu and Sanjou 2008; Fathi-Moghadam et al. 2011).

Only few literatures focused on the comparison of higher-order turbulence and Reynolds stress with vegetation and non-vegetation condition for open channel flow. In this present study, the data has been taken from previous literature (Kumar and Sharma 2022) and is therefore devoted for analyzing the higher-order turbulent parameters and Reynolds stress in a straight open channel with the presence of emerged rigid vegetation and non-vegetation condition. In this paper, higher-order turbulence flow parameter such as based on velocity fluctuation quadrant analysis, the probability distribution for the four types of quadrant and octant probability analysis has been analyzed for vegetation (S_1, S_2) and non-vegetation zone (S_0). The occurrence of probability for octant analysis has been investigated for vegetation and non-vegetation zone.

19.2   Experimental Setup and Methodology

The experiment was conducted in a 13 m long, 0.9 m wide, and 0.7 m deep recirculating straight rectangular channel. The channel sidewalls were made of glass, and the channel bed was constructed with concrete with a bed slope (S_O) of 0.002. Steel is used for the channel sidewalls, and an overhead tank was positioned upstream of the test channel to transport the water, and it is useful to maintain the flow under stable head circumstances. In this study, water is extracted from a storage tank that stores water in an intake tank using centrifugal pumps. Fig. 19.1. shows the plan view of vegetation arrangement and experimental setup in the laboratory. In this experiment, 3D velocity data has been taken by SonTek 16 MHz acoustic Doppler velocimeter (ADV). For detailed information on experimental setup and procedure, refer literature by Kumar and Sharma (2022).

In this experiment, three sections (S_0, S_1, S_2) have been taken for analysis. S_0 is the non-vegetation zone, that is, 30 cm before the upstream vegetation. Both (S_1, S_2) sections are in the vegetation zone, that is, 387 cm and 603 cm from the upstream vegetation, respectively.

19.3   Result and Discussion

19.3.1   Quadrant Analysis

Quadrant analysis is a very important parameter in analyzing fluid dynamics. The determination of quadrant analysis is based on the relative sign of velocity fluctuation. In this analysis, four quadrants will show the different bursting events. The bursting events are defined by four quadrants such as outward interactions ($i = 1$, $u' > 0$, $w' > 0$), ejections ($i = 2$, $u' < 0$, $w' > 0$), inward interactions ($i = 3$, $u' < 0$, $w' < 0$), and sweeps ($i = 4$, $u' > 0$, $w' < 0$). This analysis has been done at $Z/Y \sim 0.1$ (Z = height from bed and Y = total depth of flow) at three different points in the channel. Fig. 19.1 shows the quadrant analysis at $Z/Y \sim 0.1$, where horizontal and vertical coordinates represent velocity fluctuation in the longitudinal and vertical direction, respectively. In the non-vegetation zone shown in Fig. 19.2a, the ejection
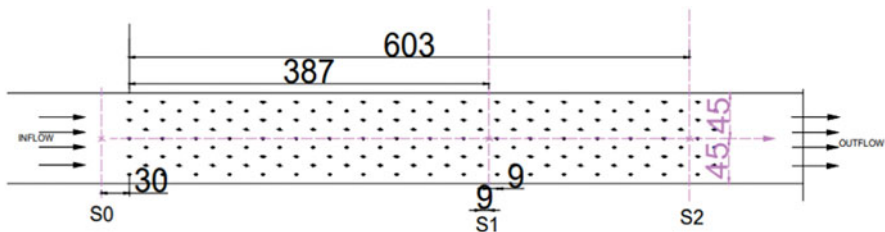
Fig. 19.1 Plan view and test section of experimental setup
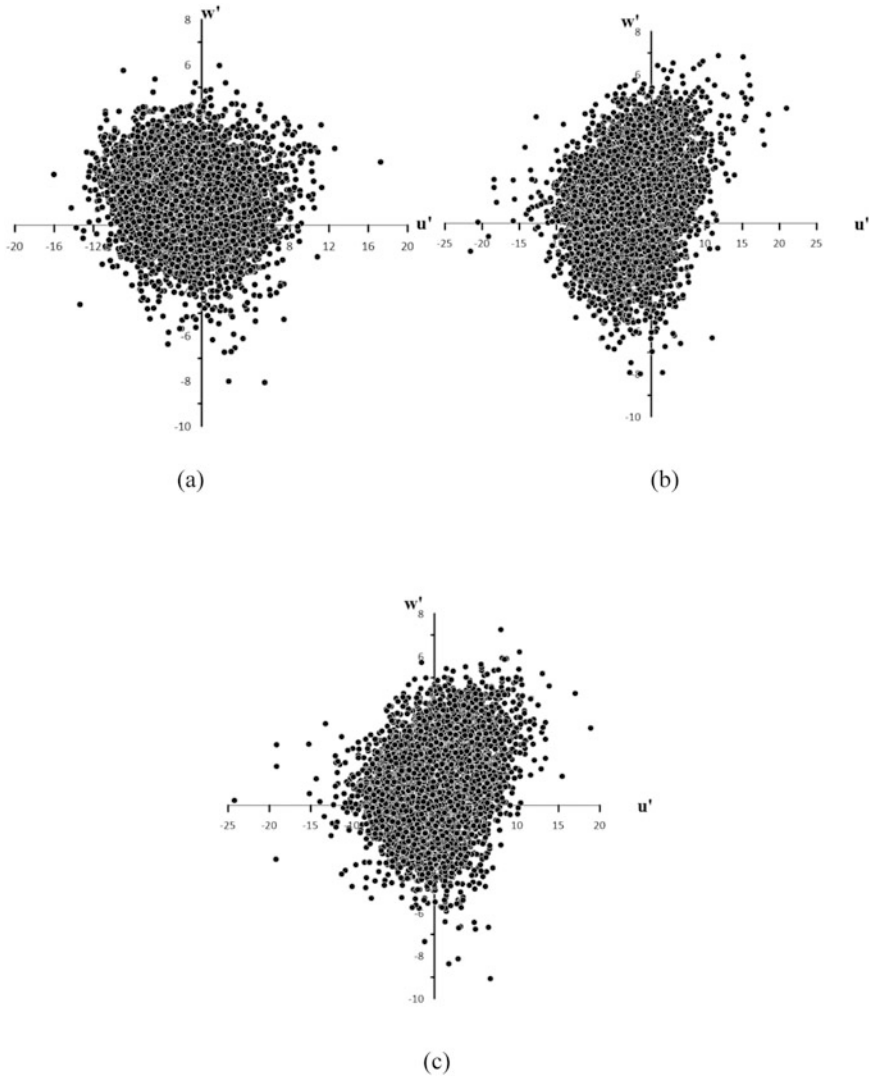
Fig. 19.2 Quadrant analysis at $Z/Y \sim 0.1$ in flows subjected to (**a**) non-vegetation (S_0) and (**b, c**) vegetation zone (S_1, S_2)

event is more dominant than other events. The least contribution is from the sweep and outward interaction. The contribution of ejection and inward interaction is 60–70%. The contribution of sweep and outward interaction is 20–30%.

Figure 19.2b shows the velocity fluctuation at the center of the vegetation zone. The ejection event is more dominant than other events. The least contribution is from the sweep event. The contribution of ejection is 70–80%. The contribution of inward and outward interaction is 30–20%. While flow is going through rigid vegetation

toward downstream, velocity fluctuation is less. The contribution of velocity fluctuation at the downstream vegetation end is shown in Fig. 19.2c. The sweep and ejection events are more dominant than other events. The least contribution is from the inward interaction event. The contribution of sweep and ejection is 50–70%. The contribution of inward and outward interaction is 40–30. Sweep and ejection event has more dominance in the non-vegetation zone (S_0), while in the vegetation zone (S_1, S_2), ejection and inward interaction have more contribution.

19.3.2 Probability Distribution

The probability $P_{i,H}$ of the occurrence of the bursting events can be obtained from Eq. 19.1 (Sharma and Kumar 2017):

$$P_{i,H} = \frac{\int_{t=0}^{t=T} I_{i,H} dt}{\int_{t=0}^{t=T} [I_{1,H} + I_{2,H} + I_{3,H} + I_{4,H}] dt} \tag{19.1}$$

$$I_{i,H}[u'(t)w'(t)] = \begin{cases} 1, \text{if} (u'w') \text{ is inquadranti and if} \\ |u'w'| = H(u'^2)^{0.5}(w'^2)^{0.5} \\ 0, \qquad\qquad\qquad \text{otherwise} \end{cases} \tag{19.2}$$

where $I_{i,H}$ is an indicator function described by the Eq. 19.2 The vertical variations of $P_{i,H}$ in flows subjected to non-vegetation zone, center of vegetation zone, and end of vegetation zone are plotted in Fig. 19.3.

In the non-vegetation zone, $P_{(1,0)}$ and $P_{(4,0)}$ are having higher probabilities as compared to the $P_{(3,0)}$ and $P_{(2,0)}$. At the center of the vegetation (S_1), the probability $P_{(4,0)}$ has the least value as compared to other quadrant probabilities. At the end of the vegetation zone (S_2), $P_{(2,0)}$ has the least value of probability, and $P_{(1,0)}$ has maximum probability.

19.3.3 Octant Analysis

The research by Keshavarzi and Gheisi (2006) also demonstrated that when there is fully three-dimensional flow in nature, two-dimensional analysis of bursting analysis cannot identify the entrainment process. They created a three-dimensional octant analysis technique to take into account for a secondary flow's impact. The aforementioned method was utilized in this study to analyze experimentally recorded velocity data in order to evaluate the coherent turbulent flow structure around bridge pier.
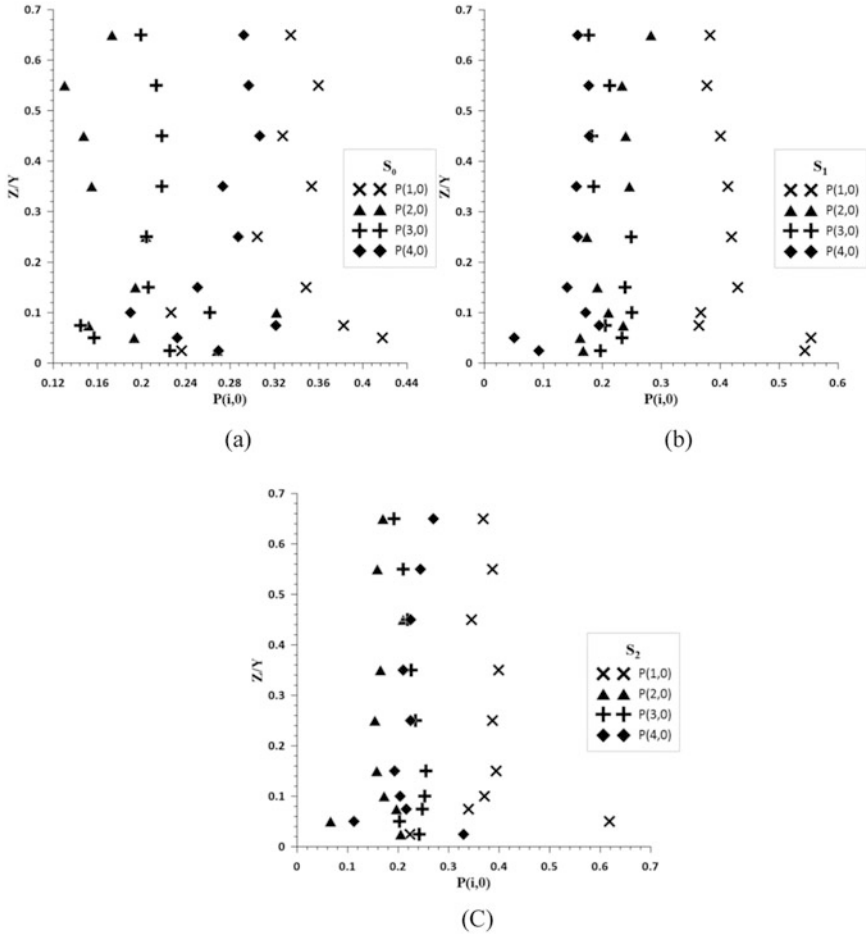
Fig. 19.3 Vertical profiles of $P_{i,H}$ in flows subjected to (**a**) non-vegetation (S_0) and (**b, c**) vegetation zone (S_1, S_2)

The classifications of bursting events were performed based on the sign of the velocityfluctuations in three dimensions that can be obtained from Eq. 19.3, and eight different events are described below:

$$u' = u_i - \overline{u}, v' = v_i - \overline{v}, w' = w_i - \overline{w} \tag{19.3}$$

1. Internal outward interaction or Class I-A ($u' > 0$, $w' > 0$, $v' > 0$);
2. Internal ejection or Class II-A ($u' < 0$, $w' > 0$, $v' < 0$);
3. Internal inward interaction or Class III-A ($u' < 0$, $w' < 0$, $v' < 0$);
4. Internal sweep or Class IV-A ($u' > 0$, $w' < 0$, $v' > 0$);
5. External outward interaction or Class I-B ($u' > 0$, $w' > 0$, $v' < 0$);

6. External ejection or Class II-B ($u' < 0$, $w' > 0$, $v' > 0$);
7. External inward interaction or Class III-B ($u' < 0$, $w' < 0$, $v' > 0$);
8. External sweep or Class IV-B ($u' > 0$, $w' < 0$, $v' < 0$);

Based on the three velocity fluctuations, the time fraction or occurrence probability of the eight orthogonal zones was calculated. To determine an event's likelihood of occurring given the sediment entrainment function, the time fraction of each event must be known. The following equation was presented by Keshavarzi and Gheisi (2006) to calculate the likelihood of occurrence for each event.

$$P_k = \frac{n_k}{N} \tag{19.4}$$

$$N = \sum_{K=1}^{8} n_k \qquad k = 1, 2, 3, 4, \dots \dots .8 \tag{19.5}$$

P_k is the occurrence probability of each bursting event, which can be determined by Eqs. 19.4 and 19.5; n_k is the number of events in each class; and N is the total number of bursting events. Using the above equations, the occurrence probabilities for the eight different bursting events were computed for vegetation (S_1, S_2) and non-vegetation zone (S_0) shown in Fig. 19.4.

The occurrence of probability in octant analysis in eight classes shows the non-vegetation zone, in Fig. 19.4a at $z/y \sim$ (0.3 to 0.4), and maximum probability of occurrence is for Class I-A and least value of probability of occurrence for Class IV-A. At the center of vegetation zone (S_1), Class III-A and Class I-A have maximum probability, while at the bed surface $Z/Y < 0.1$, Class II-B and Class IV-B have minimum probability shown in Fig. 19.4b. Fig. 19.4c shows the occurrence of probability toward the downstream of the vegetation zone (S_2) at the flow depth $z/y > 0.1$ Class IV-A has minimum probability.

19.4 Discussion

A series of quasicyclic events that take place in the wall region of turbulent flows make up the bursting process. Approximately 70% of turbulence production happens during this procedure. The most significant process in wall-bounded turbulent shear flow is considered to be bursting. To have a more thorough understanding of the dynamics of the turbulent transport process, it is essential to understand bursting phenomenon. Reynolds shear stress transport can be observed in quadrant analysis. It has been observed that sweep and ejection have more contribution in the non-vegetation zone while in the vegetation zone ejection and inward have more contribution. Probability distribution will show the occurrence of the bursting events in the flow. Probability analysis has been done for hole region ($H = 0$). $P_{(1,0)}$ has maximum value in the vegetation and non-vegetation zone. $P_{(2,0)}$ and $P_{(4,0)}$ have
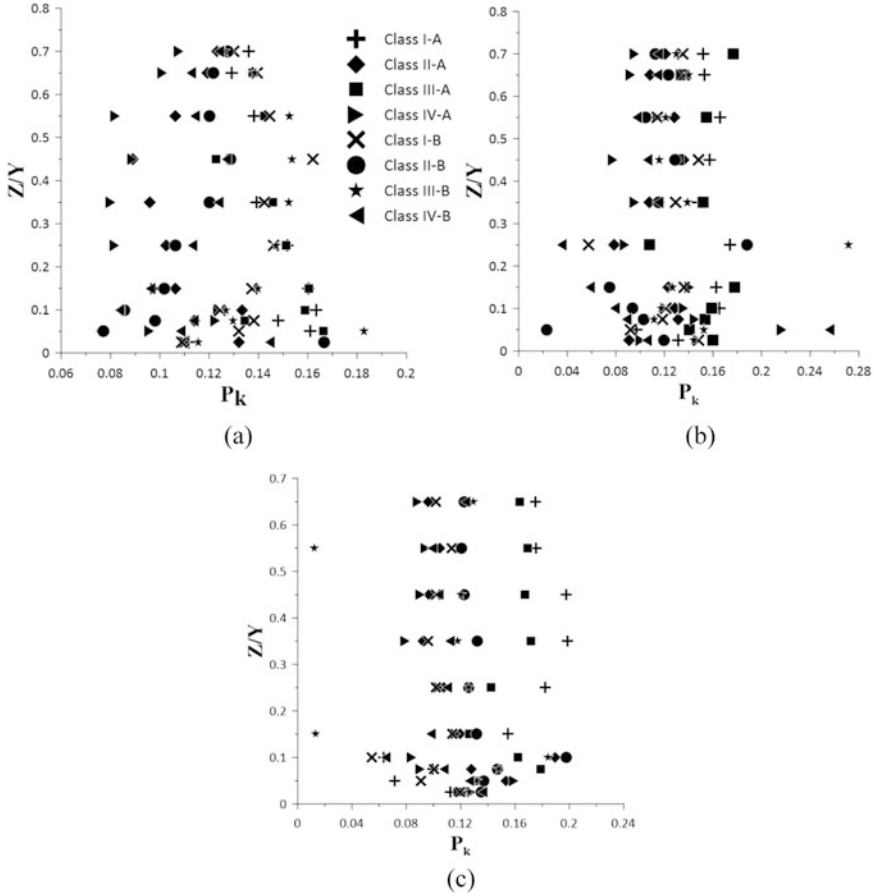
Fig. 19.4 Vertical profiles of the occurrence of probability for different bursting events (**a**) Non vegetation (S_0) and (**b**, **c**) vegetation zone (S_1, S_2)

least value in the vegetation zone. Octant analysis shows the occurrence of probability for eight classes. Class I-A and Class III-A have maximum probability in the vegetation and non-vegetation zone. Class IV-B and Class II-B have minimum probability in the vegetation and non-vegetation zone.

19.5   Conclusion

An experimental investigation was conducted to examine changes in the turbulent flow characteristics caused by the application of vegetation and non-vegetation over a rigid bed with emergent rigid vegetation. In this paper, quadrant analysis show the bursting event such as sweep and ejection has more contribution in the

non-vegetation zone. In the vegetation zone, sweep event reduces, and inward interactions have more contribution. Probability analysis shows the occurrence of bursting event. It shows $P_{(2,0)}$ and $P_{(4,0)}$ have more value in the vegetation zone as compared to the non-vegetation zone that shows the Reynolds shear stress transport by the sweep and ejection event. The probability occurrence of octant analysis shows the maximum value for Class I-A in the non-vegetation zone and at the center of the vegetation zone, while at the end of the vegetation zone, Class II-B has maximum probability. The minimum occurrence of probability for non-vegetation zone is Class IV-A, and the center of the vegetation has also similar effect, while at end of the vegetation zone, Class II-B and Class IV-B have least probability of occurrence at the bed surface.

19.6 Future Scope

In this study, analysis has been done for rigid bed with emergent rigid vegetation. In future research, detail analysis of turbulent flow characteristics can be done for flexible vegetation, and validation of the experimental results can be performed in Ansys Fluent and Flow3D.

References

Aamir M, Ahmad Z, Pandey M, Khan MA, Aldrees A, Mohamed A (2022) The effect of rough rigid apron on scour downstream of sluice gates. Water 14(14):2223. https://doi.org/10.3390/w14142223

Bennett SJ, Pirim T, Barkdoll BD (2002) Using simulated emergent vegetation to alter stream flow direction within a straight experimental channel. Geomorphology 44(1–2):115–126

Brookes A, Shields FD Jr, Brookes A, Shields FD Jr (1996) Perspectives on river channel restoration. In: River Channel Restoration. Wiley, Hoboken, NJ, pp 1–19

Carollo FG, Ferro VITO, Termini D (2002) Flow velocity measurements in vegetated channels. J Hydraul Eng 128(7):664–673

Chatelain M, Proust S (2021) Open-channel flow through emergent rigid vegetation: effects of bed roughness and shallowness on the flow structure and surface waves. Phys Fluids. https://doi.org/10.1063/5.0063288

Chembolu V, Kakati R, Subashisa Dutta S (2019) A laboratory study of fow characteristics in natural heterogeneous vegetation patches under submerged conditions. Adv Water Resour 133:103418

Fathi-Moghadam M, Arman A, Emamgholizadeh S, Alikhani A (2011) Settling properties of cohesive sediments in lakes and reservoirs. J Waterw Port Coast Ocean Eng 137(4):204–209

Gupta LK, Pandey M, Raj PA, Shukla AK (2023) Fine sediment intrusion and its consequences for river ecosystems: a review. J Hazard Toxic Radioact Waste. 27(1):04022036. https://doi.org/10.1061/(ASCE)HZ.2153-5515.0000729

Järvelä J (2002) Flow resistance of flexible and stiff vegetation: a flume study with natural plants. J Hydrol 269(1–2):44–54

Keshavarzi AR, Gheisi AR (2006) Stochastic nature of three dimensional bursting events and sediment entrainment in vortex chamber. Stoch Env Res Risk A 21:75–87

Khan MA, Sharma N, Pu JH, Pandey M, Azamathulla H (2022) Experimental observation of turbulent structure at region surrounding the mid-channel braid bar. Marine Georesour Geotechnol 40(4):448–461. https://doi.org/10.1080/1064119X.2021.1906366

Kumar P, Sharma A (2022) Experimental investigation of 3D flow properties around emergent rigid vegetation. Ecohydrology 15(8):e2474

Luhar M, Rominger J, Nepf HM (2008) Interaction between fow, transport and vegetation spatial structure. Environ Fluid Mech 8:423–439

Meijer DG, Van Velzen EH (1999) Prototype-scale flume experi-ments on hydraulic roughness of submerged vegetation. In 28th Inter-national Conference, Int. Assoc. of Hydraul. Eng. and Res., Graz, Austria

Nepf HM (1999) Drag, turbulence, and diffusion in flow through emergent vegetation. Water Resour Res 35(2):479–489

Nepf HM (2012) Flow and transport in regions with aquatic vegetation. Annu Rev Fluid Mech 44:123–142

Nezu I, Sanjou M (2008) Turburence structure and coherent motion in vegetated canopy open-channel flows. J Hydro Environ Res 2(2):62–90

Pasha GA, Tanaka N (2016) Efectiveness of fnite length inland forest in trapping tsunami-borne wood debris. J Earthq Tsunami 10(4):1650008

Pasha GA, Tanaka N, Yagisawa J, Achmad FN (2018) Tsunami mitigation by a combination of coastal vegetation and a backward-facing step. Coast Eng J 60:104–125

Righetti M, Armanini A (2002) Flow resistance in open channel flows with sparsely distributed bushes. J Hydrol 269(1–2):55–64

Sharma A, Kumar B (2017) Structure of turbulence over non-uniform sand bed channel with downward seepage. Eur J Mech B/Fluids 65:530–551

Sohrabi S, Afzalimehr H, Singh VP (2022) Estimation of drag coeffcient of emergent and submerged vegetation patches with various densities and arrangements in open channel flow. ISH J Hydraul Eng. https://doi.org/10.1080/09715010.2022.2066482

Tsujimoto T (1999) Fluvial processes in streams with vegetation. J Hydraul Res 37(6):789–803

Tsujimoto T, Kitamura T (1990) Velocity profile of flow in vegetated-bed channels. KHL Progressive Report. 1:43e55

Wang J, Liu X, Min F, Dai J, Jiang X (2021) Turbulence structure and longitudinal velocity distribution of open channel flows with reedy emergent vegetation. Ecohydrology 15(1):e2352

Chapter 20
Recirculation Region Control Behind a Partially Submerged Cylinder Due to Wave Against Current

Krishnendu Barman, Sayahnya Roy, Susanta Chaudhuri, and Koustuv Debnath

Abstract This chapter shows the effect of wave acting against the current on the modulation of vortex shedding behind a partially submerged cylinder. The effect of superimposed wave against current flow on the drag field and turbulence characteristics at downstream of the cylinder is still not been revealed. A micro Acoustic Doppler velocimeter (ADV) is used to measure the high-frequency velocity variations. Observation suggests that there is no distinct recirculation in the wake region for the lock-on (LO) case. This LO state is achieved when the frequency of the superimposed wave is two times that of natural vortex shedding (V_{ns}) frequency. Turbulent dissipative eddy creates a jacket around the cylinder that changes the flow separation due to the superimposed wave acting against the current. Further, the upward momentum flux is found in the LO case. As far as vorticity is concerned, it is completely different for LO case. Moreover, the mean flow, fluctuating velocity, and velocity derivatives interact and exchange energy in a complex way for the case of LO as evident from turbulence production. This complex interaction of energy enhances the drag force at the near bed region, which decreases toward the free stream region in the vicinity of the cylinder for LO case.

Keywords ADV · Against wave · Drag force · Turbulence · Vortex lock-on

K. Barman (✉)
Department of Applied Mathematics with Oceanology and Computer Programming, Vidyasagar University, Midnapore, India

S. Roy · K. Debnath
Department of Aerospace Engineering and Applied Mechanics, Indian Institute of Engineering Science and Technology (IIEST), Shibpur, India

S. Chaudhuri
Department of Geological Sciences, Jadavpur University, Kolkata, India

20.1 Introduction

The cylinder is studied because the study of turbulent flow around a vertically partially submerged cylinder sheds light on a wide spectrum of applications that includes flow around the offshore structures, bridge pier, and coastal structures. As will be evident later, there are a lot of strange events (vortex shedding, vortex-lock on, recirculation zone) stimulated in the wake regime downstream of a cylinder (Lin et al. 2002, 2003; Kim et al. 2006; Vandiver et al. 2009; Feng and Wang 2010; Gunnoo et al. 2016; Gupta et al. 2023). Therefore, physical interpretation of the induced oscillatory flow resonance, that is, vortex lock-on between the shed frequency and external force near the downstream of cylinder, is primary interest in spite of its engineering applications such as turbomachinery and power generation. Accordingly, in an earlier study of Sheridan et al. (1997), they describe a range of behavior that differs greatly from that of a more classical fully submerged cylinder. They observed that the occurrence of pre-existing layer of vortices around the cylinder due to localized wave-braking phenomena. Griffin and hall (1991) performed an important review to analyze the characteristic behavior of vortex lock-on phenomenon and recirculation region control. It was found that the vortex shedding resonance is exhibit due to submerged bluff body along with rotational, in-line, and transverse oscillating steady flow. In particular, Kim et al. (2006) carried out an experimental study to illustrate the coherent structures and vortex lock-on dynamics behind a circular cylinder in an oscillatory flow environment. It is observed that the vortex lock-on appeared when the applied oscillatory frequency is perturbed twice of the natural shedding frequency near downstream of the cylinder. However, Kim et al. (2009) presented a numerical simulation to describe the vortex synchronization condition due to prescribed longitudinal sinusoidal velocity perturbation. Moreover, Lin et al. (2012) investigated the flow structure at the wake region of circular cylinder. They concluded that the two larger vortices in the longitudinal and vertical direction occurred at the recirculation zone of the impulsively stated cylinder due to energy transfer from the entrainment of background flow into the recirculation region. Therefore, vortex shedding is a very imminent event in our day to day life as evident from flow past offshore structures, high rise buildings, chimneys, or bridge. The induced vortex interaction downstream of a bluff body results in large unsteady side forces, which in turn leads to heavy structural vibrations.

Of note, a mechanism of the couple interaction of waves into the following currents over the flat surface (Kemp and Simons 1982; Umeyama 2005, 2009; Dutta et al. 2022; Chaudhuri et al. 2022), ripple structures (Grant and Madsen 1979; Fredsøe et al. 1999; Khan et al. 2022), and fully and partially submerged obstacles (Banerjee et al. 2015; Barman et al. 2018) is an important topic for offshore structures, marine environment, and shore protection. Earlier studies of Grant and Madsen (1979) and Fredsøe et al. (1999) on wave induced flow with following currents over ripple-covered bottom surface. Results showed that the changes in mean flow and increased in shear stress are due to wave interaction on the current

flow. Indeed, a key experimental investigation was performed by Kemp and Simons (1982) to characterize the wave flow dynamics along the current over smooth and rough beds. However, an elaborated experimental investigation on a much-related topic was attended by Kemp and Simons (1983) for the propagating waves against the turbulent current and discussed the silent features of this combined interaction. They stated that the wave attenuation rate is increased for applying wave opposing current. Umeyama (2005, 2009) carried out a series of experiment on wave plus current over flat surface. Rey et al. (2014) studied wave-current interaction for deep water wave against current flow in the presence of tri-dimensional bathymetry. Their results confirmed that the wave amplitude and intensity were increased when waves propagated against the current flow near the two submerged mounds. Moreover, Zhang et al. (2015) proposed a developed turbulence model for a solitary wave streaming over following as well as opposing current conditions. They concluded that the turbulent kinetic energy (TKE) and level of turbulence are increased due to the addition of wave into opposing current. Recently, Barman et al. (2018) presented an experimental investigation over the submerged obstacles with the existence of wave following current. Based on the wave-current interaction, Roy et al. (2018) performed an experimental study to characterize the turbulent structure at the wake region of circular cylinder and investigated the dynamics of vortex lock-on. Their finding confirmed that the recirculation region at downstream of the partially submerged cylinder almost departed for vortex lock-on due to combined interaction of wave-current flow. Also, shear stress showed higher values near the shear layer at the wake region of cylinder for the superimposed surface wave following the current in comparison with the natural shedding frequency. Natural hazards like pier and river bank scour happen due to an increased recirculation region, resulting in bridge collapse and flood, which leads to loss of human life (Chaudhuri et al. 2022; Saikumar et al. 2022).

The purpose of this paper is to describe the statistics of the forces at the downstream of cylinder partially submerged in a "wave-against-current" environment. Streamline of mean velocity and contour of phase-averaged turbulence intensity and Reynolds shear stress are discussed in this paper. Moreover, vorticity and dissipation contour are portrayed to analyze the eddy structure and modulation of drag force on the interaction of wave into the opposing currents. Therefore, study of vorticity (and other properties) of the "wave against current" flow downstream of the cylinder can lead to many desirable results such as vortex-induced vibrations and wake turbulence, which has innumerable applications.

20.2 Experiments

All the experimental measurements were taken in a wave flume situated at Fluid Mechanics and Hydraulics Laboratory (FMHL), Department of Aerospace Engineering and Applied Mechanics, IIEST Shibpur India. A plunger-type wavemaker bench was placed at the outlet of the flume (see Fig. 20.1). For more details about the
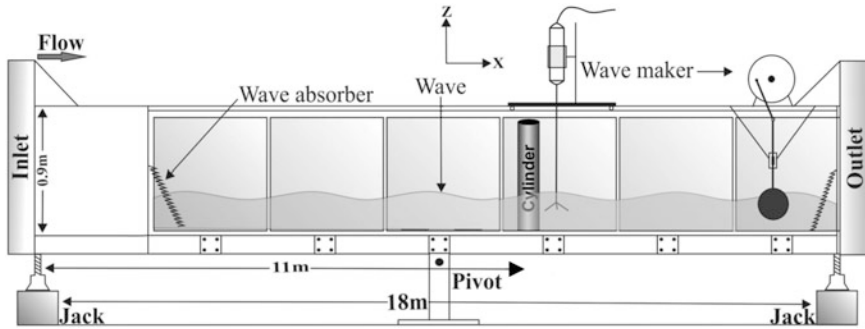
Fig. 20.1 Schematic diagram of the experimental setup

Table 20.1 Hydrodynamic parameters of mean flow

Reynolds number, Re (Uh/v)	60,000
Depth average stream-wise mean velocity, U (cm/s)	29.5
Mean flow depth, h (cm)	20
Froude Number, $Fr = \frac{U}{\sqrt{gh}}$	0.28

dimension and also the mechanism of the wave-maker, please follow previous study of Barman et al. (2018) and Roy et al. (2018). A 16 MHz Micro-ADV (acoustic Doppler velocimeter) was used to capture the induced opposing wave-current flow structures. All the instantaneous velocity data (for 3 min) measurements were taken near the downstream of the circular cylinder. The vertical cylinder was located at 9 m from the inlet, and the wavemaker was deployed at 7 m downstream from the cylinder. A number of tests (11) have been made in this experiment, but for clarity and better representation, three different cases WC1, WC2, and WC3, with wave frequencies $f = 0$, 1, and 2 Hz acting against the current are discussed. For each vertical profile, measurements were performed at 25 points. The points were chosen more densely to capture the spatial variation of turbulence. Waves were superimposed against the current of Reynolds number $Re = \frac{Uh}{v} = 60,000$, where U is the depth average mean stream-wise velocity and h is the depth of water and v is kinematic viscosity. A constant water depth 20 cm was maintained for all the experimental cases. The superimposed wave frequency was precise by varying the voltage of the input electricity to the motor, using an electronic varies. For more particulars on hydrodynamic parameters and superimposed waves, please see Tables 20.1 and 20.2.

Table 20.2 Superimposed wave parameters

	WC1	WC2	WC3	
Time period, T (s)	0	1		0.5
Frequency of wave, f (Hz)	0	1	2	
Flow depth, h (cm)	20	20	20	
Surface wave height, H_w (cm)	0	3.5	3.2	
Surface wave length, L_w (cm)	0	65	36	
Ratio of L_w/H_w		0	16	13.1
Depth average stream-wise velocity, U (cm/s)	29.5	29.4	29.2	
Wavelength-mean depth ratio	0	3.25	1.75	
Wave slope	0	7.1 9.46		

20.3 Experimental Results and Observations

The instantaneous velocity components for wave propagations into opposing current can be written as:

$$u_t = \overline{u} + \tilde{u}_t + u'; v_t = \overline{v} + \tilde{v}_t + v'; w_t = \overline{w} + \tilde{w}_t + w' \tag{20.1}$$

where $\tilde{u}_t = \langle u_t \rangle - \overline{u}$, $\tilde{v}_t = \langle v_t \rangle - \overline{v}$, $\tilde{w}_t = \langle w_t \rangle - \overline{w}$; the bar represents the time-averaged velocity, tilde signify wave-induced velocity, and a prime indicates the fluctuation velocity. For the combined wave-current environment, the normalized stream-wise and vertical phase-averaged mean velocities can be obtained as:

$$\langle \widehat{u} \rangle = \langle u_t \rangle / u_*; \langle \widehat{w} \rangle = \langle w_t \rangle / u_* \tag{20.2}$$

For induced wave opposing a current flow, the normalized phase-averaged longitudinal turbulence intensities are denoted as:

$$\langle u^+ \rangle = \frac{\left(\sqrt{\frac{1}{N} \sum_{t=0}^{N} (u_t - \langle u_t \rangle)^2} \right)}{u_*} \tag{20.3}$$

where N = total number of observation periods. And the normalized phase-averaged Reynolds shear stress is given by:

$$\langle \tau_{uw} \rangle = -\rho \overline{u'w'} = \frac{\rho}{N} \sum_{t=0}^{N} (u_t - \langle u_t \rangle)(w_t - \langle w_t \rangle) \tag{20.4}$$

All the phase-averaged turbulence parameters are determined by a similar process of Umeyama (2005) and Barman et al. (2016). In the present experiment, the vortex LO condition was achieved for the case WC2 ($f = 1$ Hz) and non LO condition evident for the case WC3, ($f = 2$ Hz).

20.3.1 Mean Velocity

Fig. 20.2a–c display the streamline of mean velocity plots for the case of WC1 ($f = 0$ Hz), WC2 ($f = 1$ Hz), and WC3 ($f = 2$ Hz). As is evident from the Fig. 20.2a ($f = 0$ Hz), the region of maximum concentration of the stream line is the region of distinction between wake/recirculation region (flow toward the cylinder, $x/h = 0$–0.5) and the main downstream flow, and this concentrated stream line region is known as reattachment region. However, there is no such distinct concentration of the streamlines at $x/h = 0.5$ observed in Fig. 20.2b, also no evidence of recirculation region for the LO case WC2 ($f = 1$ Hz). The distinction line comes into play again when the frequency is increased as mapped in the Fig. 20.2c ($f = 2$ Hz).

To understand the suppression of the recirculation region, the fast Fourier transform (FFT) of the velocity signal (measured at the $1d$ downstream on the cylinder wake center line) is calculated (not shown in here). FFT output shows that the vortex shedding natural frequency, V_{ns}, is superimposed wave frequency, $f_{vs} = 0.5$ Hz. According to Kim et al. (2006), a LO state occurs when the frequency of the wavy flow is double that of f_{vs}. In the present experiment, a similar result is noted. In the LO state, the superimposed wave frequency synchronized with the f_{vs}, which creates a resonance and modulates the flow separations around the cylinder, which suppresses the recirculation.
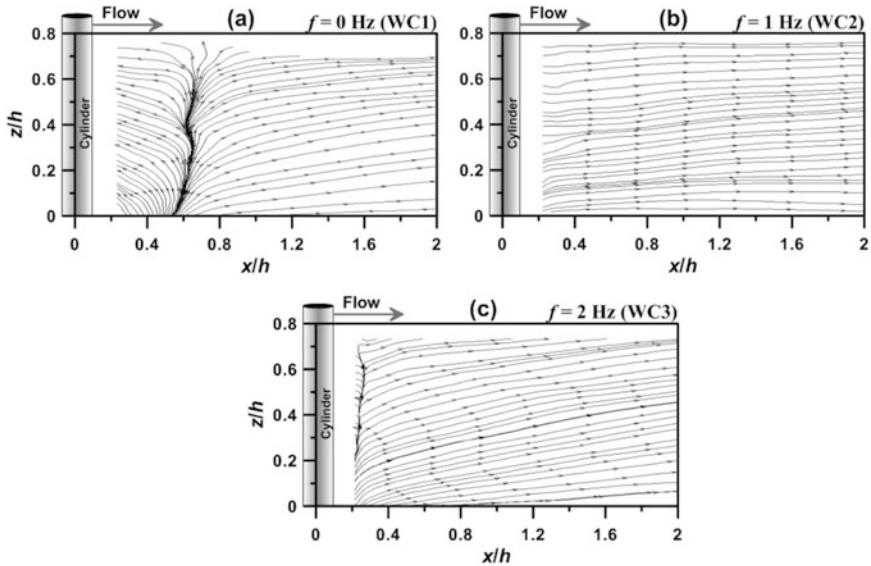

Fig. 20.2 (a–c) streamline of mean velocity plots for WC1, WC2, and WC3 cases

20.3.2 Phase-Averaged Turbulent Intensity and Reynolds Shear Stress

Turbulent intensities represent the level of turbulence within the flow field. Fig. 20.3a–c show the stream-wise turbulence intensity (U^+) contour plots for the cases WC1 ($f = 0$ Hz), WC2 ($f = 1$ Hz), and WC3 ($f = 2$ Hz). The maximum values of U^+ are observed within the recirculation region ($x/h = 0.5$–0.6) for only current over the cylinder (V_{ns}) case WC1 ($f = 0$ Hz). This is due to the interaction of vortices in the wake region and viscous region near the wall. However, the large values of U^+ shifted near the cylinder wall ($x/h = 0.1$–0.2) for the vortex LO case WC2 ($f = 1$ Hz). In this regard, Kim et al. (2006) stated that the larger values of U^+ appears close to the cylinder in the LO state compared to the V_{ns} state, and this statement supports the present results. This observation provides an insight, on the fact of modulation of turbulent eddies within the flow field due to the superimposed wave against current. Umeyama (2009) also observed that the values of U^+ are larger at the free surface region for the superimposed wave against current compared to the only current flow. As there are large values of $U+$ observed for LO case from the present and past studies, it may be stated that the superimpose wave can modulate the turbulence eddies around the cylinder. These eddies create a jacket around the cylinder, which can change the flow separation. This result shows the suppuration of recirculation region is achieved behind the cylinder. Fig. 20.3e and f show the Reynolds stress contour plots for the case of WC1 ($f = 0$ Hz), WC2 ($f = 1$ Hz), and WC3 ($f = 2$ Hz). As is evident from the above figure, within the reattachment region ($x/h = 0.5$–0.6), Reynolds stresses are four times higher in WC1 case than WC2 and WC3 cases. However, there is ten times lesser value of τ_{uw} at the immediate vicinity of cylinder for WC1 case than WC2 and WC3. Reynolds stress directly hints
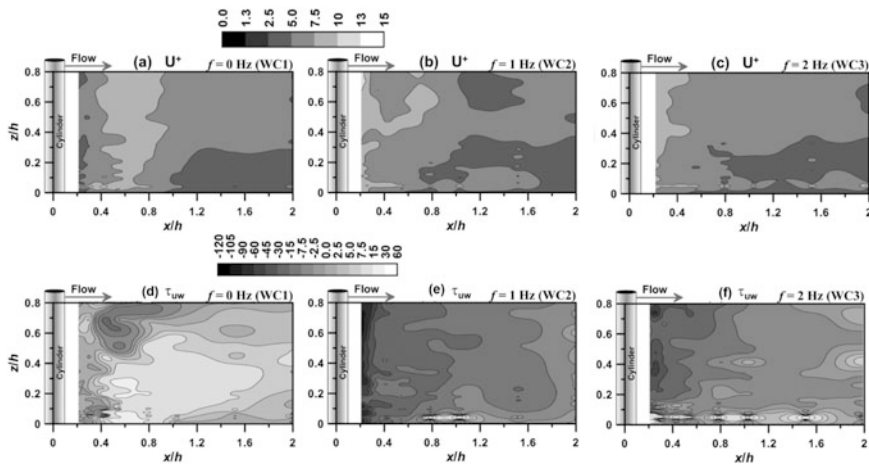

Fig. 20.3 Contour plots of phase-averaged turbulent intensities (**a–c**); and Reynolds shear stress (**d–f**) for WC1, WC2, and WC3 cases

at the fact of momentum transfer in turbulent flow. Previously, it was noted by many researchers (Umeyama 2009; Feng and Wang 2010) that the wave-current flow can decrease momentum transfer. Kemp and Simons (1983) observed that the superposed waves on flow field significantly reduce the turbulence stress at the outer flow field. The reduction of τ_{uw} is a fact of the consequent diminution in turbulent-velocity fluctuations. Moreover, the negative value of τ_{uw} signifies the upward momentum flux. In the present LO case, the large values of upward momentum flux make an envelope around the cylinder, which completely alter the flow field near the cylinder.

20.3.3 Evolution of Turbulence Vorticity and Dissipation

The vorticity vector shows the local rotational motion of a continuum. Thus, it is important to compare the behavior of vorticity vectors between LO case and natural shedding case behind the cylinder. Batchelor (2000) reported that the vorticity generation is negligible near the free surface and for a smooth surface flow. As there is no restriction in the flow field, the acceleration vector appears zero value, and the tangential stress disappears, resulting in no vorticity generation. In contrast, for a rough and wavy surface, the acceleration vector experiences some value, and the tangential stress is also increased, resulting in the generation of vorticity. Vorticity is computed as:

$$\omega_\theta = \frac{\left[\frac{\partial u_j}{\partial x_i} - \frac{\partial u_i}{\partial x_j}\right]}{2u_*^2} \tag{20.5}$$

Turbulence vorticity, ω_θ, is depicted in Fig. 20.4a–c for the case of WC1 ($f = 0$ Hz), WC2 ($f = 1$ Hz), and WC3 ($f = 2$ Hz), respectively. Fig. 20.4a shows the negative vorticity values at the vicinity of the cylinder ($x/h = 0.2$) for LO case WC2; however, there is positive vorticity for natural shedding case WC1 (Fig. 20.4b) that is observed. For the LO case, the superimposed wave against the current modulates the well-known von Kármán vortex streets and generates a new kind of vortex, which propagated downstream from the cylinder. Moreover, the change in vorticity values can also be attributed to alter in inflection points (change of sign) in the turbulence production.

Dissipation of turbulent kinetic energy t_d is portrayed in Fig. 20.4d–f for the case of WC1 ($f = 0$ Hz), WC2 ($f = 1$ Hz), and WC3 ($f = 2$ Hz), respectively. The equation used here for devising turbulent dissipation rate is taken as:

$$t_d = \frac{\left(c^3 k^{(3/2)}\right)}{l_m} \tag{20.6}$$

where l_m(mixing length), as suggested by Pope (2001):
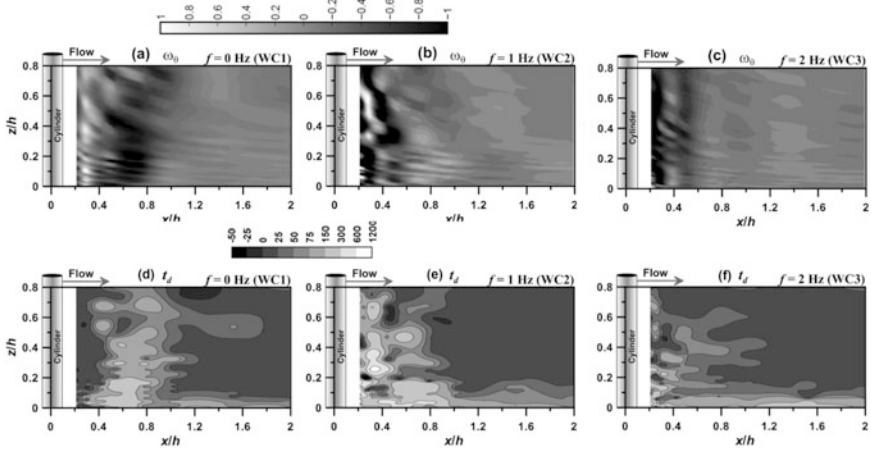
Fig. 20.4 Contour plots of turbulence vorticity (**a–c**); and dissipation (**d–f**) for WC1, WC2, and WC3 cases

$$l_m = c\sqrt{k}\left(\frac{\partial <u>}{\partial x_j}\right)^{-1}$$

According to Pope (2001) the value of "c" is close to 0.55.

The velocity gradients (du_i/dx_j) react against the fluctuating stresses, which converts the kinetic energy into the internal energy. Here, it can be seen from Figs. 20.4e and f that dissipation rate is high at a closer distance from the cylinder for the LO case (WC2) than the WC1 case. This may be due to the presence of high velocity gradients and the presence of small-scale eddies in the wave-induced flows near the cylinder.

20.3.4   Turbulence Production

Fig. 20.5a–c show the turbulence productions behind the cylinder for WC1 ($f = 0$), WC2 ($f = 1$), and WC3 ($f = 2$) cases. Turbulent kinetic energy production is computed as (Pope 2001):

$$t_p = - <u_i u_j> \frac{\partial <u_j>}{\partial x_i} \tag{20.7}$$

where i is the stream-wise direction and j is cross-stream velocity.

A lot of transaction of turbulent kinetic energy production happens for the LO case within the recirculation region ($x/h = 0.5$–0.6) of the cylinder (Fig. 20.5b). When production term is positive, energy is transferred from mean flow to
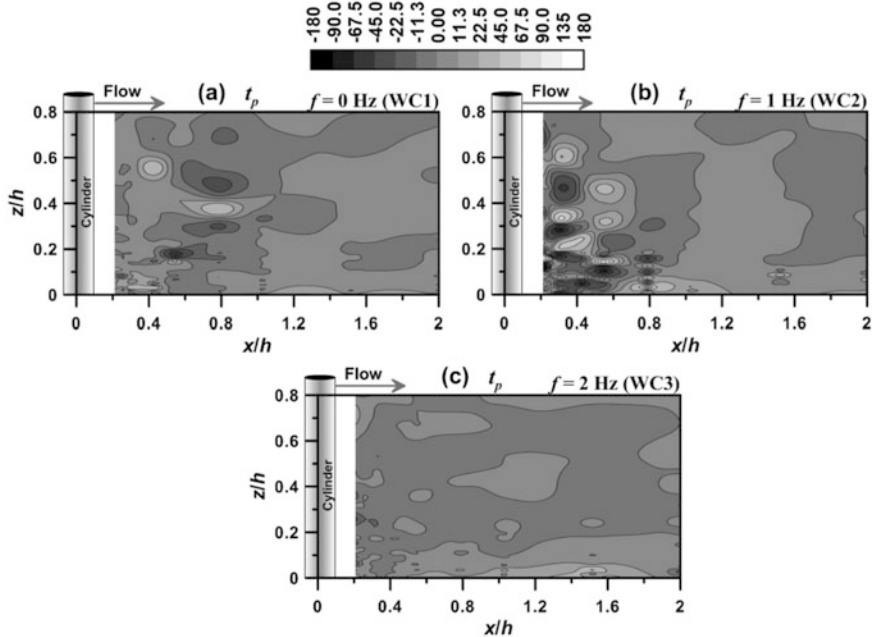
Fig. 20.5 (**a–c**) contour plots of turbulence production for WC1, WC2, and WC3 cases

fluctuating flow; this phenomenon is opposite for positive values of t_p. As is evident, it is negative near the cylinder wall region for all the cases.

However, there is some positive values of t_p observed for the LO case (WC2, Fig. 20.5b). According to Liberzon et al. (2005), there is a complex interaction and exchange of energy among the mean flow, velocity fluctuations, and derivatives. The regions with $t_p > 0$ and $t_p < 0$ may be ruled by diverse physical mechanisms, reliant on the exact type of forcing. In this experiment, alteration of drag force is observed (Please see the next section). Moreover, the circulation or transaction of energy can be attributed to high enstrophy levels or high vorticity near the cylinder. These can also be validated by the vorticity plots, which shows similar trend.

20.3.5 Modulation of the Drag force for LO state

20.3.5.1 Assessment of Governing Parameters for Drag

To develop a new drag equation for wave against current around a cylinder, the selection of the most reliable parameters is important. Further, these parameters can be used to the advancement of a new empirical equation for drag that can be used to a better prediction of drag compared to the existing ones. Turbulent parameters were included in the model to look at drag with a new spectacle. In this regard, there are

two major problems that create difficulty to evaluate the functional relationships between drag and several turbulent parameters. The first one is the inherent variability in the turbulent data with respect to time and space. Second one is the overwhelming records of self-governing variable quantity, which stimulates the drag force. Fukagata et al. (2002) proposed an expression of the frictional drag using various dynamical effects for turbulent flows in pipe and smooth boundary. Moreover, the Reynolds stress is primarily important for the calculation of wall turbulence. Also, Reynolds stress can be an appropriate parameter to derived expression for the drag force (Fukagata et al. 2002). Further, Doroodchi et al. (2008) have emphasized on the importance of turbulent intensity in the model evaluation of Drag. Further, multi-collinearity arises when some of these parameters are extremely correlated with each other, where individual parameter may characterize more than one parameter class. Hence, it is not worthy to select more than one parameter from the identical class (Fukagata et al. 2002; Doroodchi et al. 2008). Regarding multiple linear regression (MLR) analyses, one should be careful about the variable selection.

Based on previous studies (Fukagata et al. 2002; Doroodchi et al. 2008), the most significant parameters are selected as Reynolds stress (three normal stresses and six shear stresses), turbulent intensity, and vertical normalized height to evaluate drag force in the present study. To develop an empirical model for drag force at the vicinity of the cylinder, the regression analysis is applied on each and every parameter individually. In the present, the drag force is expressed as:

$D_g = f\,(R_{uu},\ R_{uv},\ R_{uw},\ U^+ \text{ and } y/h).$

$$D_g = -9.5 + 2266(z/h) - 3085(z/h)^2 \tag{20.8a}$$

$$D_g = -147 - 10.48\tau_{uv} - 19.5\tau_{uw} + 518(z/h) - 3313(z/h)^2 \\ + 0.378\tau_{uw}\tau_{uv} + 116.1\tau_{uw}(z/h) \tag{20.8b}$$

$$D_g = -2420 - 479\tau_{uu} - 56.2\tau_{uv} + 924U^+ - 5052(z/h) + 48.8\tau_{uu}(z/h) \\ + 7.7\tau_{uv}U^+ \tag{20.8c}$$

Fig. 20.6 shows the plot of D_g as a function of normalized height (z/h) for WC1 ($f = 0$), WC2 ($f = 1$), and WC3 ($f = 2$) cases. It is observed that there is a substantial decrease in the value of drag, when an oscillatory flow (WC2 and WC3) is superimposed on mean current flow (WC1) than on the case of only mean flow. As Kim et al. (2006) reported, the skin-friction drag is diminished by travelling wave superimposed on a fully developed turbulent flow. However, an important inference that can be derived is that there is a significant increase in the value of drag near the bed region, which might be an important piece of information for engineers concerned about sediment transport or pier designers. The negative value of turbulent production extracts the energy from fluctuating component to mean velocity component, which subsequently increases the drag. Intermittent increase in the value of drag near bed region can lead to enhance the sediment transport rate due to wave acting against the current. Further, Graham et al. (1993)

Fig. 20.6 Vertical profile of drag force as a function of normalized height (*z/h*) for WC1, WC2, and WC3 cases
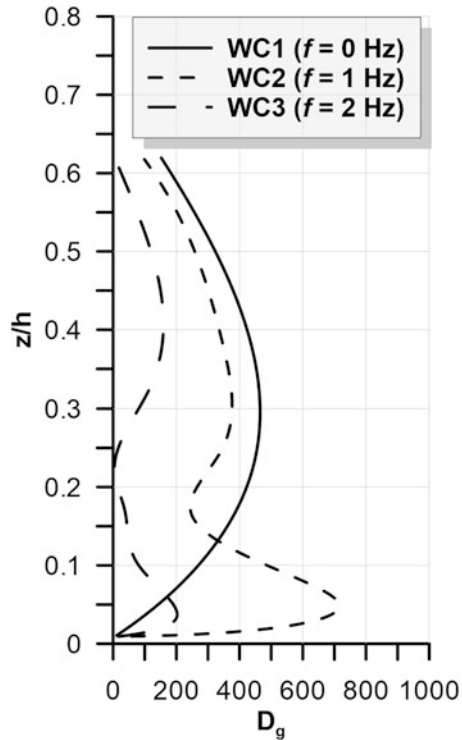
noted that the drag force in stream-wise direction on a body in unsteady flow with velocity U can be represented by Morrison's equation for a two-dimensional. The results of the present study show a good conformity with the results studied by Graham et al. (1993).

20.3.5.2 Stepwise Regression Analyses

The common idea concerned to apply the stepwise regression procedure is that the regression model should be made from a bunch of candidate predictors. In the present model, including and eliminating of these predictors are made by a stepwise manner, till there is any mathematical reason. The MLR technique is also used to inspect the connection between the dependent response and independent explanatory variables. To get best model, 20 probable regression models have been made for each case (WC1, WC2, and WC3) in this study.

While selecting the best possible regression model, four criteria were checked. The first criterion being the coefficient of determination (R_p^2). R_p^2 represents the percent of variation explicated by the regression model, which is the independent variable and intercept term $\leq n + 1$; here, n is the number of variables. The second criterion facilitating the entry or removal of predictors, which is the mean square
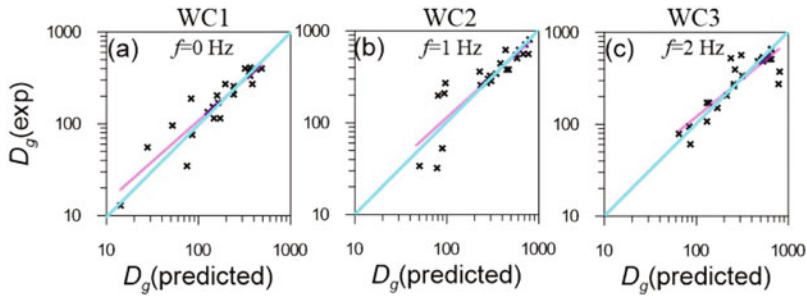
Fig. 20.7 (**a–c**) Validation plots for predicted and experimental drag forces for WC1, WC2, and WC3 cases; pink line is the linear fit; sky blue line is the diagonal line

error MSE(p). The model obtained with the least MSE(p) is selected herein. The third condition is the Mallow's Cp statistics. This statistic is applied in MLR analysis to choose the best subset of predictors. The fourth condition is the adjustments of R_p^2. The value of R_p^2 will always increase after adding a predictor, but the value of adjusted R_p^2 will increase or decrease corresponding to the explanatory power (Hair Jr. et al. 1995). In this study, the drag force variations as a function of vertical distance at the vicinity of a fixed cylinder (6 cm diameter) are carried out. The model, yielding the maximum values of adjusted R_p^2 = 98.2%, 98.5%, and 98.1% (Eq. 20.8a–c), is selected for cases WC1, WC2, and WC3, respectively. The comparative study between predicted and experimental drag forces is displayed in Fig. 20.7. Please note that values of the predicted and experimental drag forces are in good agreement for all the cases WC1, WC2, and WC3.

20.4   Conclusions

The exploration of the turbulent flow structure for wave against current was done by many researchers in the literature. However, the effect of superimposed wave against current flow over a partially submerged vertical cylinder on the drag field at downstream of the cylinder is still not revealed. To explore the vortex dynamics, turbulent characteristics, and drag force in the cylinder wake region, the distribution of vorticity, Reynolds shear stress, turbulence intensity, TKE dissipation, TKE production, and Drag field at different levels throughout the domain have been carried out in the present study. The important findings from this study are as follows:

- LO state was achieved when the frequency of the superimposed wave is two times that of f_{vs}.
- In the LO state, the superimposed wave frequency synchronized with the f_{vs}, which creates a resonance and modulates the flow separations around the cylinder, which suppresses the recirculation.

- The superimpose wave modulates the turbulence eddies around the cylinder. These eddies create a jacket around the cylinder, which can change the flow separation.
- In the present LO case, the large values of upward momentum flux make an envelope around the cylinder, which completely alter the flow field near the cylinder.
- The superimposed wave against the current modulates the well-known von Kármán vortex streets and generates a new kind of vortex, which propagated downstream from the cylinder.
- TKE dissipation rate is high at a closer distance from the cylinder for the LO case.
- Drag force at the near bed region is higher than mid depth to free stream region in the vicinity of the cylinder for LO case.

References

Banerjee T, Muste M, Katul G (2015) Flume experiments on wind induced flow in static water bodies in the presence of protruding vegetation. Adv Water Resour 76:11–28

Barman K, Debnath K, Mazumder BS (2016) Turbulence between two inline hemispherical obstacles under wave-current interactions. Adv Water Resour 88:32–52

Barman K, Debnath K, Mazumder BS (2018) Turbulence over a pair of submerged hemispheres in presence of surface waves and following current. J Offshore Mech Arctic Eng 140: 031104-1-10

Batchelor GK (2000) An introduction to fluid dynamics. First Cambridge Mathematical Library Edition

Chaudhuri S, Pandey M, Debnath K, Oliveto G (2022) A comparative study on equilibrium scour volume around circular cylinders in clay–sand mixed cohesive beds, at near threshold velocity of sand–an experimental approach. Water Supply 22(8):6777–6791. https://doi.org/10.2166/ws.2022.250

Doroodchi E, Evans GM, Schwarz MP, Lane GL, Shah N, Nguyen A (2008) Influence of turbulence intensity on particle drag coefficients. Chem Eng J 135:129–134

Dutta D, Bihs H, Afzal MS (2022) Computational Fluid Dynamics modelling of hydrodynamic characteristics of oscillatory flow past a square cylinder using the level set method. Ocean Eng 253:111211. https://doi.org/10.1016/j.oceaneng.2022.111211

Feng LH, Wang JJ (2010) Circular cylinder vortex-synchronization control with a synthetic jet positioned at the rear stagnation point. J Fluid Mech 662:232–259

Fredsøe J, Andersen KH, Sumer BM (1999) Wave plus current over a ripple-covered bed. Coast Eng 38:177–221

Fukagata K, Iwamoto K, Kasagi N (2002) Contribution of Reynolds stress distribution to the skin friction in wall-bounded flows. Phys Fluids 14:73–76

Graham JMR, Arkell RH, Zhou CY (1993) "The effect of combinations of mean current and oscillatory flow on the forces induced on a bluff body". *J. Wind Eng*. Ind Aerodyn 50:85–95

Grant WD, Madsen OS (1979) Combined wave and current interaction with rough bottom. J Geophys Res 84(C4):1797–1808

Griffin OM, Hall MS (1991) Review - vortex shedding lock-on and flow control in bluff body wakes. J Fluids Eng 113:526–537

Gunnoo H, Abcha N, Ezersky A (2016) Frequency lock-in and phase synchronization of vortex shedding behind circular cylinder due to surface waves. Phys Lett A 380(7):863–868

Gupta LK, Pandey M, Raj PA, Shukla AK (2023) Fine sediment intrusion and its consequences for river ecosystems: a review. J Hazard Toxic Radioact Waste 27(1):04022036. https://doi.org/10.1061/(ASCE)HZ.2153-5515.0000729

Hair JF Jr, Anderson RE, Tatham RL, Black WC (1995) Multivariate data analysis, 3rd edn. Macmillan Publishing Company, New York

Kemp PH, Simons RR (1982) The interaction of waves and a turbulent current: waves propagating with the current. J Fluid Mech 116:227–250

Kemp PH, Simons RR (1983) The interaction of waves and a turbulent current: waves propagating against the current. J Fluid Mech 130:73–89

Khan MA, Sharma N, Pu JH, Pandey M, Azamathulla H (2022) Experimental observation of turbulent structure at region surrounding the mid-channel braid bar. Marine Georesour Geotechnol 40(4):448–461. https://doi.org/10.1080/1064119X.2021.1906366

Kim W, Yoo JY, Sung J (2006) Dynamics of vortex LO in a perturbed cylinder wake. Phys Fluids. 18(7):074103

Kim SH, Park JY, Park N, Bae JH, Yoo JY (2009) Direct numerical simulation of vortex synchronization due to small perturbations. J Fluid Mech 634:61–90

Liberzon A, Lüthi B, Guala M, Kinzelbach W, Tsinober A (2005) Experimental study of the structure of flow regions with negative turbulent kinetic energy production in confined three-dimensional shear flows with and without buoyancy. Phys Fluids 17(9):095110

Lin C, Chiu PH, Shieh SJ (2002) Characteristics of horseshoe vortex system near a vertical plate–base plate juncture. Exp Thermal Fluid Sci 27(1):25–46

Lin C, Lai WJ, Chang KA (2003) Simultaneous particle image velocimetry and laser Doppler velocimetry measurements of periodical oscillatory horseshoe vortex system near square cylinder-base plate juncture. J Eng Mech 129(10):1173–1188

Lin C, Hsieh SC, Lin WJ, Raikar RV (2012) Characteristics of recirculation zone structure behind an impulsively started circular cylinder. J Eng Mech 138(2):184–198

Pope SB (2001) Turbulent Flows. IOP Publishing, Bristol

Pradhan A, Arif MR, Afzal MS, Gazi AH (2022) On the origin of forces in the wake of an elliptical cylinder at low Reynolds number. Environ Fluid Mech 22:1–25

Rey V, Charland J, Touboul J (2014) Wave–current interaction in the presence of a three-dimensional bathymetry: deep water wave focusing in opposing current conditions. Phys Fluids 26:096601

Roy S, Debnath K, Mazumder BS (2018) Distribution of turbulent eddies behind a monopile for vortex lock-on condition due to wave current combined flow. Coast Eng 131:70–87

Saikumar G, Pandey M, Dikshit PKS (2022) Natural river hazards: their impacts and mitigation techniques. In: River dynamics and flood hazards: studies on risk and mitigation. Springer, Singapore, pp 3–16

Sheridan J, Lin JC, Rockwell D (1997) Flow past a cylinder close to a free surface. J Fluid Mech 330:1–30

Umeyama M (2005) Reynolds stresses and velocity distributions in a wave-current coexisting environment. J Waterw Port Coast Ocean Eng 131(5):203–212

Umeyama M (2009) Changes in turbulent flow structure under combined wave-current motions. J Waterway Port Coast Ocean Eng 135(5):213–227

Vandiver JK, Jaiswal V, Jhingran V (2009) Insights on vortex-induced, traveling waves on long risers. J Fluids Struct 25(4):641–653

Zhang J, Zheng J, Jeng DS, Guo Y (2015) Numerical simulation of solitary wave propagation over a steady current. J Waterw Port Coast Ocean Eng. 141(3):04014041. ASCE

Chapter 21
Assessment of Sedimentation in Kaliasote Reservoir, Bhopal, Using Satellite Remote Sensing Techniques

K. Mishra and H. L. Tiwari

Abstract Sedimentation is the most unpreferable phenomenon for reservoirs. It originates due to soil erosion through heavy precipitation and winds. Eroded soil particles move and are eventually deposited in reservoirs via streams or channels. It affects the life of the reservoir as well as the capacity utilized to hold water in it. For the beneficial utilization of reservoirs, it is must to know about the amount of deposited sediments. The conventional techniques of capacity estimation like hydrographic surveys, stream-flow analysis, and bathymetric methods were time-consuming and laborious and also demand a lot of manpower. In this study, a remote sensing method is applied in addition to the GIS to assess the sedimentation in storage of Kaliasote reservoir located in Bhopal, capital of Madhya Pradesh state in India. Normalized difference water index (NDWI) has been applied on satellite images to clearly represent the water pixels. From the obtained results, it was clear that 4.106 Mm^3 or 11.93% of storage volume had been lost from the usable storage volume of the Kaliasote reservoir. The rate of sedimentation in the reservoir was also correlated with Varshney's and Joglekar's empirical relations.

Keywords Sedimentation · Reservoir capacity · Remote sensing · NDWI · Satellite images

21.1 Introduction

Deposition of sediments in the reservoir is not an easy process, and it is deposited in reservoirs because of a lowering in the velocity of water as a result of rapid enlargement in the cross-sectional area of rivers (Pandey et al. 2016). Transportation of sediment particles was dependent on the topographical feature of land and morphological parameter of streams (Khan et al. 2019, Gupta et al. 2023; Singh et al. 2023). The increment in the volume of deposited sediments is directly

K. Mishra (✉) · H. L. Tiwari
Department of Civil Engineering, Maulana Azad National Institute of Technology, Bhopal, India

proportional to the decrement in the irrigation capacity of reservoirs (Shatnawi 2012). This sedimentation issue, which is gradually reducing the reservoir's utility, requires attention not only during the project planning stage but also during the operating stage (Shatnawi and Diabat 2016; Jain et al. 2022). The entering sediment was collected in various zones of the reservoir depending on the form of the reservoir, the manner of reservoir utilization, silt inflow rates, and particle size distribution (Jain et al. 2010). Initially, the coarser portion of sediments settled in the upper zone of the reservoir due to a reduction in flow velocity. After that, finer portions of sediments get deposited in various elevations of the reservoir (Jain et al. 2002; Khadatare and Jedhe 2017). Sedimentation was expected to cause a loss of about 1% of the world's existing storage volume each year (Merina et al. 2016; Wagh and Manekar 2021; Saikumar et al. 2022). The quantity of sediment with its pattern of deposition at different levels of the reservoir is critical for determining the reservoir's equilibrium life (Narasayya 2013). The worldwide rate of sediments production is nearly 2×10^{10} tons per year (Goel et al. 2002).

The assessment of sediment volume by hydrographic surveys and streamflow analysis are the two most popular traditional ways. These traditional approaches are tedious, laborious, and time-consuming (Durbude and Purandara 2005; Mani and Chakravorty 2007; Jeyakanthan and Sanjeevi 2011; Singh et al. 2021). By the use of broad and multifunctional technologies of remote sensing, determining the reservoir sedimentation has shown to be both cost-effective and convenient (Avinash and Chandramouli 2018). It has also a limitation that this approach is best suitable for live storage zone (Mandwar et al. 2014). The remote sensing approach is said to be better than traditional data collecting methods because they provide data over a longer interval of time with a wider spectral range (Dadoria et al. 2017). Going through the literature review, it was found that no study had been conducted to date for estimation of sedimentation in Kaliasote reservoir located in Bhopal.

21.2   Materials and Methods

21.2.1   Study Area and Data Source

21.2.1.1   Kaliasote Reservoir

The Kaliasote reservoir is situated at Bhopal, which is the capital of Madhya Pradesh state, India (as shown in Fig. 21.1). The latitude and longitude of this dam location were 23°11′51″N and 77°24′30″E, respectively. The reservoir was constructed near Pt. Khusilal Sharma Govt. Ayurveda College in Bhopal district, on the river Kaliasote of the Betwa basin. The drainage area of the reservoir is 381.38 km^2. The designed gross storage capacity of the reservoir at full reservoir level (FRL) 505.67 m is 35.387 Mm^3, and the live storage capacity between FRL and lowest sill level (LSL) 486.16 m is 34.41 Mm^3. The initial dead storage capacity is 0.977 Mm^3. The reservoir was first impounded in the year 1988. This is a major multipurpose
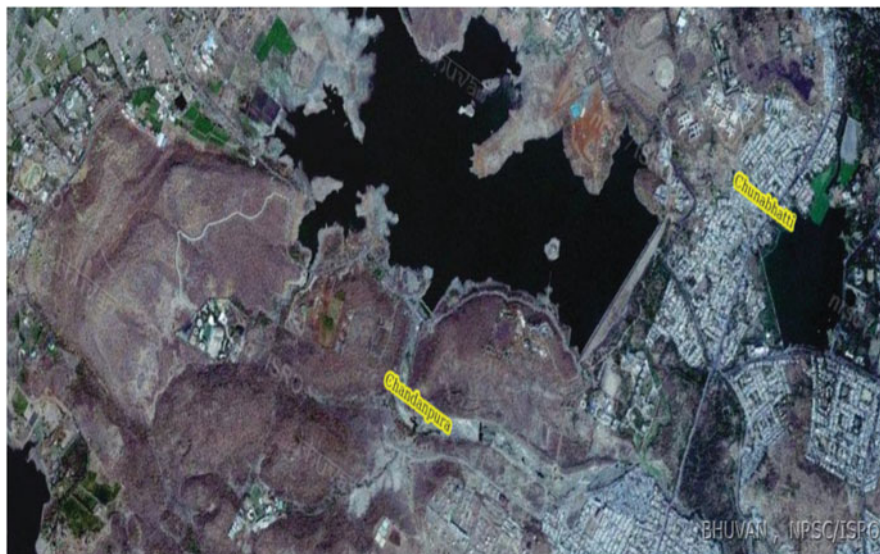
Fig. 21.1   Image of Kaliasote reservoir. **Source:** BHUVAN (https://bhuvan.nrsc.gov.in)

Table 21.1 Original elevation-capacity table (1988) of the Kaliasote reservoir

Elevation (m)	Cumulative capacity (Mm^3)
486.16	0.977
489.00	1.966
493.45	4.688
495.40	6.728
497.50	9.900
499.65	14.258
505.67	35.387

project that has been proposed for irrigation, flood control, and water supply to the Bhopal district.

This project is also linked with Upper lake, Bhopal. The dam of Kaliasote reservoir is Eathen (homogeneous) type dam. The length of the dam is 1080 m with a top width of 6.10 m. This dam is designed for the gross commanded area of 4817×10^4 m^2 including a net culturable command area of 4588×10^4 m^2.

21.2.1.2   Data Collection

Sedimentation analysis is based on two types of primary data, namely, the remotely sensed data and field data. Primarily, the remote sensing data had been downloaded from the USGS website (https://earthexplorer.usgs.gov). The original area capacity table and salient features of the Kaliasote reservoir had been collected from the divisional office of the Water Resources Department, Bhopal, as given in Table 21.1.

The water level of reservoirs based on a daily basis had been downloaded from the MPWRD website (http://www.mpwrd.gov.in).

21.2.2 Selection of Input Parameters

In this study, 6 LANDSAT 8 OLI (Operational Land Imager) of different dates were utilized with correspondence of water levels varying from MDDL to FRL as shown in Table 21.1. The major advantages of satellite imageries were freely available for the public domain along with a spatial resolution of 30 m and temporal resolution of 16 days and also cloud independent. The field data consists of the original area capacity table (given in Table 21.1), daily water level fluctuations with maximum and minimum water levels, and salient features of the respective reservoir.

According to the availability of satellite scenes, six date images were finalized, namely, 06-12-2017, 27-12-2017, 08-03-18, 28-11-2018, 08-06-19, and 14-10-19, and elevations on corresponding days were received from the MPWRD website given in Table 21.2.

21.2.3 Satellite Remote Sensing Technique

The reservoir spread region in correspondence of the satellite pass date at known elevation was the general output produced from the remote sensing investigation. The periphery of the water region was demarcated using visual and digital tools used for remote sensing data interpretation. The interpretation of visual approaches is entirely dependent on the expertise and competence of the interpreter. It was tedious to clearly distinguish between wetland and water regions about the circumference of the water spread region. Water pixels might easily be misinterpreted as land and vice versa, but various bands of related satellite pictures had been thoroughly evaluated using digital techniques. A GIS software, ArcMap, was used for digital processing in this project. The methodology taken in this study is shown in Fig. 21.2.

Table 21.2 Satellite passing date and other information

Satellite	Path	Row	Date of passing	Water levels
LANDSAT 8 OLI	145	44	December 6, 2017	**499.65**
LANDSAT 8 OLI	146	44	December 27, 2017	497.50
LANDSAT 8 OLI	146	44	March 8, 2018	493.45
LANDSAT 8 OLI	145	44	November 28, 2018	495.40
LANDSAT 8 OLI	145	44	June 8, 2019	489.00 (min. water level)
LANDSAT 8 OLI	145	44	October 14, 2019	**505.67** (max. water level)
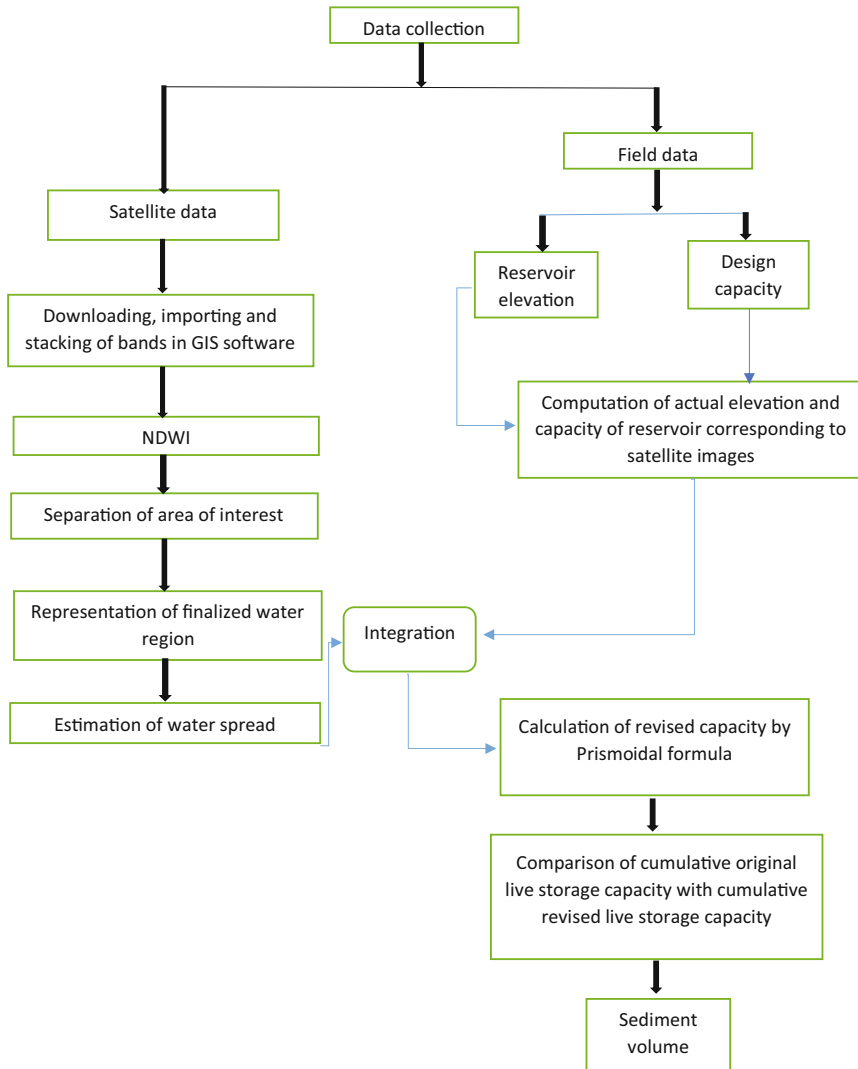
Fig. 21.2 Flow chart of adopted methodology

21.2.3.1 Downloading, Importing, and Stacking of Satellite Bands

The remote sensing data were collected from the USGS website (in .gz format). After that, all the bands of satellite images were imported into ArcMap software, and then BAND 3 and BAND 5 were stacked together. The BAND 3 and BAND 5 were known as the Green and NIR bands, respectively. This process was completed one by one for each satellite image of respective dates shown in Table 21.2.

21.2.3.2   Extraction of Water Pixels

The water transmittance is quite well in the visible band (400–700 nm), although its absorption and reflectance are very moderate. Water absorption rises rapidly in the NIR region, where both reflectivity and transmissivity are low. At NIR wavelengths, the water looked like a black mass. The number of water pixels must be determined in order to extract surface water bodies. Though water has a unique spectral signature from other land uses such as vegetation, built-up areas, and soil surface, identifying water pixels at the water/soil interface is difficult and dependent on the analyst's interpretative abilities.

Mcfeeters (1996) generated an algorithm termed as Normalized Difference Water Index (NDWI) after studying the spectral characteristics (reflectance) of water pixels. The NDWI is a method for clearly identifying water pixels by comparing the digital number (DN) value of a pixel to data from various bands. The NDWI Index is defined as follows:

$$NDWI = (Green - NIR)/(Green + NIR) \tag{21.1}$$

In our case, this formula may be written as:

$$NDWI = (BAND3 - BAND5)/(BAND3 + BAND5) \tag{21.2}$$

For NDWI > 0, pixels were treated as water, and for NDWI < 0, pixels were treated as non-water. The NDWI picture was created for each satellite image with water pixels having positive values and other than water pixels having negative values.

The deep-water bodies had a very clear and distinct representation when compared to shallow water bodies. So, water at shallow depths should be carefully investigated to ensure that pixels were not misguided, particularly at the interface of soil and water. As a result, several bands were evaluated on the basis of digital numbers in order to clearly distinguish pixels along the water-soil boundary. The use of two or more bands in a single association resulted in a clear representation of the water surface based on reflectance and absorption behavior. On each geographical grid, these raster pictures were represented by digital number values, so combining numerous bands for higher digital number values aided in the delineation of water bodies.

21.2.3.3   Separation of the Desired Area

The full scene of the satellite was very large, it contains more than two water bodies and vegetation area. This study was concerned with only the Kaliasote reservoir. Hence, it was necessary to remove other water bodies. After applying the NDWI approach to each satellite scene, images were converted into water and non-water

regions by utilizing the "RECLASSIFY" technique from the spatial analyst tool, and then "EXTRACT BY MASK" function was applied to separate the desired area of the reservoir through spatial analyst tool on ArcGIS. The finalized reservoir spread regions of minimum observed level and maximum observed level are represented in Fig. 21.3 for the considered satellite images. For masking purposes, the shapefile from Google earth pro was created. At the last, the number of water pixels was recorded for all satellite images as per Table 21.3.

21.2.3.4   Calculation of Revised Water Region Area

When the number of water pixels for all satellite images was obtained, the water region area was calculated using the given formula:

$$\text{Area of water region} = \frac{\text{Number of water pixels} \times \text{Pixel area}}{10^6}$$

Here, pixel area is defined as the resolution of the utilized LANSAT 8 OLI sensor, which is equal to 30 m × 30 m, and the calculated area is termed as the revised water region area.

21.2.3.5   Estimation of the Revised Reservoir Capacity

The reservoir capacity between two consecutive levels was estimated by the trapezoidal formula (Katiyar et al. 2006; Mukherjee et al. 2007; Foteh et al. 2018) as given below:

$$V = H \times \left[A_1 + A_2 + \sqrt{(A_1 \times A_2)}\right]/3 \qquad (21.3)$$

Here, H is the height of elevation between two consecutive water levels E_1 and E_2, A_1 and A_2 are the areas of water region at levels E_1 and E_2, and V is defined as the estimated volume of the reservoir. The calculation for the revised storage capacity of the Kaliasote dam for each successive corresponding water level is given in Table 21.4.

The original elevation-capacity table at the time of designing the dam was received from the Divisional office of Kaliasote dam, Bhopal, the government of Madhya Pradesh. The designed capacity at the intermediate water levels was estimated from the original elevation-capacity table by the application of linear interpolation. The comparison between revised capacity and original capacity at the corresponding water level had been done, and the difference between these two capacities resulted in a loss in storage due to sedimentation as shown in Table 21.5. At the lowest sill level (486.16 m), cumulative revised capacity was taken as zero.

Fig. 21.3 Finalized water spread region of minimum and maximum observed levels for Kaliasote reservoir
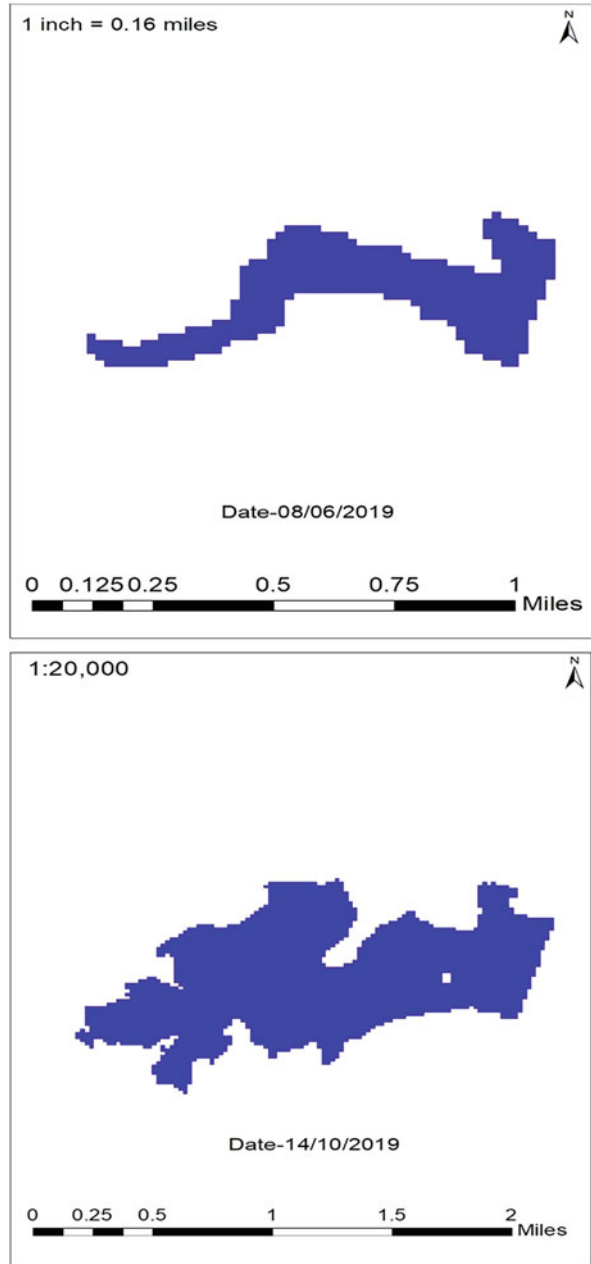
Above this level, the consecutive volumes were summed together up to the full reservoir level to obtain the final cumulative revised reservoir capacity.

Table 21.3 Number of water pixels in satellite images corresponding to elevations

Passing date of satellite	Elevation (m)	No. of water pixels
June 8, 2019	489.00	457
March 8, 2018	493.45	1444
November 28, 2018	495.40	1571
December 27, 2017	497.50	2249
December 6, 2017	499.65	2344
October 14, 2019	505.67	3405

Table 21.4 Calculation of revised reservoir capacity and comparison with original capacity of reservoir

Water levels (m)	Revised area (Mm^2)	Revised live storage capacity (Mm^3)	Cumulative revised live storage capacity (Mm^3)
486.16	0.052	–	0
489.00	0.411	0.576	0.576
493.45	1.299	3.603	4.179
495.40	1.413	2.631	6.811
497.50	2.024	3.582	10.390
499.65	2.109	4.438	14.830
505.67	3.064	15.47	30.304

Table 21.5 Estimation of loss in storage volume of Kaliasote reservoir due to sedimentation

Water level (m) I FRL	Gross storage volume in 1988 (Mm^3) II	Live storage volume in 1988 (Mm^3) III	Live storage volume as per this remote sensing survey upto 2019 (Mm^3) IV	Loss in live storage volume (Mm^3) V = III–IV
505.67	35.387	34.410	30.304	4.106

21.3 Results and Discussions

The whole study revealed that the Kaliasote reservoir's revised capacity (2019) in the zone of live storage zone, levels varying from 486.16 to 505.67 m was 30.304 Mm^3, whereas the initial capacity (1988) was 34.410 Mm^3. The gap between the initial capacity and the revised capacity, 4.106 Mm^3, was caused by sediment deposition during the past 31 years as calculated in Table 21.5. In the last 31 years, the reservoir had lost over 11.93% of its useful storage volume. As a result, the rate of sedimentation in Kaliasote reservoir was determined to be 0.132 Mm^3 per year, or 0.385% per year, which lies below the range of 0.5 to 1.5% per year reported by a survey done in several Indian reservoirs in 2004.

The change in the revised capacity curve with respect to the original capacity curve represents the loss in storage volume due to sedimentation at various elevations in the live storage of the reservoir. If the sediment deposition is further

increasing, it will have an adverse impact on a reservoir's usable life. Vegetative treatment and structural intervention can help to reduce the sediment entering in reservoir. People in nearby communities should be educated on proper land management methods in order to safeguard the watershed and minimize erosion caused by intensive irrigated cultivation.

It can also be found that the Kaliasote reservoir lost 0.132 Mm^3 of storage each year, with an average rate of 0.035 $Mm^3/100\ km^2$/year. The siltation rate calculated from the remote sensing method had been correlated with Varshney's and Joglekar's empirical relations. The Varshney's and Joglekar's formulas can be given as follows:

Varshney's equation:

$$Y = 0.392/A^{0.202} \tag{21.4}$$

Khosla's equation:

$$Y = 0.323/A^{0.28} \tag{21.5}$$

where Y is the yearly silting rate from a watershed of 100 km^2 and A is the catchment area in km^2. Because the catchment area of the Kaliasote reservoir in Bhopal is 381.38 km^2, the rates of sedimentation calculated using Varshney's formula and Khosla's equation are 0.118 $Mm^3/100\ km^2$/year and 0.06 $Mm^3/100\ km^2$/year. It was clear that both Khosla's formula and Varshney's equation indicate a higher rate of siltation than what was seen in Bhopal's Kaliasote reservoir.

According to the results of this survey, if sedimentation is going on at this rate, it will definitely deplete the whole storage capacity of the reservoir in the next 230 years. Hence, it is necessary to take proper measures for preventing the entry of sediments into the reservoir, and also removal of deposited sediments must be done.

21.4   Conclusions

The use of remote sensing to estimate revised elevation-area-capacity curves for a reservoir saves time and money. Though it has certain drawbacks, it is a highly practical method for analyzing sedimentation in a reservoir's active storage zone. The technique is fully automated, beginning with the identification of water pixels and ending with the estimation of the water spread area. Traditional procedures, such as hydrographic surveys, and streamflow analysis, are time-consuming, tedious, and costly since they require considerable data collection in order to estimate reservoir capacities and surface area for matching reservoir stages. As a result, hydrographic surveys are being conducted over a longer period of time, ranging from 5 to 15 years,

despite the fact that the recommended time interval for reservoir sedimentation evaluation is every 5 years, which can easily be done by remote sensing approach.

The following conclusions are derived from the foregoing study:

1. The sedimentation in the reservoir's live storage is estimated to be 4.106 Mm^3, during a 31-year period (1988–2019).
2. In the Kaliasote reservoir, the rate of sedimentation will be 0.132 Mm^3 per year, or 0.385% per year, which lies below from the range of 0.5–1.5% per year, with an average rate of 0.035 Mm^3 /100 km^2/year.
3. Varshney's formula and Khosla's equations yield the rate of siltation as 0.118 and 0.06 Mm^3/100 km^2/year, respectively.

References

Avinash G, Chandramouli PN (2018) Assessment of reservoir sedimentation using RS and GIS techniques-A case study of Kabini Reservoir, Karnataka, India. Int Res J Eng Technol 5(08):630–635

Dadoria D, Tiwari HL, Jaiswal RK (2017) Assessment of reservoir sedimentation in Chhattisgarh State using remote sensing and GIS. Int J Civil Eng Technol 8(4):526–534

Durbude DG, Purandara BK (2005) Assessment of sedimentation in the Linganmakki Reservoir using remote sensing. J Indian Soc Remote Sens 33(4):503–509

Foteh R, Garg V, Nikam BR, Khadatare MY, Aggarwal SP, Kumar AS (2018) Reservoir sedimentation assessment through remote sensing and hydrological modelling. J Indian Soc Remote Sens 46(11):1893–1905

Goel MK, Jain SK, Agarwal PK (2002) Assessment of sediment deposition rate in Bargi Reservoir using digital image processing. Hydrol Sci J 47(S1):S81–S92

Gupta LK, Pandey M, Raj PA, Shukla AK (2023) Fine sediment intrusion and its consequences for river ecosystems: a review. J Hazard Toxic Radioact Waste. 27(1):04022036. https://doi.org/10.1061/(ASCE)HZ.2153-5515.0000729

Jain SK, Singh P, Seth SM (2002) Assessment of sedimentation in Bhakra Reservoir in the western Himalayan region using remotely sensed data. Hydrol Sci J 47(2):203–212

Jain MK, Mishra SK, Shah RB (2010) Estimation of sediment yield and areas vulnerable to soil erosion and deposition in a Himalayan watershed using GIS. Curr Sci 98(2):213–221

Jain R, Timani K, Pandey M (2022) Influence of cohesion on California bearing ratio of clay-gravel mixtures. Int J Sediment Res. https://doi.org/10.1016/j.ijsrc.2022.12.005

Jeyakanthan VS, Sanjeevi S (2011) Assessment of reservoir sedimentation using Indian satellite image data. IUP J Soil Water Sci 4(1):7–15

Katiyar R, Garg PK, Jain SK (2006) Watershed prioritization and reservoir sedimentation using remote sensing data. Geocarto Int 21(3):55–60

Khadatare MY, Jedhe SH (2017) Sediment assessment of UJJANI Reservoir in Maharashtra by using remote sensing technique. Int Res J Eng Technol 4(8):1255–1258

Khan M, Sharma A, Goyal MK (2019) Assessment of future water provisioning and sediment load under climate and LULC change scenarios in a peninsular river basin, India. Hydrol Sci J 64:405–419. https://doi.org/10.1080/02626667.2019.1584401

Mandwar ES, Hajare HV, Gajbhiye AR (2014) Critical analysis of sedimentation assessment of reservoirs of nagpur region done by satellite remote sensing. Int J Civil Eng Technol 5(10): 74–81

Mani P, Chakravorty B (2007) Remote sensing based sedimentation study of Maithon reservoir. J Indian Soc Remote Sens 35(1):117–120

McFeeters SK (1996) The use of the Normalized Difference Water Index (NDWI) in the delineation of open water features. Int J Remote Sens 17(7):1425–1432

Merina NR, Sashikkumar MC, Rizvana N, Adlin R (2016) Sedimentation study in a reservoir using remote sensing technique. Appl Ecol Environ Res 14(4):296–304

Mukherjee S, Veer V, Tyagi SK, Sharma V (2007) Sedimentation Study of hirakud reservoir through remote sensing techniques. J Spat Hydrol 7(1):122–130

Narasayya K (2013) Assessment of reservoir sedimentation using remote sensing satellite imageries. Asian J Geoinform 12(4):1–8

Pandey A, Chaube UC, Mishra SK, Kumar D (2016) Assessment of reservoir sedimentation using remote sensing and recommendations for desilting Patratu Reservoir, India. Hydrol Sci J 61(4): 711–718

Saikumar G, Pandey M, Dikshit PKS (2022) Natural river hazards: their impacts and mitigation techniques. In: River dynamics and flood hazards: studies on risk and mitigation. Springer, Singapore, pp 3–16

Shatnawi A (2012) Siltation of Alghadeer Alabyadh reservoir. Jordan J Civil Eng 6(1):28–38

Shatnawi A, Diabat A (2016) Siltation of Wadi Al-Arab reservoir using GIS techniques. Jordan J Civil Eng 10(4):431–441

Singh S, Yadav AK, Mishra AP (2021) Reservoir Sedimentation Assessment of Rihand Reservoir Using Remote Sensing Technique. Groundw Resour Dev Plan Semi-Arid Reg, Springer, Cham, pp 453–465

Singh S, Prasad B, Tiwari HL (2023) Sedimentation analysis for a reservoir using remote sensing and GIS techniques. ISH J Hydraul Eng 29(1):71–79

Wagh S, Manekar V (2021) Assessment of reservoir sedimentation using satellite remote sensing technique (SRS). J Inst Eng (India) Ser A 102(3):851–860

Chapter 22
Development of River Atlas Using Space and Ground-Based Inputs for Brahmaputra and Barak Valleys in Assam, India

B. M. Arjun, Diganta Barman, Gokul Anand, Nilay Nishant, Anupal Baruah, Biren Baishya, and S. P. Aggarwal

Abstract The Brahmaputra and Barak basins regularly face the problems of flooding and riverbank erosion. Better management of water resources in this region needs detailed data and information about the river systems. However, the existing river database is of coarser resolution and lacks information only except few major rivers of Assam. Also, some of the small non-perennial flashy rivers that cause intense flooding during the peak monsoon are not traced in the present database. Therefore, this study has been carried out with the aim to develop a river atlas for all 33 districts of Assam comprising of river database at a finer scale. As a part of this study, different maps are prepared such as district-wise river maps, land use/land cover maps, and catchment maps. District river map contains all the major and minor rivers at a scale of 1:5000. These maps also have the details of river banks, names of rivers, sand deposits, embankments, sluice gates, locations of hydro-meteorological observatories, major locations, roads, railway networks and stations, bridges, and administrative boundaries. Further, these maps also have the details of the length of rivers, length of embankments, and river flood level charts showing warning levels and danger levels. The land use land cover (LULC) maps are prepared with a defined buffer on either side of major and minor rivers. Catchments maps are prepared to show the origin of all the rivers entering the respective district of Assam. These maps have information on the area of catchments in different states and countries, the source of origin of rivers, and the names of rivers. A user-friendly web portal is developed incorporating all the layers generated under this study. The geoportal is made available in the public domain (https://riveratlas.nesdr.gov.in/) for carrying out various analysis related to river system features. The outcomes of the study will be

B. M. Arjun · D. Barman (✉) · G. Anand · N. Nishant · A. Baruah · S. P. Aggarwal
North Eastern Space Applications Centre, Umiam, Meghalaya, India
e-mail: diganta.barman@nesac.gov.in

B. Baishya
Assam State Disaster Management Authority, Guwahati, Assam, India

beneficial for the concerned authority of the state for proper monitoring and management of the water resources system in the state of Assam, India.

Keywords River Atlas · Mapping · Catchment · LULC · Hydrology

22.1 Introduction

The northeastern part of the Indian subcontinent is endowed with huge water resources and alone generates one-third of the country's total runoff through the Brahmaputra and Barak river systems (Sharma 2015). The Brahmaputra, with a catchment area of 5,80,000 km^2, is one of the largest river systems in the world that spreads over China (2,93,000 km^2), India (1,95,000 km^2), Bhutan (45,000 km^2), and Bangladesh (47,000 km^2) (Barman and Bhattacharjya 2015; Kumar and Chatterjee 2005; Feng et al. 2019). Originating from the great glacier mass of Chema-Yung-Dung, south-east of the Mansarovar lake in the Kailash range of southern Tibet at an elevation of 5300 m, the river Brahmaputra travels for a total distance of 2880 km out of which 1625 km in China, 918 km in India and 337 km in Bangladesh before emptying into the Bay of Bengal through a joint channel with the Ganga (Sarma 2004). Flowing eastward over the Tibetan plateau, the Brahmaputra, or the Yarlung Tsangpo, enters a deep narrow gorge at Pe and twists around the Namcha Barwa Peak forming a sharp hairpin bend and dropping more than 2000 m in altitude giving up huge energy potential on its way (Bailey 1914). From the gorge, it descends to the north-eastern corner of India and joins two rivers, the Dibang and the Lohit near Pashighat, and the combined flow then flows westward through Assam until near Dhubri, where it abruptly turns south and enters Bangladesh (Sarma 2005). The gradient of the Brahmaputra river is as steep as 4.3–16.8 m/km in the gorge section upstream of Passighat, but near Guwahati, it is as flat as 0.1 m/km (Goswami 1985). The highest recorded daily discharge in the Brahmaputra at Pandu was 72,726 m^3/s in August 1962, while the lowest was 1757 m^3/s in February 1968 (Pradhan et al. 2021). However, the mean annual flood discharge of this river is of magnitude 47,608 m^3/s at Pandu, Assam (Bhattachaiyya and Bora 1997). Another major river that covers a large part of southern Assam is the Barak river. The river originates in the Manipur hills, south of Mao bordering Nagaland and Manipur (Annayat and Sil 2020). After traversing the Barak valley in a westerly direction up to Karimganj, it bifurcates into two branches known as the Surma and the Kushiyara, which reunite near Bhairab Bazar in Bangladesh. The joint stream is called the Meghna, which later meets the Brahmaputra, locally known as the Padma, and eventually flows into the Bay of Bengal (Mirza et al. 2001). From its origin to its outfall with the Meghna river in Bangladesh, the Barak river traverses a total length of 902 km, of which the Indian reach is 564 km long (Jain et al. 2007). The Barak river systems cover a catchment area of 41,157 km^2, and 62% of this total area lies within India (Deka et al. 2013).

Comprising of fluvial plains, the Brahmaputra and the Barak basins regularly face the problems of flooding and riverbank erosion (Kumar 2021). Effective flood

hazard management requires a thorough understanding of the hazards, their potential impact on society, and the available strategies for managing them (Saikumar et al. 2023, Jain et al. 2018). This includes not only responding to floods when they occur but also mitigating their impact through proper land use land cover planning, flood early warning, and mapping of all river system features and other measures (Ranjan 2017). Better management of the water resources of this region needs detailed data and information about the river systems and also continuous monitoring of the river bank lines. However, the existing river database is of coarser resolution and lacks the bank information only except few major rivers. Currently, the river system database, which is available in the public domain, is at a scale coarser than 1:10.000 from India Water Resources Information System (India-WRIS) (Nagaveni et al. 2019). Further, these database does not have information related to the local names of the rivers, embankments, sluice gates, sand deposits, etc. Also, some of the small non-perennial flashy rivers that cause intense flooding during the peak monsoon are not traced in the present database. The river details can also be extracted from global platforms such as Google Earth, Bing Maps, Open Street maps, etc., but they do not provide the details of the catchment of the river, local names of the river, and flood protection structures and have minimal functionalities for river analysis. Therefore, a detailed River Atlas comprising of river database at a finer scale of 1:5000, their bank information including land use land cover, catchment information, and structural measures taken for flood and erosion management is of utmost need for decision-making, which is attempted in this study. Further, a robust and user friendly geoportal is developed incorporating all the river related features for carrying out various analyses for effective management and planning of water resource systems.

This study mainly involves mapping all major and minor rivers of the Brahmaputra and Barak basin in Assam at a very high-resolution scale. The mapping of other river system features outside Assam and those falling under the Brahmaputra and Barak basin has been carried out at a coarser scale. Hence, extensive information on river system features has been generated as a part of this study. Since this study emphasizes mainly the rivers and other features, the authors found it suitable to include this study under the theme "River, Sediment and Hydrological Extremes: Causes, Impacts and Management."

22.2 Study Area

The study is focused on developing a high resolution river database for Brahmaputra and Barak valleys in Assam, India. The state of Assam is located in the tropical latitudes (24°08′N. 27°59′N) and eastern longitudes (89°42′E, 96°01′E). The state is surrounded by hills and mountains on three sides and shares administrative boundaries with six northeastern states and two countries. The state of Assam consists of 33 districts out of which 30 districts fall under the Brahmaputra basin, and three districts fall under the Barak basin. The state is rich in water resources, and around 10.5% of the total geographical area of the state is occupied by surface water bodies,
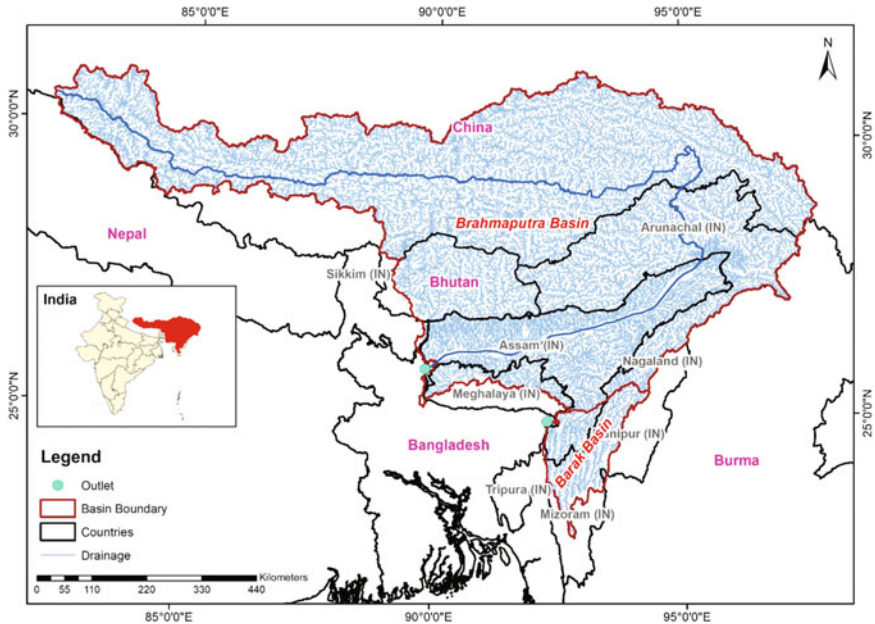
Fig. 22.1 Study area showing the Brahmaputra and Barak basin

which include Brahmaputra and Barak rivers, natural wetlands and marshy areas (Chakraborty et al. 2014). The tributaries of the river Brahmaputra have originated mainly in Bhutan, Arunachal, Nagaland, Meghalaya, and a few within Assam (Kuehl et al. 2011). The total number of tributaries joining the river Brahmaputra within its Assam reach is around 63, and the number of sub-tributaries joining the main tributaries is around 215 (Sarma 2005). The catchment area of the tributaries ranges between 300 km^2 and 31,000 km^2 and that of the sub-tributaries ranges between 500 km^2 and 3000 km^2. The tributaries of the Barak river have their sources mainly in the land of Manipur, Mizoram, and Assam. The total number of tributaries joining the Barak river within its Assam reach is around 10, and the number of sub-tributaries joining the main tributaries is around 5 (Das et al. 2007; Alam and Phukon 2013). The catchment area of the tributaries ranges between 300 km^2 and 4200 km^2, and that of the sub-tributaries ranges between 100 km^2 and 2000 km^2. Fig. 22.1 shows the Brahmaputra and Barak basin.

22.3 Materials and Data Used

For the creation of the river atlas database, several datasets have been used. The important datasets used are Digital Elevation Model (DEM), satellite imagery, land use land cover, road, railways networks, major locations, flood protection structures, and hydro-meteorological observatories. The list of datasets used is described below:

Digital Elevation Model (DEM): DEMs are used for the delineation of drainage networks and catchment boundaries for all tributaries of the Brahmaputra and Barak basin. A high-resolution CartoDEM v3 that has a spatial resolution of 10 m is used for the delineation of river networks for all the rivers, which are within the Indian administrative boundary. For rivers that are outside the Indian administrative boundary, Shuttle Radar Topography Mission (SRTM) DEM of 30 m resolution is used.

Satellite Imagery: The mapping of all the river networks inside the state of Assam at a scale of 1:5000 is carried out using high-resolution satellite imagery. The images used for mapping are KOMPSAT imagery (1 m resolution) from Bhuvan web services and Bing hybrid maps (2.39 m resolution) (Basemaps).

Land Use/Land Cover (LULC): The LULC is being generated using LISS IV satellite imagery of 5.8 m resolution using supervised classification and fine-tuned with ground control points.

Road, Railway Network, and Major Locations: The district maps generated in this study contain details of roads, railway networks, and major locations in the districts. These datasets are downloaded and generated from several global sources such as Trimble Date marketplace, Google Earth, Bing maps, etc.

Embankments, Sluice Gates, Rain Gauge, Water Level Gauge: The district maps also contain important structures such as embankments, sluice gates, and hydro-meteorological observations (rain gauge and water level gauges). These datasets are obtained from the Assam State Water Resource Department (AWRD), Government of Assam, and Assam Water Research and Management Institute Society (AWRMIS), Government of Assam.

22.4 Methodology

In this study, four different maps are generated using geospatial and ground inputs for each district of Assam (comprising 33 districts). Those are river district maps (with revenue circles in the background), river district maps (with DEM in the background), land use/land cover maps, and catchment maps. The below section describes the methodology involved in the generation of individual district wise river atlas maps.

22.4.1 Preparation of District Wise River Atlas Maps

Preparation of River District Map: The river district map contains all the river system features of the respective district at a finer scale. All the major and minor rivers entering the respective district of Assam are mapped at a scale of 1:5000 using KOMPSAT satellite imagery and other global sources in the Geographic Information System (GIS) platform using software such as QGIS and ArcGIS. The map contains the details of the left and right banks, names of rivers, sand deposits, embankments, major locations, roads, railway lines, railway stations, revenue circle boundaries, bridges, etc. The data obtained from the concerned line departments of the state such as sluice gates and locations of hydro-meteorological observatories are also incorporated in the map. Important information such as the length of the embankment, the origin of rivers entering the district, warning level, and danger level of the rivers has been extracted from the database and collected during field visits.

Preparation of Land Use/Land Cover Maps: The land use land cover maps are prepared with a defined buffer of 1 km on either side of major and minor rivers. The area corresponding to different classes in the respective district is attributed in the maps.

Preparation of Catchment Maps: CartoDEM v3 and SRTM DEMs are used to generate the catchment maps using the automatic catchment delineation technique in the GIS platform. The source of origin of all the rivers entering the respective district of Assam is identified. These auto-delineated catchments are further verified manually for the correctness of delineation. Information such as the area of catchments in different states and countries, the source of origin of all the rivers, and the local names of the rivers is generated.

22.4.2 Development of River Atlas Geoportal

Assam River Atlas geoportal is a gateway to web-based geospatial resources related to river systems such as rivers, catchment areas, LULC, and river sources of the Assam, enabling users to discover, view, and access this information and services. This user-friendly web portal allows users to interact with all the layers available in the application seamlessly. River Atlas will be used for better management of water resources of the Brahmaputra and Barak river basins, thus addressing the problems of intense flooding and riverbank erosion. This geoportal enables the different user agencies working in the field of water resources and management to visualize and analyze geospatial data. Multiple layers related to the river systems are accessible at a very fine resolution. Advanced functionalities help in performing analysis and planning during the disaster period for taking quick actions. Tools built into the application ensure the fusion of data from multiple sources via WMS integration and the ability to overlay local data. Users can also generate statistical reports for custom
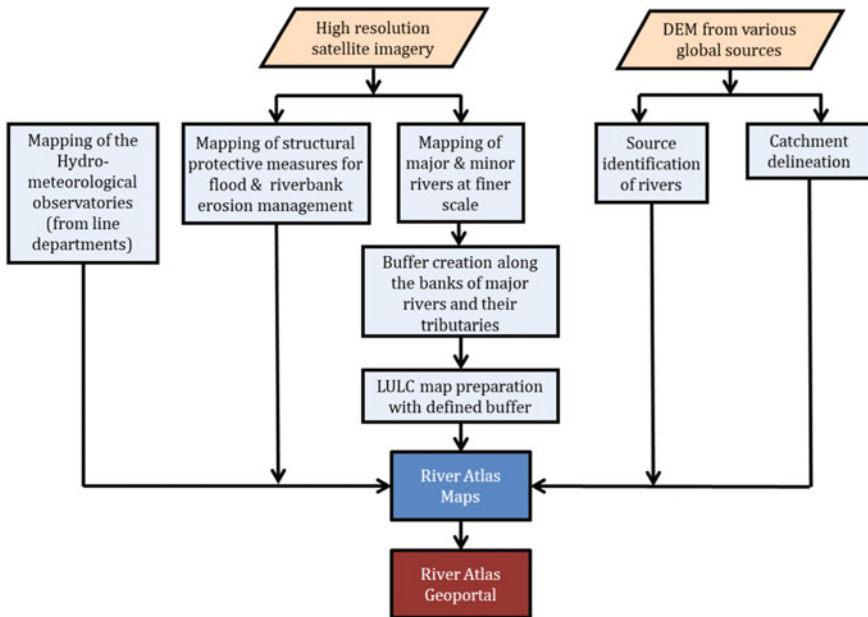
Fig. 22.2 Study area showing the Brahmaputra and Barak basins

areas and create custom maps and custom data extracts, which can be used in their existing workflow.

Fig. 22.2 shows the methodology involved in the development of the river atlas.

22.5 Results

The outputs that are generated using the above described methodology are presented in the below sections:

22.5.1 District River Map

A total of 66 district river maps are prepared, that is, two district maps for each district of Assam. These maps are (1) district river map with a revenue circle in the background and (2) district river map with DEM in the background. A sample map for the Lakhimpur district, Assam, is shown in Figs. 22.3 and 22.4. These maps are prepared with different layers in the background for easy interpretation and understanding by the concerned administrative authorities of the district and state. From the figure, it is observed that several layers are incorporated in the maps such as
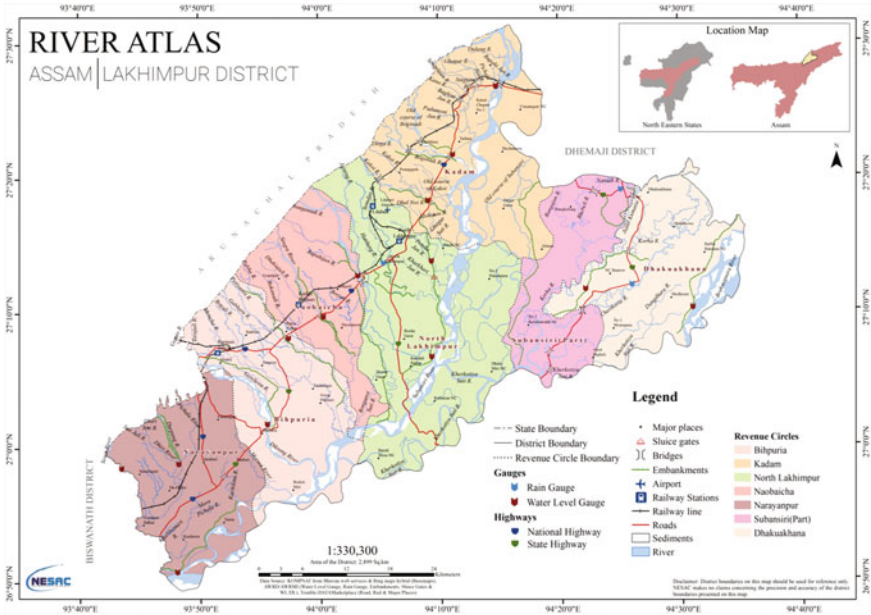
Fig. 22.3 District river map with revenue circle (RC) in the background for Lakhimpur district, Assam
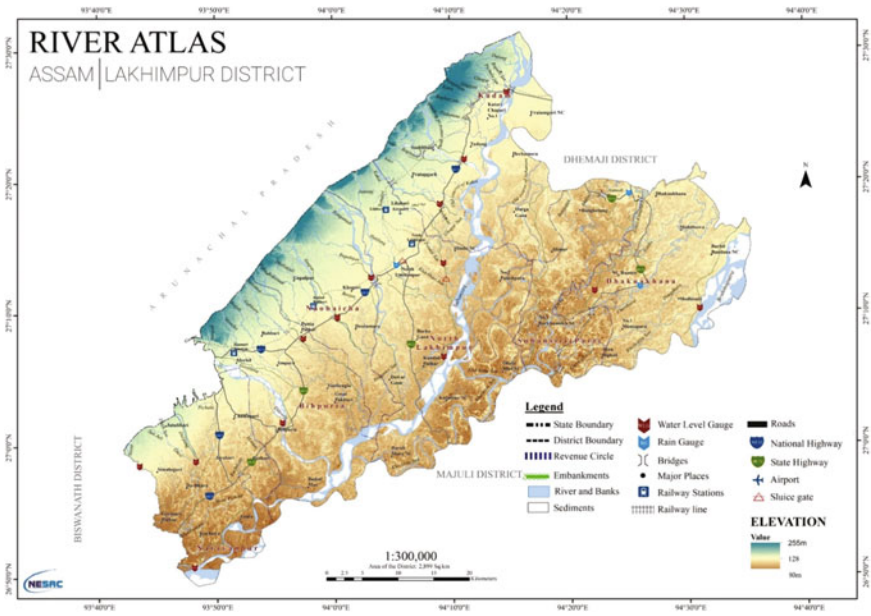
Fig. 22.4 District river map with DEM in the background for Lakhimpur district, Assam

Table 22.1 Details of embankments along with different rivers and their construction year in the Lakhimpur district, Assam

River name	Embankment length (in km)	Year of construction
Brahmaputra	33.72	1955–1957
Subansiri	42.80	1954–1988
Ranganadi	60.81	1951–1982
Dikrong	33.21	1953–1958
Boginadi	6.90	1953–1954
Singra	26.25	1954–1955
Pabha	30.43	1957–1958
Durpang	15.37	1969–1970
Dirgha	9.60	1952–1953
Kakoi	9.50	1951–1952
Pichala(Sessa)	6.40	1961–1962
Goriajan	3.20	1948–1949
Sumdiri	16.11	1963–1989
Hatilung	9.10	1952–1953
Korha	32.65	1952–1955

Table 22.2 River flood level chart for Lakhimpur district, Assam

Rivers	WL (m)	DL (m)
Boginadi	98.16	99.16
Brahmaputra	78.3	79.3
Dikrong	85.6	86.6
Durpang	111.32	112.32
Kakoi	92.39	93.39
Pabho	90.97	91.97
Ranganadi	94.02	95.02
Sessa	97.9	98.9
Singora	92.16	93.16
Subansiri	89.4	90.4

administrative boundaries (state, district, and revenue), gauges, highways, major places, sluice gates, embankments, airports, railways lines, sand deposits, banks of the rivers, and elevation ranges. The elevation information will be useful in carrying out developmental related activities on the banks of the river such as flood protection and mitigation structures. The attributes of a few important features have been extracted from the generated database and tabulated such as length of embankments (Table 22.1), river flood levels (danger level, warning level, high flood level) (Table 22.2), source of origin of rivers entering respective district (Table 22.3), etc. From Table 22.1, it is noticed that the maximum length of embankment in the Lakhimpur district is across the Ranganadi river with a length of 60.81 km constructed from 1951 to 1982. Similarly, the longest river flowing in the district is Subansiri with a length of 137 km (Table 22.3). The level of detailing available in the map is shown in Fig. 22.5.

Table 22.3 List of rivers in Lakhimpur district along with length and source of origin

Rivers	Source	Length (km)
Bogali	Denka, Lakhimpur, Assam	13.27
Boginadi	Boginadi Forest Beat, Papumpare, Arunachal Pradesh	13.64
Bokanadi	Dhemagarh No.1, Lakhimpur, Assam	14.35
Brahmaputra	Konggyu Tso, China	18.08
Borjan	Borbam Pathar, Lakhimpur, Assam	46.67
Charikoria	Kakabari Kamal Pur, Dhemaji, Assam	51.00
Dhekiajuli	Assam-Arunachal Boundary	15.30
Dikrong	Rachi, Papumpare, Arunachal Pradesh	33.00
Durpang	Arunachal-Assam Boundary	25.66
Hatilung	Dafla Range, Lower Subansiri, Arunachal Pradesh	16.18
Jiatal-Kumatia	Richi-Rite, West Siang, Arunachal Pradesh	31.00
Kakoi	Kakoi Forest Beat, Papumpare, Arunachal Pradesh	31.24
Meneha	Shopo, Papumpare, Arunachal Pradesh	14.27
Mora Pichala	Hatbor Bori, Lakhimpur, Assam	17.22
Mornoi	Daffala Pathar, Lakhimpur, Assam	18.45
Pabha	Tomru, Papumpare, Arunachal Pradesh	19.84
Petuka Jan	Puta Pukhuri, Lakhimpur, Assam	11.21
Ranganadi	Dafla Range, Lower Subansiri, Arunachal Pradesh	32.29
Ronganoi Suti	Dafla Range, Lower Subansiri, Arunachal Pradesh	12.47
Singra	Tanio Happa, Papumpare, Arunachal Pradesh	40.97
Somdiri	Assam-Arunachal Boundary	14.74
Subansiri	Comai, China	137.00

22.5.2 District LULC Map

The LULC maps will help in understanding the type of classes available on the banks of rivers in a particular district. The LULC maps are broadly classified into four major classes, that is, agriculture, forest, built-up, and waterbody (Fig. 22.6). Further, the area that falls under these classes in the respective district is incorporated in the maps (Table 22.4). From Table 22.4, it is noticed that the maximum area of a district is dominated by agriculture, that is, 1066.7 km^2 followed by forest, water, and built-up, respectively.

22.5.3 District Catchment Map

The catchment maps are prepared to identify the origin of rivers entering the respective district of Assam. These maps will be useful for understanding the catchment area contributing to a particular district and carrying out various analyses during flooding. This map will also provide details about the catchment area falling in different states and countries. From Fig. 22.7, it is observed that the largest river
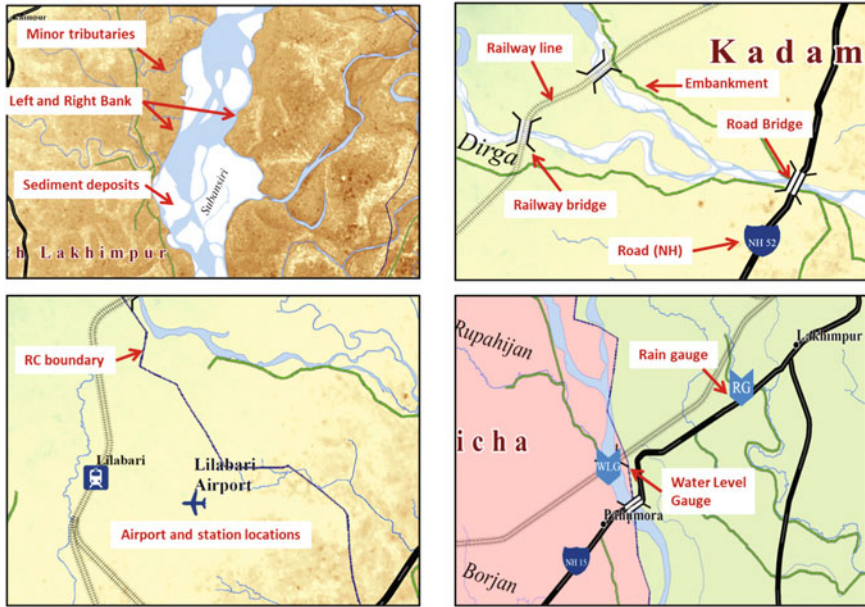
Fig. 22.5 Level of detailing available in the maps
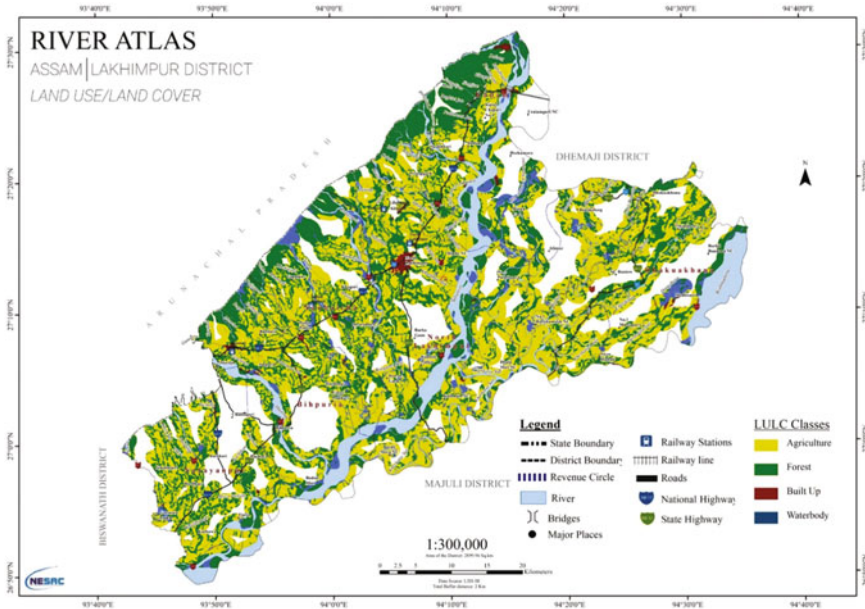
Fig. 22.6 District LULC map for Lakhimpur district, Assam

Table 22.4 LULC area in
Lakhimpur district

Class	Area (km^2)
Water	402.7
Agricultural land	1066.7
Forest	807.97
Built-up	14.71
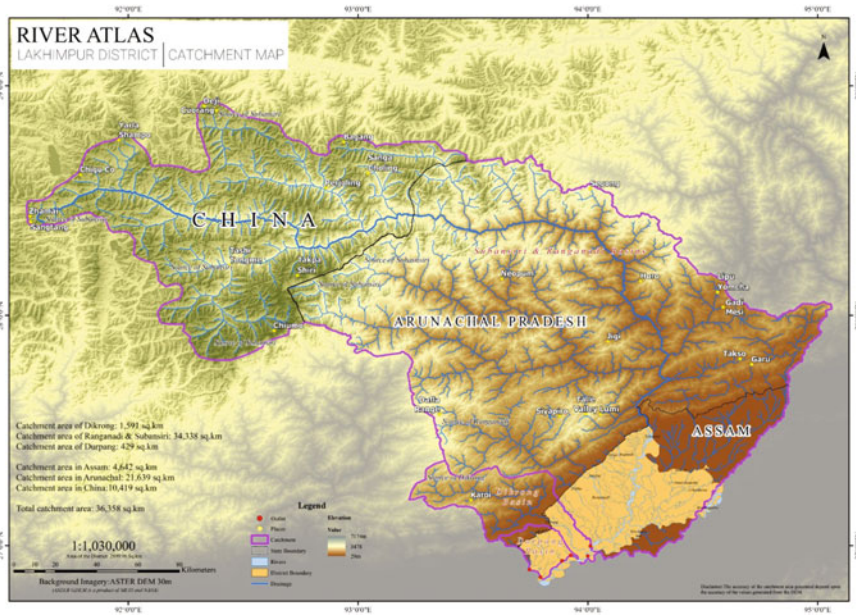
Fig. 22.7 District catchment map

flowing in the Lakhimpur district of Assam is Subansiri, which originates from China and then flows to Arunachal Pradesh and Assam. The total catchment area of all the rivers entering Lakhimpur district is 36,700 km^2 out of which 10,419 km^2 lies in China, 21,639 km^2 lies in Arunachal Pradesh, and 4642 km^2 lies in Assam.

Similarly, district-wise river atlas maps have been prepared for all 33 districts of Assam (4 maps per district comprising 132 maps). A few sample river atlas maps for Dhemaji, Dibrugarh, Cachar, Baksa, Salmara Mancachar, Sonitpur, Kamrup Metro, and Bongaigaon districts are shown in Figs. 22.8 and 22.9. Other district maps can be accessed from the river atlas geoportal under the "MAPS" section (one can access the "MAPS" section after registering in the geoportal).
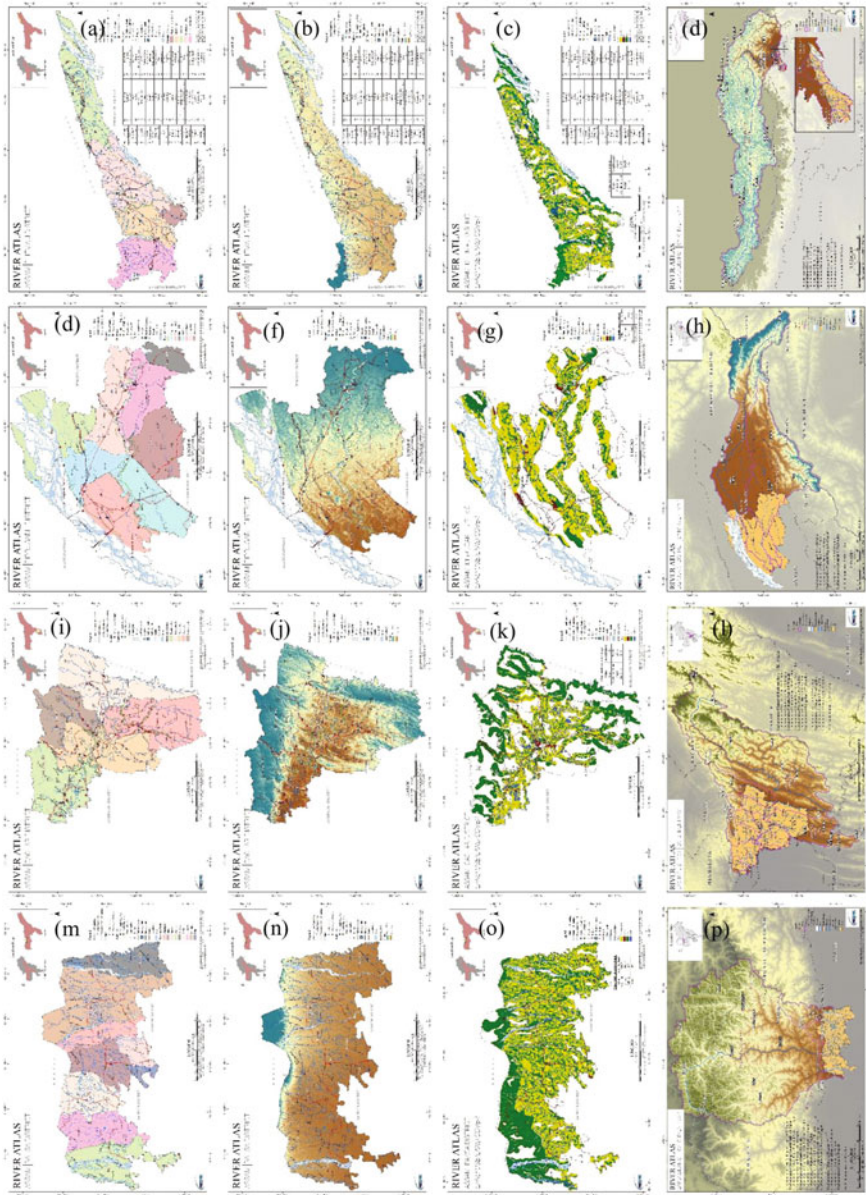
Fig. 22.8 River map (RC and DEM in the background), LULC map and catchment map for Dhemaji (**a–d**), Dibrugarh (**e–h**), Cachar (**i–m**), and Baksa (**n–q**) districts
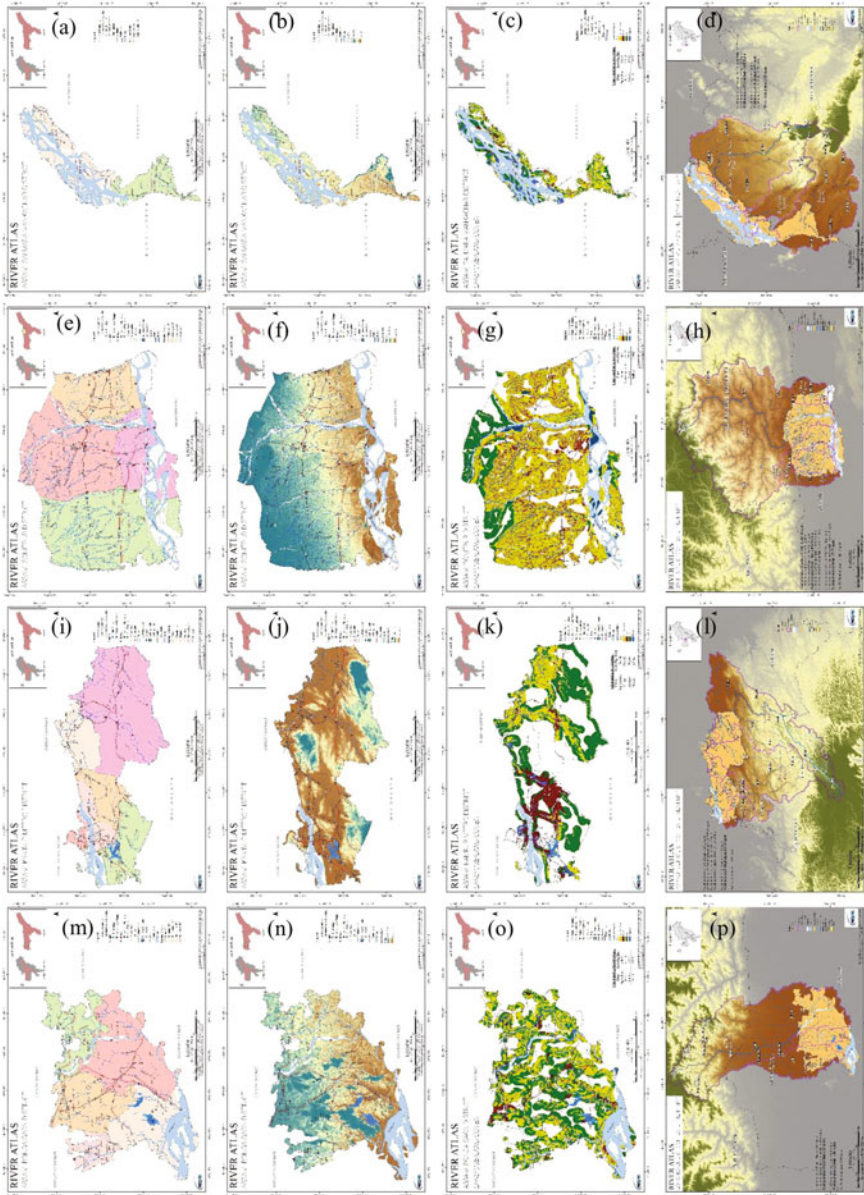
Fig. 22.9 river map (RC and DEM in the background), LULC map and catchment map for Salmara Mancachar (**a**–**d**), Sonitpur (**e**–**h**), Kamrup Metro (**i**–**m**), and Bongaigaon (**n**–**q**) districts

22.5.4   River Atlas Geoportal

In this study, several district maps have been prepared, and these maps are static maps with no facility for carrying out analysis. To utilize the potential of high-resolution layers and carry out analysis using multiple layers, a user-friendly geoportal has been developed, which can be accessed using the link https://riveratlas.nesdr.gov.in/. This geoportal has 132 maps, 50 layers, and 15 tools for carrying out various analyses. The list of layers and important tools available in the geoportal is presented in Fig. 22.10. Fig. 22.11 shows the landing page of the river atlas geoportal.

22.6   Uniqueness and Impact on Society

It is found that there is no river atlas available for the entire state of Assam along with various features such as roads, railway lines, bridges, embankments, sluice gates, hydro-meteorological observatories, etc. None of the state government departments has sufficient documented information on the exact source of origin of rivers, especially in the case of transboundary rivers. The high-resolution river database of 1:5000 scale developed as a part of this study is a unique and first ever GIS database made available for concerned government authority. The present mapping has reasonably acceptable details of LULC for all major and minor rivers in the district with a defined buffer. The maps provide elevation information for all districts along with river networks. The maps and geoportal generated as a part of this study can be used efficiently for water resource management, flood management, preparation of detailed project reports (DPRs), etc. In the event of flooding in the state of
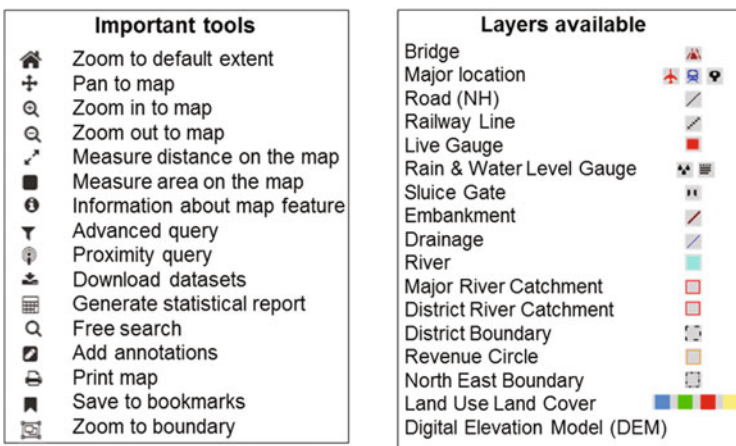
Fig. 22.10 Functionalities and layers available in the geoportal
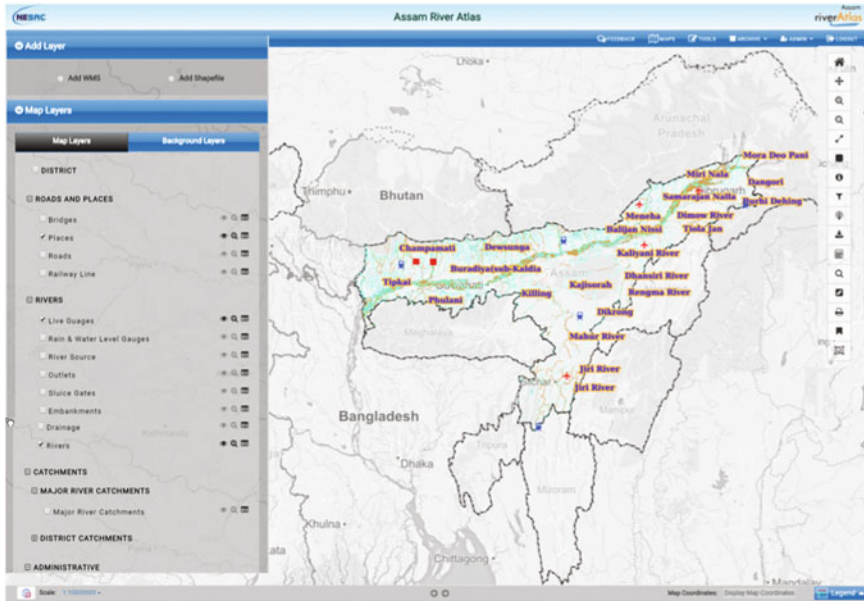
Fig. 22.11 River atlas geoportal

Assam, it is necessary to have ancillary details of the flood causing rivers such as catchment area, the origin of river, length and width, embankment across the river, hydro-meteorological observatories, LULC near the river, etc. Further, it is important to carry out analysis using these layers and generate the outputs on the fly during the time of disaster. Using the river atlas maps and geoportal, the necessary outputs can be generated on a near real-time basis. The Honourable Chief Minister of Assam expressed satisfaction and optimism on the usefulness of the developed maps in river planning and development in Assam (https://thenortheasttoday.com/states/assam/first-ever-river-atlas-in-assam-to-be-released-soon/cid2544454.htm) (Fig. 22.12).

22.7 Conclusion

In this study, high-resolution river atlas maps have been generated for all districts of Assam. The maps are generated mainly using geospatial inputs and field datasets. Three types of maps have been prepared such as district river maps, district LULC maps, and district catchment maps. As a part of this study, 132 maps have been generated comprising four maps each for 33 districts of Assam. To utilize the layers generated up to a maximum extent, a user-friendly geoportal (https://riveratlas.nesdr. gov.in/) has been developed and made available in the public domain. The outputs generated as a part of this study are the first ever high-resolution maps (1:5000) and geoportal available for the concerned authority of the Government of Assam. The

Fig. 22.12 Release of river atlas maps by Honourable Chief Minister of Assam

outputs generated will be useful for the proper management of water resources and also to mitigate floods in the state of Assam. Since the Brahmaputra basin is one of the largest basins in India, the high-resolution database of 1:5000 along with river system features generated as a part of this study will contribute to the overall water resources system of India. Since the information generated is available in the public domain, several analysis can be carried out by the research community on various applications such as flood hazard mapping, flood early warning, and bank erosion studies, which in turn will contribute to the development of water resources system of India.

No study is complete by itself; the database generated is a one-time database, and since the river course is dynamic in nature, periodic updation of the river networks is required. The fluvial geomorphology component of individual rivers can be incorporated into the map, which will provide a better understanding of the river process and how they change over time. The generation of watershed maps for all the rivers will help in the prioritization of watersheds, and further, it can be used to adopt catchment conservation measures.

References

Alam Laskar A, Phukon P (2013) Structural control on landscape development of Barak Valley, northeast India. J Geol Soc India 81:232–240. https://doi.org/10.1007/s12594-013-0026-6

Annayat W, Sil BS (2020) Assessing channel morphology and prediction of centerline channel migration of the Barak River using geospatial techniques. Bull Eng Geol Environ 79:5161–5183. https://doi.org/10.1007/s10064-020-01894-9

Bailey FM (1914) Exploration on the Tsangpo or upper Brahmaputra. Scott Geogr Mag 30:561–582. https://doi.org/10.1080/00369221408734154

Barman S, Bhattacharjya RK (2015) Change in snow cover area of Brahmaputra river basin and its sensitivity to temperature. Environ Syst Res 4:16. https://doi.org/10.1186/s40068-015-0043-0

Bhattachaiyya NN, Bora AK (1997) Floods of the Brahmaputra River in India. Water Int 22:222–229. https://doi.org/10.1080/02508069708686709

Chakraborty P, Sakthivel S, Kumar B, Kumar S, Mishra M, Verma VK, Gaur R (2014) Spatial distribution of persistent organic pollutants in the surface water of River Brahmaputra and River Ganga in India. Rev Environ Health 29. https://doi.org/10.1515/reveh-2014-0014

Das JD, Dutta T, Saraf AK (2007) Remote sensing and GIS application in change detection of the Barak River channel, N.E. India. J Indian Soc Remote Sens 35:301–312. https://doi.org/10.1007/BF02990786

Deka RL, Mahanta C, Pathak H, Nath KK, Das S (2013) Trends and fluctuations of rainfall regime in the Brahmaputra and Barak basins of Assam, India. Theor Appl Climatol 114:61–71. https://doi.org/10.1007/s00704-012-0820-x

Feng Y, Wang W, Liu J (2019) Dilemmas in and Pathways to Transboundary Water Cooperation between China and India on the Yaluzangbu-Brahmaputra River. Water (Basel) 11:2096. https://doi.org/10.3390/w11102096

Goswami DC (1985) Brahmaputra River, Assam, India: physiography, basin denudation, and channel aggradation. Water Resour Res 21:959–978. https://doi.org/10.1029/WR021i007p00959

Jain SK, Agarwal PK, Singh VP (2007) Brahmaputra and barak basin. In: Hydrology and water resources of india. Springer, Dordrecht, pp 419–472

Jain SK, Mani P, Jain SK, Prakash P, Singh VP, Tullos D, Kumar S, Agarwal SP, Dimri AP (2018) A Brief review of flood forecasting techniques and their applications. Int J River Basin Manag 16:329–344. https://doi.org/10.1080/15715124.2017.1411920

Kuehl SA, Allison MA, Goodbred SL, Kudrass H (2011) The Ganges–Brahmaputra Delta. In River deltas-concepts, models, and examples. SEPM (Society for Sedimentary Geology), pp 413–434

Kumar R (2021) Flood damage assessment in a part of the Ganga-Brahmaputra plain region, India. In: Advances in remote sensing for natural resource monitoring. Wiley, Hoboken, NJ, pp 389–404

Kumar R, Chatterjee C (2005) Regional flood frequency analysis using L-moments for North Brahmaputra Region of India. J Hydrol Eng 10:1–7. https://doi.org/10.1061/(ASCE)1084-0699(2005)10:1(1)

Mirza MMQ, Warrick RA, Ericksen NJ, Kenny GJ (2001) Are floods getting worse in the Ganges, Brahmaputra and Meghna basins? Environ Hazards 3:37–48. https://doi.org/10.3763/ehaz.2001.0305

Nagaveni C, Kumar KP, Ravibabu MV (2019) Evaluation of TanDEMx and SRTM DEM on watershed simulated runoff estimation. J Earth Syst Sci 128:2. https://doi.org/10.1007/s12040-018-1035-z

Pradhan NS, Das PJ, Gupta N, Shrestha AB (2021) Sustainable management options for healthy rivers in South Asia: the case of Brahmaputra. Sustainability 13:1087. https://doi.org/10.3390/su13031087

Ranjan R (2017) Flood disaster management. In: River system analysis and management. Springer, Singapore, pp 371–417

Saikumar G, Pandey M, Dikshit PKS (2023) Natural river hazards: their impacts and mitigation techniques. Springer, Cham, pp 3–16

Sarma JN (2004) An overview of the Brahmaputra river system; pp 72–87

Sarma JN (2005) Fluvial process and morphology of the Brahmaputra River in Assam, India. Geomorphology 70:226–256. https://doi.org/10.1016/j.geomorph.2005.02.007

Sharma N (2015) Sustainable development of water resources in the Brahmaputra and Barak River system of northeast India. pp 835–845

Chapter 23
Numerical Study of Flow Through Linear Weir

Amiya Abhash, Ravi Prakash Tripathi, Padam Jee Omar, Nitesh Gupta, and K. K. Pandey

Abstract The use of computational fluid dynamics (CFD) for simulating flow around weirs and hydraulic structures is gaining popularity, as constructing physical models every time for analysis takes up lots of time and energy and not economical as well. With the availability of advanced software like CFD, Fluent, and Flow 3D, there have been significant improvements in the modeling of stepped spillway flows. CFD is increasingly used for study of flow around old as well as new structures and for studying their behavior to flow dynamics. The study of flow around a linear weir has been undertaken in this paper. A linear weir model was established, and a simulation study was carried out to investigate the flow behavior through the linear weir. The simulation result has been compared to the experimental result from literature. The head-discharge relationship of the weir has also been compared to standard equations available in literature. The paper confirms the use of CFD as a tool for accurately predicting flow patterns around hydraulic structures. The comprehensive information provided in the article can be useful to professionals in the field of flood risk management and hydraulic engineering, helping them to design and construct safer and more cost-effective structures to mitigate the impact of floods.

A. Abhash · K. K. Pandey
Department of Civil Engineering, Indian Institute of Technology (BHU), Varanasi, Uttar Pradesh, India
e-mail: amiyaa.rs.civ16@itbhu.ac.in

R. P. Tripathi
Department of Civil Engineering, Rajkiya Engineering College, Sonbhadra, Uttar Pradesh, India
e-mail: ravi.tripathi@recsonbhadra.ac.in

P. J. Omar (✉)
Department of Civil Engineering, Babasaheb Bhimrao Ambedkar University, Lucknow, India

N. Gupta
Department of Civil Engineering, Nirama University, Ahmedabad, India
e-mail: nitesh.gupta@nirmauni.ac.in

397

23.1 Introduction

Precipitation is a significant source of water resources on the planet. Freshwater constitutes only 2.5% of all water on earth and is fundamental for all life forms (Sathe et al. 2012; Saikumar et al. 2022). The substantial population growth has initiated a water stress scenario (Shukla et al. 2013; Gleick 2014). The rivers are the main contributors of fresh water among the surface sources along with providing groundwater requirements (Omar et al. 2017). The water distribution of big rivers creates water disputes between countries or states. The recent political tension between India and Pakistan regarding Indus Treaty, the increasing dispute over Nile Basin, Afghanistan, and Iran water dispute, long time tensions in the Euphrates-Tigris, Cauvery water dispute in India within states, and the Israel and its Arab neighbors are some examples of river water dispute. This use of a finite resource has led researchers around the world to move toward a sustainable and optimum use of water. Hydraulic structures are frequently used for water resources development and management (Hirshleifer et al. 1969; Griffin 2016; Pandey et al. 2022a; b). Dams, barrages, weirs, head, and cross regulators are some significant structures, and they are applied to store and regulate the surface water of river (Gaur et al. 2023;). The flow domain in the vicinity of these hydraulic structures consists of spatial as well as temporal variation of velocity. India is a monsoon country with rainfall not falling throughout the year but concentrated in 3–4 months (Gaur et al. 2021; Omar et al. 2020). This implies India gets all of its fresh water resource in around 3–4 months. This leads a greater responsibility on the water resource professionals to better manage this finite water source so that its sustainable use can be availed all around the year.

Dams are the most former and elemental type of civil engineering hydraulic structures. All great cultures have been discovered with the construction of dams and reservoir appropriate to their demands, to meet drinking and irrigation demands originating through the evolution and elaboration of engineered farming (Omar et al. 2022).

Transverse hydraulic structures are structures placed across the open channel river and are used for to modify flow in the open channel (Naik et al. 2008; Tripathi and Pandey 2020; Guguloth and Pandey 2023). A linear weir is the simplest type of transverse hydraulic structure, which is basically an obstruction constructed perpendicular to the flow of open channel covering entire width of the channel. The water flows over the linear weir and thus allows the measurement of discharge by measuring the upstream head. A linear weir is abundantly used in irrigation systems along with industries and laboratories. Weirs have different shapes such as rectangular, triangular, trapezoidal, labyrinth, and morning glory types (Arvanaghi and Oskuei 2013; Pourshahbaz et al. 2022).

Weirs are generally used for following purposes:

1. Flow discharge control and measurement
2. Channel stabilization
3. Water level moderation
4. Environmental improvement

Flow system is complex over a weir; however, taking the energy principles into account, the discharge flowing through over a linear weir can be related to the head over the weir crest (Horton 1906) (Eq. 23.1).

$$Q = \frac{2}{3} Cd \sqrt{2g}\, LH^{1.5} \tag{23.1}$$

where Q = flow rate (m³/s)
   h = head on the weir (m)
   l = crest length of the weir (m)
   g = acceleration due to gravity (9.81 m/s²)
   C_{d} = discharge constant of the weir.

Linear weirs are commonly used in hydraulic engineering to regulate flow in open channels, divert water for irrigation or hydroelectric power generation, and prevent flooding in urban areas (Tripathi and Pandey 2022). However, predicting the hydraulic performance of linear weirs can be a challenging task due to the complex flow patterns that develop near the weir crest. Numerical modeling offers a promising approach for understanding these flow patterns and optimizing the design of linear weirs (Pandey et al. 2019; Shivashankar et al. 2023).

In this study, we present a numerical investigation of the flow characteristics of linear weirs. The objective of this research is to provide a better understanding of the flow dynamics through linear weirs by utilizing numerical simulations. The numerical model used in this study is validated through comparison with experimental data from previous studies, and the effects of various geometric and hydraulic parameters on the flow behavior are analyzed. The results of this study can help in the design of efficient and effective linear weirs, ultimately contributing to the sustainable management of water resources.

23.2   Experimental Results and Numerical Models

The numerical model is constructed based on experimental model of Tiwari and Sharma (2017) and Afzal and Dutta (2023). A linear weir of height 160 mm was placed perpendicular in open channel flow over the entire width of 84 mm taken for three-dimensional numerical simulation.

23.2.1 Meshing and Boundary Condition

The top and outlet of the numerical model was designated as pressure outlet, while the two side lengths were taken as symmetry. The primary phase was taken as air while the secondary phase as water. The model was run as transient simulation in presence of gravity (Afzal et al. 2020). The phase interaction between air and water was provided in the form of surface tension force (Jana et al. 2021; Pandey et al. 2022a; b; Dutta et al. 2023). The upstream distance from inlet to weir was taken as 3.0 meters, while the total length of channel was 4.16 meters. Height of inlet was taken as 125 mm. Around 650,000 elements were created for linear weir meshing.

Computational fluid dynamics (CFD) simulation using FLUENT solver is selected for our numerical study for flow over. Free surface as determined with CFD study has been compared with experimental results.

PISO algorithm for pressure-velocity coupling method was used. Also, the realizable (k-ε) model is used in the present study as the viscous model to simulate the effect of turbulence. "Realizable" model implies that the model is consistent with the physics of turbulent flow and satisfies certain mathematical constraints on the Reynolds stresses.

To validate the numerical model, experimental tests were conducted in a laboratory flume with a linear weir. The weir had a length of 1 meter and a height of 0.1 meter. The upstream water level was varied to achieve different discharges. The height of water over the weir was measured using a probe tool shown in Fig. 23.1. The flow rate through the weir was measured using a flowmeter. The experimental results were compared with the numerical simulations for the same range of discharges.

The experimental results showed good agreement with the numerical simulations, indicating that the numerical model was able to accurately simulate the flow behavior through the linear weir. The flow rate through the weir increased with increasing discharge, as expected, and the numerical model was able to accurately predict the flow rate over the entire range of discharges tested. The agreement between the experimental results and the numerical simulations was within 5%, which is considered to be a reasonable level of accuracy for hydraulic engineering applications.

23.2.2 Verification of the Numerical Model

CFD analysis shows the discharge capacity of linear rectangular weir to be in close agreement with the experimental results from literature. A probe tool was used to ascertain the height over the weir across the direction of flow over the weir as shown in Fig. 23.1. Time step of the analysis for linear weir was taken up as 0.01 s. The solution converged, and the continuity error was well within the limit.
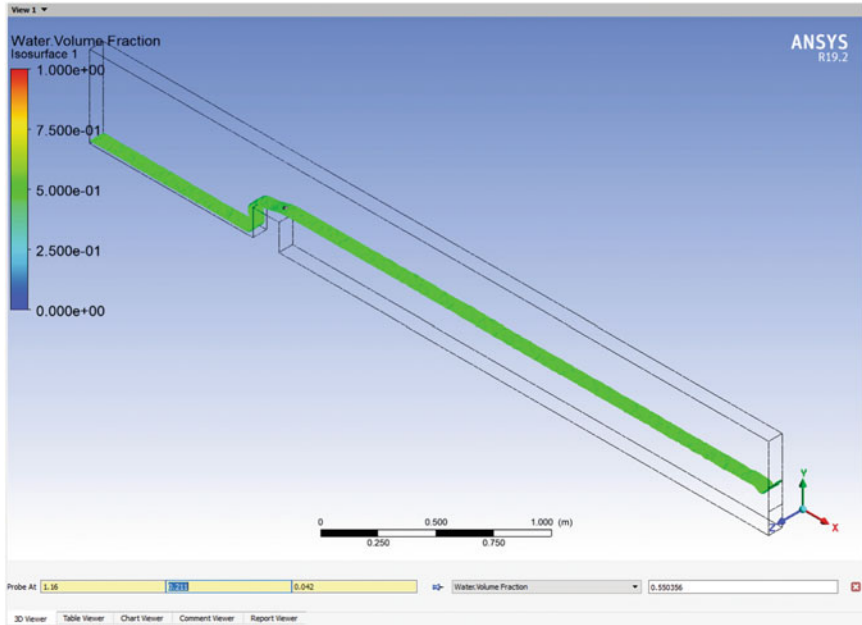
Fig. 23.1   Probe at the center of the linear weir for volume fraction

The numerical model used in the study was based on the Reynolds-Averaged Navier-Stokes (RANS) equations, which were solved using the commercial software ANSYS Fluent. The simulations were conducted using a 3D, unstructured grid with approximately 1.5 million cells. The turbulence model used was the standard k-ε model. The simulations were conducted for a range of geometric and hydraulic parameters, including weir length, weir height, upstream water level, and discharge.

The numerical simulations showed good agreement with the experimental results, indicating that the numerical model was able to accurately predict the flow behavior through the linear weir. The simulations showed that the flow behavior through the linear weir is complex and depends on several factors, including weir length, weir height, upstream water level, and discharge. The simulations also revealed the formation of recirculation zones downstream of the weir crest, which agreed with the experimental observations.

Overall, the combination of experimental results and numerical models provided a comprehensive understanding of the flow behavior through linear weirs. The validation of the numerical model with experimental data gave confidence in the accuracy of the numerical simulations, and the simulations allowed for a more detailed analysis of the flow behavior than could be achieved with experimental tests alone. The results of this study can help to improve the design and optimization of linear weirs for hydraulic engineering applications.

23.3   Results and Discussion

The scaled residuals in continuity dropped well below the third order of magnitude
(10^{-3}) for discharges and remained steady, while other residuals in X-velocity, Y-
velocity, Z-velocity, k, ε, and volume fraction (air) dropped to fifth order of magni-
tude (Fig. 23.2), and thereafter, the residuals attained a constant value. The probe
tool used for ascertaining height of water over the weir for a constant discharge is
shown in Fig. 23.1. The Iso-surface plot for a discharge is shown in Fig. 23.3.
Iterations were kept constant at 10 for all the different discharges in the numerical
model.

The result from the CFD analysis is in very close agreement with the experimen-
tal finding as presented in Fig. 23.4 where series 1 is the data from literature and
series 2 is the data from numerical model. The maximum error obtained was well
within 3% for all discharges.

The numerical model developed in this study was used to investigate the flow
characteristics through linear weirs. A range of geometric and hydraulic parameters
were considered, including weir length, weir height, upstream water level, and
discharge. The simulations were conducted for a range of discharges, and the results
were analyzed in terms of the flow behavior and the hydraulic performance of the
linear weirs.

The results showed that the numerical model was able to accurately simulate the
flow characteristics through linear weirs. The scaled residuals in continuity dropped
well below the third order of magnitude for discharges and remained steady,
indicating that the numerical solution was accurate and converged to a stable result.
The other residuals for X-velocity, Y-velocity, Z-velocity, k, ε, and volume fraction
(air) dropped to the fifth order of magnitude before attaining a constant value,
indicating that these variables had a lower level of accuracy but still reached a stable
value.
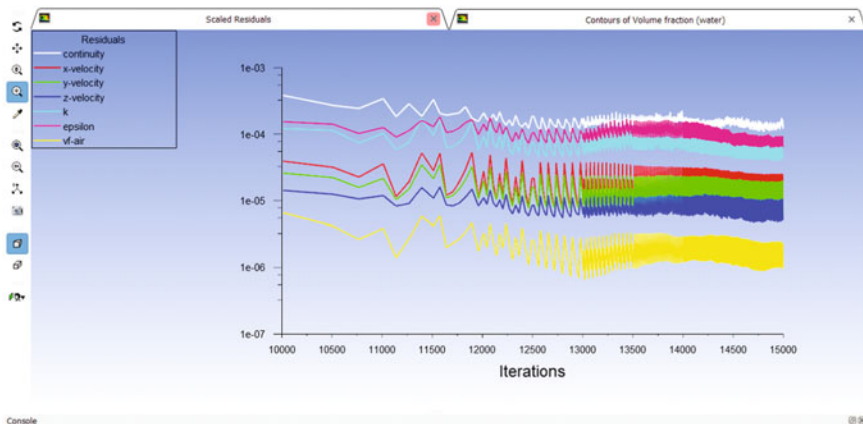
Fig. 23.2 Residuals of CFD Analysis for linear weir
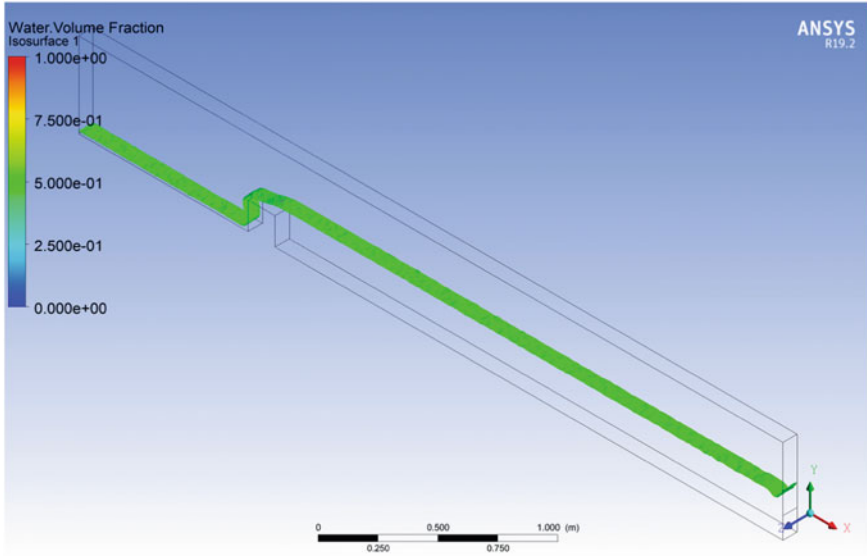
Fig. 23.3 Iso-surface plot for the linear weir
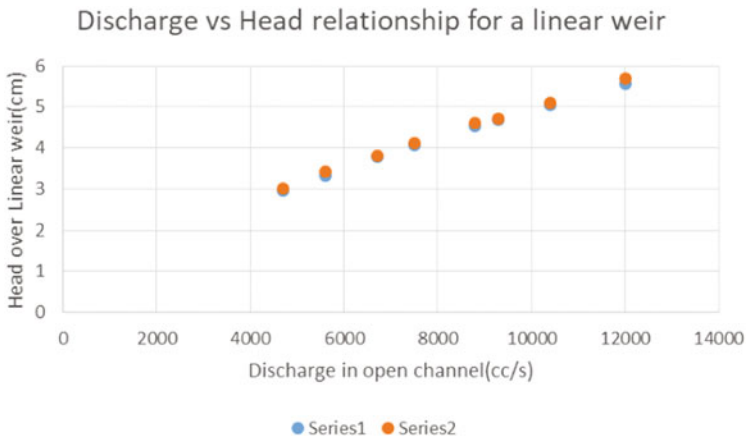
Fig. 23.4 Discharge versus head for linear weir

The simulations also showed that the flow behavior through linear weirs is complex and depends on several factors, including weir length, weir height, upstream water level, and discharge. For instance, the flow rate through the weir increased with increasing discharge, as expected. However, the effect of weir height on the flow rate was more complex, with an initial increase followed by a decrease as the weir height was increased. The simulations also revealed the formation of

recirculation zones downstream of the weir crest, which could have implications for the hydraulic performance of the weir.

The numerical simulations presented in this study provide valuable insights into the flow behavior through linear weirs. The simulations demonstrated the accuracy and stability of the numerical model and highlighted the complexity of the flow behavior through linear weirs. The results showed that the hydraulic performance of linear weirs depends on several factors, including weir length, weir height, upstream water level, and discharge.

The findings of this study can help in the design and optimization of linear weirs for hydraulic engineering applications. For instance, the results suggest that increasing weir height beyond a certain point may not lead to a corresponding increase in the flow rate through the weir and may even lead to a decrease in the flow rate. The formation of recirculation zones downstream of the weir crest could also have implications for the hydraulic performance of the weir, and further studies may be needed to understand these effects.

Overall, the numerical simulations presented in this study provide a valuable tool for understanding the flow behavior through linear weirs and optimizing their design for hydraulic engineering applications. The findings of this study can help to improve the efficiency and effectiveness of linear weirs for regulating flow in open channels, diverting water for irrigation or hydroelectric power generation, and preventing flooding in urban areas.

23.4   Conclusion

This study has demonstrated the value of numerical modeling in understanding the complex flow patterns of linear weirs. By utilizing numerical simulations and validating the model with experimental data, we have gained a better understanding of the flow dynamics through linear weirs and analyzed the effects of various geometric and hydraulic parameters on the flow behavior. This research provides useful insights for the design of efficient and effective linear weirs, which are important for regulating flow in open channels, diverting water for irrigation or hydroelectric power generation, and preventing flooding in urban areas.

The results of this study have important implications for the sustainable management of water resources. Effective and efficient linear weirs can help to conserve water, protect against flooding, and facilitate the sustainable development of hydropower and irrigation systems. By contributing to our understanding of the hydraulic performance of linear weirs, this research can help to improve the design and implementation of these important engineering structures, ultimately promoting the sustainable use of water resources for future generations. It can hence be concluded from our study of a numerical model that CFD can effectively be applied to solve natural flow patterns in open channel flow. It also paves a way to utilize CFD to analyze flows in complex hydraulic structures like labyrinth weirs and morning glory spillways or the recently founded Piano Key Weirs (PKW). This area needs

further study as numerical models save lot of time and resources and thus are gaining popularity.

References

Afzal MS, Dutta D (2023) Numerical study of local scour around rectangular cylinder due to combined wave-current effect. In Coastal Sediments 2023: The Proceedings of the Coastal Sediments 2023; pp 1020–1034

Afzal MS, Bihs H, Kumar L (2020) Computational fluid dynamics modeling of abutment scour under steady current using the level set method. Int J Sediment Res 35(4):355–364

Arvanaghi H, Oskuei NN (2013) Sharp-crested weir discharge coefficient. J Civil Eng Urbanism 3(3):87–91

Dutta D, Afzal MS, Alhaddad S (2023) 3D CFD study of scour in combined wave–current flows around rectangular piles with varying aspect ratios. Water 15(8):1541

Gaur S, Johannet A, Graillot D, Omar PJ (2021) Modeling of groundwater level using artificial neural network algorithm and WA-SVR model. In: Pande CB, Moharir KN (eds) Groundwater resources development and planning in the semi-arid region. Springer, Cham, pp 129–150. https://doi.org/10.1007/978-3-030-68124-1_7

Gaur S, Omar PJ, Eslamian S (2023) Advantage of grid-free analytic element method for identification of locations and pumping rates of wells. In: Saeid E, Faezeh E (eds) Handbook of hydroinformatics. Elsevier, Amsterdam, pp 1–10. https://doi.org/10.1016/B978-0-12-821962-1.00003-9

Gleick PH (2014) The world's water.: the biennial report on freshwater resources, Vol. 8

Griffin RC (2016) Water resource economics: the analysis of scarcity, policies, and projects. MIT Press, Cambridge

Guguloth S, Pandey M (2023) Accuracy evaluation of scour depth equations under the submerged vertical jet. AQUA-Water Infrastruct Ecosyst Soc. 72(4):557–575

Hirshleifer J, De Haven JC, Milliman JW (1969) Water supply: economics, technology, and policy

Horton RE (1906) Weir experiments, coefficients, and formulas (Vol. 16). US Government Printing Office

Jana P, Pandey R, Semeraro T, Alatalo JM, Areteno R, Todaria NP, Tripathi R (2021) Community perspectives on conservation of water sources in Tarkeshwar sacred groves, Himalaya, India. Water Supply 21(8):4343–4354

Naik B, Panda R, Nayak S, Sharma S (2008) Hydraulics and salinity profile of pitcher irrigation in saline water condition. Agric Water Manag 95(10):1129–1134

Omar PJ, Gupta N, Tripathi RP, Shekhar S (2017) A study of change in agricultural and forest land in Gwalior city using satellite imagery. SAMRIDDHI J Phys Sci Eng Technol 9(02):109–112

Omar PJ, Dwivedi SB, Dikshit PKS (2020) Sustainable development and management of groundwater in Varanasi, India. In: AlKhaddar R, Singh R, Dutta S, Kumari M (eds) Advances in water resources engineering and management, Lecture notes in civil engineering, vol 39. Springer, Singapore. https://doi.org/10.1007/978-981-13-8181-2_15

Omar PJ, Shivhare N, Dwivedi SB, Dikshit PKS (2022) Identification of soil erosion-prone zone utilizing geo-informatics techniques and WSPM model. Sustain Water Resour Manage 8(3):66. https://doi.org/10.1007/s40899-022-00654-9

Pandey KK, Abhash A, Tripathi RP, Dayal S (2019) Flow-field near forty-five degree dividing open channel. Int J Recent Technol Eng. https://doi.org/10.35940/ijrte.C4917.098319

Pandey P, Mishra AR, Verma PK, Tripathi RP (2022a) Study and implementation of smart water supply management model for water drain region in India. In: VLSI, microwave and wireless technologies: select proceedings of ICVMWT 2021. Springer, Singapore, pp 711–721

Pandey M, Azamathulla H, Pu, J. H. (Eds.). (2022b) River dynamics and flood hazards: studies on risk and mitigation. Springer, Singapore

Pourshahbaz H, Abbasi S, Pandey M, Pu JH, Taghvaei P, Tofangdar N (2022) Morphology and hydrodynamics numerical simulation around groynes. ISH J Hydraul Eng 28(1):53–61

Saikumar G, Pandey M, Dikshit PKS (2022) Natural river hazards: their impacts and mitigation techniques. In: River dynamics and flood hazards: studies on risk and mitigation. Springer Nature Singapore, Singapore, pp 3–16

Sathe B, Khir M, Sankhua R (2012) Rainfall analysis and design flood estimation for Upper Krishna River Basin Catchment in India. Int J Sci Eng Res 3(8), pp 1–20

Shivashankar M, Pandey M, Shukla AK (2023) Numerical investigation on the evaluation of the sediment retention efficiency of invert traps in an open rectangular combined sewer channel. J Hazard Toxic Radioact Waste. 27(1):04022045

Shukla S, Khire MV, Gedam SS (2013) Effects of urbanization on river basin ecosystem-A framework. Geoscience and Remote Sensing Symposium (IGARSS), IEEE International

Tiwari H, Sharma N (2017) Empirical and mathematical modeling of head and discharge over piano key weir. Development of Water Resources in India. Springer, Cham, pp 341–354

Tripathi RP, Pandey KK (2020) Experimental study of local scour around T-shaped spur dike in a meandering channel. Water Supply. 21(2):542–552. https://doi.org/10.2166/ws.2020.331

Tripathi RP, Pandey KK (2022) Scour around spur dike in curved channel: a review. Acta Geophys 70(5):2469–2485

Chapter 24
Artificial Intelligence-Based Fully Scalable Real-Time Early Flood Warning System

Praveen Rathod, Manish Pandey, and Anil Kumar Gupta

Abstract The Early Flood Warning System (EFWS) being developed is an innovative approach to mitigate the negative impacts of flooding in flood-prone areas. The system consists of several components, including hydrologic and hydraulic models, AI-based flood map generation, and a mobile application for real-time alerts and geo-location-based messaging. The hydrologic and hydraulic models use a variety of data sources to simulate multiple scenarios, including rainfall intensity, water level in reservoirs, and lateral flow to sites. By analyzing these scenarios, the models can predict the probable flood-prone areas in a basin or city. The AI-based flood map generation component of the system then utilizes the data collected by rainfall and reservoir level sensors to create artificial flood maps indicating the depth and specific areas that are likely to be affected. This system uses AI models to create accurate predictions and can quickly produce results, allowing for timely and efficient warnings to be issued. The mobile application component of the system is a crucial tool for disseminating information and alerts to people in flood-prone areas. It is enabled with geo-location-based messaging, allowing for targeted alerts to be sent to specific neighborhoods or areas. The application also provides personalized flood maps, emergency resources, and two-way communication with users. This real-time information can help users to understand the level of risk they face and take appropriate precautions to stay safe during a flood. From the study, it is concluded that using AI in the EFWS provides several advantages, including improved accuracy, scalability, customization, cost-effectiveness, and real-time monitoring. The system can be tailored to suit the specific needs of a particular area, and the AI algorithms can analyze complex data sets to provide highly accurate predictions.

P. Rathod (✉)
Neram Civil Environmental Solution Pvt. Ltd., Pune, India

M. Pandey
NIT, Warangal, India

A. K. Gupta
Centre for Excellence on Climate Resilience, Environment Climate and DRM Division,
National Institute of Disaster Management, New Delhi, India

This approach is scalable and cost-effective, and the real-time monitoring allows for immediate responses to changing conditions, reducing the impact of floods and mitigating the risk of property damage and loss of life.

24.1   Introduction

India is extremely susceptible to flooding. Over 40 million hectares (mha) of the 329 million hectares (mha) total geographic area are at risk of flooding. Floods are a frequent occurrence that result in significant human casualties as well as damage to property, infrastructure, and public services. The fact that flood-related damages are on the rise is cause for alarm. In the past 10 years, from 1996 to 2005, the average yearly flood damage was Rs. 4745 crore, compared to Rs. 1805 crore, the corresponding average for the prior 53 years. Numerous factors, such as a sharp rise in population, rapid urbanization, an increase in economic and development activity in flood plains, and global warming, can be blamed for this (NDMA, India 2020). Floods affect 75 lakh hectares of land on average each year, claim 1600 lives, and cost Rs. 1805 crores in damage to public facilities, residences, and agriculture. The most lives lost (11,316) occurred in the year 1977. Major floods occur more than once every 5 years. Floods have also happened in places that weren't previously thought to be prone to flooding. These guidelines make an effort to address every aspect of flood management. Rainfall occurs 80% of the time from June to September, during the monsoon season. Heavy loads of silt are transported by rivers from catchments. These, along with rivers' insufficient carrying capacity, are to blame for floods, backed-up drainage systems, and riverbank erosion. Flash floods are caused by cyclones, cyclonic circulations, and cloud bursts, which result in significant losses. It is a truth that some of the rivers harming India originate in nearby nations, giving the issue a further complicated layer. It has been repeatedly noted that over the past 10 years, significant advancements have been made in the development and application of Early Warning Systems (EWS) for natural hazards (Hallegatte 2012). Success stories from both rich and developing nations demonstrate the value of EWS as a tool for preserving life, averting harm, and boosting societal resilience (UNISDR 2015; Golnaraghi 2012; UNEP 2012; Baudoin et al. 2014). Several developments have driven the increasing deployment of early warning systems (EWS) for disasters in recent years. Some of the key developments are as follows:

(1) Technological advancements: Advances in technology have enabled the development of more sophisticated and reliable early warning systems. For instance, the use of remote sensing technologies such as satellite imagery and drones has made it possible to detect and monitor natural hazards more accurately and in real time (Alfieri et al. 2012).

(2) Increase in disaster frequency and severity: The frequency and severity of natural disasters have been on the rise in recent years due to climate change, which has led to an increased demand for early warning systems that can help mitigate their impact (Hellmuth et al. 2007).

(3) Growing recognition of the importance of disaster risk reduction: There is now a growing recognition among governments, organizations, and communities of the importance of disaster risk reduction, including the deployment of early warning systems, as a critical component of disaster preparedness and response (Zommers and Singh 2014).

(4) The need to protect vulnerable populations: Early warning systems are especially important for protecting vulnerable populations, such as those living in low-lying coastal areas or in areas prone to landslides and flash floods (Baudoin et al. 2014).

(5) Improved technology for communication and sharing of information, including mobile phones, the internet, and social media (Webster 2013; UNISDR 2015).

(6) Recent studies showing that early warning systems can have significant benefits exceeding their costs (World Bank 2011).

Numerous projects are being developed to create stronger and "smarter" flood protection systems in response to recent catastrophic floods that have occurred all over the world. Numerous initiatives, including FLOODsite, FloodControl 2015, and the International Levee Handbook (Krzhizhanovskaya et al. 2011), make an effort to address some of the flood control issues. The creation of Early Warning Systems (EWS) for flood mitigation and disaster management is one of the most difficult issues. According to UNISDR (2015), an early warning system is "the set of capacities needed to generate and disseminate timely and meaningful warning information to enable individuals, communities, and organizations threatened by a hazard to prepare and to act appropriately and in sufficient time to reduce the possibility of harm or loss" (emphasizing that an effective early warning system needs to span all components from hazard detection through to community response). EWS typically include the following four elements: Risk awareness is ranked first, followed by monitoring, forecasting, and warning, followed by communication of an early warning and response capacity (Perera et al. 2019). For all these components to work, EWS mainly relies on the forecasting of rainfall and level of reservoir in real time. India Meteorological Department's (IMD) forecasting accuracy of heavy rainfall events is almost 78% for 24-h warnings. However, there is still a lot of scope to improve this accuracy (M Mohapatra, director general, IMD). IMD and ministry of earth sciences (MoES) is working to improve the modeling and observational systems to increase the accuracy of forecasting systems. While there is more accuracy in cyclone prediction as it is a larger system and a lot of R&D has gone into developing it, there has been a lot of improvement in the accuracy of heavy rainfall warning from around 50% in 2014 to 77% in 2020. Precipitation early-warning indices and water level early-warning indexes are two common early-warning indicators. The early-warning index for water levels is typically used for warning in small- or medium-sized basins. The early-warning index, particularly the rainfall threshold, is the subject of extensive study on flash flood avoidance worldwide (Golian et al. 2010). The value of rainfall intensity and total precipitation that occurs just before flash flood events is presented as the rainfall threshold. There are several technical difficulties that can arise in the development

and implementation of early flood warning systems (EWS). Some of these technical difficulties include the following:

(1) Data availability and quality: EWS rely on accurate and timely data from a range of sources, including rainfall gauges, river flow sensors, and satellite imagery. However, in some areas, data may be incomplete or unreliable, which can limit the accuracy of the system.

(2) Integration of multiple data sources: In order to provide accurate and reliable flood warnings, EWS must integrate data from multiple sources, including weather forecasts, river flow data, and topographic data. Integrating these data sources can be complex and require sophisticated data processing and modeling techniques.

(3) Infrastructure limitations: EWS require a range of infrastructure, including sensors, communication networks, and data processing systems. In some areas, particularly in developing countries, the infrastructure required for an effective EWS may not be in place or may be inadequate.

(4) Cost: The development and implementation of an effective EWS can be expensive, particularly in areas with limited resources. This can be a major challenge for many developing countries, which may not have the financial resources to invest in a comprehensive EWS. Many of the early flood warning system relies on real-time simulation of flood due to rain or breach of hydraulic structure; however, simulation time is considerably high, which makes the system inefficient. UrbanFlood EU FP7 project or Virtual Dike Project, which is an ambitious project from Europe, requires in situ monitoring and simulation, which sometime causes difficult to disseminate the flood warning system in real time.

24.2   Requirement of Ideal Early Flood Warning System

While flood simulation models can be an important tool for early flood warning systems (EWS), it is possible to develop an effective EWS that does not rely on simulation models. Some of the ideal characteristics of an early flood warning system that does not require flood simulation include the following:

1. Early detection: The EWS should be able to detect the onset of floods at an early stage, allowing for early warning and preparedness actions.
2. Scalability: The EWS should be scalable to different geographical areas and populations at risk, from small communities to large cities even at the country level.
3. Reliability: The EWS should be reliable, with a low rate of false alarms and missed events.
4. Accessibility: The EWS should be accessible to all, regardless of location, language, or disability. The warning messages should be easily understandable and available in the local language.

5. Sustainability: The EWS should be sustainable, with long-term planning and maintenance and with the capacity to adapt to changing conditions, such as climate change.
6. Integration with emergency response: The EWS should be integrated with emergency response plans and procedures, enabling an effective response to a flood event.
7. Cost-effectiveness: The EWS should be cost-effective, with a balance between the cost of implementation and the benefits of reducing flood damage and loss of life.
8. Community engagement: The EWS should engage with communities at risk, encouraging community participation in the development and implementation of the system, as well as public education and awareness campaigns to increase preparedness.
9. Real-time monitoring: An effective EWS should include real-time monitoring of rainfall, river levels, and other key indicators to provide timely warnings of potential flood events.
10. Historical data analysis: Historical data can be a valuable source of information for predicting future flood events. An EWS that analyzes historical data can help to identify patterns and trends that may indicate an increased risk of flooding.
11. Multi-hazard approach: An EWS that takes a multi-hazard approach can provide warnings for a range of potential hazards, including flash floods, river floods, and coastal flooding.
12. Community engagement: An effective EWS should engage with communities at risk to ensure that warning messages are understood and acted upon. This may involve the use of multiple communication channels, including social media, radio, and text messages.
13. Timely and accurate warnings: An effective EWS should provide timely and accurate warnings of potential flood events, with sufficient lead time to allow people to take necessary actions to protect themselves and their property.

In the present study, a scalable, reliable, and sustainable early flood warning system has been proposed, which is based on sensor equipment, data communication, and visualization technologies integrated with artificial intelligence.

24.3   Early Flood Warning System

AI-based proposed early flood warning system consists of several components as shown in Fig. 24.1, including the development of a hydrologic and hydraulic model, the use of artificial intelligence (AI) to develop flood maps, and the dissemination of these maps via mobile devices. The first component of your system involves the development of a hydrologic and hydraulic model. This involves collecting and analyzing data on various factors that contribute to flooding, such as rainfall, topography, and river flow. Once the data is collected, it is used to develop models

Fig. 24.1 Early flood warning system flow diagram

that simulate various scenarios and predict which areas are most likely to be affected by flooding. By simulating multiple scenarios, system can provide more accurate and reliable flood warnings.

The second component of this system is the use of artificial intelligence to develop flood maps. Once the hydrologic and hydraulic models have been developed, AI model will be trained for all the scenarios that is capable of producing the flood maps. These maps indicate the depth and specific areas that are likely to be flooded based on the data collected by the rainfall and reservoir level sensors. In addition to quick result production, using AI in your early flood warning system has several advantages:

- Improved accuracy: AI algorithms can analyze complex and diverse data sets in real time to produce highly accurate flood maps and predictions. By using machine learning, the system can continually improve its accuracy as new data becomes available, resulting in more precise and reliable warnings.
- Scalability: AI-based systems can be easily scaled to cover large areas and populations, making it possible to provide timely warnings to a wide range of people. This is especially important in areas with high population densities or where flood risk is particularly high.
- Customization: The AI-based model can be customized to suit the specific needs of a particular area or situation. The system can take into account factors such as topography, land use, rainfall patterns, and river flow rates, providing accurate and tailored predictions that reflect the unique characteristics of the area.
- Cost-effectiveness: Once the initial investment is made, an AI-based early flood warning system can be very cost-effective to operate. Since the system is automated, there is no need for a large workforce to monitor and maintain the system, which can result in significant cost savings over time.

- Real-time monitoring: AI-based systems can provide real-time monitoring of flood conditions, allowing for immediate responses to changing conditions. This can help to minimize the impact of floods and reduce the risk of property damage and loss of life.

The final component of this system involves the dissemination of these maps via mobile devices. Once a given scenario is fed into the system, the AI model selects the appropriate empirical model and generates the flood maps, which are then sent to mobile devices in the affected areas. This allows individuals and communities to take action to protect themselves and their property before the flood occurs.

There are several advantages to your proposed early flood warning system. First, the use of hydrologic and hydraulic models allows for more accurate predictions of which areas are likely to be affected by flooding. Second, the use of AI-based models to develop flood maps can provide more detailed and accurate information about the depth and specific areas that are likely to be flooded. Finally, the dissemination of these maps via mobile devices allows for more rapid and widespread dissemination of flood warnings, allowing individuals and communities to take action to protect themselves and their property.

24.4   Functionality of Integrated Mobile Application in Early Flood Warning System

The mobile application in your early flood warning system can be a game changer in several ways.

Firstly, the mobile application can provide real-time notifications and updates to residents in flood-prone areas, which can help them to take timely and appropriate action to protect themselves and their property. By using geolocation-based message transmission, the system can send targeted alerts to specific areas that are most at risk, ensuring that the right people receive the right information at the right time. Secondly, the mobile application can enable residents to access up-to-date flood maps and other relevant information, such as evacuation routes and emergency contact numbers, from their mobile devices. This can help to increase awareness and preparedness among residents and can help them to make informed decisions about how to respond to flood warnings. Thirdly, the mobile application can provide a means for residents to report flood-related incidents and share information with other residents and authorities. This can help to improve coordination and communication during a flood event and can facilitate a more effective response. Process flow of integrating with the AI model with the AI is shown in the Fig. 24.2. Flooding can occur at any location mainly due to rain, rain and release from the reservoir, or excess release from the reservoir including breach. Considering these variables different scenarios will be generated making possible combinations with different rainfall and release data. For each scenario, hydrologic and hydraulic models were developed to assess the flood damage. Area of interest will be divided into small
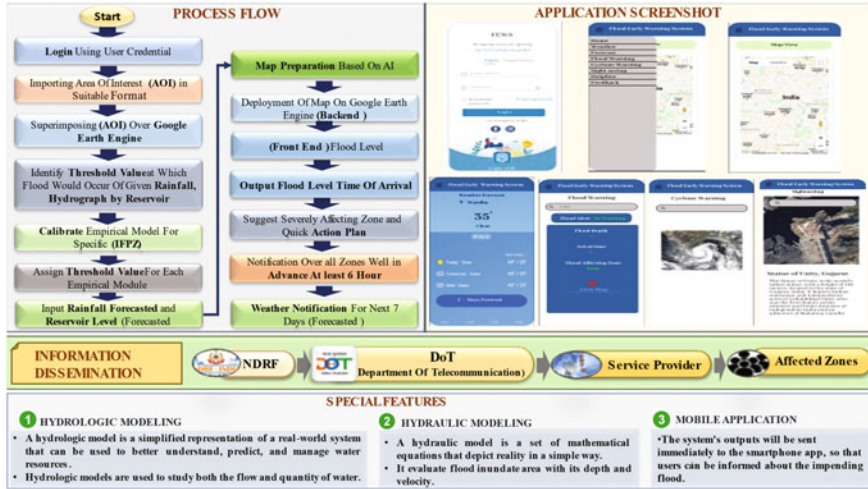
Fig. 24.2 Process flow of mobile application

grids, and each grid will store the information such as input variables (rainfall, reservoir level, initial moisture, and lateral flow if any) and flood depth. Once the assessment is done, scenarios respective to the variable combinations are saved and used for AI model training. AI model will be capable of giving the flood depth and generating flood map from the saved input data at the grids. AI model is trained and validated for each scenarios. Here, AI will have tree architecture so as to suite best for the different scenarios. A real-time assessment will be carried out for each 5 min to 1 h frequency in the background of the system. Background system will be accessing the rainfall data from the IMD forecast and sensor data such as reservoir level land moisture from the field through Internet of Things (IoT).

Once the anomalies detected by the system, which will probably cause the flood, first message will be delivered to the responsible authoritarian to assess the situation, and once authoritarian accepts the message produced by the system, message will be disseminated to all mobile user through messaging service and notification through mobile app.

24.5 Conclusions

The early flood warning system (EFWS) developed in this study is a game-changer for mitigating the negative impacts of flooding in flood-prone areas. The system takes a scenario modeling approach to predicting accurate results and does not rely on traditional flood simulation methods. By integrating advanced technologies like AI and mobile applications, the EFWS can provide timely and accurate information to people in flood-prone areas, allowing them to take necessary precautions to stay

safe during a flood. The scenario modeling approach considers multiple factors such as rainfall intensity, water level in reservoirs, initial moistures and lateral flow to sites, providing a more comprehensive prediction of the probable flood-prone areas in a basin or city. The AI-based flood map generation component utilizes grid-based models to create accurate predictions of flood depths, which can be integrated with mobile application to provide personalized flood maps, emergency resources, and two-way communication with users.

The EFWS provides several advantages over traditional flood warning systems, including improved accuracy, scalability, customization, cost-effectiveness, and real-time monitoring. The system can be tailored to suit the specific needs of a particular area, and the AI algorithms can analyze complex data sets to provide highly accurate predictions. This approach is cost-effective, and the real-time monitoring allows for immediate responses to changing conditions, reducing the impact of floods and mitigating the risk of property damage and loss of life.

References

Alfieri L, Salamon P, Pappenberger F, Wetterhall F, Thielen J (2012) Operational early warning systems for water-related hazards in Europe. Environ Sci Pol 21:35–49

Baudoin MA, Henly-Shepard S, Fernando N, Sitati A (2014) Early warning systems and livelihood resilience: exploring opportunities for community participation

FLOODsite. http://www.floodsite.net, Flood Control 2015 http://www.floodcontrol2015.com, The International Levee Handbook project http://www.leveehandbook.net/about-project.asp

Golian S, Saghafian B, Maknoon R (2010) Derivation of probabilistic thresholds of spatially distributed rainfall for flood forecasting. Water Resour Manag 24:3547–3559

Golnaraghi M (2012) An Overview: building a global knowledge base of lessons learned from good practices in multi-hazard early warning systems. Institutional Partnerships in Multi-Hazard Early Warning Systems: A Compilation of Seven National Good Practices and Guiding Principles, 1-8

Hallegatte S (2012) A cost effective solution to reduce disaster losses in developing countries: hydro-meteorological services, early warning, and evacuation. World Bank policy research working paper, 6058

Hellmuth, M. E., Moorhead, A., Thomas, M. C., & Williams, J. (2007). Climate risk management in Africa: Learning from practice

Krzhizhanovskaya VV, Shirshov GS, Melnikova NB, Belleman RG, Rusadi FI, Broekhuijsen BJ et al (2011) Flood early warning system: design, implementation and computational modules. Procedia Comput Sci 4:106–115

NDMA India (2020) National Disaster Management Authority (**NDMA**) Government of India https://ndma.gov.in/Mitigation_Preparedness/FRMS

Perera D, Seidou O, Agnihotri J, Rasmy M, Smakhtin V, Coulibaly P, Mehmood H (2019) Flood early warning systems: a review of benefits, challenges and prospects. UNU-INWEH, Hamilton

UNEP (2012) Early warning systems: a state of the art analysis and future directions. United Nations Environment Programme (UNEP)

UNISDR (2015) Making development sustainable: the future of disaster risk management. Global assessment report on disaster risk reduction

World Bank (2011) Thai Flood 2011: Rapid Assessment for Resilient Recovery and Reconstruction Planning. © World Bank, Bangkok. http://hdl.handle.net/10986/26862

Webster P (2013) Improve weather forecasts for the developing world. Nature 493:17–19. https://doi.org/10.1038/493017a

Zommers Z, Singh A (eds) (2014) Reducing disaster: Early warning systems for climate change. Springer, Cham

Chapter 25
Sustainability Through Integrated Resilience and Risk Management: Rivers and Disasters in Changing Climate

Fatima Amin, Mushtaq Ahmad Dar, and Anil Kumar Gupta

Abstract The world over the years has been subject to various significant natural hazards and has experienced their catastrophic impacts. Recurring hydro-meteorological occurrences tend to impact individuals unfavorably and result in severe economic loss compared to other natural disasters. Climate change will impose a wide array of stressors on urban areas. River flooding is an annual phenomenon in most of the big rivers. River system morphology is a significant study area for research on higher and lower hydrological extremes and their effects. River systems have undergone a massive transformation since the Anthropocene. Extreme events are part of the natural environment creating diverse habitats through processes of erosion and deposition. Human-induced climate change is predicted to increase average temperature, leading to an increase in variables, so a well-developed sustainable approach to managing risks is needed for the integrity of nature.

Keywords Resilience · Sediment · SDGs · Flood Risk Management

25.1 Introduction

The world over the years has been subject to various significant natural hazards and has experienced their catastrophic impacts. Recurring hydro-meteorological occurrences tend to impact individuals unfavorably and result in severe economic loss compared to other natural disasters (Saikumar et al. 2022). The Asia Pacific region,

F. Amin (✉)
Environment, Climate and Disaster Risk Management (ECDRM) National Institute of Disaster Management, (NIDM) Ministry of Home Affairs, Govt. of India, New Delhi, India

M. A. Dar
Department of Education, Government of Jammu and Kashmir, UT, India

A. K. Gupta
Centre for Excellence on Climate Resilience, Environment Climate and DRM Division, National Institute of Disaster Management, New Delhi, India

with its geographical location, has the highest risk of disasters in the world. From 1970 to 2011, approximately two million people have been killed due to natural hazards accounting for 75% of the global fatality. The International Decade of Natural Disaster Reduction (IDNDR) term also concluded that for mitigation and prevention of natural disasters to be achievable, environment-friendly practices must be entailed in sustainable advancement.

Climate change will impose a wide array of stressors on urban areas. Water stress, water-related hazards, and water quality pose increasing challenges to modern society. Some of these will likely involve the direct and easily understood impacts of storms, sea level rise, temperature change, and extreme climatic events, but others will involve indirect effects that reverberate through the systems, namely, energy, transport, communications, etc. that urban areas depend on. Planning for urban resilience allows cities to prepare for and respond to these stressors. Resilience can be defined as the "ability of a system, community, or society exposed to hazards to resist, absorb, accommodate, and recover from the effects of a risk in a timely and efficient manner by preserving and restoring its essential basic structures and functions" (UNISDR 2009). Urban resilience generally refers to the ability of a city or urban system to withstand a wide array of shocks and stresses (Gupta et al. 2023).

Climate change has significant impacts on sediment transport in rivers. Changes in precipitation patterns and temperature can alter the hydrological cycle, leading to changes in water availability and runoff. This can cause changes in sediment transport, as increased runoff can increase sediment loads and transport rates. Additionally, changes in vegetation patterns and land use can affect sediment transport by altering erosion rates and vegetation cover. Climate change can also exacerbate extreme events, such as floods and droughts, which can cause significant changes in sediment transport. Overall, the impacts of climate change on sediment transport in rivers are complex and varied, and further research is needed to fully understand the implications of these changes.

Operationalizing urban resilience is a complex, even conflicting subject. Because of its multidisciplinary origin and many approaches, resilience meanings sometimes need to be revised. This contradiction is because resilience belongs to many disciplines such as physics, psychology, and ecology. This conceptual vagueness makes using resilience and its integration into risk management complex. Despite its growing use in official communications, the concept's operational relevance is constantly being questioned.

In India, earthquakes, floods, cyclones, drought, tsunami, landslides, and avalanches are significant hazards. Almost 85% of India's area is vulnerable to one or multiple risks (Purkayastha and Afzal 2022). Approximately 60% of the landmass is prone to earthquakes of various intensities; over 40 million hectares are prone to floods; about 8% of the total area is prone to cyclones, and 68% is susceptible to drought in the country. More than 50 million people are affected by droughts annually. In the decade 1990–2000, an average of about 4344 people lost their lives, and about 30 million people were affected by disasters every year. India's long coastline of 7516 kilometers is exposed to nearly 10% of the world's tropical

cyclones. River flooding is an annual phenomenon in most of the big rivers (Aamir et al. 2022). In the hilly terrain of India, including the Himalayas, landslides have been a major and widely spread natural disaster that often strike life and property and occupy a position of significant concern. Forest fire, though not causing much loss of human life, is a major hazard for forest cover in the country. As per the Forest Survey of India report, 50% of the country's forest cover is fire-prone, out of which 6.17% is prone to severe fire damage causing extensive loss to forest vegetation and the environment.

25.2 Introduction to Rivers and Sediments

River system morphology is a major study area for research on higher and lower hydrological extremes and their effects (Pourshahbaz et al. 2022). River pathways have a direct bearing on flood risk because they influence the speed and attenuation of the flood wave as it passes through the drainage network and controls the local relationship between discharge and water level during a flood event (Lane and Thorne 2007).

As defined, changes in the morphology of catchment areas and the river channel and sediment load affect water conveyance in rivers during floods (Afzal et al. 2021). The overall risk results of flooding during higher hydrological extremes and the risk and effects of water scarcity during low hydrological extremes are a combined effect of topographical, morphological, hydrological, and geological and management of the catchment areas (Schumm 1969). The morphological characteristics of river systems respond to changes in the input regimes of sediment (Qs) and water (Qw) (Schumm 1969; Shivashankar et al. 2022).

25.2.1 Key Issues of Resilience and Sustainability

With the 2030 Agenda for Sustainable Development, the United Nations has established a catalogue of 17 Sustainable Development Goals (SDGs) to achieve a better and more sustainable future for all by 2030. One crucial aspect, formulated as Goal 6, is ensuring the availability and sustainable management of water and sanitation for all. Achieving SDG 6 represents a challenge for planning, governance, and water management, especially in prosperous water-scarce regions, where water demand rises steadily and outgrows sustainable supply (Bondy et al. 2021) (Fig. 25.1).

According to S.N Lane & C.R. Thorne, There is considerable uncertainty in flood risk change as a result of four sources:

Integrated water management concept for achieving SDG -6
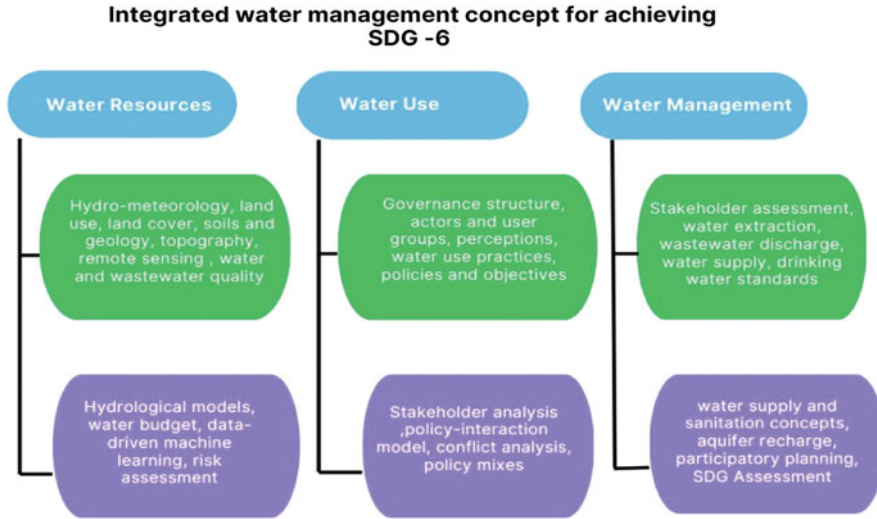
Fig. 25.1 Water resources water use and water management

1. Degree and rate of change in flow and sediment regimes
2. Nature, extent, and rate of morphological response in terms of deepening and widening
3. The impact of morphological responses on channel conveyance capacity and flood level and future probabilities
4. Impact of morphological adjustments on the condition of flood defenses

In the Indian subcontinent, all these factors, along with the vast geographical, climatic, and management components, the uncertainty may be higher, and hence, risks of various types of disaster occurrences during higher and lower hydrological extremes (both) are higher.

25.2.2 Challenges of River Systems

River systems have undergone a massive transformation since the Anthropocene. The natural properties of river systems have been drastically altered and reshaped, limiting the use of management frameworks, their scientific knowledge base, and their ability to provide adequate solutions for current problems and those of the future, such as climate change, biodiversity crisis and increased demands for water resources.

Water management has been pivotal in human evolution and fundamental in societal advancement, for example, the development of agriculture and the establishment of permanent settlements. However, with increasing economic and social demands, river systems have undergone dramatic, worldwide, and often irreversible

transformations in geomorphic and eco-hydrological properties (Hossain and Mertig 2020), culminating in the era of the Anthropocene (Waters et al. 2016). As the fundamental properties and interactions within riverine landscapes have changed, for example, the connectivity patterns, the majority of large river systems can no longer be considered natural (Crook et al. 2015).

25.2.3 Rivers and Catchment: The Nexus

Agricultural land management affects catchment runoff, river vegetation affects conveyance, and relative sea level affects the frequency with which land adjacent to coasts and estuaries is flooded (Thorne et al., 2007). Agricultural land management is an essential factor in the management of flood risks during higher and lower hydrological extremes. Agricultural land management in catchment areas defines the level of infiltration of rainwater and runoff, which in turn defines the severity of erosion and sediment deposition in the lower part of a river basin. Well-maintained and well-planned agricultural land management will help in both good crop production and low flood risk downstream. Coastal and fluvial flooding affects the physical characters of the environment, coastal riverine and floodplain ecosystems and species living in these ecosystems. Contrarily, regular flooding is vital for the survival of these ecosystems; for example, wetland ecosystems around river channels are fed and maintained by inundation.

25.2.3.1 Causes of Sedimentation in Low-Lying Areas

Erosion leads to snow avalanches and glacier slip that causes flash floods, and other causes heavy rainfall, and rapid snow melting is due to increased temperature (high intensity and frequency due to CC). Due to all these activities, abraded and eroded material from upper reaches is washed down and deposited in low-lying areas of youth and mature stages of the river basin. This causes to swallowing of river basins downstream, which along with the increase in encroachment in floodplain areas due to human activities (Settlements, roads and etc.) forces waters during floods to go sideways, causing lateral erosion, and hence at times, damage to croplands, roads, bridges, forest areas, and green reservoirs. This causes loss of life and property, economic losses on a large scale, food insecurity, and damage to aquatic life. In some cases, especially during the second stage, when the river water flows toward less sloppy terrain and deposits sediments, lateral erosion is more rapid, causing more damage in these areas.

Contrarily, unplanned mining in and around river basins, which is common throughout the country most of the time (non-flooding times) deepens the river bed, which enhances the dragging of the sediments from upper areas during high flow. This, in turn, leads to an increase in the probability of erosion activities like landslides, mud slips, etc., due to an increase in the steepness of slopes and

gravitational pull*. It also affects the supply of water to croplands through irrigation canals and streams, especially during low rainfall/snowfall periods. Sometimes, it can result in the decline of the water table and hence the availability of subsurface water through tube wells, wells bore wells, etc. Changing climatic conditions further worsen these causes and, along with the rise in average temperature and low rainfall/snowfall, lead to severe drought, thus affecting crop production and food supplies (Das et al. 2021a; b, 2022). All these conditions invite high investment in farmlands by farmers, which further destroys their economy and badly affects the agriculture sector.

25.2.4   Erosion and Bed Load

When shear stress exerted by a river on its bed exceeds a threshold, superficial sediment is entertained by the flow. Moderate values of rolling, sliding, and bouncing while gravity maintains them close to the bed surface. This so-called bed load transport deforms the bed, and the resulting interaction between flow and sediment transport generates a beautiful variety of river-shaped and coastal morphologies (Lajeunesse et al. 2017).

A complete description of sediment transport requires a theoretical formulation of the velocity distribution of particles F (v) and its dependency on the flow conditions.

The erosion deposition model is a simple model treating the bed load layers as a uniform reservoir of independent particles moving at velocity V. The equation of the model is:

$$q_s = nV$$

where q_s is the average sediment (bed load) transport rate, V is the average particle velocity, and n is surface concentration to the flow condition.

It is the erosion of the sediment in the river basin, which supplies bed load and is higher during higher hydrological extremes of flooding and then the deposition of this bed load in the lower parts of the river system where the intensity of flow velocity decreases. The process changes the river morphology and affects the river ecosystem. During lower hydrological extremes, the water flow is much less and may disappear in loosely deposited bed load sediment as infiltration and percolation are high, leading to water shortages. Based on detailed research and inputs of E-D and other models, better planning of our river systems can be developed for sustainable ecological development and long-term goal achievement in these river systems.

25.3 Impact of Climate Change on Mountains and Waters

Climate change is a phenomenon that has become a major issue globally due to its significant impact on the environment. One of the areas that are greatly affected by climate change is the mountains and waters. Mountains and water are crucial ecosystems, and their environmental impact is profound. The changing climate has been causing significant changes in the ecology of mountains and water systems, negatively impacting the environment, wildlife, and human communities that depend on them.

One of the most significant impacts of climate change on mountains is the melting of glaciers. Glaciers are an essential water source for many rivers and lakes globally, and their melting directly impacts the water supply for millions of people. The melting of glaciers can lead to increased water runoff, which can cause floods, landslides, and other natural disasters. Additionally, the melting of glaciers can also cause a rise in sea levels, leading to the destruction of coastal communities and the loss of critical habitat for marine life.

Climate change is also causing changes in mountainous regions' temperature and precipitation patterns. These changes directly impact the ecology and wildlife that reside in these areas. For instance, the warmer temperatures have caused an increase in the number of invasive species that can survive in these environments. These invasive species can displace native plants and animals, leading to the loss of biodiversity. Additionally, the changing precipitation patterns can lead to droughts, wildfires, and other natural disasters, negatively impacting the environment and human communities that rely on these areas for their livelihoods (Treesa et al. 2017). Moreover, the climate change is expected to alter the sub-daily patterns of precipitation resulting in intensification of storms (Das and Umamahesh 2016; Manikanta et al. 2023).

The impact of climate change on water systems is equally significant. Changes in temperature and precipitation patterns can decrease the quality and quantity of water available for human consumption (Das et al. 2022a, 2023). Additionally, climate change can cause rising sea levels, leading to saltwater intrusion into freshwater systems. This intrusion can cause the loss of habitat for freshwater species and lead to soil salinization, making it difficult for crops to grow.

Another significant impact of climate change on water systems is the increased frequency and severity of floods and droughts. These events can cause damage to infrastructure, displace communities, and lead to food shortages. In areas where water is scarce, droughts can be particularly devastating. Water scarcity can lead to conflicts between communities and cause a decline in economic activity.

Hydrological extremes include river water flow's upper and lower levels (Extremes). These two conditions may occur periodically/non-periodically in the rivers depending upon the aforementioned reasons, like rainfall/snowfall and other climatic causes /disturbances. The fluctuation of these two extremes affects and continuously keeps changing the geomorphology of the landscape in the river basin in all its stages differently. The drastic climatic changes make the fluctuation pattern

of upper and lower extremes of water flow more complicated spatially and temporally, making planning challenging to contain floods and droughts, erosion and sedimentation, development and land-use pattern, etc., for administration.

The country's rapid population increase demands more settlement areas, agricultural land, and other amenities like industries, roads, and construction materials. Due to rapid urban and rural settlement expansion, pressure on land around river basins has increased too much. Unplanned expansion of these settlements and other human activities leads to encroachment of drainage areas around the river basins, which becomes an obstruction to drainage during higher extremes of water flow and leads to a rise in water level around the floodplains and low-lying areas of the river basin posing a danger to submergence of settlements and other amenities during floods, for example, 2014 floods in Kashmir valley, which almost submerged the Srinagar City and causing massive damage to south Kashmir.

On the other hand, lower hydrological extremes caused due to low rainfall and snowfall for long durations cause droughts and water scarcity affecting all spheres of life, including drinking water supply, irrigation and industrial water supply, etc. (Shukla et al. 2019a, 2019b). It damages the agriculture and horticulture sector and thus affects the economy on at large scale. For example, the low rainfall and snowfall in Pir-Panjal range continuously for a few years, around 1999–2002, caused severe drought in Karewas of Kashmir and damaged apple orchards and other crops in these areas on a large scale affecting the economy of the farming sector badly. It took decades to renew these apple orchards up to full growth with huge inputs of time, money, and effort.

25.4 Integrated Risk and Vulnerability: Understanding the Relationship

Integrated risk and vulnerability are two concepts that are closely related to each other. Both concepts are essential in understanding the challenges communities and countries face in dealing with natural and human-made disasters.

Integrated risk refers to the likelihood of an event or hazard and its potential consequences or impacts. This concept considers the environment's complexity and the interconnectedness of various systems that can be affected by a hazard. Integrated risk assessment involves identifying the hazards, assessing their likelihood and potential impact, and developing strategies to mitigate and manage the risks.

Vulnerability, on the other hand, refers to the susceptibility of a community or system to the impacts of a hazard. A range of factors, including social, economic, and environmental factors, can influence vulnerability. For instance, socially marginalized or economically disadvantaged communities may be more vulnerable to the impacts of a hazard. Vulnerability assessment involves identifying the factors contributing to vulnerability and developing strategies to reduce vulnerability and build resilience.

The relationship between integrated risk and vulnerability is that vulnerability influences integrated risk, and integrated risk can also exacerbate vulnerability. For example, communities that are vulnerable to the impacts of a hazard may be more likely to experience the full consequences of a hazard. They may need more resources or capacity to prepare for and respond to the hazard. Conversely, an event or hazard can increase vulnerability by causing damage to infrastructure, displacing communities, or disrupting economic activity.

It is essential to consider both concepts together to manage risks effectively and reduce vulnerability. Integrated risk assessment should consider the factors that contribute to vulnerability, and vulnerability assessments should consider the potential impacts of hazards. Combining the two concepts makes it possible to develop strategies that effectively reduce the likelihood and impacts of hazards while also building resilience in vulnerable communities.

25.5 Sustainability of River Systems

Stresses and shocks can significantly impact the long-term sustainability of water resources. Stresses refer to persistent pressures on water resources, such as overexploitation, pollution, and climate change, while shocks are sudden and unexpected events, such as natural disasters or infrastructure failures.

One of the most significant impacts of stresses and shocks on water resources is the depletion of water resources. Overexploitation of groundwater resources can lead to declining water tables, which can have long-term impacts on water availability for drinking, agriculture, and industry (Agrawal et al. 2021; Hinge et al. 2022). Water pollution can also make water resources unusable, affecting human health and ecosystems. Stresses and shocks can also impact the quality of water resources. For example, droughts and floods can cause changes in water temperature and chemical composition, negatively impacting aquatic life and the quality of water for human consumption. Pollution and other sources of contamination can further degrade the quality of water resources, making it more challenging to use and treat for human and industrial needs.

Another impact of stresses and shocks is the loss of ecosystem services provided by water resources (Sharma et al. 2022). For instance, wetlands provide critical services such as flood mitigation, water filtration, and habitat for aquatic species. Pollution, habitat degradation, and other stresses can lead to the loss of these critical ecosystem services, which can have long-term implications for human and environmental sustainability. Stresses and shocks can also exacerbate existing social and economic inequalities related to access to water resources. For example, droughts can disproportionately affect low-income communities, which may not have access to sufficient water supplies or the resources to adapt to water scarcity. Floods can also impact marginalized communities, which may lack access to adequate infrastructure and resources to recover from the impacts of the disaster (Mangukiya and Sharma 2022).

Rivers are critical freshwater resources that support numerous ecosystems, provide habitats for wildlife, and supply water for human and industrial use. However, many rivers worldwide face significant challenges, including pollution, habitat degradation, and overexploitation. Renewability and rejuvenation of rivers are critical for their long-term sustainability, and several strategies can be used to achieve these goals.

Promoting sustainable water management practices is one of the most effective strategies for renewing and rejuvenating rivers. This involves ensuring that water resources are used efficiently, reducing pollution, and conserving water resources. Sustainable water management practices include reducing water demand, promoting water conservation, and protecting riverine ecosystems. Another effective strategy for renewing and rejuvenating rivers is to restore degraded river habitats. This involves restoring the natural flow of water, improving water quality, and restoring degraded ecosystems. River habitat restoration can involve removing dams and other barriers, reducing the impact of erosion, and planting vegetation along riverbanks.

Additionally, community engagement is essential for the renewal and rejuvenation of rivers. Communities living near rivers are critical in promoting sustainable river management practices and protecting riverine ecosystems. Local communities can engage in river management through programs encouraging public participation, education, and outreach. Water governance is also critical for the renewal and rejuvenation of rivers. This involves the development of policies and regulations that promote sustainable river management practices, protect water resources, and provide access to water resources for all stakeholders. Effective water governance requires collaboration between various stakeholders, including government agencies, communities, and the private sector.

Investments in infrastructure and technology are critical for the renewal and rejuvenation of rivers. For instance, the construction of water treatment plants, sewage treatment plants, and other infrastructure can improve water quality and reduce pollution. Using new technologies such as remote sensing and geographic information systems can help monitor and manage riverine ecosystems.

Water is critical in achieving sustainable development, as it is essential for human and environmental well-being. Access to clean and safe water is a fundamental human right and essential for meeting basic needs such as drinking, hygiene, and sanitation. Moreover, water is essential for agriculture, energy production, industry, and transportation, making it a vital resource for economic development.

However, water availability is becoming increasingly scarce due to population growth, urbanization, climate change, and pollution. The scarcity of water resources is already affecting many regions of the world, causing social and economic disruptions and threatening the environment's sustainability. Therefore, it is essential to ensure the sustainable management of water resources to achieve long-term development sustainability.

One of the ways to ensure the sustainable management of water resources is through water conservation and efficiency measures. This involves reducing water demand by adopting sustainable water management practices such as water recycling, rainwater harvesting, and efficient irrigation techniques. These measures

can help reduce water waste and ensure the efficient use of water resources, ensuring their availability for future generations.

Another way to ensure the sustainable management of water resources is through protecting and restoring aquatic ecosystems. Aquatic ecosystems play a vital role in regulating the water cycle, supporting biodiversity, and providing essential ecosystem services such as water filtration and flood control. Therefore, protecting and restoring these ecosystems can help maintain the availability and quality of water resources. In addition, promoting the equitable distribution of water resources is critical for achieving sustainable development. Ensuring all stakeholders have access to clean and safe water promotes social equity and reduces poverty. Moreover, the equitable distribution of water resources can promote regional stability, reduce conflicts, and foster cooperation between different stakeholders.

Effective water governance is critical for achieving sustainable development. This involves the development of policies and regulations that promote the sustainable management of water resources, ensure equitable access to water resources, and protect water resources from pollution and degradation. Effective water governance requires collaboration between various stakeholders, including government agencies, communities, and the private sector.

The Sustainable Development Goals (SDGs) related to water are crucial for achieving sustainable development and achieving these goals requires a comprehensive and collaborative approach. The following are some strategies that can be used to achieve SDGs related to water:

Increase access to safe and clean water: One of the SDGs' main goals is to ensure universal access to safe and clean water. To achieve this goal, governments, international organizations, and private entities need to invest in water infrastructure, such as water treatment plants, and distribution networks. This should be done to ensure access to water for all people, regardless of their socioeconomic status.

- Improve sanitation: Another fundamental goal related to water is to improve sanitation, which is critical for reducing waterborne diseases and improving public health. This can be achieved by constructing sanitation facilities, such as toilets and waste treatment plants, and public education campaigns to promote hygiene and safe sanitation practices.
- Protect water resources: To ensure the availability of clean and safe water, it is essential to protect water resources from pollution and degradation. This can be achieved by implementing policies and regulations that regulate water use and ensure that industries and communities do not pollute water resources.
- Increase water-use efficiency: The efficient use of water is critical for achieving water-related SDGs, particularly in water-scarce regions. This can be achieved through the adoption of sustainable water management practices such as water recycling, rainwater harvesting, and efficient irrigation techniques.
- Promote integrated water resource management: Integrated water resource management involves coordinating water resources and considering ecological, social, and economic considerations. This approach helps ensure that water resources are managed sustainably, and it can also promote cooperation between

different stakeholders, such as government agencies, communities, and the private sector.

- Promote community participation: Communities living in areas where water-related SDGs are most challenging should be encouraged to participate in water management processes. Community participation helps ensure that water management strategies are culturally and socially appropriate and helps foster a sense of ownership and responsibility for water resources.

Relationship of prevention and recovery strategies with resilience and sustainability, etc. River Restoration: In the youth stage, embankments and abetments in a landslide and avalanche hazard areas can prevent sliding, causing effects on the river basin downward. The same is the case with mudflows. The construction of these protection walls should be well planned in relation to the geology and geomorphology of the area.

Rapid deforestation in the upper reaches of river basins drastically enhances erosion and landslide activity. Along with afforestation activities by relevant organizations, there is a need to protect existing plantations in forest and non-forest areas, predominantly hilly areas around river banks, on a priority basis as only this plantation cover can stop the soil erosion till new plants get mature and spread their roots fully and take over as the guards to soil erosion.

Nowadays, unplanned and illogical mining activities have increased too much in and around the river basins and expanded to the forest areas. It results in increased activity of erosion, landslide, tree felling, etc. These activities, along with other causes, affect the ecological balance of the area and enhance the already citied causes and impacts of hydrological extremes and river sediments.

Mining activities thus need to be done under regulations in a planned manner to be helpful in river restoration and prevention of ecological and environmental degradation.

While constructing road and rail links in hilly areas, tunnelling is preferred to cutting of slopes, which otherwise enhances land sliding and erosion risks on a large scale. This way plantation cover on these slopes can also be prevented and restored wherever possible. Combined, these activities will ultimately have lasting effects on the prevention of soil erosion and river restoration.

25.5.1 Flood Risk Management

Extreme floods are part of the natural environment and may have significant and long-lived environmental impacts (Hall et al. 2003). Factors that influence the impact of large floods include characteristics of flood preparedness regime, channel gradient, bed load characteristics (particle size etc.), the strength of the river bank, and the shape of channels.

Table 3.2 shows changes in flood flows and sediment discharge under different drivers and potential impacts on the form of natural river channels.

Table 25.1 Measures for flood risk

Measures to reduce the flood risk	Example measures
Reduce the physical hazard	Flood embankments/sea defenses
	River channelization
	Wash land storage
	Reservoir impoundment
	Catchment management
Reduce exposure to the hazard	Land-use planning
	Property-scale flood proofing
Reduce vulnerability to the hazard	Warning and insurance

Andrew R Watickson et al., in the topic, environmental impacts of future flood risks, have given in a table form examples of measures to reduce flood risks, which are reproduced here (Table 25.1).

The management plans to reduce flood risks during higher hydrological extremes may show good results if the measures shown in the table above and these measures can be explained and elaborated for better flood risk management and study purpose as well.

The principal reason for floods in the Indian sun continent lies in their natural ecological systems—the monsoon, the high sediment river systems, and the steep and higher erodible mountains, particularly of the Himalayan region (SAARC 1992).

The average rainfall of India is about 1150 mm, with variations in its vast geographical divisions. Nearly 80% of the rainfall occurs in the rainy season (SW monsoons) from June to September. Most of the floods also occur in this period. Thus, the rivers in the whole Indian subcontinent have high extremes of flow during these months and also carry most of the sediment load down to low-lying areas. Similarly, the geographical vastness, climatic turbulences, disturbances, and climatic changes cause low rainfall in various areas of the subcontinent. Sometimes, the monsoons bring low rains, and these factors result in low rainfall and hence water scarcity, and thus, rivers are at lower hydrological extremes. Droughts are common in some areas due to this. Of all SAARC countries, India is most affected by droughts, and most of the countries in the Indian subcontinent feel that their flood control management system are still inadequate (SAARC 1992 DM Report).

Flood management has included channel and floodplain morphology modification to increase conveyance, reduce flood levels, or contain higher flood elevations. Channel maintenance is also in use to reduce sediment accumulations or vegetation growth, channel realignment, and artificial channel from its flood plain.

Increasing water convergence or reducing storage capacity at a site in the river system increases flood peaches downstream, and habitual diversity at the site tends to decline and eliminate the natural connection between channel and floodplain and thus has substantial impacts on riparian and flood plain fauna and flora. Downstream changes in water flow and sediment load also impact ecosystem structure and function, while secondary ecological impacts are associated with changes in land use and water quality.

Along with the implementation actions to be taken for river restoration, some major activities for flood risk management can be taken up. Artificial check dames and hefty pounds, if constructed at feasible locations where the water during higher extremes of flow in river basins can be diverted into these, will lessen not only the impact of flooding in lower-lying areas but also enhance the stable supply of irrigation and drinking water during low hydrological extremes and dry spells. Banking of riverside plantation of these river banks and maintaining the river's flow capacity by proper planning also lowers the flood risks and thus helps in flood risk management in a more protracted planning manner.

25.5.2 Diversion Canals

Construction of extra canals other than the existing ones based on an in-depth study of the terrain and the landform of the river basin, which will lead and drain extra water to reservoirs at proper sites upstream and downstream, will also help in flood risk management for long-term planning. It will also help sustain water availability for drinking and irrigation purposes. Depending upon the geographical location, terrain geology and rock type. (Upstream), soil type, landforms, settlements, crop patterns, availability, and demand of mineral resources and their extraction and planning (Fig. 25.2).

25.5.3 Sustainable Development and Policies

Sustainable development is the concept of meeting the needs of the present without compromising the ability of future generations to meet their own needs. It requires balancing economic growth, social well-being, and environmental protection.

Fig. 25.2 Development and SDGs

Policies are essential for achieving sustainable development goals, as they provide a framework for guiding actions toward a sustainable future.

There are several policies that governments and organizations can implement to promote sustainable development. One such policy is the promotion of renewable energy sources such as wind, solar, and hydropower. These energy sources are sustainable, unlike fossil fuels, which are finite and significantly impact the environment. Governments can incentivize using renewable energy by providing tax credits, subsidies, and other financial incentives.

Another policy that promotes sustainable development is the adoption of sustainable land use practices. This involves protecting and preserving natural resources such as forests, wetlands, and other ecosystems. It also involves responsible land management for agricultural purposes and the prevention of soil erosion and land degradation. Governments can develop policies and regulations encouraging sustainable land use practices, such as zoning laws and environmental impact assessments.

Sustainable transportation policies are also essential for promoting sustainable development. This involves promoting public transportation, walking, and cycling as alternatives to private cars. Governments can develop policies prioritizing public transportation, such as building more bike lanes, sidewalks, and public transportation systems. This can help reduce greenhouse gas emissions and air pollution, contributing to climate change and negatively impacting public health.

Policies promoting sustainable consumption and production are also important for sustainable development. This involves reducing waste, promoting recycling, and encouraging the use of sustainable products. Governments can implement policies that incentivize sustainable production practices, such as green manufacturing processes and environment-friendly materials.

25.5.4 Conclusion and the Way Forward

Both higher and low hydrological extremes and its risk are affected by various river processes, including the sediment load carried by river water after it is eroded and transported through the channel. The sediment deposition affects the conveyance capacity of the channel and results in lateral erosions and flood risks.

On the other hand, the channel depth and no sediment enhance the erosion of the stream bed and its banks. Thus, a long-term planning considering both factors is needed for river restoration.

25.5.5 Traditional Harvesting Techniques

The ancient civilization had progressed in many ways, including innovative and judicious water harvesting methods. Community-level systems like big ponds, mini

lakes, reservoirs, and canals collected rainwater during heavy rains and preserved it and supplied water during dry periods. These reservoirs and other water bodies were developed at feasible spots in farmlands, for example, a Karewa (Wular Lake) of J&K UT and elsewhere in the country. This prevented runoff and hence soil erosion also. Thus, less sediment was carried downstream hence keeping the river ecosystem stable.

However, in past times, these systems have eroded, and people encroached upon these systems, thus deteriorating the fragile landforms and river ecosystem. Rapid population increase affects many aspects like land use and cropping patterns, rendering these systems ineffective.

Various governments are already taking measures to revive these traditional water harvesting structures, but the climatic, ground, and other factors still need to support the new plans fully. So, there is a need to research more on the methodology and come up with better solutions, which may include fully adopting old traditional ways of water harvesting so that extreme hydrological flows are checked and a balanced flow remains stable in river channels, which will help sustainable growth of agriculture, river ecosystem, water facilities, etc.

Afforestation on a large scale in the forest and non-forest areas and identification of infiltration zones in these areas, if protected, will help reduce runoff and recharge groundwater. Recharging groundwater will renew the springs that once flourished in most areas. Planned ways and judicious use of mined resources from the river and its catchment areas are much needed, which can help maintain the channel depth and other characteristics to avoid swallowing or much deepening of river beds and streams. This will help a long way in balancing the fragile river ecosystems.

25.5.6 Research and Modeling

The primary purpose of modeling is to gain insight into physical processes by solving an equation devised to predict the evolution of variables and describe the system's dynamics.

Based on the geographical location and hence the topography and other relevant factors of a river system, modeling may be done for every river basin. Based on detailed research of the inputs for modeling, the best models may be chosen feasible for maintaining the river ecosystem in a particular area.

Sediment transport in rivers is a complex process that is influenced by various climatic, hydrological, geological, ecological, and human factors. Climate change can significantly affect sediment transport through changes in precipitation patterns, temperature, hydrological cycle, water availability, runoff, erosion rates, vegetation cover, and extreme events like floods and droughts. The impacts of sediment transport in rivers are complex and varied, affecting human and natural systems in both positive and negative ways. Effective management of sediment transport under hydrological extremes induced by climate change requires a comprehensive understanding of the complex interactions between climate, hydrology, geology, ecology,

and human activities, as well as the implementation of a range of management strategies that promote the resilience of human and natural systems.

References

Aamir M, Ahmad Z, Pandey M, Khan MA, Aldrees A, Mohamed A (2022) The effect of rough rigid apron on scour downstream of sluice gates. Water 14(14):2223. https://doi.org/10.3390/w14142223

Afzal MS, Holmedal LE, Myrhaug D (2021) Sediment transport in combined wave–current seabed boundary layers due to streaming. J Hydraul Eng 147(4):04021007. https://doi.org/10.1061/(ASCE)HY.1943-7900.0001862

Agrawal P, Sinha A, Kumar S et al (2021) Exploring artificial intelligence techniques for ground-water quality assessment. Water (Switzerland) 13. https://doi.org/10.3390/w13091172

Bondy J, Brauer F, Cardona J, Chamorro J, Fischer T, Hahne L, Hinz S, Hügler M, León CD, Keller S, Zahumensky Y (2021) Integrated water management solutions in the Lurín Catchment, Lima, Peru: supporting United Nations' Sustainable Development Goal 6: final report of the joint project TRUST

Crook DA, Lowe WH, Allendorf FW, Erős T, Finn DS, Gillanders BM et al (2015) Human effects on ecological connectivity in aquatic ecosystems: integrating scientific approaches to support management and mitigation. Sci Total Environ 534:52–64

Das J, Umamahesh NV (2016) Downscaling monsoon rainfall over river godavari basin under different climate-change scenarios. Water Resour Manag 30:5575–5587. https://doi.org/10.1007/s11269-016-1549-6

Das S, Das J, Umamahesh NV (2021a) Nonstationary modeling of meteorological droughts: application to a region in India. J Hydrol Eng 26:5020048

Das S, Das J, Umamahesh NV (2021b) Nonstationary modeling of meteorological droughts: application to a region in India. J Hydrol Eng 26(2):05020048

Das J, Manikanta V, Umamahesh NV (2022a) Population exposure to compound extreme events in India under different emission and population scenarios. Sci Total Environ 806. https://doi.org/10.1016/j.scitotenv.2021.150424

Das S, Das J, Umamahesh NV (2022b) Copula-based drought risk analysis on rainfed agriculture under stationary and non-stationary settings. Hydrol Sci J 67:1683–1701. https://doi.org/10.1080/02626667.2022.2079416

Das J, Das S, Umamahesh NV (2023) Population exposure to drought severities under shared socioeconomic pathways scenarios in India. Sci Total Environ:867. https://doi.org/10.1016/j.scitotenv.2023.161566

Gupta LK, Pandey M, Raj PA, Shukla AK (2023) Fine sediment intrusion and its consequences for river ecosystems: a review. J Hazard Toxic Radioact Waste. 27(1):04022036. https://doi.org/10.1061/(ASCE)HZ.2153-5515.0000729

Hall JW, Meadowcroft IC, Sayers PB, Bramley ME (2003) Integrated flood risk management in England and Wales. Nat Hazards Review 4(3):126–135

Hinge G, Bharali B, Baruah A, Sharma A (2022) Integrated groundwater quality analysis using Water Quality Index, GIS and multivariate technique: a case study of Guwahati City. Environ Earth Sci 81. https://doi.org/10.1007/s12665-022-10544-0

Hossain MB, Mertig AG (2020) Socio-structural forces predicting global water footprint: socio-hydrology and ecologically unequal exchange. Hydrol Sci J 65(4):495–506

Lajeunesse E, Devauchelle O, Lachaussée F, Claudin P (2017) Bedload transport in laboratory rivers: the erosion–deposition model. Gravel-Bed Rivers: Processes and Disasters, pp 415–438

Lane SN, Thorne CR (2007) River processes. Future flooding and coastal erosion risks. ICE Publishing, a division of Thomas Telford Ltd, the commercial arm of the Institution of Civil Engineers, pp 82–99

Mangukiya NK, Sharma A (2022) Flood risk mapping for the lower Narmada basin in India: a machine learning and IoT-based framework. Nat Hazards 113:1285–1304. https://doi.org/10.1007/s11069-022-05347-2

Manikanta V, Ganguly T, Umamahesh NV (2023) A Multi criteria Decision Making based nonparametric method of fragments to disaggregate daily precipitation. J Hydrol:617. https://doi.org/10.1016/j.jhydrol.2022.128994

Pourshahbaz H, Abbasi S, Pandey M, Pu JH, Taghvaei P, Tofangdar N (2022) Morphology and hydrodynamics numerical simulation around groynes. ISH J Hydraul Eng 28(1):53–61

Purkayastha S, Afzal MS (2022) Review of smooth particle hydrodynamics and its applications for environmental flows. J Inst Eng (India) Ser A 103(3):921–941

Saikumar G, Pandey M, Dikshit PKS (2022) Natural river hazards: their impacts and mitigation techniques. In: River dynamics and flood hazards: studies on risk and mitigation. Springer, Singapore, pp 3–16

Schumm SA (1969) River metamorphosis. J Hydraul Div 95(1):255–274

Sharma A, Baruah A, Mangukiya N et al (2022) Evaluation of Gangetic dolphin habitat suitability under hydroclimatic changes using a coupled hydrological-hydrodynamic approach. Ecol Inform:69. https://doi.org/10.1016/j.ecoinf.2022.101639

Shivashankar M, Pandey M, Zakwan M (2022) Estimation of settling velocity using generalized reduced gradient (GRG) and hybrid generalized reduced gradient–genetic algorithm (hybrid GRG-GA). Acta Geophys 70(5):2487–2497

Shukla R, Agarwal A, Gornott C et al (2019a) Farmer typology to understand differentiated climate change adaptation in Himalaya. Sci Rep:9. https://doi.org/10.1038/s41598-019-56931-9

Shukla R, Agarwal A, Sachdeva K et al (2019b) Climate change perception: an analysis of climate change and risk perceptions among farmer types of Indian Western Himalayas. Clim Chang 152:103–119. https://doi.org/10.1007/s10584-018-2314-z

South Asian Association for Regional Cooperation (1992) Regional Study on the Causes and Consequences of Natural Disasters and the Protection and Preservation of the Environment. South Asian Association for Regional Cooperation

Thorne CR, Evans EP, Penning-Rowsell EC (eds) (2007) Future flooding and coastal erosion risks. Thomas Telford, London

Treesa A, Das J, Umamahesh NV (2017) Assessment of impact of climate change on streamflows using VIC model. Eur Water 59:61–68

UNISDR U (2009) Making disaster risk reduction gender sensitive: Policy and practical guidelines

Waters CN, Zalasiewicz J, Summerhayes C, Barnosky AD, Poirier C, Gałuszka A, Cearreta A, Edgeworth M, Ellis EC, Ellis M, Jeandel C, Reinhold Leinfelder JR, Mcneill DD, Richter W S, Syvitski J, Vidas D, Wagreich M, Williams M, Zhisheng A, Grinevald J, Odada E, Oreskes N, Wolfe AP (2016) The Anthropocene is functionally and stratigraphically distinct from the Holocene. Science 351(6269):aad2622